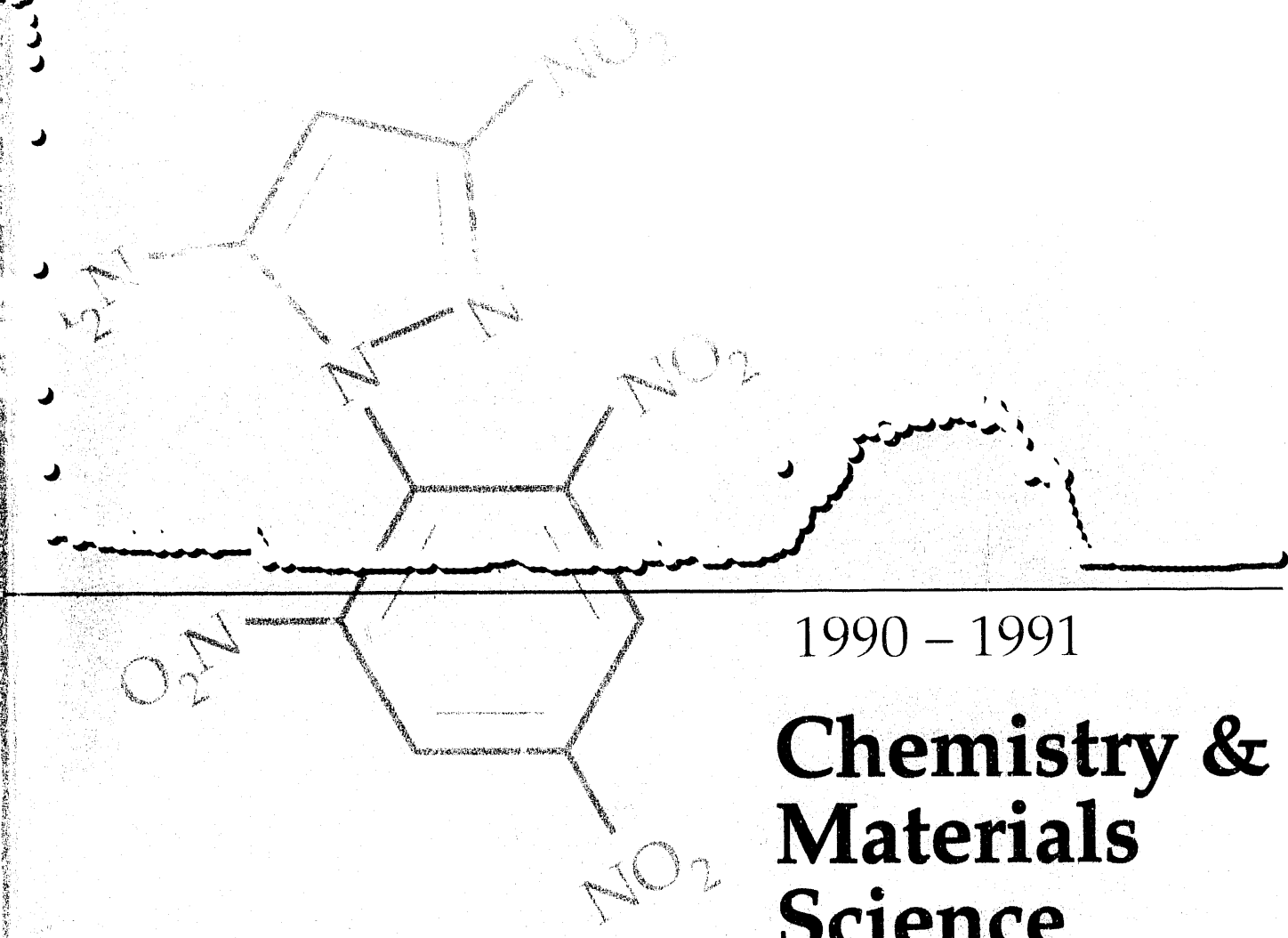
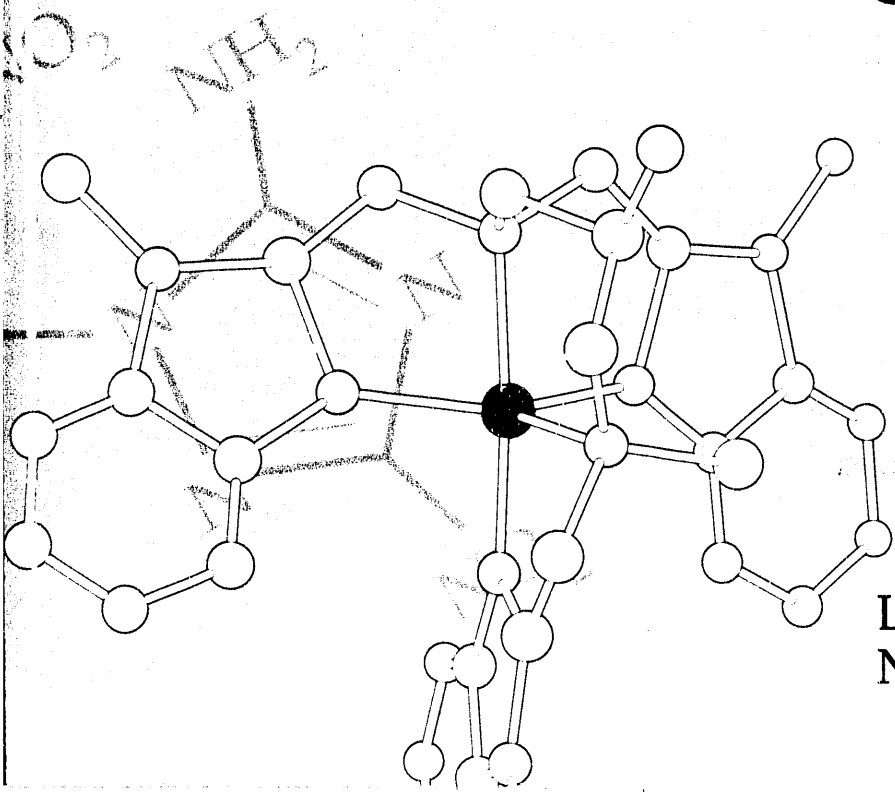


59/10-26-92 J-59  
UCRL-53943-91



1990 - 1991

# Chemistry & Materials Science



Lawrence Livermore  
National Laboratory

Disclaimer

This document was prepared as an account of work sponsored by an agency of the United States Government. Neither the United States Government nor the University of California nor any of their employees makes any warranty, express or implied, or assumes any legal liability or responsibility for the accuracy, completeness, or usefulness of any information, apparatus, product, or process disclosed, or represents that its use would not infringe privately owned rights. Reference herein to any specific commercial products, process, or service by trade name, trademark, manufacturer, or otherwise, does not necessarily constitute or imply its endorsement, recommendation, or favoring by the United States Government or the University of California. The views and opinions of authors expressed herein do not necessarily state or reflect those of the United States Government or the University of California and shall not be used for advertising or product endorsement purposes.

UCRL-53943-91

Work performed under the auspices of the U.S. Department of Energy by Lawrence Livermore National Laboratory under Contract W-7405-Eng-48.

UCRL-53943-91  
Distribution Category UC-700

UCRL--53943-91


DE93 001761

---

1990-1991

**Chemistry &  
Materials  
Science**

**MASTER**

DISTRIBUTION OF THIS DOCUMENT IS UNLIMITED 

Lawrence Livermore National Laboratory  
University of California  
Livermore, California 94551

---

# Acknowledgments

Christopher Gatrousis is the Associate Director for Chemistry & Materials Science. Thomas T. Sugihara is the Deputy Associate Director for Research, Larry L. Schwartz is the Deputy Associate Director for Administration, and D. Rex Beach is the Deputy Associate Director for Assurances. The three Division Leaders are Jeffery H. Richardson, Chemical Sciences Division; Michael J. Fluss, Condensed Matter and Analytical Sciences Division; and Jeffrey N. Kass, Materials Division.

The following people served as the publication staff for this *Report*:

**Scientific Editor** Thomas T. Sugihara

**C&MS Department Coordinator** Linda M. Brown

**Publication Editors** James M. Bruner  
Lori A. McElroy

**Designer and Art Coordinator** Ellen L. Baldwin

# Contents

Overview	vii
<b>1 Research Sampler</b>	
Overview	2
<b>Organic Aerogels: The Next Generation</b> R. W. Pekala and C. T. Alviso	4
<b>High-Performance Nano-engineered Multilayer Materials</b> T. W. Barbee, Jr.	7
<b>Nuclear Spin Polarization</b> P. C. Souers	9
<b>Studies of the Omega Phase Transformation in the Titanium-Molybdenum Alloy System</b> L. E. Tanner, D. Schryvers, and S. M. Shapiro	11
<b>Surface Reactions Induced and Measured by Scanning Probe Microscopy</b> M. Balooch, W. J. Siekhaus, and R. J. Tench	14
<b>Atomic-Resolution Imaging with Photoelectron Holography</b> L. J. Terminello and J. J. Barton	16
<b>2 Metals and Alloys</b>	
Overview	20
<b>First-Principles Approach to Alloy Phase Stability</b> P. E. A. Turchi and M. Sluiter	22
<b>A First-Principles Study of Phase Stability in Nickel-Aluminum Alloys</b> M. Sluiter and P. E. A. Turchi	26
<b>Ordering in the Ti-Pd Alloy System</b> A. F. Jankowski and P. E. A. Turchi	29
<b>Deformation Behavior of Pre-shocked Copper as a Function of Strain Rate and Temperature</b> W. H. Gourdin and D. H. Lassila	32
<b>Fatigue Behavior of U-6Nb Alloys</b> M. J. Strum, J. W. Elmer, N. Q. Nguyen, and D. C. Freeman	36
<b>A Model for the Formation of Bands of Ultrafine Particles in Rapidly Solidified Al-Be Alloys</b> J. Elmer, L. E. Tanner, and M. J. Aziz	39
<b>3 Energetic Materials</b>	
Overview	42
<b>Pressure Dependence of the Reaction Propagation Rate of TATB at High Pressure</b> M. F. Foltz	44

	<b>The Synthesis of New, Insensitive Energetic Materials</b> P. F. Pagoria, C. L. Coon, and A. R. Mitchell _____	47
	<b>Modeling Chemistry in the TOPAZ Heat-Flow Code</b> A. L. Nichols III _____	50
	<b>Harmonic Analysis of Phonon Echoes in Liquids</b> J. D. Bauer and D. F. Calef _____	53
	<b>Low-Vulnerability Composite Explosives (LOVEX)</b> C. O. Pruneda, D. M. Hoffman, E. S. Jessop, and D. M. Walkup _____	57
<b>4</b>	<b>Chemistry and Physics of Advanced Materials</b>	
	<b>Overview</b> _____	60
	<b>Synthesis of Very High-Porosity Silica Aerogels</b> L. W. Hrubesh, T. M. Tillotson, and J. F. Poco _____	62
	<b>Elimination of Scattering Centers from Cr:LiCaAlF<sub>6</sub></b> J. J. De Yoreo, L. J. Atherton, and D. H. Roberts _____	65
	<b>Preparation and Properties of Brominated Plasma Polymer Coatings</b> S. A. Letts, C. W. Price, F. M. Kong, S. R. Buckley, M. D. Saculla, E. F. Lindsey, C. E. Moore, and P. Welch _____	68
	<b>Epoxy Adhesive with High Fracture Toughness</b> R. E. Lyon and J. D. LeMay _____	71
<b>5</b>	<b>Bonding and Reactions at Surfaces and Interfaces</b>	
	<b>Overview</b> _____	76
	<b>LEED Determination of Multilayer Relaxation in Stepped Surfaces</b> A. Gonis _____	78
	<b>Experimental and Theoretical Determination of the Atomic Structure of the (310) Twin in Niobium</b> G. H. Campbell, W. E. King, S. M. Foiles, P. Gumbsch, and M. Rühle _____	81
	<b>The Real-Space Multiple-Scattering Theory and the Electronic Structure of Grain Boundaries</b> E. C. Sowa and A. Gonis _____	84
	<b>Laser-Induced Desorption of Aluminum from Al<sub>2</sub>O<sub>3</sub>(1120)</b> M. A. Schildbach and A. V. Hamza _____	87
	<b>Thermal Stability of Mo/Si Multilayers</b> R. S. Rosen, D. G. Stearns, M. A. Viliardos, M. E. Kassner, and S. P. Vernon _____	90
<b>6</b>	<b>Superconductivity</b>	
	<b>Overview</b> _____	94
	<b>Magnetic and Transport Properties of Some High-Temperature Superconductors</b> J. Z. Liu, Lu Zhang, Y. X. Jia, M. D. Lan, P. Klavins, and R. N. Shelton _____	96
	<b>Quasiparticles in Doped La<sub>2</sub>CuO<sub>4</sub></b> J. B. Grant and A. K. McMahan _____	99

	<b>Fermi-Surface Measurements and Planar Orthorhombic Order in <math>\text{La}_{2-x}\text{Sr}_x\text{CuO}_4</math></b>	
	P. A. Sterne, R. H. Howell, F. R. Solal, M. J. Fluss, J. H. Kaiser, R. N. West, H. Kojima, and K. Kitazawa	102
	<b>Photoelectron Studies of <i>In Situ</i> Cleaved Crystals of <math>\text{YBa}_2\text{Cu}_3\text{O}_7</math></b>	
	C. Colmenares, J. Z. Liu, C. Evans, and R. L. Smith	105
	<b>The Valence Bands and Fermiology of Untwinned, Single-Crystal <math>\text{YBa}_2\text{Cu}_3\text{O}_{6.9}</math></b>	
	J. G. Tobin, C. G. Olson, C. Gu, J. Z. Liu, F. R. Solal, M. J. Fluss, R. H. Howell, J. C. O'Brien, H. B. Radousky, and P. A. Sterne	108
<b>7</b>	<b>Energy Research and Development</b>	
	<b>Overview</b>	112
	<b>Biomimetic Methane Oxidation: Synthesis and Kinetics</b>	
	M. W. Droege, J. H. Satcher, Jr., R. A. Reibold, and T. J. R. Weakely	114
	<b>Theoretical Description of Biomimetic Complexes</b>	
	N. W. Winter and M. W. Droege	117
	<b>Subunit Resolution for Active Site Identification of <i>Methylosinus trichosporium</i> OB3b Soluble Methane Monooxygenase</b>	
	M. M. Himmelsbach, R. T. Taylor, and M. W. Droege	120
	<b>Bioreactor Cultivation of <i>Methylosinus trichosporium</i> OB3b for Production of Particulate Methane Monooxygenase</b>	
	N. N. Shah, R. T. Taylor, and M. W. Droege	124
	<b>Coking and Cracking Reactions of Oil Vapor Over Oxidized Shale</b>	
	P. H. Wallman, M. F. Singleton, and C. B. Thorsness	128
<b>8</b>	<b>Waste Processing and Management</b>	
	<b>Overview</b>	132
	<b>Stochastic Models for Predicting Pitting Corrosion Damage of Radioactive-Waste Containers</b>	
	G. A. Henshall	134
	<b>Mediated Electrochemical Oxidation of Hazardous and Mixed Wastes</b>	
	J. C. Farmer, F. T. Wang, R. C. Hickman, R. A. Hawley-Fedder, P. R. Lewis, L. J. Summers, and L. Foiles	137
	<b>Molten Salt Destruction Process for Mixed Wastes</b>	
	R. S. Upadhye and J. F. Cooper	141
<b>9</b>	<b>Characterization and Analysis</b>	
	<b>Overview</b>	146
	<b>A Time-Resolved Diffraction Study of the Ta-C Solid Combustion System</b>	
	J. Wong, E. M. Larson, J. B. Holt, P. A. Waide, B. Rupp, and L. J. Terminello	148
	<b>Preparation of Solid-Membrane Ion-Selective Electrodes by Ion Implantation</b>	
	R. S. Glass, R. G. Musket, and K. C. Hong	152
	<b>Tensile Failure in Metal-Matrix Composites</b>	
	J. H. Kinney, M. L. Sattler, E. Zywicz, R. A. Saroyan, and M. C. Nichols	155

	<b>Determination of Absolute Transition Probabilities in Neutral Cerium</b>	
	S. E. Bisson, E. F. Worden, J. G. Conway, and B. Comaskey	159
	<b>New Analytical Approach for Screening and Identifying Trace Levels of Nitrogen-Containing Compounds</b>	
	A. Alcaraz, W. H. Martin, and B. D. Andresen	161
	<b>Bio-organic Molecules on Surfaces: Atomic Structure of Ordered Monolayers of Adenine on Graphite by STM and Analysis of Sperm Nuclear Volumes by AFM</b>	
	W. J. Siekhaus, M. Balooch, R. J. Tench, R. Balhorn, M. J. Allen, N. V. Hud, C. Lee, G. Pogany, and S. Subbiah	164
<b>10</b>	<b>Facilities and Instrumentation</b>	
	<b>Overview</b>	168
	<b>Applications of Ultrashort-Pulse Laser Technology to Materials Characterization and Investigations of Condensed-Phase Energy-Transfer Dynamics</b>	
	A. J. Ruggiero	170
	<b>4-MV Ion-Accelerator System for Materials Studies</b>	
	R. G. Musket	173
	<b>LLNL/UC Davis High-<math>T_c</math> Collaboration: Highlights of the University Program</b>	
	R. N. Shelton	176
	<b>Glenn T. Seaborg Institute for Transactinium Science</b>	
	T. T. Sugihara	178
<b>11</b>	<b>Department Personnel and Professional Contributions</b>	
	<b>Overview</b>	
	L. M. Brown	180
	<b>Personnel</b>	182
	<b>Consultants</b>	188
	<b>Scientific Advisory Committees</b>	188
	<b>Collaborations</b>	189
	<b>Research Communications</b>	191
	<b>Patents</b>	234
<b>12</b>	<b>Budget Information</b>	237
	<b>Acronyms and Abbreviations</b>	240



# Overview

T. T. Sugihara

## Introduction

This is the second "annual" report of the Chemistry & Materials Science (C&MS) Department. Our general purpose is to concisely summarize technical and scientific accomplishments of the recent past. Originally we had planned that this would be done annually. For a variety of reasons, we have found a two-year cycle to be more realistic. Thus, this report covers the fiscal years 1990 and 1991. We intend the report to be also an archival record of the Department's research activities.

The technical part of the report consists of 49 articles in ten sections. The first section presents a cross section of Departmental R&D; that is, it is a sample of the broad range of science and technology that the chemical and materials sciences include. This is followed by eight sections, each organized around a single topic. The tenth section includes articles on advances in instrumentation and facilities as well as descriptions of institutional changes.

Section 11 lists Department personnel and their publications, patents, and presentations. Consultants and collaborators are listed also. The report concludes with a summary of Departmental budgets.

## The Laboratory and the C&MS Department

The mission of Lawrence Livermore National Laboratory is "to serve as a national resource of scientific, technical, and engineering capability with a special focus on national security. This mission includes research and development, strategic defense, arms-control and treaty-verification technology, energy, the environment, biomedicine, the economy, and education." This statement is taken from a recent notice in the Federal Register (4/3/92) concerning the Draft Environmental Impact Statement for LLNL.

However, LLNL Director J. H. Nuckolls recently pointed out in his report to the Regents of the University of California, "Revolutions in geopolitics, technology, and the global economy are creating new challenges for the Laboratory," and the words in the mission statement assume new meanings. In addressing these challenges, the Laboratory is working toward achieving a smaller weapons stockpile with enhanced safety, security, and reliability. A new program has been proposed to detect and deter nuclear proliferation. The national laboratories have also been put on notice to join with industry in directing federally sponsored research toward meeting economic needs as well as national security.

Education in mathematics and science continues to be a significant element in the Laboratory's programs. Partnerships with the University of California and the state educational system have been encouraged.

Since C&MS is a supporting disciplinary department, its mission statement would naturally parallel that of the Laboratory but would be supplemented by emphasis on providing expertise in the chemical and materials sciences. Many of the technical articles in this report originated in mission-oriented programs, but they emphasize nonprogrammatic research activities.

## Organization of the Department

The table of organization and management structure is given in Section 11. The staff has always been multidisciplinary. In mid-1991, 31% were chemists, 6% physicists, 8% metallurgists, 13% engineers, and 4% postdoctorates distributed among the various disciplines. Technicians constituted 27% of the staff, and 10% were administrative personnel. About 50% have PhD degrees. In mid-1991, the total FTE count was 357. Since then, the number has dropped substantially because of early retirement opportunities offered in late 1991.

Most of the support for C&MS personnel comes from the major Laboratory programs such as Defense Systems, Lasers, and Energy (see Table 1). Personnel assigned to programs tend to work on projects directly related to short-term programmatic goals.

The Department has managed two critical facilities, the Tritium Facility and the Plutonium Facility, for a number of years. In FY 1992, however, these responsibilities were transferred to Defense Systems. The Department has a major involvement in the Laboratory's environmental protection and waste management program because of C&MS expertise in analytical chemistry and materials characterization.

About 10% of the Department's resources are directly managed by C&MS and provide the basis for most of the R&D presented in this report. Chief elements are Weapons-Supporting Research, Basic Energy Sciences (Office of Energy Research), Laboratory Directed Research and Development (formerly Institutional Research and Development), and work for non-DOE agencies (such as the Department of Defense).

The C&MS role in education and training of scientists has been expanding. A new research institute devoted to the study of the heaviest elements (see Section 10, "Institute

for Transactinium Science") commenced operations in 1991. The number of postdoctoral scientists in the Department has steadily increased from 1 or 2 in 1985 to 20 in 1991.

The Department plays a significant role in Laboratory-wide educational programs such as the Undergraduate Summer Institute in Applied Science, the Science and Engineering Research Semester (a DOE-wide program), and the Summer Employment Program that brings nearly 300 undergraduate students to the Laboratory each summer. Also, a number of C&MS staff are individually involved in educational activities in local schools and colleges.

## State of the Department

As times change and the Laboratory's mission evolves, so has the Department's direction begun to shift in its discretionary activities to increase the emphasis on technology transfer and dual-use technologies. Effort and resources devoted to educational activities are expected to increase in the near term, with more undergraduate and graduate students resident at the Laboratory.

The research program has been well recognized for accomplishments in a number of areas of basic science. It is expected to change only in evolutionary ways, although of course unusual scientific observations occur in unpredictable ways from time to time (e.g., discovery of fullerenes) and entirely new efforts are begun that could not have been planned in advance. The guiding principle for inclusion in the C&MS program will continue to be good science, but there must also be a good reason for a program to be here rather than elsewhere, such as unique facilities, unusually qualified staff, potential for commercialization, or likelihood of spawning a major new program.

A few recent accomplishments are listed here as examples of C&MS research. This list is not intended to be a preview of the report, which contains a much broader range of topics and more detailed descriptions, but rather a glimpse of the Department at work.

- Applications of x-ray diffraction and absorption have taken on new dimensions with the advent of high-intensity, high-resolution beams from synchrotrons. Joe Wong has taken diffraction data over a  $2\theta$  range of several degrees in a few tens of milliseconds, permitting him to

follow the course of solid-state reactions by observing phase changes. The formation of TaC from its constituent elements is an example of such a reaction. John Kinney has obtained spatial resolution of a few micrometers in the three-dimensional imaging of ceramic composites by x-ray absorption. Kinney calls this technique x-ray tomographic microscopy, which also has diverse applications in biological systems.

- Multilayers in which thin alternating layers of two substances (e.g., metals) are deposited are usually thought of and studied as materials on the nanometer scale. Troy Barbee has produced foils of macroscopic thickness (e.g., 20  $\mu\text{m}$ ) in which individual layers are only a few nanometers thick. Such foils frequently have exceptional strength and other mechanical properties.
- The spectroscopic properties of energetic materials in a diamond-anvil cell have been investigated by Fran Foltz. The reaction propagation rate as a function of pressure shows discontinuities corresponding to phase changes in a high explosive such as triaminotrinitrobenzene. Such microscopic information about the detonation process has not previously been available.
- Aerogels are polymers synthesized by a sol-gel process. They have very special properties of very low density and very high specific area. Rick Pekala and Larry Hrubesh have synthesized aerogels from pure silica and substituted silica compounds with densities as low as 5  $\text{mg}/\text{cm}^3$ , only four times that of air. More recently, aerogels have been synthesized from organic monomers as well, some of which have record low thermal conductivities. The manifold applications of these extraordinary materials are being explored vigorously.
- A group led by Mike Fluss has addressed some fundamental questions regarding high-temperature superconductivity in the perovskite compounds. This group showed, by advanced experimental methods such as angular correlation of positron annihilation radiation and angle-resolved photoemission, that the hole carriers in perovskite planes are metallic; so also are the electrons along the CuO chains. These observations explain anomalous transport effects observed in the normal and superconducting states of the perovskite superconductors.

---

## Overview

Chemistry is the central science that deals with materials, their properties, and the transformations they undergo. It treats materials as simple as an atom of a light element or as complex as the large molecules that make up a polymer or an enzyme. Materials science, on the other hand, is an enabling science that seeks new levels of understanding of the basic building blocks of materials: atoms, molecules, crystals, and noncrystalline arrays. Among these materials are pure metals, alloys, ceramics, composites, biomaterials, or glasses, and they may have special electronic, optical, or magnetic properties. A department that is charged with the responsibility for providing the Laboratory with leading-edge knowledge in "chemistry and materials science" thus has a large territory to cover. Naturally, some focus is needed; the C&MS Department has tended to emphasize those topics and materials that are of most importance to the programs of the Laboratory.

This first section of the report provides a sample of the Department's research that illustrates the breadth and novelty of research that has recently been completed. The first article is concerned with aerogels synthesized from organic monomers, basically a new class of materials with extraordinary physical and mechanical properties. Because substituent groups can be placed on the organic backbone, aerogels with specific chemical properties are possible as well.

The capability to produce multilayer structures has become a well-established art and technology in C&MS. The first structures, relatively thin, were found to be very useful and important in x-ray optics, opening up new areas for research. Reported here are the properties of multilayers of macroscopic thickness with remarkable mechanical properties that derive from the perfection of the layers.

For a number of years, a group at the Tritium Facility has been investigating the cryogenic properties of the molecule DT, which in the simplest approximation should resemble molecular hydrogen H<sub>2</sub>. Quantum mechanically, however, symmetry rules are different for the two, and in

addition, the radiation damage from the  $\beta$  decay of tritium converts DT to a mixture (generally called D-T) of D<sub>2</sub>, DT, and T<sub>2</sub>. The recent goal of this group has been to align the nuclear spins of the deuterium and tritium atoms because the cross section for fusion of the aligned species is thought to be significantly higher than that of the randomly oriented species. Substantial progress toward this goal has been achieved, but the final steps have had to be deferred because of the closure of the Tritium Facility. Nevertheless, a wealth of new data has been obtained for the behavior of D-T at liquid-helium temperatures.

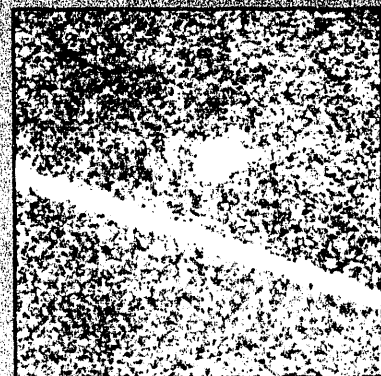
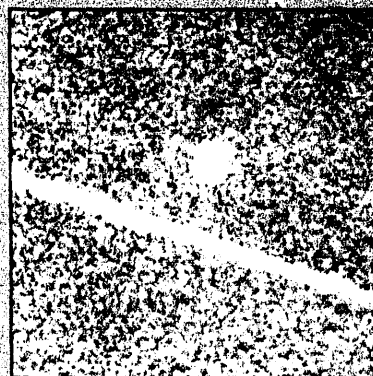
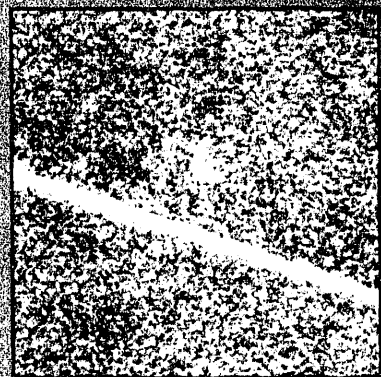
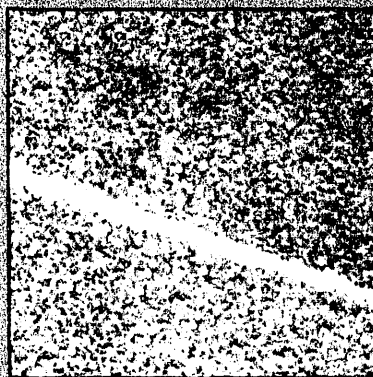
Pioneering studies of displacive and repiactive solid-state phase transformations have been done in this department. Reported here are the most recent studies of the transformation of the Ti-Mo  $\beta$  phase. In this system, it is found that the high-pressure-stable  $\omega$  phase can be nucleated by a displacive mechanism and that the metastable  $\omega$  phase can compete with stable phases during thermal aging treatments.

Scanning probe microscopy is now widely used to scan surfaces with atomic resolution. In the work reported here, it was found that the very high electric field generated by a very sharp tip in the presence of a reactive gas can cause chemical reactions to occur. The oxidation of silicon leads to a path on the order of 20 nm wide, a structural feature observed by the same microscope that cut the path.

Obtaining structural information regarding a buried layer, such as an interface, has not been easy. A recently developed method based on photoelectron holography promises to overcome many of the problems. A photoelectron hologram is the constant-energy, angle-dependent photoelectron intensity derived from a chemically specific core level. This method promises to provide interface structural information that surface imaging spectroscopies such as scanning tunneling microscopy cannot reach. First proof-of-principle results are reported here.

Section 1

**Research  
Sampler**



**Oxide pattern formed on  
clear silicon substrate by  
induced reaction.**

# Organic Aerogels: The Next Generation

R. W. Pekala and  
C. T. Alviso

*The aqueous sol-gel polymerization of melamine with formaldehyde, followed by supercritical extraction, leads to the formation of a new type of organic aerogel. Low density (0.1 to 0.8 g/cm<sup>3</sup>), large surface area (~1000 m<sup>2</sup>/g), and optical clarity are only a few of the promising characteristics of melamine-formaldehyde aerogels.*

## Introduction

Aerogels differ from conventional open-cell foams or membranes, in that they have ultrafine cell/pore sizes (<50 nm), large surface areas (400 to 1100 m<sup>2</sup>/g), and solid matrices composed of interconnected, colloidal-like particles or polymeric chains with characteristic diameters of 10 nm. The ability to synthesize aerogels from a variety of monomers while controlling structure and properties at the nanometer scale opens up exciting possibilities for these unique materials. Potential applications include thermal insulation, permselective membranes, catalyst supports, battery electrodes, supercapacitors, and acoustic impedance-matching devices.

The most common aerogels are silica based.<sup>1</sup> They are formed from the hydrolysis and condensation of tetramethoxysilane (TMOS) or tetraethoxysilane (TEOS) in dilute solution. The major variables in the process include water/silicon ratio, solution pH, type of alkoxy silane, and the use of high-temperature vs low-temperature supercritical drying. In general, acid catalysis favors the formation of lightly branched silica species that covalently link together to form a gel. Under alkaline conditions, highly crosslinked

colloidal structures form. An understanding of these sol-gel polymerizations and their effect on the silica microstructure has been established over the past decade.<sup>2,3</sup>

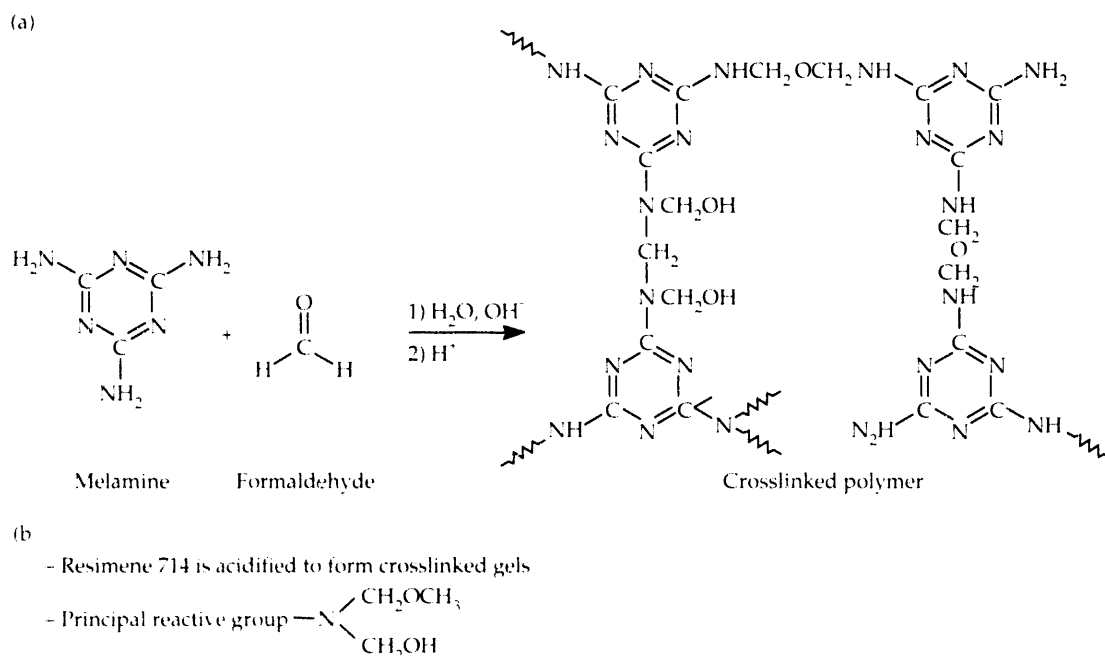
In 1985, the first organic-based aerogels were synthesized from the aqueous polycondensation of resorcinol (1,3-dihydroxybenzene) with formaldehyde. These low-density materials were found to be the organic analogs of silica aerogels, but with the advantage of having a lower average atomic number. The major disadvantage of resorcinol-formaldehyde aerogels is their dark red color, which results from oxidation products formed during the sol-gel polymerization. Recently, however, colorless aerogels have been formed from the aqueous polycondensation of melamine (2,4,6-triamino-s-triazine) with formaldehyde. Polymerization conditions have been found to affect the transparency and microstructure of this new generation of organic aerogels.

## Experimental Methods

Figure 1 shows two approaches for synthesizing melamine-formaldehyde (MF) aerogels. In the monomer

**Figure 1.**

Schematic of the (a) monomer and (b) oligomer approaches for preparing MF aerogels. The oligomer approach is simpler and works over a wider pH range.



approach, melamine and formaldehyde are mixed in a 1:3.7 molar ratio and diluted with deionized/distilled water to control the overall reactant concentration. We use sodium hydroxide (10 to 100 millimoles) as the base catalyst in the initial part of this polymerization. Because melamine is a crystalline solid with limited water solubility, this slurry must be heated for ~15 min at 70°C to form a clear solution. We then cool the solution to 45°C and acidify it with HCl. For transparent gels, the pH of the MF solution must be 1.5 to 1.8 (measured at room temperature). Outside this range, opaque or translucent gels form.

Melamine is a hexafunctional monomer capable of reaction at each of the amine hydrogens. Under alkaline conditions, formaldehyde adds to these positions to form hydroxymethyl (-CH<sub>2</sub>OH) groups. In the second part of the polymerization, we acidify the solution to promote condensation of these intermediates, leading to gel formation. The principal crosslinking reactions include the formation of (1) diamino methylene (-NHCH<sub>2</sub>NH-) and (2) diamino methylene ether (-NHCH<sub>2</sub>OCH<sub>2</sub>NH-) bridges.<sup>4</sup>

In the oligomer approach, MF gels are formed by diluting a low-molecular-weight MF polymer, Resimene 714,\* with an appropriate amount of deionized/distilled water and adjusting the pH with HCl. Transparent gels form in the pH range of 2 to 3. We prefer the oligomer approach because it works over a wider pH range and is simpler.

All MF solutions develop a blue haze as they cure (2 d at 50°C followed by 5 d at 95°C). This phenomenon is associated with Rayleigh scattering from MF clusters generated in solution. These clusters contain surface functional groups (e.g., -CH<sub>2</sub>OH) that eventually crosslink to form a gel. The aggregation and crosslinking processes show a strong pH dependence. Furthermore, the synthesis approach used (monomer vs oligomer) affects the pH range for the preparation of transparent gels and aerogels.

MF gels are converted to aerogels by supercritical extraction of carbon dioxide. Because water is not miscible with liquid CO<sub>2</sub>, we first exchange the aquagels with an organic solvent (e.g., acetone). Next, we exchange CO<sub>2</sub> for the organic solvent and take it above its critical point ( $T_c = 31^\circ\text{C}$ ;  $P_c = 7.4\text{ MPa}$ ) inside a temperature-controlled pressure vessel. The resultant aerogels are both colorless and transparent.

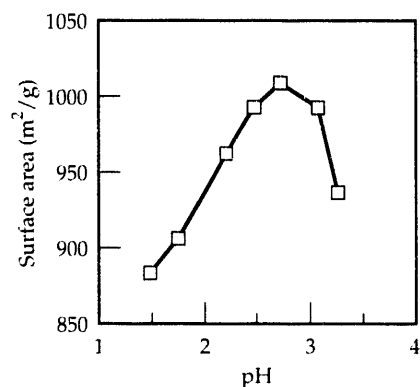


**Figure 2.**

Effect of pH on surface area of MF aerogels prepared by using the oligomer approach.

## Results and Discussion

The pH of a melamine-formaldehyde solution appears to be the most critical parameter controlling the optical clarity of a dried MF aerogel. Aerogels prepared by the monomer approach at pH 1.7 were transparent, whereas those prepared at pH 0.7 were opaque. Infrared (IR) absorption peaks and intensity ratios of the two aerogels were identical. Solid-state, nuclear magnetic resonance (NMR) measurements also revealed identical chemical shifts and relaxation parameters. From these data, solution pH does not appear to influence the type or degree of crosslinking in the aerogels. Rather, it affects the aggregation of clusters, which ultimately determines pore size and optical clarity.

MF aerogels have extremely large surface areas, ranging from 880 to 1020 m<sup>2</sup>/g (the largest being obtained at pH 2.7). Figure 2 shows the dependence of specific surface area on solution pH. Extinction coefficients calculated for these same aerogels in the ultraviolet/visible spectrum (UV/VIS) (see Fig. 3) show that MF aerogels with good transmissive properties form in the pH range of 2 to 3.

MF aerogels are similar to silica aerogels in many ways (e.g., large surface areas, optical transparency). In order to investigate the structure-property relationships of these new aerogels, we measured compressive moduli as a function of density and compared them to those of silica aerogels. As Fig. 4 shows, compressive modulus increases with aerogel density. The linear relationship shown in the log-log plot in each case demonstrates a power-law density dependence that has been observed in many other low-density materials. This relationship is expressed as  $E = \rho^\alpha$ , where  $\rho$  is the bulk density and  $\alpha$  is a noninteger scaling exponent that usually ranges from 2 to 4 (see Ref. 5).

For silica aerogels, the scaling exponent shows a strong dependence on catalyst conditions.<sup>6</sup> Acid-catalyzed, base-catalyzed, and partially condensed silica aerogels have exponents of  $3.4 \pm 0.1$ ,  $2.9 \pm 0.2$ , and  $3.8 \pm 0.2$ , respectively. Interestingly, all transparent MF aerogels have a scaling exponent of  $3.3 \pm 0.1$  and moduli that approximate those

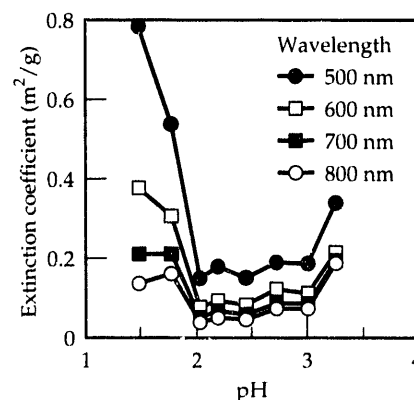


**Figure 3.**

Effect of pH on UV/VIS extinction coefficient of MF aerogels prepared by using the oligomer approach.

of acid-catalyzed silica aerogels. These data suggest similar microstructures for the two aerogels, even though one is organic and the other is inorganic.

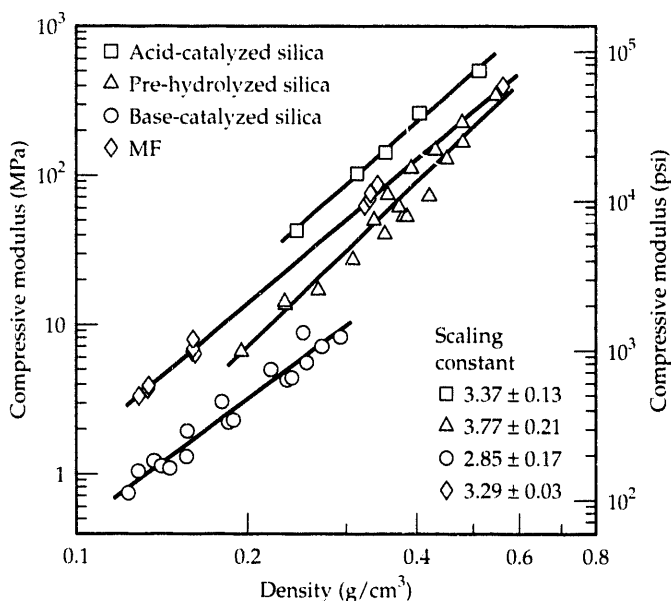
## Summary

Sol-gel polymerizations are not unique to metal alkoxides; in theory, any multifunctional monomer can be polymerized in dilute solution to form an aerogel. Our work has

demonstrated that organic-based aerogels can be successfully synthesized from the aqueous polycondensation of melamine with formaldehyde. These transparent, low-density materials (0.1 to 0.8 g/cm<sup>3</sup>) have continuous porosity, ultrafine cell/pore sizes ( $\leq 50$  nm), and large surface areas ( $\sim 1000$  m<sup>2</sup>/g). The catalyst concentration (solution pH) is the major variable controlling the structure and properties of these new aerogels.

*This work was funded by Laboratory Directed Research and Development.*

**Figure 4.** Effect of density on compressive modulus (uniaxial stiffness) for MF and silica aerogels.



\* A product of Monsanto Chemical Co., Resimene 714 results from the condensation of melamine with formaldehyde followed by partial methoxylation. This oligomer is supplied as an 80% solution in water.

## References

1. L. W. Hrubesh, T. M. Tillotson, and J. F. Poco, "Synthesis of Very High-Porosity Silica Gels," elsewhere in this Report.
2. C. J. Brinker and G. W. Scherer, *Sol-Gel Science* (Academic Press, New York, 1990).
3. J. Fricke, "Aerogels," *Sci. Am.* **258**(5), 92 (1988).
4. I. H. Updegraff, in *Encyclopedia of Polymer Science and Engineering* (Wiley, New York, 1985), p. 752.
5. L. J. Gibson and M. R. Ashby, "The Mechanics of Three-Dimensional Cellular Materials," *Proc. Royal Soc. Lond.*, **382**(A), 43 (1982).
6. J. D. LeMay, R. W. Hopper, L. W. Hrubesh, and R. W. Pekala, "Low-Density Microcellular Materials," *MRS Bull.* **15**(12), 19 (1990).

# High-Performance Nano-engineered Multilayer Materials

T. W. Barbee, Jr.

*We are designing and producing nanostructure multilayer materials at atomic and near-atomic scales. These nanostructure materials have the potential for extremely high mechanical performance that approaches their theoretical strengths.*

## Introduction

Multilayers are depth-periodic structures fabricated from alternating layers of elemental materials, alloys, or compounds. As a result of the atomic-level control of its composition and microstructure, a multilayer is a unique material that has the potential for extremely high mechanical performance that approaches the theoretical strength of its component materials.<sup>1</sup>

Atomic engineering pertains to multilayers having periods smaller than four atomic layers (~1.0 nm); microstructure engineering pertains to multilayers having periods greater than this; and both are collectively called nano-engineering.<sup>2</sup> Nano-engineering involves procedures for reproducibly synthesizing materials and design tools that allow the property of interest to be optimized. Such synthesis control can eliminate or reduce flaws that often limit the mechanical performance of conventional materials. Physical vapor deposition<sup>3</sup> is one method commonly used for multilayer synthesis at LLNL.

## Experiment

We have synthesized multilayer samples up to 200  $\mu\text{m}$  thick and  $\sim 300\text{ cm}^2$  in area containing more than 40,000 individual layers with periods between 0.5 and 400 nm. Layer substances include elemental copper, zirconium, titanium, chromium, tantalum, tungsten, and platinum and the alloys monel (70 Ni/ 30 Cu), 304 stainless steel, and tungsten-26%rhenium. As an example of the relationships observed between synthesis, structure, and properties, we briefly discuss here the mechanical properties of copper/monel multilayers.

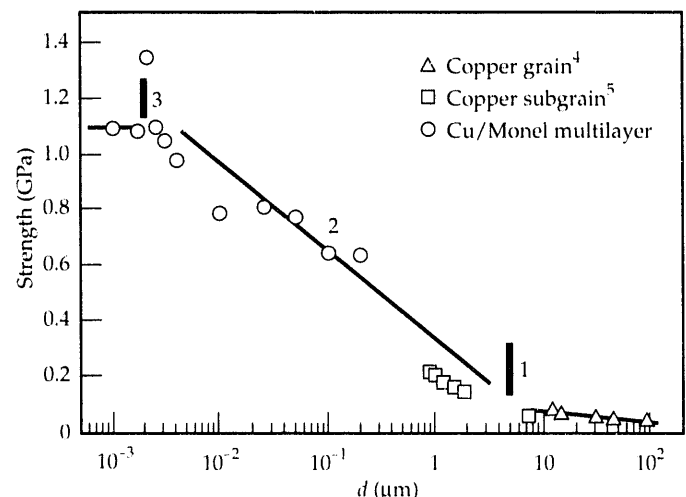
## Results

Figure 1 shows the tensile strengths of copper/monel multilayers fabricated and tested at LLNL. These multilayers have total thicknesses greater than 25  $\mu\text{m}$ ; the thicknesses of individual layers are equal; and the periods are 0.5 to

200 nm. We also show, from the literature,<sup>3,4</sup> the tensile strength of copper. The independent variable,  $d$ , is the multilayer period for copper/monel and the grain size or dislocation subgrain size for copper. Three regions of structural scale dependence are indicated: (1)  $d > 5\ \mu\text{m}$ ; (2)  $0.002 < d < 5\ \mu\text{m}$ ; and (3)  $d < 0.002\ \mu\text{m}$ . Region 1 is characteristic of polycrystalline materials, in which grain/subgrain size strengthening is inversely proportional to the square root of the grain size. Region 2 is a new structural scale domain for which accepted theory is not available. In region 3, the multilayers are chemically uniform as a result of the very thin layers (<0.5 nm).

The theoretical strengths of copper and nickel are 1.2 and 2.4 GPa, respectively. On the basis of a simple rule-of-mixtures argument, the maximum strength expected for a copper/monel multilayer was  $\sim 1.8$  GPa. The strength of the actual multilayer at  $d \approx 2.0$  nm was  $\sim 1.35$  GPa, greater

**Figure 1.** Comparison of the tensile strengths of bulk copper (from the literature) and equal-layer-thickness copper/monel multilayers (this work). The horizontal axis,  $d$ , represents the multilayer period (for Cu/monel) and the grain and subgrain sizes (for copper).





than 70% of the theoretical maximum. This laboratory result, an indicator of the potential of nanostructure multilayer materials, marks the first time such a high strength has been in a "bulk" sample. Previously, such a strength<sup>5</sup> was attainable only in perfect microscopic whiskers (diameter  $\leq 4 \mu\text{m}$ ).

## Conclusion

The properties of macroscopic, nanostructure, multilayer materials and their dependence on the synthesis process demonstrate the developing ability to fabricate "designer" materials by controlling structure at heretofore inaccessible levels. This ability, which will facilitate rapid development of the base of scientific understanding needed to guide technological application of these new materials, presents new scientific and technological opportunities.

*This work was funded by Weapons-Supporting Research.*

## References

1. A. Kelly and N. H. Macmillan, *Strong Solids* (Oxford Press, Oxford, England, 1986).
2. T. W. Barbee, Jr., "Multilayer Structures: Atomic Engineering in Its Infancy," in *Physics, Fabrication and Applications of Multilayered Structures*, P. Dhez and C. Weisbuch, Eds. (Plenum Press, New York, 1988), p. 17.
3. T. W. Barbee, Jr., "Synthesis of Multilayer Structures by Physical Vapor Deposition Techniques," in *Synthetic Modulated Structures*, L. L. Chang and B. C. Giessen, Eds. (Academic Press, New York, 1985), p. 313.
4. R. P. Carreker and W. R. Hibbard, "Tensile Deformation of High-Purity Copper as a Function of Temperature, Strain Rate, and Grain Size," *Acta Metall.* **1**, 654 (1953).
5. D. H. Warrington, "Dependence of Tensile Strength on Dislocation Subgrain Structure," in *Proc. Electron Microscope Conf.*, Delft, The Netherlands, 1961 (de Nederlandse Vereniging Voor Electronenmicroscopie, Amsterdam, 1961), p. 392.

# Nuclear Spin Polarization

P. C. Souers

*Magnetic-resonance studies of solid, normal, deuterium-tritium (DT) have shown that the nuclear relaxation times are too short for nuclear polarization. Removal of the first-excited ( $J = 1$ ) rotational state of molecular hydrogen increases these times, but tritium radioactivity decreases them again. Hydrogen atoms have been found in densities adequate to support nuclear polarization. Synthesis of superpure molecular DT is the most likely future solution to the problem of creating a DT sample capable of sustaining polarization.*

## Introduction

It has been suggested that alignment of the nuclear magnetic moments in deuterium-tritium (D-T) would produce a hydrogen fusion fuel with a 50% higher cross section, thereby possibly obtaining fusion with a laser driver of half the normal size.<sup>1</sup> For five years, we have studied solid D-T at temperatures as low as 1.4 K in an attempt to find conditions conducive to eventual nuclear polarization. With the closure of the LLNL Tritium Facility, the work has ended, and this report summarizes the entire five-year effort.

From the start, we recognized that the greatest problem would be short nuclear relaxation times, which would severely limit the life of nuclear polarization.<sup>2</sup> These short relaxation times in solid hydrogen are caused by free molecular rotation. It was feared that tritium radioactivity would create new, rotationally excited,  $J = 1$  D<sub>2</sub> and  $J = 1$  T<sub>2</sub>, which would further shorten the relaxation times. Also unknown were the concentration and relaxation times of hydrogen atoms needed for the microwave pumping that creates nuclear polarization.

## Experiment

We used pulsed nuclear magnetic resonance (NMR) at 5 to 50 MHz to measure the nuclear relaxation times and frequency-swept, unmodulated, 9.4-GHz, electron spin resonance (ESR) to measure the hydrogen atom concentrations and relaxation times. Most D-T was a mixture of 25% D<sub>2</sub>-50% DT-25% T<sub>2</sub>, but up to 93% of molecular DT was synthesized by the reaction of lithium tritide and deuterated methanol. To reach our target temperature of 1.4 K, we used liquid-helium cryostats. At times, the samples were frozen into silica aerogel foam.

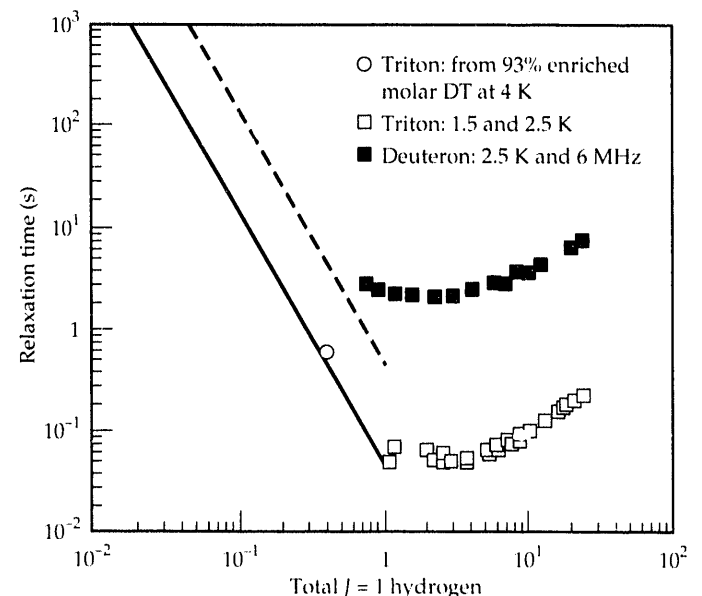
## Results

In normal D-T, the relaxation times of triton and deuteron were about 0.1 and 10 s, respectively (see Fig. 1)—much too short for the 1000 s required for nuclear polarization.

Worse yet, tritium radioactivity decreased the normal  $J = 1$  concentrations to about 0.75%, just where a relaxation-time minimum occurred. On the other hand, radiation-caused formation of new  $J = 1$  hydrogen prevented the  $J = 1$  concentration from dropping lower. Also, we found that the relaxation time of triton in 93% DT was about 1 s, showing that removal of  $J = 1$  T<sub>2</sub> increased the relaxation time.

Using ESR, we measured radiation-created hydrogen-atom concentrations as high as 2000 ppm in solid D-T (a number that is entirely acceptable for nuclear polarization) with electron relaxation times of about 0.1 to 1 s (somewhat long considering the short nuclear relaxation times). The atoms were spread over five hyperfine states of different

**Figure 1.** Summary of longitudinal nuclear relaxation times,  $T_1$ , for T and D nuclei in solid D-T for various total  $J = 1$  concentrations. The triton samples were all taken at 30 MHz. Estimated relaxation times for tritons (solid) and deuterons (dashed) at low  $J = 1$  concentrations are from the calculations of Drabold and Fedders.<sup>3</sup>



energies—two for tritium atoms and three for deuterium atoms. Pumping all atoms would, therefore, require five different frequencies. The atom concentration increased dramatically with decreasing temperature.

Using NMR to study a solid mixture of  $D_2$  and  $T_2$ , we obtained an exchange time constant of 200 h for DT formation. This was a measure of the radioactive destruction of the hydrogen composition. Because even small  $J = 1$  concentrations are harmful to nuclear relaxation, this experiment shows that a long-relaxing sample has a lifetime of less than 1 h.

We found that nuclear relaxation times varied greatly as a function of  $J = 1$  hydrogen but not of temperature or NMR frequency. This is characteristic of the electric quadrupole mechanism that dominates nuclear relaxation in solid hydrogen for large  $J = 1$  concentrations. The cause is a crystal-wide energy band that is created by the overlap of closely packed  $J = 1$  hydrogen molecules. Because the electron relaxation times are temperature-independent, they also can be dominated by a quadrupole mechanism. Long nuclear relaxation times were seen for thin layers of D-T frozen inside 96% porous silica aerogel. It was suggested that electric field gradients from the foam walls would destroy the quadrupole energy band, but only in a few of the nearest layers of hydrogen molecules.

Below 2 to 3 K, so many hydrogen atoms built up inside the solid D-T that a heat step or fluctuation caused most atoms to cooperatively recombine, releasing large quantities of heat. (The cryostat cell rose 5 K!) Heavy cooling suppressed these “heat spikes,” which clearly destroyed the atom population needed for polarization pumping. The absence of the ESR signal after a spike showed that the spike was related to the atoms.

## Discussion

The net result of our experiments was to show that normal D-T or even 93% DT was not usable as polarized fusion fuel. The next step is to quickly synthesize pure molecular DT, containing a small impurity concentration of  $J = 1$  hydrogen. We were designing such a method that uses a 23-K adsorption column, and we saw some separation in the first trial run.

The degree to which the DT must be purified is still uncertain. Ongoing analysis of old hydrogen-deuteride data suggests that our experiments and some in the literature may have sat long enough for  $J = 1$  pair condensation to occur inside the sample. In this case, quadrupole energy levels would form in localized parts of the sample and cause fast nuclear relaxation. The hope is that a rapidly quenched sample, which has to be made anyway because of the tritium radioactivity, might have longer relaxation times at relatively low  $J = 1$  hydrogen levels. This important experiment has never been thoroughly tested in any solid hydrogen and must await future research.

Once the quadrupole energy band has been brought close to breaking by the fast reduction of  $J = 1$  hydrogen, the further effect of electric-field gradients from the silica aerogel may be helpful across broader sections of the crystal. One may postulate an adsorption column system that makes a small amount of DT containing low amounts of  $J = 1$  hydrogen at 23 K in a few minutes and then quenches the sample to 1.4 K inside aerogel foam.

## Conclusions

The creation of solid D-T with sufficiently long nuclear relaxation times will be difficult but not impossible. The purification and freezing process must be done in minutes, which is a considerable challenge at liquid-helium temperatures. Once the crystal-wide quadrupole energy band is broken, however, then relaxation may be lengthened (faster than linearly) by decreasing the temperature and increasing the magnetic resonance frequency.

*This work was funded by Weapons-Supporting Research.*

## References

1. R. M. Kulsrud, H. P. Furth, E. J. Valeo, and M. Goldhaber, “Fusion Reactor Plasmas with Polarized Nuclei,” *Phys. Rev. Lett.* **49**, 1248 (1982).
2. P. C. Souers, E. M. Fearon, E. R. Mapoles, J. R. Gaines, J. D. Sater, and P. A. Fedders, “Nuclear Spin Polarization of Solid Deuterium-Tritium,” *J. Vac. Sci. Technol. A* **4**, 1118 (1986).
3. D. A. Drabold and P. A. Fedders, “Nuclear Spin-Lattice Relaxation Times for Mixtures of Ortho- and Para- $H_2$ . II. Low Ortho- $H_2$  Concentration,” *Phys. Rev. B* **39**, 6325 (1989).

# Studies of the Omega Phase Transformation in the Titanium-Molybdenum Alloy System

L. E. Tanner, D. Schryvers\*  
and S. M. Shapiro†

**High-resolution electron microscopy and neutron-scattering studies have documented that in the course of transformation of the Ti-Mo  $\beta$  phase, the high-pressure-stable  $\omega$  phase can be nucleated by an atomic displacive mechanism. This is accomplished by a local heterogeneous process involving the coupling of a  $\beta$ -phase phonon anomaly with the strain fields of lattice defects. The studies have also shown that the metastable  $\omega$  phase can compete effectively with stable phases during certain thermal aging treatments.**

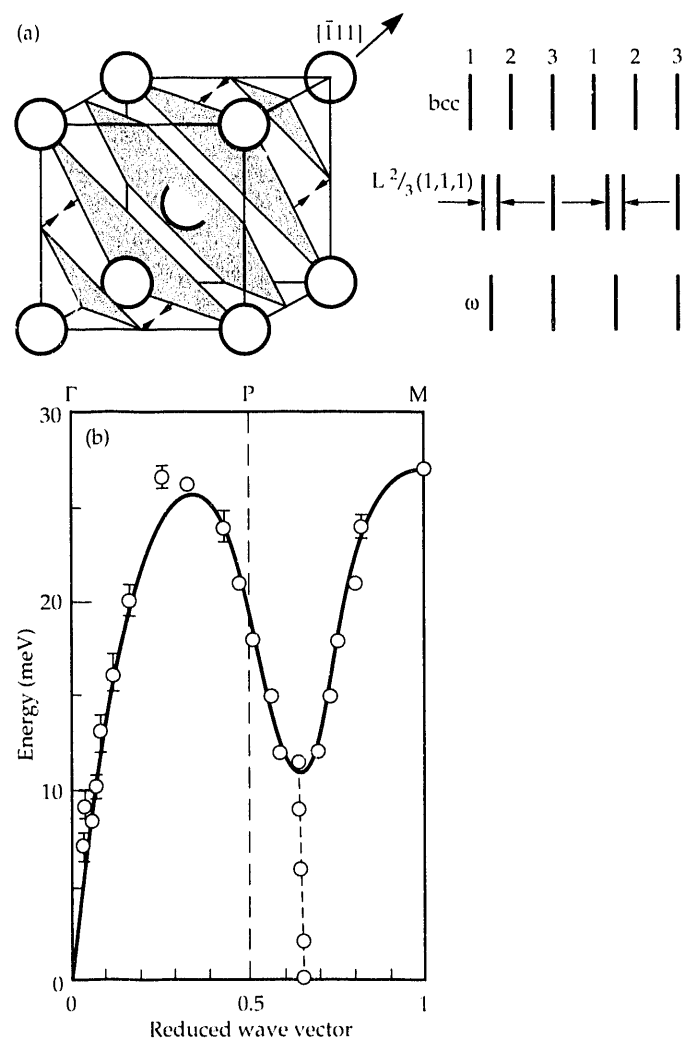
## Introduction

The majority of displacive transformations of metallic-alloy phases are of the martensitic type. They usually occur when a high-temperature-stable phase, quenched to avoid diffusional decomposition to multiphase equilibrium, reaches the critical undercooling (below  $T_0$ , the temperature of equal free energy between parent and product phases) to initiate a composition-invariant symmetry change. This transformation involves a cooperative shear displacement of atoms by fractions of lattice spacings. Our recent work<sup>1</sup> shows how this is facilitated by the unusually low energies of the appropriate symmetry-related transverse acoustic (TA) phonon mode. The product phase is invariably structurally related to one of the stable phases at lower temperatures, but is metastable; hence, only a partial decrease in total free energy can be realized by the transition.

A somewhat different scenario appears to develop with the  $\beta$  (bcc)  $\rightarrow$   $\omega$  (simple hexagonal) displacive phase transformation observed in alloys based on the Group-IV transition metals titanium, zirconium, and hafnium.<sup>2,3</sup> Certain aspects remain unclear, and our new insights<sup>1</sup> help explain this behavior. In these cases,  $\omega$  is metastable but is *structurally distinct* from the equilibrium  $\beta$  and  $\alpha$  (hcp) phases of these systems; it is truly stable only at high pressures.<sup>2</sup> However, it can be displacively generated from high-temperature-stable  $\beta$  by an oscillatory shifting of its  $\{111\}$  planes [see Fig. 1(a)]; this is driven by a prominent low-energy anomaly in the longitudinal acoustic (LA)  $\langle 111 \rangle$  mode, which is present in the  $\beta$  phonon spectra at ambient pressure [see Fig. 1(b)].<sup>4</sup>

The transition initiates during quenching but does not go to completion at or below room temperature. Complete transformation has been observed only with thermal assistance during the initial stages of aging treatments at temperatures designed to produce the equilibrium phases by decomposition of  $\beta$ . Elucidation of this unique coupling

**Figure 1.** (a) The relationship between bcc  $\beta$  and simple hexagonal  $\omega$ . (b)  $\langle 111 \rangle$  longitudinal acoustic phonon dispersion for Ti-8 at.% Mo.



of distortive with diffusional atomic movements required us to examine microstructural changes at the atomic level using transmission electron microscopy (TEM) at high resolution.<sup>5</sup>

## Experimental Procedure

We heat-treated single and polycrystalline Ti-Mo alloys at 950°C in the high-temperature  $\beta$  phase field and quenched them into iced brine. Subsequently, we aged them in the equilibrium  $\alpha + \beta$  phase field at temperatures between 300 and 400°C. By the use of conventional contrast TEM (CTEM), high-resolution TEM (HRTEM) and electron diffraction (ED) in conjunction with elastic and inelastic neutron scattering, we determined microstructural evolution, static strains, and lattice dynamic variations with time at aging temperature.

## Results and Discussion

CTEM images of quenched in Ti-8 at.% Mo exhibit a fine-scale strain contrast, and elastic neutron scattering confirms the presence of local static distortions similar to  $\omega$  crystal symmetry. However, only HRTEM can reveal any meaningful structural detail. Figure 2 shows a  $(1\bar{1}0)$  oriented image of  $(110)$  bcc plane fringes (spacing: 0.23 nm). The fringes are perturbed by local enhancements (dots) grouped as linear arrays or “chains” (~1 to 2 nm long) lying along the two  $\langle 111 \rangle$  directions in this orientation. The ED pattern (inset) reveals bcc Bragg spots plus arcs of diffuse scattering with enhancements at the  $\omega$  Bragg positions of  $(2/3)\langle 111 \rangle^*$ . The arcs are sections of sheets of scattering in reciprocal space that are consistent with rod-like configurations in real space.

Aging at 350°C induces a continuous rearrangement, ordering, and coalescence of the linear chains to produce 3-D domains with a structure uniquely different from bcc  $\beta$ . The  $(1\bar{1}0)$  HRTEM image after 100 h is shown in Fig. 3(a), and ED (inset) reveals that sharp  $\omega$  spots have replaced the diffuse scattering. Two of the four possible structural variants

of  $\omega$  are in contrast, where each domain contains a characteristic rectangular white dot pattern, which is the projected image of columns of atoms parallel to the incident electron beam.<sup>6</sup> The short dot spacing is along  $[11\bar{1}]$  (or  $[\bar{1}11]$ ), and the long spacing is along  $[11\bar{2}]$  (or  $[\bar{1}12]$ ), respectively.

The pattern is readily understood in terms of the structural change from  $\beta$  to  $\omega$  indicated earlier [see Fig. 1(a)] and shown in Fig. 3(b) for the  $(1\bar{1}0)$  projection related to the image. A longitudinal lattice displacement modulation is induced with wave-vector  $(2/3)(\pi/d)\langle 111 \rangle$  of appropriate amplitude and phase, where  $d$  is the interplanar space.<sup>2,3</sup> This is related to the position of the sharp dip in vibrational energy of the LA $\langle 111 \rangle$  phonon mode [see Fig. 1(b)].<sup>4</sup>

The result is the sequential displacement of bcc  $(111)$  planes such that two out of three planes collapse toward each other, while the third remains positionally unchanged. We have grouped the atoms of the fully collapsed planes as “pairs” (enclosed by ellipses) for convenience in order to deal with HRTEM resolution limitations. The instrumental limit of resolution is 0.17 nm, and the spacing of the atomic pairs in projection is 0.13 nm. Hence, a single dot represents two columns within a plane and gives rise to the rectangular arrays observed in the images. We confirmed this interpretation by using real-space methods for computer simulation.

**Figure 3.**

(a) HREM image and diffraction pattern of aged 8Mo. (b) Schematic of the structural relationship between bcc  $\beta$  and  $\omega$  as seen along the  $[1\bar{1}0]$  direction, including the longitudinal displacement wave.

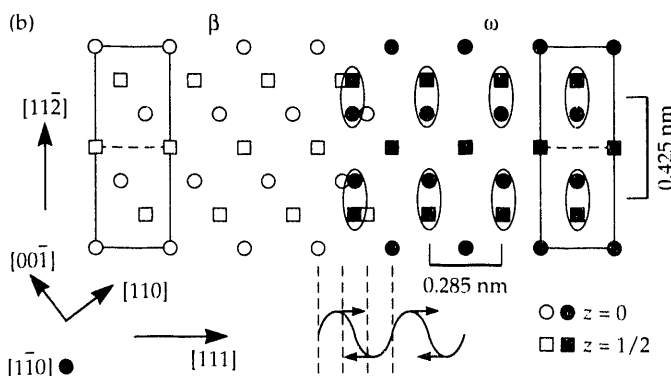
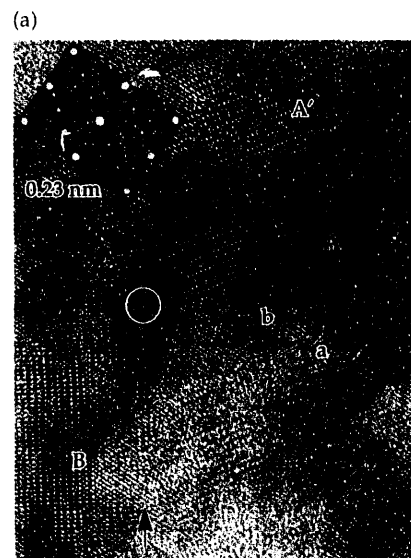
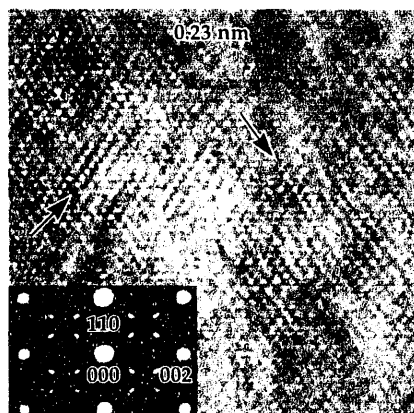


**Figure 2.**

The  $[1\bar{1}0]$  HREM image and diffraction pattern of as-quenched 8Mo, revealing small, nearly commensurate one- and two-dimensional  $\omega$  regions (“chains”).



Applying this imaging code to the initial structure (see Fig. 2), we are convinced that the displacive stage during the quench involves the formation of the linear chains (viz.,  $\omega$  nuclei). The question to be addressed at this point is, "What sets this process in motion with a phase that is stable only at elevated pressure?" From our studies of the formation of martensites,<sup>1</sup> we know that the critical enabling step is related to heterogeneous nucleation linked to the transformation-related phonon anomaly.

Petry et al.<sup>4</sup> recently established that the (2/3)LA<111> phonon dip persists into the high-temperature  $\beta$  field in these alloys and that it couples to the strain fields of defects such as solute atoms and clusters.<sup>4,7</sup> Consequently, these elastic distortions are biased toward  $\omega$ -like symmetry so that the parent  $\beta$  lattice becomes populated with a profusion of strain embryos (potential nuclei). They are "frozen" into their characteristic linear morphology when quenched through the metastable  $T_0^{\beta \rightarrow \omega}$  (calculated in Ref. 8 to be  $\sim 400^\circ\text{C}$ ).

The subsequent continuation of  $\beta \rightarrow \omega$  with aging simply concerns the thermodynamic and kinetic competition between structurally distinct phases with differing relative stabilities. Once formed and then aged at a thermodynamically appropriate temperature ( $350^\circ\text{C} < T_0^{\beta \rightarrow \omega}$ ),<sup>8</sup> metastable  $\omega$  has a clear energetic advantage over equilibrium  $\alpha$ , which still must overcome its nucleation barrier with time at temperature. Hence, during the incubation period for  $\alpha$  nucleation,  $\omega$  is free to continue to develop by rearrangement and coalescence because a partial reduction in free energy will result. Once  $\alpha$  is able to form, however,  $\omega$  must revert to allow the stable  $\alpha + \beta$  microstructure to develop as aging continues.

## Conclusions

With these experimental observations, we have established that when the Ti-Mo  $\beta$  phase is quenched from high temperatures, it undergoes an incomplete displacive transformation to the metastable high-pressure phase,  $\omega$ . The

displacive process is initiated because heterogeneous nucleation results from the coupling of a transformation-related phonon anomaly with lattice-defect strain fields. The  $\beta \rightarrow \omega$  transformation will go to completion with thermal aging, temporarily preempting equilibrium  $\alpha$ , if the aging temperature is lower than  $T_0^{\beta \rightarrow \omega}$ .

## Acknowledgments

The HRTEM studies were carried out at the National Center for Electron Microscopy at the Lawrence Berkeley Laboratory, Berkeley, CA. Neutron-scattering experiments were carried out at Brookhaven National Laboratory, Upton, NY.

*This work was funded by the U.S. DOE Office of Basic Energy Studies, Division of Materials Science.*

\*Permanent address: University of Antwerp, Antwerp, Belgium.

†Permanent address: Brookhaven National Laboratory, Upton, NY.

## References

1. S. Shapiro, B. Yang, Y. Noda, L. Tanner, and D. Schryvers, "Neutron Scattering and Electron Microscopy Studies of the Premartensitic Phenomena in  $\text{Ni}_x\text{Al}_{(100-x)}$ ," *Phys. Rev. B* **44**, 9301 (1991).
2. S. Sikka and Y. Vohra, "Omega Phase in Materials," *Prog. Mater. Sci.* **27**, 245 (1982).
3. D. deFontaine, "Simple Models for the Omega Phase Transformation," *Metall. Trans. A* **19**, 169 (1988).
4. W. Petry, A. Heiming, and G. Vogl, "Phonon Dispersion of the bcc Phase of Group-IV Metals. I Titanium; II Zirconium; III Hafnium," *Phys. Rev. B* **43**, 10933, 10948, 10963, (1991).
5. D. Schryvers and L. E. Tanner, "HRTEM Observations of Athermal Omega Phase in Ti-Mo Alloys," *Mater. Sci. Forum* **56-58**, 329 (1990).
6. J. Spence, *Experimental High Resolution Electron Microscopy* (Oxford Univ. Press, New York, 1980).
7. A. Heiming, W. Petry, and G. Vogl, "The Local Displacement Field Around Co and Nb Solute in Omega-phase forming bcc-Zr at High Temperatures," *Z. Physik. B/Condensed Matter* **85**, 239 (1991).
8. D. Moffat and U. Kattner, "The Stable and Metastable Ti-Nb Phase Diagrams," *Metall. Trans. A* **19**, 2389 (1988).

# Surface Reactions Induced and Measured by Scanning Probe Microscopy

M. Balooch, W. J. Siekhaus,  
and R. J. Tench

*We have used scanning tunneling microscopy (STM) to investigate the kinetics of surface reactions that occur at individual reaction sites. Specifically, we studied the gasification of graphite by oxygen and hydrogen over a wide range of conditions, including variations in temperature, reactant pressure, and exposure time. We also succeeded in enhancing the graphite-ozone reaction at specific sites. In separate experiments, we used atomic force microscopy (AFM) to study polymer coatings on inertial confinement fusion (ICF) spheres, starting with nucleation and proceeding through the growth process to the final product.*

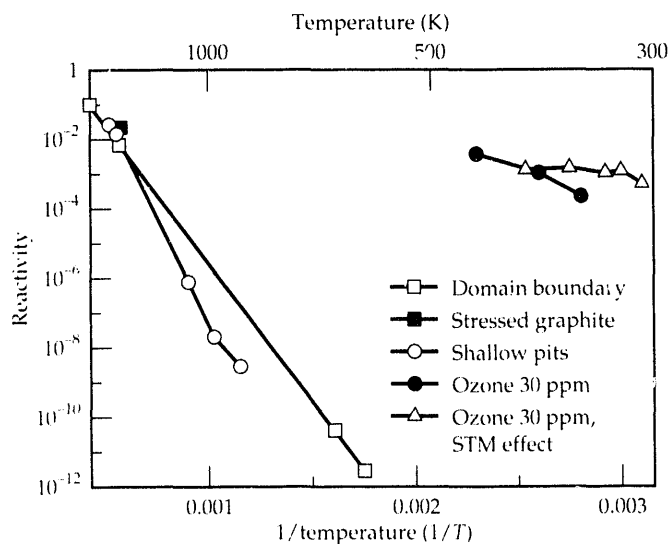
## Introduction

The advancement of many modern technologies depends on a better understanding of the specific mechanisms by which etching and deposition occur. For the past two decades, many powerful techniques—e.g., gravimetry, thermal desorption, and modulated molecular beam mass spectrometry—have helped to elucidate the basic steps that determine the kinetics of gas-surface reactions. In all of these, scientists have tried to understand how the surface participates in the chemical reaction. They have shown or postulated that surface characteristics—including periodic structure, point defects, atomic steps, grain

boundaries, and impurities—strongly influence the kinetics of the reaction process. Many surface-sensitive techniques such as Auger electron spectroscopy (AES), x-ray photoelectron spectroscopy (XPS), and low-energy electron diffraction (LEED) relate the “global” surface structure and composition to surface-reaction kinetics. However, none of these techniques provide detailed information about the physical structures of specific reaction sites and the reaction rates at those sites.

The development of scanning probe microscopy (SPM)—which includes scanning tunneling and atomic force microscopies (STM and AFM)—has made it possible to observe individual atomic sites.<sup>1</sup> We have, for the first time, used STM to investigate the carbon-combustion kinetics of particular sites on graphite under a wide range of conditions. In addition, we have observed the enhancement of a localized graphite-ozone reaction under the STM tip.

**Figure 1.** Reaction of HOPG basal plane with O<sub>2</sub> and O<sub>3</sub>, and the STM effect on O<sub>3</sub> reaction.



## Experimental Methods and Results

We have studied the nanometer-scale kinetics of graphite oxidation by heating graphite conventionally (for long-term measurements) or by short-pulse laser heating (for millisecond exposure times) in an STM. Using STM, we can locate specific sites—such as steps on a highly ordered pyrolytic graphite (HOPG) basal plane—and measure their reactivity by determining the local rate of atom removal. (Reactivity, the reaction probability at a site, is the fraction of reactants striking that site that undergo a chemical reaction.)

We can use STM to determine reactivity over a range of 12 orders of magnitude. The lower limit of reactivity measured by this technique corresponds to removal of one atom per site per day. The results suggest an activation energy of 36 kcal/mole at the grain boundaries and 53 kcal/mole for

steps and shallow pits. The literature for graphite oxidation reports the "gross" activation energy to be between 35 and 80 kcal/mole. Most probably, the graphite samples used in previous experiments had various densities of grain boundaries, point defects, and other local surface perturbations where gasification most readily occurs, which would account for the wide range of values.

Figure 1 shows the site-specific reactivity of oxygen (air) with graphite as a function of inverse temperature for specific sites. Here we can see that ozone (at a partial pressure of  $10^{-3}$  Torr in air) reacts with graphite much more than air does with graphite. This is especially true at higher voltages ( $>2$  V) in the vicinity of the STM tip, where the high electric field and the intense electron current between the tip and the site immediately below it further increase the reactivity by more than an order of magnitude.

We have extended these STM studies to catalytic reactions and found that STM provides great insight into these reaction mechanisms as well. For instance, we knew that impingement of atomic (but not molecular) hydrogen leads to carbon gasification in amounts sufficient to be detectable in molecular beam experiments<sup>2</sup> and postulated that molecular hydrogen dissociatively adsorbed onto platinum clusters would spill over onto the graphite and gasify the carbon.<sup>2</sup> To catalytically enhance gasification with molecular hydrogen, we deposited platinum on graphite and heated it in a vacuum. XTM revealed that the platinum formed clusters along steps on the surface, and when the surface was exposed to hydrogen, carbon atoms on the elevated step next to the platinum cluster reacted with the hydrogen, and gasification occurred. The platinum cluster then migrated into the void vacated by these carbon atoms, etching shallow channels into the graphite surface.

Only on rare occasions can conventional analytical surface-science tools be used on insulating surfaces. Although STM reaction studies are limited to conductive substrates, AFM provides a means to study surface reactions such as deposition and corrosion of insulating materials—a major DOE concern. To show that we can study the details of reactions on insulators, we used AFM to study the nucleation, growth, and surface roughness of the polymer coatings of inertial confinement fusion (ICF) spheres (see Fig. 2). By using AFM, we easily measured the typical roughness and sphericity of such spheres with nanometer accuracy. AFM nucleation and growth studies also will be essential in searching for parameters that influence desirable film properties.

## Summary

We have demonstrated that SPM can be used for surface-reaction studies on both conductors and insulators over a wide range of temperatures, pressures, exposure times, and chemical environments (e.g., in high vacuum and in gases at and above atmospheric pressure). This flexibility is not possible with other techniques.

We have determined site-specific kinetics and morphology changes for thermal and catalytic corrosion reactions and observed a polymer-deposition reaction from nucleation to finished product.

Detailed material-removal studies on conductors and insulators are important in studies of environmental corrosion, waste-product containment, and material erosion in space. Detailed deposition studies are essential for film production in many technologies.

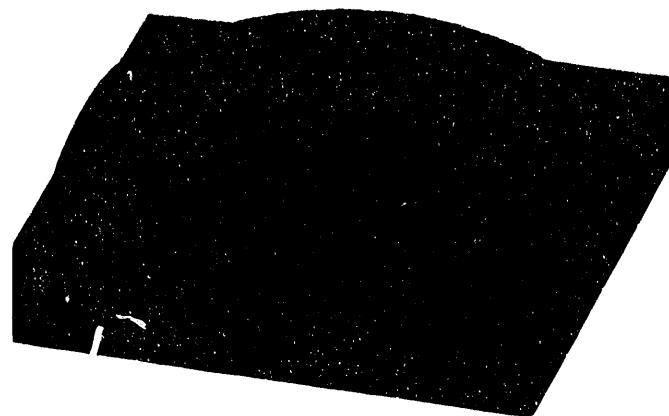
In addition, we have used the high electric field and electron current density between the STM tip and the sample to enhance local reactivity. Locally induced reaction may be the technique by which future nanometer-scale lithography is achieved.

*This work was funded by Weapons-Supporting Research.*

## References

1. G. Binnig and H. Rohrer, "Scanning Tunneling Microscopy," *IBM J. Res. Devel.* **30**, 355 (1986).
2. D. R. Olander and M. Balooch, "Platinum Catalyzed Gasification of Graphite by Hydrogen," *J. Catalysis* **60**, 41 (1979).

**Figure 2.** Surface morphology of a polymer-coated sphere.





# Atomic-Resolution Imaging with Photoelectron Holography

L. J. Terminello and  
J. J. Barton\*

*We have imaged copper atoms near a (100) single-crystal face using photoelectron holography. The Cu 3p hologram, measured at 577 eV using synchrotron radiation, was two-dimensionally Fourier transformed to obtain three dimensions of atomic structural information. This structural technique can then be used to better understand solid-state atomic interactions with future applications.*

## Introduction

From a scientific standpoint, atomic-resolution structural probes of single crystals, surfaces, and other unique interfaces provide challenging new venues with which to learn about chemical bonding in the solid state. Many solid-state structural probes already exist, but few can provide atomic-resolution images of the regions being studied. Scanning tunneling microscopy (STM) can stunningly image a surface with atomic resolution but cannot reveal directly what is below the surface. Other penetrating probes, such as x-ray crystallography, give detailed structural information but do so indirectly. The recently pioneered<sup>1,2</sup> atom imaging technique of photoelectron holography can image not just the surface of a solid-state sample, but also the near surface region.

In this article, we describe one of the first photoelectron-holography experiments to image atoms within a single crystal: the near-surface atoms of a Cu(001) crystal face. By studying this simple prototype system, we intend to learn how to apply this technique to more-complicated and technologically interesting systems.

A photoelectron hologram is the constant-energy, angle-dependent photoelectron intensity derived from a chemically specific core level. Photoelectron holography is experimentally the same as photoelectron diffraction, which has been shown to be an effective tool for determining surface structure.<sup>3,4</sup> However, when described as a holographic process, the diffraction (interference) between the core-level electron measured directly from the photoemitter (i.e., the reference beam) and the same photoelectron wave that has scattered off neighboring atoms (i.e., the object wave) forms a true hologram.<sup>2</sup> Photoelectron holography is uniquely suited to provide near-surface structural information because it can probe buried regions that surface-imaging spectroscopies (e.g., STM) cannot reach. At the same time,

it can yield elemental and oxidation-state-specific data that surface-penetrating probes [e.g., extended x-ray absorption fine structure (EXAFS), x-ray standing wave, and ion scattering] inadequately provide. The chemical specificity of a hologram is a consequence of using element-specific core-level photoelectrons. Oxidation-state sensitivity occurs when high-resolution photoelectron spectroscopy is used to select the oxidation state or interfacially shifted core-level electron.<sup>5</sup> Preliminary studies have shown that the holography technique can reach buried interfaces when used in this manner.<sup>6</sup>

The elegance of the holography technique permits the multiple-angle photoelectron interference pattern to be two-dimensionally Fourier transformed to produce a real-space, three-dimensional intensity map of the electron-scattering atoms neighboring the photoemitter.<sup>3</sup> High-precision (0.02-Å error) structural information can be obtained by comparing the interference pattern to multiple-scattering simulations.<sup>3,4</sup> No other combination of techniques can provide such comprehensive geometric and chemical information.

## Experimental Methods

We measured Cu 3p photoelectron holograms from a clean, Cu(001) crystal face that we prepared according to well-established cleaning and annealing procedures. Monitoring with core-level photoelectron spectroscopy showed that after we prepared the new surface, it remained clean for 6 to 10 h. We used valence-band photoemission to orient the electron emission directions with respect to the analyzer and measured core-level and valence-band photoelectron spectra using an ellipsoidal mirror analyzer.<sup>7</sup> This band-pass electron-energy analyzer can measure both angle-resolved and angle-integrated spectra, thus permitting easy alternation between characterization of the sample (angle-integrated) and measurement of the 3p photoelectron holograms (angle-resolved).

To obtain Cu 3p photoelectron holograms at a kinetic energy of 577 eV, we performed these measurements with monochromatized synchrotron radiation as the excitation source. We conducted our measurements on the IBM/U8 beamline<sup>8</sup> at the National Synchrotron Light Source, which provided the 650-eV photons needed for this experiment. We measured Cu 3p electron angular distributions of 82° full-angle acceptance at 577 eV. The total collecting time for a single hologram at this energy was 4 h; if we had used a more typical hemispherical electron analyzer to make this measurement, it would have taken nearly 10 times longer.

## Results

The top left corner of Fig. 1 shows the raw Cu 3p electron interference pattern. Immediately evident is the strong analyzer signature that must be removed before the oscillatory portion of the data (the hologram) becomes clear. To remove this signature, we first normalized the 3p electron angular distribution to an isotropically emitted electron source measured at the same kinetic energy. Next, we moved the photopeak far from the energy window of the analyzer—a procedure possible only with synchrotron radiation. Finally, we measured the inelastically scattered electrons from the same sample. The bottom left corner of Fig. 1 shows the resultant interference pattern.

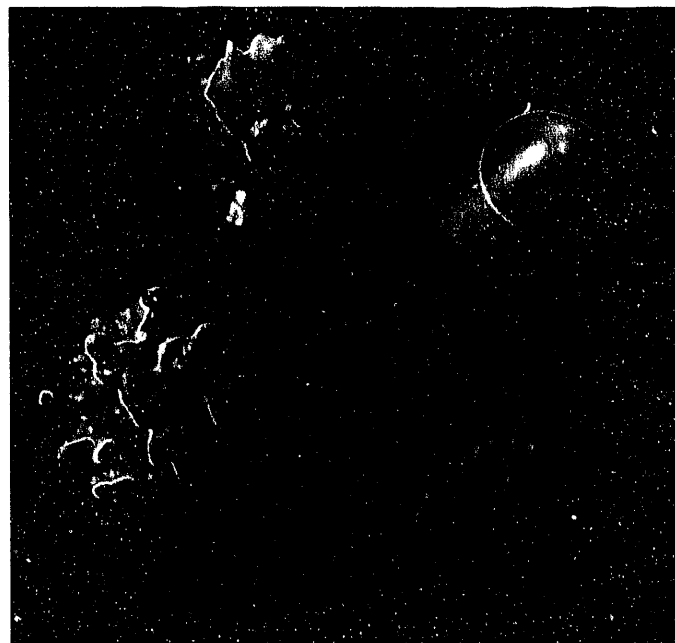
We then converted this electron angular distribution pattern to a constant inverse-space (k-space) grid for further data processing. We did this because the two-dimensional Fourier transform operates on inverse-space data ( $\text{\AA}^{-1}$ ) to obtain real-space ( $\text{\AA}$ ) intensities of atoms located near the emitter. The algorithms used for transforming the hologram are given in Ref. 3. However, prior to Fourier transformation, the data needed to be “windowed” so that the edges of the finite data range of the hologram did not lead to truncation errors in the real-space images. Attenuation of the edges of the data range reduced the ringing that would otherwise be present in the atom images. This window function is a two-dimensional Gaussian pictured at the upper right corner of Fig. 1.

Initially, we had difficulty visualizing the three-dimensional intensity information obtained from the Fourier transform. Perhaps the most effective means of representing the data was to take two-dimensional slices through the volume and project that intensity information as a surface. This has been effective with other holographic images,<sup>2</sup> and it worked with these data as well. The lower right corner of Fig. 1 shows a two-dimensional slice through the real-space intensity volume. This slice was taken through a plane that is parallel to the crystal surface and intersects the layer of atoms 1.8  $\text{\AA}$  directly above a given emitter.

## Discussion and Conclusions

In the slice through the Fourier-space volume shown in Fig. 1, the peaks arise from scattering atoms that lie in the plane immediately above any Cu 3p photoelectron emitter. The volume slice shown is representative of the structural information obtained from this system. Because of the symmetry of the sample, nearly all the atoms in the near-surface region are equivalent emitters. The four peaks around the central intensity appear at approximately the correct distance from the emitter (at the origin). The atom-position resolution of these peaks is 0.7  $\text{\AA}$ , but they are translated from their ideal position by 0.3  $\text{\AA}$  because of the forward electron scattering that dominates the hologram. As an electron is forward-scattered through an atom, the scattered wave is slightly phase-shifted an additional amount when it interacts with the atom potential. This phase shift adds to that which normally occurs from the geometry-induced diffraction, the part that gives rise to the structural information we seek. Hence, the forward-scattering phase shift causes the four peaks to appear at slightly shifted positions.

**Figure 1.** (Upper left) The unprocessed Cu 3p electron angular distribution at 577 eV. The angular acceptance displayed is 82°, and electron intensity is proportional to height on the surface plot. (Lower left) The raw hologram isolated from the electron angular distribution pattern. (Upper right) The Gaussian window function used to process the hologram prior to transformation. (Lower right) Two-dimensional slice through the atom-position volume taken at a distance 1.8  $\text{\AA}$  above the emitter. Note the four symmetric peaks that arise from the atoms located directly above the emitter.



Streaking of the intensity from the atom that lies 3.61 Å directly above the emitter causes the intensity at the center of the Fourier slice. Even though this atom is two atomic layers away, we can still see it in the slice taken through the layer below. Apparently, the resolution of the holographic transform in the direction perpendicular to the crystal surface is poorer than that within the plane. We expected this result, which was observed previously,<sup>2</sup> when considering the diffraction limit of structural information that we could obtain from the hologram. Nevertheless, the structural information obtained from this prototype system indicates that the photoelectron holography technique has sufficient resolution and accuracy to be applied to more-complex solid-state systems.<sup>9</sup>

Many important problems, especially those regarding next-generation materials, can be addressed with this imaging technique. For example, the effect of photoactivation on interface growth mechanisms and structure can be investigated by using photoelectron holography.<sup>10</sup> Examples from other technologically important areas include the atomic structure of magnetic thin-film interfaces and supported nanocrystal quantum dots. These topics are ideal challenges that may be successfully addressed by photoelectron holography.

*This work was funded by IBM Research through a postdoctoral research position (Terminello) and by Weapons-Supporting Research at LLNL.*

\* IBM Research, Yorktown Heights, NY

## References

1. A. Szöke, "X-Ray and Electron Holography Using a Local Reference Beam," in *Short Wavelength Coherent Radiation: Generation and Applications*, *AIP Conf. Proc.* **147**, D. T. Atwood and J. Boker, Eds. (American Institute of Physics, New York, 1986), pp. 361-367.
2. G. R. Harp, D. K. Saldin, and B. P. Tonner, "Atomic-Resolution Electron Holography in Solids with Localized Sources," *Phys. Rev. Lett.* **65**, 1012 (1990).
3. J. J. Barton, "Photoelectron Holography," *Phys. Rev. Lett.* **61**, 1356 (1988).
4. L. J. Terminello, X. S. Zhang, Z. Q. Huang, S.-H. Kim, A. E. Schach von Wittenau, K. T. Leung, D. A. Shirley, "The Surface Structure of  $\text{Cr}(2 \times 2)\text{S}$ :  $\text{Cr}(001)$  Determined by Angle-Resolved Photoelectron Extended Fine Structure," *Phys. Rev. B* **38**, 3879 (1988).
5. F. J. Himpsel, U. O. Karlsson, J. F. Morar, D. Rieger, and J. A. Yarmoff, "Determination of Interface States for  $\text{CaF}_2/\text{Si}(111)$  from Near-Edge X-Ray-Absorption Measurements," *Phys. Rev. Lett.* **56**, 1497 (1986).
6. L. J. Terminello and J. J. Barton, "Auger Electron Angular Distributions," *Science* **252**, 1218 (1991).
7. D. E. Eastman, J. J. Donelon, N. C. Hien, and F. J. Himpsel, "An Ellipsoidal Mirror Display Analyzer System for Electron Energy and Angular Measurements," *Nucl. Instrum. Methods* **172**, 327 (1980).
8. F. J. Himpsel, Y. Jugnet, D. E. Eastman, J. J. Donelon, D. Grimm, G. Landgren, A. Marx, J. F. Morar, C. Oden, R. A. Pollack, J. Schreier, and C. Crider, "A 10-Meter Toroidal Grating Monochromator for VUV-SXR Synchrotron Radiation Sources," *Nucl. Instrum. Methods Phys. Res.* **222**, 107 (1984).
9. L. J. Terminello and J. J. Barton, "Holographic Imaging of Atoms Using Multiple-Energy Electron Angular Distribution Patterns," to be submitted to *Phys. Rev. Lett.* [see LLNL Preprint UCRL-JC-109201 (1992)].
10. L. J. Terminello, F. J. Himpsel, E. R. McFeely, and A. B. McLean, " $\text{Si}_2\text{Cl}_6$  and  $\text{Si}_2\text{H}_6$  Adsorption on  $\text{CaF}_2/\text{Si}(111)$ ," *J. Vac. Sci. Technol.* **8(3)**, 3038 (1990).

---

## Overview

The C&MS Department provides research and development services in materials science and technology to meet the demands of all the major LLNL programs. In particular, we design and develop advanced materials for special—and frequently, extremely harsh—operating conditions. We also test and characterize such materials to obtain the necessary parameters for weapon design codes. To meet these commitments, we maintain laboratory facilities that fulfill nearly all of the requirements of modern metallurgical and ceramic applied research and development. These capabilities include arc, induction, and resistance furnaces for melting and heat-treating in a variety of atmospheres, and facilities for hot pressing, sintering, grinding and milling, and sputtering and vapor deposition. We also perform mechanical testing of specimens in a variety of ways and environments.

Research and development is carried out primarily in the following general areas: physical metallurgy, joining, forming and processing, coatings and surface modification, and corrosion and compatibility.

The study of phase transformations is a very important aspect of physical metallurgy. Tailoring alloys to specific applications usually requires an understanding of the effects of impurities, microstructure, and heat treatment on the transformations leading to the desired product. We study both the thermodynamics of phase transformations and their transformation mechanisms and associated kinetics. For several years, we have focused on the details of displacive transformations and developed a mechanistic theory to explain the origins of martensite nuclei and the importance of inhomogeneous strain fields associated with potent defects in the formation of martensite embryos, a coherent precursor to the nucleus. A very thorough study of the relationship between embryo formation and the phonon spectrum has produced an understanding at the atomic level of the selection process between different martensitic transformations. It is worth noting that the diffusionless martensitic transformation is the basis for our most important alloy, steel.

The synthesis of a wide range of coatings by physical and chemical vapor deposition and their characterization remain an important materials thrust. We now have the ability to synthesize true bulk multilayer samples hundreds of micrometers thick over tens of centimeters composed of tens of thousands of precisely reproduced individual layers. This breakthrough has enabled conventional mechanical characterization of these materials, revealing remarkable tensile and other properties. Strengths approaching theoretical in material combinations not normally allowed by nature (e.g., copper/stainless steel) have been measured. We have continued to develop the x-ray optical properties of these materials and to employ them as an experimental benchmark for alloy theory developments.

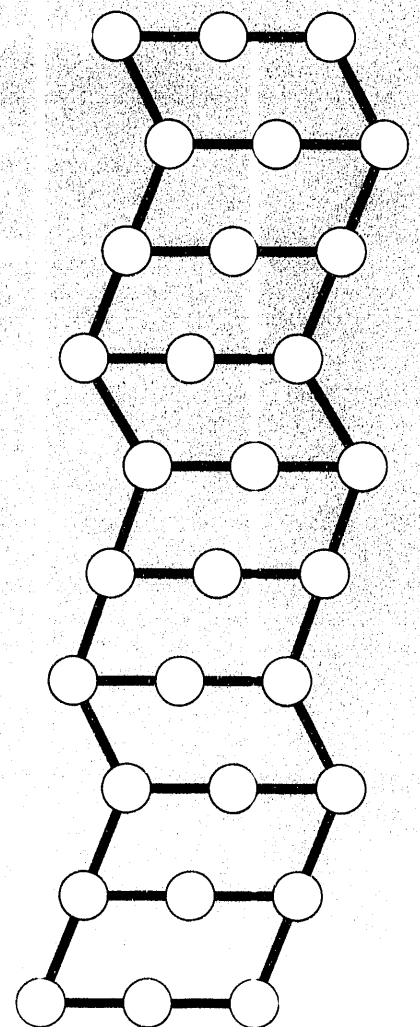
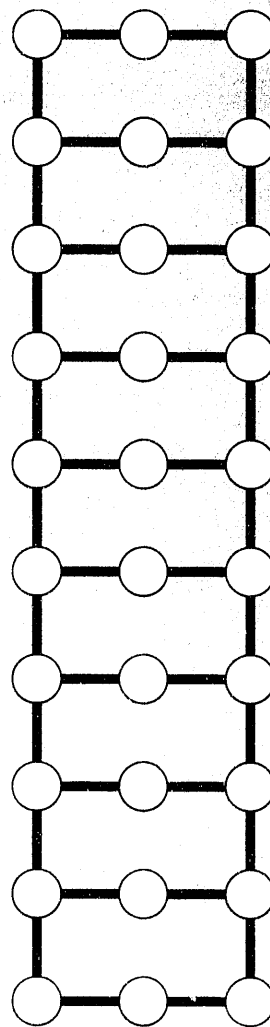
C&MS has a very strong and growing effort in *ab initio* alloy theory, including the development of new codes to address previously intractable problems and the extension of the application of existing codes to new alloy systems. Recent effort has focused on applying these codes to predicting phase stability and transformation routes with impressive success and on expanding them to include relativistic effects in order to treat the actinides. This activity is closely tied to state-of-the-art alloy-synthesis techniques, such as magnetron sputtering to both benchmark and guide the *ab initio* effort.

The materials effort includes an important component of process metallurgy and joining activity. We have directed our expertise in metal fatigue and corrosion toward developing a better understanding of their relationship to processing for uranium alloys important to the Nuclear Weapons Program. We have continued our study of superplastic deformation in steels and completed the phenomenological modeling of rapidly solidified Al-Be alloys. This modeling has very successfully explained the banded precipitate structure observed in rapidly solidified Al-Be and has predicted several other systems that should show this effect.

---

Section 2

**Metals  
and Alloys**



Two of the three structures  
observed in  $\text{Ti}_{50}\text{Pd}_{50-x}\text{Cr}_x$  alloys.

# First-Principles Approach to Alloy Phase Stability

P. E. A. Turchi and M. Sluiter

*The study of phase stability, including order-disorder phenomena and structural transformations, in substitutional alloys is of great theoretical and technological interest. Our approach combines accurate quantum-mechanical and statistical descriptions of the configurational part of the total free energy of an alloy. We have successfully illustrated the interplay between electronic-structure properties, crystalline effects, and configurational order at the microscopic level for copper-zinc, iron-chromium, and iron-vanadium alloys, thus demonstrating the validity and the predictive power of this advanced methodology.*

## Introduction

Three factors motivate us to use first-principles methodologies to study alloy phase stability from a proper combination of quantum mechanics and statistical thermodynamics. First, parameter-free calculations of total energies within the local density approximation are successful in predicting equilibrium properties of substitutional alloys at zero temperature.<sup>1</sup> Second, the cluster variation method (CVM) or Monte Carlo simulations used in conjunction with a 3-D Ising model can accurately describe thermodynamical properties at nonzero temperature.<sup>2</sup> Finally, the link between these two fields was made possible by introducing approaches justifying an Ising-like expression for the ordering contribution to the total energy. Such approaches include the generalized perturbation method (GPM), the embedded cluster method, and the concentration functional theory (CFT).<sup>2</sup> They all rely on the sole knowledge of a configurationally disordered state of matter, as described (for example) within the coherent potential approximation (CPA). With reference to this random medium, the energy difference between a specific state of order and the chemically random state (also called the ordering energy) can be properly evaluated. For reasons discussed elsewhere,<sup>2</sup> the ordering energies in the following examples are calculated within the GPM, if not stated otherwise.

To lowest order in perturbation, the ordering energy for an alloy consisting of A and B atoms takes the form

$$\Delta E_{\text{ord}}(\{q_s\}) \approx \sum_s q_s V_s \quad \text{with } q_s = \frac{c}{2}(n_s^{\text{BB}} - cn_s), \quad (1)$$

where  $n_s^{\text{BB}}$  and  $n_s$  refer to the number of BB pairs and total number of pairs, per site, associated with the sth-neighbor

shell.  $V_s$  is an sth-neighbor effective pair interaction (EPI) given by

$$V_s = V_s^{\text{AA}} + V_s^{\text{BB}} - 2V_s^{\text{AB}}. \quad (2)$$

These expressions, in terms of electronic quantities describing the random medium, are documented elsewhere.<sup>3</sup> In this GPM expansion, a set of parameters  $\{q_s\}$  that depend only on site occupancies specify a state of order. These EPIs provide an immediate answer to the existence of the most probable ground states (i.e., the ordered states stable at zero temperature) by reference to the studies performed on the Ising model for various crystalline structures. (See, for example, the results established for bcc<sup>4</sup> and fcc<sup>5</sup> lattices.) Equation (1) can be extended to higher order to include many-body interactions, although these are usually negligible because of disorder effects. Furthermore, in most of the alloy cases studied so far, the EPIs converge rapidly with distance, making the statistical treatment easier. One should mention that, as derived from the three methods mentioned above, the EPIs are concentration-dependent, in clear contrast to the ones deduced from a more phenomenological approach first introduced by Connolly and Williams,<sup>6,7</sup> which is not yet supported on fundamental grounds.

We performed all electronic-structure calculations on the basis of charge self-consistent Korringa Kohn Rostoker CPA muffin-tin potentials up to an angular momentum index  $l$  equal to 3. We present only the main results here. The only required input data are the atomic numbers of the alloy species and the crystalline structure.

## Phase-Stability Properties of Cu-Zn Alloys

We obtained total energies of the disordered state and EPIs for both fcc ( $\alpha$ )- and bcc ( $\beta$ )-based alloys as a function of composition.<sup>1,8</sup> Both quantities suggest a strong tendency

toward phase formation and ordering. The EPIs converge rapidly with distance and indicate that the most probable ground states are (1)  $LI_2$  (at  $Cu_3Zn$  and  $CuZn_3$ ) and  $LI_0$  (at  $CuZn$ ) for  $\alpha$ -based alloys and (2)  $DO_3$  (at  $Cu_3Zn$  and  $CuZn_3$ ) and B2 (at  $CuZn$ ) for  $\beta$ -based alloys. At  $T \neq 0$  K, we used the tetrahedron-octahedron (irregular tetrahedron) approximation of the CVM for  $\alpha(\beta)$ -based alloys to solve the statistical part of the problem.

Figure 1(a) shows the copper-rich part of the resulting phase diagram, and Fig. 1(b) is the corresponding experimental phase diagram.<sup>9</sup> In (a), fcc is the domain of stability of the  $\alpha$ -solid solution indicated by Cu in (b). It is remarkable that the two regions with the  $\beta$ -solid solution and the B2 ordered structure are not only properly located but also exhibit the correct behavior with temperature. Vibrations (the effect of which are described within the simple Debye theory) affect the high-temperature part of this phase diagram (i.e., above 600 K). Excess vibrational entropy, a characteristic of bcc-based systems, is mainly responsible for the typical curvature of the two-phase region ( $\alpha + \beta$ ) in the copper-rich part of the phase diagram.

The  $\alpha$ -solid solution exhibits short-range order (SRO), a deviation from randomness that causes diffuse scattering intensity away from the Bragg peaks (see Fig. 2). Indeed, SRO-caused diffuse scattering, as calculated using CFT<sup>10</sup> for an  $\alpha$ - $Cu_{80}Zn_{20}$  alloy slightly above the order-disorder temperature  $T_c$ , shows maxima at the  $[1\frac{1}{2}0]$  positions in reciprocal space. These maxima indicate the existence of long-period superstructure (LPS) of the  $DO_{23}$ -type, as also suggested experimentally.<sup>11</sup> This state, a precursor to the formation of an ordered  $LI_2$  compound [see Fig. 1(a)], has a small antiphase boundary energy (less than  $24$  mJ/m<sup>2</sup>,

as computed from the EPIs), which also strongly suggests the existence of LPS. The ordered phase itself has not yet been observed experimentally, probably because of prohibitively slow diffusion kinetics at low temperature. The predicted order-disorder transition temperature from  $\beta$  (bcc) to B2 (783 K) is only 40 K higher than the experimental value. At the boundary between B2 and  $LI_0$ , their internal energies at  $T = 0$  K become almost equal, strongly suggesting a structural transformation of the martensitic-type (i.e., diffusionless) in a narrow range of composition, as is indeed experimentally observed. The dotted lines in the theoretical phase diagram indicate the metastable zone boundaries. Hence, the most striking features that control the stability properties of Cu-Zn, as a function of concentration and temperature, are revealed by the first-principles approach used throughout this study. These features, in turn, provide a detailed description of the thermodynamics of both the stable and the metastable states of this alloy.

### Ordering Tendencies in FeCr and FeV Alloys

We selected Fe-Cr and Fe-V alloys primarily to gain a better understanding of the possible role played by SRO in the high-temperature bcc-solid solution in driving the structural transformation to a complex  $\sigma$  phase upon cooling. Figure 3(a) shows the calculated EPIs for the nonmagnetic equiatomic alloys. These rapidly convergent sets of EPIs show that FeCr tends to phase separate, whereas FeV clearly exhibits a B2 order. The ordering energy of B2-FeV is about  $-8.25$  mRy/atom, which is high relative to theoretical estimates for other B2 alloys ( $CuZn$ :  $-2.70$ ,  $NiTi$ :  $-5.71$ ,  $NiAl$ :  $-22.05$  mRy/atom). In the case of FeCr, the

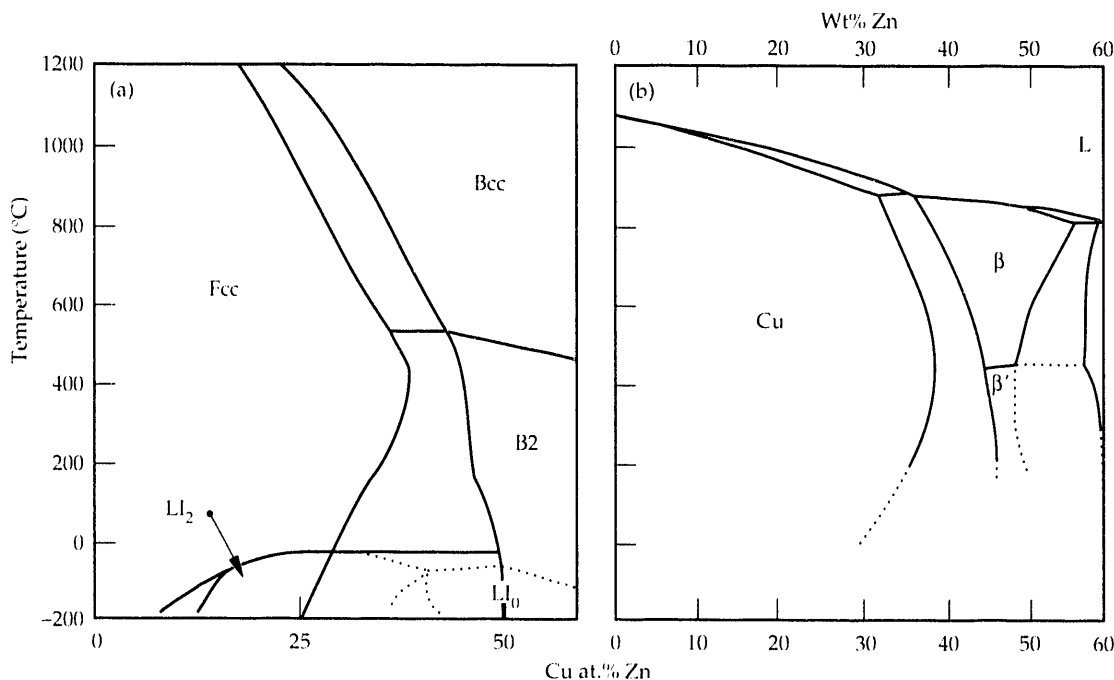


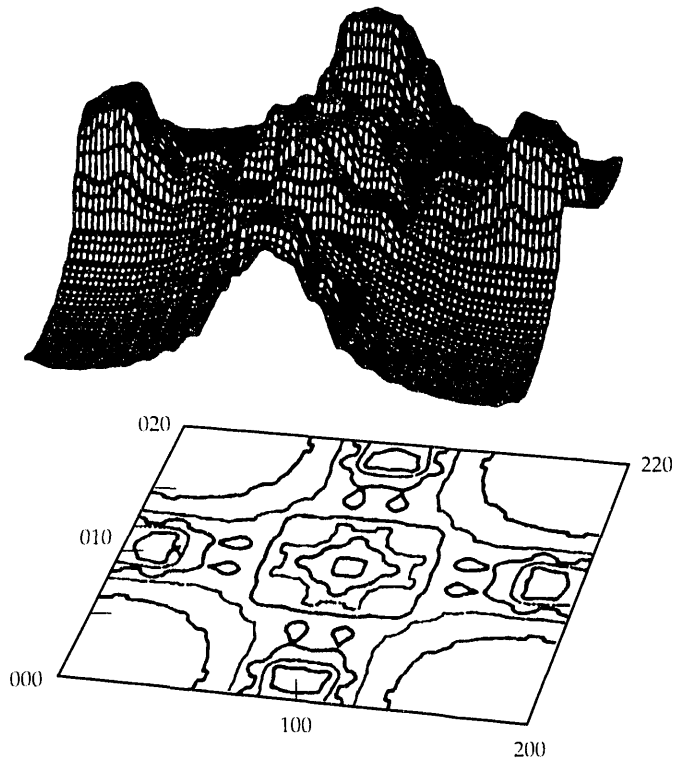
**Figure 1.**

Copper-rich part of the theoretical Cu-Zn phase diagram (a) compared with the assessed one (b).<sup>9</sup> Dotted lines refer to metastable boundaries.

EPIs closely agree with the inverse Monte Carlo simulations performed on the information deduced from x-ray diffuse scattering measurements,<sup>12</sup> as shown in Fig. 3(a). The origin of this difference in the ordering tendencies between the two alloys relies on an argument based on bandfilling, or average number of valence electrons,  $N$ , as shown in Fig. 3(b), where the first EPIs are plotted vs  $N$  ( $N$

= 6.5 for FeV and 7 for FeCr). This fact supports general tight-binding arguments made in the past.<sup>13</sup> The average number of valence electrons plays a critical role in deciding whether or not an alloy will have a tendency to order or phase separate, whereas the difference in the number of valence electrons of the alloy species (3 for FeV and 2 for FeCr) determines the strength of the tendency, as shown in Fig. 3(b). These findings are important insofar as the formation of complex phases and the stability of multicomponent systems are concerned.

**Figure 2.** Calculated SRO diffuse scattering intensity for the (001) plane, at  $T/T_c \approx 1.26$ , and for  $\alpha$ -based  $\text{Cu}_{80}\text{Zn}_{20}$  alloy.

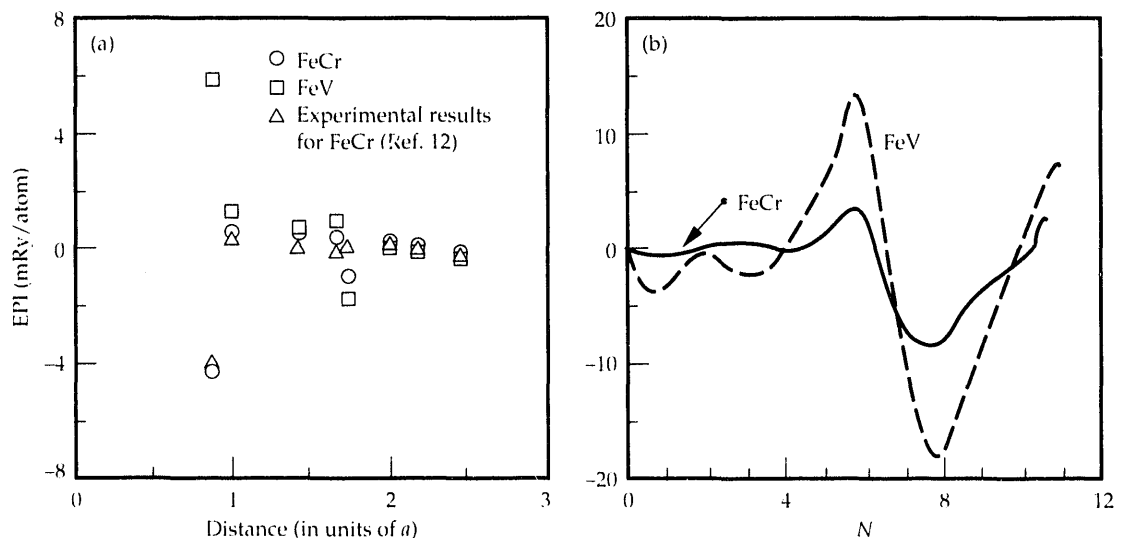


## Conclusion

The results of our first-principles approach to transformations in substitutional alloys show that a better understanding of phase stability properties may be gained at a microscopic level. Order-disorder phenomena and structural transformations can be explained and predicted from an accurate electronic description of the configurationally disordered state of the alloy. Crystalline structure and atomic numbers of the alloy species constitute the only required input information. This work reemphasizes, on fundamental grounds, the critical role played by the average number of valence electrons in determining the sign of the interactions that build up the ordering energy and thus in deciding whether an alloy may order or phase separate. The diagonal disorder effect, driven by the difference in the number of valence electrons of the alloy constituents, quantitatively controls the strength of the tendency. These predictive capabilities provide valuable information on the relative stability and metastability of ordered configurations and on the origin of phase formation of alloys based on complex crystalline structures. We hope that such methodology, besides predicting important aspects of phase transformations, will soon play a key role in the design of new classes of high-performance materials.

**Figure 3.**

(a) Theoretical EPIs for FeCr and FeV and experimental results for FeCr as a function of distance (in units of the bcc lattice parameter,  $a$ ). (b) First EPIs for FeCr and FeV, as a function of the number of valence electrons.





This work was funded by the Division of Materials Science of the DOE Office of Basic Energy Sciences, by Weapons-Supporting Research (FY90), and by Laboratory Directed Research and Development (FY91).

## References

1. P. E. A. Turchi, M. Sluiter, F. J. Pinski, D. D. Johnson, D. M. Nicholson, G. M. Stocks, and J. B. Staunton, "A First-Principles Description of Phase Stability in Cu-Zn Substitutional Alloys," *Phys. Rev. Lett.* **67**, 1779 (1991), and *Erratum* **68**, 418 (1992).
2. P. E. A. Turchi, "Electronic Structure and Phase Stability: Effect of a Bain Transformation on the Thermodynamic Properties of Substitutional Alloys," *Mater. Sci. Eng.* **A127**, 145 (1990) and references therein.
3. P. E. A. Turchi, G. M. Stocks, W. H. Butler, D. M. Nicholson, and A. Gonis, "First-Principles Study of Ordering Properties of Substitutional Alloys Using the Generalized Perturbation Method," *Phys. Rev. B* **37**, 5982 (1988).
4. A. Finel and F. Ducastelle, "Ordered Structures on the bcc Lattice with First, Second, Third and Fifth Neighbour Interactions," in *Phase Transformations in Solids*, T. Tsukalagos, Ed. (North Holland, Amsterdam, 1984), p. 293.
5. J. Kanamori and Y. Kakehashi, "Conditions for the Existence of Ordered Structure in Binary Alloy Systems," *J. Phys. (Paris), Colloq.* **83**, C7-274 (1977).
6. J. W. D. Connolly and A. R. Williams, "Density-Functional Theory Applied to Phase Transformations in Transition-Metal Alloys," *Phys. Rev. B* **27**, 5169 (1983).
7. M. Sluiter and P. E. A. Turchi, "Electronic Theory of Phase Stability in Substitutional Alloys: The Generalized Perturbation Method Versus the Connolly-Williams Method," *Phys. Rev. B* **40**, 11215 (1989).
8. M. Sluiter, P. E. A. Turchi, D. D. Johnson, F. J. Pinski, D. M. Nicholson, and G. M. Stocks, "A First-Principles Study of Short-Range Order in Cu-Zn," *Mater. Res. Soc. Symp. Soc.*, **166**, 225 (1990).
9. *Binary Alloy Phase Diagrams*, T. B. Massalski, Ed. (American Society for Metals, Metals Park, OH, 1990), 2nd Ed., Vols. 1-3.
10. B. L. Györfy and G. M. Stocks, "Concentration Waves and Fermi Surfaces in Random Metallic Alloys," *Phys. Rev. Lett.* **50**, 374 (1983).
11. L. T. Reinhard, B. Schönfeld, G. Kostorz, and W. Bührer, "Short-Range Order in  $\alpha$ -Brass," *Phys. Rev. B* **41**, 1727 (1990).
12. L. T. Reinhard, J. L. Robertson, S. C. Moss, G. E. Ice, P. Zschack, and C. J. Sparks, "Anomalous X-Ray Scattering Study of Local Order in bcc Fe<sub>0.53</sub>Cr<sub>0.47</sub>," *Phys. Rev. B* **45**, 2662 (1992).
13. P. Turchi and F. Ducastelle, "Continued Fractions and Perturbation Theory: Application to Tight Binding Systems," in *The Recursion Method and Its Applications*, D. G. Pettifor and D. L. Weaire, Eds. (Springer Verlag, New York, 1985), Vol. 58, p.104.

# A First-Principles Study of Phase Stability in Nickel-Aluminum Alloys

M. Sluiter and P. E. A. Turchi

*We have studied the thermodynamic stability of bcc- and fcc-based ordered phases in nickel-aluminum alloys with a highly accurate first-principles electronic-structure method. We can now predict the correct ground states, explain the solid solubility (or the lack thereof) in the terminal solid solutions, predict the occurrence of a martensitic transformation in a narrow composition range, and relate it to the competition between bcc- and fcc-based ordered structures. We computed the nickel-rich portion of the phase diagram, and the excellent agreement of our calculations with experimental determinations confirms the accuracy of our present approach.*

## Introduction

The properties of nickel-aluminum alloys make them promising candidates for a new generation of high-performance alloys. This in itself constitutes sufficient grounds for studying this alloy system, but in addition, nickel-aluminum alloys exhibit phenomena that are very interesting for theoretical study. In particular, both replacive and displacive transformations occur, and in a narrow range of composition, both processes can take place consecutively. Nickel-rich nickel-aluminum alloys, with a high-temperature B2 phase, undergo a martensitic transformation in a narrow range of composition in which, at low temperature, an ordered phase of Pt<sub>5</sub>Ga<sub>3</sub>-type exists.<sup>1</sup> Moreover, line compounds with complex crystal structures form at the nickel-poor side of the phase diagram.<sup>2</sup>

We now know that most physical properties of metals and alloys can be understood on the basis of their electronic structure. Because of the recent development of efficient and accurate electronic structure methods based on the local-density approximation, many properties of metals and alloys can

now be explained and computed with reasonable accuracy.<sup>3,4</sup> In particular, it has become possible to examine the thermodynamic properties and study the phase stability of alloys from first principles (i.e., from the sole knowledge of the atomic numbers of the constituents).<sup>5</sup> Such first-principles approaches are of great benefit for several reasons:

- A true understanding of phenomena can be obtained as their causes and origins are pinpointed.
- Phenomena that are inherently difficult to control experimentally can be studied without special problems in a theoretical approach (e.g., metastable intermetallic phases).
- Hazardous and expensive experimentation (e.g., experiments involving highly radioactive elements) can be avoided.

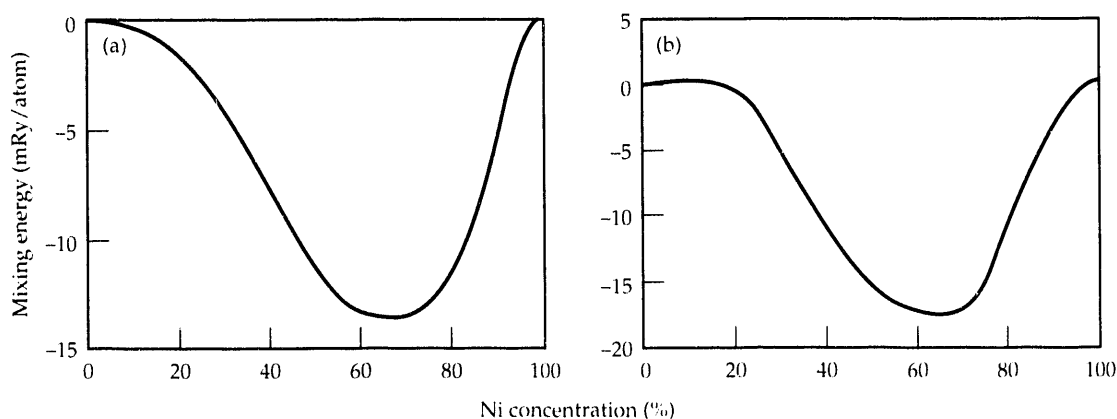
An additional benefit is that first-principles approaches are versatile (i.e., they can be applied to any alloy system).

## The Generalized Perturbation Method

We used the generalized perturbation method (GPM),<sup>6</sup> a rather successful method implemented within a

**Figure 1.**

The computed energy of mixing as a function of composition in nickel-aluminum alloys on the fcc lattice (a), and on the bcc lattice (b).



multiple-scattering formalism. The GPM is based on a perturbative treatment of completely disordered alloys, the energetics of which are described by the mixing energy (a function of composition only). For alloys with long- or short-range order, another energy term needs to be considered: the ordering energy, which consists of products of composition deviations and effective interactions. With both energy terms, the GPM furnishes an expression for the energy of any arbitrary configuration of the alloy. As such, it makes possible a ground-state analysis (i.e., a systematic search for the most probable states of order at zero temperature) and a statistical treatment of temperature (or entropy), so that composition-temperature (phase) diagrams can be derived.

## Results and Discussion

The negative energy of mixing in nickel-aluminum alloys (see Fig. 1) indicates that alloy formation is favored over phase separation. Phase segregation is predicted too, but only at low nickel concentrations in which the energy of mixing has an upward curvature. This feature gives rise to the insolubility of nickel in fcc aluminum. Conversely, on the nickel-rich side, the curvature is downward, and appreciable solubility of aluminum in nickel is predicted. Both predictions agree with experimental observations.

Pair interactions (see Fig. 2) support these predictions. In aluminum-rich alloys, pair interactions tend to be very weak or negative, indicating phase segregation. Weak interactions prevent the usual competing superstructures from forming, thus allowing complex phases to exist.<sup>7</sup> At other compositions, the interactions are strongly positive, which indicates that ordered compounds can be expected.

A ground-state analysis, which uses the interactions as sole input, indicates that several ordered structures can occur. On the fcc lattice, the most probable compounds are NiAl with an L1<sub>0</sub> crystal structure and Ni<sub>3</sub>Al with the L1<sub>2</sub> structure. On the bcc lattice, three phases are possible: NiAl with the B2 structure, Ni<sub>5</sub>Al<sub>3</sub> with a "phase 9"-type of structure (see Fig. 3), and Ni<sub>3</sub>Al with a DO<sub>3</sub> structure. When the structural energy difference between bcc and fcc is considered<sup>8</sup> for the pure elements, the bcc-based ordered structure in NiAl evidently is much more stable than the fcc superstructure. In Ni<sub>3</sub>Al, the situation is reversed, and the fcc superstructure is more stable than the bcc-based structure. In alloys with compositions between NiAl and Ni<sub>3</sub>Al, the fcc- and bcc-based structures clearly are almost equally stable. Therefore, in a narrow range of composition, an alloy may have one structure at high temperature and another at low temperature.

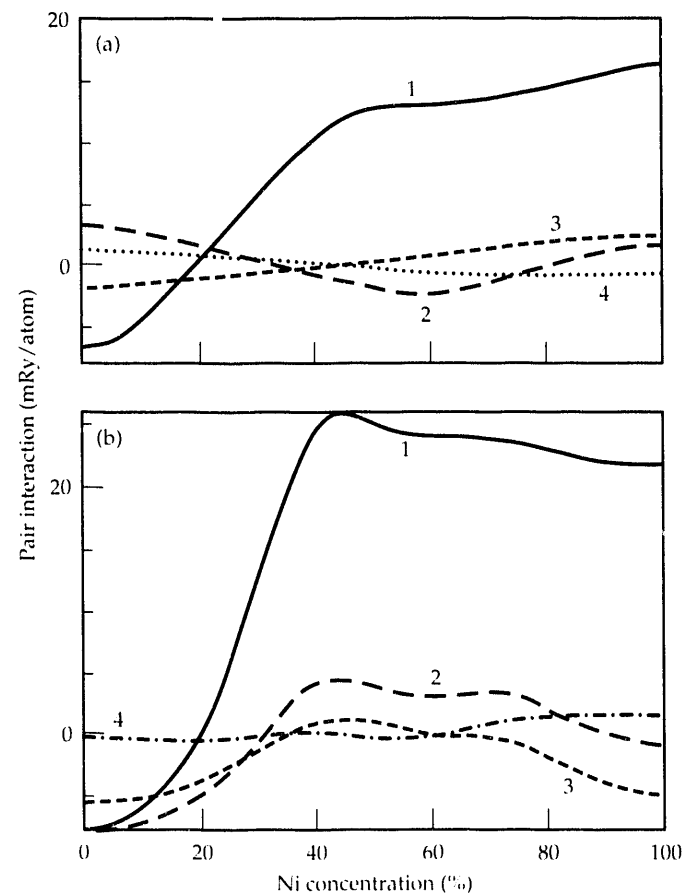
Such a phenomenon gives rise to martensitic transformations, which occur in actual nickel-aluminum alloys with compositions of about 62.5 at.% Ni.<sup>9</sup> In those alloys, we have predicted a bcc-based superstructure, "phase 9," which is almost identical to the actually occurring structure of the Pt<sub>5</sub>Ga<sub>3</sub> type (see Fig. 3). The latter is based on a

bct lattice, which is an interpolation between the fcc and bcc lattices, as one would expect on the basis of these first-principles results.

In addition to revealing the most-probable ordered structures in alloys, we can also use pair interactions to compute the diffuse scattering induced by short-range order. We have found these computations to agree remarkably well with highly accurate measurements of neutron small-angle scattering.<sup>7</sup>

When mixing energies and pair interactions are introduced into a statistical thermodynamic description of the Ising model such as the cluster variation method (CVM), the free energy can be evaluated as a function of temperature so that the phase diagram can be obtained. We computed the nickel-rich portion of the nickel-aluminum phase diagram (see Fig. 4) and found agreement with the experimental phase diagram to be very good. The phases and phase boundaries agree well with experiment, and the only shortcomings of our approach are that we do not have a theoretical framework that allows us to consider the liquid phase, nor can we at present properly include the Ni<sub>5</sub>Al<sub>3</sub> phase on the bcc lattice. Because features in the phase diagram are

**Figure 2.** The computed pair interactions in the 1st, 2nd, 3rd, and 4th neighbor shells as functions of composition in nickel-aluminum alloys on the fcc lattice (a), and on the bcc lattice (b).



extremely sensitive to minor inaccuracies in the free energy, we conclude that our approach produces a very accurate description of the energetics of nickel-aluminum alloys. In addition, we have evaluated the stability of metastable phases (such as Ni<sub>3</sub>Al with the DO<sub>3</sub> structure) that is not readily available from experiment.

Other applications of our first-principles description of nickel-aluminum alloys include the computation of antiphase boundaries (APB). For example, the ratio of the APB energies on the [111] plane to those on the [100] plane is an important parameter for dislocation behavior in Ni<sub>3</sub>Al. Our calculations produce a ratio that is very close to the most reliable experimental determination.<sup>7</sup> In short, first-principles calculations are rapidly expanding in areas where previously only experimental measurements were possible. First-principles results will increasingly augment experimental work.

*This work was funded by the Materials Science Division of the Office of Basic Energy Sciences, U.S. Department of Energy.*

## References

1. K. Enami and S. Nenno, "A New Ordered Phase in Tempered 63.8Ni-1Co-Al Martensite," *Trans. JIM* **19**, 571 (1978).
2. M. F. Singleton, J. L. Murray, and P. Nash, "Al-Ni (Aluminum-Nickel)," in *Binary Alloy Phase Diagrams*, 2nd ed., T. B. Massalski, Ed. (American Society for Materials, Metals Park, OH, 1990), p. 181.
3. P. E. A. Turchi, M. Sluiter, F. J. Pinski, D. D. Johnson, D. M. Nicholson, G. M. Stocks, and J. B. Staunton, "First-Principles Study of Phase Stability in Cu-Zn Substitutional Alloys," *Phys. Rev. Lett.* **67**, 1779 (1991)
4. M. Sluiter, D. de Fontaine, X. Guo, R. Podloucky, and A. J. Freeman, "First-Principles Calculation of Phase Equilibria in the Aluminum-Lithium System," *Phys. Rev. B* **42**, 10460 (1990).
5. G. M. Stocks, D. M. Nicholson, F. J. Pinski, W. H. Butler, P. Sterne, W. M. Temmerman, G. L. Gyorffy, D. D. Johnson, A. Gonis, X.-G. Zhang, and P. E. A. Turchi, "Ab Initio Theory of the Ground State

- Properties of Ordered and Disordered Alloys and the Theory of Ordering Processes in Alloys," in *High-Temperature Ordered Alloys II*, *MRS Symp. Proc.* **81**, N. S. Stoloff, C. C. Koch, C. T. Liu, and O. Izumi, Eds (Materials Research Society, Pittsburgh, PA, 1987), p. 15.
6. P. E. A. Turchi, G. M. Stocks, W. H. Butler, D. M. Nicholson, and A. Gonis, "First-Principles Study of Ordering Properties of Substitutional Alloys Using the Generalized Perturbation Method," *Phys. Rev. B* **37**, 5982 (1988).
  7. M. Sluiter, P. E. A. Turchi, F. J. Pinski, and G. M. Stocks, "A First-Principles Study of Phase Stability in Ni-Al and Ni-Ti Alloys," *J. Mater. Sci. Eng.*, in press (1991).
  8. N. Saunders, A. P. Miodownik, and A. T. Dindale, "Metastable Lattice Stabilities for the Elements," *Calphad* **12**, 351 (1988).
  9. Y. Noda, S. M. Shapiro, G. Shirane, Y. Yamada, and L. E. Tanner, "Martensitic Transformation of a Ni-Al Alloy I. Experimental Results and Approximate Structure of the Seven-Layered Phase," *Phys. Rev. B* **42**, 10397 (1990).

**Figure 4.** Nickel-rich portion of the nickel-aluminum phase diagram computed with first-principles energies of mixing and pair interactions and with structural-energy differences from Ref. 8.

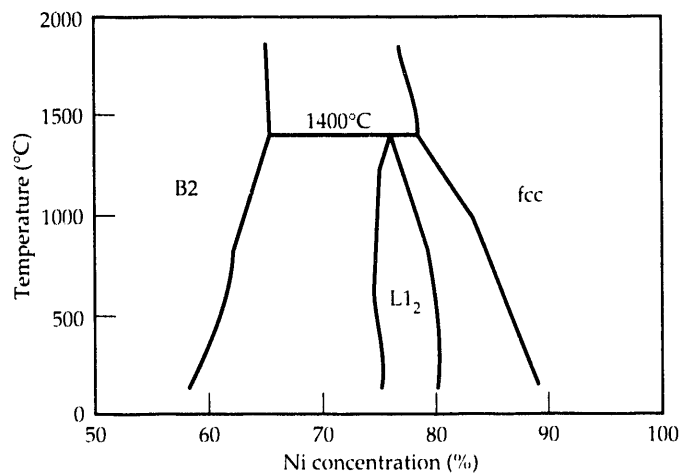
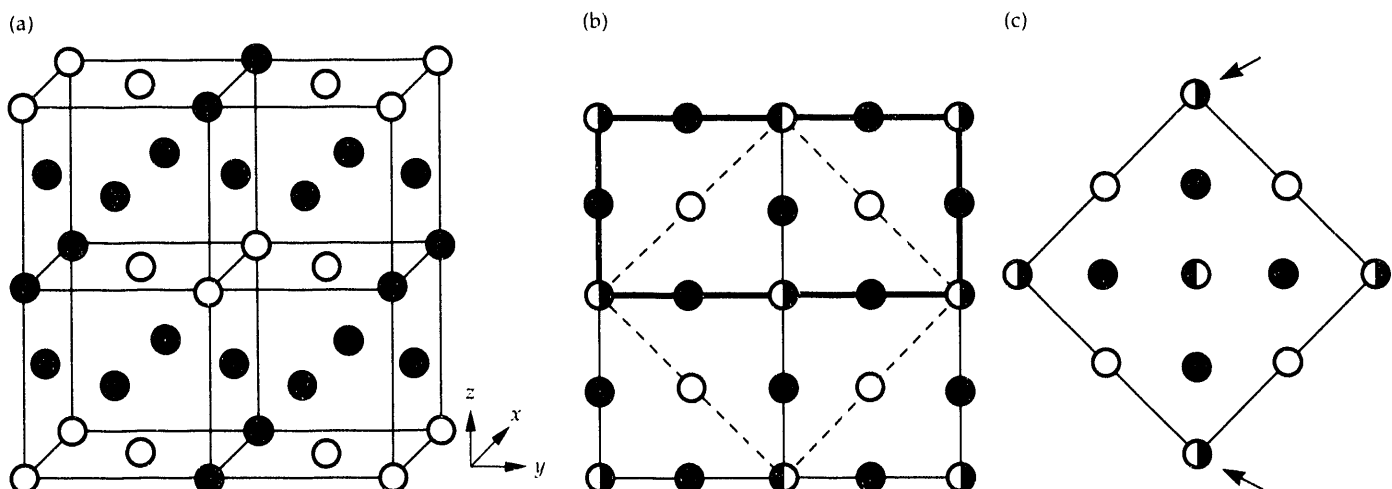


**Figure 3.** Crystal structures with stoichiometry Ni<sub>5</sub>Al<sub>3</sub>: (a) Pt<sub>5</sub>Ga<sub>3</sub> type, (b) Pt<sub>5</sub>Ga<sub>3</sub> type viewed along the z axis, and (c) "phase 9" viewed along a cube axis. The arrows in (c) indicate the difference in atomic occupancy with (b). Black circles denote nickel, and white circles denote aluminum.



# Ordering in the Ti-Pd Alloy System

A. F. Jankowski and P. E. A. Turchi

*Physical vapor deposition provides a direct means to prepare specimens for the study of order-disorder transformations in complex crystal systems, such as titanium-palladium. Rapid quenching takes place from the vapor phase to the solid state, leading to the formation of high-temperature and metastable structures. We observed subsequent ordering by using hot stage electron microscopy in situ. Amorphous (Pd > 33 at.%) and A15 (Pd < 33 at.%) phases are found in the as-deposited structures for the first time.*

## Introduction

The titanium-palladium system is composed of complex crystalline structures, as can be seen in the assessed equilibrium phase diagram.<sup>1</sup> Several examples include Ti<sub>2</sub>Pd (a C11<sub>b</sub> structure of the MoSi<sub>2</sub> type), the high-temperature β-TiPd phase (a B2 structure of the CsCl type), the low-temperature α-TiPd (a B19 structure of the AuCd type) and the reported existence<sup>2,3</sup> of a Ti<sub>4</sub>Pd compound (with an off-stoichiometric A15 structure that may be stabilized by oxygen).

We chose the Ti-Pd system to study short-range order (SRO), which develops in the body-centered-cubic (bcc) solid solution, above or near the possible domain existence of the long-range order of an A15 structure. Predictions from electronic-structure calculations applied to transition-metal alloys show that competition exists between a DO<sub>3</sub> ordered configuration (of the Fe<sub>3</sub>Al type) and an A15 ordered state for Ti-Pd.<sup>4</sup>

The Ti-Pd system is also a good candidate for obtaining an amorphous phase by the use of the physical vapor deposition (PVD) technique for the following reasons.<sup>5-8</sup> The alloy system consists of two or more elements with compositions different from the stoichiometry of a known compound. A large and negative heat of mixing should occur for the binary system. The mobility of one or more of the elements in the amorphous state should be low. The atomic size difference of the constituents is substantial. In addition, a low substrate temperature is used to enhance the rapid quenching rates attainable with PVD.

Therefore, from experimental synthesis of Ti-Pd films, we know that it may be possible to find amorphous phases,<sup>9</sup> study ordering from disordered high-temperature solutions, and create an A15 phase (of A<sub>3</sub>B stoichiometry).<sup>10</sup>

## Experimental Method

As our PVD method, we used dc-mode planar magnetron sputtering, in which we monitored and controlled a sequential deposition of titanium and palladium to produce the

desired film stoichiometry. By alternating source materials to produce nearly submonolayer-thick layers, we formed an atomic-scale intermixing in the deposited film. We sequentially passed (at 0.012 rev/s) substrates of Si(111) and cleaved mica mounted on a copper platen 20 cm over each of three planar magnetrons. Of these, two were for titanium (the major constituent) and the third was for palladium. The contribution in thickness from each magnetron source was constant, ranging from 0.1 to 0.3 nm/rev. The resultant 0.25-μm-thick foils were specular and silver-metallic. The substrate temperature did not exceed 71°C for any deposition run.

We measured the uniformity of composition through the deposited coating using Auger electron spectroscopy (AES) coupled with depth profiling. In AES, the surface is bombarded with a 3-keV, 10-μA electron beam, resulting in Auger electrons being ejected with energies characteristic of each element (i.e., 330 eV for palladium and 418 eV for titanium). A 5-keV, 1.16-μA argon ion beam is used to sputter etch through the sample. We base our calculation of the concentration on the heights of energy peaks (within a 10- to 20-eV window of the characteristic peak) of data acquired in the derivative mode. The Auger composition profiles produce palladium concentration values consistent with calibrated, quartz-crystal monitors. We found oxygen contamination to be completely removed from the top 5- to 7-nm layer of the free surface.

We removed the Ti-Pd films from the mica substrates by immersing the substrates in a bath of 80°C distilled water. We initially examined the foils by using a powder diffractometer operated in the θ/2θ mode, with a graphite monochromator and copper Kα radiation. High-angle scans indicated the crystalline texture, or lack thereof, in the Ti-Pd deposits. The amorphous structure, or very fine grain size, of the deposits and preferred growth orientation do not readily permit crystal-structure identification. Therefore, electron microscopy is the preferred analytic technique for structure determination.

Using bright field (BF) imaging, we examined (in plan view) the Ti-Pd films that floated off the mica substrates and analyzed the crystal structure of the deposits using the selected area diffraction (SAD) patterns. We equated the planar spacing corresponding with the principal reflection in each SAD pattern with the accurate planar spacing measured for that reflection in the  $\theta/2\theta$  scans. Then, we examined samples from each nominal composition in the as-deposited state and annealed them *in situ* to study any ordering that may have occurred. We used a single-tilt temperature stage in a JEOL-200CX side-entry TEM to increase the sample temperature from 25 to 725°C with heating rates of 2 to 10°C/min and an energy-dispersive spectrometer (EDS) in the scanning transmission electron microscopy (STEM) imaging mode for composition analysis of the deposited films. We used the 4.51 keV-Ti K and 2.82-keV Pd L lines in the semiquantitative analysis. The STEM composition data obtained was affected by less than 1 at.% for absorption correction.

We used differential scanning calorimetry (DSC) to identify the temperature of transformations, both the onset of crystallization and the subsequent ordering. Because the foils were very thin, typical DSC samples weighed only 0.33 to 0.41 mg. A sealed pan arrangement helped to isolate such small sample volumes in order to enhance the definition of transformations in the DSC trace. We ran the DSC using a 10°C/min heating rate, comparable to the TEM *in situ*, hot-stage experiments.

## Results

We produced Ti-Pd foils with nominal palladium concentrations ranging from 20 to 66 at.%. We found excellent agreement among the experimental measurements of composition. For example, a film with a nominal concentration

of 25% Pd measured 25.2% using AES and 28.2% using STEM. We also found foils to be amorphous above and crystalline below 33% Pd.

The amorphous foils showed no diffraction contrast in BF imaging and had a characteristic broad, amorphous halo in electron diffraction. The foils underwent amorphous-to-crystalline transformation characterized by a nucleation and grain-growth process (see Fig. 1), typical of many metallic glasses.<sup>11</sup> The crystallite composition measured 52% Pd, whereas the adjoining untransformed matrix measured 63%, indicating the existence of palladium enrichment in the matrix adjoining the crystallization front.

We measured the onset temperature of amorphous-to-crystalline transformation by using a thermocouple attachment to the TEM temperature stage and by DSC. The sequence of transformations, beginning with the crystallization exotherm, are clearly identifiable in the DSC trace (see Fig. 2). The "double" crystallization peak (249 to 280°C) may be attributable to primary crystallization or to the coarsening<sup>12</sup> of micrograins. This behavior is consistent with that of the Ti-Pd alloy at 0.4 to 0.65 $T_{\text{melt}}$  (1393 K). The initial crystalline phase, cubic  $\beta$ -TiPd, is followed upon heating by orthorhombic  $\alpha$ -TiPd and tetragonal  $\text{Ti}_2\text{Pd}$  (< 370°C), and later by  $\alpha \rightarrow \beta$  allotropic transformation (>440°C). The initially observed  $\beta$ -TiPd phase was somewhat unusual because it occurred at a temperature assessed to be above the  $\alpha$ -TiPd phase.

The crystalline films were nanocrystalline in the as-deposited state, with grain sizes typically less than 20 nm. In general, the selected area diffraction patterns (with the exception of the 25% Pd foil) can be indexed using a bcc structure (the high-temperature, disordered crystalline structure sought to study SRO), which may develop before transformation to the A15 phase. The 30% Pd sample has a lattice parameter of 0.345 nm, and the 20% Pd sample has a lattice parameter of 0.322 nm. We annealed samples at 450°C for 70 h and at 550°C for several hours. (Note that both temperatures were below the assessed 595°C temperature of phase separation to  $\text{Ti}_2\text{Pd}$  and to  $\alpha$ -Ti.) The bcc

**Figure 1.** A BF image of crystallites that form in the amorphous matrix with an accompanying SAD pattern along the [011] projection, identifying the B2 structure of  $\beta$ -TiPd. Bar = 0.3  $\mu\text{m}$ .

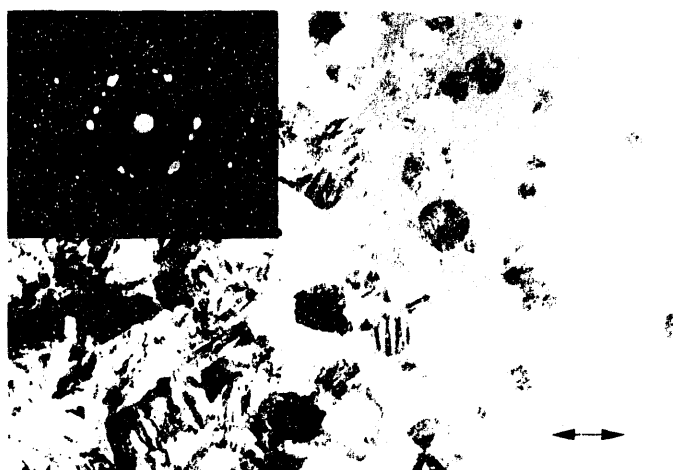
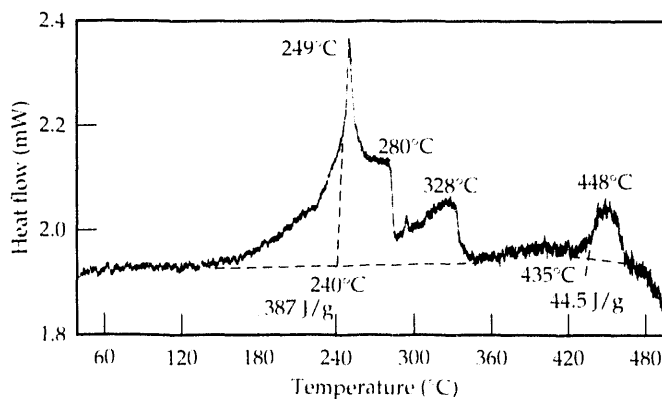


**Figure 2.** A DSC trace of heat flow as a function of temperature, indicating crystallization and grain growth and subsequent ordering.



phase transformed to  $Ti_2Pd$  without any appearance of the A15 structure. Further annealing produced weak  $\alpha$ -TiPd reflections. The as-deposited 25% Pd sample was an A15 phase. The SAD pattern can be completely indexed only to an A15 structure with a lattice parameter of 0.482 nm. A possible fit (see Table 1) to the  $\alpha$ -TiPd phase<sup>12</sup> is not likely because of discrepancies in the planar spacings for the (101) and (311) reflections. The *in situ* annealed sample orders to  $Ti_2Pd$ .

## Discussion

Formation of the bcc structures in the Ti-Pd films, with nominal compositions of 20 and 30% Pd, results from direct quenching from the vapor (i.e., the solid-solution equivalent of the high-temperature  $\beta$ -Ti phase). A nanocrystalline structure results directly from such a quenching process. The lattice parameter for the 20% Pd film follows a Vegard's rule-of-mixtures value, whereas the 30% Pd sample shows a positive deviation. The A15 structure formed at 25% Pd on a room-temperature substrate. Failure of the 20 and 30% Pd samples to exhibit bcc-to-A15-to- $Ti_2Pd$  transformations indicates that the A15 phase field probably lies between approximately 23 and 28% Pd. The observed ordering to the  $Ti_2Pd$  structure at  $450 < T < 550^\circ C$  indicates that the  $Ti_2Pd$  phase may occur in this range, and not at  $595^\circ C$  as indicated in the established phase diagram. Ordering from the bcc structure to an A15 phase may be possible by vapor-depositing 25% Pd films onto cryogenically cooled substrates. In this way, a bcc parent phase may form for Ti-Pd films with compositions between 23 and 28% Pd.

## Summary

We have rigorously identified, for the first time, amorphous and A15 structures of  $Ti_3Pd$ . The amorphous phase occurs in sputtered films with compositions above 33 at.% Pd. The

significance of this composition needs to be theoretically established. The observed A15 structure of  $Ti_3Pd$  agrees with predictions from electronic-structure calculations.<sup>4</sup>

## Acknowledgments

The authors thank the following individuals for their contribution to this effort: L. Summers (XRD), R. Bedford (DSC), L. Schrawyer (AES), and M. Wall (TEM).

*This work was funded by Weapons-Supporting Research.*

## References

1. T. B. Massalski (Ed.), *Binary Alloy Phase Diagrams* (American Society for Metals, Metals Park, OH, 1986), p. 1878.
2. S. Zhang, K. Sumpiyama, and Y. Nakamura, "Nonequilibrium Crystalline and Amorphous Ti-Pd Alloys Produced by Vapor Quenching," *Mater. Trans. JIM* **30**, 733 (1989).
3. E. Raub and E. Roschel, "Die Titan-Palladium-Legierungen," *Z. Metallk.* **59**, 112 (1968).
4. P. E. A. Turchi, G. Treglia, and F. Ducastelle, "Electronic Structure and Phase Stability of A15 Transition Metals and Alloys," *J. Phys. F* **13**, 2543 (1983).
5. R. B. Schwarz and W. L. Johnson, "Formation of an Amorphous Alloy by Solid-State Reaction of the Pure Polycrystalline Metals," *Phys. Rev. Lett.* **51**, 415 (1983).
6. R. B. Schwarz, "Formation of Amorphous Alloys by Solid-State Reactions," *Mater. Sci. Eng.* **97**, 71 (1988).
7. R. B. Schwarz and W. L. Johnson, "Remarks on Solid-State Amorphizing Transformations," *J. Less-Common Met.* **140**, 1 (1988).
8. T. Egami and Y. Waseda, "Atomic Size Effect on the Formability of Metallic Glasses," *J. Non-Cryst. Solids*, **64**, 113 (1984).
9. A. F. Jankowski, M. Wall, and P. E. A. Turchi, "Crystallization of Amorphous Ti-Pd," *J. Less-Common Met.* **161**, 115 (1990).
10. A. F. Jankowski, "A15 Structure Formation in Ti-Pd," *J. Alloys Comp.* **178** (in press) [see LLNL Preprint UCRL-JC-107291 (1991)].
11. R. L. Freed and J. B. Vander Sande, "The Metallic Glass  $Cu_{56}Zr_{44}$  Devitrification and the Effects of Devitrification on Mechanical Properties," *Acta Metall.* **28**, 103 (1980).
12. A. E. Dwight, R. A. Conner, Jr., and J. W. Downey, "Equiatomic Compounds of the Transition and Lanthanide Elements with Rh, Sr, Ni, and Pt," *Acta Crystallogr.* **13**, 835 (1965).

**Table 1.** Planar spacings (nm) and indices (hkl) of the 25-at.% Pd film.

A15 ( $a = 0.482$ )	0.341 (110)	0.241 (200)	0.2155 (210)	0.170 (220)	0.139 (222)	0.134 (320)	0.1205 (400)	0.114 (330)	0.108 (420)
As deposited	0.3399	0.2403	0.2155	0.1640	0.1394	0.1336	0.1212	0.1152	0.1064
$\alpha$ -TiPd	0.332 (101)	0.243 (011)	0.215 (111)	0.1665 (211)	0.141 (020)	0.129 (311)	0.1195 (220)	0.1175 <sup>a</sup>	

<sup>a</sup> Unknown/unreported.

# Deformation Behavior of Pre-shocked Copper as a Function of Strain Rate and Temperature

W. H. Gourdin and  
D. H. Lassila\*

*From quasistatic compression data for 30- $\mu\text{m}$  grain-size samples of oxygen-free electronic (OFE) grade copper shocked to 10 GPa for 1  $\mu\text{s}$ , we derive a value for the thermal component of the mechanical threshold stress (MTS). Model calculations of the flow stress based on this value provide an excellent description of the uniaxial deformation of pre-shocked specimens tested in compression at low and high strain rates. We have obtained excellent agreement with data obtained from electromagnetically launched expanding-ring experiments in which excursions of both temperature and strain rate are large.*

## Introduction

Accurate modeling of material flow behavior at high strain rates is a critical part of realistically simulating warheads for conventional munitions. In such munitions, however, materials are frequently subjected to strong shocks followed by extensive subsequent deformation. Although shock waves are known to alter material constitutive behavior, quantitative treatments have only recently appeared.<sup>1,2</sup> We have studied the stress-strain behavior of previously shock-loaded oxygen-free electronic (OFE) grade copper with 10- and 30- $\mu\text{m}$  grain sizes. Our studies included testing it in compression using conventional equipment and in tension using electromagnetically launched expanding rings (discussed elsewhere<sup>3,4</sup>). Our results show that once the initial value of the threshold stress is specified, the evolution of the flow stress during subsequent deformation is well described by the mechanical threshold stress (MTS) model,<sup>5-7</sup> even for the complex temperature and strain-rate histories experienced during electromagnetic ring expansion.

## Experiment

We fabricated OFE copper test specimens for quasistatic and split Hopkinson pressure bar (SHPB) experiments from cross-rolled plate that we heat-treated to yield a grain size of approximately 30  $\mu\text{m}$ . Copper disks were shock-loaded to 10 GPa for 1  $\mu\text{s}$  by the impact of a copper flyer plate moving at 518 m/s<sup>1,8,9</sup> and then caught in a water bath, which also served as a thermal quenching medium.<sup>1,2,9</sup> We then electrodischarge-machined cylinders 0.5 cm in diameter and 0.5 cm long from the shocked disks (axes normal to the shock front) and tested them for compression at room temperature and an engineering strain rate of  $10^{-3}$  s<sup>-1</sup>. We

tested similar specimens 0.25 cm in diameter by 0.25 cm long with the SHPB at a rate of 2700 s<sup>-1</sup>.

We fabricated specimens for the expanding-ring experiments into disks 4.0 cm in diameter and 0.3 cm thick from forged OFE hot-rolled plate,<sup>6</sup> heat-treated them to yield a grain size of approximately 10  $\mu\text{m}$ , and subsequently shock-loaded them to 11.5 GPa for 1.5  $\mu\text{s}$  by impacting them with a copper plate moving at  $587 \pm 5$  m/s. We used both lateral and forward momentum traps and recovered the specimens in a low-density foam. Thickness measurements after recovery indicated that the residual plastic strain was generally less than 1%, although it did range as high as 2%. We made no attempt to cool the specimens rapidly after shock-loading, and they were warm to the touch (30 to 40°C) when we extracted them from the foam. Finally, we fabricated two sets of rings from the shocked disks, one set with 3.2-cm mean diameters and 0.1- $\times$ 0.1-cm square cross sections and the other with 3.1-cm mean diameters and 0.05- $\times$ 0.05-cm square cross sections.

Figure 1 shows strain-rate and temperature histories typical of the expansion of copper rings with these two cross sections. In Fig. 1(b), we see that rings with the smaller cross section can reach temperatures as high as 400°C.<sup>6,3</sup> Because of the simultaneous variations of strain rate and temperature on a very short time scale, expanding-ring data is uniquely valuable in interrogating material constitutive models.

## Analysis and Results

Within the MTS model,<sup>5,6</sup> the flow stress is given by

$$\sigma = \dot{\sigma}_a M(T) + \dot{\sigma}_t M(T) \left\{ 1 - \left[ \frac{kT}{G_0} \ln \left( \frac{\dot{\epsilon}_0}{\dot{\epsilon}} \right) \right]^{1/q} \right\}^{1/p}, \quad (1)$$



where  $M(T)$  is the ratio of the shear modulus  $\mu$  at temperature  $T$  to its value at  $T = 295 \text{ K}$ ,<sup>4</sup>  $G_0$  is the activation energy ( $G_0 = g_0 \mu b^3$ , where  $\mu$  is the shear modulus and  $b$  is the burgers vector),  $p$  and  $q$  ( $0 \leq p \leq 1$  and  $1 \leq q \leq 2$ ) describe the modification of the activation barrier by the "thermal" portion of the applied stress  $\hat{\sigma}_t$ , and  $\dot{\epsilon}$  is the strain rate. Definitions and values of the various quantities are discussed in detail in Ref. 6. The MTS,

$$\hat{\sigma} = \hat{\sigma}_a + \hat{\sigma}_t \quad (2)$$

characterizes the influence of structure on the flow stress through Eq. (1). The "athermal" portion,  $\hat{\sigma}_a$ , is independent of both temperature and deformation and varies with grain size according to<sup>6</sup>

$$\hat{\sigma}_a = \frac{2.78 \times 10^{-4}}{\sqrt{d}} \quad (3)$$

where  $d$  is the grain size in meters. The "thermal" portion,  $\hat{\sigma}_t$ , is independent of the grain size but changes with

deformation, as specified by an empirical expression for the rate of change of the threshold stress with strain,  $d\hat{\sigma}_t/d\epsilon$ .<sup>5,6,9</sup> Under uniaxial strain in the shock front, we cannot presume that relationships derived for uniaxial stress apply. However, we can reasonably assume that they do describe the evolution of the MTS during subsequent deformation, provided that the initial value of  $\hat{\sigma}_t$  after shock loading is known.

We determined  $\hat{\sigma}_t$  for copper shocked to 10 GPa for 1  $\mu\text{s}$  as follows. Figure 2 shows the stress-strain data for copper tested in compression at a strain rate of  $10^{-3} \text{ s}^{-1}$ . We see that the stress rises abruptly to a yield value well above that typical of the unshocked material.<sup>6</sup> We assume that this yield stress is representative of the threshold stress immediately after final release from shock loading through Eq. (1). By extrapolating the flow curve back to zero strain, we find a characteristic value of about 0.25 GPa for the yield.

For a grain size of 30  $\mu\text{m}$ , Eq. (3) yields  $\hat{\sigma}_a = 0.051 \text{ GPa}$ , and at room temperature,  $M(298) = 1$ . By inverting Eq. (1), we find  $\hat{\sigma}_t = 0.227 \text{ GPa}$ . The calculated isothermal stress-strain response obtained by using this initial value for  $\hat{\sigma}_t$  and the model parameter values given in Ref. 6 agrees well with the experimental data in Fig. 2. A similar calculation under adiabatic conditions<sup>†</sup> for a strain rate of  $2700 \text{ s}^{-1}$  likewise yields excellent agreement with compression SHPB data, also shown in Fig. 2.

For 10- $\mu\text{m}$  grains, Eq. (3) yields  $\hat{\sigma}_t = 0.088 \text{ GPa}$ . We assume that this is simply superimposed on the thermal component of the threshold stress produced by the shock, which we take to be 0.227 GPa. In Fig. 3, calculations and

**Figure 1.** Temperature and strain rate vs true strain for expanding rings with cross sections of  $0.1 \times 0.1 \text{ cm}$  (a) and  $0.05 \times 0.05 \text{ cm}$  (b).

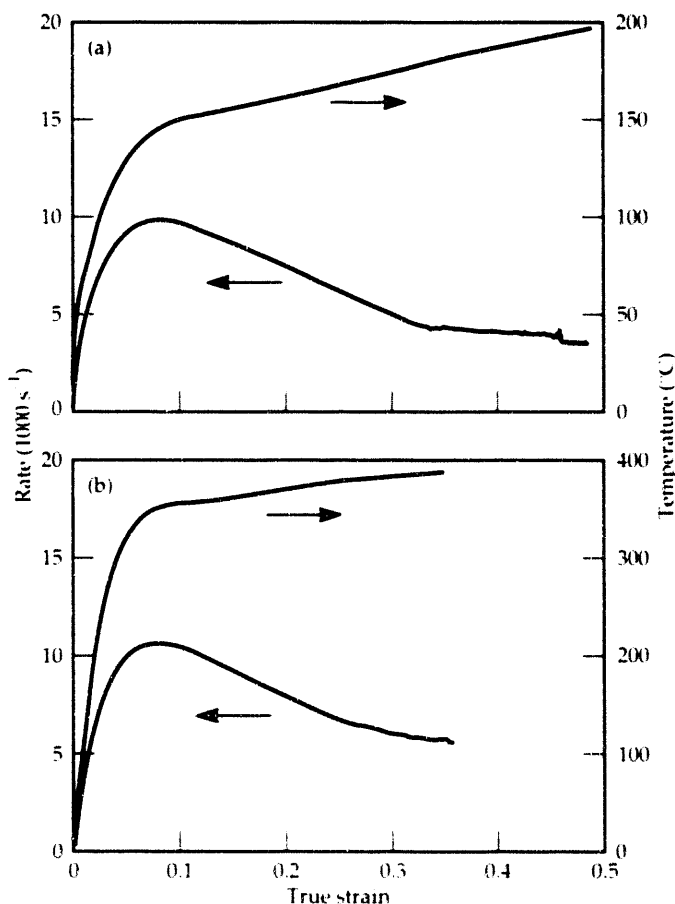
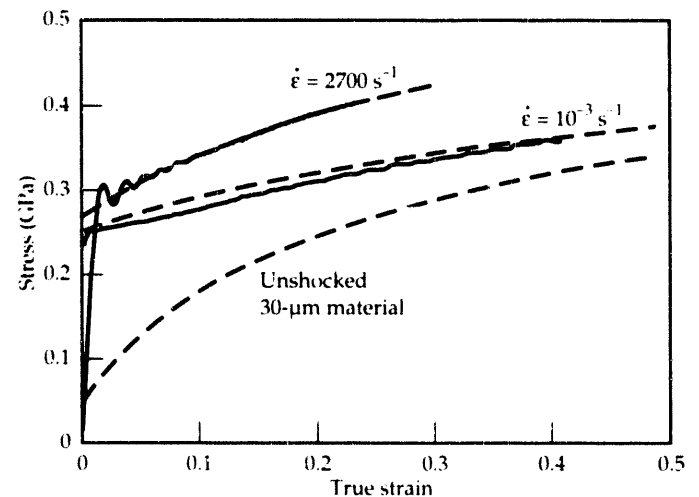


**Figure 2.** Comparison between compression data (solid line) and calculations (broken line) with the MTS model for OFE copper previously shocked to 10 GPa for 1  $\mu\text{s}$ . The calculated (dashed) flow curve for unshocked 30- $\mu\text{m}$  material tested at a constant engineering strain rate of  $10^{-3} \text{ s}^{-1}$  is shown for comparison.



expansion data for rings with both large (150–200°C) and small (350–400°C) square cross sections shocked to 11.5 GPa are in excellent agreement. Of particular interest is the negative slope of the flow stress at low strains for rings with small cross section.

## Discussion

We have used the same value of  $\hat{\sigma}_t$  for calculations of both the compression and ring experiments, even though the shock amplitudes (10 and 11.5 GPa) and shock durations (1 and 1.5  $\mu$ s) applied to the starting materials were different. Gray and Follansbee,<sup>1</sup> however, have noted that both amplitude and duration may affect the structural evolution (and hence  $\hat{\sigma}_t$ ) in the shock front. To address this issue, we interpolated their data in two variables and estimated  $\hat{\sigma}_t = 0.243$  GPa for an 11.5-GPa, 1.5- $\mu$ s shock. The range of experimentally determined values for copper shocked to 10 GPa for 1  $\mu$ s reported by Follansbee and Gray<sup>2</sup> is 0.2 to 0.27 GPa, scattered  $\pm 15\%$  about a mean of 0.235 GPa. This scatter is large compared to the difference (0.016 GPa) between our interpolated value of  $\hat{\sigma}_t$  and the experimental value (0.227 GPa). Thus, we ignore any effect on the flow stress from small differences in the shock amplitudes and durations applied to our specimens. The effect of the residual heat following shock loading and release likewise appears to be negligible.<sup>10</sup>

From Fig. 3, it is clear that the nonmonotonic behavior of the calculated flow stress is crucial to the close agreement between calculation and experiment for the small cross-section ring. The flow stress declines slightly at first, reaches a minimum, and then increases gradually. The unique characteristics of electromagnetic ring expansion play a critical role in inducing this unusual flow-stress

behavior. For strains less than about 4%, the change of temperature with strain  $dT/d\epsilon$  is so large [Fig. 1(b)] that the change in  $\mu$  dominates the behavior of the flow stress. Because the function  $M(T)$  decreases with temperature, the net slope is negative. As strain increases beyond 4%,  $dT/d\epsilon$  declines rapidly, and the moderate increase in  $\hat{\sigma}_t$  with strain (i.e., "strain hardening") overwhelms the effects of any further decline in the shear modulus. The slope  $d\sigma/d\epsilon$  therefore changes sign and becomes slightly positive.

## Conclusion

The MTS model successfully captures the subtleties of temperature and strain-rate effects on the post-shock deformation behavior of 10- and 30- $\mu$ m OFE copper, provided that the initial value of the thermal component of the MTS,  $\hat{\sigma}_t$ , is specified. The value we find, 0.227 GPa, is in good agreement with values in the literature. We conclude specifically that

- When an appropriate initial value of the MTS is specified, the post-shock flow stress of OFE copper is well described by relationships derived independently for unshocked materials.
- The structural changes produced by a shock wave are superimposed on both the initial structural characteristics of a material and the structural changes that accompany subsequent deformation.
- The temperature dependence of the shear modulus is crucial to the proper description of the evolution of the flow stress when heating rates and temperatures are high.

## Acknowledgments

The authors gratefully acknowledge the invaluable help of Patricia Lewis, Ralph Boling, Larry Crouch, and Stuart Weinland in carrying out the expanding-ring experiments, and Mary LeBlanc in carrying out the mechanical testing. G. T. Gray III shock-loaded the 30- $\mu$ m specimens.

*This work was funded by the Joint DoD/DOE Munitions Development Program.*

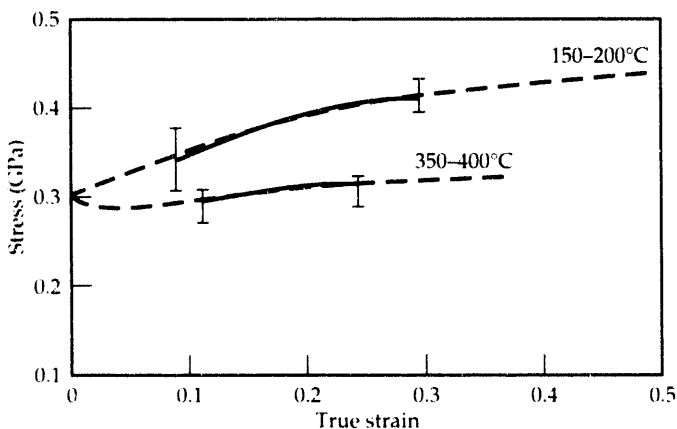
\* Mechanical Engineering Department, LLNL

† All of the plastic work is assumed to be deposited in the sample as heat.

## References

1. G. T. Gray III and P. S. Follansbee, "Influence of Peak Pressure and Pulse Duration on Substructure Development and Threshold Stress Measurements in Shock-Loaded Copper," in *Impact Loading and Dynamic Behaviour of Materials (Proc. IMPACT '87 Int. Conf. Impact Loading and Dynamic Behaviour of Materials, Bremen, 1987)*, C. Y. Chiem, H.-D. Kunze and L. W. Meyer, Eds. (DGM Informationsgesellschaft mbH, Oberursel, FRG, 1988), pp. 541–548.

**Figure 3.** Comparison of tensile data (solid lines) and calculations (broken lines) for expanding rings of OFE copper with 10- $\mu$ m grain size previously shocked to 11.5 GPa for 1.5  $\mu$ s.



2. P. S. Follansbee and G. T. Gray III, "Dynamic Deformation of Shock Prestrained Copper," submitted to *Mater. Sci. Eng.* [see Los Alamos National Laboratory, Los Alamos, NM, Preprint LA-UR90-528 (1991)].
3. W. H. Gourdin, "Analysis and Assessment of Electromagnetic Ring Expansion as a High-Strain-Rate Test," *J. Appl. Phys.* **65**, 411 (1989).
4. W. H. Gourdin, S. L. Weinland, and R. M. Boling, "Development of the Electromagnetically Launched Expanding Ring as a High-Strain-Rate Test Technique," *Rev. Sci. Instrum.* **60**, 427 (1989).
5. P. S. Follansbee and U. F. Kocks, "A Constitutive Description of the Deformation of Copper Based on the Use of the Mechanical Threshold Stress as an Internal State Variable," *Acta Metall.* **36**, 81 (1988).
6. W. H. Gourdin and D. H. Lassila, "Flow Stress of OFE Copper at Strain Rates from  $10^{-3}$  to  $10^4$  s $^{-1}$ : Grain-Size Effects and Comparison to the Mechanical Threshold Stress Model," *Acta Metall. Mater.* **39**(10), 2337 (1991).
7. P. S. Follansbee, "High-Strain-Rate Deformation of fcc Metals and Alloys," in *Metallurgical Applications of Shock-Wave and High-Strain-Rate Phenomena*, L. E. Murr, K. P. Staudhammer, and M. A. Meyers, Eds. (Marcel Dekker, Inc., New York, 1986), Ch. 24, pp. 451–479.
8. D. H. Lassila, M. LeBlanc, and G. T. Gray III, "High Strain Rate Deformation Behavior of Shocked Copper," *Proc. Int. Conf. on Shock-Wave and High-Strain-Rate Phenomena in Materials*, EXPLOMET '90, San Diego, CA, August 12–17, 1990 (in press) [see LLNL Preprint UCRL-JC-103469 (1990)].
9. G. T. Gray III, P. S. Follansbee, and C. E. Frantz, "Effect of Residual Strain on the Substructure Development and Mechanical Response of Shock-Loaded Copper," *Mater. Sci. Eng.* **A111**, 9 (1989).
10. W. H. Gourdin and D. H. Lassila, "The Mechanical Behavior of Pre-Shocked Copper at Strain Rates of  $10^{-3}$ – $10^4$  s $^{-1}$  and Temperatures of 25–400°C," *Mater. Sci. Eng.* (in press) [see LLNL Preprint UCRL-JC-107280 (1991)].

# Fatigue Behavior of U-6Nb Alloys

M. J. Strum, J. W. Elmer,  
N. Q. Nguyen, and  
D. C. Freeman\*

***We evaluated the fatigue behavior of uranium alloy U-6Nb aged at 200°C for 2 h using fracture mechanics methods. We found that crack closure associated with crack branching results in a fatigue threshold of 3.2 MPa√m at a load ratio of 0.1. Tests at high load ratio eliminate crack closure and reduce the fatigue threshold to 0.9 MPa√m in air and to 1.5 MPa√m in dry nitrogen. Fatigue-crack growth rates drop by a factor of 5 in dry nitrogen because of corrosion fatigue in air at 50% relative humidity.***

## Introduction

The strength and corrosion properties of U-6Nb strongly depend on the thermal history of the material. Two heat-treatment conditions are commonly used: a low-yield-strength, solution-quenched condition or a higher-yield-strength, quenched-and-aged condition heat treated at 200°C for 2 h. We evaluated both conditions for fatigue-crack-propagation behavior, emphasizing the properties in the aged condition.

By determining the fatigue crack growth rate (FCGR) behavior of U-6Nb, we could then use fracture-mechanics methods to assess the lifetime of the U-6Nb components. To support the fracture-mechanics assessments, we identified the crack initiation sites by analyzing the fracture surfaces of stress-life test specimens. We also evaluated the sensitivity of fatigue behavior to the test environment and mean tensile stresses. From this approach, we obtained a full set of design data for U-6Nb structural applications.

The general corrosion resistance of U-6Nb decreases substantially when aged to peak strength, although it remains high for material aged at 200°C for 2 h. Aging imparts a more significant decrease in the resistance to stress corrosion cracking (SCC). We evaluated the potential for synergism between corrosion and fatigue damage in aged U-6Nb by comparing FCGRs in laboratory-air and dry-nitrogen environments. No fatigue-crack-propagation data has been previously reported for U-6Nb in any environment. However, Finnerty et al.<sup>1</sup> reported that smooth-bar fatigue strengths of oil-quenched U-6Nb decrease from 260 MPa in humid nitrogen to 240 MPa in humid air. Susceptibility to SCC also depends strongly on environmental conditions: increasing moisture content increases SCC susceptibility in H<sub>2</sub> or O<sub>2</sub> environments, but not in N<sub>2</sub> environments.<sup>2</sup>

Of particular interest in high-cycle fatigue designs is the fatigue threshold, commonly defined as the critical stress intensity range for growth rates below 10<sup>-7</sup> mm/cycle. Many investigators have reported sensitivity of the fatigue

threshold to microstructure and environment. They most often attributed the effects to closure of the crack tip prior to reaching the minimum load in a fatigue cycle. Crack closure increases the apparent fatigue threshold but does not represent the intrinsic fatigue resistance of the material. Short cracks, noncorrosive environments, and mean tensile loads can all reduce the fatigue threshold by reducing or eliminating crack closure.

We measured the degree of crack closure in U-6Nb for long cracks, and we determined the fatigue threshold for both standard and high mean tensile loads for the environments mentioned.

## Experimental Methods

The U-6Nb material used in this study was as-quenched, 16-mm-thick, cross-rolled plate produced at the Oak Ridge Y-12 Plant in Tennessee. We cut all test specimens such that their loading direction was parallel to the plane of the cross-rolled plate and heat-treated the rough-machined samples at 200°C for 2 h in an air furnace. We then finish-machined the test specimens using a series of decreasing cut depths, with a finish cut depth of 0.025 mm.

The FCGR measurements followed the procedures recommended in American Society for Testing Materials (ASTM) Standard E647-88 for compact tension specimens. We obtained all near-threshold FCGR data by means of decreasing-*K* tests, in which we used a stepped load-shedding technique, applying the fatigue cycle by a hydraulic actuator with a square-wave function-generator at a frequency of 20 Hz.

We measured crack length by two methods. In early testing, we wedged the crack open at the minimum load and measured the crack length to the nearest 0.025 mm by optical measurements at 100× magnification. In later tests, including all environmental testing, we used an *in situ* DCPD (direct-current potential-drop) method to measure crack length (see Ref. 3 for detailed procedures). We evaluated environmental effects using a leak-tight environmental chamber operated at a slight, positive, purge-gas pressure.

## Results

We measured the baseline fatigue-crack propagation behavior for aged U-6Nb (200°C/2h) in laboratory air at a load ratio of 0.1 using a total of six test specimens. The relationship between FCGRs and cyclic stress intensities (see Fig. 1) consists of three distinct regions of crack growth-rate behavior. As stress intensities ( $\Delta K$ ) increase above  $20 \text{ MPa} \sqrt{\text{m}}$ , the FCGRs increase rapidly. This low-cycle fatigue region is bordered by a mid-growth-rate region that can be characterized as low- $n$  Paris Law behavior,

$$da/dN = C(\Delta K)^n, \quad (1)$$

where  $da/dN$  is the crack growth rate (length per cycle),  $C$  is an empirically determined coefficient, and  $n$  decreases from 3.9 in the low-cycle fatigue range to as low as 0.4 in the mid-growth-rate region. With further decreases in  $\Delta K$ ,  $n$  rapidly increases, and a fatigue threshold is reached at which growth rates rapidly decrease to below  $10^{-7} \text{ mm/cycle}$ . The fatigue threshold occurs at a cyclic stress intensity of  $3.2 \text{ MPa} \sqrt{\text{m}}$  under these conditions.

The dependence of the fatigue-threshold value on testing conditions was further evaluated. For long cracks cycled at a load ratio of 0.1 in laboratory air, we determined that crack-tip closure occurs above the minimum cyclic load. Compliance measurements of crack opening displacement vs load indicated the stress intensity required to open the crack tip to be  $1.2 \text{ MPa} \sqrt{\text{m}}$ . The effective cyclic stress intensity at threshold was therefore actually  $2.2 \text{ MPa} \sqrt{\text{m}}$  vs the applied value of  $3.2 \text{ MPa} \sqrt{\text{m}}$ . This crack-tip closure was eliminated when the fatigue crack was widened with a saw cut to within approximately 1.5 mm of the crack tip.

We further evaluated fatigue behavior in the absence of crack-tip closure effects by instituting fatigue test cycles with constant maximum stress intensity,  $K_{\text{max}}$ . We also used these tests to impose increased mean tensile stresses onto the fatigue cycles. We evaluated two levels of  $K_{\text{max}}$ :  $14.6$  and  $30.5 \text{ MPa} \sqrt{\text{m}}$ . Under these conditions, the fatigue threshold decreased to  $0.9 \text{ MPa} \sqrt{\text{m}}$  and below  $0.6 \text{ MPa} \sqrt{\text{m}}$ , respectively.

We also evaluated the influence of test environment on FCGRs at high mean loads. The shape of the curve of growth rate vs cyclic stress intensity in dry nitrogen is similar to that in laboratory air at 50% relative humidity (RH), as shown in Fig. 2. However, the growth rates decreased in dry nitrogen by a factor of 5. At growth rates of  $10^{-7} \text{ mm/cycle}$  in dry nitrogen, the threshold stress intensity decreased from  $1.5$  to  $0.8 \text{ MPa} \sqrt{\text{m}}$  as  $K_{\text{max}}$  increased from  $14.6$  to  $30.5 \text{ MPa} \sqrt{\text{m}}$ .

The crack propagation behavior in all tests became notably anisotropic as the cyclic stress intensity decreased below approximately  $10 \text{ MPa} \sqrt{\text{m}}$ . Crack propagation deviated from that of a single crack-front to the propagation of multiple cracks in a lightning-bolt morphology, as shown in Fig. 3. The crack path was in all cases transgranular in nature, often characterized by closely spaced jogs in two directions within a particular grain orientation. The crack path also preferentially intercepts inclusions identified as both oxides and carbides.

We also found the sites of fatigue-crack initiation by examining the fracture surfaces of smooth-bar fatigue specimens, as described in Ref. 3. In all cases, the point of

**Figure 1.** Fatigue-crack growth rates in aged U-6Nb at 200°C/2 h for increasing- and decreasing- $K$  tests on 12.7- and 2.5-mm-thick plates at  $R = 0.1$  in air.

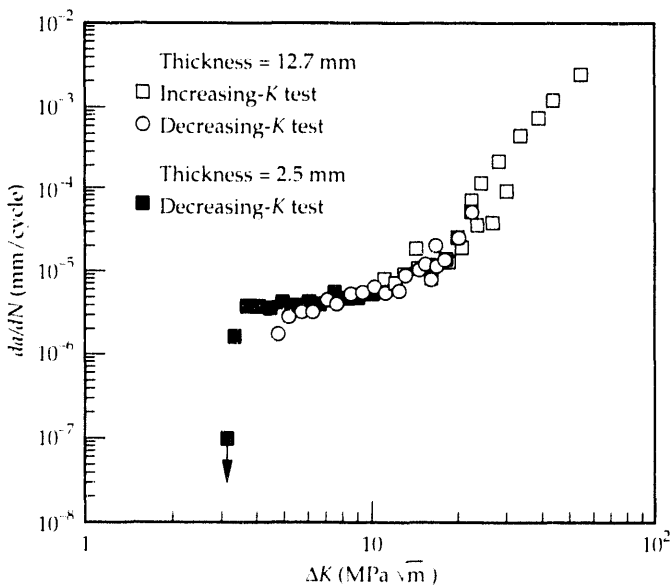
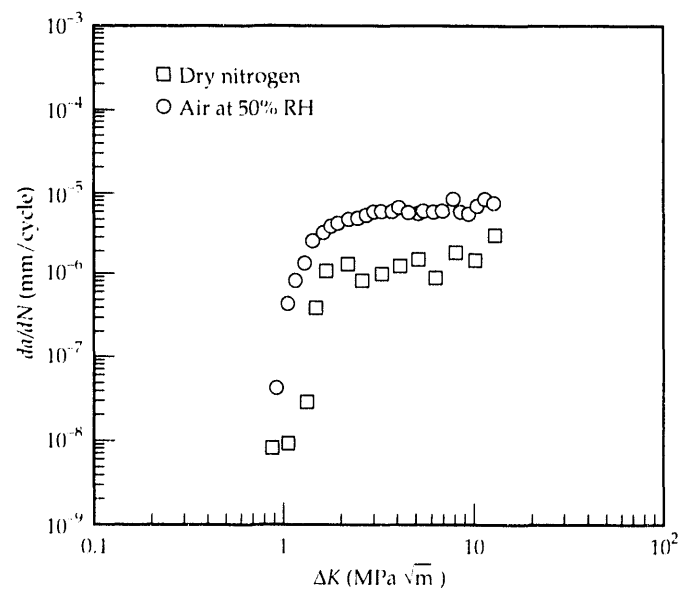


**Figure 2.** Comparison of fatigue-crack growth rates in air and dry nitrogen at a constant maximum stress intensity of  $14.6 \text{ MPa} \sqrt{\text{m}}$ .



crack initiation was a prominent inclusion or inclusion cluster, identified by x-ray fluorescence spectroscopy as niobium carbide and uranium oxide. When we compared the distribution of these inherent defects in U-6Nb plates with producer data, we found it to be typical in terms of maximum size (0.016 mm) and number.

## Discussion

The mechanical behavior of U-6Nb is characterized by high fracture toughness, high resistance to low-cycle fatigue, and low fatigue thresholds. Linking the low-cycle fatigue and the fatigue threshold regimes is a plateau in FCGRs below approximately  $10 \text{ MPa} \sqrt{\text{m}}$ , where  $n$  decreases to as low as 0.4, much lower than the values typical of steels ( $2 < n < 4$ ). While mid-growth rates are not typically sensitive to testing conditions in other systems, the fatigue threshold behavior is well known to be sensitive to mean tensile loads and environment. Aggressive environments can also influence mid-growth-rate behavior through a corrosion-fatigue mechanism. We evaluated these variables of mean tensile loads and test environment to ensure that fatigue-lifetime predictions were not overestimated.

The source of crack closure for long cracks at a load ratio ( $R$ ) of 0.1 in laboratory air was clarified by opening the crack width to within 1.5 mm of the crack tip. The crack closure disappeared, indicating that the source of the observed closure phenomena is long range in nature. Although surface oxidation increased at low growth rates, we expected oxidation-induced closure to be most significant near the crack tip and unaffected by the saw cut. Conversely, we expected the effects of crack branching to be a longer range interaction. Crack surface roughness is known to cause

asperities behind the crack tip to come into contact prior to complete unloading. This mechanism is consistent with the saw-cut results.

We also eliminated far-field closure by imposing fatigue cycles at constant maximum stress intensity. We chose the value of  $14.6 \text{ MPa} \sqrt{\text{m}}$  to maintain minimum stress intensities many times higher than the observed closure value of  $1.2 \text{ MPa} \sqrt{\text{m}}$  and to stay above the region of pronounced crack branching. Although closure was eliminated, crack branching persisted when the cyclic stress intensity range decreased below  $10 \text{ MPa} \sqrt{\text{m}}$ . The fatigue threshold in laboratory air decreased under these conditions from  $3.2 \text{ MPa} \sqrt{\text{m}}$  ( $R = 0.1$ ) to  $0.9 \text{ MPa} \sqrt{\text{m}}$  ( $R = 0.93$ ). This drop is larger than was expected from closure effects alone.

Environmental effects were evaluated by comparison testing in an inert environment of dry nitrogen. FCGRs in dry nitrogen were reduced relative to laboratory air, but the mid-growth-rate plateau remained. This behavior is indicative of corrosion fatigue without stress corrosion cracking. The nitrogen environment did not significantly affect the fatigue threshold or the extent of crack branching.

## Conclusions

We have fully characterized the fatigue-crack-growth behavior of U-6Nb in laboratory air and at a load ratio of 0.1. The results show a high resistance to low-cycle fatigue, a mid-growth-rate plateau insensitive to cyclic stress intensity, and a fatigue threshold of  $3.2 \text{ MPa} \sqrt{\text{m}}$ . By measuring crack closure loads, an effective fatigue threshold of  $2.1 \text{ MPa} \sqrt{\text{m}}$  was calculated for a load ratio of 0.1. Tests at high load ratios with a constant maximum stress intensity eliminated closure and reduced the fatigue threshold at  $10^{-7} \text{ mm/cycle}$  to  $0.9 \text{ MPa} \sqrt{\text{m}}$  at a load ratio of 0.93. Comparison tests in dry nitrogen show a mild sensitivity to environment but no change in the shape of the curves of growth rate vs cyclic stress intensity. A significant degree of crack branching occurs in the mid-growth-rate fatigue range for both environments and with preferential cracking of oxide and carbide inclusions.

*This work was funded by the W-89 Program.*

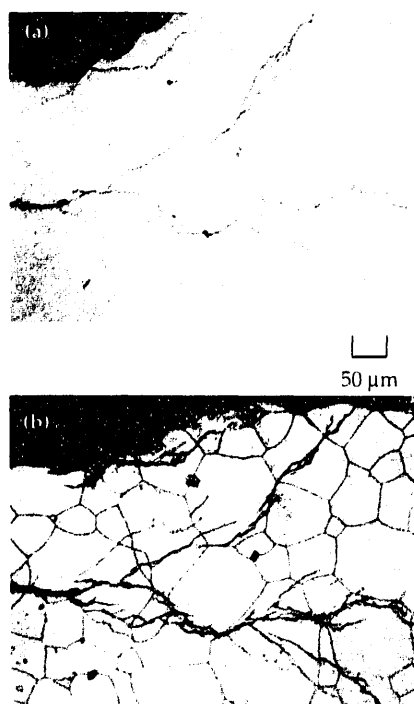
\* Mechanical Engineering Department, LLNL.

## References

1. P. M. Finnerty, S. J. Hull, and P. A. Mackett, "The Effect of Quench Rate on the Corrosion and Mechano-Chemical Properties of the U-6Nb Alloy," *Proc. JOWOG 22C (Uranium) Meeting, June 9-11, 1987*, Lawrence Livermore National Laboratory, Livermore, CA, CONF-8706387 (1987).
2. N. J. Magnani, Sandia National Laboratories, "Stress Corrosion Cracking in U-6Nb Alloys," Sandia National Laboratories, Albuquerque, NM, SAND78-0439 (1978).
3. M. J. Strum, J. W. Elmer, and D. C. Freeman, *Fracture and Fatigue of U-6Nb*, Lawrence Livermore National Laboratory, Livermore, CA, UCRL-JC-110446 (1992).

**Figure 3.**

Profile of fatigue fracture surface, displaying extensive secondary cracking and crack branching at  $\Delta K < 10 \text{ MPa} \sqrt{\text{m}}$ .



# A Model for the Formation of Bands of Ultrafine Particles in Rapidly Solidified Aluminum-Beryllium Alloys

J. W. Elmer, L. E. Tanner,  
and M. J. Aziz\*

*Rapid-solidification processing of aluminum-beryllium alloys produces a dispersion of ultrafine beryllium particles in an aluminum alloy matrix. This dispersion is highly desirable because it strengthens the alloy while providing macroscopically homogeneous mechanical properties. In Al-5 at.% Be, the rapidly solidified microstructure consists of 10-nm-diameter, beryllium-rich particles that are periodically spaced in arrays parallel to the solidification front. To model and explain the formation of this unique banded microstructure, we used a numerical method with liquid-phase nucleation.*

## Introduction

Dispersions of ultrafine beryllium particles in aluminum alloys increase their strength-to-weight ratio while maintaining favorable ductility and fracture toughness. Such dispersions are desirable and have been produced directly through rapid solidification processing by such techniques as melt spinning, arc-splat quenching, and electron-beam resolidification.<sup>1-4</sup> The resulting microstructures contain randomly oriented, ultrafine beryllium particles that lie in arrays parallel to the solidification front. When viewed on edge, these arrays appear as rows of ultrafine particles.

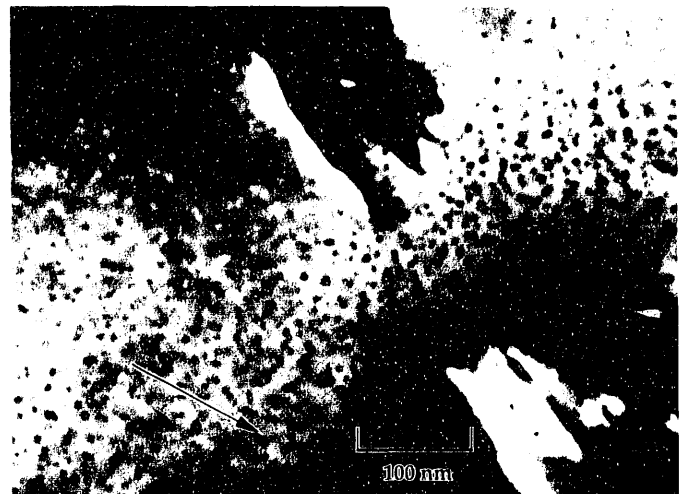
Figure 1 shows a transmission electron microscope (TEM) micrograph of the typical ultrafine particle microstructures produced by electron-beam resolidification at scan speeds greater than 0.1 m/s.<sup>2</sup> Rows of nanometer-sized beryllium-rich particles are evident with a spacing of approximately 25 nm. These rows of particles are aligned parallel to the solidification front, and selected area diffraction further shows that these particles have a random crystallographic orientation.<sup>2</sup>

The periodic nature of this banded microstructure suggests that the ultrafine particles form by a nonsteady-state solidification mechanism. The random orientation of these particles further suggests that they nucleate directly from the liquid ahead of the liquid/solid (L/S) interface. Conventional solidification theory cannot describe the formation of this unusual microstructure. We have developed a model of macroscopically steady-state but microscopically oscillatory motion of the solidification front to explain the formation of this new class of microstructures.

## Rapid-Solidification Model

The aluminum-beryllium phase diagram is a simple eutectic system that exhibits severely limited solubility in the terminal solid phases. Figure 2 shows that the major feature of this phase diagram is the hcp beryllium liquidus, which is flat over a wide range of compositions. This flat liquidus indicates the likely presence of a metastable liquid-phase miscibility gap that may be accessible by rapid-solidification processing.<sup>5</sup> A subregular thermodynamic

**Figure 1.** TEM micrograph of an Al-5 at.% Be alloy solidified at 0.2 m/s. The arrow indicates the solidification direction.

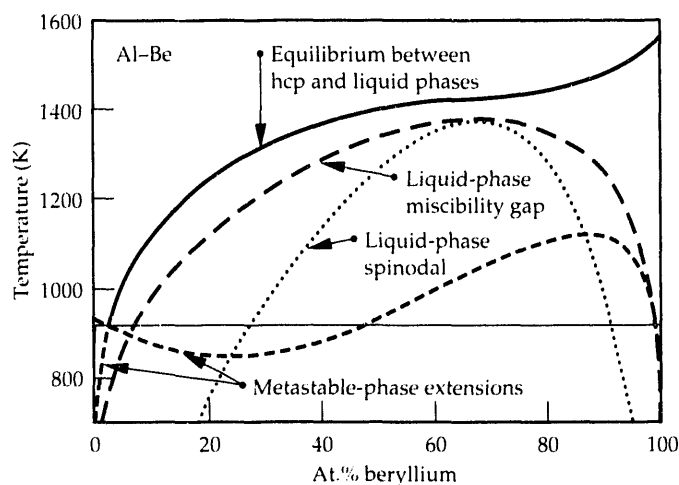


solution model of the aluminum-beryllium alloy system<sup>6</sup> confirms the presence of a liquid miscibility gap, which is a key feature in forming ultrafine particles by rapid-solidification processing.

The solidification mechanism that we propose relies on liquid-phase nucleation (LPN) to form the ultrafine particles. This mechanism involves (1) stabilization by rapid solidification of a plane-front solvent-rich phase; (2) buildup of rejected solute in a diffusional boundary layer ahead of this interface, which slows down the growing crystal matrix; (3) boundary layer composition entering a metastable liquid miscibility gap; (4) homogeneous nucleation of solute-rich liquid droplets in the boundary layer; (5) rapid droplet growth, which is limited by the small size of the boundary layer and accompanied by depletion of excess solute from this layer; and (6) growth of the matrix past the droplets and reformation into a planar interface. Repetition of this mechanism on a nanometer scale accounts for the banded microstructure.

In this investigation, we developed a numerical approach to study the formation of ultrafine particles by modeling the effects of rapid solidification on the diffusive boundary layer and by modeling the homogeneous nucleation of solute-rich droplets from this layer. Inputs to the model are (1) approximate pseudo-steady-state, one-dimensional solute and thermal-diffusion equations; (2) nonequilibrium interface response functions; (3) the kinetics of homogeneous nucleation; and (4) a thermodynamic model of the alloy system, which is needed for quantitative results in (2) and (3). Details of the model are provided in Ref. 2. Results of the model correlate well with experimental data.

**Figure 2.** Al-Be phase diagram, showing the metastable liquid-miscibility gap.



## Results

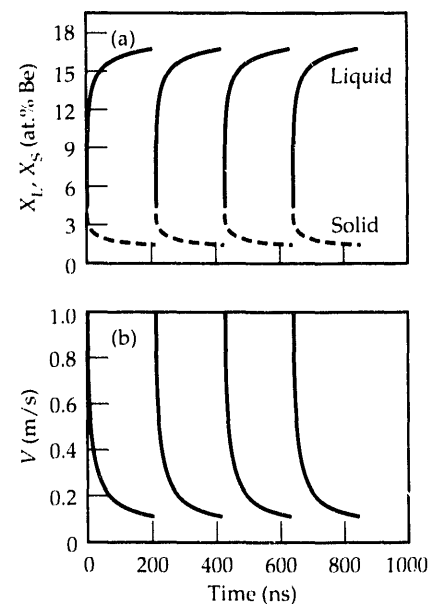
We first used the model to compare the homogeneous nucleation kinetics of liquid beryllium-rich droplets to the kinetics of solid beryllium-rich particles. These results showed that ultrafine particles can form only through nucleation of liquid droplets and that the nucleation time was on the order of 100 ns for typical rapid solidification conditions.<sup>2</sup> These significant findings indicate that bands of ultrafine particles can form by LPN, but only when access to a liquid-miscibility gap exists.

We then used the numerical model to calculate the liquid and solid compositions and the velocity and temperature of the L/S interface as functions of the solidification time for rapidly solidified Al-5 at.% Be alloys. For an average interface velocity of 0.2 m/s, the model shows that the concentration of solute in the liquid increases and the concentration of solute in the solid decreases as the solidification front advances. These results, plotted in Fig. 3(a), show that solute (beryllium) builds up in the liquid boundary layer, reaching 16 at.% just prior to nucleation of beryllium-rich droplets at a solidification time of 220 ns. After accounting for the effects of nucleation on the L/S interface and on the diffusive boundary layer, the calculations show that the nucleation process will continue, leading to a periodic spacing of the ultrafine particles.

During formation of the droplets, the interface velocity oscillates considerably about its mean value. Figure 3(b) is the calculated velocity profile for the nucleation events in Fig. 3(a). The velocity exceeds 1 m/s just after droplet nucleation, but it decreases rapidly as solute builds up in the boundary layer. Therefore, for an average interface velocity of 0.2 m/s, we calculate that the actual interface

**Figure 3.**

Results of the model showing, during four nucleation events, (a) the calculated concentration of Be in the liquid (solid lines) and the solid (dashed lines), and (b) the interface velocity.



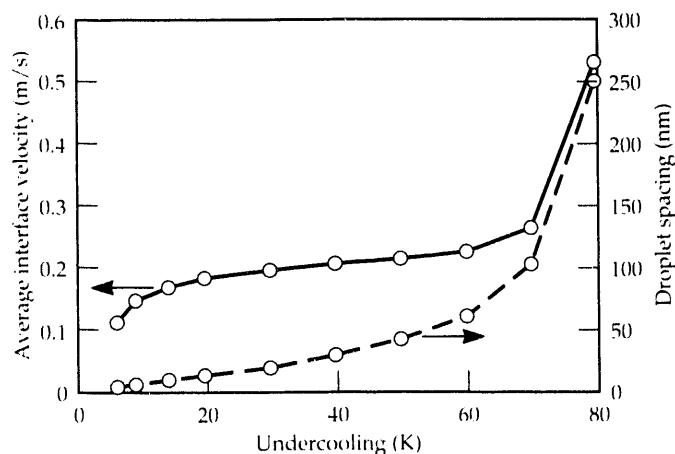


velocity oscillates more than an order of magnitude during the 220-ns nucleation period. Calculations of the interface temperature also show periodic fluctuations, but these fluctuations are small ( $\sim 50$  mK), thus allowing us to consider the solidification process to be isothermal.

The model also calculated the droplet size and further confirmed the LPN mechanism. These calculations predict droplets 11 nm in diameter for the solidification conditions presented in Fig. 3, where the undercooling is approximately 50 K and the average interface velocity is 0.2 m/s. This calculated particle diameter agrees well with the experimentally measured values, which showed particle sizes varying between 7 and 12 nm for electron-beam scan speeds between 0.1 and 0.5 m/s.

Finally, we used the numerical model to calculate the range of initial undercoolings for which ultrafine particles would form in Al-5 at.% Be. These results showed that, for undercoolings lower than 6 K, the supersaturation of the liquid in the diffusive boundary layer is insufficient to reach the miscibility gap, whereas for undercoolings higher than 80 K, complete solute trapping of the beryllium would occur. For all undercoolings between 6 and 80 K, the model predicts periodic nucleation of ultrafine particles. Figure 4 shows the results of the particle spacing and the average interface velocity calculated for a range of initial undercoolings. As the undercooling increases from 6 to 80 K, the average interface velocity increases from 0.1 to 0.53 m/s, and the droplet spacing increases from 5 to 250 nm. These calculations also agree with experimental results, further supporting the proposed LPN solidification mechanism.

**Figure 4.** Results of the model, showing calculations of the average droplet spacing and the average interface velocity as functions of initial undercooling.



## Summary

The rapid-solidification model explains semiquantitatively the diameter and periodic spacing of the ultrafine particles in rapidly solidified aluminum-beryllium alloys. In Al-5 at.% Be, the model predicts that homogeneous nucleation will periodically interrupt the development of the diffusive boundary layer and will produce a banded microstructure that consists of 10-nm-diam, beryllium-rich particles spaced approximately 25 nm apart. Experimental results from rapidly solidified aluminum-beryllium alloys agree with these calculations and support the LPN mechanism. This mechanism relies on thermodynamic access to a liquid-miscibility gap to form the ultrafine particles. Therefore, the rapid solidification model can be further used to predict ultrafine particle formation in other alloy systems with similar phase-diagram features.

## Acknowledgments

The authors acknowledge the assistance of M. A. Wall for transmission electron microscopy and thin-foil specimen preparation, R. Castro for aluminum-beryllium alloy preparation, and L. J. Atherton for helpful discussions and for donating FORTRAN subroutines.

*This work was funded by Weapons-Supporting Research and by the Division of Materials Science of the DOE Office of Basic Energy Sciences.*

\* Harvard University, Cambridge, MA.

## References

1. L. E. Tanner, L. Jacobsen, and R. Gronsky, "Rapidly Solidified Microstructures in Eutectic Alloys," in *Proc. 43rd Annual Meeting of the Electron Microscopy Society of America, 1985* (San Francisco Press, San Francisco, CA, 1985), pp. 50-51.
2. J. W. Elmer, L. E. Tanner, and M. J. Aziz, "Formation of Bands of Ultrafine Particles During Rapid Solidification: Modeling and Direct Observations," submitted to *Acta Metall. Mater.* [see LLNL Preprint UCRL-JC-109384 (1991)].
3. L. E. Tanner, Lawrence Livermore National Laboratory, Livermore, CA, private communication (1991).
4. D. C. Van Aken, and H. L. Fraser, "The Microstructure of Rapidly Solidified Hyper-Eutectic Al-Be Alloys," *Acta Metall.* **33**(6), 963 (1985).
5. W. J. Boettinger and J. H. Perepezko, "Rapidly Solidified Crystalline Alloys," in *Proc. TMS-AIME Regional Meeting, Morristown, NJ, May, 1985*, S. K. Das, B. H. Kear, and C. M. Adam, Eds. (The Metallurgical Society, Inc., Warrendale, PA, 1985), pp. 21-58.
6. J. L. Murray and D. J. Kahan, *Phase Diagrams of Binary Beryllium Alloys*, H. Okamoto and L. E. Tanner, Eds. (American Society for Metals, Metals Park, OH, 1987).

---

## Overview

Energetic materials—that is, compounds of high energy content per unit weight—have long been an area for research and development at the Laboratory because of their obvious importance in the nuclear weapons program. In recent years, emphasis has shifted toward the development, experimental characterization, and theoretical understanding of high-energy-density compounds in a more microscopic way. A special concern has been on safety—to understand how the molecular structure of a compound affects its sensitivity to shock and ultimately to detonation.

The rate at which a reaction triggered by a laser pulse is propagated in triaminotrinitrobenzene has been studied as a function of pressure in a diamond-anvil cell. Discontinuities in the relationship between rate and pressure are correlated with phase changes in the molecular crystal structure, but mechanisms are not yet understood.

The response of a high explosive in an abnormal thermal environment is a critical matter in assessing safety. The heat-conduction code TOPAZ can model part of the response. However, chemical kinetics clearly must play a role as well. The kinetics part has recently been added to produce a revised code TOPAZCHM, which has been used to calculate the time to explosion of realistic explosive assemblies.

The time-honored skills of the synthetic organic chemist continue to contribute to the development of new compounds that may possess more energy than TATB (the usual reference standard for an insensitive high explosive) and that have comparable insensitivity. Such compounds are high-nitrogen, heterocyclic nitro compounds with a high degree of hydrogen bonding, thermal stability, and a planar graphitic structure.

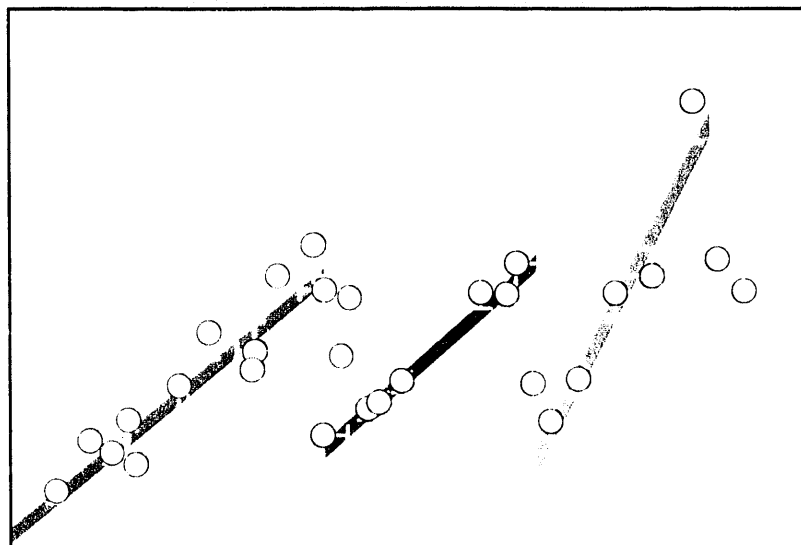
Theoretical interpretations of high-explosive phenomena depend on a molecular-level understanding of matter subjected to a very high pressure over a short time scale. The behavior of a liquid under shock compression has been investigated by the methods of molecular dynamics.

The Energetic Materials Section has traditionally dedicated a significant effort to the development of composite explosives, especially those of lower vulnerability than conventional explosives and with comparable performance and cost. A recent successful formulation consists of inexpensive solid fillers in an elastic, energetic plasticizer-urethane binder matrix.

---

Section 3

**Energetic  
Materials**



**TATB burn velocity in a  
diamond anvil cell.**

# Pressure Dependence of the Reaction Propagation Rate of TATB at High Pressure

M. F. Foltz

*The insensitive high explosive 1,3,5-triamino-2,4,6-trinitrobenzene (TATB), ignited by a laser under high pressure in a diamond anvil cell, exhibits reaction propagation rates (RPR) that are strongly pressure dependent. The observed sawtooth shape of the RPR-vs-pressure curve suggests pressure-induced transitions to higher density phases. A proposed molecular rearrangement, such as that of graphite to diamond, would produce a very stable, dense 3-D network of stacked molecular rings.*

## Introduction

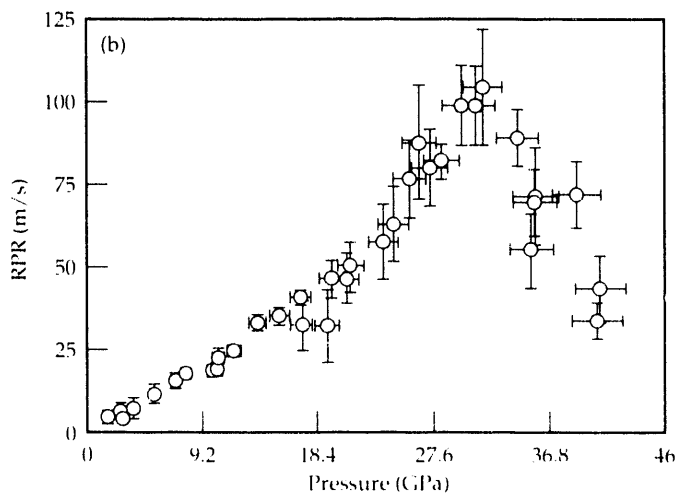
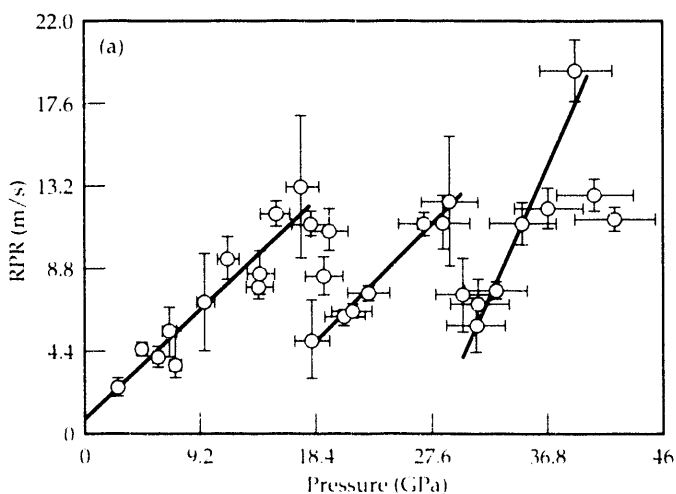
The dynamics of fast chemical reactions in the hostile environment of explosions is poorly understood, although such information is needed to design new insensitive, high-yield explosives. Attempts to quantify the chemistry of the hot reaction zone in large-scale shock experiments<sup>1</sup> have so far met with insurmountable technical problems. As a result, interest has turned to the small-scale (<1- $\mu\text{g}$ ), static, high-pressure testing regime afforded by the diamond anvil cell (DAC). To date, much of the small-scale work done to probe chemistry as a function of pressure and/or temperature has been in a static or thermally reacting scenario.<sup>1-3</sup> The use of a pulsed laser ignition source has been confined primarily to experiments using macroscopic pressed pellets.<sup>4</sup> In this study, the unique use of laser ignition of a sample pressurized in the DAC is coupled with measurements of the rapid reaction propagation rate (RPR) by streak-camera imaging of the reaction zone. We chose the compound 1,3,5-triamino-2,4,6-trinitrobenzene (TATB) for

study as a prototypical insensitive, thermally stable explosive. The phase diagram of TATB is poorly understood, and there is inherent interest in searching for possible high-pressure transitions that affect reactivity.

## Experimental

We used the experimental technique and apparatus similar to those used previously for nitromethane RPR measurements.<sup>5</sup> The Bassett-type DAC consists of two opposing 0.1-carat diamonds sandwiching a drilled stainless-steel gasket. Pressure measurements were made by the standard ruby fluorescence technique,<sup>6</sup> with an argon-ion laser's 514-nm beam focused onto ruby chips embedded in the sample. To load the cell, powdered TATB and ruby chips were compacted between the diamonds to form a gasket-contained pellet. After the pressure was measured, the same argon-ion laser was defocused to fully illuminate the sample area. The reflection of the sample's laser-speckle image was magnified and projected onto the entrance slit

**Figure 1.** (a) Plot of the measured RPR of TATB as a function of pressure. The linear least-squares fit to the data for the three pressure regimes are, with increasing pressure,  $(6.2 \pm 0.71) \times 10^{-1}$ ,  $(6.7 \pm 0.40) \times 10^{-1}$  and  $(15.0 \pm 2.16) \times 10^{-1}$  m/s/GPa. (b) Plot of the measured RPR of nitromethane as a function of pressure (Ref. 5).

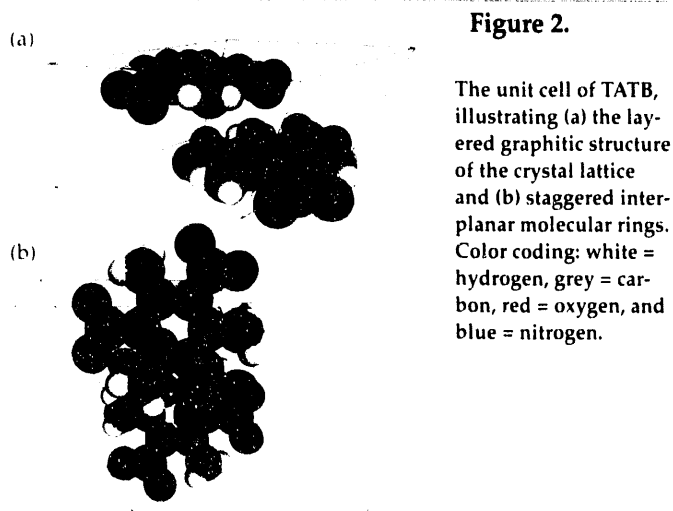


of a streak camera. A single, tightly focused light pulse from a frequency-doubled Nd:YAG laser (532 nm) ignited the sample and triggered the streak camera to capture the reaction event on film. This procedure was repeated anew for all pressure points measured. Because TATB strongly absorbs visible laser light, we placed the ignition zone just beneath the diamond anvil/sample interface, instead of in the center of the sample as in previous work.

## Results

Increasing pressure on TATB caused a progressive shift in color: from yellow at ambient pressure, to red, then to black above 19 GPa. A magnified view of TATB under high pressure prior to ignition revealed inclusions in the highest-pressure region of the sample. These inclusions were distinct from the surrounding highly colored sample. Although pressure release restored most of the sample to the original yellow color, the inclusions remained distinguishable from the bulk. As samples were compressed to pressures up to about 40 GPa, these crystalline zones encompassed an increasing fraction of the total sample area. The inclusions exhibited a very different compressibility from the surrounding material, producing a larger pressure gradient across the cell than is typical in a gasketed DAC.<sup>7</sup>

Figure 1(a) shows the RPR measurements of TATB, with fits to the data for the three pressure regimes. Previous measurements made on the simple energetic molecule nitromethane (NM),<sup>5</sup> are shown for comparison in Fig. 1(b). The RPRs of TATB are 10 times slower than those of NM but also increase generally with greater pressure. Unlike NM, TATB has three distinct pressure regimes distinguished by (1) the pressure dependence of the RPR, (2) the degree of burn completion, and (3) the nature of final products. Each pressure regime is made distinct by saw-tooth breaks in the RPR curve.

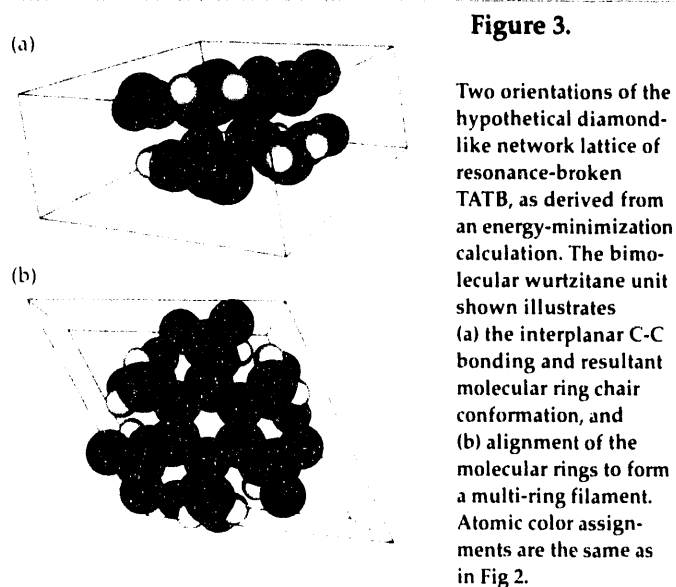


## Discussion

One way to explain the RPR data of TATB is to focus on changes at the molecular level as a function of pressure. Significant changes at this level ultimately are reflected in changes in the bulk thermal material properties. These properties govern conduction and convection of heat from behind the reaction zone to the unreacted explosive ahead of the zone, thereby determining the rate of reaction.

It is reasonable to ask whether the breaks in the RPR curve and the production of high-pressure polycrystalline inclusions are evidence of pressure-induced phase transitions. If not, can they be explained by pressure-induced rearrangement of chemical bonds to form molecules that are more stable than TATB? A reaction in TATB between neighboring amino and nitro groups would form furoxan or furazan cyclic rings by excluding water,<sup>8</sup> a suggested early product in thermal decomposition.<sup>9</sup> Conflicting data, however, suggest that the water produced may be from a limited source (e.g., molecules trapped in the lattice).<sup>10,11</sup> In addition, our preliminary FTIR spectra of high-pressure TATB do not support this theory.

An analogy has been drawn between the structural features of TATB and graphite.<sup>12</sup> The graphitic layered structure and staggered molecular ring configuration of TATB<sup>13</sup> are illustrated in Fig. 2. An increase in pressure would cause the rings to slide into alignment, yielding a high-pressure phase in which infinite stacks of parallel molecules (3-D network TATB) are formed. The lattice structure resulting from an energy minimization calculation (Molecular Simulation Software, Biodesign, Inc.)<sup>14</sup> is shown in Fig. 3. This bond rearrangement gives a more densely packed crystal structure, with stabilization coming from breaking the resonance of the ring and formation of interplanar C-C



bonds. A simple bimolecular unit would be substituted wurtzite. <sup>15</sup> However, the slight twist seen between rings caused by Van der Waals repulsion between neighboring functional groups reveals a source of destabilizing strain. Release of pressure may allow strained, nonbonded rings to spring apart into a structure different from ambient TATB.

The rate of chemical reaction, which is limited by heat loss to the surroundings, increases with temperature. Pressure-induced changes in reaction dynamics affect the temperature of the burn <sup>16</sup> and are seen to affect reaction rate. <sup>17</sup> In addition, thermal decomposition studies of another explosive <sup>18</sup> illustrate phase-dependent chemistry. Phase transitions involve a change in relative molecular orientation. This change can lead to large differences in reactivity, a concept well studied in experiments with oriented molecular beams. <sup>19</sup> The comparison of relative reactivity of crystal phases is the solid-state equivalent to such experiments. Knowledge of the structure of the high-pressure phases should allow construction of simplified potential-energy surfaces necessary for understanding condensed-phase chemistry.

*This work was funded by Weapons-Supporting Research.*

## References

1. W. M. Trott and A. M. Rentlund, "Single-Pulse Raman Scattering Study of Triaminotrinitrobenzene Under Shock Compression," *J. Phys. Chem.* **92**, 5921 (1988).
2. P. J. Miller, S. Block, and G. J. Piermarini, "Effects of Pressure on the Thermal Decomposition, Chemical Reactivity, and Phase Behavior of RDX," *Combustion and Flame* **83**, 174 (1991).
3. A. G. Landers, and T. B. Brill, "Pressure-Temperature Dependence of the Beta-Delta Polymorph Interconversion in Octahydro-1,3,5,7-tetranitro-1,3,5,7-tetrazocine," *J. Phys. Chem.* **84**, 3573 (1980), and references therein.
4. M. W. Leeuw, A. J. Th. Rooijers, and A. C. van der Steen, "Fast Spectrographic Analysis of Laser Initiated Decomposition Reactions in Explosives," in *Proc. Eighth Int. Detonation Symp.* (Albuquerque, NM, 1985), p. 710.
5. S. F. Rice and M.F. Foltz, "Very High Pressure Combustion: Reaction Propagation Rates of Nitromethane Within a Diamond Anvil Cell," *Combustion and Flame* **87**, 109 (1991).
6. R. J. Hemley, P. M. Bell, and H. K. Mao, "Laser Techniques in High-Pressure Geophysics," *Science* **237**, 605 (1987).
7. G. J. Piermarini, S. Block, and J. D. Barnett, "Hydrostatic Limits in Liquids and Solids to 100 kbar," *J. Appl. Phys.* **44**(12), 5377 (1973).
8. J. Sharma, J. D. Hoffsommer, D. J. Glover, C. S. Coffey, J. W. Forbes, T. P. Liddiard, W. L. Elban, and F. Santiago, "Sub-ignition Reactions at Molecular Levels in Explosives Subjected to Impact and Underwater Shock," *Proc. Eighth Internat. Detonation Symp.* (Albuquerque, NM, 1985) p. 725.
9. G. W. Taylor, and G. H. Andrews, Jr., "Flowing Afterglow Spectroscopy: an Untrasensitive Probe into Solid-Phase Decomposition Kinetics," *Proc. Fifth Symp. Chem. Probl. Connected Sub. Explos.* (Sandbyberg, Sweden, 1979), p. 297.
10. E. Catalano, and C. E. Rolon, "A Study of the Thermal Decomposition of Confined Triaminotrinitrobenzene. The Gaseous Products and Kinetics of Evolution," *Thermochim. Acta* **61**, 37 (1983).
11. R. Garza, "A Thermogravimetric Study of TATB and Two TATB-Based Explosives," Lawrence Livermore National Laboratory, Livermore, CA, UCRL-82723 (1979).
12. J. R. Kolb and H. F. Rizzo, "Growth of 1,3,5-Triamino-2,4,6-trinitrobenzene (TATB) I. Anisotropic Thermal Expansion," *Propellants and Explosives* **4**, 10 (1979).
13. H. H. Cady and A. C. Larson, "The Crystal Structure of 1,3,5-Triamino-2,4,6-trinitrobenzene," *Acta Crystall.* **18**, 485 (1965).
14. A. L. Nichols, III, Lawrence Livermore National Laboratory, Livermore, CA, private communication (1991).
15. D. P. G. Hamon and G. F. Taylor, "A Synthesis of Tetracyclo [5,3,1,1<sup>2,6</sup>,0<sup>4,9</sup>]dodecane (Iceane)," *Aust. J. Chem.* **29**, 1721 (1976).
16. C. E. H. Bawn, "The Decomposition of Organic Solids," in *Chemistry of the Solid State*, W. E. Garner, Ed. (Academic Press, New York, 1955), p. 254.
17. S. Srivastava, A. P. Marchand, V. Vidyasagar, J. L. Flippen-Anderson, R. Gilardi, C. George, Z. Zachajka, and W. J. Le Noble, "Pressure Effect on the Product Distribution in Competing Reactions: Formation of a Bis Diels-Alder Adduct via an Aromatizable Intermediate," *J. Org. Chem.* **54**, 247 (1989), and references therein.
18. B. B. Goshgarian, *The Thermal Decomposition of Cyclotrimethylene-triamine (RDX) and Cyclotetramethylene-tetramine (HMX)*, Air Force Rocket Propulsion Laboratory, Edwards AFB, CA, AFRPL-TR-78-76 (1978).
19. R. D. Levine and R. B. Bernstein, *Molecular Reaction Dynamics* (Clarendon Press, Oxford, 1974), p. 88.

# The Synthesis of New, Insensitive Energetic Materials

P. F. Pagoria, C. L. Coon,  
and A. R. Mitchell

*We are synthesizing a series of new, heterocyclic, insensitive energetic materials that possess more energy than 1,3,5-triamino-2,4,6-trinitrobenzene (TATB), currently the industry standard in insensitive high explosives (IHEs). We have synthesized and characterized the first target compound in this series, one of few materials shown to have both sensitivity and performance properties similar to TATB.*

## Introduction

In synthesizing new, energetic materials from the milligram scale to the multikilogram scale, we concentrate in two general areas: (1) new materials with more energy than the highly energetic but somewhat sensitive 1,3,5,7-tetranitro-1,3,5,7-tetraazacyclooctane (HMX) and (2) new, insensitive materials with more energy than 1,3,5-triamino-1,3,5-trinitrobenzene (TATB). TATB is the currently accepted standard in insensitive high explosives (IHEs), which are important in the design of nuclear and conventional weapons. TATB's lack of sensitivity to spark, friction, or impact and its excellent thermal stability are well documented.<sup>1</sup> However, because of its low energy content, alternatives to TATB have long been desired. This, coupled with a growing interest in enhanced safety, has led us to investigate a series of new, insensitive compounds that are predicted to be more energetic than TATB.<sup>2,3</sup>

## Design Approach

The approach taken in the design of these target molecules was to incorporate known, small, insensitive molecules [nitroguanidine (NQ) and 3-amino-5-nitro-1,2,4-triazole (ANTA)] that have a large degree of hydrogen bonding (see Fig. 1) into the target compounds as substituents on an energetic, heterocyclic backbone. We expect this approach to generate new energetic materials with the same physical properties as TATB<sup>1</sup> (i.e., a high degree of hydrogen bonding, good thermal stability, and graphitic crystalline structure), thus giving them similar insensitivity. In addition, the materials should have a higher energy content than TATB because their high nitrogen content should give them higher molecular density and heat of formation, both important contributors to the performance of an explosive. Finally, the synthetic schemes for these molecules are amenable to scale-up and are relatively inexpensive.

## Synthesis and Performance

We synthesized and measured the performance of the first material in this series of new IHEs, and it compares favorably with TATB in tests that measure the insensitivity of a new material (spark, friction, and impact sensitivity tests). It is also thermally stable, with a decomposition point of 330°C (vs 350°C for TATB), and has a density of 1.84 g/cm<sup>3</sup>. The synthesis of this material was scaled up to produce 330 g, enough for a 12-in.-long × 1-in.-diameter cylinder shot used to calculate the material's performance. To produce the material in the form needed, we formulated it with an epoxy resin binder system. This yielded a plastic bonded explosive (PBX), which was mechanically pressed to densities between 97 and 99% of theoretical maximum density (TMD). The cylinder-shot results showed this material to be one of the few known molecules that is essentially equal to TATB in both energy and insensitivity.

This encouraging result led us to investigate other compounds in the series. We synthesized several target molecules (see Fig. 2) on a small scale and determined their structures either spectroscopically or, in many instances, by x-ray crystallographic analysis (XRCA).<sup>\*</sup> Soon, we will subject these compounds to small-scale sensitivity tests to determine which are the most promising candidates for scale-up and performance testing.

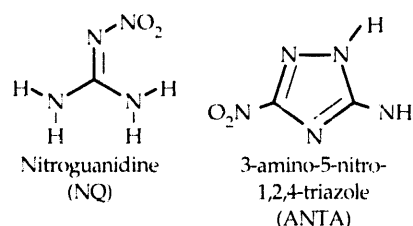


**Figure 1.**

Small, insensitive,  
energetic compounds.

The synthesis of these new target compounds generally involved condensing the sodium salt of ANTA (NaANTA) with a commercially available energetic heterocycle. The synthesis of 2-[1-(3-amino-5-nitro-1,2,4-triazoyl)]-3,5-dinitropyridine [see Fig. 2(a)] involved condensing NaANTA at room temperature with 2-chloro-3,5-dinitropyridine in dimethylformamide (DMF). We poured the reaction mixture into water to precipitate the product as a yellow-orange solid. Recrystallization from  $\text{CH}_3\text{CN}$  yielded the product as yellow needles. XRCA confirmed the structure and showed it to have a crystal density of  $1.86 \text{ g/cm}^3$ .

The reaction of NaANTA with picryl chloride at room temperature in DMF yielded 1-(2,4,6-trinitrophenyl)-3-amino-5-nitro-1,2,4-triazole [see Fig. 2(b)] in 50% yield. Recrystallization from  $\text{CH}_3\text{CN}$  yielded the product as yellow needles. This compound has a complexed solvent of recrystallization, a property that seems to be common in this new class of compounds.

The synthesis of 1,5-bis-[1-(3-amino-5-nitro-1,2,4-triazoyl)]-2,4-dinitrobenzene [see Fig. 2(c)] involved the reaction of 1,5-difluoro-2,4-dinitrobenzene with NaANTA in dry DMF at room temperature for 30 min. Dilution of the reaction mixture with water, followed by acidification, yielded the desired product as a yellow-orange solid in 60% yield. Recrystallization from  $\text{CH}_3\text{CN}$  yielded the product as yellow needles. This compound also has a complexed solvent of recrystallization.

An important intermediate in the synthesis of these target molecules was ANTA, the first reported synthesis of which was a multistep synthetic process with an overall yield of less than 5% (see Fig. 3).<sup>4</sup> This procedure was attractive in

that the starting material, 3-amino-1,2,4-triazole, was commercially available. However, we found the synthesis difficult to reproduce; specifically, nitration of 3-acetamido-1,2,4-triazole did not give the desired product in the yield claimed. In general, the yields were less than 1%, and in many instances, zero. The irreproducibility of this step was attributed to the precipitation of a second major product (3-acetamido-1,2,4-triazolidin-2-one), which resulted from oxidation at the reactive 2-position. By lowering the reaction temperature to  $-25^\circ\text{C}$ , we controlled the precipitation of this unwanted product and obtained 15 to 25% reproducible yields of ANTA. This synthesis still was not considered for scale-up because it was too long, had a low overall yield, and involved a labor-intensive solvent extraction in the nitration step.

The original scale-up procedure, developed at Los Alamos, was a short, two-step procedure with good yields in which commercially available 3,5-diamino-1,2,4-triazole (DAT) was converted to ammonium 3,5-dinitro-1,2,4-triazolate (ADNT), which was then reduced with hydrazine hydrate to give ANTA in a 60 to 70% overall yield.<sup>5</sup> In modifying this procedure to improve safety and convenience, we found that the conversion of DAT to ADNT can be facilitated by using more efficient cooling (dry ice/ $\text{CCl}_4$  rather than ice/salt). This reduced the reaction time from 3 h to between 1 and 2 h. Further, 3,5-dinitro-1,2,4-triazole (DNT), the precursor to ADNT, can be isolated directly from the reaction mixture as a dicyclohexylammonium (DCHA) salt (see Fig. 4), thus avoiding the undesirable extraction step in the ADNT synthesis. The DCHA salt itself has an advantage over ADNT: it is not explosive. The DCHA can be reduced to ANTA in a manner similar to the reduction of ADNT. Further, pouring the hydrazine reaction mixture into 1-M citric acid produces ANTA in sufficient purity to use in subsequent steps, thus avoiding a recrystallization step.

**Figure 2.** New target compounds recently synthesized.

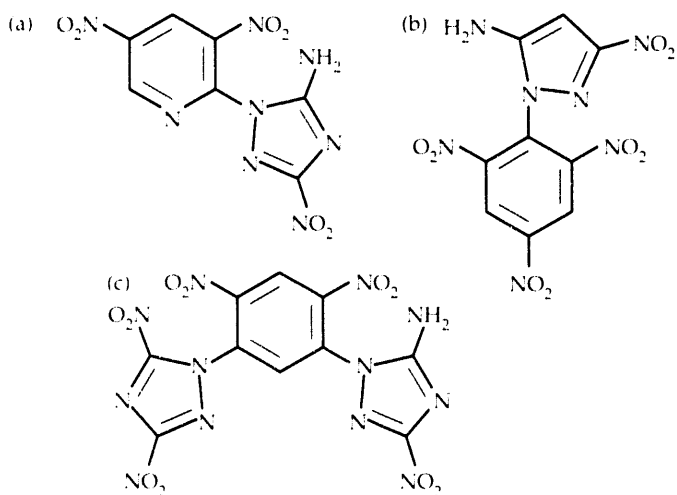
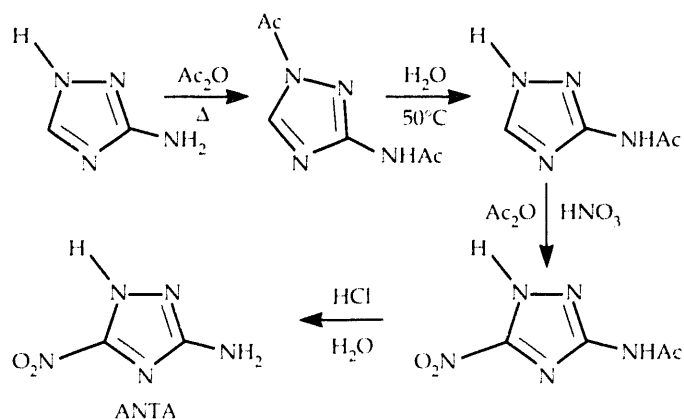


**Figure 3.** First reported synthesis of ANTA.<sup>5</sup>

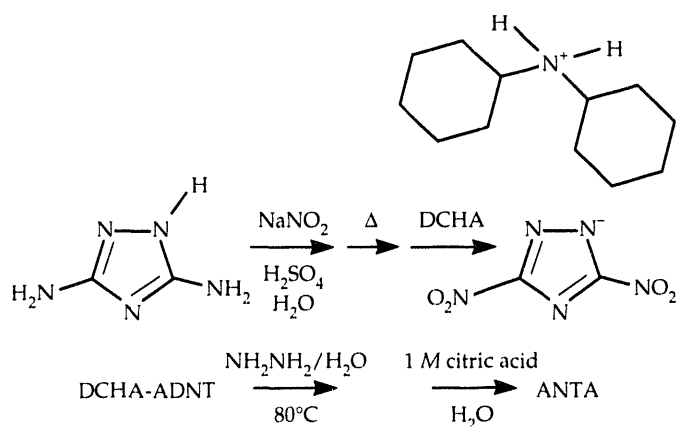




## Summary

We have identified a promising new class of insensitive energetic materials and have synthesized and scaled up the first example of this class of new materials to produce 330 g of material. Performance and sensitivity measurements show it to be one of the few known compounds with performance and sensitivity properties equal to or better than TATB. We are continuing to synthesize other target compounds and to identify small, insensitive compounds that may be used as substituents in energetic, heterocyclic systems.

**Figure 4.** Improved synthesis of ANTA.



The original proposal to design and synthesize high-nitrogen, insensitive, energetic materials was funded by Laboratory Directed Research and Development. Additional funding was provided by B Program/Nuclear Design and the Office of Munitions.

\* X-ray crystallographic analysis courtesy of R. L. Gilardi, Naval Research Laboratory, Washington, DC.

## References

1. S. F. Rice and R. L. Simpson, *The Unusual Stability of TATB: A Review of the Scientific Literature*, Lawrence Livermore National Laboratory, Livermore, CA, UCRL-LR-103683 (1990).
2. M. Cowperthwaite and W. H. Zwisler, *TIGER Computer Program Documentation*, Stanford Research Institute, Menlo Park, CA, Z106 (1973).
3. A. L. Nichols and F. H. Ree, *CHEQ 2.0 User's Manual*, Lawrence Livermore National Laboratory, Livermore, CA, UCRL-MA-106754 (1990).
4. M. S. Pevzner, T. N. Kulibabina, N. A. Povarova, L. V. Kilina, "Heterocyclic Nitro Compounds. 24. Nitration of 5-amino-1,2,4-triazole and 5-acetamido-1,2,4-triazole with Acetyl Nitrate and Nitronium Salts," *Khim. Geterotsikl. Soedin.*, 929 (English translation, 1979).
5. K. Y. Lee, C. B. Storm, *Preparation and Properties of 3-amino-5-nitro-1,2,4-triazole*, Los Alamos National Laboratory, Los Alamos, NM, LA-11907-MS (1978).

# Modeling Chemistry in the TOPAZ Heat-Flow Code

A. L. Nichols III

*The behavior of solid explosives at elevated temperatures is of extreme importance if we are to understand the hazards associated with these materials. Modifications to the LLNL heat-flow code TOPAZ2D incorporate the many effects of chemistry on these materials, making it applicable to a variety of important and interesting problems.*

## Introduction

Although every effort is made to ensure that an explosive is kept in a safe environment, situations may occur in which the "environment" is less than ideal. Two major non ideal "environments" can assault the explosive. The first type of assault is the addition of kinetic energy in the form of a shock wave to the explosive. This type of assault has been reasonably well studied by incorporating a phenomenological pressure-dependent rate law into hydrodynamic codes like DYNA.<sup>1</sup> The second type of assault is the addition of thermal energy in the form of heat, such as by a fire or other means. This work<sup>2</sup> aims to model the thermal assault on explosives by incorporating arbitrary chemistry with Arrhenius kinetics into the LLNL thermal-transport code TOPAZ2D.<sup>3</sup>

## Theory

Chemistry deals with mixtures. If a block of pure material undergoes a chemical reaction, it is no longer a pure material. Consider the reaction  $A \rightarrow B$ . As soon as the reaction begins, the block of material will be a mixture of both materials A and B. To model chemistry in TOPAZ, it was necessary to introduce "mixture materials." A mixture material is a list of the material composition by mole fraction. We assume that mole-fraction-weighted averages of the constituent materials describe the heat capacity  $C_v$  and the thermal conductivity  $\lambda$  of the mixture material:

$$\rho C_v = \sum_i [N_i] \rho_i C_{vi} \quad (1)$$

$$\lambda_l = \sum_i [N_i] \lambda_{li} \quad (\text{Arithmetic}) \quad (2)$$

or

$$\frac{1}{\lambda_l} = \frac{\sum_i [N_i]}{\lambda_{li}} \quad (\text{Harmonic}) \quad (3)$$

where  $\rho_i$  and  $[N_i]$  are the density and the mole fraction, respectively, of the  $i$ th component.

Chemical reactions would be very uninteresting if their only effect were to modify the material properties. However, reactions are normally accompanied by a change in energy. In the case of explosives, for example, the bulk of the thermal energy in the material arises from the chemical reaction. Although a reaction can be written in the form  $A \rightarrow B + \Delta E$  to indicate that energy is being released, the amount of energy released does not depend on the reaction, but rather on the state of the initial and final products. In a constant-volume code like TOPAZ, the appropriate energy is called the internal energy, which is a function of the volume, composition, and entropy. The entropy, while not explicitly used in TOPAZ, can be inferred from the temperature. The internal energy is determined by integrating the heat capacity from the reference temperature to the desired temperature and then adding the reference energy. The energy  $E$  of a mixture material is defined just like the heat capacity:

$$\rho E = \sum_i [N_i] \rho_i E_i \quad (4)$$

As the composition changes, the change in energy between the reactants and the products is fed back into the thermal-transport code as a heat load.

The stoichiometry of the reaction is described by using standard algebraic form. That is, the  $j$ th chemical reaction in a set of reactions is written

$$\sum_i \nu_{i,j} N_i = 0 \quad (5)$$

where  $N_i$  designates the species identity and  $\nu_{i,j}$  shows how much of the  $i$ th species is involved in the  $j$ th reaction. To describe the chemical processes, one must also describe the reaction kinetics. The rate of change of the concentration of the  $i$ th species is

$$\frac{d[N_i]}{dt} = \sum_j \nu_{i,j} k_j \prod_l [N_l]^{\mu_{l,j}} \quad (6)$$

where  $k_j$  is the reaction rate of the  $j$ th reaction. The coefficient  $\mu_{l,j}$  is the order of the  $l$ th species in the  $j$ th reaction. We assume that the reaction rates are functions of temperature only and can be represented with Arrhenius kinetics:

$$k_{i,j}(T) = A_j^0 e^{-E_j^*/k_B T}, \quad (7)$$

where  $A_j^0$  is the pre-exponential frequency factor,  $E_j^*$  is the activation energy, and  $k_B$  is Boltzmann's constant. Therefore, to completely describe a reaction, one must include the complete stoichiometry, reaction-order exponents, the pre-exponential factor, and activation energy.

The chemistry is tightly coupled both to the material properties and to the thermal transfer portions of the code. The actual calculation of the extent of reaction uses an implicit-in-time, self-correcting Newton-Raphson technique on the composition vector in an element. This technique greatly improves the stability and rate of convergence over techniques used previously. The code also reorders and groups the input reactions to improve the run-time efficiency. Minimum and maximum temperatures can be defined to help speed up the calculation. The code ignores all reactions when the temperature is lower than the minimum temperature and will execute only one pass on the Newton-Raphson solver when the temperature is above the maximum temperature.

### Example #1: 1-D HE Burn

Figure 1 shows the modeling of a deflagration of high explosive by using Chemical TOPAZ. The system is a 20- $\mu\text{m}$  cylinder of TATB at an initial temperature of 300 K. The outside temperature is ramped to 1500 K over a period of 5  $\mu\text{s}$ .

The reaction scheme used for the kinetics is the same as that given by McGuire and Tarver.<sup>4</sup> The HE first undergoes an endothermic reaction that creates an intermediate compound, which can then either react with itself or with the original HE to form the final products. This is known as an autocatalytic reaction.

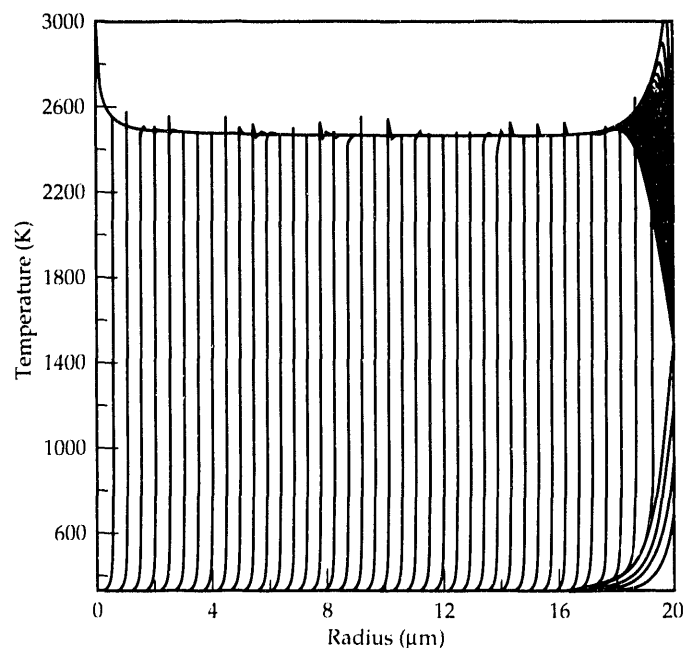
In this example, an initial period in which the HE is heated from the outside precedes a period of rapid transition to a self-sustaining reaction. Note that the rate of deflagration appears to slow to an asymptotic value as the reaction front moves from the preheated material to the bulk material.

Using the times given, we calculate a deflagration velocity for the HE to be approximately 6 m/s. Using an equation-of-state code such as CHEQ,<sup>5</sup> we find that the pressure for the constant-volume burn of TATB is  $12.5 \pm 1$  GPa. The actual burn velocity in the diamond anvil cell at this pressure is  $7.7 \pm 1.6$  m/s,<sup>6</sup> which is in excellent agreement with the calculated velocity, given the simplicity of the model.

### Example #2: Initiator Explosion

In this example, we model the initiator experiment described in Ref. 7. Briefly, the initiator consists of a steel cylinder containing pellets of TATB and PETN. The initiator assembly hangs by tungsten wires in a 55-gal barrel. The bottom of the barrel is filled with water and jet fuel that is ignited at the beginning of the experiment. Figure 2 shows the results of two different calculations for the temperature contours at the point in time when the explosive is going into thermal runaway. The figures on the left correspond to the experiment as performed, while the figures on the right correspond to a related set of experiments. The experimental and calculated times for the event on the left are 360 and 378 s, respectively. In the experiment on the right, the bolts holding the apparatus together did not break, so no experimental time is known. By examining the calculated results, one can understand the difference in these two experiments. A small hole for the slapper wire (not pictured) exists at the base of the PETN pellet. In the system on the left, the PETN starts burning away from this hole, and so any gases that form will pressurize the assembly. In the system on the right, the PETN starts burning next to the hole, and so any gases that form can escape through it, relieving pressure on the assembly.

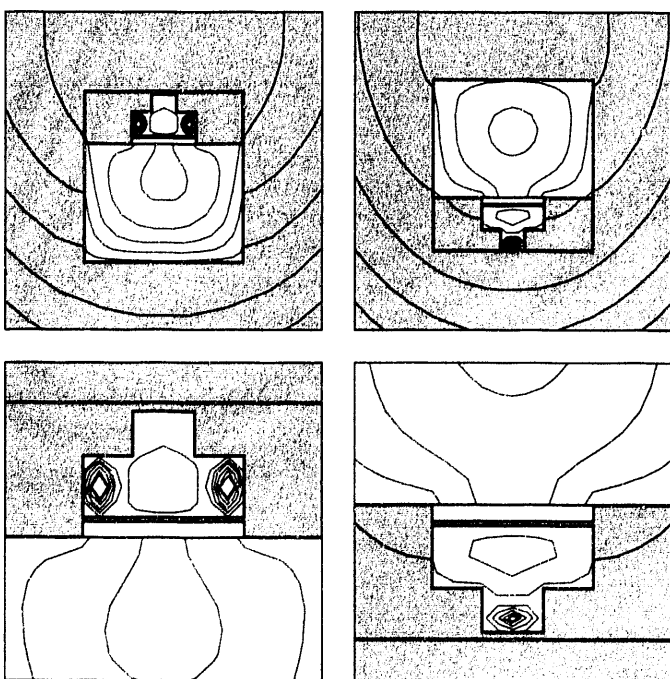
**Figure 1.** The temperature profile of burning TATB at several different times. Burning initiates at the right side and propagates to the left. The time states are 0.5, 1.5, 2.5, 3.5, 4.5, 4.6, 4.7, 4.8, ...



## Conclusion

The chemical version of TOPAZ is being used successfully to model several widely different systems. Although the underlying theory is straightforward, we have developed

**Figure 2.** Temperature contour plots (25 °C apart, increasing from the inner contours) for an initiator at the onset of PETN burn. The flame is below the initiator in each case. The upper figures show the complete device, and the lower figures focus on the PETN. The dark regions are steel; the square region is TATB; the light, T-shaped region is PETN; and the white rectangle is air. The entire device is 2 in. tall and 2 in. in diameter and is symmetric about the vertical axis through the center. The difference between the left and right onset times is about 1 min; the one at right ignites first at about 5 min.



several phenomenological chemical-reaction models that can be applied to a range of problems.

In addition to models for the two types of problems presented in this article, models have been constructed for studying other thermochemical processes such as thermite burns and the deflagration of unconfined explosives.

*This work was funded by the Enhanced Safety, B, and Weapons-Supporting Research Programs.*

## References

1. J. O. Hallquist, *User's Manual for DYNA2D—An Explicit Two-Dimensional Hydrodynamic Finite Element Code with Interactive Rezoning and Graphical Display*, Lawrence Livermore National Laboratory, Livermore, CA, UCID-18756 Rev. 3 (1986).
2. A. L. Nichols III, *Chemical TOPAZ: Modifications to the Heat Transfer Code TOPAZ: the Addition of Chemical Reaction Kinetics and Chemical Mixtures*, Lawrence Livermore National Laboratory, Livermore, CA, UCID-20824, Addendum 1 (1990).
3. A. B. Shapiro, *TOPAZ2D—A Two-Dimensional Finite Element Code for Heat Transfer Analysis, Electrostatic, and Magnetostatic Problems*, Lawrence Livermore National Laboratory, Livermore, CA, UCID-20824 (1986).
4. R. R. McGuire and C. M. Tarver, *Chemical Decomposition Models for the Thermal Explosion of Confined HMX, TATB, RDX, and TNT Explosives*, Lawrence Livermore National Laboratory, Livermore, CA, UCRL-84986 (1981).
5. A. L. Nichols III and F. H. Ree, *CHLQ 2.0 User's Manual*, Lawrence Livermore National Laboratory, Livermore, CA, UCRL-MA-106754 (1990).
6. M. F. Foltz, "Pressure Dependence of the Reaction Propagation Rate of TATB at High Pressure," elsewhere in this Report.
7. R. S. Lee, R. C. Weingart, and J. D. Berg, *Generic Initiation Train for IHE Fuzing*, presented at the 1990 Government/Industry Symp. on Insensitive Munition Technology, White Oak, MD, Mar 13-14, 1990 [Available as LLNL Preprint UCRL-JC-103107 (1990)].

# Harmonic Analysis of Phonon Echoes in Liquids

J. D. Bauer and D. F. Calef

*We have compared phonon quench echoes in supercooled liquid argon with a normal mode analysis of the echoes. The phonon echoes are produced by molecular dynamics simulation. We model the echoes by considering a collection of harmonic oscillators whose frequency distribution is defined by the density of normal modes in the liquid under consideration. For times less than 300 fs, we find that the fluid behaves in a relatively harmonic manner. We also find that low temperatures and short times are best suited to harmonic analysis.*

## Introduction

Our understanding of the dynamics of liquids tends to be based on the perception of a liquid as a “dense gas.” This perception, however, stresses the long time behavior of the liquid. For a short time scale (e.g., shock compression), we need to view liquids more like solids.

Recently, intense interest has been exhibited in the phonon spectrum of simple liquids and clusters.<sup>1–5</sup> Researchers have used both analytic<sup>1</sup> and numerical approaches<sup>3,6</sup> to describe phonon modes in liquids and glasses; here we are concerned with a direct numerical approach. The other approaches have been basically “static,” deriving the distribution of phonon modes from equilibrium averages. Our approach, using “phonon echoes,” is inherently dynamic and can probe questions that equilibrium methods cannot.

The basic theoretical concept behind previous work is very simple. Essentially, a “snapshot,” or single configuration, of a fluid is treated as if it were an enormous molecule, and normal modes are calculated for this “molecule.” The eigenvalues of these modes are taken to yield the squares of the vibrational frequencies of the system. An average is then taken over configurations to obtain the density of states for these phonons.

In general, both positive and negative eigenvalues, or real and imaginary modes, will occur in a fluid. The imaginary modes can be perceived as arising from saddle points or barriers on the many-dimensional potential surface.

However, this perception may be neither reliable nor useful. As the distribution of the modes is calculated by the use of an equilibrium average, no information about the lifetimes of these modes is provided. If the modes lose their identity in less than a vibrational period, they simply represent the static average of the second derivative of the

Hamiltonian, giving little information about true dynamics. Clearly, a method that dynamically probes these modes would greatly clarify the situation.

We are interested in the phenomenon of phonon echoes. Phonon echoes, first discovered by Grest et al.,<sup>7–10</sup> are temperature echoes in computer simulations of liquids and glasses that result from the coherence of particle motions. This coherence is set up in the liquid by pulsing the system through temperature quenches. We believe a better understanding of the harmonic analysis can be gained from the echo phenomenon in liquids. In an actual computer simulation, the intermolecular and intramolecular couplings are, in general, anharmonic. By directly comparing quantities obtained through computer simulations of liquid systems with simple analytic expressions, we can anticipate where the harmonic approximation can be useful. Similarly, by using computer simulation, we can better understand anharmonic effects in phonon-mediated processes. In the particular case of phonon echoes, we can probe the time scale and the regime of density and temperature over which the harmonic approximation is valid.

A related question about the role of homogeneous and inhomogeneous dephasing of these modes remains. If we prepare our system in some initial state (i.e., some set phase relationship exists between the modes characterizing the system), then what is the time scale over which this phase relationship is destroyed? Our methods can address this question.

Ultimately, we anticipate that probing phonon modes will provide insight into the energy transfer between intramolecular and intermolecular degrees of freedom in complex liquids. However, we first want to understand how the normal mode analysis applies to dynamics in simple systems. It is important to realize that the existence

of these modes can be validated by using computer simulation, which allows for experimental verification and exploitation of the theoretical picture.

In this article, we present a comparison of phonon echoes in supercooled argon, obtained via simulation, with the results of simple expressions obtained from harmonic analysis incorporating numerically obtained phonon densities of states.

## Method

We experiment with phonon echoes by means of molecular dynamics (MD) simulation. In an MD simulation, Newton's equations are numerically integrated to give the positions, velocities, and accelerations of the particles that comprise the system of interest. We will consider a Lennard-Jones liquid, a set of particles with an interaction potential of the form

$$V(r) = 4\epsilon[(\sigma/r)^{12} - (\sigma/r)^6] . \quad (1)$$

The parameters suitable for argon are  $\sigma = 3.405 \text{ \AA}$  and  $\epsilon/k = 120 \text{ K}$ . We generally use 500 particles in our simulations.

We start with a well-equilibrated liquid at specified reduced density  $\rho^* = \rho\sigma^3$  and time-averaged temperature  $T^* = kT/\epsilon$ . In our experiment, we chose  $\rho^* = 1.00$  and then studied  $T^* = 0.8$  and  $1.25$ . We produce the echoes by quenching the liquid to  $T^* = 0$  at two separate times separated by an interval  $\tau$ . We produce the quench by setting the velocities of all the particles instantaneously to zero. We then monitor the temperature of the system, defined by the average kinetic energy, and observe an echo—a dip in the temperature—at a time  $\tau$  from the second quench.

The origin of this echo is most easily seen for a harmonic oscillator<sup>7</sup> of frequency  $\omega$ . We consider a particle moving in a potential given by

$$V_H(x) = (1/2) m\omega^2 x^2 , \quad (2)$$

where  $m$  is the particle mass,  $\omega$  is the frequency of the potential well, and  $x_\omega(t)$  is the coordinate that describes the displacement of the particle from equilibrium. If we consider the particle, initially displaced from equilibrium, to be undergoing its natural motion but subject to two velocity quenches separated by a time  $\tau$ , we find the equation of motion for this particle to be given by

$$x_{\tau,\omega}(t) = x_{0,\omega} \cos(\omega\tau) \cos(\omega t) . \quad (3)$$

Here, we measure time from the second quench. If we equate the temperature and the kinetic energy, we find

$$kT(t) = m\omega^2 x_{0,\omega}^2 \cos(\omega\tau) \sin^2(\omega t) , \quad (4)$$

where  $k$  is Boltzmann's constant.

Given a distribution of oscillators, we can express the temperature as an integral over the density of such oscillators:

$$kT(t) = \int D(\omega) m\omega^2 x_{0,\omega}^2 \cos^2(\omega t) d\omega , \quad (5)$$

where  $D(\omega)$  is the density of phonon (vibrational) states.

In our situation, both real and imaginary modes exist. Because only stable modes contribute to making the echo, the appropriate quantity for our purposes is the real part of the liquid density of states, normalized to unity.  $D_R(\omega)$  denotes this quantity. We do not know the initial positions of the oscillators, so we consider an initial distribution of starting positions that is given by a Boltzmann distribution. The probability of finding an  $x_0$  is then given by

$$\rho(x_0) = \left( \frac{m\omega^2}{2\pi kT_0} \right)^{1/2} \exp(-m\omega^2 x_0^2 / 2kT_0) . \quad (6)$$

We note that the average of  $x_{0,\omega}^2$  is  $kT_0/m\omega^2$ , which leads to the final form for the time-dependent reduced temperature:

$$T^*(t) = T_0^* \int D_R(\omega) \cos^2(\omega\tau) \sin^2(\omega t) d\omega . \quad (7)$$

Within the harmonic approximation, Eq. (7) provides a direct connection between the echoes and the phonon density of states.

As previously mentioned, the density of phonon states can be determined via the method put forth by McTague et al.<sup>6</sup> and more recently by Keyes et al.<sup>3</sup> The dynamical matrix elements are given by

$$\mathbf{G}_{i,j,\mu,\nu} = \left. \frac{\partial^2 U_N}{\partial r_i^\mu \partial r_j^\nu} \right|_{\mathbf{R}_0} , \quad (8)$$

where  $U_N = U_N(r_1, \dots, r_N)$  is the  $N$ -body potential,  $r_i^\mu$  is the  $\mu$ th cartesian component of the coordinate of the  $i$ th particle, and  $\mathbf{R}_0$  is the initial configuration about which the potential is expanded. Because the details of this procedure have already been outlined many times (see Refs. 2–6), we do not detail them here. The matrix  $\mathbf{G}$  can be obtained for 20 configurations of a 500-particle system and can be diagonalized for each configuration. The density of states is given by

$$D(\omega) = \frac{1}{3N} \left\langle \sum_{\alpha} \delta(\omega - \omega_{\alpha}) \right\rangle . \quad (9)$$

The brackets denote an ensemble average. As stated previously, we use the real part of this quantity, normalized to unity, and remove the three zero eigenvalues that correspond to uniform translation.

## Results and Discussion

We performed quench experiments for quench times of  $\tau^* = 0.125, 0.15,$  and  $0.2$ , where  $\tau^* = \tau/t_0$ . The characteristic time in the simulation,  $t_0$ , is 2.15 ps. The real times of our quenches correspond to  $\tau = 269, 323,$  and  $430$  fs.

Figure 1 shows the relevant densities of states. Figure 2 shows a trace of  $T^*(t)$  vs  $t^*$  for  $T_0^* = 0.8$  as compared with the results of Eq. (7). The trace represents the average over eight different runs; time zero corresponds to the instant of the second quench.

We note that for  $T_0^* = 0.8$ , the agreement for  $\tau^* = 0.125$  is quite good. At  $\tau^* = 0.15$ , the agreement is not as good because the echo from the simulation has broadened and becomes shallow relative to the harmonic result. By  $\tau^* = 0.2$ , the differences are much greater, but qualitative agreement is still interesting. For the higher-temperature case (not shown), a greater difference occurs, with the best agreement corresponding to the shortest quench time.

We also compared the results of Eq. (7) with MD data from quench sequences starting with  $T_0^* = 0.06$ . At this temperature, where we find 99.3% of the modes to be real and the extent of the excitation to be very small, we expect good agreement with harmonic theory. In fact, we find essentially exact agreement for the 0.125, 0.15, and 0.2 quench times.

An immediate observation from our harmonic model is that, for such a broad distribution of frequencies, no second

echo occurs. The absence of these echoes in the harmonic model results solely from “inhomogeneous” dephasing processes; hence, the lack of these additional echoes in the simulation data is no proof of the breakdown of the harmonic approximation.

Figure 2 clearly shows that the harmonic result tends to be narrower and deeper than the MD data. As we discussed previously, the harmonic model includes inhomogeneous dephasing (i.e., a spectrum of frequencies). Information about homogeneous dephasing is found in the broadening and decreasing depth of the quench. An interesting observation, however, is that, for the longest quench times (Fig. 2, bottom), small echoes resulting from harmonics higher in frequency are seen before the major echoes. Considering the simplicity of the harmonic approximation, these results are encouraging.

The next step in our analysis will be to formulate a harmonic Langevin model. The introduction of a frequency-dependent friction would create a generalized Langevin equation. We hope that this will facilitate studying dephasing processes in liquid systems and also enable us to realize and to compare a simple quantified description of these modes with experiment. We also plan to investigate more-complex systems such as molecular fluids.

**Figure 1.**  $D(\omega)/t_0$  vs  $\omega t_0$  for  $\rho^* = 1.00$ . The solid line represents  $T^* = 1.25$ , and the dotted line represents  $T^* = 0.8$ .

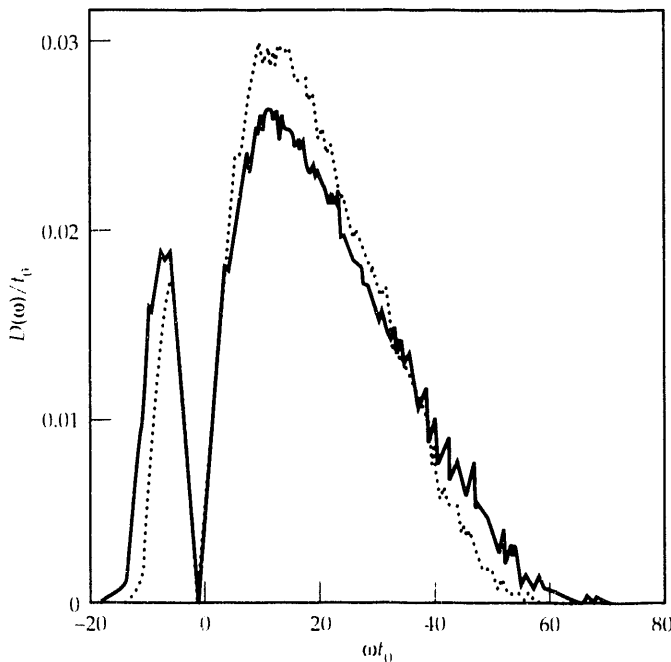
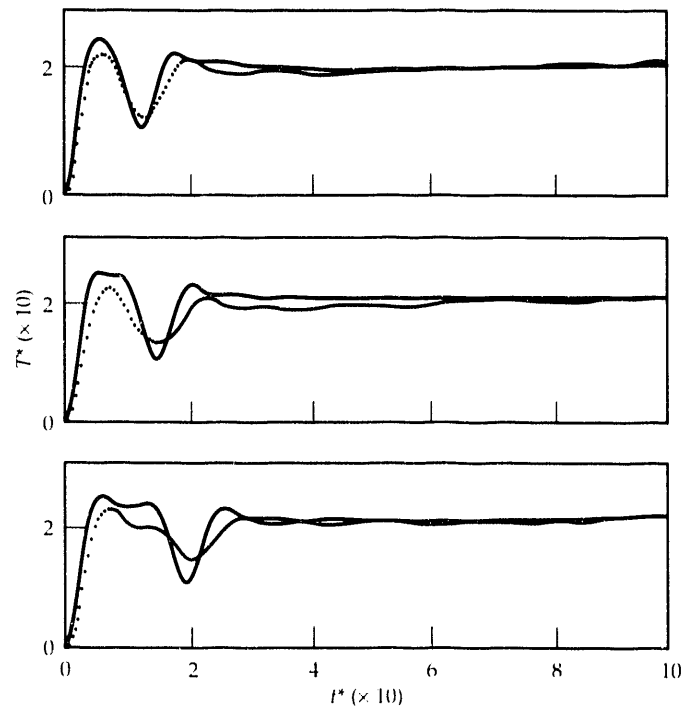


**Figure 2.** Trace of  $T^*(t)$  vs  $t/t_0$  for  $T_0^* = 0.8$ . Top to bottom:  $\tau^* = 0.125, \tau^* = 0.15,$  and  $t^* = 0.20$ , respectively. The dots represent the MD data, and the solid line is the result of Eq. (7).



## Acknowledgment

The authors thank Professor David Coker for helpful discussions.

*This work was funded by Weapons-Supporting Research.*

## References

1. B.-C. Xu and R. M. Strat, "Liquid Theory for Band Structure in a Liquid. II. *p*-Orbitals and Phonons," *J. Chem. Phys.* **92**, 1923 (1990).
2. J. E. Adams and R. M. Strat, "New Insight into Experimental Probes of Cluster Melting," *J. Chem. Phys.* **93**, 1332 (1990).
3. G. Seeley and T. Keyes, "Normal-Mode Analysis of Liquid-State Dynamics," *J. Chem. Phys.* **91**, 5581 (1989).
4. B. Madan, T. Keyes, and G. Seeley, "Diffusion in Supercooled Liquids via Normal Mode Analysis," *J. Chem. Phys.* **92**, 7565 (1990).
5. B. Madan, T. Keyes, and G. Seeley, "Normal Mode Analysis of the Velocity Correlation Function in Supercooled Liquids," *J. Chem. Phys.* **94**, 6762 (1991).
6. A. Rahman, M. J. Mandell, and J. P. McTague, "Molecular Dynamics Study of an Amorphous Lennard-Jones System at Low Temperature," *J. Chem. Phys.* **64**, 1564 (1976).
7. G. S. Grest, S. R. Nagel, and A. Rahman, "Quench Echoes in Molecular Dynamics—A New Phonon Spectroscopy," *Solid State Commun.* **36**, 875 (1980).
8. G. S. Grest, S. R. Nagel, and A. Rahman, "Quench Echoes in Lennard-Jones and Rubidium Frozen Fluids—Temperature Dependence of the Anharmonic Behavior," *J. Phys. Coll.* **C8**, 293 (1980).
9. S. R. Nagel, A. Rahman, and G. S. Grest, "Normal-Mode Analysis by Quench-Echo Techniques: Localization in an Amorphous Solid," *Phys. Rev. Lett.* **47**, 1665 (1981).
10. S. R. Nagel, A. Rahman, and G. S. Grest, "Phonon Localization and Anharmonicity in Model Glasses," *Phys. Rev. Lett.* **53**, 368 (1984).



# Low-Vulnerability Composite Explosives (LOVEX)

C. O. Pruneda,  
D. M. Hoffman, E. S. Jessop,  
and C. M. Walkup

*We have an ongoing program to develop explosives with significantly lower vulnerability to battle/accident environments (bullets, fires) than conventional explosives without sacrificing performance or increasing costs. We have developed a composite explosive, RX-35-BX, which is made of inexpensive fillers, sodium nitrate, aluminum metal powder, and a binder system that consists of a polymeric component and an energetic liquid that acts as a plasticizer for the polymer.*

## Introduction

New-generation munitions for use in fragmentation and penetrator applications have operational and insensitive munition (IM) requirements that pose unique design and materials-technology problems not found in current munitions. The development and production costs of these technologies will be greater than current munition costs; therefore, the per-munition cost is a critical consideration in making design and material-selection decisions. Although little latitude exists in making some unique munition-design technologies less expensive, some cost flexibility may be possible in selecting the explosive fill. When 200 to 300 lb of explosive is used per munition, a dollar per pound of explosive makes a significant difference in the cost over the production life cycle. However, low cost at the expense of performance and insensitivity, as usually specified by munition operational requirements, is not an acceptable compromise. Therefore, multicomponent, composite explosives offer maximum flexibility in adjusting component contents in order to optimize performance, vulnerability, and cost.

## Design Approach

We design an explosive to meet performance, vulnerability, and cost criteria by formulating a composite explosive (a nonideal explosive) with a low-modulus polymeric binder. Formulators of explosives must understand the role of each component in these compositions so that they can better optimize the characteristics of explosives to these competing criteria. A key to this understanding is knowing how the fuel and oxidizer that comprise a composite will react on detonation. Ideally, the fuel and oxidizer reside within the same molecule [as in hexahydro-1,3,5-trinitro-1,3,5-triazine (RDX), where carbon and hydrogen are the fuel, and oxygen is the oxidizer]. In a composite explosive with separate fuel and oxidizer components, the detonation behavior results in longer reaction times because of the relatively

distant fuel and oxidizer components. For high performance and reliable initiation at the low temperatures usually specified in munition operational requirements, a sensitive crystalline explosive, RDX, and an energetic liquid component must be combined in the composite explosive.

We have tailored a specific formulation, identified as RX-35-BX, for use as a main-charge explosive fill in general-purpose munitions. We have performed cylinder expansion tests on RX-35-BX and a series of other low-vulnerability explosives (LOVEX) formulations to determine their metal-acceleration ability.

## Formulation

Table 1 gives the compositions of RX-35-BX and two other LOVEX composite explosives. The BX composite contains spherical aluminum (Alcoa S-8122) as a fuel and a blast

**Table 2.** Chemical properties of RX-35-BX binder and plasticizers.

	Mol wt	$T_m$ (°C)	$\rho$ (g/cm <sup>3</sup> )	$f$ (OH) <sup>a</sup>	$\eta$ (cp) <sup>b</sup>
Binder structure					
TONE 0260	3,000	50–60	1.07	2	1,490 <sup>c</sup>
TONE 3000	6,000	50–60	—	3	—
N-100	675–694	—	1.14	3.5–3.6	10,000
T-131	—	-23	1.11	—	33
Explosive plasticizers					
TMETN	255.15	-3	1.47	—	156
TEGDN	240.2	-19	1.335	—	13.2
Stabilizers					
MNA	152	150	1.201	—	Solid
2-NDPA	214.22	75	—	—	Solid

<sup>a</sup> OH functionality (number of OH groups available for reaction).

<sup>b</sup> Viscosity, in centipoise.

<sup>c</sup>  $T = 55^\circ\text{C}$  for viscosity measurements of TONES.

enhancer, and sodium nitrate as the oxidizer. Only 24 wt% RDX is used. The total solids loading is 68%. A blend of energetic nitrate ester plasticizers [trimethylol ethane trinitrate (TMETN) and triethyleneglycol dinitrate (TEGDN)] controls the initial viscosity to allow the use of melt-cast kettles for processing. A polyurethane binder based both on polycaprolactone polyols (Union Carbide TONE 0260 and TONE 6000) dissolved in the nitrate esters and on the biuret polyisocyanate of hexamethylene diisocyanate (Mobay Desmodur N-100) provides an insensitive, elastomeric matrix for the solids. A latent, mercaptotin catalyst (DABCO T-131) coordinated in the polyol/plasticizer provides long potlife, overnight cure at ambient temperature, and no observable cure exotherm in mixes of up to 120 lb. Table 2 lists some typical properties and structures of the various components.

## Processing

The polyols and plasticizers dissolve at 60°C overnight. After dissolving, the polycaprolactone polyols will not crystallize from the lacquer until well below ambient temperature (−18°C). After this solution cools to ambient, we add the DABCO T-131 to the lacquer and allow it to coordinate with the polyols for at least 10 min. Because T-131 is a catalyst that can be master-batched, the coordinated lacquer can be made well in advance and stored for several months.

We then slowly add the N-100 isocyanate to this lacquer and stir it until it completely disperses. Once the liquids mix, we add the solids—aluminum, RDX, and sodium nitrate—in that order. The explosive remains castable for at least 6 h. Vacuum casting is preferred, but pours could also be made without vacuum. We set aside the castings to cure overnight at ambient. Because of the high solids loading and urethane cure chemistry, very little shrinkage occurs.

**Table 1.** Formulation of RX-35-BS, -BT, and -BX.

Component	Composition (wt%)			Name
	BS	BT	BX	
TMETN <sup>a</sup>	15.66	15.66	18.01	Trimethylol ethane trinitrate
TEGDN <sup>a</sup>	5.21	5.21	5.87	Triethylene glycol dinitrate
MNA <sup>a</sup>	0.11	0.11	0.11	A nitro-amine stabilizer
TONE 0260 <sup>a</sup>	5.33	5.33	6.06	Polycaprolactone polyols
TONE 6000 <sup>a</sup>	0.80	0.80	0.90	Polycaprolactone polyols
DABCO 131	0.0019	0.0019	0.0019	Latent catalyst
N-100	0.92	0.92	1.04	Isocyanate
Aluminum	14.0	14.0	14.00	Metal fuel
RDX	48.0	42.0	24.00	Type II, Class V
NaNO <sub>3</sub>	10.0	16.0	30.00	Grade A, Class 1

<sup>a</sup>A lacquer can be made from the first five components and stored until needed. The lacquer would be added at 30.96 parts by weight and mixed with the solids at ambient temperature.

## Curing Behavior

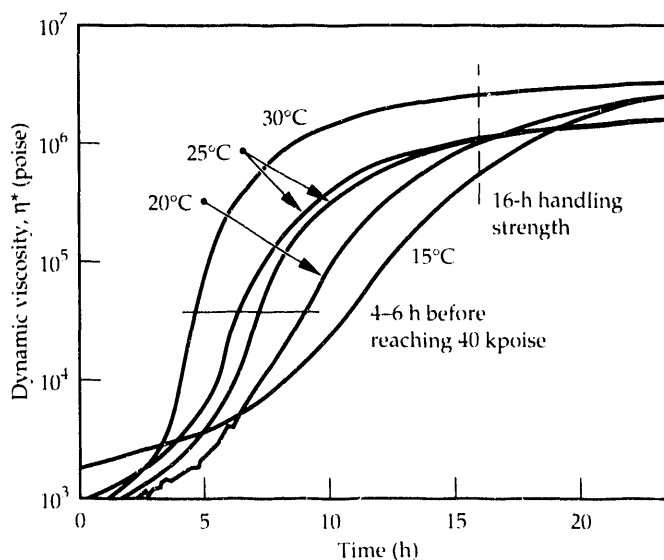
The polymeric isocyanate, N-100, reacts sluggishly with uncatalyzed polyols. Excess isocyanate (NCO) is almost always used in urethane polymerizations because of side reactions. The equivalent weight ratio of NCO to OH in RX-35-BX is 1.16. This ratio worked well in over 50 small-scale (50-g) formulations (not all RX-35-BX) and in 25 mixes between 1 and 120 lb. We did not observe any evidence of moisture foaming or surface tackiness, which is characteristic of unreacted isocyanate. Of a variety of catalysts evaluated in the early developmental work, T-131 (a latent, mercaptotin catalyst) was found to be superior to all others tested with TMETN/TEGDN/TONE polyol mixtures cured with N-100.

We evaluated the curing behavior of RX-35-BX with dynamic viscosity tests at temperatures between 15 and 30°C. We used a Rheometrics Mechanical Spectrometer model 800 at an oscillating frequency of 1 Hz and a 0.05% strain with parallel-plate fixtures separated by a gap of ~0.5 cm. We prepared several 50-g mixes at ambient conditions, degassed them under vacuum for 30 to 45 min, and transferred them to the spectrometer, which was previously equilibrated to the desired cure temperature. Figure 1 shows the dynamic viscosity,  $\eta^*$ , of RX-35-BX as a function of time at various temperatures. At ambient temperatures, this formulation had 6 h of castable life. By 16 h, the sample had cured to handling strength.

## Rheological Behavior

We measured the initial viscosities of larger mixes with a Brookfield HTB viscometer with helipath stand and T-bar spindle C. The apparent viscosity of RX-35-BX varied

**Figure 1.** Dynamic viscosity of RX-35-BX at various temperatures. At ambient temperatures, this formulation had 6 h of castable life. By 16 h, the sample had cured to handling strength.



slightly with rotational speed. At 0.5 rpm, RX-35-BX mix viscosities remained fairly constant between 2 and  $3 \times 10^3$  poise for 4 to 6 h. According to the Brookfield data, the apparent viscosity followed a power law of the form  $\eta = KS^{0.29}$ , where  $\eta$  is the Brookfield viscosity in poise,  $S$  is the rotational speed of the T-bar spindle in rpm, and  $K$  is the proportionality constant ( $K = 2.74 \times 10^3$  poise/rpm<sup>0.29</sup>).

## Conclusion

We have developed a high-performance, low-vulnerability, and low-cost composite explosive that may have main-charge applications in general-purpose munitions. This explosive, RX-35-BX, which matches or may surpass conventional explosive performance, passes the very difficult

slow cookoff test in 8-in.-diameter hardware and uses available low-cost materials and processing facilities. Brookfield viscosity measurements of uncured RX-35-BX show slight variations in apparent viscosity with varying spindle rotational speed, but at 0.5 spindle rpm, mix viscosities remained relatively constant for 4 to 6 h. To follow the curing behavior of RX-35-BX, we used dynamic viscosity measurements of the uncured composition. We have determined that the use of a latent-cure, mercaptotin catalyst results in a long potlife, and it cures and reaches handling strength overnight at ambient temperature.

*This work was funded by the Office of Munitions through the Advanced Conventional Weapons Program.*

---

## Overview

The term "advanced materials" can refer to a variety of materials not in common use, and this lack of common usage may reflect the novelty or difficulty of synthesis. In other cases, the material may have been designed for use under environmentally hostile conditions and is too expensive for ordinary applications. The Department, in response to the Laboratory's programmatic needs, frequently carries out research and development of extraordinary substances. Some of these are described here.

For several years, the Department has been synthesizing foams with unusual properties. A sol-gel process has been used to produce silica-based aerogels of truly extraordinary physical properties. The density, which can be as low as a few milligrams per cubic centimeter, barely exceeds that of the air in the pores of the foam. Synthetic pathways are discussed. Elsewhere in this *Report*, aerogels synthesized from organic compounds are described.

The inertial confinement fusion program required polymer films in which bromine was atomically dispersed. A

solution was found in a plasma polymerization process in which a brominated feed gas was used.

Bonding substrates of high surface energy (such as metals and ceramics) with low surface-energy substances (such as plastics and fiber-reinforced polymer composites) requires an adhesive of low surface energy to promote wetting. A high-fracture-toughness epoxy used in bonding beryllium oxide components, developed for other purposes, has been found to have wide application.

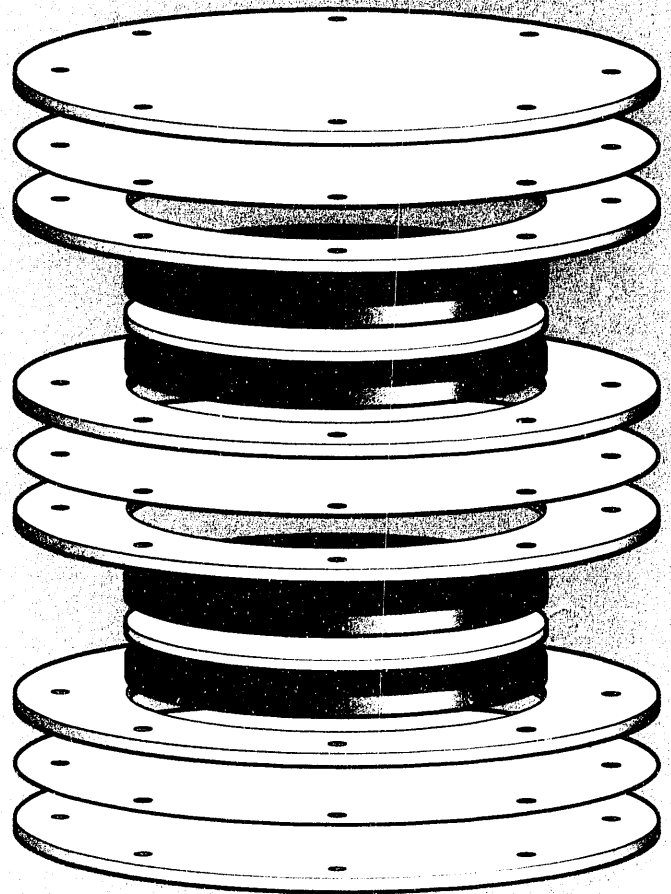
A new laser host consisting of crystalline  $\text{LiCaAlF}_6$  doped with chromium has recently been discovered to have very favorable characteristics as a broadband absorber and emitter. Growing the crystal with acceptable optical characteristics has become a challenge because of defects that produce scattering losses. Annealing has been found to overcome the problem.

The Department also has both experimental and theoretical programs in fiber-reinforced composite materials. This work will be reported in a future *Report*.

---

Section 4

**Chemistry and  
Physics of  
Advanced  
Materials**



**Compression seal high  
voltage bipolar superca-  
pacitor design.**

# Synthesis of Very High-Porosity Silica Aerogels

L. W. Hrubesh,

T. M. Tillotson, and J. F. Poco

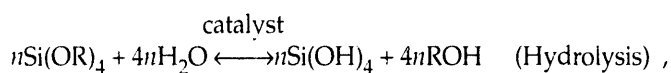
*Aerogels are among the lightest of all man-made materials, but until now the ability to make truly high-porosity aerogels has been limited. We have successfully formed silica aerogels that are barely as dense as the gas that fills their pores and that have a different microstructure than conventional, lower-porosity aerogels. They also have unique optical, mechanical, and thermal properties that result directly from the especially large proportion of trapped air in their pores.*

## Introduction

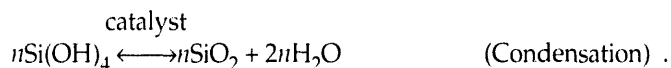
We are interested in very high-porosity (i.e., porosity >99%), transparent silica aerogels for charged-particle detection via the Cerenkov effect and as targets for NOVA experiments. Silica aerogels characteristically have a high porosity (i.e., the pore-volume fraction of the bulk) because their nanometer-size particles are linked together to form a gel with an open, three-dimensional structure that survives removal of the liquid phase with minimal collapse. For producing transparent aerogels with porosities greater than 99%, however, conventional silica sol-gel chemistry is limited because gelation is either too slow or completely unachievable, and even when gelation is achieved, the large pore sizes result in loss of transparency. We have developed a two-step sol-gel process that bypasses the limitations of the conventional process and forms very high-porosity silica aerogels that are transparent up to the highest porosities achieved.

## Experimental Method

The standard sol-gel chemistry leading to high-porosity aerogels involves hydrolyzing and condensing silicon alkoxides according to the reactions



and



Usually, this is done in a single mixing step in which tetraalkoxysilane [ $\text{Si}(\text{OR})_4$ ], water, catalyst, and excess alcohol used to assist mixing are brought together in a container. Both types of reactions proceed simultaneously,

silica particles form, gelation occurs, and syneresis (i.e., spontaneous shrinkage caused by bond formation between particles) continues to strengthen the structure. When the single-step method is used to attempt to make very high-porosity aerogels, it is necessary to dilute the silica concentration by adding large quantities of solvent to the mixture. If alcohol is used as the solvent, the backward hydrolysis reactions (esterification and alcoholysis) can prevent a gel from forming at all. Even when gelation occurs after high dilution by this method, the resulting aerogel is no longer transparent for porosities greater than 99% because the pore-size distribution includes too many pores larger than 50 nm in diameter.<sup>1</sup>

We developed a two-step process that circumvents these limitations and allows us to make very high-porosity gels. First, we form a partially hydrolyzed, partially condensed, silica mixture as a gel precursor. Second, we process the precursor to a gel. Using this process, we make silica aerogels with porosities as high as 99.86%. A technically important part of this process is to remove all alcohol by distillation during the reactions and replace it with a non-alcohol solvent. Similar two-step sol-gel chemistry was reported by Brinker, et al.<sup>2</sup> for xerogels (i.e., very low-porosity gels), and Schaefer et al.<sup>3</sup> for conventional aerogels, but alcohol was used as a solvent in those processes.

Although the clearest aerogels have been produced with tetramethoxysilane (TMOS) and methanol as the solvent, our procedure works equally well with tetraethoxysilane (TEOS) and ethanol as the solvent.

To make the precursor, we first purify the TMOS (Dynasil, Inc.) by triple distillation. Next, we mix the TMOS with methanol and an amount of water insufficient for complete hydrolysis (e.g., molar ratios of 1 TMOS: 1.3 H<sub>2</sub>O: 2.4 MeOH: 10<sup>-5</sup> HCl). Then, we reflux the mixture under acidic conditions for 16 h, distill it, remove all of the alcohol initially added to aid mixing and subsequently produced by reaction, and collect the remaining condensed silica, which has an oily consistency. The oil can be

either sealed in a container to protect it against moisture, or diluted with a nonalcoholic solvent (e.g., acetonitrile or acetone) and stored indefinitely for later use. The nonalcoholic solvent inhibits backward reactions and stabilizes the oligomeric silica mixture against reactions leading to gelation.

Using the condensed silica oil as the precursor, we produce the gel by generating reactions that complete the hydrolysis under basic conditions and with a large excess of nonalcoholic solvent. This is accomplished by mixing the condensed silica oil with 2.5 moles of water, sufficient nonalcoholic (typically acetonitrile) solvent to achieve the targeted porosity, and 2 mL of  $\text{NH}_4\text{OH}$  catalyst per liter of solution. The gel typically forms within 72 h.

To obtain a very high-porosity aerogel, we place the glass mold containing the gel directly into an autoclave to extract the solvent from the gel under conditions that cause the solvent to be a supercritical fluid. (Such fluid lacks the surface tension that would tend to collapse the tenuous gel structure as the fluid is withdrawn.) We ramp the temperature to  $300^\circ\text{C}$  at a rate of  $20^\circ\text{C}/\text{h}$  while holding the pressure generated by the solvent vapor at approximately 136 bar. Finally, we depressurize the autoclave at a rate of 20 bar/h and allow the resulting aerogel to cool slowly while the vessel is purged with dry nitrogen gas.

Very high-porosity aerogels produced by direct extraction of the solvent are hydrophobic and are stable in air. However, very high-porosity aerogels produced by first exchanging the solvent with carbon dioxide and then supercritically drying the resultant product are hydrophilic and shrink badly when exposed to air.

## Results and Discussion

Figure 1 shows the transparency of an aerogel with porosity greater than 99.8%. We have characterized the microstructure of very high-porosity aerogels to determine how they can remain transparent with such high porosity and to compare them with the microstructure of conventional, lower-porosity aerogels. The methods used were transmission electron microscopy (TEM), nitrogen adsorption porosimetry (BET), and spectrophotometry using visible through



**Figure 1.**

A very high-porosity silica aerogel made by the two-step process. The resulting aerogel is relatively transparent and strong.

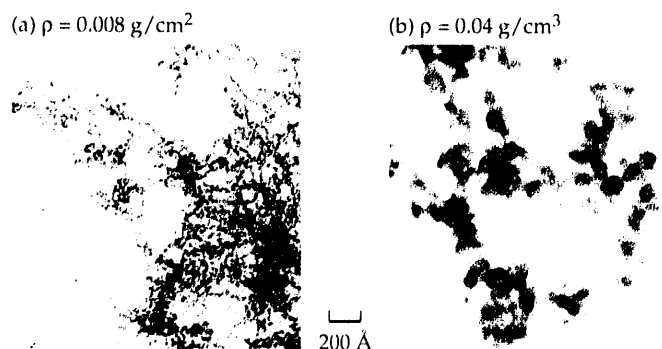
ultraviolet light. Recent measurements of the compressive modulus, sound velocity, and thermal conductivity\* clearly show the effects of trapped air within these aerogels.

Figure 2 shows TEM micrographs of aerogels produced by both the two-step method and the single-step method. The silica aerogel with 99.8% porosity exhibits a chainlike microstructure, with many chain lengths as long as 20 nm between apparent connections. The average width of the chains is approximately 2 nm. In contrast, the TEM for a single-step, base-catalyzed, TMOS aerogel with a 98.2% porosity shows strings of spheroidal particles. The particles have an average diameter of 12 nm and appear to be connected with minimal necking. The two structures are significantly different, the first being polymer-like and the latter bead-like.

The BET surface-area measurements for very high-porosity silica aerogels range from  $550$  to  $650\text{ m}^2/\text{g}$ , anomalously low compared with surface areas of lower-porosity aerogels derived by the two-step method ( $850$  to  $950\text{ m}^2/\text{g}$ ) and the single-step method ( $700$  to  $750\text{ m}^2/\text{g}$ ). Very high-porosity aerogels may have many pores that are too small to be probed by nitrogen molecules, thus giving low BET-measured values for the surface area. In fact, results from helium pycnometry also suggest such microporosity; the measured skeletal density for very high-porosity aerogels is  $1.81\text{ g}/\text{cm}^3$  vs  $2.09\text{ g}/\text{cm}^3$  for aerogels derived by the single-step method, but both are lower than the normal density of silica.

The transmittance of very high-porosity aerogels is considerably higher than that of aerogels derived by the single-step method for all wavelengths between 200 and 800 nm. This enhanced transmittance, coupled with improved thermal insulative properties, has renewed commercial interest in the use of aerogels as thermal-pane windows. Figure 3 compares transmittances of both types of aerogels. All three aerogels compared have the same thickness, but the two

**Figure 2.** TEMs of two-step and single-step aerogels. The former (a) is filamentary, and the latter (b) is colloidal.



aerogels produced by the two-step method have different porosities. The enhanced transmittance is surprising because increased extinction at all wavelengths from ultraviolet to visible was expected as a result of scattering from the larger pores within the high-porosity silica aerogel. The pores of very high-porosity aerogels either are smaller than expected or are very uniform in size. We have not been able to measure either accurately.

The compressive modulus ( $E$ ) of aerogels as a function of density ( $\rho$ ) has been studied for several kinds of low-porosity aerogels<sup>4</sup> and is represented by the relation  $E \sim \rho^x$ , where  $2.8 < x < 3.8$ . However, results for very high-porosity aerogels deviate from this relation (see Fig. 4). Sound-velocity data also show similar differences in behavior between very high-porosity and conventional aerogels.<sup>5</sup> The ambient thermal conductivity of very low-density aerogels decreases with porosity to a minimum at about 98% porosity but then increases with porosity as radiative transport dominates the conductivity through a structure with a higher ratio of air to solid material.<sup>6</sup> The minimum thermal conductivity of very high-porosity silica aerogels is only  $0.016 \text{ W/m}^2$ , the lowest conductivity measured for any silica aerogel. This property of the silica aerogel is currently being exploited by commercial interests for highly efficient and environmentally friendly super insulation to replace chlorofluorocarbon (CFC) foams in refrigerator insulation.

## Conclusions

Our experimental results suggest a microstructure for the very high-porosity silica aerogel that differs from the bead-like structure typical of single-step, base-catalyzed TMOS aerogels. The suggested microstructure is an

interlinked chain-like polymer with an average chain diameter of 2 to 3 nm and an average chain length greater than 15 nm. The increased transparency of these new aerogels also indicates that they have very small particles and uniform pores smaller than 50 nm in diameter. The increased light transmittance and low thermal conductivity of our newly developed aerogels have stimulated considerable interest in their potential commercial use in thermal-pane windows and other insulation applications.

*This work was funded by R Program and by Weapons-Supporting Research.*

\* Made for us by Prof. J. Fricke, University of Wurzburg, FRG.

## References

1. C. F. Bohren and D. R. Huffman, *Absorption and Scattering of Light by Small Particles* (Wiley-Interscience, New York, 1983), Chapter 5.
2. C. J. Brinker, K. D. Keefer, D. W. Schaefer, and C. S. Ashley, "Sol-Gel Transition in Simple Silicates," *J. Non-Cryst. Solids* **48**, 47 (1982).
3. D. W. Schaefer, K. D. Keefer, C. S. Ashley, R. K. Pearson, and I. M. Thomas, "Origin of Porosity in Synthetic Materials," in *Physics and Chemistry of Porous Media II*. J. R. Banavar, J. Koplik and K. W. Winkler, Eds. (American Institute of Physics, New York, 1987), p. 63.
4. J. D. Lemay, T. M. Tillotson, L. W. Hrubesh, and R. W. Pekala, "Microstructural Dependence of Aerogel Mechanical Properties," *Mater. Res. Soc. Symp. Proc.* **180**, 321 (1990).
5. J. Gross, J. Fricke, and L. W. Hrubesh, "Sound Propagation in  $\text{SiO}_2$  Aerogels," *J. Acoust. Soc. Am.* **113**, 48 (1992).
6. J. Fricke, University of Wurzburg, FRG, private communication (1991).

**Figure 3.** Relative transmittance of aerogels. The effective clarity of two-step aerogels is higher than that of single-step aerogels.

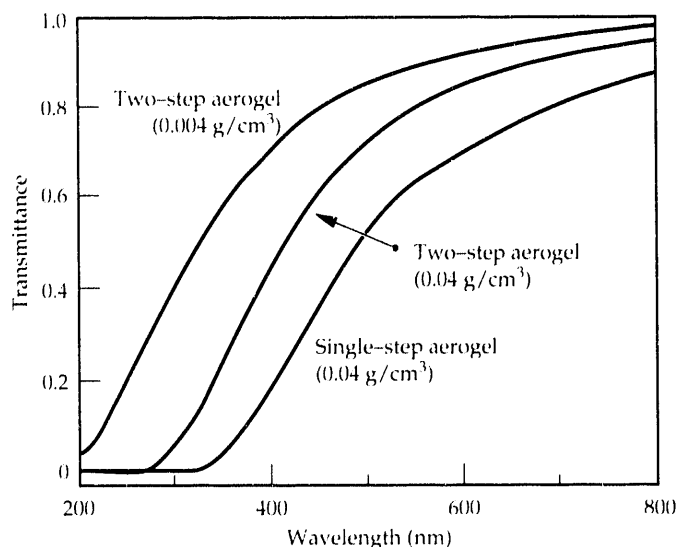
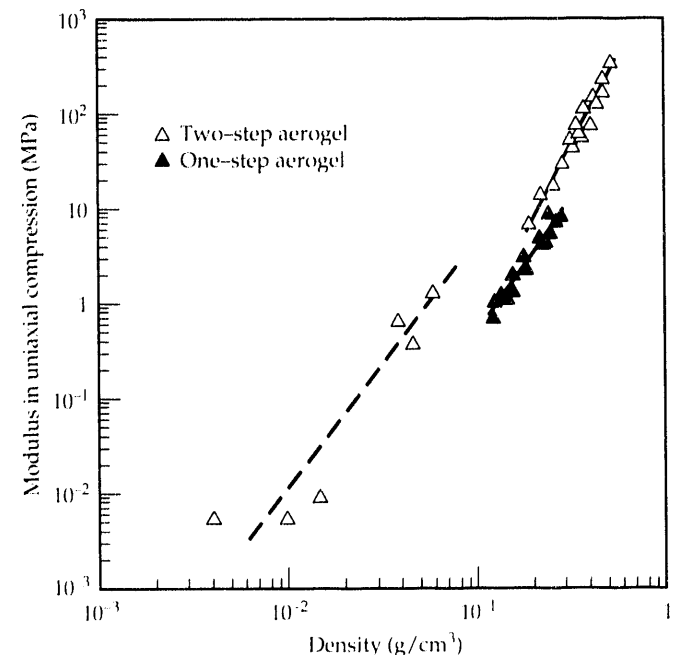


**Figure 4.** The compressive modulus of aerogels as a function of density. The modulus of high-porosity aerogels (lower left) is less affected by density because of the larger amount of air trapped within the pores.





# Elimination of Scattering Centers from Cr:LiCaAlF<sub>6</sub>

J. J. De Yoreo, L. J. Atherton,  
and D. H. Roberts\*

*We have determined the morphology and composition of submicrometer-sized defects in single crystals of the laser host LiCaAlF<sub>6</sub> (LiCAF). Annealing within 50°C of the melting point eliminates these defects and reduces passive scattering losses in the crystals by an order of magnitude. During annealing, these defects dissolve into the matrix and then diffuse out of the crystal. We hypothesize a mechanism for the growth and elimination of defects in LiCAF.*

## Introduction

In a series of recent papers, Payne et al.<sup>1–3</sup> and Atherton et al.<sup>4</sup> detailed the properties, performance, and growth of the laser crystal, Cr<sup>3+</sup>:LiCaAlF<sub>6</sub> (hereafter referred to as LiCAF). As is the case with many other Cr<sup>3+</sup> laser crystals, LiCAF is both a broadband absorber and a broadband emitter. Its output wavelength, which is tunable between 720 and 840 nm, exhibits negligible thermal lensing. In addition, it has a measured quantum slope efficiency in excess of 0.70.<sup>1</sup> The strontium and gallium analogs Cr<sup>3+</sup>:LiSrAlF<sub>6</sub> (LiSAF) and Cr<sup>3+</sup>:LiSrGaF<sub>6</sub> (LiSGaF) have similarly attractive laser properties.<sup>5,6</sup> Unfortunately, the utility of “as-grown” single crystals of LiCAF has been limited by passive scattering losses, in the range of 1 to 5 × 10<sup>–2</sup> cm<sup>–1</sup>, as a result of submicrometer-to micrometer-sized defects, which are present in roughly 10 to 100 ppm by volume. We have shown elsewhere<sup>7</sup> that these defects are composed of a lithium-rich phase of the major constituents of LiCAF. Here, we demonstrate that the defects can be eliminated and the scattering losses reduced to less than 2 × 10<sup>–3</sup> cm<sup>–1</sup> by annealing LiCAF crystals at high temperatures.

## Crystal Growth

We grew the LiCAF crystals for this study by both the Bridgman and the gradient freeze methods using graphite ampoules. In the gradient freeze process, we established a temperature gradient in the furnace and grew the crystal by ramping the furnace temperature (or power) down with time to advance the melt/crystal interface upward. Likewise, in the Bridgman method, we advanced the melt/crystal interface upward through the ampoule but held the temperature profile constant while lowering the ampoule from a hot zone to a cold zone. For these experiments, the temperature gradient and growth rate ranged from 6 to 10°C/cm and 0.5 to 1.0 mm/h, respectively.

The LiCAF growth was seeded with 0.25- × 1.0-in. crystals oriented along the *a* axis (i.e., in the direction of growth). The starting material for these crystals was previously grown Czochralski (CZ) crystals, also produced in our laboratory. We grew the CZ crystals from stoichiometric quantities of Johnson-Mathey high-purity GFI powders

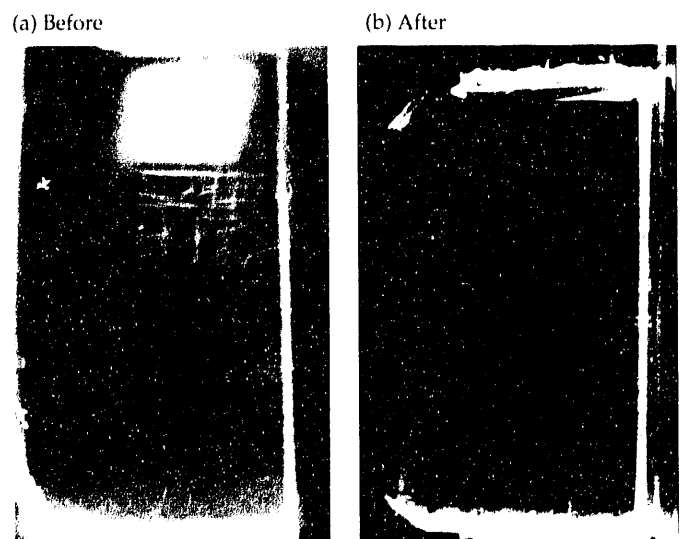
of LiF, CaF<sub>2</sub>, and AlF<sub>3</sub>, doped with 2 mol% of Johnson-Mathey Aesar CrF<sub>3</sub>. The mixture was hydrofluorinated with pure HF at 800°C for 4 h prior to growth in order to prevent oxide formation.

We used CZ feedstock to avoid (temporarily) the determination of the congruent composition of LiCAF for our starting material. Subsequent to this initial work, we grew single LiCAF crystals from stoichiometric mixtures and mixtures that were up to 3 (mol)% LiF-rich, 3% LiF-lean, 3% AlF<sub>3</sub>-rich, and 3% CaF<sub>2</sub>-lean. We doped these crystals with approximately 3 mol% CrF<sub>3</sub> substituted for AlF<sub>3</sub>. We have observed no dependence of defect density on starting composition. Table 1 lists some of the samples used in the annealing studies, along with the measured scattering losses.

## Defect Morphology

Figure 1(a) shows a section of crystal GF031389 cut perpendicular to the *a* axis and illuminated from the side. Regions of strong scattering are clearly visible, and as Table 1

**Figure 1.** Crystal GF031389 (1B): (a) before annealing and (b) after annealing. The bright areas are regions of strong scattering. Crystal dimension is approximately 4 × 10 × 20 mm.



shows, the measured scattering losses for this crystal are about  $2 \times 10^{-2} \text{ cm}^{-1}$ . As shown in Fig. 2, these regions consist of arrays of discrete, micrometer to submicrometer scattering centers. Furthermore, these arrays of defects exhibit three distinct morphologies: curvilinear “feathers,” planar “nebulae,” and 3-D clouds of randomly distributed defects or “smoke.” When a nebula lies within a region of smoke, it is surrounded by a nearly defect-free material whose boundary follows that of the nebula. The spatial distribution of these three morphologies appears to be random and displays no consistency from boule to boule.

Both the nebulae and the feathers lie almost exclusively within the  $c$  plane, which is a plane of easy slip in this uniaxial crystal. The feathers are made up of short line segments of defects that almost always lie along either the  $a$  or  $a^*$  axis. Transmission electron microscopy (TEM) studies show that dislocation lines exhibit these same orientations. In contrast, the particles of smoke are randomly distributed. These observations suggest that dislocations associated with shear-induced slip in the  $c$  plane provide low-energy nucleation sites for the defects, but in the absence of dislocations, the defects will nucleate randomly, producing regions of smoke. Finally, as-grown crystals of LiCAF always exhibit an approximately 1-mm defect-free region around the perimeter of the crystal.

## Annealing

In an effort to reduce the scattering losses, we annealed small ( $4 \times 10 \times 20$ -mm) crystals of LiCAF from boules GF031389 and GF051589 within a graphite crucible open to a flowing argon atmosphere inside a platinum tube furnace. We annealed the samples at 690 to 804°C for 1 to 14 d, after which they cooled at a rate of 200°C/h. For times  $\geq 4$  d and temperatures  $>750^\circ\text{C}$ , annealing removed defects and reduced scattering (see Table 1). Figure 1(b) shows the effect of annealing on a crystal of LiCAF—the same crystal

**Table 1.** Samples used in the annealing studies and their measured scattering losses.

Sample ID	Annealing history			Measured scattering losses ( $10^{-2}\text{cm}^{-1}$ )	
	Time (d)	Temp. ( $^\circ\text{C}$ )	Cool rate ( $^\circ\text{C}/\text{h}$ )	Before	After
GF031389 (1B)	1	750	200	2–4	1–2
	15	785	200	1–2	$<0.3$
	4	796	3	$<0.3$	$<0.3$
GF031389 (2B)	4	780	200	2–4	a,b
GF031389 (3B)	1	805	200	2–5	2–5
	4	796	3	2–5	$<0.5$
GF051589	1	790	200	2–5	2–5
	1	801	200	2–5	a

<sup>a</sup> Sample too small for accurate loss measurements.

<sup>b</sup> Visual observation clearly showed that sample was nearly defect free.

shown in Fig. 1(a) prior to annealing. Losses in annealed crystals are less than  $2 \times 10^{-3} \text{ cm}^{-1}$ , an order-of-magnitude reduction. We observed no changes in defect concentration or morphology for annealing below 750°C.

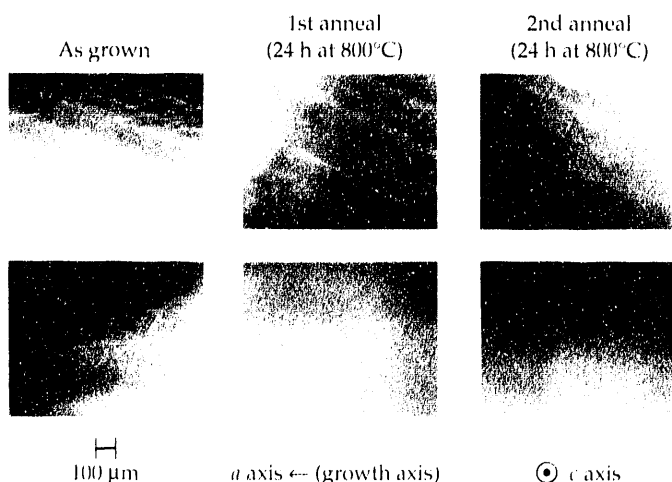
We performed a set of 1-d annealing runs on a sample from GF051589 to examine the affects of partial annealing on the defect structures. The results, shown in Fig. 2, lead to the following observations and conclusions:

- The defect arrays undergo dispersal to more-disordered structures with each successive anneal. This indicates that the defects undergo dissolution followed by diffusion during annealing, and regrowth during cool-down.
- The smoke disappears first, thus strengthening our suggestion that the dislocations provide low-energy nucleation sites; hence, the smoke particles are the last to form and the first to disappear.
- The maximum defect size increases by about a factor of 2. Although particle coarsening is the thermodynamically favored means of reducing the surface free energy,<sup>8</sup> it also suggests that the limit on defect size is due to an increase in strain energy with size. Annealing may relieve the strain and increase the maximum defect size.

Despite these observations, the cooling rates after annealing (200°C/h) were so much longer than during crystal growth (1 to 3°C/h) that we could not rule out the possibility that, following dissolution of the defects into the matrix, the samples were being quenched into a metastable state with the defects atomically dispersed. To differentiate between a mechanism of quenching and one of diffusion, we carried out the following experiment.

We cut two,  $4 \times 10 \times 20$ -mm, defect-rich crystals from adjacent positions in boule GF031389. We annealed one for 4 days at 796°C and then cooled it at 200°C/h, producing a defect-free crystal. We then annealed both samples for 4 d at 796°C and then cooled them at 3°C/h from 796 to 580°C

**Figure 2.** Examples of the three common defect morphologies and effect of annealing. Top sequence: curvilinear feathers. Bottom sequence: planar nebula and nearby smoke. Note that after one day, the smoke particles have disappeared. During annealing, the other defect structures become increasingly dispersed.



and at 20°C/h from 580 to 20°C. Both crystals were defect free. Hence, we conclude that, after dissolution, atomically dispersed defects diffuse out of the sample because of a concentration gradient between the sample and the surrounding atmosphere.

## Discussion

From these annealing experiments, we can estimate a diffusion constant for the atomically dispersed defects near 800°C. We assume that, following dissolution, the annealing process can be approximated by the diffusion of a mobile species with initial concentration,  $C_0$ , from a semi-infinite slab between  $x = -l$  and  $+l$  into an infinite medium with concentration  $C(x,t) = 0$  for all time  $t$ . The solution is given by<sup>9</sup>

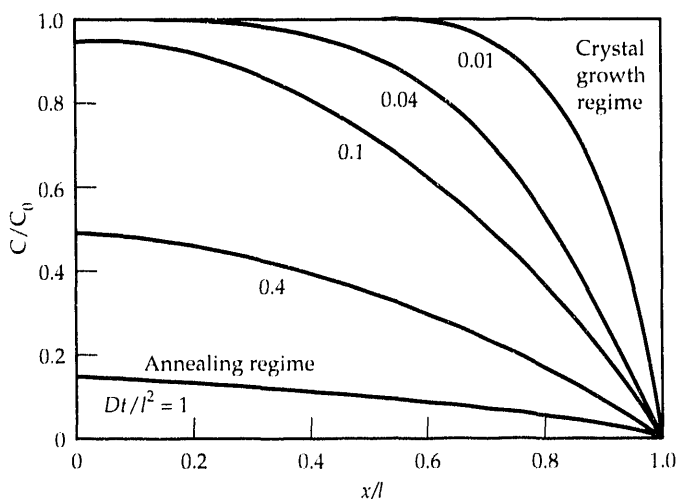
$$C(x,t) = C_0 - C_0 \sum_{n=1}^{\infty} (-1)^n \left\{ \operatorname{erfc} \left[ \frac{(2n+1)l-x}{2\sqrt{Dt}} \right] + \operatorname{erfc} \left[ \frac{(2n+1)l+x}{2\sqrt{Dt}} \right] \right\}. \quad (1)$$

This solution is shown graphically in Fig. 3.

For "complete" annealing (scattering losses reduced by an order of magnitude), we assume  $C/C_0 \leq 0.1$ . From Fig. 3, this indicates  $Dt/l^2 \approx 1.0$ . With  $l = 2$  mm and  $t \approx 100$  h, we calculate  $D \approx 10^{-7}$  cm<sup>2</sup>/s. This is similar in magnitude to the diffusion constant for self-diffusion of lithium in LiF and sodium in NaCl near their melting points.<sup>10</sup>

Based on our annealing experiments, diffusion can occur only when  $T > 750^\circ\text{C}$ . During crystal growth, with a cooling rate of 1°C/h, the time available for diffusion is  $< 60$  h. For  $l \approx 1$  cm, and  $D \approx 10^{-7}$  cm<sup>2</sup>/s,  $Dt/l^2 \approx 0.01$ . This constraint establishes a boundary-layer regime for the concentration during crystal growth. The value of  $C/C_0$  is in excess of 0.5

**Figure 3.** Variation of concentration,  $C/C_0$ , with position,  $x/l$ , during diffusion from an infinite slab of thickness  $2l$  into an infinite medium with  $C(t) = 0$ . Curves are given for various values of  $Dt/l^2$ , where  $D$  is the diffusion constant. (Adapted from Ref. 9.)



for  $x/l < 0.90$  and falls below 0.1 only for  $x/l < 0.95$ . This value accounts for the presence of a defect-free region around the perimeter of as-grown crystals of LiCAF. We have shown elsewhere<sup>7</sup> that, by growing crystals slowly enough in a sufficiently shallow gradient, it is possible to grow LiCAF that is defect free throughout its volume.

Based on the above observations we propose the following framework for understanding the formation, growth, and elimination of defects in LiCAF. As the growing crystal moves away from the melt/solid interface, it reaches a critical temperature,  $T_c$ , of about 750°C, below which LiCAF becomes supersaturated in either an extrinsic impurity species or an excess of an intrinsic major constituent. At some temperature below  $T_c$ , nucleation of the defects occurs both randomly and along dislocations. Initially, surface-energy reduction favors the growth of defects, but eventually, increasing strain energy imposes a limiting size on the defects. During annealing, the defects dissolve back into the LiCAF matrix and then diffuse out of the sample along a concentration gradient.

## Acknowledgments

We gratefully acknowledge the assistance of Wayne Kway in materials preparation and the production of Czochralski grown crystals.

*This work was funded by Weapons-Supporting Research.*

\*Mechanical Engineering Department, LLNL

## References

1. S. A. Payne, L. L. Chase, H. W. Newkirk, L. K. Smith, and W. F. Krupke, "A Promising New Solid-State Laser Material," *IEEE J. Quantum Electron.* **24**, 2243 (1988).
2. S. A. Payne, L. L. Chase, L. K. Smith, and B. H. T. Chai, "Flashlamp-Pumped Performance of LiCaAlF<sub>6</sub>:Cr<sup>3+</sup>," *Opt. Quantum Electron.* **22**, S259 (1990).
3. S. A. Payne, L. L. Chase, and G. D. Wilke, "Optical Spectroscopy of the New Laser Materials, LiSrAlF<sub>6</sub>:Cr<sup>3+</sup> and LiCaAlF<sub>6</sub>:Cr<sup>3+</sup>," *J. Lumin.* **44**, 167 (1989).
4. L. J. Atherton, J. J. DeYoreo, S. A. Payne, D. H. Roberts, J. F. Cooper, and R. W. Martin, "Growth of Cr:LiCaAlF<sub>6</sub> by the Bridgman and Gradient Freeze Processes," *AACG Newsletter*, **21**, 10 (1991).
5. S. A. Payne, L. L. Chase, L. K. Smith, W. L. Kway, and H. W. Newkirk, "Laser Performance of LiSrAlF<sub>6</sub>:Cr<sup>3+</sup>," *J. Appl. Phys.* **66**, 1051 (1989).
6. L. K. Smith, S. A. Payne, W. L. Kway, L. L. Chase, and B. H. T. Chai, "Investigation of the Laser Properties of Cr<sup>3+</sup>:LiSrGaF<sub>6</sub>," *Proc. Conf. Lasers and Electro-Optics*, Baltimore, MD, 1991 (in press).
7. J. J. De Yoreo, L. J. Atherton, D. H. Roberts, R. W. Martin, and R. C. Morris, "Study of Defect Formation, Growth, and Elimination in Cr:LiCaAlF<sub>6</sub>," *J. Appl. Phys.* (in press) [see LLNL Preprint UCRL-JC-109908 (1991)].
8. B. Lewis, "Nucleation and Growth Theory," in *Crystal Growth*, 2nd ed., B. R. Pamplin, Ed. (Pergamon, New York, 1980), p. 23.
9. H. S. Carslaw and J. C. Jaeger, *Conduction of Heat in Solids* (Oxford University Press, Oxford, U.K., 1959), pp. 92-99.
10. R. J. Borg and G. J. Dienes, *An Introduction to Solid State Diffusion* (Academic Press, Berkeley, CA, 1988), pp. 111-114, 265-266.

# Preparation and Properties of Brominated Plasma Polymer Coatings

S. A. Letts, C. W. Price,  
F. M. Kong, S. R. Buckley,  
M. D. Saculla,\* E. F. Lindsey,\*  
C. E. Moore,\* and P. Welch

*We have developed a plasma polymerization process for depositing brominated polymer coatings for laser experiments. We used an x-ray radiographic gauging technique and x-ray microfluorescence to measure composition and used atomic force microscopy to measure the surface finish of the coatings. We found that the surface finish improved to better than 50 nm peak-to-valley with increased total gas flow rates.*

## Introduction

Hydrodynamic instability experiments related to inertial confinement fusion have recently required polymer films seeded with bromine.<sup>1</sup> To prepare these films, we developed a process for producing a polymer with atomically dispersed bromine in the range of 1 to 5 at.% and with excellent uniformity and surface finish. Previous work in our laboratory had produced coatings with silicon or sulfur atomically dispersed in a hydrocarbon polymer.<sup>2</sup> We used the established plasma polymerization apparatus and introduced a brominated feed gas.

Quantitative analysis of the films, which usually had a mass of less than 50  $\mu\text{g}$ , presented an additional challenge. We developed several methods for measuring bromine composition, including combustion chemical analysis, density measurement, radiographic analysis, and x-ray microfluorescence. The analysis revealed compositional variations within our coating apparatus and irregularities in flow control. We are now able to deposit coatings with predictable thickness and uniform composition up to 100  $\mu\text{m}$  thick.

## Experimental Method

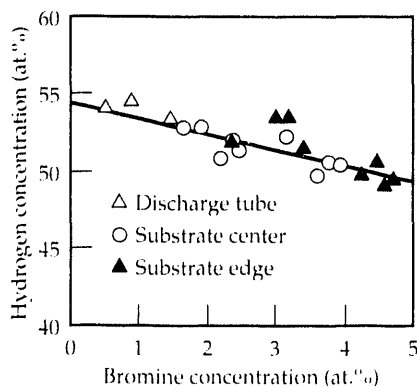
The plasma coating process and system have been described in previous reports.<sup>2-4</sup> Briefly, the coating system consists of four main components: a gas supply manifold, an rf-discharge generator, a coating chamber, and a vacuum pump. Electrically actuated valves control the flow rate of the various reactant gases. The valves are feedback controlled by pressure-drop measurements. For bromine-seeded coatings, we use a combination of three gases: ethylbromide, trans-2-butene, and hydrogen. We measure the pressure in the coating chamber with a capacitance manometer and control it at a constant 75 mTorr with a variable-conductance throttle valve that separates the coating chamber and the vacuum-pumping section. Polymer deposition occurs in a region of glow discharge driven by an rf helical resonator. In this region, electrons collide with the gas molecules, causing fragmentation and ionization. The reactive fragments chemically recombine in the gas phase and on nearby surfaces to form a polymer coating.

## Composition Analysis

We used combustion chemical analysis to measure bromine concentration of our samples to an accuracy of 0.1%, calibrated by known standards. We separated and analyzed polymer collected from the discharge tube from the center of the substrate area and from the outer edge of our substrate (3 cm from the center of the coating chamber). The bromine content increased as the sample was collected farther from the discharge. Figure 1 shows hydrogen concentration as a function of bromine concentration for various bromine-seeded polymers. The line through the data has a slope of  $-1$ , indicating that the addition of one bromine atom results in the loss or displacement of one hydrogen atom. The bromine-carbon bond is weaker than the carbon-hydrogen bond, and continual electron bombardment may break it in the immediate area of the discharge, resulting in

**Figure 1.**

Hydrogen and bromine concentrations in plasma polymers, measured by chemical analysis, show that bromine concentration is lowest in the discharge tube and highest at the edge of the substrate. The  $-1$  slope of the line through the data indicates that one hydrogen atom is removed for each bromine atom added to the polymer structure.



bromine depletion. Farther downstream, away from the discharge, the material receives less electron bombardment and therefore has a higher bromine content.

Although we ultimately controlled bromine composition in the polymer by controlling the flow rate of the brominated feed gas, we found that other process parameters also influenced the composition, including the trans-2-butene and hydrogen flow rates, the discharge power, and the system pressure. These variables may ultimately provide the means to further improve the plasma polymer coatings by controlling oxidation, stress, and surface finish.

## Density Analysis

Densities of the bromocarbon polymers accurately reflect the bromine concentration of the polymers. We used a density gradient column (a mixture of two liquids) to measure polymer density. The measurements of density and composition of matching samples are plotted in Fig. 2. The samples for the density measurements came from the discharge tube, the center of the substrate, and 25 mm from the center; the concentration of bromine increased in the same order. Density and composition appear to be linearly related in the range of 0 to 5 at.%. The zero-intercept density is  $1.06 \text{ g/cm}^3$ , the value for pure hydrocarbon polymer on this coater.

## Surface Finish Analysis

Scanning electron microscopy has been our primary means of characterizing surface finish. Recently we used atomic force microscopy (AFM) to more quantitatively measure the microstructure of the plasma polymer films. Figure 3, an AFM scan of one of our films, shows surface roughness to be about 50 nm peak-to-valley. The film appears to be composed of an aggregate of smaller particles 50 nm in diameter. Previous work on hydrocarbon films showed that the surface finish improves with increased total gas flow rate.<sup>4</sup> The improved surface finish appears to result from less gas-phase nucleation because of the short residence time of the

gas species in the discharge zone. In this study, we again found that the size of particles in the coating decreased with increased gas flow rate. We also found the bromine composition to decrease with increased flow and, hence, the proportion of bromoethane had to be increased to maintain a constant 2-at.% bromine composition.

## Radiography

We use x-ray radiography to measure the thickness and uniformity of coatings. Because radiographs of coatings deposited with irregular gas flow control reveal density and composition variations, radiography is an important tool in diagnosing deposition conditions. In particular, radiographic density of the coatings varies with the bromine content. To use the radiographs to quantitatively measure bromine content, we constructed a calibration step wedge consisting of 30 layers of polymer film and precision-machined a brominated polystyrene<sup>5</sup> step wedge. We then matched the optical density of the brominated film to a thickness within the step wedge.

## X-Ray Microfluorescence

To more accurately and more rapidly measure bromine concentrations, we set up an x-ray microfluorescence (XRMF) apparatus, which consists of a movable stage and an x-ray beam collimated to a diameter as small as  $50 \mu\text{m}$ . We measured fluorescence in the brominated films with an energy dispersive detector. Figure 4 is a  $50\text{-}\mu\text{m}$ -aperture scan across the precision-machined brominated polystyrene step wedge. We found the counting rate to be a linear function of thickness to at least a thickness of  $140 \mu\text{m}$ .

**Figure 2.**

The density of bromine-seeded plasma polymers, as measured in a density gradient column, is linear in bromine concentration below 5 at.%.

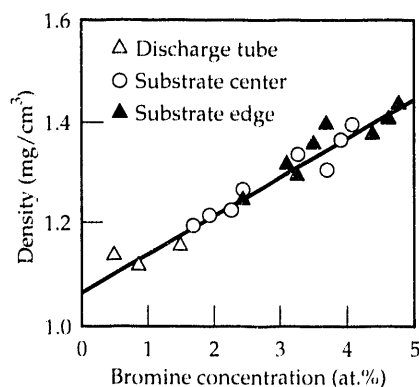
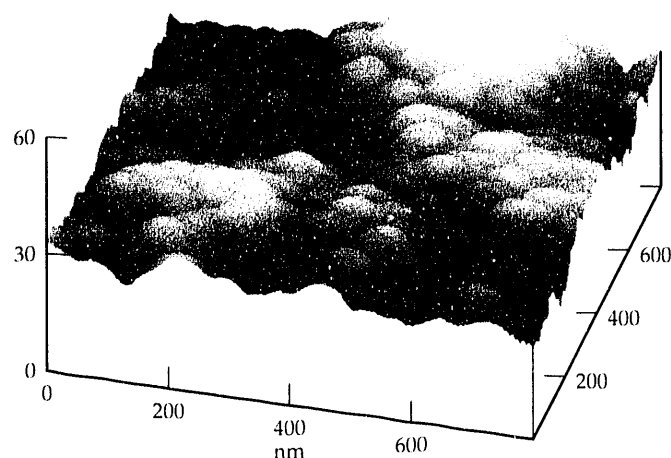


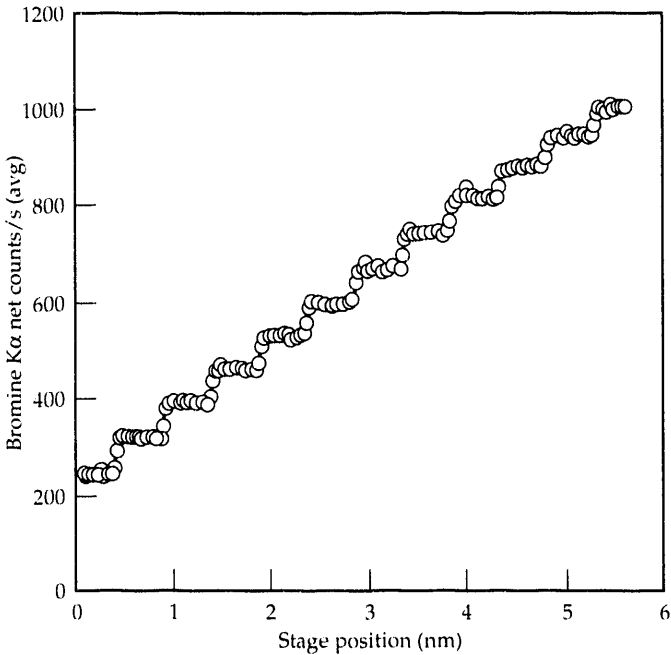
**Figure 3.** AFM scans of bromine-seeded plasma polymers revealed a structure composed of an aggregate of particles 50 nm in diameter.



## Summary

We have developed a plasma polymerization process for deposition of bromine-seeded coatings with controlled composition up to 5 at.%. Surface finish was improved at

**Figure 4.** A precision-machined brominated polystyrene (2.05 at.% bromine) was scanned in 25- $\mu\text{m}$  increments by using a 50- $\mu\text{m}$  collimated x-ray beam to calibrate the XRMF apparatus.



higher gas flow rates. We have developed a radiographic technique to quantitatively measure bromine concentration and have found x-ray microfluorescence to be both rapid and quantitatively accurate.

*This work was funded by the ICF Project in Y Program.*

\*Mechanical Engineering Department, LLNL

## References

1. B. A. Remington, S. W. Haan, S. G. Glendinning, J. D. Kilkenny, and R. J. Wallace, "Planar Rayleigh-Taylor Experiments on Nova," presented at the 3rd Int. Workshop Physics Compressible Turbulent Mixing, June 17-19, 1991, Royaumont, France [see LLNL Preprint UCRL-JC-107506 (1991)].
2. S. A. Letts, D. E. Miller, R. A. Corley, T. M. Tillotson, and L. A. Witt, "Summary Abstract: Microscopic Target Development with Seeded and Patterned Plasma Polymers," *J. Vac. Sci. Technol.* **A3**(3), 1277 (1985).
3. W. L. Johnson, S. A. Letts, C. W. Hatcher, L. E. Lorensen, and C. D. Hendricks, "Plasma Polymerization Coating of DT-Filled Glass Shells for Laser Fusion Targets," in *Plasma Polymerization, ACS Symposium Series 108*, M. Shen and A. T. Bell, Eds. (American Chemical Society, Washington, DC, 1979), Ch. 20, p. 315.
4. S. A. Letts, D. W. Myers, and L. A. Witt, "Ultrasoother Plasma Polymerized Coatings for Laser Fusion Targets," *J. Vac. Sci. Technol.* **19**(3), 739 (1981).
5. R. C. Cook, G. E. Overturf III, and S. R. Buckley, "Preparation and Properties of Halogenated Polystyrenes," *Inertial Confinement Fusion* **1**(4), 135 (1991) (Lawrence Livermore National Laboratory, Livermore, CA, UCRL-LR-105821-91-4).

# Epoxy Adhesive with High Fracture Toughness

R. E. Lyon and J. D. LeMay

*We have developed a structural epoxy adhesive that has a fracture toughness of  $1.3 \text{ MPa}\sqrt{\text{m}}$  and cures completely at  $75^\circ\text{C}$ . Originally developed to bond BeO components in an LLNL weapon system, this adhesive has proven effective as a general-purpose structural adhesive for a variety of high-surface-energy substrates, including metals, metal-oxide ceramics, and glasses. The low surface tension of the liquid adhesive,  $32 \text{ mJ/m}^2$ , promotes wetting of low-surface-energy solids (such as plastics and fiber-reinforced polymer composites) for high bond strength.*

## Introduction

The LLNL Weapons Program requested us to develop an improved structural adhesive for BeO/BeO bonded joints to replace an epoxy adhesive that had failed in component vibration tests and had exhibited wide variability in static bond-strength tests. The improved adhesive was to have a high degree of reliability, high bond strength, and good fracture toughness over both the entire weapon lifetime and the stockpile-to-target sequence (STS) temperature range of  $-50$  to  $+75^\circ\text{C}$ . Moreover, the bond between the adhesive and the BeO substrates would have to be formed in the existing component production cycle, which involves fixturing the assembly and heating to a temperature of  $75^\circ\text{C}$  under vacuum.

To completely cure at  $75^\circ\text{C}$  and maintain mechanical properties at the upper STS temperature, the adhesive should have an equilibrium glass transition (softening) temperature in the range of  $85$  to  $95^\circ\text{C}$ . Desirable processing characteristics included low viscosity in the liquid state for easy mixing and a pot-life (working time at room temperature) of 2 to 4 h prior to solidification in order to allow sufficient time for assembly. Wetting of the BeO surfaces by the adhesive in the liquid state was also required to achieve a high-quality bonded joint. Wetting ensures intimate contact and a continuous interface between the two phases because the liquid adhesive fills microcracks and crevices in the BeO surfaces to provide mechanical interlocking and to displace air pockets that could act as fracture-initiation sites.

The  $75^\circ\text{C}$  temperature of the processing cycle precludes the use of commercially available, high-fracture-toughness, organic adhesives, which typically require a temperature greater than  $120^\circ\text{C}$  and moderate pressure to form a structural bond. These processing constraints also prohibit the use of all of the conventional ceramic joining methods such as inorganic cements, glass solders, and metallization—which require temperatures above  $800^\circ\text{C}$ .

## Technical Approach

Our approach was to develop a two-phase structural adhesive based on epoxide/amine (epoxy) reaction chemistry. We selected epoxy adhesives because they can form high-strength bonds with ceramic substrates and can be formulated to cure at moderate temperature ( $50$  to  $100^\circ\text{C}$ ) without generating volatile by-products. In addition, we believed that an epoxy adhesive could be developed in which the chemical reaction would go to completion at the  $75^\circ\text{C}$  vacuum bake-out temperature used in production. However, pure epoxies such as the one that failed in the component tests have notoriously poor fracture properties, with fracture energies ( $G_{1c}$ ) of about  $120 \text{ J/m}^2$  and fracture toughnesses ( $K_{1c}$ ) of about  $0.6 \text{ MPa}\sqrt{\text{m}}$ . The relationship between these two measures of fracture resistance is (for plane stress)

$$K_{1c}^2 = EG_{1c} \quad (1)$$

where  $E$  is the Young's modulus or stiffness of the material. The relationship of  $G_{1c}$  and  $K_{1c}$  in Eq. (1) shows the importance of the elastic properties of the material in determining the intensity of the stresses at a crack tip. For example, a brittle, high-modulus ceramic such as BeO, which exhibits no plastic deformation at a crack tip, can have a low fracture energy ( $\approx 40 \text{ J/m}^2$ ) but a high fracture toughness ( $\approx 1$  to  $2 \text{ MPa}\sqrt{\text{m}}$ ) relative to epoxy. Given the lower fracture toughness for the epoxy, we would expect a bondline crack to form more easily and propagate more readily through a pure epoxy adhesive layer than through the adjacent BeO. Therefore, assuming perfect interface bonding, the fracture resistance of a BeO/epoxy/BeO joint can only be improved by increasing the fracture toughness of the epoxy layer to equal that of the BeO. From Eq. (1), using a typical Young's

modulus for the epoxy (3 GPa), we can calculate the minimum fracture energy for the epoxy, 600 to 800 J/m<sup>2</sup>, needed to approach the fracture toughness of the BeO.

To achieve the required factor-of-6 increase in fracture energy of the epoxy, we decided to incorporate rubber particles in the epoxy matrix. Rubber-toughening of epoxies, a well-established way to increase fracture toughness, is thought to result from localized shear banding and cavitation mechanisms that nucleate at rubber particles to dissipate strain energy.<sup>1</sup> We examined a variety of liquid-rubber additives that were initially soluble in the liquid epoxy but phase-separated during cure to form discrete rubber particles. We evaluated amine-terminated poly(tetramethylene oxide) rubbers, carboxy-terminated butadiene-acrylonitrile (CTBN) copolymer rubbers having various acrylonitrile content, and epoxide- and amine-terminated CTBNs.

## Experimental Procedures

We used differential scanning calorimetry (DSC) to determine the glass transition temperature and completeness of reaction<sup>2</sup> for candidate adhesives after a cure cycle of 24 h at 75°C. Using molded epoxy specimens, we measured torsional shear strength and modulus at a strain rate of 0.05/min at temperatures of 22 and 75°C.<sup>3</sup> Using the pendant drop technique, we measured surface tensions of epoxies in the liquid state<sup>4</sup> to identify adhesives with low surface tensions that would provide good wetting of the BeO surfaces. Using a double torsion fracture test,<sup>5</sup> we determined the  $G_{Ic}$  values of candidate epoxies as a function of composition and bond thickness. We obtained all  $G_{Ic}$  values reported in this work at 22°C and at a deformation rate of 0.013 mm/min by using tool steel adherends measuring 150 × 40 × 6 mm. We examined adhesive microstructure by using scanning electron microscopy (SEM) and determined the shear strength of BeO adhesive joints by using a tubular-butt torsion test.<sup>6</sup>

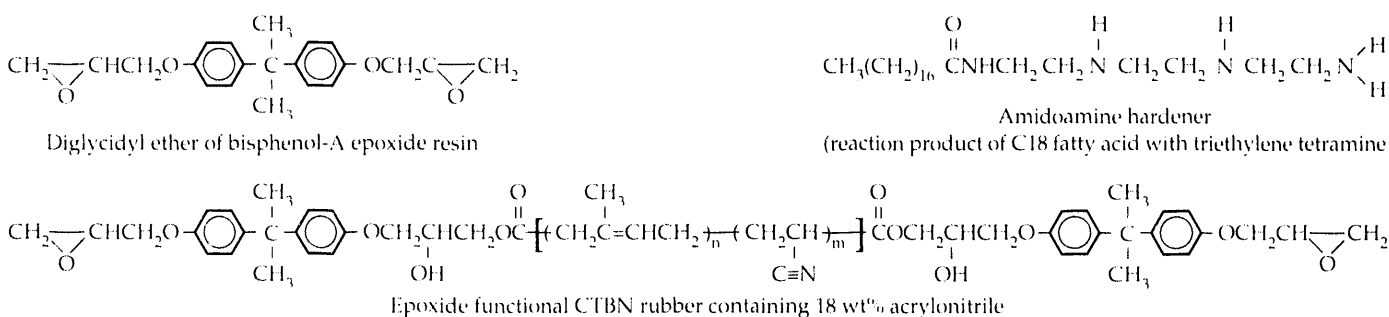
## Results and Discussion

Of several epoxies containing only an epoxide resin and an amine hardener, we found only one that had low toxicity, consistently high bond strengths, and good processing characteristics. The resin component of the selected epoxy is the diglycidyl ether of bisphenol-A, (DER 332, Dow Chemical). The hardener is an amidoamine (HY-955, Ciba-Geigy), which is a reaction product of a C<sub>18</sub> fatty acid with triethylene tetramine. This epoxy had a high static shear strength of 47 MPa and a ductile failure mode with homogeneous yielding and ultimate shear strain approaching 25%. Despite the inherent ductility of this single-phase polymeric glass, its fracture energy was only 130 J/m<sup>2</sup>, far below the target value of 600 to 800 J/m<sup>2</sup>.

Adding the amine-terminated poly(tetramethylene oxide) rubber, the CTBN copolymer rubber, or the amine-terminated CTBN at the 10-wt% level produced no significant increase in fracture toughness of the epoxy, although SEM micrographs showed evidence of a phase-separated morphology with rubber particles dispersed in the epoxy matrix. In contrast, the epoxide-terminated CTBN produced a marked improvement in fracture energy. Figure 1 shows the chemical structures of the epoxy-terminated CTBN (Epi-Rez 58006, Rhone-Poulenc), the diglycidyl ether of bisphenol-A epoxide resin, and the amidoamine hardener of the selected epoxy adhesive.

Figure 2 shows the softening temperature, shear modulus, shear strength, and fracture energy of the epoxy adhesive as functions of rubber concentration. The softening temperature is independent of rubber concentration over the range tested, indicating complete separation of the rubber phase from the epoxy matrix. The shear modulus and shear strength at both 22 and 75°C decrease monotonically with increasing rubber concentration. The shear strength falls to the minimum acceptable values [represented by the dashed lines in Fig. 2(b)] in the range of 10 to 13% rubber. The decrease in modulus with increasing rubber concentration

**Figure 1.** Chemical structures of 89-15 adhesive components.





is a property of the two-phase morphology, which is predicted from micromechanics by a rule-of-mixtures calculation that takes into account the volume fractions and elastic properties of the separate epoxy and rubber phases. Figure 2(a) shows fracture energies obtained at room temperature in 100- $\mu\text{m}$ -thick bondlines. A plateau in the fracture energy at  $900 \text{ J/m}^2$  occurs in the range of 10 to 13% rubber in the epoxy matrix. This value translates into a fracture toughness of  $1.3 \text{ MPa}\sqrt{\text{m}}$  for the rubber-modified epoxy, which is the target value for BeO.

The optimum adhesive formulation occurred at a rubber concentration of about 10 wt%, where we obtained high fracture toughness without significantly compromising shear strength, modulus, or glass transition temperature. We designated the optimum adhesive formulation of 10% rubber in the 1:1 stoichiometric ratio of diglycidyl ether of bisphenol-A with the amidoamine hardener as 89-15. Table 1 summarizes its properties.

**Figure 2.** The effects of rubber concentration on adhesive fracture energy, shear modulus, shear strength, and softening temperature of adhesive 89-15.

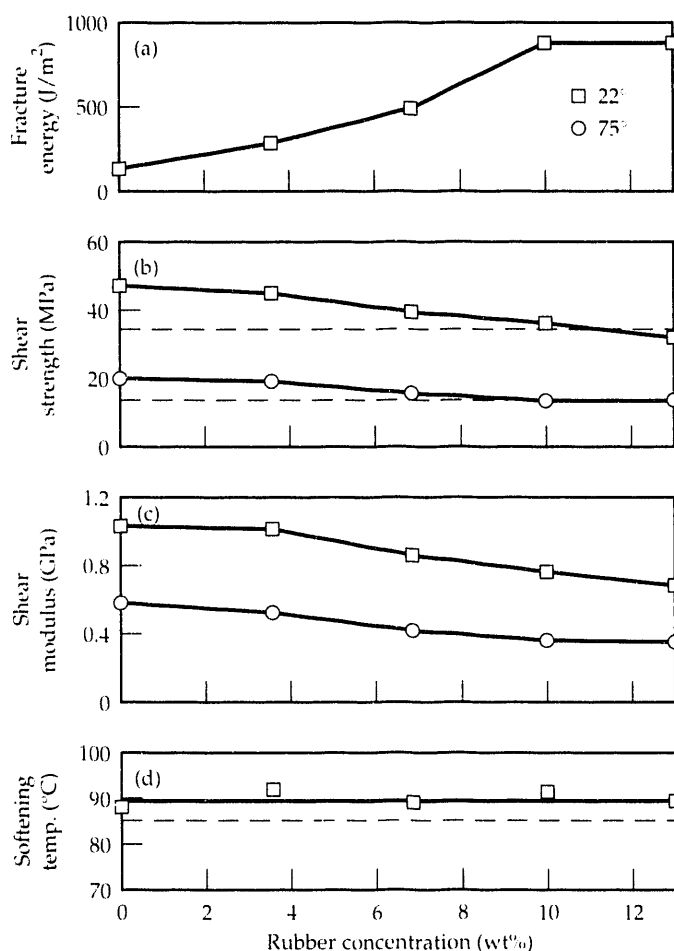


Figure 3 shows the microstructure of the 89-15 rubber-toughened epoxy adhesive. The liquid copolymer rubber additive is initially soluble in the liquid parent epoxy, forming a clear solution on mixing. At the gel point of the epoxy, the rubber phase precipitates from solution to form rubber-rich spherical domains, which are 1 to 2  $\mu\text{m}$  in diameter. Because the rubber particles are larger than the wavelength of visible light, they scatter the light, making the adhesive appear opaque. The relative solubility parameters of the rubber and epoxy, the interfacial tension, and the chemorheology of the system all determine the final size of the rubber particles. Typical rubber particles range from 1 to 10  $\mu\text{m}$  in rubber-toughened epoxies. Particle size is independent of rubber concentration in the 89-15 adhesive, but the number of particles increases with the concentration of rubber.

**Table 1.** Adhesive 89-15 properties.

Property	Value
Softening temperature, $T_g$ (°C)	86
Fracture energy, $G_{Ic}$ ( $\text{J/m}^2$ )	$800 \pm 100$
Fracture toughness, $K_{Ic}$ ( $\text{MPa}\sqrt{\text{m}}$ )	$1.3 \pm 0.1$
Shear modulus (GPa)	0.76
Shear strength (MPa)	36
Surface tension ( $\text{mJ/m}^2$ )	32
Initial viscosity (Pa·s)	5
Gel time (min)	180
Density, liquid ( $\text{g/cm}^3$ )	1.08
Joint shear strength (MPa)	
BeO	43
Tool steel	43
Alumina	40



**Figure 3.**

SEM micrograph of adhesive 89-15 fracture surface, showing phase-separated rubber particles.

## Conclusions

We obtained a consistent joint shear strength of 43 MPa for adhesive 89-15 with BeO, tool steel, and aluminum oxide substrates. Cohesive failure of the epoxy occurred in each case. The measured surface tension of 89-15 in the liquid state is slightly lower, because of added liquid rubber, than that of the parent epoxy. It is also significantly lower than the surface tension of the epoxy that failed in the component tests, thus promoting better wetting of the BeO surfaces. The 89-15 adhesive has an initial viscosity after mixing of 5 Pa·s, a liquid density of 1.08 g/cm<sup>3</sup>, and a gel time at room temperature of 180 min.

*This work was funded by the Nuclear Weapons Program.*

## References

1. A. I. Kinloch and R. J. Young, *Fracture Behavior of Polymers* (Elsevier, London, 1985), Ch. 11.
2. R. B. Prime, in *Thermal Characterization of Polymeric Materials*, E. A. Turi, Ed. (Academic Press, New York, 1981), Ch. 5.
3. R. E. Lyon, "Shear Strength of a Ductile Material from Torsion of Solid Cylinders," *J. Test. Eval.* **19**(3), 240 (1991).
4. A. A. Adamson, *Physical Chemistry of Surfaces* (Wiley-Interscience, New York, 1960), pp. 36-37.
5. A. C. Moloney, H. H. Kausch, and H. R. Stieger, "The Use of the Double Torsion Test Geometry to Study the Fracture of Adhesive Joints," *J. Mater. Sci. Lett.* **3**, 776 (1984).
6. W. I. McCarvill and J. P. Bell, "Torsional Test Method for Adhesive Joints," *J. Adhesion* **6**, 185 (1974).

---

## Overview

Surfaces and interfaces have long dominated the development and use of new materials. For example, much that is important in controlling the course of a chemical reaction is thought to occur at a surface. Adhesion, though long studied and perhaps understood phenomenologically, cannot be described on a molecular basis, and no theory of adhesion exists that has a predictive capability.

The Department faces short-term programmatic challenges to solve surface and interface problems and has long-term opportunities to develop a basic understanding of them. Both experimental and theoretical approaches are in use, some of which are described in this *Report*.

High-resolution methods of characterizing surfaces have been known for some time, among them low-energy electron diffraction (LEED). When applied to surfaces of high Miller index, such as stepped or kinked surfaces, LEED experimental data have not been amenable to quantitative interpretation. A new theoretical approach, based on a first-principles formalism called real-space multiple scattering theory (RSMST), has been used to determine atomic relaxations in stepped platinum surfaces.

The question of what occurs at an interface might be addressed most simply if the substances on both sides of the interface are the same chemically and crystallographically and differ only in crystal orientation. Such a system is described in which two single crystals of niobium are cleaned, polished flat in particular crystal planes, oriented to form a particular twin boundary, and then diffusion-bonded. The results of a subsequent analysis by high-resolution electron microscopy of the grain boundary were compared with model predictions.

The theoretical basis for RSMST and for its application to the niobium twist boundary studied experimentally is presented in the form of the density of electronic states at the grain boundary. Detailed comparison with experimental data is not yet possible.

The interaction of laser radiation with surfaces is a matter of great practical interest, particularly at or near the threshold of intensity and wavelength at which observable damage occurs. In an experiment reported here, laser radiation incident on a sapphire surface at two frequencies—the higher corresponding to 3.5 eV—has been found to produce aluminum ions with kinetic energies averaging 7 eV, a result difficult to understand without a mechanism that includes electronic desorption.

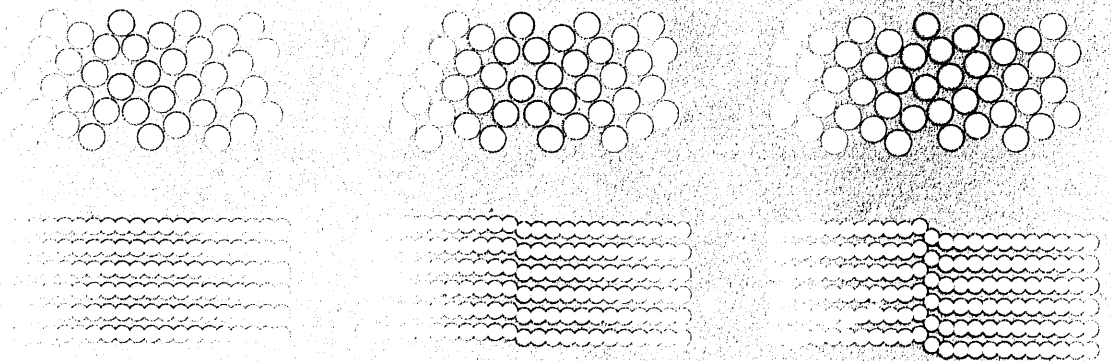
The preparation of multilayer structures for use in x-ray optics has been described previously. A particularly useful multilayer in lithography consists of alternating layers of molybdenum and silicon. Interdiffusion at the interface can alter its optical performance. High-resolution electron microscopy of the interfacial region of samples annealed at various temperatures indicates that reflectivity and wavelength dependence of the Mo/Si multilayer were unlikely to be affected at operating temperatures near ambient.

Our diffusion bonding of niobium samples was done in Germany because no U.S. facility can carry out the bonding under ultrahigh-vacuum (UHV) conditions. Such a diffusion-bonding facility has been under design and construction in the Department since 1988 and is scheduled to go into operation early in fiscal year 1993.

---

Section 5

**Bonding and  
Reactions  
at Surfaces  
and Interfaces**



**Ball models of the (310) twin in niobium.**

# LEED Determination of Multilayer Relaxation in Stepped Surfaces

A. Gonis

*The real-space multiple scattering theory (RSMST), combined with an automated tensor low-energy electron diffraction (LEED) method, is used to determine atomic relaxations in the stepped platinum(210) surface for which conventional mechanisms fail. These relaxations are found to be primarily perpendicular to the surface and nonalternating in sign. Also, they are in good qualitative agreement with new results from using the embedded-atom method.*

## Introduction

The study of systems with reduced symmetry, such as surfaces and interfaces, is of great importance to science and technology. However, the lack of translational invariance characterizing these systems has hampered the study of such systems by means of first-principles, quantum mechanical methods. Only recently have theoretical/computational developments allowed an essentially unified treatment of bulk, translationally invariant materials and of systems containing extended, two-dimensional defects such as surfaces and interfaces. We have applied these new methods to the study of the multilayer relaxation of a stepped surface, that of platinum in the (210) direction.

High-Miller-index surfaces, also called stepped or kinked surfaces, are of great importance in fields as diverse as catalysis, crystal growth, crack propagation, and tribology. Yet very few structures of stepped surfaces, such as multilayer relaxations and adsorption geometries, have been determined on the sub-angstrom scale. Structural determination has so far been confined almost exclusively to low-Miller-index surfaces for which conventional methods yield reliable results.

The primary technique used to analyze stepped surfaces has been low-energy electron diffraction (LEED).<sup>1</sup> However, the application of LEED has been hampered by difficulties in dealing with the small interlayer spacings that usually characterize high-Miller-index surfaces. Small spacings result from wide terraces and from kinks in the steps (i.e., nonalignments of the atoms in the steps, resulting in jagged step edges).

A stepped surface is characterized by the relatively large area,  $A$ , of its two-dimensional unit cell and by the small interplanar spacing,  $d$ , between atomic layers parallel to the surface. These factors cause two major difficulties in LEED theory.<sup>1</sup> First, the size of the plane-wave basis set necessary to represent electronic wave-functions at a given

energy scales roughly as  $A/d$ , so that it soon becomes prohibitively large for a stepped surface. Second, a traditional LEED approach relies on a layer-doubling method for obtaining the reflectivity of a surface, a process that can fail to converge for small interplanar spacings. Some improvements may result for the use of stacks of planes<sup>2-5</sup> rather than a single plane in the layer-doubling method, but this technique only delays the onset of divergent behavior and does not cure it. Thus, conventional LEED theory has been applied only sparingly to the analysis of stepped surfaces. An application to the Cu(410) surface has been reported,<sup>6</sup> but that study did not provide reliable details on multilayer relaxation.

The Al(210) surface structure, very similar to that of Pt(210), was analyzed some years ago<sup>7</sup> using LEED in connection with the layer-doubling method. This analysis was possible only because of the unusually weak multiple scattering of electrons by aluminum atoms, which permitted the method to converge better than in almost any other metal. By contrast, platinum causes particularly strong multiple scattering and thus serves as a severe test case for a LEED theory. The failure of conventional LEED methods (i.e., layer doubling) to converge, thus precluding the analysis of experimental data, motivated us to choose platinum. The structure could be solved,<sup>8</sup> however, by applying the RSMST method<sup>9</sup> coupled with an automated tensor LEED search<sup>10-13</sup> for the many unknown structural parameters.

## General Theory

The RSMST<sup>9</sup> allows us to determine the scattering properties of materials with reduced symmetry and is ideally suited for the treatment of two-dimensional extended defects such as surfaces, interfaces, and grain boundaries.<sup>14</sup> In our application of the RSMST method to LEED, we use the two-dimensional surface periodicity and a Fourier transform to convert the surface problem into a one-dimensional problem. Then, we apply the concept of

removal invariance, which states that removing one layer, or a repeating unit, from a semi-infinite periodic stack of layers does not change the properties of the surface. Within multiple-scattering theory, this process leads to a self-consistent equation from which the scattering matrix of the surface for each vector in the two-dimensional Brillouin zone of the surface and in the angular momentum representation can be determined. This self-consistent equation replaces the layer-doubling process and alleviates the difficulties of convergence caused by small interlayer spacing.

From the surface-scattering matrix, the amplitudes of the reflected electron beams can be calculated by a straightforward transformation to a plane-wave basis. Once the scattering matrix for the unrelaxed substrate is known, the intensities for a given relaxed configuration can be obtained in at least two ways. The first approach is to calculate the scattering matrix for each relaxed configuration by adding the relaxed planes onto the substrate. The second approach is to use the tensor LEED technique,<sup>10-13</sup> which is essentially a perturbation expansion of the scattering matrix in terms of the displacement of the atoms in the surface region with respect to the unrelaxed reference structure (the substrate). We chose the latter approach, coupled with an automated structural search<sup>13</sup> as being by far the more efficient of the two methods. This method is valid for relaxations less than about 0.4 Å and is particularly efficient when it is necessary to fit many unknown parameters. The former approach (layer addition), which should ideally be combined with the tensor LEED method, would be used for reconstruction, overlayers of adsorbates, etc.

For comparison, we also calculated the Pt(210) surface relaxation using the embedded-atom method (EAM).<sup>15,16</sup> As discussed below, these two very different methods gave quite similar results, thus increasing our confidence in both of them.

## Experimental Details

We measured the LEED spectra on a sample cut from a high-purity (99.999%) single-crystal rod and oriented this sample within  $\pm 0.5^\circ$  using the Laue method. After polishing the sample with diamond paste (0.25  $\mu\text{m}$ ), we cleaned it *in situ* by a combination of argon-ion sputtering, annealing, and oxygen treatment. From this process, we obtained an impurity-free surface, as judged by Auger electron spectroscopy, displaying a sharp LEED pattern.

We took LEED intensities near liquid-air temperature using a video camera operated under computer control.<sup>17</sup> Between the measurements of different beams, we flashed the surface to avoid residual gas absorption, which could easily affect the surface multilayer relaxation. Experimental spectra extend up to 300 eV, while the theory-experiment fit used only the data between 15 and 120 eV. Our purpose here was to reduce (1) the dimensions of the various matrices used in the calculation and (2) the computational times. We were able to make the incident beam fall into the (001)

surface mirror plane, causing the  $(k,h)$  and  $(h,k)$  spots to be symmetrically equivalent. We then averaged the intensity spectra of such spot pairs to increase the quality of the data.

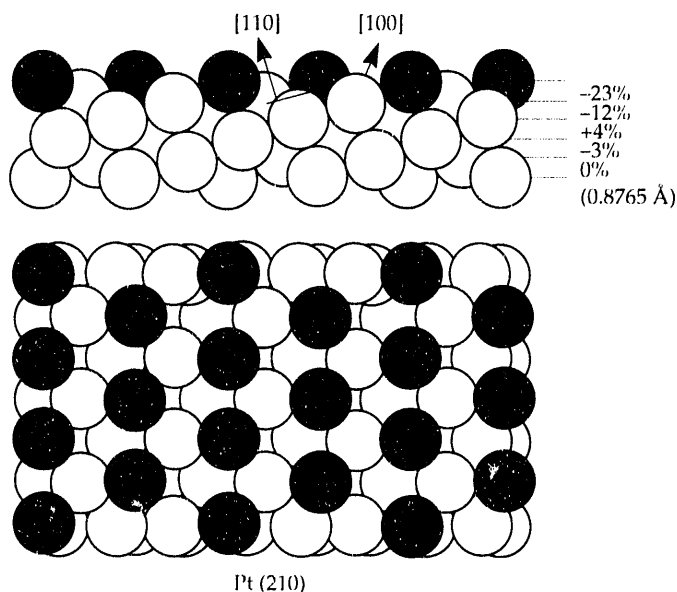
## Calculational Details

The nonstructural parameters for the LEED calculation were as follows: phase shifts up to  $l_{\text{max}} = 6$  were included, based on a relativistic potential<sup>18</sup> for platinum. The muffin-tin zero (the zero of potential in the solid) was set at 10 eV below vacuum and later adjusted during the tensor LEED search to an optimum 14 eV. The mean free path was simulated by an imaginary part of the muffin-tin constant that was made proportional to the cube root of the energy.<sup>18</sup> A Debye temperature of 230 K was used, and the temperature was set at 100 K.

## Results

The resulting structure of the Pt(210) surface is illustrated in Fig. 1, which shows both a side view (a) and a top view (b) of the surface, along with the interlayer relaxation in terms of the unrelaxed (bulk) interplanar values. Negative numbers indicate a contraction, and positive numbers indicate an expansion of the interlayer spacing. The first interlayer spacing contracts by 23%, the second contracts by 12%, the third expands by 4%, and the fourth contracts by 3%. These results agree reasonably well with those predicted by the EAM calculations, which yielded the relaxations -31%, -10%, +10%, and -7%, respectively. Lateral relaxations, as predicted by both methods, were virtually nonexistent. Similar agreement between the two methods occurred in the case of the Al(210) surface, thus increasing

**Figure 1.** Side view (a) and top view (b) of the reconstructed Pt (210) surface.



our confidence in the reliability of both techniques. The value of the unrelaxed interlayer spacing, given next to the 0% relaxation spacing, is 0.8765 Å.

The magnitude of the contraction of the first interlayer spacing is not surprising. It fits well with observed trends of "rougher" surfaces to have larger relaxations. Of particular interest is the lack of alternation in sign of the spacing relaxations, as if these occurred with an oscillation that is badly mismatched with the interlayer spacing. Such behavior has occasionally been observed before, namely for the bcc Fe(111), Fe(210), and fcc Al(331) surfaces.<sup>19</sup> In view of such findings, a trend appears to emerge: such nonalternation in sign seems to occur only on the more open surfaces that expose the *third*-layer atoms most prominently to the vacuum. The exposure of highly coordinated metal atoms should be particularly beneficial for catalytic activity.

The success of the RSMST technique demonstrates that it is well suited for the structural study of stepped surfaces, especially when coupled with automated tensor LEED. Our study opens the way for the detailed analysis of stepped surfaces that were heretofore unreachable with conventional LEED analysis.

*This work was funded by Weapons-Supporting Research.*

## References

1. M. A. Van Hove, W. H. Weinberg, and C.-M. Chan, *Low-Energy Electron Diffraction* (Springer, Heidelberg, 1986).
2. D. W. Jepsen, "New Transfer-Matrix Method for Low-Energy-Electron Diffraction and Other Surface Electronic-Structure Problems," *Phys. Rev. B* **22**, 5701 (1980).
3. P. J. Rous and J. B. Pendry, "Diffuse LEED from Simple Stepped Surfaces," *Surf. Sci.* **173**, 1 (1986).
4. J. M. MacLaren, S. Crampin, and D. D. Vvedensky, "Layer Korringa-Kohn-Rostoker Theory for Close-Spaced Planes of Atoms," *Phys. Rev. B* **40**, 12176 (1989).
5. P. Pinkava and S. Crampin, "On the Calculation of LEED Spectra from Stepped Surfaces," *Surf. Sci.* **233**, 27 (1990).
6. A. J. Algra, S. B. Luitjens, E. P. Th. M. Suurmeijer, and A. L. Boers, "The Relaxation of the Copper(410) Surface," *Appl. Surf. Sci.* **10**, 273 (1982).
7. D. L. Adams, V. Jensen, X. F. Sun, and J. H. Vollesen, "Multilayer Relaxation of the Al(210) Surface," *Phys. Rev. B* **38**, 7913 (1988).
8. X.-G. Zhang, M. A. Van Hove, G. A. Samorjai, P. J. Rous, D. Tobin, A. Gonis, J. M. MacLaren, K. Heinz, M. Michl, H. Linder, K. Müller, M. Ehsasi, and J. H. Block, "Efficient Determination of Multilayer Relaxation in the Pt(210) Stepped and Densely Kinked Surface," *Phys. Rev. Lett.* **67**, 1298 (1991).
9. X.-G. Zhang, P. J. Rous, J. M. MacLaren, A. Gonis, M. A. Van Hove, and G. A. Samorjai, "A Real-Space Multiple Scattering Theory of Low Energy Electron Diffraction: A New Approach for the Structure Determination of Stepped Surfaces," *Surf. Sci.* **239**, 103 (1990).
10. P. J. Rous, J. B. Pendry, D. K. Saldin, K. Heinz, K. Müller, and N. Bickel, "Tensor LEED: A Technique for High-Speed Surface-Structure Determination," *Phys. Rev. Lett.* **57**, 2951 (1986).
11. P. J. Rous and J. B. Pendry, "The Theory of Tensor LEED," *Surf. Sci.* **219**, 355 (1989).
12. P. J. Rous and J. B. Pendry, "Applications of Tensor LEED," *Surf. Sci.* **219**, 373 (1989).
13. P. J. Rous, M. A. Van Hove, and G. A. Samorjai, "Directed Search Methods for Surface Structure Determination by LEED," *Surf. Sci.* **226**, 15 (1990).
14. E. C. Sowa, A. Gonis, X.-G. Zhang, and S. M. Foiles, "Electronic Structure of Grain Boundaries," *Phys. Rev. B* **40**, 9993 (1989).
15. M. S. Daw and M. I. Baskes, "Semiempirical, Quantum Mechanical Calculation of Hydrogen Embrittlement in Metals," *Phys. Rev. Lett.* **50**, 1285 (1983).
16. M. S. Daw and M. I. Baskes, "Embedded-Atom Method: Derivation and Application to Impurities, Surfaces, and Other Defects in Metals," *Phys. Rev. B* **29**, 6443 (1984).
17. K. Heinz, K. Müller, T. Engel, and K. H. Rieder, "Springer Tracts in Modern Physics," in *Structural Studies of Surfaces*, **91**, G. Hoehler, Ed. (Springer-Verlag, Berlin, 1982), p. 1.
18. D. F. Ogletree, M. A. Van Hove, and G. A. Samorjai, "LEED Intensity Analysis of the Structures of Clean Pt(111) and of CO Adsorbed on Pt(111) in the c(4 × 2) Arrangement," *Surf. Sci.* **173**, 351 (1986).
19. F. Jona and P. Marcus, "Surface Structures from LEED: Metal Surfaces and Metastable Phases," in *The structure of Surfaces II*, J. F. Van der Veen and M. A. Van Hove, Eds. (Springer, Heidelberg, 1988), p. 90.

# Experimental and Theoretical Determination of the Atomic Structure of the (310) Twin in Niobium

G. H. Campbell, W. E. King,  
S. M. Foiles,\* P. Gumbsch,<sup>†</sup>  
and M. Rühle<sup>‡</sup>

*We fabricated a (310) twin boundary in niobium by diffusion-bonding oriented single crystals, characterized it using high-resolution electron microscopy, and predicted the atomic structures for the boundary using different interatomic potentials. After comparing the theoretical models to the high-resolution images by image simulation, we have ruled out one of the low-energy structures predicted by theory.*

## Introduction

The predictive power of the embedded-atom method (EAM) and other interatomic-potential methods for determining the atomic structure of defects in face-centered cubic (fcc) metals is well established.<sup>1,2</sup> However, it is desirable for models of large assemblies of atoms to be more generally applicable to other crystal systems. Defect structures in body-centered cubic (bcc) metals are assumed to be more difficult to predict because their atoms are less isotropic. That is, an atom in a bcc structure has 8 nearest neighbors vs 12 in fcc. Comparison of experimentally determined defect structures in a bcc metal with theoretically predicted structures should provide information on the relative strengths of the interatomic potentials.

We chose the (310) twin boundary in the bcc structure for this study because calculations of the energy of symmetric tilt grain boundaries in bcc metals on planes perpendicular to the [001] direction show a cusp at the position of the (310) plane.<sup>3</sup> Because grain boundaries tend to facet, lower-energy structures are easier to fabricate with segments of atomically flat grain boundary suitable for study. Finally, we chose niobium as the model bcc metal because it is available in high purity and large single crystals.

## Model Structure Calculations

The structure of the (310) twin has been simulated by using several interatomic potentials for niobium: EAM,<sup>4</sup> Finnis-Sinclair,<sup>5</sup> and the model-generalized pseudopotential theory (MGPT).<sup>6</sup> Different translational states of the adjacent crystals were used as initial conditions for the energy minimization calculation, but the presence of periodic vacancies or interstitials was not considered. We consider here those structures predicted using the Finnis-Sinclair potential, which are essentially the same as those predicted by using the EAM.

## Experiment

We oriented two single crystals of high-purity niobium using Laue backscatter x-ray diffraction and flat surfaces corresponding to (310) planes and polished them using specialized optical polishing techniques. We then cleaned them by sputtering, oriented them to form a (310) twin, and diffusion-bonded them under ultrahigh vacuum (UHV). Finally, we prepared specimens of this grain boundary for observation by high-resolution transmission electron microscopy (HREM).

## Results

Figure 1 shows the model grain-boundary structures predicted using the Finnis-Sinclair interatomic potential, along with the calculated values of the grain-boundary energy. The first structure shown, labeled "Relaxed CSL," has strict mirror symmetry at the interface and is very close to a purely geometric model, where a reflection operation is performed at a (310) plane of the perfect bulk bcc structure. The other models shown are the two lowest-energy configurations determined by the calculation. These models differ from the Relaxed CSL, in that relative translations occur between the adjacent crystals. In Model 1, the crystal positions undergo a relative translation of 0.078 nm in the [001] direction. In Model 2 a 0.083-nm component of the crystal translation occurs in the [001] direction, and a 0.052-nm component occurs in the  $[\bar{1}30]$  direction. The difference in grain-boundary energies between Model 1 and Model 2 is within the error range of the interaction model, but they are both significantly lower than the energy of the Relaxed CSL model.

In the high-resolution micrograph of Fig. 2, both crystals are viewed in the [001] direction, the same direction as that shown in the top row of model structures in Fig. 1.



Crystallographically flat, straight sections of the boundary on (310) planes in both crystals are separated by small regions of severe mismatch. The important experimental parameters to know are microscope focus and specimen thickness. From a combination of image simulation in the bulk crystal<sup>7</sup> and a record of the focus setting of the microscope during operation, we determined a focus value of  $-30$  nm for this micrograph. The contrast in the simulated images is relatively insensitive to thickness in the thin areas of the specimen. Under these conditions, maxima in projected atomic potential correspond to minima in image intensity ("black atom contrast").

Using image simulation, we compared the predictions of theoretical grain-boundary-structure models to the experimental high-resolution images. In Fig. 3 (simulated images of the structures in Fig. 1), the images from the Relaxed CSL model and Model 1 appear to be identical. Indeed, the intensities differ by less than 1% for all values of thickness and defocus investigated. When viewed in the [001] direction, crystal shifts in that direction are indiscernible, but when a shift occurs in the  $[\bar{1}30]$  direction, as in Model 2, the contrast in the boundary is changed considerably.

Figure 4 compares the simulated image obtained by using the Relaxed CSL model or Model 1 to the experimental image for the determined values of focus and thickness. (Clearly, we can discard the simulation of Model 2, based on the mirror symmetry of the experimental image.) Not only was the match good for the value of focus in Fig. 4, but also for the other focus values investigated.

## Discussion

By comparing the experimental and simulated images, we concluded that the interface, when viewed in this projection, possesses mirror symmetry. Because no relative shift of the crystals occurs in the  $[\bar{1}30]$  direction, Model 2 definitely does not represent the structure of *this* interface. However, the statistical significance of an HREM observation is always questionable because of the extremely small area examined. Boundary-structure multiplicity cannot be ruled out, especially when the theory predicts multiple structures with similar energies.<sup>8,9</sup>

A complete structural determination of the interface would allow us to choose just one model structure as the

**Figure 1.**

Ball models of the (310) twin in niobium predicted by Finnis-Sinclair interatomic-potential calculations. Their energies, the lowest of all structures predicted, are shown as values of  $\gamma_{GB}$ . The structures differ by the respective translational states of the adjoining crystals.

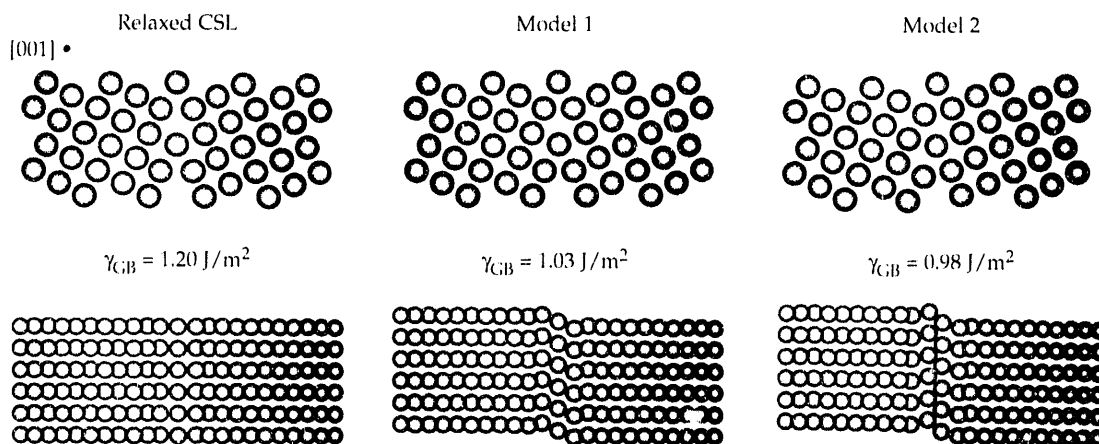


**Figure 2.** High-resolution micrograph of the (310) twin in niobium. The electron beam is parallel to [001] in both crystals, and crossed (110) are imaged ( $d = 0.23$  nm). Flat regions of the interface indicate faceting into a metastable structure.

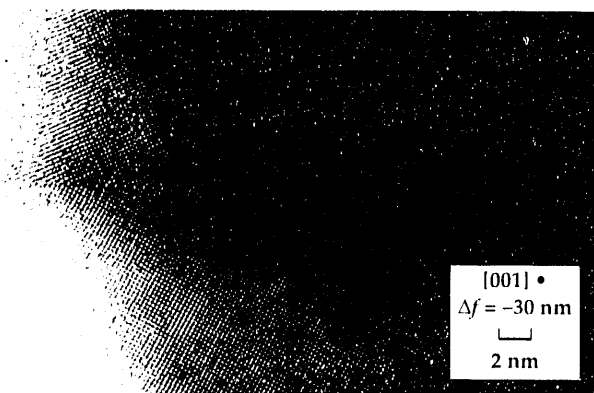
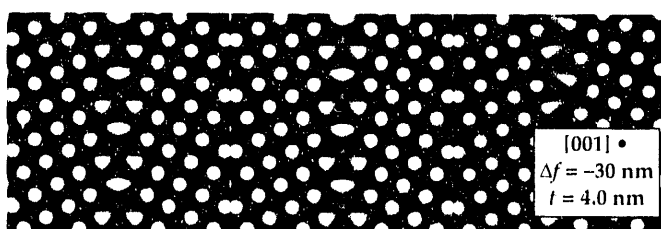


**Figure 3.** Comparison of the computer-simulated images obtained by slicing the model atomic structure from Fig. 1 and using the microscope parameters from Fig. 2. Note the different appearances of the interface in Model 1 and Model 2.



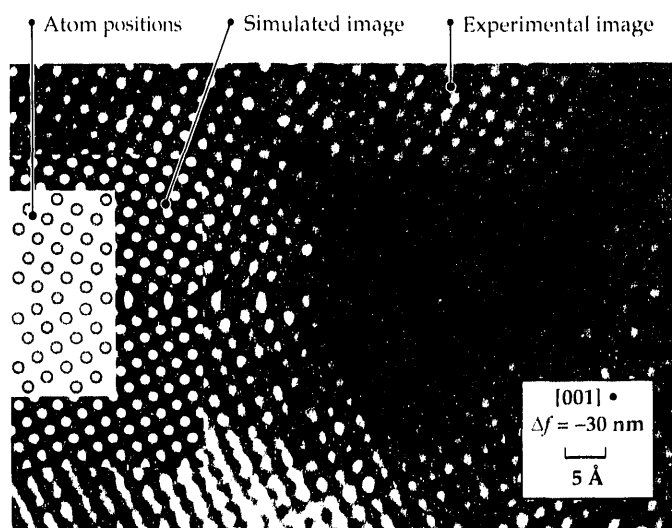
The focus deviation from Gaussian,  $\Delta f$ , and crystal thickness,  $t$ , are shown.

best for that interface. Determining the projected structure of the interface in another direction, when combined with such a structural determination, would give us a complete characterization. However, structural imaging of interfaces by HREM is subject to strict geometrical constraints.<sup>10</sup> The plane of the interface, as well as zone axes in both crystals, must be aligned with the electron beam. Observing structures in other directions would require resolution of the (310) planes, which are parallel to the interface and only 0.1 nm apart. This degree of accuracy is currently not obtainable.

## Conclusion

We have used HREM to determine the atomic structure of faceted grain boundaries of diffusion-bonded single crystals of niobium oriented to form a twin about the (310) plane. The EAM and Finnis-Sinclair interatomic-potential methods predict two structures with nearly identical energies for this grain boundary. In one structure, the adjacent crystals shift in the [130] direction at the interface, and in the other, they do not. When we used image simulation to compare and evaluate these predicted structures, we concluded that the actual crystal structure has no component of shift in the [130] direction. By viewing projected images along the [001] direction, we confirmed that the structure has a mirror symmetry about the twin grain boundary and thus ruled out one of the two predicted low-energy structures.

**Figure 4.** Comparison of the experimental image (enlargement of Fig. 2) with the simulated image, overlaid by atom positions from Model 1.



## Acknowledgment

We thank W. Wien for his careful preparation of the niobium crystals for diffusion bonding and D. Korn for his help with the UHV diffusion-bonding machine.

*This work was funded by the Division of Materials Science of the DOE Office of Basic Energy Sciences and by the Alexander von Humboldt Foundation.*

\*Sandia National Laboratories, Livermore, CA.

†Max-Planck-Institut für Metallforschung, Institut für Werkstoffwissenschaft, Stuttgart, Germany.

## References

1. S. M. Foiles, "Calculation of the Surface Segregation of Alloys Using the Embedded Atom Method," in *Surface Segregation Phenomena*, P. A. Dowben and A. Miller, Eds. (CRC Press, Boca Raton, 1990), pp. 79-106.
2. M. I. Baskes, S. M. Foiles, and M. S. Daw, "Application of the Embedded Atom Method to Interfaces in Metals," *Materials Science Forum* **46**, 187 (1989).
3. D. Wolf, "Correlation Between the Energy and Structure of Grain Boundaries in b.c.c. Metals: II. Symmetrical Tilt Boundaries," *Philos. Mag. A* **62**, 447 (1990).
4. R. A. Johnson and D. J. Oh, "Analytic Embedded Atom Method Model for BCC Metals," *J. Mater. Res.* **4**, 1195 (1989).
5. G. J. Ackland and R. Thetford, "An Improved N-Body Semi-Imperical Model for Body-Centered Cubic Transition Metals," *Philos. Mag. A* **56**, 15 (1987).
6. J. A. Moriarty, "First-Principles Interatomic Potentials in Transition Metals: Multi Ion Interactions and Their Analytic Representation," in *Many-Atom Interactions in Solids*, R. N. Nieminen, M. J. Puska, and M. J. Manninen, Eds. (Springer-Verlag, Berlin, 1990), pp. 158-167.
7. W. E. King, G. H. Campbell, A. Coombs, M. J. Mills, and M. Rühle, "HREM Investigation of the Structure of the  $\Sigma=5(310)/[001]$  Symmetric Tilt Grain Boundary in Nb," in *Defects in Materials*, *Mater. Res. Soc. Proc.* **209**, P. D. Bristowe, J. E. Epperson, J. E. Griffith, and Z. Liliental-Weber, Eds. (Materials Research Society, Pittsburgh, PA, 1990), pp. 39-46.
8. V. Vitek, Y. Minonishi, and G.-J. Wang, "Multiplicity of Grain Boundary Structures: Vacancies in Boundaries and Transformations of the Boundary Structure," *J. Phys. (Paris)* **46** (suppl. 4), 171 (1985).
9. W. Krakow, "Structural Multiplicity Observed at a  $\Sigma=5/[001]$  53.1° Tilt Boundary in Gold," *Philos. Mag. A* **63**, 233 (1991).
10. P. Pirouz and F. Ernst, "High Resolution Electron Microscopy: Possibilities and Limitations," in *Int. Workshop on Metal/Ceramic Interfaces*, M. Rühle, A. G. Evans, M. F. Ashby, and J. P. Hirth, Eds. (Pergamon, New York, 1990), pp. 199-233.

# The Real-Space Multiple-Scattering Theory and the Electronic Structure of Grain Boundaries

E. C. Sowa and A. Gonis

*We have used the real-space multiple-scattering theory (RSMST) to perform non-charge-self-consistent electronic-charge calculations on the  $\Sigma 5$  (310) tilt grain boundary in copper and on the  $\Sigma 5$  (100)  $36.9^\circ$  twist grain boundary in copper and niobium. These calculations show the effect of the atomic environment on the local density of electronic states near the grain boundary. We have begun work on a charge-self-consistent version of the method that will be able to calculate total energies.*

## Introduction

Interfaces often dominate the properties of a technologically interesting material by either enhancing or limiting its desirable characteristics. To design new materials at the atomic level and characterize existing materials, we need to understand structure-property relationships in materials with interfaces. This can be achieved only by means of an interdisciplinary approach in which experimentalists and theorists work together on the same systems.

An interface system is not as symmetric as a perfect crystal, which is what current state-of-the-art electronic-structure techniques are designed to treat. Thus, interfaces pose an important conceptual and technical challenge to researchers in theoretical solid-state physics. This challenge is more serious for fully quantum-mechanical treatments of the electronic structure at interfaces than for the atomistic simulations of interface systems<sup>1-3</sup> that have been so successful recently. Besides providing information about electronic states that is not accessible with atomistic simulations, electronic-structure calculations can also serve as benchmarks for atomistic simulations and provide information for deriving or fitting interatomic potentials. However, such information may not be available from experiments on buried interface systems.

## Real-Space Multiple-Scattering Theory

The use of Bloch's theorem makes the theoretical treatment of pure, periodic crystals practical. Unfortunately, the presence of an interface breaks the required translational invariance. This issue can be sidestepped, but not completely avoided, by approximating the isolated interface as a periodic array of repeating slabs of finite thickness (i.e., a supercell). Large repeat distances in the interface plane, combined with slabs thick enough to avoid interference between adjacent interfaces, can result in a unit cell with too many atoms for current techniques and computers to handle. Another

way to approximate the interface system is to forgo the use of Bloch's theorem and consider a free cluster of atoms with the geometry of the interface at the center of the cluster. Once again, however, a cluster large enough to eliminate the effect of its free surfaces on the interface at its center is too large to fit into current computers.

Many of the techniques developed for perfect crystals assume translational invariance from the start. However, the Green-function method, as developed by Korringa<sup>4</sup> and Kohn and Rostoker<sup>5</sup> (KKR), is more flexible for systems with reduced symmetry. When cast in the language of multiple-scattering theory (MST), the Green-function method does not require translational invariance explicitly, although Bloch's theorem may still be used in calculations when it is appropriate. However, one still must find a way to reduce the electronic-structure problem for systems with extended defects to a tractable size without making unwarranted approximations such as artificial periodic boundary conditions.

The answer to this challenge lies in replacing translational invariance with semi-infinite periodicity (SIP), which is defined by the regular repetition along a given direction of a scattering unit (e.g., an atom or plane of atoms), starting from a given point. A bicrystal, for example, has the SIP property because, far away from the interface itself, the system becomes bulk-like. Clearly, SIP is a property of a more general class of systems than is full translational invariance.

The symmetry principle that we shall apply to such systems is *removal invariance*, which states simply that the scattering properties of a system with SIP will not be changed by adding to or removing from its free end an integral number of scattering units. By using this principle in conjunction with MST, we can solve the Schrödinger equation to obtain the Green function of the extended system directly in real space. Then, we can use the Green function to determine the charge density and the local electronic density of states (DOS). The key idea is to treat the interface system as a finite cluster in real space but use removal invariance to

renormalize the boundary sites of the cluster to represent the scattering properties of the infinite medium surrounding the cluster. This real-space MST (RSMST)<sup>6,7</sup> converges much more rapidly with respect to cluster size than does a free cluster. Unlike Bloch's theorem, we cannot use removal invariance to construct the wave function of the extended system directly. Replacing reciprocal-space methods with real-space methods represents a trading of formal power in a restricted domain for wider applicability.

## Current Results

We have implemented the RSMST as a computer code that solves the Schrödinger equation and determines the local DOS at any atom of interest in a cluster. At its present stage, we can apply this code to known atomistic configurations with known electronic one-particle potentials. We use the self-consistent potentials for bulk copper and niobium given by Moruzzi, Janak, and Williams (MJW).<sup>8</sup> The atomic coordinates of the unrelaxed grain boundaries are easily found by appropriately twisting or tilting one half of the underlying lattice. In particular, we have used the code on copper twist and tilt grain boundaries and on a niobium twist grain boundary to obtain DOSs at sites in the interface regions for both relaxed and unrelaxed interfaces. For example, we took relaxed coordinates from the results of simulations that use the embedded-atom method<sup>9–11</sup> and compared these DOSs to those at bulk-like sites far from the interface.

We consider here the case of the  $\Sigma 5$  (310) tilt grain boundary in copper, which is formed by cutting a copper crystal to expose its (310) faces, rotating one half with respect to the other by  $180^\circ$  about the normal to the interface plane, and joining them. (The choice of their relative alignment, or the three microscopic degrees of freedom in the interface, is somewhat arbitrary for the unrelaxed configuration, which is not mirror-symmetric.) The primary effect of the relaxation predicted by the embedded atom method is that the interface becomes mirror-symmetric. In the RSMST calculation, we included relaxations to six layers on either side of the boundary.

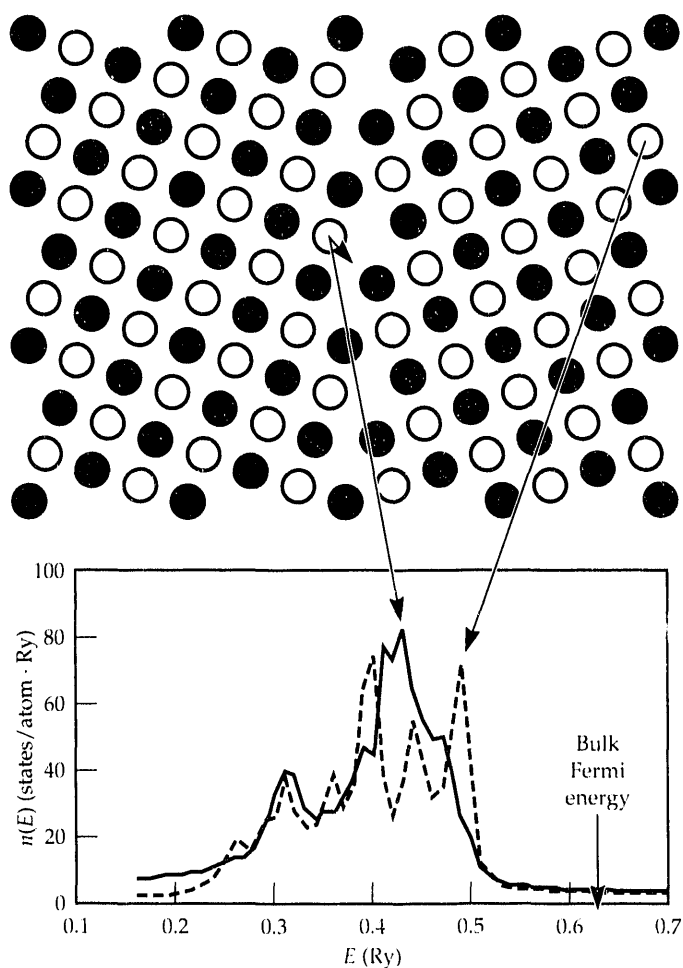
Figure 1, which shows the  $\Sigma 5$  (310) tilt grain boundary structure in copper, reveals how we interpret the DOS comparison. We compare the DOS at the interface atom that moves the most upon relaxation to the bulk-copper DOS computed by using the same method. The clusters used for all the calculations shown here contain approximately 120 atoms; for clusters of this size, we need a supercomputer with large memory such as a Cray-2. The integral of the DOS yields the charge density, and the integral of the energy-weighted DOS yields the band energy, an important contribution to the total energy of the system.

In Fig. 2, the solid lines show the local DOS at the black atom in the interface plane, which happens to be a coincidence site (a site common to the lattices on both sides of the interface). In the unrelaxed configuration, Fig. 2(a), the DOS

undergoes considerably more smearing and loss of structure than does the bulk (dashed lines). This is associated with the lowered symmetry and consequent destruction of the associated Van Hove singularities. One peak in particular, the second from the right, has essentially disappeared—it is associated with the periodicity of the (100) plane and is, of course, present in the (100) twist boundary that we have calculated. Upon relaxation, some of the peaks recover some amplitude [see Fig. 2(b)]. The local DOS at the moving (white) atom (the unrelaxed case is shown in Fig. 1) exhibits similar features.

We have also performed this calculation for the  $\Sigma 5$  (100)  $36.9^\circ$  twist grain boundaries in niobium and copper. Niobium represents a significant extension of the method because its bcc structure is more open than copper's fcc structure, and the Fermi level lies in the middle of the  $d$ -band. The qualitative features are similar to the cases described above.

**Figure 1.** The geometry of the  $\Sigma 5$  (310) tilt grain boundary in copper. The shading of the atoms represents location perpendicular to the plane of the figure. The small arrow on the atom at the center of the interface region indicates the direction in which it moves upon relaxation. Two local DOS curves are shown for this structure—the solid line is the DOS at a site in the interface region, while the dashed line is the DOS at a site far enough away from the interface to be bulk-like. Both curves are computed with the RSMST method.



As these calculations illustrate, the RSMST method allows us to solve the Schrödinger equation for materials with extended defects, such as surfaces and interfaces, without using inappropriate boundary conditions. From these calculations, we can see that DOS changes that result *only* from local geometry are significant, although not as large as those seen in similar calculations on free surfaces. However, the solution of the Schrödinger equation is only part of a complete electronic-structure calculation.

## Total-Energy Calculations

One of the primary goals of a complete electronic-structure calculation is to calculate energy differences, which are useful both for finding the ground state of the system and for predicting mechanical properties such as elastic constants. The standard procedure for calculating total energies is to solve the Hohenberg-Kohn-Sham equations of density-functional theory self-consistently in the local-density approximation. Briefly, for each structure considered, we use the output charge density from the solution of the Schrödinger equation to determine a new input potential by solving the Poisson equation, and we repeat the whole cycle until the input and output charge densities no longer change significantly. We then evaluate the energy functional, which includes both band-energy (the energy-weighted integral of the density of states described previously) and electrostatic contributions.

By restricting our attention to systems that are two-dimensionally periodic in the plane of the interface, we can take advantage of a total-energy code for layered systems that already exists. This code,<sup>12</sup> the Layer KKR (LKKR), uses Bloch's theorem within each layer and uses layer doubling to stack layers to form a bicrystal. The LKKR has been used to treat a (210) grain boundary in nickel.<sup>13</sup> This version of the LKKR cannot handle all interesting grain boundaries because layer doubling does not converge for closely spaced layers (e.g., high-Miller-index planes). However, because the removal invariance algorithm of the RSMST *can* handle closely spaced layers, we have substituted it for the layer-doubling algorithm. As a test of this hybrid code, the LKKR-RSMST, we can show that an interface formed by cleaving bulk copper and rigidly pulling the halves apart (or pushing them together) does indeed have a higher energy than the pure crystal. We are now preparing an application to a grain-boundary system.

## Acknowledgment

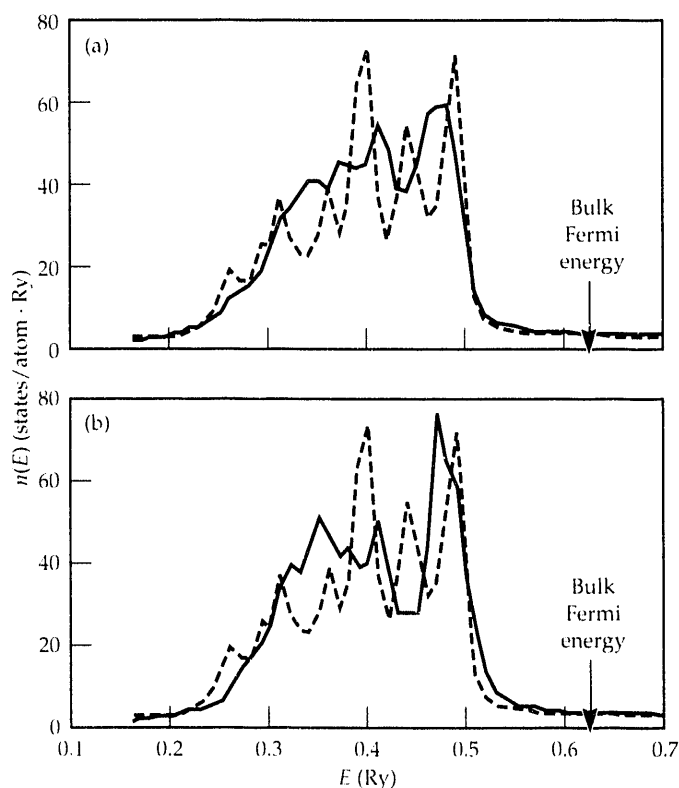
Computations were performed at the National Energy Research Supercomputing Center.

*This work was funded by the Division of Materials Science, DOE Office of Basic Energy Sciences.*

## References

1. S. M. Foiles and D. N. Seidman, "Solute-Atom Segregation at Internal Interfaces," *MRS Bull.* **15**(9), 51 (1990).
2. K. L. Merkle and D. Wolf, "Structure and Energy of Grain Boundaries in Metals," *MRS Bull.* **15**(9), 42 (1990).
3. S. R. Phillpot, D. Wolf, and S. Yip, "Effects of Atomic-Level Disorder at Solid Interfaces," *MRS Bull.* **15**(10), 38 (1990).
4. J. Korringa, "On the Calculation of the Energy of a Bloch Wave in a Metal," *Physica* **13**, 392 (1947).
5. W. Kohn and N. Rostoker, "Solution of the Schrodinger Equation in Periodic Lattices with an Application to Metallic Lithium," *Phys. Rev.* **94**, 1111 (1954).
6. X.-G. Zhang, A. Gonis, and J. M. MacLaren, "Real-Space Multiple-Scattering Theory and the Electronic Structure of Systems with Full or Reduced Symmetry," *Phys. Rev. B* **40**, 3694 (1989).
7. X.-G. Zhang and A. Gonis, "A New, Real-Space, Multiple-Scattering-Theory Method for the Determination of Electronic Structure," *Phys. Rev. Lett.* **62**, 1161 (1989).
8. V. L. Moruzzi, J. F. Janak, and A. R. Williams, *Calculated Electronic Properties of Metals* (Pergamon, New York, NY, 1978).
9. M. S. Daw and M. I. Baskes, "Embedded-Atom Method: Derivation and Application to Impurities, Surfaces, and Other Defects in Metals," *Phys. Rev. B* **29**, 6443 (1984).
10. S. M. Foiles, M. I. Baskes, and M. S. Daw, "Embedded-Atom-Method Functions for the fcc Metals Cu, Ag, Au, Ni, Pd, Pt, and their Alloys," *Phys. Rev. B* **33**, 7983 (1986).
11. E. C. Sowa, A. Gonis, X.-G. Zhang, and S. M. Foiles, "Electronic Structure of Grain Boundaries," *Phys. Rev. B* **40**, 9993 (1989).
12. J. M. MacLaren, S. Crampin, D. D. Vvedensky, R. C. Albers, and J. B. Pendry, "Layer Korringa-Kohn-Rostoker Electronic Structure Code for Bulk and Interface Geometries," *Comput. Phys. Commun.* **60**, 365 (1989).
13. S. Crampin, D. D. Vvedensky, J. M. MacLaren, and M. E. Eberhart, "Electronic Structure Near (210) Tilt Boundaries in Nickel," *Phys. Rev. B* **40**, 3413 (1989).

**Figure 2.** Electronic DOSs associated with a coincidence site in a copper  $\Sigma 5$  (310) tilt grain boundary (solid lines), compared with bulk copper (dashed lines): (a) unrelaxed configuration; (b) relaxed configuration.



# Laser-Induced Desorption of Aluminum from $\text{Al}_2\text{O}_3(11\bar{2}0)$

M. A. Schildbach and  
A. V. Hamza

*We investigated the laser-induced desorption of particles from a well-characterized sapphire ( $11\bar{2}0$ ) surface at laser wavelengths of 1064 nm (1.17 eV) and 355 nm (3.51 eV). Below the laser ablation threshold, only aluminum ions desorbed, with average kinetic energies of  $7.0 \pm 0.7$  eV at both photon energies. These high kinetic energies indicate an electronic desorption mechanism. Upon heating to over 1600 K, the surface reconstructed, exhibiting a  $(12 \times 4)$  low-energy electron diffraction pattern. The electron energy-loss spectrum for this surface, with a broad ( $\sim 2$  eV FWHM) loss feature centered at 3.6 eV, revealed surface electronic states in the bulk band gap of sapphire. We believe that the surface electronic states participate in the photon absorption process.*

## Introduction

Recently, multiphoton absorption by wide band gap materials has been proposed as an important mechanism for energy absorption on surfaces ultimately leading to laser-induced surface damage. Many authors have observed nonthermal, photon-stimulated desorption of particles with radiation at energies less than the band gap of the solid material sample.<sup>1</sup> The multiphoton nature of the process is gleaned from the dependence of the particle yield on photon fluence. In cases where the number of photons required in the process is large ( $>3$ ), the assistance of surface or defect states in the band gap has been proposed. These states may be the origin of photon absorption or may resonantly enhance the multiphoton absorption. However, the surfaces studied have not been sufficiently well characterized to confirm the proposed mechanism.

We have attempted to identify the mechanism by which the surfaces of transparent materials absorb photons with energies significantly less than the band gap. We chose sapphire surfaces for study because of their importance in laser and optics technology, their large bulk-projected band gap, and their low threshold for secondary electron emission, which allows the use of electron spectroscopies to characterize the surfaces. Our results for  $\text{Al}_2\text{O}_3(11\bar{2}0)$  irradiated with 1064- and 355-nm photons show that absorption by the surface may be multiphoton in nature and that surface states are present in the band gap that may participate in the photon absorption.

## Experiment

The experimental apparatus was an ultrahigh vacuum chamber, with base pressure of  $2 \times 10^{-10}$  Torr, equipped with reverse-view low-energy electron diffraction (LEED) optics and a double-pass cylindrical mirror analyzer (CMA) for surface-structure and composition determination. We focused the 1064-nm, 8-ns and 355-nm, 6-ns output of a Nd:YAG laser to a 0.5-mm-diameter spot at approximately  $15^\circ$  to the surface normal. We measured time of flight (TOF) for laser-induced desorption with a differentially pumped quadrupole mass spectrometer using the laser pulse to trigger a transient digitizer with a resolution of  $1 \mu\text{s}/\text{channel}$ . The distance from the sample to the multiplier was 45.8 cm. The quadrupole was oriented such that the desorbing flux passed down the centerline of the mass filter.

$\text{Al}_2\text{O}_3(11\bar{2}0)$  samples were  $12 \times 12 \times 1$  mm. Tantalum strips mounted between two samples served as resistive heaters, as described in Refs. 2 and 3. A chromel-alumel thermocouple, held in contact with the surface by a high-temperature ceramic adhesive, monitored the surface temperature. The only significant surface impurity on the samples, as received, was carbon. We cleaned the surface by heating it to  $\sim 1100$  K and then sputtering it with  $\text{Ar}^+$  ions to remove the residual carbon contaminant. After sputtering, annealing to 1700 K produced the equilibrium  $(12 \times 4)$  pattern. Auger electron spectra for the equilibrium surface showed no contaminants and a surface stoichiometry of two aluminum atoms to three oxygen atoms.

## Results and Discussion

After we exposed the  $(12 \times 4)$  surface to a series of 50,000 laser pulses at  $\sim 3.5 \text{ J/cm}^2$ , the LEED pattern had gradually degraded to the point that we could no longer detect fractional-order diffraction beams at any incident electron energy. We also observed changes in the electronic properties of the surface after photon exposure. The clean and well-annealed surface exhibited stable LEED patterns down to incident electron energies of 80 eV (i.e., surface charging was negligible). With increasing exposure to 1064-nm photons, the threshold electron energy for stable LEED patterns increased. After 50,000 pulses, we could observe stable patterns only at incident electron energies above 115 eV. Annealing the laser-degraded surface to 1700 K restored the original  $(12 \times 4)$  LEED pattern.

The exposure of the surface to 1.17-eV photons revealed the intimate relationship between the atomic and electronic structures of the surface. The surface electric conductivity increases as the surface structure nears its equilibrium structure. Thus, a plausible explanation for the increased conductivity of the  $(12 \times 4)$  surface may be surface electronic states that facilitate the removal of surface charge. Gignac et al.<sup>3</sup> observed a surface electronic state in the bulk band gap at  $\sim 4 \text{ eV}$  below the conduction band minimum for  $\text{Al}_2\text{O}_3(1\bar{1}02)$  and suggested that the presence of this state may enable impinging electrons to flow rapidly away from the point of impact, thereby reducing the charging of the surface.

We used reflection electron-energy-loss spectroscopy (ELS) to probe the surface for electronic states in the band gap. Figure 1 shows the EL spectrum for the  $\text{Al}_2\text{O}_3(11\bar{2}0)-(12 \times 4)$  surface. The prominent loss features appear at 22

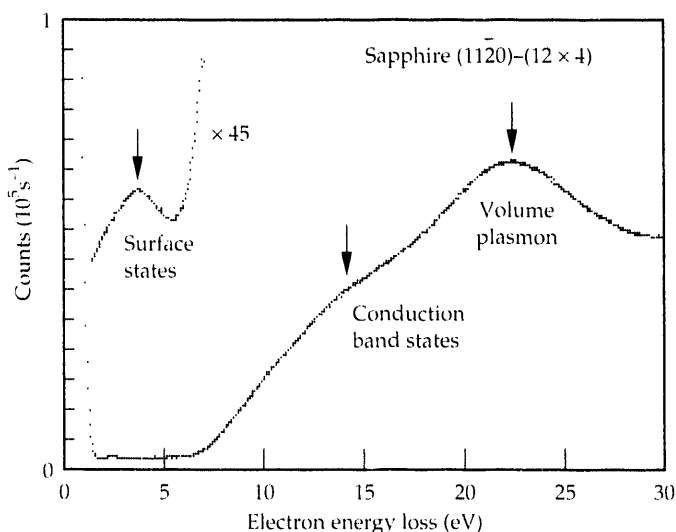
and 14 eV. The 22-eV loss, which is assigned to the excitation of the sapphire bulk plasmon, agrees well with previous ELS measurements.<sup>3,4</sup> The 14-eV loss feature is assigned to interband transitions from the valence band maximum (VBM) to empty states in the conduction band formed from empty aluminum 3s and 3p orbitals (based on calculations by Ciraci and Batra<sup>5</sup>). The enlargement of the bulk-projected band gap region reveals the presence of a broad loss feature in the band gap centered at 3.6 eV. This loss feature relates to either a transition from an occupied surface electronic state 3.6 eV below the conduction band minimum (CBM) to the CBM or a transition from the VBM to an unoccupied surface electronic state 3.6 eV above the VBM. Ciraci and Batra<sup>5</sup> also predicted the presence of a surface electronic state 3 eV above the VBM in the bulk-projected band gap for the  $\text{Al}_2\text{O}_3(0001)$  surface as a result of the  $s + p_z$  dangling bonds from the surface aluminum atoms. The surface state observed here may be derived from these same dangling bonds because aluminum atoms on the  $(11\bar{2}0)-(12 \times 4)$  surface also may not be fully coordinated. However, because the loss feature is present in the absolute bulk band gap, surface electronic states are available to participate in a multiphoton absorption and in the conduction of electrons on the surface.

Aluminum ions desorbed at laser fluences of 5 to  $10 \text{ J/cm}^2$ , which are below the visible damage threshold of  $12 \text{ J/cm}^2$ . Below the visible damage threshold, we observed no other desorbing species.

We used TOF to measure velocity distributions for the desorbing aluminum ions during the pre-damage events. The most striking feature of the TOF distributions is the high kinetic energy of the desorbing aluminum. Also noteworthy is the shot-to-shot stability of the TOF distribution. The average kinetic energy of the desorbing aluminum is  $7.0 \pm 0.7 \text{ eV}$  for both the single-shot and the 10-shot-averaged distributions at both laser wavelengths. The high average kinetic energy indicates a nonthermal desorption mechanism. Because incident photon energies as low as 1.17 eV produce these high kinetic energies, a multiphoton absorption process may also be occurring.

Desorption of particles with energy of  $\sim 7 \text{ eV}$  requires a surface excitation of at least 7 eV. Sapphire exhibits an exciton that is bound by approximately 1 eV,<sup>6,7</sup> and because the band gap of sapphire is  $\sim 9 \text{ eV}$ , the exciton lies  $\sim 8 \text{ eV}$  above the VBM. Decay of this exciton would yield energy up to 8 eV. In addition, the exciton is localized on the aluminum atom, and no oxygen-centered excitons have been observed for sapphire.<sup>4,6</sup> This is consistent with the desorption of predominantly aluminum particles. Thus, exciton decay at surface aluminum atoms could lead to the observed desorption energies of  $\sim 7 \text{ eV}$ . Because the unaided absorption of seven 1.17-eV photons to excite the exciton is unlikely, the presence of surface electronic states

**Figure 1.** ELS spectrum for  $\text{Al}_2\text{O}_3(11\bar{2}0)-(12 \times 4)$ . The 201.5 eV elastic peak registered  $1.6 \times 10^6$  counts with an FWHM of 0.8 eV. CMA pass energy was 50 eV.



in the band gap that could resonantly enhance the absorption of photons makes this desorption mechanism plausible. If occupied, the surface electronic states could also be the origin of the photoabsorption, thereby reducing the number of photons required to produce the exciton.

*This work was funded by the Division of Materials Science of the DOE Office of Basic Energy Sciences.*

## References

1. E. Matthias, H. B. Nielsen, J. Reif, A. Rosen, and E. Westin, "Multiphoton-Induced Desorption of Positive Ions from Barium Fluoride," *J. Vac. Sci. Technol. B* **5**, 1415 (1987) and references therein.
2. C. C. Chang, "Silicon-on-Sapphire Epitaxy by Vacuum Sublimation: LEED-Auger Studies and Electronic Properties of the Films," *J. Vac. Sci. Technol.* **8**, 500 (1971).
3. W. J. Gignac, R. S. Williams, and S. P. Kowalczyk, "Valence- and Conduction-Band Structure of the Sapphire ( $1\bar{1}02$ ) Surface," *Phys. Rev. B* **32**, 1237 (1985).
4. J. Olivier and R. Poirer, "Electronic Structure of  $Al_2O_3$  from Electron Energy Loss Spectroscopy," *Surf. Sci.* **105**, 347 (1981).
5. S. Ciraci and I. P. Batra, "Electronic Structure of  $\alpha$ -Alumina and Its Defect States," *Phys. Rev. B* **28**, 982 (1983).
6. A. Balzarotti, F. Antonangeli, R. Girlanda, and G. Martino, "Core Excitons in Corundum," *Solid State Commun.* **44**, 275 (1982).
7. I. A. Brytov and Y. N. Romashchenko, "X-Ray Spectroscopic Investigation of the Electronic Structure of Silicon and Aluminum Oxides," *Sov. Phys. Solid State* **20**, 384 (1978).



# Thermal Stability of Mo/Si Multilayers

R. S. Rosen, D. G. Stearns,\*

M. A. Viliardos,<sup>†</sup>

M. E. Kassner,<sup>†</sup>

and S. P. Vernon<sup>‡</sup>

*By means of annealing studies at relatively low temperatures for various times, we investigated the thermal stability of Mo/Si multilayers. We found two distinct stages of thermally activated interlayer growth: a primary "surge," followed by a (slower) secondary "steady-state" growth where the interdiffusion coefficient is constant. The interdiffusion coefficients for the interlayer formed by deposition of Mo on Si are 200 times greater than those of the interlayer formed by deposition of Si on Mo. The interdiffusion coefficient and apparent activation energy for the secondary stage of Mo-on-Si interlayer growth are comparable to values for diffusion of silicon in hexagonal MoSi<sub>2</sub>.*

## Introduction

Mo/Si multilayer coatings have demonstrated the highest normal-incidence reflectivity at soft x-ray wavelengths to date<sup>1</sup> and are used in x-ray optical applications such as soft x-ray projection lithography (SXPL). The operational wavelength of SXPL is chosen to be 13.0 nm in order to optimize the normal incidence reflectivity of the Mo/Si multilayer coatings. Under these conditions, the multilayer structure is required to have a period (bilayer spacing) of ~6.7 nm, where the ratio of the Mo layer thickness to the period is in the range of 0.3 to 0.4. The fundamental requirements for precision-imaging multilayer mirrors in SXPL include high reflectivity and long-term stability at the operating temperature, which is estimated to be at or very near ambient temperature. However, the reflectivity is known to decrease with the formation of interlayer regions of mixed composition resulting from interdiffusion at the Mo/Si interfaces.<sup>2,3</sup> The objective of this study is to

perform a series of annealing treatments of Mo/Si multilayers at relatively low temperatures over long times in order to reliably assess stability during multilayer mirror service at ambient and near-ambient temperatures.

## Experimental Methods

The multilayers in this study consisted of 40 bilayers of molybdenum and silicon sputter-deposited onto polished single-crystal silicon wafers. The nominal bilayer spacing was 7.0 nm, and the ratio of molybdenum thickness to bilayer thickness was ~0.4. Reference 1 describes in detail the vacuum system and deposition procedures. First, we annealed the coated silicon substrates at 260 to 342°C for 0.5 to 2000 h. Next, we examined the structure of the as-deposited (unannealed) and annealed multilayers using large-angle x-ray diffraction (LAXS), selected-area electron diffraction (SAED), and high-resolution electron microscopy (HREM). Finally, we assessed the thermal stability from HREM measurements of the silicide interlayer thicknesses and from normal-incidence reflectivity (NIR) measurements using synchrotron radiation.

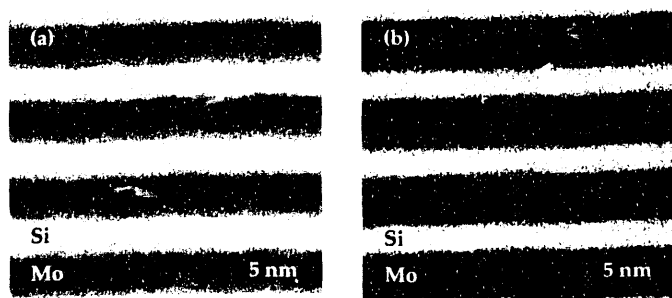
## Results and Discussion

The unannealed multilayer consists of amorphous silicon layers and crystalline molybdenum layers separated by thin, amorphous, Mo/Si interlayer regions. SAXS measurements of the bilayer spacing indicated that the multilayer structures had contracted during annealing, consistent with the formation of higher-density silicides from the pure layers. HREM confirmed that the Mo/Si interlayer regions thicken with annealing, as shown in Fig. 1. Although not shown in this figure, the structure after 100 h at 316°C consists of relatively thick layers of hexagonal MoSi<sub>2</sub> (as identified by

**Figure 1.** HREM micrographs of Mo/Si multilayers

(a) unannealed and (b) annealed for 1 h at

316°C (substrate oriented below the layers). These micrographs show growth of the (substantially) amorphous Mo/Si interlayer regions.



LAXS and SAED) separated by thin layers of “unreacted” crystalline molybdenum. The pure silicon layers were completely consumed by the formation of  $\text{MoSi}_2$ . We reduced the NIR of specimens annealed at  $316^\circ\text{C}$  for 1, 10, and 40 h to 54, 50, and 44%, respectively, from the unannealed value of 57%. After 80 h at  $316^\circ\text{C}$ , the NIR was less than 10% of the original value.

We determined the secondary-stage growth kinetics of the Mo/Si interlayers by assuming that the interlayer growth is diffusion limited with constant concentrations at the interfaces between the Mo/Si interlayer and elemental layers, and that the concentration gradient across the interlayer is linear. We then related the interlayer width  $w(t)$  after annealing time  $t$  to the interdiffusion coefficient  $D$  by

$$D = [w^2(t) - w^2(0)]/2t, \quad (1)$$

where  $w(0)$  is the initial interlayer width. Empirically,  $D$ , the interdiffusion coefficient of the Mo/Si couple as a function of temperature, can be described by relating it to a pre-exponential coefficient,  $D_0$ , which is independent of temperature, and an effective activation energy of interdiffusion,  $E_a$ :

$$D = D_0 \exp(-E_a/kT). \quad (2)$$

Figure 2 shows an Arrhenius plot of  $\log D$  vs  $1/T$  for the thick and thin Mo/Si interlayers (evaluated from secondary-stage growth rates) and, for comparison, interdiffusion results of other studies.<sup>2,4-8</sup> The interdiffusion coefficients for the thick (Mo-on-Si) interlayer are  $\sim 200$  times greater than those of the thin (Si-on-Mo) interlayer, despite the fact that the apparent activation energies are nearly identical over the temperature range studied. The apparent activation energy,  $E_a \approx 2.5$  eV, and interdiffusion coefficient,  $D_0 \approx 100 \text{ cm}^2/\text{s}$ , for the secondary stage of thick interlayer growth are comparable to interdiffusion values for Mo/Si multilayers at temperatures of 400 to  $500^\circ\text{C}$ ,<sup>2,7</sup> and to diffusion values for silicon in hexagonal  $\text{MoSi}_2$  evaluated from Mo/Si couples at temperatures of 475 to  $1200^\circ\text{C}$ .<sup>4-6,8</sup> Previous studies have shown that silicon is the principal diffusing species in hexagonal  $\text{MoSi}_2$  for specimens annealed at 560 to  $580^\circ\text{C}$ .<sup>4</sup>

## Conclusions

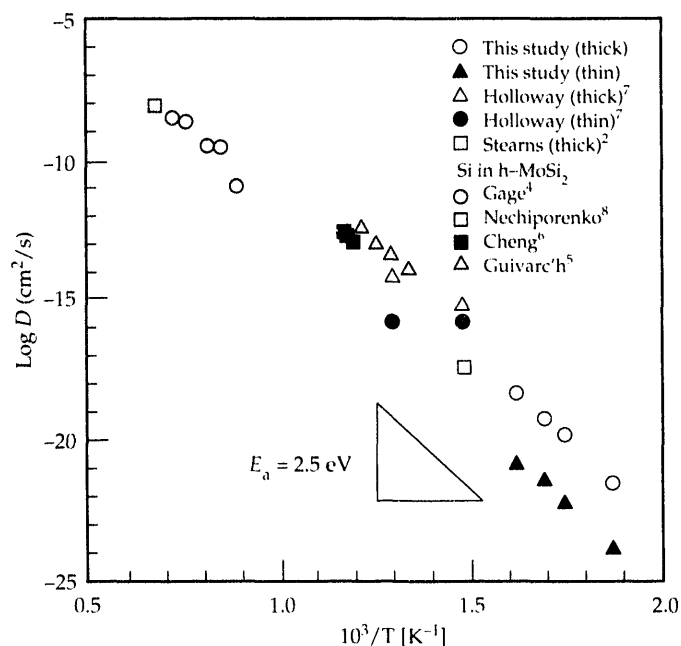
Annealing experiments performed on Mo/Si multilayers at temperatures of 260 to  $342^\circ\text{C}$  for 0.5 to 1000 h indicate two distinct stages of thermally activated silicide growth: a primary “surge” of  $\sim 0.3$  nm, followed by a (slower) secondary “steady-state” growth with constant  $D$ . The interdiffusion coefficients for the interlayer formed by deposition of molybdenum on silicon are 200 times greater than those of

the interlayer formed by deposition of silicon on molybdenum. The apparent activation energy,  $E_a \approx 2.5$  eV and interdiffusion coefficient,  $D_0 \approx 100 \text{ cm}^2/\text{s}$ , for the secondary stage of thick interlayer growth are comparable to values for diffusion of silicon in hexagonal  $\text{MoSi}_2$ . The increased growth rate during the primary stage may result from a decrease in free energy associated with the relaxation of residual interfacial stresses that are present in the as-deposited multilayer. A decrease in multilayer x-ray reflectance occurs as a result of interdiffusion (believed to be predominantly silicon) in the (principally) amorphous Mo/Si interlayer region, causing growth of this interlayer region that eventually crystallizes to hexagonal  $\text{MoSi}_2$ . If we assume a constant  $E_a$  at temperatures below  $200^\circ\text{C}$ , our data suggest, however, that changes in peak reflectivity and peak wavelength of Mo/Si multilayer mirrors at ambient temperature are negligible over the time scale relevant to SXPL.

## Acknowledgments

Y. Cheng prepared and viewed the HREM samples at the Facility for High-Resolution Electron Microscopy within the Center for Solid State Science at Arizona State University. The normal-incidence x-ray reflectance measurements were accomplished through a collaborative association with the

**Figure 2.** Arrhenius plot for the thick and thin Mo/Si interlayers, evaluated from secondary-stage growth rates, compared with interdiffusion results from other studies.<sup>2,4-8</sup> The apparent activation energy,  $E_a \approx 2.5$  eV, and interdiffusion coefficient,  $D_0 \approx 100 \text{ cm}^2/\text{s}$ , for the secondary stage of thick interlayer growth are comparable to diffusion values for silicon in hexagonal  $\text{MoSi}_2$ .



VUV Radiometric Laboratory of the Physikalisch Technische Bundesanstalt (PTB) at the Berlin Electron Storage Ring (BESSY). The principal collaborators were M. Krumrey and P. Müller from the PTB, D. Gaines from Brigham Young University, and N. Ceglio from Lawrence Livermore National Laboratory.

*This work was funded by the Advanced X-Ray Optics Program.*

\*Laser Program, LLNL

†Department of Mechanical Engineering, Oregon State University, Corvallis

‡Vernon Applied Physics, Torrance, CA

## References

1. D. G. Stearns, R. S. Rosen, and S. P. Vernon, "Fabrication of High-Reflectance Mo-Si Multilayer Mirrors by Planar-Magnetron Sputtering," *J. Vac. Sci. Technol. A*, **9**, 2662 (1991).
2. D. G. Stearns, M. B. Stearns, Y. Cheng, J. H. Stith, and N. M. Ceglio, "Thermally Induced Structural Modification of Mo-Si Multilayers," *J. Appl. Phys.* **67**, 2415 (1990).
3. R. S. Rosen, M. A. Viliardos, M. E. Kassner, D. G. Stearns, and S. P. Vernon, "Thermal Stability of Mo/Si Multilayers," *Proc. Multilayer Optics for Advanced X-Ray Applications, SPIE* **1547**, 212 (1991).
4. P. R. Gage and R. W. Bartlett, "Diffusion Kinetics Affecting Formation of Silicide Coatings on Molybdenum and Tungsten," *Trans. Metall. Soc. AIME* **233**, 832 (1965).
5. A. Guivarc'h, P. Auvray, L. Berthou, M. Le Cun, J. P. Boulet, P. Henoc, and G. Pelous, "Reaction Kinetics of Molybdenum Thin Films on Silicon (111) Surface," *J. Appl. Phys.* **49**, 233 (1978).
6. J. Y. Cheng, H. C. Cheng, and L. J. Chen, "Cross-Sectional Transmission Electron Microscope Study of the Growth Kinetics of Hexagonal MoSi<sub>2</sub> on (001)Si," *J. Appl. Phys.* **61**, 2218 (1987).
7. K. Holloway, K. B. Do, and R. Sinclair, "Interfacial Reactions on Annealing Molybdenum-Silicon Multilayers," *J. Appl. Phys.* **65**, 474 (1989).
8. E. P. Nechiporenko, E. P. Poltavtsev, N. S. Kapustin, V. V. Kapustin, and Yu. T. Kondratov, *Izv. Akad. Nauk SSSR, Neorg. Mater.* **10**, 1829 (1973).

---

## Overview

The discovery in 1986 of perovskite superconductors with transition temperatures much higher than those of previously known substances led many organizations to study the new phenomenon and attempt to synthesize compounds of still higher transition temperature. The C&MS effort, which later became the LLNL program, was directed to address substantive fundamental questions, synthesize high-quality, well-characterized samples, and combine experiment and theory in complementary ways.

This superconductivity program started from scratch because there was little base in condensed matter physics to draw on at the Laboratory. We began a fruitful collaboration with the University of California at Davis and other academic institutions (see Section 10 of this *Report*) and hired a number of condensed-matter physicists. By 1991, the program had an operating budget of about \$2 million. Since then, the search for sustained funding has been unsuccessful, and the program is being phased out in 1992.

Among the papers in this section is one dealing with the magnetic and transport properties of several copper-oxide superconductors. The key to these measurements is the ability to synthesize single crystals of these compounds. Thermodynamic properties such as upper critical field and coherence length were deduced from the data.

The electronic structure of untwinned single crystals of the yttrium-barium-copper-oxide (YBCO) superconductor was investigated by photoemission studies with synchrotron radiation. No large superconducting gap was observed.

X-ray and ultraviolet photoelectron spectroscopy of YBCO single crystals that had been freshly cleaved in an ultrahigh vacuum showed that the surfaces are stable for several days at ambient temperature. Exposure to air causes a variety of oxides and possibly hydroxides and carbonates to form.

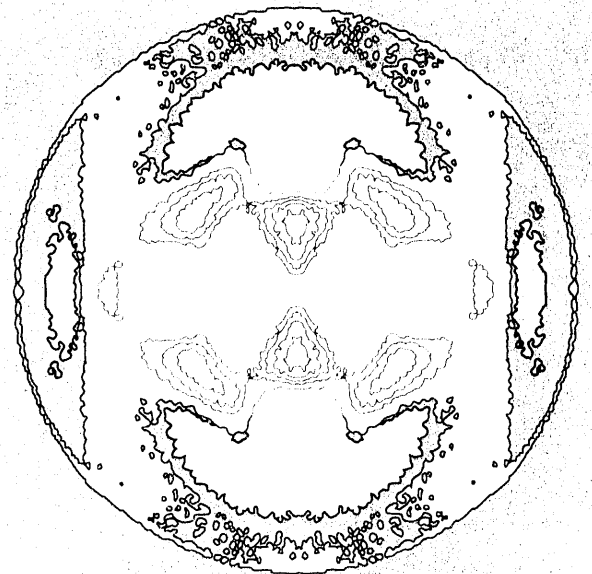
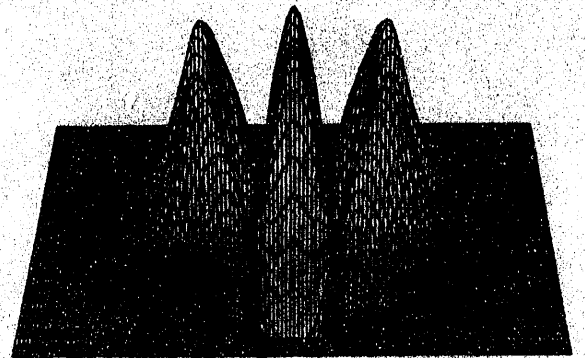
A theoretical analysis of the electronic structure of  $\text{La}_2\text{CuO}_4$  (or LSCO when doped with strontium) has been made. With a chemically realistic, eight-band effective Hamiltonian, the quasiparticle dispersion curves agree with experimental data.

A nearly unique experimental capability of the C&MS group is the ability to acquire high-precision electron-positron momentum distributions by angular correlation of annihilation radiation. The application of this technique to LSCO showed sharp features that indicated the presence of a Fermi surface and that agreed with calculations of the copper-oxygen plane bands.

---

Section 6

**Superconductivity**



**Positron angular correlation data for YBCO after subtracting the average isotropic component.**

# Magnetic and Transport Properties of Some High-Temperature Superconductors

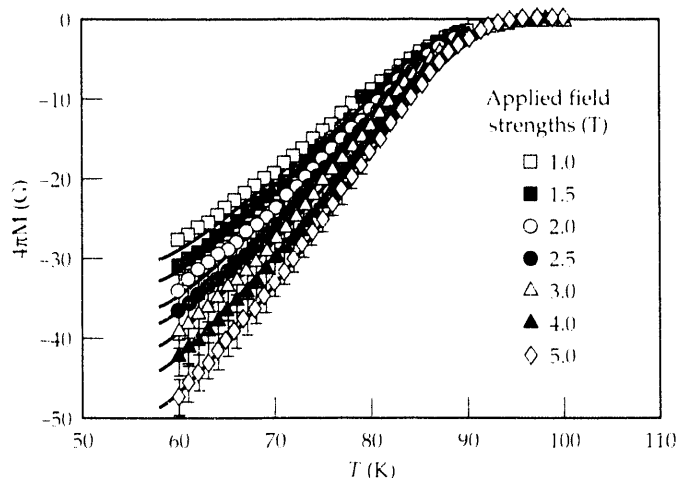
J. Z. Liu,\* Lu Zhang,\*  
Y. X. Jia,\* M. D. Lan,\*  
P. Klavins,\* and  
R. N. Shelton\*

We measured magnetic and transport properties of single crystals of  $\text{Bi}_{1.7}\text{Pb}_{0.3}\text{Sr}_2\text{CaCu}_2\text{O}_8$  (BPSCCO) and  $\text{Y}_{1-x}\text{Pr}_x\text{Ba}_2\text{Cu}_3\text{O}_7$  (YBCO-Pr) over wide temperature and field ranges. We determined important thermodynamic properties, such as the Ginzburg-Landau parameter  $\kappa$ , orbital critical field  $H_{c2}$ , and coherence length  $\xi$ .

## Introduction

The basic superconducting parameters, such as the Ginzburg-Landau constant  $\kappa$ , upper critical field  $H_{c2}$ , superconducting coherence length  $\xi$ , magnetic penetration depth  $\lambda$ , and pinning energy  $U_0$ , are important to understanding the mechanism of various newly discovered high-temperature superconductors. Unfortunately, because of the high transition temperatures, fluctuations near the critical temperature  $T_c$  are quite strong. This effect hinders the use of the classic London or Abrikosov models in determining these basic parameters. Recently, Hao et al.<sup>1</sup> developed a variation model to calculate the total free energy and obtained an analytical expression for the reversible magnetization in the range  $H_{c1} \ll H \ll H_{c2}$ . The basic parameters of single crystals of  $\text{YBa}_2\text{Cu}_3\text{O}_7$  (YBCO) were determined by fitting the reversible magnetization curves with this model.<sup>1,2</sup> In this article, we present our results<sup>3</sup> for high-quality single crystals of  $\text{Bi}_{1.7}\text{Pb}_{0.3}\text{Sr}_2\text{CaCu}_2\text{O}_8$  (BPSCCO) with  $T_c = 94$  K and  $\Delta T_c = 2$  K and our results on transport measurement in YBCO-Pr crystals.

**Figure 1.** Magnetization vs temperature for fields parallel to the  $c$  axis of  $\text{Bi}_{1.7}\text{Pb}_{0.3}\text{Sr}_2\text{CaCu}_2\text{O}_8$  crystal. Solid lines indicate fit to theory.



## Results and Discussion

We measured the reversible magnetization at applied fields up to 5 Tesla and temperatures between 60 and 100 K. Figure 1 shows the resultant magnetization curves in the reversible region for different fields applied parallel to the  $c$  axis. The magnetization curves are nearly linear functions of temperature from a point about 10 K below  $T_c$  down to 60 K. By using a computer program to fit these magnetization curves with an analytical equation of the reversible magnetization, in which  $\kappa$  is taken to be an adjustable parameter, we determined the thermodynamic parameters such as  $H_c$ ,  $\lambda$ , and  $\kappa$  simultaneously. In Fig. 1, the experimental measurements agree very well with the model, which yields  $\kappa = 94 \pm 4$  for sample No.1 and  $\kappa = 92 \pm 5$  for sample No. 2.

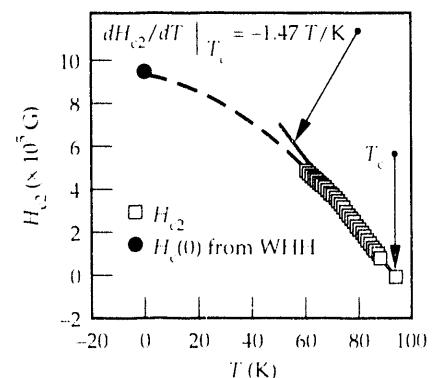
We calculated the upper critical field by

$$H_{c2} = \kappa \sqrt{2} H_c(T). \quad (1)$$

For the critical fields  $H_{c2}(T)$  shown in Fig. 2, the slopes of  $dH_{c2}(T)/dT$  near  $T_c$  are  $-1.5\text{ T K}^{-1}$  and  $-1.3\text{ T K}^{-1}$  for samples 1 and 2, respectively. The orbital critical fields, extrapolated to  $T = 0$  K using the Werthamer, Helfand, and Hohenberg (WHH) formula,<sup>4</sup>

**Figure 2.**

Upper critical field vs field for  $H$  parallel to  $c$  in a  $\text{Bi}_{1.7}\text{Pb}_{0.3}\text{Sr}_2\text{CaCu}_2\text{O}_8$  crystal.



$$H_{c2}(0) = 0.69 \left. \frac{dH_{c2}(T)}{dT} \right|_{T_c} T_c, \quad (2)$$

are  $H_{c2}(0) = 95$  and  $83$  T for the two samples. To find the coherence length at zero temperature, we used the expression

$$H_{c2}(0) = \frac{\Phi_0}{2\pi\xi_{ab}^2(0)}, \quad (3)$$

where  $\Phi_0 = 2.07 \times 10^{-7}$  G cm<sup>2</sup> is the flux quantum. We then calculated the  $\xi_{ab}(0)$  values of  $1.9$  and  $2.0$  nm, assuming a clean limit. For both crystals, the London penetration depth  $\lambda_{ab}$  is estimated to be  $178$  nm, in good agreement with the result of  $172$  nm obtained from a direct-penetration depth measurement in a muon-spin rotation experiment.<sup>5</sup>

Although the reversible magnetization calculation developed by Hao et al. has been used successfully with YBCO and BPSCCO crystals, it is difficult to use for determining the basic superconducting parameters of single crystals of YBCO-Pr because of the difficulty in separating the perfect diamagnetization from the paramagnetic contribution. Therefore, we used electrical transport measurements for these compounds.<sup>6</sup>

Using a self-flux method, we prepared single crystals of YBCO-Pr with  $x = 0, 0.1, 0.2, 0.28, 0.44,$  and  $0.56$  and measured the electrical resistivity with a standard dc four-probe ohmmeter with a current of  $5$  mA. Figure 3 shows the typical temperature dependence of the resistive transition for  $x = 0.2$  crystals under different magnetic fields applied parallel (a) and perpendicular (b) to the  $c$  axis. The broadening of the resistive transition is very similar to that seen in YBCO crystals. The dominant contribution to this broadening is from fluctuation effects at high temperature and flux flow at low temperature. The transition width with  $H$  parallel to  $c$  is much broader than that with  $H$  perpendicular to  $c$  for equal magnitudes of the applied field. All of the samples with  $0 < x < 0.56$  have a metallic-like behavior when  $T > 100$  K. To determine the upper critical field, we used a scaling formula,<sup>7,8</sup>

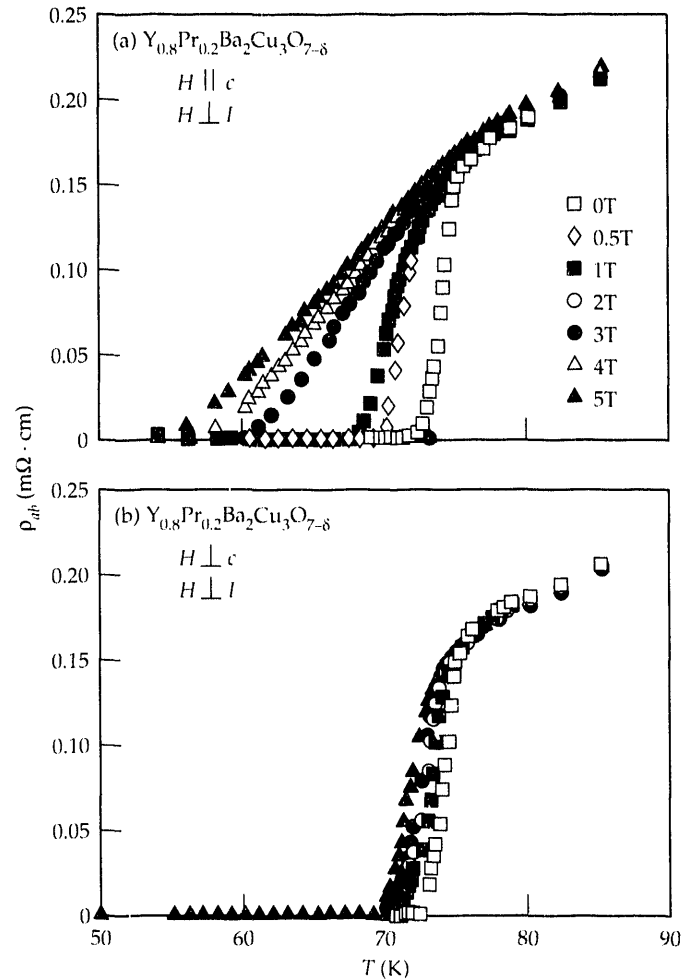
$$(H^{1/3}T^{2/3})\sigma_f = g(x) \frac{A[T - T_c(H)]}{(TH)^{2/3}}, \quad (4)$$

which describes the effect of fluctuation on conductivity in the high field limit, to analyze our data. Here,  $\sigma_f$  is the fluctuation conductivity,  $H$  is the applied magnetic field, and  $T_c(H)$  is the mean field transition temperature.  $T_c(H)$ , the only free parameter in this scaling relation, is field dependent.  $A$  is a field- and temperature-independent coefficient.

The scaling function  $g(x)$  should be the same for all fields. Equation (4) is valid in the immediate neighborhood of  $T_c(H)$  and at high fields. Welp et al.<sup>9</sup> successfully used this scaling law to obtain the  $H_{c2}(T)$  phase diagram of YBCO crystals. We extended this analysis to our single-crystal data across the entire series YBCO-Pr to obtain the temperature dependence of  $H_{c2}$ . Figure 4(a) presents the results of  $H_{c2}$  vs  $T$  for  $H$  parallel to the  $c$  axis. Figure 4(b) shows  $H_{c2}(T)$  for the same praseodymium compositions (except  $x = 0.28$ ) with the field perpendicular to the  $c$  axis. In both (a) and (b),  $H_{c2}$  vs  $T$  follows approximately a Ginsburg-Landau linear variation.

By using the WHH formula, we calculated the zero-temperature upper critical field  $H_{c2}(0)$ . We obtained the coherence length  $\xi$  by using mean-field Ginsburg-Laundau

**Figure 3.** Temperature dependence of the resistivity under several applied fields on the transition region for YBCO-Pr. In (a),  $H$  is parallel to  $c$  and perpendicular to  $I$ . In (b),  $H$  is perpendicular to both  $c$  and  $I$ .



predictions in the clean limit  $H_{c2}(0) = \Phi_0/2\pi\xi(0)^2$ , and we obtained the effective mass anisotropy  $\varepsilon^2 = m_{ab}/m_c$  from

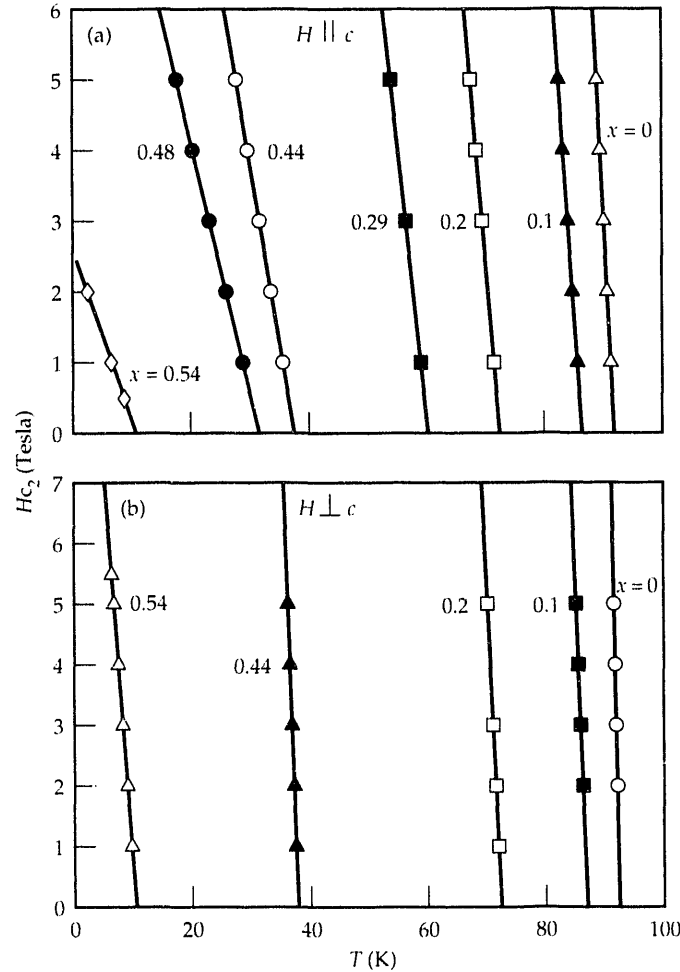
$$\varepsilon = \frac{dH_{c2}^{\parallel}}{dT} / \frac{dH_{c2}^{\perp}}{dT} \quad (5)$$

Table 1 presents all of the calculated data. Our values of these parameters for YBCO agree very closely with recent published values from magnetization measurements.<sup>1,2,9</sup>

*This work was funded by Laboratory Directed Research and Development.*

\* University of California, Davis

**Figure 4.** Temperature dependence of  $H_{c2}$  for  $Y_{1-x}Pr_xBa_2Cu_3O_{7-\delta}$  crystals with  $x = 0, 0.1, 0.2, 0.28, 0.44$ , and  $0.56$ . In (a),  $H$  is parallel to  $c$  and in (b),  $H$  is perpendicular to  $c$ .



## References

1. Z. Hao, J. R. Clem, M. W. McElfresh, L. Civale, A. P. Malozemoff, and F. Holtzberg, "Model for the Reversible Magnetization of High- $\kappa$  Type-II Superconductors: Application to High- $T_c$  Superconductors," *Phys. Rev. B* **43**, 2844 (1991).
2. U. Welp, S. Fleshler, W. K. Kwok, K. G. Vandervoort, J. Downey, B. Veal, and G. W. Crabtree, "Determination of the Upper and Lower Critical Fields of  $YBa_2Cu_3O_{7-d}$  from the Logarithmic Field Dependence of the Magnetization," *Proc. Workshop on Physical Phenomena at High Magnetic Fields*, Tallahassee, FL, E. Manousakis, P. Schlottmann, P. Kumar, K. Bedell, and S. N. Mueller, Eds. (Addison-Wesley Co., 1992), p. 403.
3. L. Zhang, J. Z. Liu, and R. N. Shelton, "Upper Critical Field of  $(Bi,Pb)_2Sr_2CaCu_2O_8$  Single Crystals," *Phys. Rev. B* **45**, 4978 (1992).
4. N. R. Werthamer, E. Helfand, and P. C. Hohenberg, "Temperature and Purity Dependence of the Superconducting Critical Field,  $H_{c2}$ , III. Electron Spin and Spin-Orbit Effects," *Phys. Rev.* **147**, 295 (1966).
5. M. Weber P. Birrer, F. N. Gygax, B. Hitti, et al., "Measurements of the London Penetration Depth in Bi-Based High- $T_c$  Compounds," *Hyperfine Interactions*, **63**, 93 (1990).
6. Y. X. Jia, J. Z. Liu, M. D. Lan, P. Klavins, R. N. Shelton, and H. B. Radousky, "Upper Critical Field  $H_{c2}$  of Single-Crystal  $Y_{1-x}Pr_xBa_2Cu_3O_{7-\delta}$ ," *Phys. Rev. B* **45**, 10609 (1992).
7. S. Ullah and A. T. Dorsey, "Effect of Fluctuations on the Transport Properties of Type II Superconductors in a Magnetic Field," *Phys. Rev. B* **44**, 262 (1991).
8. S. Ullah and A. T. Dorsey, "Critical Fluctuations in High-Temperature Superconductors and the Etingshausen Effect," *Phys. Rev. Lett.* **65**, 2066 (1990).
9. U. Welp, S. Fleshler, W. K. Kwok, R. A. Klemm, et al., "High-Yield Scaling Behavior of Thermodynamic and Transport Quantities of  $YBa_2Cu_3O_{7-\delta}$  Near the Superconducting Transition," *Phys. Rev. Lett.* **67**, 3180 (1991).

**Table 1.** Upper critical field parameters for  $Y_{1-x}Pr_xBa_2Cu_3O_{7-\delta}$  ( $0 \leq x \leq 0.56$ ).<sup>a</sup>

$x$	0	0.1	0.2	0.28	0.44	0.56
$T_c$ (K)	92	86	73	60	36	11
$-[dH_{c2}^{\parallel}/dT]T_c$ (T/K)	1.7	1.3	1.1	0.79	0.53	0.25
$-[dH_{c2}^{\perp}/dT]T_c$ (T/K)	9.9	4.2	3.4	—	3.3	1.3
$H_{c2}^{\parallel}(0)$ (T)	112	79.3	56.2	33.2	13.4	1.93
$H_{c2}^{\perp}(0)$ (T)	639	252	174	—	83.2	10.0
$\xi_c(0)$ (nm)	0.30	0.64	0.78	—	0.80	2.5
$\xi_{ab}(0)$ (nm)	1.7	2.0	2.4	3.2	5.0	13
$\varepsilon = (dH_{c2}^{\perp}/dT)/(dH_{c2}^{\parallel}/dT)$	5.7	3.2	3.1	—	6.2	5.2
$m_{ab}/m_c$	32.7	10.1	9.5	—	38.8	27.0

<sup>a</sup> Here,  $H_{c2}^{\parallel}$  stands for  $H$  parallel to  $c$ ,  $H_{c2}^{\perp}$  stands for  $H$  perpendicular to  $c$ , and  $\xi_{ab}$  and  $\xi_c$  are the coherence lengths in the  $ab$  plane and along the  $c$  axis, respectively.



# Quasiparticles in Doped $\text{La}_2\text{CuO}_4$

J. B. Grant\* and  
A. K. McMahan†

*We have carried out limited-configuration interaction calculations for a chemically realistic, eight-band, effective Hamiltonian for  $\text{La}_2\text{CuO}_4$ . The resultant quasiparticle dispersion curves agree with available experimental data. These results suggest that the first holes doped into  $\text{La}_2\text{CuO}_4$  are of predominant oxygen  $2p_\sigma$  character, have momentum  $\mathbf{k} = (\frac{1}{2}, \frac{1}{2}, 0)\pi/a$  and have spins that are continually flipping as a result of spin exchange with the intrinsic copper spins, at a rate characterized by  $J_{pd} \approx 0.33$  eV. The copper  $3d_{3z^2-r^2}$  and apical oxygen  $2p_z$  states are crucial to the quasiparticle dispersion.*

## Introduction

High-temperature superconductivity occurs in compounds that exhibit both strong electron-electron correlation and significant electron dispersion. Traditional electronic-structure techniques are suited to one or the other of these characteristics, but not both. The combination present in the cuprates has made it exceedingly difficult to provide a realistic theoretical description of these materials. One strategy used to confront this problem has been to remove extraneous degrees of freedom, creating effective Hamiltonians more amenable to rigorous solution. The danger here, typified by the one-band Hubbard model, is that such Hamiltonians may become too simplified to be chemically realistic. The purpose of this work is to generate and approximately solve a more realistic effective Hamiltonian for  $\text{La}_2\text{CuO}_4$  to identify those quasiparticle states that are occupied by the additional holes introduced into this insulator by doping.

## Theoretical Basis

Although local-density functional theory fails to describe  $\text{La}_2\text{CuO}_4$  completely—it incorrectly yields metallic behavior for this material—there is growing evidence that it does provide reasonable values for one- and two-body interactions, which can be used to define the desired effective Hamiltonians. The specific approach used here has been described in detail elsewhere.<sup>1</sup> In the present application, we have obtained parameters describing all states that appear with any significant weight at and near the local-density functional Fermi energy. These are primarily  $3d_{x^2-y^2}$  and  $3d_{3z^2-r^2}$  states on the copper atoms,  $2p_\sigma$  states on the in-plane oxygens, and  $2p_z$  states on the apical oxygen atoms. We have also included the less-important (but not negligible)  $2p_\pi$  states on the oxygens lying in the  $\text{CuO}_2$  layers, leading in total to an eight-band effective Hamiltonian.

The quasihole energies are defined by  $\epsilon_{\mathbf{k}} = E_{\mathbf{k}}^{N+1} - E_0^N$ , where  $E_0^N$  is the ground-state energy of the antiferromagnetic insulator with  $N$  holes, and  $E_{\mathbf{k}}^{N+1}$  is the lowest total energy of the system with one added hole and total momentum  $\mathbf{k}$ . We have evaluated these total energies by means of a combined unrestricted Hartree-Fock (HF) and limited configuration-interaction (CI) treatment of the effective Hamiltonian, as described in more complete accounts of this work.<sup>2-4</sup> For the present lightly doped charge-transfer insulators, the important correlations omitted by HF are spin fluctuations of two kinds:

- The correct antiferromagnetic ground state involves zero-point spin fluctuations away from the Néel order (up-down-up-down) obtained in HF.
- The extra hole present in the  $N+1$  system can disrupt the local spin order.

We generate these additional, metastable spin configurations by means of HF calculations with initial occupations imposed on the copper sites. The number of configurations, therefore, scales with the number of holes and not the number of orbitals. This important distinction enables the present calculations for an eight-band effective Hamiltonian.

## Results

Table 1 presents our results for  $E_X^{N+1}$  and  $\epsilon_X - \epsilon_M$ , where  $X$  and  $M$  signify  $\mathbf{k} = (\frac{1}{2}, \frac{1}{2}, 0)\pi/a$  and  $(1,0,0)\pi/a$ , respectively. The HF solution for the  $N$ -hole insulator provides excited-state eigenvalues  $\epsilon_{\mathbf{k}}$ , which correspond to placing an additional  $N+1$ st hole into one or another of the various empty orbitals (the lowest of which is predominantly oxygen in character), *without* altering the disposition of the pre-existing  $N$  holes. The eigenvalue difference (and Koopman's theorem total energy  $E_X^{N+1}$ ) in the first line of Table 1 corresponds to such a "doped Néel" configuration.

This HF configuration is indicated schematically in Fig. 1(a), where the arrows designate spins, the circled “down spin” is the oxygen hole moving in a state of well-defined crystal momentum,  $\mathbf{k}$ , along the oxygen plaquettes (shaded regions), and the remaining arrows signify the predominantly copper holes of the Néel state. If, on the other hand, an HF calculation is carried out for  $N+1$  holes, it is possible to obtain a self-consistent solution (not necessarily the lowest energy HF solution in the case of the multiband Hamiltonians) of the character sketched in Fig. 1(b). Here, the spins of the central copper hole and the circled oxygen hole are exchanged relative to the doped Néel state in Fig. 1(a), with the important consequence that the oxygen hole is localized, bound to the local region of antiparallel copper holes by the strong antiferromagnetic copper-oxygen exchange interaction in these materials. This localized configuration in Fig. 1(b) may be translated to other sites, and the set of such translated configurations provides multiconfigurational wave functions for the  $N+1$  system of well-characterized momentum and the results labeled “spin exchanged” in Table 1.

The row labeled “both” in Table 1 is the result of limited CI calculations in which both the doped Néel configurations and the spin-exchanged configurations are included. Note that the X- and M-point quasihole energies are nearly degenerate in this more complete CI calculation, in contrast to the conflicting results of the first two entries. Finally, the results labeled “+SF2” and “+SF4” add configurations in which spins are flipped on two and four sites, respectively. These additional configurations are seen to significantly improve the total energy for the system of  $N+1$  holes, yet leave the quasihole dispersion  $\epsilon_X - \epsilon_M$  relatively unaffected.

## Discussion

It is well accepted that the preexisting holes in the insulating parent compounds of the high- $T_c$  cuprates are of predominantly copper character, and that holes doped into

these materials—those that introduce metallic conductivity and enable superconductivity—are primarily of oxygen character. The results in Table 1 provide two important quantitative details about the nature of these oxygen quasiparticles in  $\text{La}_2\text{CuO}_4$ :

- They have momentum  $\mathbf{k} = (\frac{1}{2}, \frac{1}{2}, 0)\pi/a$ .
- Their motion throughout the crystal is described by an intrinsically multiconfigurational wave function that represents continual, high-frequency ( $J_{\text{pd}} \approx 0.33$  eV) spin exchange with copper holes of the opposite spin in the antiferromagnetic background.

On the basis of Table 1, we suggest that the essential aspects of these quasiparticles are contained in the combination of doped Néel and spin-exchanged configurations, and that the additional double and quadruple spin-flip configurations serve to introduce the appropriate zero-point fluctuations in the host spin background but are not crucial to the quasiparticle dispersion.

It is generally believed that the doped holes must go at the X point in the Brillouin zone because only there does symmetry constrain the oxygen states to be fully polarized in the  $x, y$  plane, in apparent consistency with polarized spectroscopic data. Quantitative theoretical calculations have persistently shown the M point to be competitive.<sup>2,3</sup> Moreover, as shown in Table 1, the pure HF calculations suggest that the M point, which is dominated by apical oxygen  $2p_z$  states hybridized with copper  $3d_{3z^2-r^2}$  states, is favored by 0.23 eV.

The configurations in Fig. 1 derive their stability from strong overlap of copper  $3d_{x^2-y^2}$  and oxygen  $2p_\sigma$  states within the  $\text{CuO}_2$  layers. The spin-exchanged configuration,

**Figure 1.** Doped ( $N+1$  hole) configurations obtained from unrestricted Hartree-Fock (HF) calculations. In each configuration, the circled arrow represents the predominantly oxygen hole, while the remaining arrows indicate the predominantly copper holes with Néel order. In the “doped Néel” HF configuration (a), the oxygen hole has well-defined crystal momentum along the oxygen plaquettes (shaded region). In the spin-exchanged HF configuration (b), the oxygen hole is bound to a copper hole of opposite spin by the strong antiferromagnetic copper-oxygen exchange interaction.

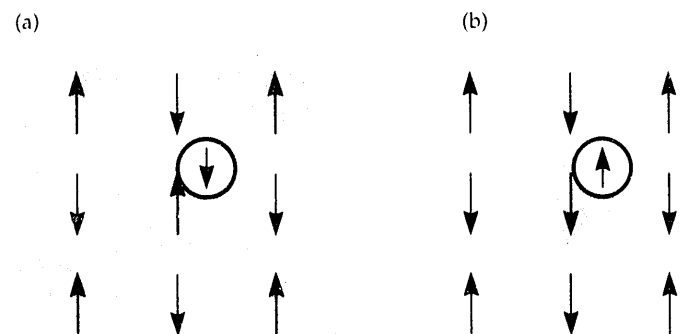


**Table 1.** Results for the eight-band Hamiltonian of  $\text{La}_2\text{CuO}_4$ , obtained for a periodic cluster of 16 formula units. Energies are in eV.

Configurations	$E_X^{N+1}$	$\epsilon_X - \epsilon_M$
Doped Néel	-31.58	+0.23
Spin exchanged	-31.98	-0.24
Both	-32.10	-0.02
+SF2	-32.40	-0.04
+SF4	-32.50	-0.03

Fig. 1(b), is further stabilized by hopping with its neighbors, a condition not allowed in the doped Néel configuration because of the Pauli exclusion principle. As noted previously, we believe that the true multiconfigurational wave function includes admixtures of both the doped Néel configurations and the spin-exchanged configurations. Furthermore, the dispersion between X and M is relatively flat because of the influence of the copper  $3d_{3z^2-r^2}$  and apical oxygen  $2p_z$  states on the configurations at M. There is, in fact, evidence in some transport data that the dispersion is indeed relatively flat, notably that the spectroscopic data requires only that the X point be at least slightly lower than the M point.

## Conclusions

We have developed a limited CI solution of a chemically realistic, eight-band, effective Hamiltonian describing  $\text{La}_2\text{CuO}_4$ . Our results suggest that the first carrier holes doped into this material are of mostly oxygen  $2p_\sigma$  character, have momentum  $\mathbf{k} = (\frac{1}{2}, \frac{1}{2}, 0)\pi/a$ , and are intrinsically multiconfigurational quasiparticles constantly flipping

their spins because of spin exchange with antiparallel copper spins in the host background. The copper  $3d_{3z^2-r^2}$  and apical oxygen  $2p_z$  states are crucial to the quasiparticle dispersion between X and M.

*This work was funded by Laboratory Directed Research and Development.*

\*Electronics Engineering Department, LLNL

†Physics Department, LLNL

## References

1. A. K. McMahan, J. F. Annett, and R. M. Martin, "Cuprate Parameters from Numerical Wannier Functions," *Phys. Rev. B* **42**, 6268 (1990).
2. J. B. Grant and A. K. McMahan, "Realistic Electronic Structure Calculations of Magnetic Insulators Like  $\text{La}_2\text{CuO}_4$ ," *Phys. Rev. Lett.* **66**, 488 (1991).
3. J. B. Grant, *Realistic Electronic Structure Calculations of Magnetic Insulators Like  $\text{La}_2\text{CuO}_4$* , PhD Dissertation, University of California, Davis/Lawrence Livermore National Laboratory, Livermore, CA, UCRL-LR-107714 (1991).
4. J. B. Grant and A. K. McMahan, "Spin Bags and Quasiparticles in Doped  $\text{La}_2\text{CuO}_4$ ," *Phys. Rev. B*, to be published (1992).

# Fermi-Surface Measurements and Planar Orthorhombic Order in $\text{La}_{2-x}\text{Sr}_x\text{CuO}_4$

P. A. Sterne, R. H. Howell,\*  
 F. R. Solal, M. J. Fluss,  
 J. H. Kaiser,<sup>†</sup> R. N. West,<sup>†</sup>  
 H. Kojima,<sup>‡</sup> and K. Kitazawa<sup>§</sup>

*We have made new, highly precise measurements of the room-temperature electron-positron momentum spectra of  $\text{La}_{1.87}\text{Sr}_{0.13}\text{CuO}_4$  and corresponding calculations based on the local-density approximation. The data show sharp features indicative of a Fermi surface, in remarkable agreement with calculations of the copper-oxygen plane bands. Strong planar orthorhombicity is revealed in the electronic structure above the tetragonal-orthorhombic transition temperature.*

## Introduction

The existence and shape of the Fermi surface of superconducting oxides is a subject of intense investigation. The experimental observation of the Fermi surface puts severe constraints on the theory of high-temperature superconductivity. Recent experiments using angle-resolved photoemission,<sup>1,2</sup> the de Haas-van Alphen effect,<sup>3</sup> and angular correlation of annihilation radiation (ACAR)<sup>4</sup> have all provided evidence for the existence of a Fermi surface in  $\text{YBa}_2\text{Cu}_3\text{O}_{7-x}$  (YBCO) and  $\text{Bi}_2\text{Sr}_2\text{CaCu}_2\text{O}_8$  (BSCCO). In spite of this success, little detailed information exists about the Fermi surface of the Cu-O planes. In ACAR, the recent model-independent demonstration of a Fermi surface in YBCO was restricted to the electron ridge associated with the Cu-O chains.<sup>4</sup> To date, no observations of a Fermi surface in  $\text{La}_{2-x}\text{Sr}_x\text{CuO}_4$  (LSCO) have been reported.

We have made a new, highly precise measurement of the electron-positron momentum (EPM) distribution performed on LSCO, with  $x = 0.13$ , and associated calculations of the EPM using the local-density approximation (LDA). LSCO is an excellent system for studying the Fermi surface of the Cu-O planes because the other planes in the system are not expected to contribute to the electronic states in the region of the Fermi energy. In addition, the positron wavefunction and the plane region of the unit cell overlap quite a bit, in contrast to YBCO and BSCCO, where the positron primarily samples the Cu-O chains and the Bi-O layers, respectively.

## Experiment

We performed the ACAR measurements on a single crystal of LSCO with great statistical precision, collecting the data at room temperature in the LLNL spectrometer. Single-crystal samples were prepared by the traveling solvent floating-zone technique at Kofu and Tokyo. Measurements of the dc magnetic susceptibility showed that the crystal had an onset of superconductivity above 33 K. A second-order

phase transition from tetragonal to orthorhombic symmetry occurs at 210 K, as determined from neutron diffraction.

We mounted the sample in a ring goniometer, attached by epoxy to two 50- $\mu\text{m}$  wires and aligned the crystal to within  $0.5^\circ$  by Laue x-ray photography so that the  $c$  axis of the sample was along the line connecting the detector centers, and the  $a$  and  $b$  sample axes were along the  $x$  and  $y$  data axes, respectively. The angular resolution of the ACAR spectrometer was 0.5 mrad ( $3.86 \text{ mrad} = 1 \text{ \AA}^{-1}$ ). The data were collected in a  $256 \times 256$  matrix with bins 0.167 mrad wide and were stored every  $2 \times 10^7$  counts. Later we summed these data into one total distribution of  $4.3 \times 10^8$  counts and corrected for the efficiency function of the detector after individual analyses to ensure the stability of the detection system.

To guide our interpretation of the data, we performed theoretical calculations of the full EPM density using the linear muffin-tin orbital (LMTO) method and LDA for both electron-electron and electron-positron interactions. In the LMTO method, the electron-charge density is calculated self-consistently, and the positron wavefunction is determined as described in Ref. 5. The electron and positron wavefunctions are used to calculate the theoretical EPM densities, which are then manipulated in a manner identical to that used to analyze the experimental data.

To identify Fermi-surface-related effects, we performed calculations for both insulating and metallic cases. We did metallic calculations with a range of rigid band shifts to represent strontium doping. We formed the model insulator by constraining the occupancy of electron states in a self-consistent antiferromagnetic calculation to stabilize an insulator<sup>6</sup> and performed calculations for both the high-temperature body-centered-tetragonal (bct) phase and the low-temperature orthorhombic structure.

## Results and Discussion

The experimental EPM distribution is an extended pattern in momentum space of the electronic distribution in the Brillouin zone. We can sum all the data back into a single

zone by using the Lock-Crisp-West (LCW) theorem, which enhances the contribution of the Fermi break to the data and partially averages the wavefunction effects, which then appear as a more slowly varying background. A Fermi surface then appears as a sharp break in the momentum density, and hence metallic and insulating data look very different in this representation.

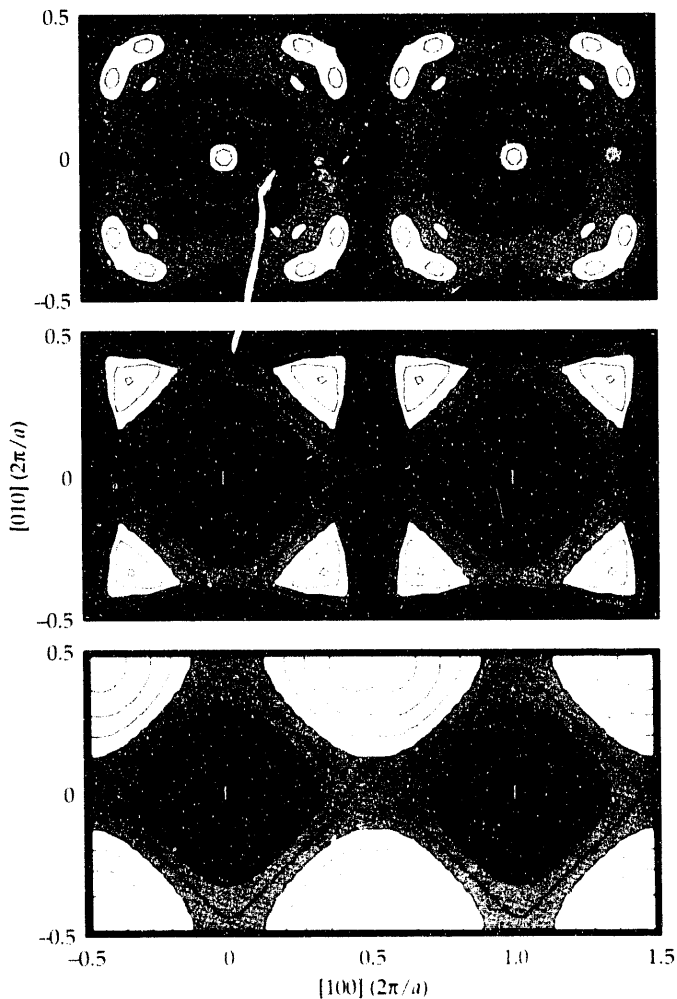
Sharp breaks in the LCW experimental spectrum can be ascribed to a Fermi surface. However, it is difficult to use such a feature alone to identify the Fermi surface without supporting evidence. For LSCO, the LMTO calculations show the Fermi surface as a feature clearly distinguishable from the wavefunction effects when the electron momentum density is displayed in the reduced zone. Also, the calculations for the insulating states are distinctly different from the metallic cases.

Figure 1 shows the results of the LCW operation based on the low-temperature orthorhombic structure. The metallic calculation obtained by rigidly shifting the Fermi energy

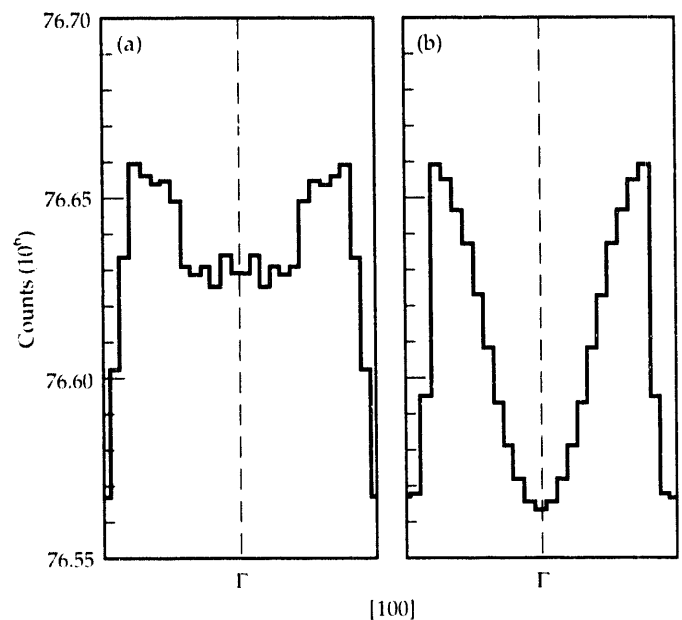
is notably similar to the experimental LCW, whereas the insulator calculation performed using the procedure described in Ref. 6 slowly varies throughout the zone and shares no obvious features with the experimental data. The comparison of the shape and position of the Fermi edge near the zone boundary in the calculation and the continuously connected sharp break near the same momenta in the data strongly suggest the existence of a Fermi surface in the Cu-O planes. The sharpness of the measured Fermi surface is also close to that calculated, as seen in Fig. 2, where we have summed both the theory and the data in the LCW along the (010) direction. Figures 1 and 2 both show a rise in the experimental spectrum around  $\Gamma$  that is not present in the theory. This may be due either to background contributions for which we have not corrected or to positron trapping in defects.

When we used the LCW on the low-temperature orthorhombic lattice, a simple picture of the Fermiology emerged. If we had used the LCW procedure on the high-temperature tetragonal lattice, we would have obtained a much more complicated picture, with apparent closed Fermi surfaces around both the  $\Gamma$  and X points of the tetragonal zone. Rigid band calculations suggest that the Fermi surface in this case should consist of a single closed section around either the  $\Gamma$  point or the X point, depending on the amount of doping. When the data are analyzed on the orthorhombic lattice, the X point of the tetragonal zone maps onto the  $\Gamma$  point of the orthorhombic zone, and the two closed Fermi surface sections then coincide. In addition, other features with no obvious correspondence with

**Figure 1.** LCW data folded onto the projected orthorhombic Brillouin zone for experiment (top), metallic calculation (middle), and antiferromagnetic insulator calculation (bottom).



**Figure 2.** Experimental (a) and theoretical (b) LCW spectrum integrated along the (010) direction in the orthorhombic lattice.



the Fermi surface become less prominent in the orthorhombic analysis. The appearance of two distinct Fermi surface sheets in the tetragonal LCW and the simplicity of the picture in the orthorhombic structure all indicate a planar orthorhombic symmetry in the electronic structure.

Orthorhombic symmetry in the positron measurement might be expected from a careful analysis of the characteristics of the orthorhombic-tetragonal (O-T) phase transition. A tilting of the oxygen octahedra around each copper atom produce local orthorhombic distortions. LDA calculations<sup>7</sup> suggest that this local order is stable at temperatures above the observed O-T transition and that the transition results from long-range ordering. The oxygen octahedra share a common oxygen atom, are strongly coupled within the  $a$ - $b$  planes, and are only weakly coupled along the  $c$  axis. Orthorhombic domains, extended in two dimensions, would consequently exist above the O-T transition.

This description of the phase characteristics is consistent with several other experimental observations. Diffraction data on the orthorhombic superlattice peak result from a coherent average over the  $c$ -axis direction. As ordering along the  $c$  axis is lost, the peak becomes less intense and is broadened. In our geometry, positron angular-correlation measurements sample electrons individually and then sum the distribution for electron momenta along the  $c$  axis, leading to the twinned orthorhombic symmetry we observe. Additionally, resistivity measurements done along specified crystalline directions show a clear change in the  $c$ -axis resistivity at the O-T transition and no change in the  $a$ - $b$  plane.<sup>8</sup> Also, neutron-diffraction determinations of the interatomic distances are unchanged by the O-T transition and have orthorhombic values in the tetragonal region.<sup>9</sup>

## Summary

Using the two-dimensional ACAR technique, we performed a high-statistics measurement of the EPM density in LSCO. The LCW procedure revealed a Fermi-surface feature in substantial agreement with the predictions of band-structure calculations. The pronounced two-dimensional

nature of this system produces large planar regions of orthorhombic symmetry, which persist above the O-T phase-transition temperature. The positron provides a potentially powerful probe of these domains through its influence on the observed Fermi surface.

*This work was funded at LLNL by Weapons-Supporting Research and Laboratory Directed Research and Development and at the University of Texas at Arlington by the Robert A. Welch Foundation and the Texas Advanced Research Program.*

\*Physics Department, LLNL

†University of Texas at Arlington

‡Yamanashi University, Kofu, Japan

§University of Tokyo, Tokyo, Japan

## References

1. J. G. Tobin, C. G. Olsen, C. Gu, D. W. Lynch, J. Z. Liu, F. R. Solal, M. J. Fluss, R. H. Howell, J. C. O'Brien, H. B. Radousky, and P. A. Sterne, "The Valence Bands and Fermiology of Untwinned Single-Crystal  $\text{YBa}_2\text{Cu}_3\text{O}_{6.9}$ ," *Phys. Rev. B* **45**, 5563 (1992).
2. C. G. Olsen, R. Liu, D. W. Lynch, R. S. List, A. J. Arko, B. W. Veal, Y. C. Chang, P. Z. Jiang, and A. P. Paulikas, "High-Resolution, Angle-Resolved Photoemission Study of the Fermi Surface and the Normal-State Electronic Structure of  $\text{Bi}_2\text{Sr}_2\text{CaCu}_2\text{O}_8$ ," *Phys. Rev. B* **42**, 381 (1990).
3. F. M. Mueller, C. M. Fowler, B. L. Freeman, W. L. Hults, J. C. King, and J. L. Smith, "Measurement of the de Haas-van Alphen Effect in  $\text{YBa}_2\text{Cu}_3\text{O}_{6.97}$  Using Megagauss Fields," *Physica B* **172**, 253 (1991).
4. H. Haghghi, J. H. Kaiser, S. Rayner, R. N. West, J. Z. Liu, R. Shelton, R. H. Howell, F. Solal, and M. J. Fluss, "Direct Observation of Fermi Surface in  $\text{YBa}_2\text{Cu}_3\text{O}_{7-\delta}$ ," *Phys. Rev. Lett.* **67**, 382 (1991).
5. P. A. Sterne and J. Kaiser, "First-Principles Calculation of Positron Lifetimes in Solids," *Phys. Rev. B* **43**, 13892 (1991).
6. P. A. Sterne and C. S. Wang, "Oxygen Vacancies and Antiferromagnetism in  $\text{La}_2\text{CuO}_4$ ," *Phys. Rev. B* **37**, 7472 (1988).
7. R. E. Cohen, W. E. Pickett, and H. Krakauer, "First Principles Phonon Calculations for  $\text{La}_2\text{CuO}_4$ ," *Phys. Rev. Lett.* **62**, 831, (1989).
8. S. Kambe, K. Kitazawa, M. Naito, A. Fukuoka, I. Tanaka, and H. Kojima, "Anisotropic Resistivity in the 2-Dimensional Metal  $(\text{La}_{1-x}\text{Sr}_x)_2\text{CuO}_4$ ," *Physica C* **160**, 35 (1989).
9. T. Egami, W. Domowski, J. D. Jorgenson, D. G. Hinks, D. W. Capone II, C. U. Segre, and K. Zhang, *Rev. Solid State Sci.* **1**, 247 (1987).

# Photoelectron Studies of *In Situ* Cleaved Crystals of $\text{YBa}_2\text{Cu}_3\text{O}_7$

C. Colmenares, J. Z. Liu,\*  
C. Evans, and R. L. Smith†

*We have used x-ray and ultraviolet photoelectron spectroscopies (XPS and UPS) to study the near-surface chemistry of  $\text{YBa}_2\text{Cu}_3\text{O}_{7-x}$  (YBCO) single crystals cleaved in ultrahigh vacuum (UHV) at 300 K. Oxygen loss from this material was not detectable under these conditions with the instrumentation used. Core-level and valence-band measurements showed that YBCO decomposed rapidly when irradiated by x rays and ultraviolet light. Also, exposure of freshly cleaved YBCO surfaces to atmospheric air reduced the oxidation state of copper from  $\text{Cu}^{+2}$  to  $\text{Cu}^{+1}$ , while the yttrium and barium components formed oxides, hydroxides, and carbonates.*

## Introduction

Recent work by Fowler et al.<sup>1</sup> has shown that very high-quality single crystals of  $\text{YBa}_2\text{Cu}_3\text{O}_{7-x}$  (YBCO) do not lose oxygen under vacuum at 300 K, contrary to many reports in recent literature. They also defined the core-level spectra of yttrium, barium, copper, and oxygen for these high-purity crystals, which were reported to have a nearly undetectable level of carbon. We initiated the present program to test the purity and quality of YBCO single crystals used for many measurements at LLNL. We had the following goals:

- To measure the carbon and gold content of our crystals: carbon because of the use of carbonates in synthesizing the crystals, and gold because gold crucibles were used in preparing single crystals.
- To verify that high-quality YBCO crystals do not lose oxygen in ultrahigh vacuum (UHV) at 300 K.
- To determine the superconducting quality of our crystals by comparing their core levels and valence band spectra to those of Fowler et al.<sup>1,2</sup>
- To study the transformation that a clean, freshly cleaved surface of YBCO undergoes when exposed to air.

The last goal is of particular importance to many physical probe techniques and to technological applications in electronics and high-frequency devices.

X-ray and ultraviolet photoelectron spectroscopies (XPS and UPS) are particularly well suited for our study. The valence band in XPS is dominated by copper 3d-derived states, and the electronic core levels of yttrium, barium, copper, and oxygen can yield the chemical state data that we seek. In UPS, on the other hand, the HeI oxygen 2p-derived features of the valence band predominate. For HeII, the cross sections for the copper 3d and the oxygen 2p shells are nearly equal. Thus, these spectra should reflect the total density of states of the valence band.

## Experiment

We studied small (2- × 2-mm) single crystals of YBCO with sharp superconducting transitions from 80 to 92 K ( $1 < \Delta T < 15$  K) using XPS with HeI (21.2-eV) and HeII (40.8-eV) radiations. We examined cleaved surfaces for carbon by Auger electron spectroscopy (AES) using an Auger microprobe. We cleaved the crystals in UHV ( $\sim 1 \times 10^{-10}$  Torr) at 300 K to produce clean surfaces and also used air-cleaved surfaces to study the effect of air contamination on the core levels and the valence band. To detect the possible oxygen loss by the cleaved samples, we monitored the oxygen partial pressure in the vacuum chamber with a residual gas analyzer (RGA), operated at very high sensitivity.

## Results and Discussions

In the XPS and UPS study of crystals fractured in vacuum, we often detected strong signals from carbon, which is not supposed to be in these samples. To determine the origin of this carbon, we examined several of the fracture surfaces in the Auger microprobe. Some of the samples showed the surface to be covered with inclusions varying in size from 1 to 30  $\mu\text{m}$ , the largest of which were usually conical. Auger analysis of these inclusions disclosed that they were predominantly graphitic carbon with traces of chlorine and nitrogen. To avoid these carbon inclusions in our fractured samples, we grew YBCO single crystals using oxides rather than carbonates as the starting materials.

We used XPS to look for gold in several samples, and we found concentrations varying from 0.1 to 0.5 at. %.

We did not detect any measurable oxygen loss when cleaving single crystals under UHV at 300 K or during prolonged storage under these conditions ( $\sim 1$  week). The partial pressure of oxygen measured with the RGA was  $\sim 3 \times 10^{-13}$  Torr at a total pressure of  $1 \times 10^{-10}$  Torr for vacuum-

cleaved crystals; we believe this to be part of the residual-gas contribution to the base pressure of the system.

Yttrium, barium, copper, oxygen, and traces of carbon and gold were the only elements detected. The core levels for these elements, obtained by XPS, agree with those of Fowler et al.<sup>1</sup> In the measurements taken in ~1 h, no change was measurable in the core levels. However, x-ray exposures exceeding 3 h resulted in complete reduction of  $\text{Cu}^{+2}$  to  $\text{Cu}^+$  ( $\text{Cu}_2\text{O}$ ) and/or metallic copper. It is also possible that the "green phase" of orthorhombic  $\text{Y}_2\text{BaCuO}_5$  formed.<sup>2</sup> The yttrium and barium spectra did not change. Crystals cleaved under UHV conditions have a relatively broad  $\text{Cu } 2p_{3/2}$  (933.5-eV) core peak and a satellite on the high-binding-energy side with an area of ~0.46 of the main peak (see Fig. 1), in agreement with the data of

Fowler et al. This spectrum is practically identical to that of a sample of  $\text{CuO}$ . In air-cleaved crystals, the  $\text{Cu } 2p_{3/2}$  is narrower and shifts to lower binding energy (932.5 eV), indicating a change in oxidation state.

From these data and the x-ray-generated Auger peak at ~335 eV ( $\text{L}_3\text{VV}$  transition), we have concluded that this peak consists of  $\text{CuO}$  and  $\text{Cu}_2\text{O}$  and/or metallic copper. The oxygen 1s level of the vacuum-cleaved superconductor (see Fig. 2) is clearly at 528 eV, in agreement with Fowler's data. Exposure of the sample to air removes this peak, and a very broad peak appears that can be deconvoluted into four components. These probably correspond to yttrium, barium, and copper oxides, hydroxides, and carbonates. The XPS core levels of these elements also show this behavior.

**Figure 1.**

The copper  $2p_{3/2}$  level for vacuum- and air-cleaved single crystals of YBCO.

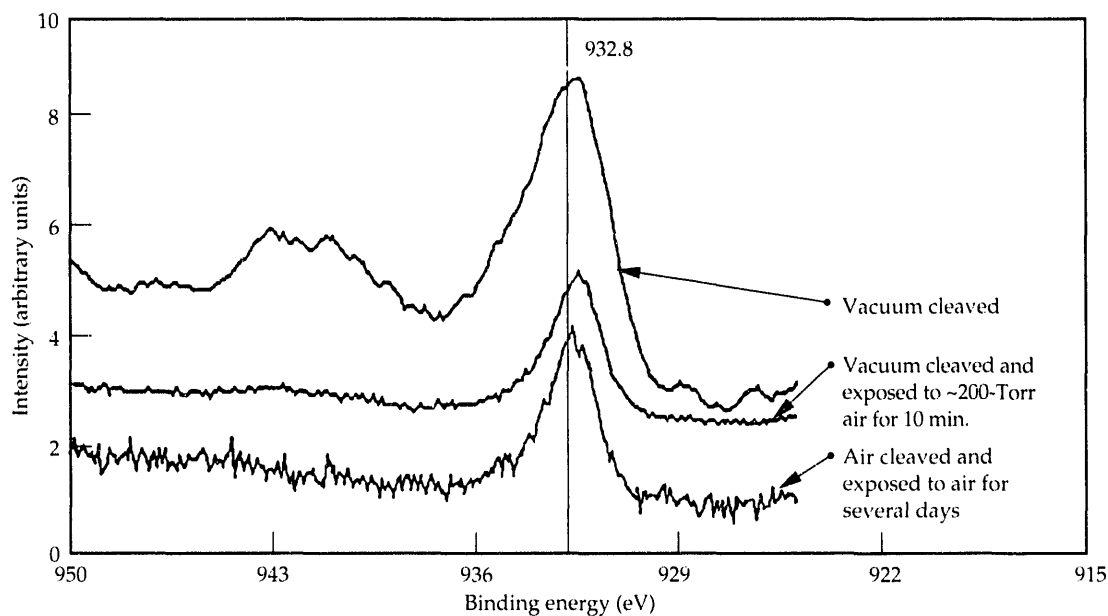
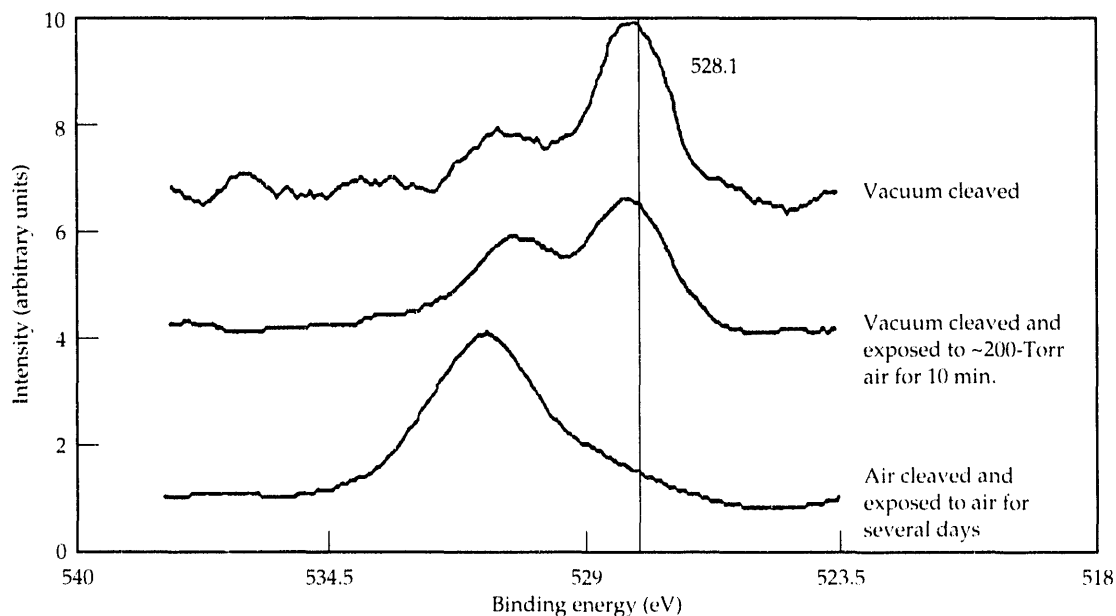


**Figure 2.**

The oxygen 1s level for vacuum- and air-cleaved single crystals of YBCO.





## Conclusions

- Freshly cleaved YBCO surfaces are stable under UHV conditions for several days at 300 K. If decomposition occurs, the oxygen partial pressure is below  $\sim 3 \times 10^{-13}$  Torr.
- Exposure of freshly cleaved YBCO surfaces to air results in the formation of  $\text{Cu}_2\text{O}/\text{Cu}$ ,  $\text{BaO}$ ,  $\text{Y}_2\text{O}_3$ , and possibly some yttrium hydroxides and carbonates, as shown by the behavior of core and valence-band levels.
- Exposure of freshly cleaved YBCO surfaces to x-ray or ultraviolet radiation reduces  $\text{Cu}^{+2}$  completely to  $\text{Cu}^{+1}/\text{Cu}$  in  $\sim 3$  h. The yttrium and barium core levels do not change.

*This work was funded by Weapons-Supporting Research.*

\*University of California, Davis

†Mechanical Engineering Department, LLNL

## References

1. D. E. Fowler, C. R. Brundle, J. Lezczak, and F. Holtzberg, "Core and Valence XPS Spectra of Clean, Cleaved, Single Crystals of  $\text{YBa}_2\text{Cu}_3\text{O}_7$ ," *Trans. Elect. Spect. Related Phenom.* **52**, 323 (1990) and references therein.
2. R. M. Hazen, L. W. Finger, R. J. Angel, C. T. Prewitt, N. L. Ross, H. K. Mao, and C. G. Hadjilacos, "Crystallographic Description of Phases in the Y-Ba-Cu-O Superconductor," *Phys. Rev. B* **35**, 7238 (1987).

# The Valence Bands and Fermiology of Untwinned, Single-Crystal $\text{YBa}_2\text{Cu}_3\text{O}_{6.9}$

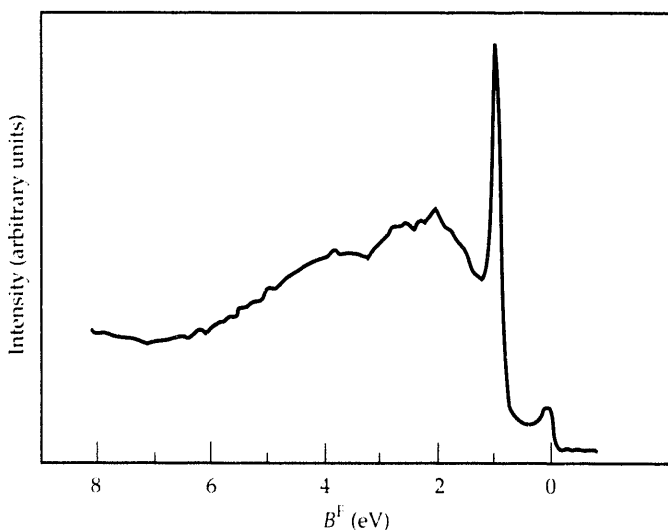
J. G. Tobin, C. G. Olson,\*  
 C. Gu,\* J. Z. Liu,†  
 F. R. Solal, M. J. Fluss,  
 R. H. Howell,† J. C. O'Brien,†  
 H. B. Radousky,† and  
 P. A. Sterne

*We probed the cleaved surfaces of untwinned, single-crystal  $\text{YBa}_2\text{Cu}_3\text{O}_{6.9}$  (YBCO) with photoemission induced by synchrotron radiation, using high-energy and high-angular resolution. We observed acute spectral structure, both at the Fermi energy and at higher binding energies, particularly near the high-symmetry points of the two-dimensional Brillouin zone (e.g.,  $\bar{\Gamma}$ ,  $\bar{X}$ ,  $\bar{Y}$ , and  $\bar{S}$ ). Our data are consistent with a superconducting gap of less than 10 meV.*

## Introduction

The utility of probing the electronic structure of high-temperature superconductors with photoemission has been well established.<sup>1</sup> Using high-angular resolution ( $\pm 1^\circ$ ) and high-energy resolution (FWHM  $\approx 32$  meV) photoelectron spectroscopy, Olson et al.<sup>1</sup> directly observed and measured the superconducting gap ( $\Delta = 24$  meV) of cleaved  $\text{Bi}_2\text{Sr}_2\text{CaCu}_2\text{O}_8$  (BSCCO) at various specific points in reciprocal space. Their photoemission results provided a fairly stringent test for theoretical models of the electronic structure. That is, the experimental Fermi surface preserved not only the volume, but also the essence of the Fermi surface calculated by the local-density approximation (LDA).<sup>1</sup> The experimental bands near the Fermi level strongly resembled the LDA bands, but with a moderate mass enhancement.

**Figure 1.** Angle-resolved photoelectron spectrum of untwinned YBCO. The Brillouin zone near  $\bar{X}$  was sampled, using  $h\nu = 24$  eV. Note the acute special structure at  $B^F = 1$  eV and  $B^F = 0$ .



The success of this approach with BSCCO encouraged us to apply photoelectron spectroscopy to a more complicated system,  $\text{YBa}_2\text{Cu}_3\text{O}_{7-\delta}$  (YBCO).

In our photoemission study of YBCO, we used the highest resolution and best samples available. Figure 1 is an example of our data. Note the acute spectral structure at both  $B^F = 1$  eV and  $B^F = 0$  eV. ( $B^F$  is the binding energy with respect to the Fermi energy.) The combination of improved samples—in particular, high-quality, untwinned, single crystals of YBCO and high-resolution, angle-resolved photoemission—can provide the type of detail that was previously missing in earlier investigations. Using this detailed information, we mapped the valence bands and investigated Fermi crossings and superconducting gaps throughout the two-dimensional Brillouin zone, with emphasis on differentiating the nature and contributions of chain (1-D) and plane (2-D) states. The Fermiology of the cleaved surfaces of untwinned, single-crystal YBCO can be summarized as follows:

- Crossings are seen throughout the two-dimensional Brillouin zone and are identified with plane- and chain-derived states.
- The electronic structures at nondegenerate corners of the Brillouin zone (e.g.,  $\bar{X}$  and  $\bar{Y}$ ) are distinctly different.
- The measured gap is zero or small throughout the two-dimensional Brillouin zone for all observed bands (including bands of both chain and plane origin), contrary to the preliminary reports of others.<sup>1</sup>

In this study, we concentrate on the gap measurements.

## Experiment

We performed photoemission measurements on the 1 GeV storage ring, Aladdin, at the University of Wisconsin Synchrotron Radiation Center (UWSRC) and on the Iowa State University/Montana State University ERG/SEYA Beamline, using an angle-resolved photoelectron spectrometer from Vacuum Science Workshop. We optimized the electron and x-ray optics of the instrument for small

(typically  $\sim 1 \times \sim 1$ -mm) YBCO samples. The total-energy and electron-momentum resolutions are quite high; energy bandpasses of 30 meV or less are typical, and the electron angular acceptance is  $\pm 1^\circ$ . The single crystals were grown and detwinned at the University of California at Davis under the direction of J. Z. Liu.<sup>1</sup>

Prior to the photoemission experiments, measurements of the Meissner effect confirmed the superconducting nature of the crystals. Before and after cleaving, we used Laue backscattering measurements to orient the samples. The sample normal and other high-symmetry directions such as  $\bar{\Gamma}-\bar{X}$ ,  $\bar{\Gamma}-\bar{Y}$ , and  $\bar{\Gamma}-\bar{S}$ , determined *in situ* by the symmetry of the photoemission measurements, were consistent with the crystal orientation, as determined by the Laue measurements.

Typically, the sample temperature was 20 K during all operations, including cleaving and photoemission measurements, and base pressures in the experimental chamber were 3 to  $6 \times 10^{-11}$  Torr. Optical-microscopic observation complemented all spectroscopic characterization *in situ*, especially when the samples were removed from the vacuum chamber.

## The Superconducting Gap

An important property of a high-temperature superconductor is the width of the superconducting gap.<sup>1</sup> Unfortunately, substantial confusion exists concerning this property in YBCO. Infrared spectroscopy measurements of the CuO planes indicate gaps of  $2\Delta_{a,b} \approx 8 k_B T_c$  (53 to 60 meV) and  $2\Delta_c = 3 k_B T_c$  (24 meV). Tunneling measurements also suggest a double-gap structure,  $2\Delta_{a,b} = 39$  meV and  $2\Delta_c = 8$  meV, with both a nonzero conductance at zero bias and a linear background conductance near zero bias. The subscripts *a*, *b*, and

*c* relate to gaps parallel (*a*,*b*) and perpendicular (*c*) to the plane of the *a* and *b* axes. Similarly, nuclear magnetic resonance (NMR) experiments indicate a two-gap structure assigned to the CuO plane states ( $2\Delta = 3.8$  to  $6.2 k_B T_c$  or 29 to 48 meV) and the CuO chain states ( $2\Delta = 3.52 k_B T_c = 27$  meV). Other measurements suggest that electronic density exists inside the superconducting gap.

Angle-resolved photoelectron spectroscopy is an attractive means of unraveling this problem because it can directly probe the occupied electronic states in a momentum-resolving mode. Because of inferior samples (e.g., twinning) and poorer resolution (100 meV or more), no previous photoemission measurements have properly addressed these issues. Although other researchers reported a large gap (25 meV), we can find a gap no greater than 10 meV ( $\Delta \leq 5 \pm 5$  meV) using *untwinned*, single-crystal YBCO with an energy resolution (FWHM) of 30 meV and an angular resolution of  $\pm 1^\circ$ . Mante et al.<sup>1</sup> recently reached the same conclusion as we, using higher angular resolution, lower energy resolution, and twinned crystals of slightly lower oxygen concentration.

In Figs. 2 and 3, a shoulder or peak occurs near the Fermi energy, which is well up the slope on the low-energy side. This peak suggests a small or zero gap. In Fig. 4, which

**Figure 2.** Spectrum taken from untwinned, single-crystal YBCO near the high symmetry point  $\bar{Y}$ . The sharp, intense peak near the Fermi energy is not observed at  $\bar{X}$ . The FWHM of the peak is about 40 meV, including an instrumental broadening of about 30 meV. The photon energy was 17 eV.

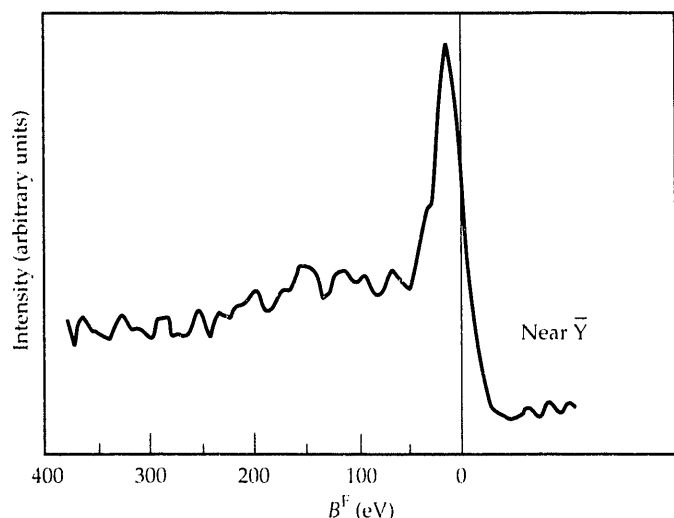
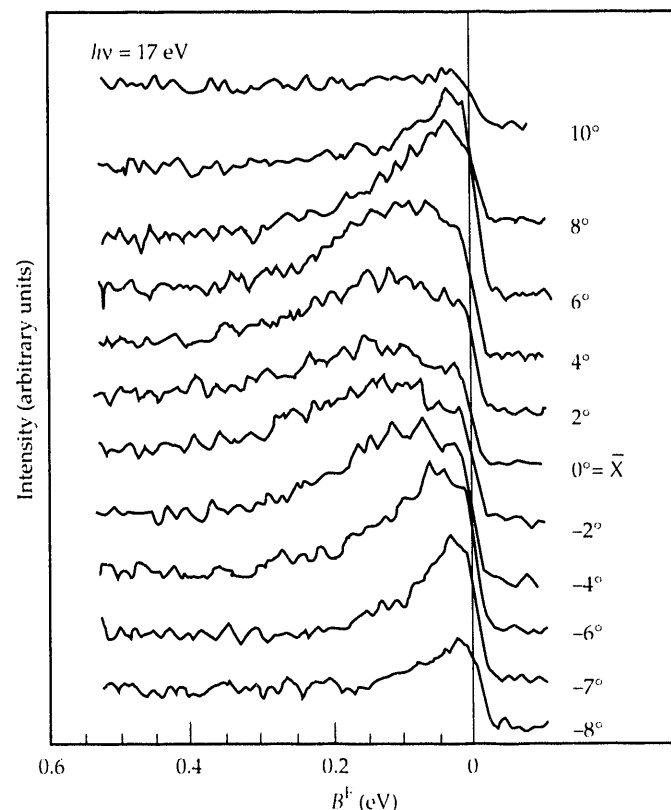


**Figure 3.** Spectra collected near  $\bar{X}$  using 17-eV photons. The rotation was approximately along  $\bar{S}-\bar{X}-\bar{S}$ . The emission direction and light polarization were fairly well aligned. The ratio of the effective mass to the reduced mass for the data shown here is approximately 1.6.



confirms this interpretation, we obtained these spectra in sequence: (a) YBCO at 100 K (above  $T_c$ ), (b) YBCO at 20 K (below  $T_c$ ), and (c) platinum at 20 K, with no adjustments to the apparatus except to cool the samples between (a) and (b) and to move the sample holder between (b) and (c). [A spectrum taken before warming agrees with spectrum (b) taken after warming.] The Fermi energy runs through the middle of the rise in spectra (a) and (c) but is adjacent to the peak in spectrum (b). The differences between these spectra and those of BSCCO are startling. For BSCCO at 20 K, the peak is approximately 40 meV from the Fermi energy, which crosses at the bottom of the rise, whereas YBCO at 20 K has a peak within approximately 10 meV of the Fermi energy, which crosses near the top.

Therefore, if a gap does exist, its width should be  $\Delta \leq 5 \pm 5$  meV. The presence of electronic density near the Fermi energy is consistent with several other seemingly anomalous observations about YBCO. For example, tunneling measurements exhibit both a nonzero conductance at zero bias and a linear background conductance in the gap.<sup>1</sup> Specific-heat, Raman-scattering, and microwave-resistivity measurements<sup>1</sup> suggest that electronic density exists inside a large gap. Although (1) our rough estimate of the apparent gap width applies to all observed crossings (both

chain- and plane-derived) and (2) assignment of the electronic density to specific electronic structure must await further analysis, we can make the following observations.

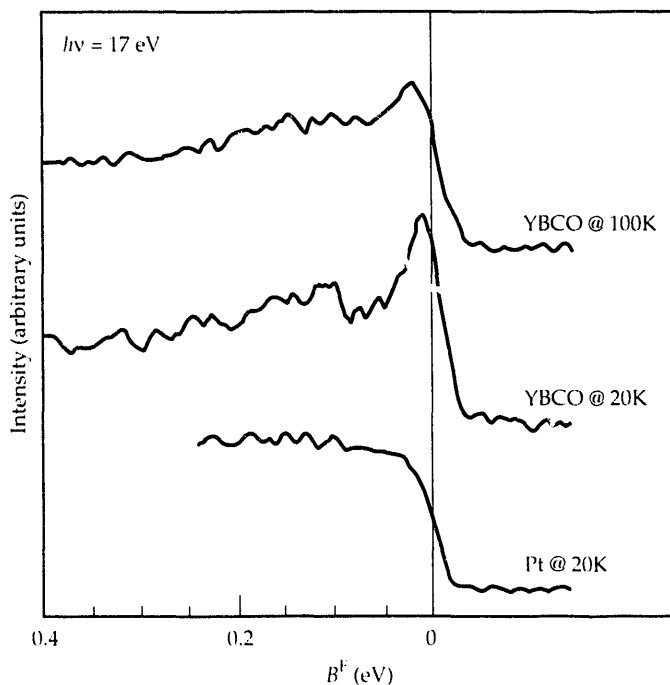
The apparent discrepancy between the results for cleaved BSCCO<sup>1</sup> and cleaved YBCO really is not surprising. In two ways, BSCCO's lattice structure is noticeably simpler than YBCO's: (1) it lacks chains, and (2) it has mirror plane symmetry *between* the two weakly bonded cleavage layers, so that intact unit cells survive cleavage and thus exist on the surface for photoemission measurements. Because such mirror cleavage planes do not exist in YBCO, cleaving implies some sort of asymmetry or a rupturing of the topmost unit cell.

Further, the chain states may be masking a gap in the plane state.<sup>1</sup> Our estimate of the apparent gap comes from what are believed to be chain states, and all of our crossings, including those of the plane-derived bands, have nearby chain bands. Perhaps the small gap is only a chain property, and the CuO plane gaps are hidden by the chain intensity near the Fermi energy. This possibility is appealing in light of other measurements of a large CuO plane gap and two gap structures, of which the smaller is for the chains.<sup>1</sup>

Another possibility is the combination of cleavage-induced surface reconstruction and a proximity effect. Perhaps the process of cleaving produces a subtle but telling shift of atoms. Despite the rupturing of unit cells, the two-dimensional periodicity would necessarily remain intact, based on our observation of such detailed spectral structure around  $\bar{\Gamma}$ ,  $\bar{X}$ ,  $\bar{Y}$ , and  $\bar{S}$ . Perhaps a slight vertical expansion or contraction of the lattice is occurring. For example, a reduced volume could give rise to the increased orthorhombicity and decreased critical temperature proposed by Hayashi et al.<sup>1</sup> If the critical temperature dropped below 20 K, the surface of the material would be normal. (Perhaps then the changes that are seen in Fig. 4 are solely due to thermal broadening.) Alternatively, as suggested by resistivity measurements, chain imperfections (oxygen depletion) may give rise to a metallic band. Perhaps cleavage causes oxygen loss in the chain bands. To address the issue of surface obfuscation of bulk gaps, we performed a series of gas-adsorption studies with argon and O<sub>2</sub>, either of which might have changed the reconstruction and opened a large gap. These effects did not occur, but it is unclear whether gas adsorption is sufficiently severe to perturb a reconstruction that may be half a unit cell deep ( $\sim 6$  Å).

Therefore, although it is not possible to uniquely assign the origin of the small gap, it seems fairly likely that it is strongly chain-related. The observation of the  $\bar{Y}$  Fermi-energy peak and the differences with BSCCO both point toward strong participation by the chain-derived states.

**Figure 4.** High-resolution spectra, where nothing has been changed except to cool the YBCO sample (a to b) and move the samples (b to c). See text for discussion.



## Acknowledgments

Work at Ames Laboratory was performed under DOE Contract No. W-7405-Eng-82. We performed the synchrotron radiation investigations at the University of Wisconsin Synchrotron Radiation Center. Conversations with Vladimir Kresin were highly enlightening, enjoyable, and appreciated.

*This work was funded by Laboratory Directed Research and Development.*

---

\*Ames Laboratory and the Iowa State University, Ames

† Department of Physics, University of California, Davis

‡ Physics Department, LLNL

## Reference

1. J. G. Tobin, C. G. Olson, C. Gu, J. Z. Liu, F. R. Socal, M. J. Fluss, F. H. Howell, J. C. O'Brien, H. B. Radowsky, and P. A. Sterne, "Valence Bands and Fermi-Surface Topology of Untwinned, Single-Crystal  $\text{YBa}_2\text{Cu}_3\text{O}_{6.9}$ ," *Phys. Rev. B* **45**, 5563 (1992) and references therein.

---

## Overview

The Chemical & Materials Science organization is technically active in a number of Laboratory programs related to energy production both to meet future energy needs and to provide alternate solutions to environmental problems associated with energy production. Among these are controlled thermonuclear energy (inertial confinement fusion), laser isotope separation of uranium, disposal of nuclear waste, and a number of fossil energy projects. In this section, we highlight projects related to liquid-fuel production in which C&MS is actively involved.

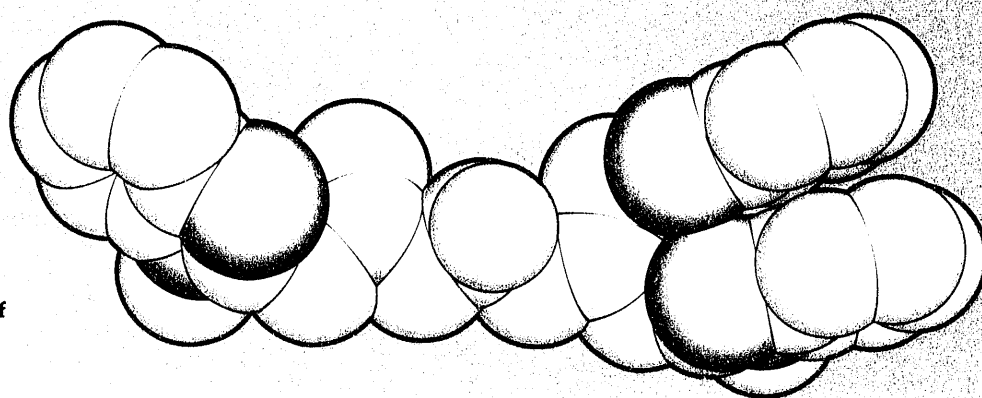
Inexpensive and abundant energy supplies are vital to the U.S. economy. Although our resources in nuclear fuels, natural gas, oil shale, and coal are abundant, domestic supplies of fuel for transportation are inadequate. Because our petroleum production has peaked and is in decline, we are faced with the continuing need to import significant quantities of oil. The present surplus of oil on the world market has held prices at a level that both discourages conservation and inhibits commercial development of alternate energy sources. Our reliance on imported oil also lessens our security in energy supplies. Consequently, it is in our long-term national interest to actively pursue technologies that have the potential to provide alternate sources of liquid fuels to power our transportation infrastructure.

The first four papers in this section report on research directed toward converting methane from our abundant natural-gas resources into hydrocarbon liquids. The objectives of the research are to develop a biomimetic catalyst that will partially oxidize methane to methanol at moderate temperatures and at pressures near atmospheric. This work is in collaboration with biomedical researchers at LLNL and is jointly funded by DOE and the Gas Research Institute.

The last paper in this section reports on work that is part of our continuing research to understand the kinetics of oil-shale retorting. This research provides the technical base for developing economical commercial production of oil from shale. The LLNL oil-shale program represents the only remaining substantial U.S. effort—either government or commercial—to develop the technology for recovering oil from shale. The focus of this effort is a pilot-scale retort based on the LLNL-developed hot-recycled-solid process. The overall technology development includes research in chemical processes that occur during pyrolysis and combustion of oil shale, processes of heat and material transfer, and the flow of solid materials.

**Energy  
Research and  
Development**

**A space-filling model of  
an asymmetric ligand  
used to synthesize  
biomimetic catalysts.**



# Biomimetic Methane Oxidation: Synthesis and Kinetics

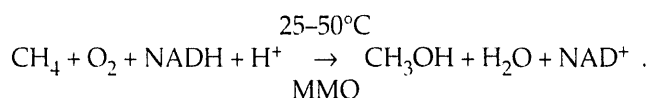
M. W. Droege,  
J. H. Satcher, Jr.,  
R. A. Reibold, and  
T. J. R. Weakely\*

*We have designed and prepared a binuclear, unsymmetric, coordinating ligand that is an effective metal chelator. The new ligand reacts rapidly with copper(II) to form a variety of copper coordination complexes. We have synthesized and characterized a binuclear copper complex, including a single-crystal, x-ray structure analysis. This complex is of significant interest because it represents proof of principle for developing coordinatively asymmetric, binuclear, metal-chelate complexes. Although this structural type of chelator now appears to be common in biological systems, it has not been previously described for inorganic synthetic coordination complexes.*

## Introduction

Catalytic oxidation of light hydrocarbons, especially methane derived from natural gas, is an important research area that is attracting considerable attention. The potential for natural-gas (methane) processing will depend on the development of catalyzed routes that directly convert methane into higher-valued products (heavier hydrocarbons, olefins, and alcohols). However, methane is chemically quite inert and so far has not been easy to convert to liquid hydrocarbons. As a result, no technologies are currently available to process methane economically.

It is well known that a select group of aerobic soil/water bacteria called methanotrophs can efficiently and selectively use methane as their sole source of energy and carbon for cellular growth.<sup>1</sup> The enzyme methane monooxygenase (MMO) catalyzes the first reaction in this metabolic pathway to form methanol:



The technical challenge is to selectively oxidize the relatively inert methane but not to oxidize the relatively reactive methanol to carbon oxides.

Microorganisms can produce MMO in two distinct forms: a membrane-bound particulate form or a discrete soluble form. The soluble form consists of three main proteins: A, B, and C. Protein A is an iron-containing oxygenase that reacts with methane to produce methanol.<sup>2-4</sup>

Spectroscopic and thermodynamic studies have postulated that the metals in Protein A occur in a binuclear iron center and function as the active site for methane oxidation.<sup>5-8</sup> Although some of the details vary, the general description of the iron site in Protein A is a binuclear cluster that contains some type of  $\mu$ -oxo ligand between the iron atoms. The remaining ligands (derived from amino acid residues) are either nitrogen- or oxygen-containing, and the Fe-Fe distance is between 3.0 and 3.5 Å. On the other hand, the particulate form of MMO is poorly characterized and is thought to contain copper ions at the active site. This form also is active in methane oxidation in the biological system.<sup>9,10</sup>

Our work centers on the synthesis and characterization of inorganic/organic chemical models of the active site of MMO (both particulate and soluble). We have focused on the synthesis of an unsymmetric, binuclear chelating ligand with an alkoxo group that can serve as a bridging  $\mu$ -oxo ligand. The advantage of such a ligand system is twofold: (a) metal complexes of an unsymmetric binucleating ligand will provide coordinative unsaturation at only one metal, resulting in focused substrate reactivity at that site, and (b) a single ligand with binuclear coordination will provide a more robust environment for metal oxidation-state changes and accompanying chemical reactivity.

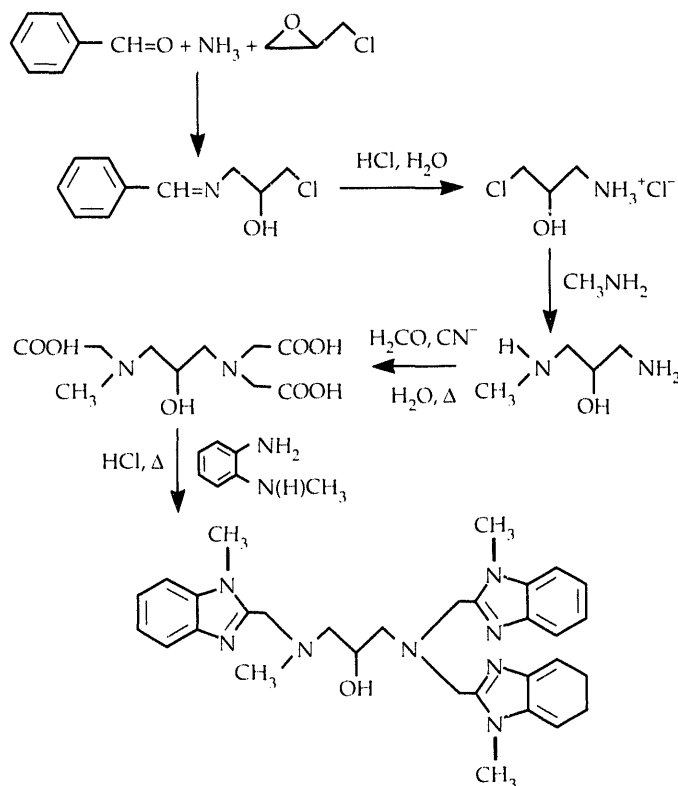
We report here the synthesis of a prototype unsymmetric binuclear chelating ligand, its reactivity with copper ion, and the characterization of two new copper chelate complexes. This work provides the first proof of concept for the formation of a binuclear complex with a different coordination at each metal ion. Such complexes are relevant to the development of model systems for the active site of MMO.



## Results and Discussion

Figure 1 shows the synthetic route for the prototype binuclear chelating ligand HMeL. Elemental analysis and nuclear magnetic resonance (NMR) studies confirm the composition and structure of the ligand. It has a hydroxo functionality that could serve as a bridging alkoxo group and aliphatic and aromatic nitrogen coordination groups (benzimidazole). With the C-OH bond as a bisecting line in this molecule, it is clear that the ligand could coordinate two metal ions in different environments. One half of the ligand provides three coordination sites (two nitrogens and one bridging oxygen), while the other half provides four coordination sites (three nitrogens and one bridging oxygen). Reactions with copper ion demonstrate that the ligand is a potent chelating agent. Blue or blue-green complexes form rapidly in the presence of copper(II). Stoichiometric reactions in methanol synthesize the complexes using hydrated metal salts. Characterization by elemental analysis and single crystal x-ray crystallography show that either mononuclear or binuclear complexes form. For a metal-to-ligand ratio of 1:1, a mononuclear complex forms (see Fig. 2). The structure of the complex shows a distorted, trigonal, bipyramidal coordination environment around copper with five Cu-N bonds (average Cu-N distance  $\sim 2$  Å). In this case, the hydroxo functionality does not coordinate to the metal and is located far from the metal in the structure.

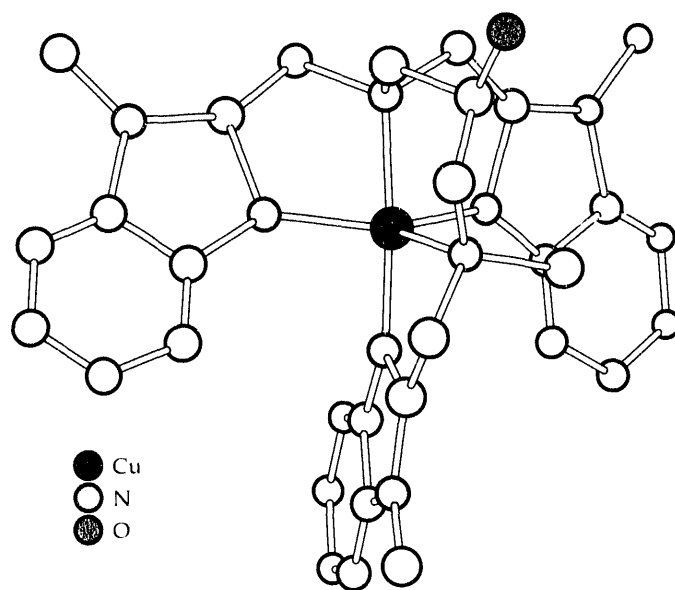
**Figure 1.** Reaction pathway that produces the chelating ligand HMeL.



With a metal-to-ligand ratio of 2:1 and in the presence of two equivalents of sodium acetate, a binuclear complex forms (see Fig. 3). The structure shows that the ligand has chelated two copper ions, that the copper ions share the alkoxo oxygen (bridging  $\mu$ -oxo), and that a coordinated acetate ion bridges the two metals. As a result, one copper ion is coordinatively saturated (five-coordinate, distorted, trigonal pyramid), while the other copper ion is only four-coordinate (distorted, square pyramid). The mixed oxygen-nitrogen ligation has average Cu-N(O) distances of  $\sim 2$  Å, typical of Cu(II) coordination complexes. In this reaction, acetate serves both as a coordinating bridge between the two copper sites and as a general base that assists in deprotonation of the organic hydroxo group forming the charged alkoxo bridging species. Interestingly, the crystal structure shows that, in the solid state, an oxygen from one of the  $\text{ClO}_4^-$  counterions binds weakly to the four-coordinate copper ion (about 2.6 Å away). This suggests that this copper ion is coordinatively unsaturated and that there is a potential fifth site for binding. Initial attempts to demonstrate this binding site have been successful, and an azido-bridged binuclear copper complex has been prepared and isolated.<sup>11</sup> It appears that complexes of this type can show selective reactivity at one metal site. Such behavior is a key requirement for bioinorganic mimics of the MMO active site.

We explored catalytic activity under atmospheric pressure in acetonitrile in a Fisher-Porter bottle, with cyclohexane as the hydrocarbon substrate, with hydrogen peroxide as the oxidant, and with a metal complex; the ratio was 1000:100:1. When the mononuclear copper

**Figure 2.** Structure of mononuclear Cu(II) complex. Open circles represent carbon atoms. For clarity, hydrogen atoms are not shown.



complex or copper(II)tetrafluoroborate acted as the catalyst species, cyclohexane was not converted to cyclohexanol and/or cyclohexanone, according to our gas-chromatography/mass-spectrometry (GC/MS) analysis of the reaction media sampled over a 48-h period. We also found hydrogen-peroxide decomposition, as monitored by titration with potassium permanganate, to be zero during this period. In contrast, the binuclear copper complex as a catalyst consumed 40% of the hydrogen peroxide over a 48-h period and produced cyclohexanol and cyclohexanone in a 1:1 molar ratio. The alcohol and ketone produced represents a 10% yield based on oxidizing equivalents consumed, and there is a turnover ratio of three moles of oxidized product to one mole of catalyst. Although this is a modest conversion of a selected hydrocarbon to oxidized species, it demonstrates the utility of the asymmetric-coordination/directed-reactivity concept. From this type of information, we may obtain kinetic parameters for the reaction and can postulate a mechanism of reaction. A change in solution color upon adding peroxide suggests that binding occurs at the coordinatively unsaturated copper atom (as found in the azido bridged species), but this remains to be confirmed by x-ray crystallography.

## Conclusions

We have designed and prepared a binuclear, unsymmetric coordinating ligand that is an effective metal chelator. The new ligand reacts rapidly with copper(II) to form a variety

of copper coordination complexes. The binuclear complex is of significant interest because it represents proof of principle for developing coordinatively unsymmetric, binuclear metal-chelate complexes. Although this structural type of chelator now appears to be common in biological systems, this is the first time a synthetic organometallic complex has been prepared with these structural features. We expect this ligand and its derivatives to play an important role in the development of bioinorganic complexes that aim to mimic enzymes whose active site contains a multimetal complex (such as MMO).

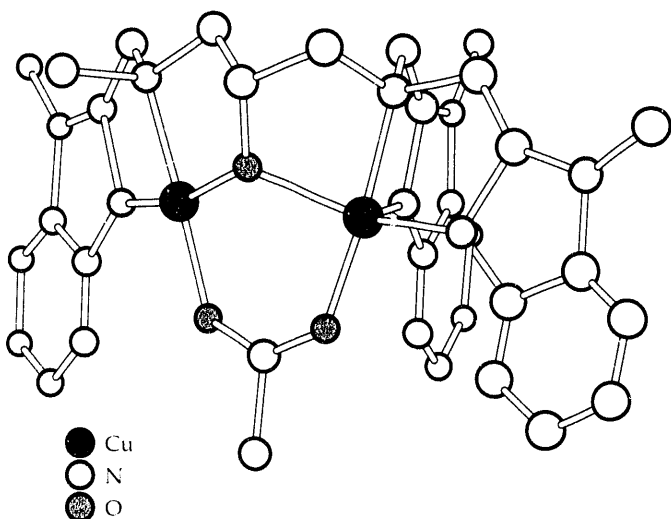
*This work was funded by the DOE Morgantown Energy Technology Center, Gas Research Institute, and LLNL's Laboratory Directed Research and Development.*

\* Department of Chemistry, The University of Oregon, Eugene

## References

1. H. Dalton, "Oxidation of Hydrocarbons by Methane Monooxygenase from a Variety of Microbes," *Adv. Appl. Microbiol.* **26**, 71 (1980).
2. M. P. Woodland and H. Dalton, "Purification and Characterization of Component A of the Methane Monooxygenase from *Methylococcus capsulatus* (Bath)," *J. Biol. Chem.* **259**, 53 (1984).
3. J. Green and H. Dalton, "Protein B of Soluble Methane Monooxygenase from *Methylococcus capsulatus* (Bath)," *J. Biol. Chem.* **260**, 15795 (1985).
4. B. G. Fox, W. A. Froland, J. E. Dege, and J. D. Lipscomb, "Methane Monooxygenase from *Methylosinus trichosporium* OB3b. Purification and Properties of a Three-Component System with High Specific Activity from a Type II Methanotroph," *J. Biol. Chem.* **264**, 10023 (1989).
5. M. P. Woodland, D. W. Patil, R. Cammack, and H. Dalton, "ESR Studies of Protein A of the Soluble Methane Monooxygenase from *Methylococcus capsulatus* (Bath)," *Biochim. Biophys. Acta* **873**, 237 (1986).
6. B. G. Fox, K. K. Surerus, E. Munck, and J. D. Lipscomb, "Evidence for a  $\mu$ -Oxo-Bridged Binuclear Iron Cluster in the Hydroxylase Component of Methane Monooxygenase," *J. Biol. Chem.* **263**, 10553 (1988).
7. R. C. Prince, G. N. George, J. C. Savas, S. P. Cramer, and R. N. Patel, "Spectroscopic Properties of the Hydroxylase of Methane Monooxygenase," *Biochim. Biophys. Acta* **952**, 220 (1988).
8. A. Ericson, B. Hedman, K. O. Hodgson, J. Green, H. Dalton, J. G. Bentsen, R. H. Beer, and S. J. Lippard, "Structural Characterization by EXAFS Spectroscopy of the Binuclear Iron Center in Protein A of Methane Monooxygenase from *Methylococcus capsulatus* (Bath)," *J. Am. Chem. Soc.* **110**, 2330 (1988).
9. S. H. Stanley, S. D. Prior, D. J. Leak, and H. Dalton, "Copper Stress Underlies the Fundamental Change in Intracellular Location of Methane Monooxygenase in Methane-Oxidizing Organisms: Studies in Batch and Continuous Cultures," *J. Biotechnol. Lett.* **5**, 487 (1983).
10. S. Park, M. L. Hanna, R. T. Taylor, and M. W. Droege, "Batch Cultivation of *Methylosinus trichosporium* OB3b. I: Production of Soluble Methane Monooxygenase," *Biotechnol. Bioeng.* **38**, 423 (1991).
11. M. W. Droege, J. H. Satcher, Jr., and T. J. R. Weakley, Lawrence Livermore National Laboratory, Livermore, CA, unpublished results.

**Figure 3.** Structure of binuclear Cu(II) complex. Open circles represent carbon atoms. For clarity, hydrogen atoms are not shown.



# Theoretical Description of Biomimetic Complexes

N. W. Winter\* and  
M. W. Droege

*In support of the development of new types of inorganic catalysts for converting methane to liquid fuels, we are investigating computational models to study intermediate reaction complexes that occur during the selective partial oxidation of methane. We have carried out first-principles calculations of the electronic structure at the active transition-metal sites in the catalysts to understand the relationship between structure, functionality, and catalytic activity and to guide the development of new materials.*

## Introduction

Catalytic oxidation of light hydrocarbons, such as methane derived from natural gas, is an economically important industrial research area. Biocatalytic enzymatic processes known to perform partial oxidation of alkanes<sup>1,2</sup> provide a model for developing biomimetic chemical catalysts that can convert methane to higher-valued products. In support of the experimental study of biomimetic materials, we are developing computational models for the enzymatic system methane monooxygenase (MMO) and newly synthesized chemical complexes designed to mimic the active site in this enzyme.

The major difficulty in the theoretical characterization of these materials is that energy-minimization and molecular dynamics (MD) models based on parameterized valence force fields cannot adequately treat the transition metals that are an integral part of the active site. Our emphasis in this work is to calculate, using first principles, the electronic structure of the transition metal sites by using cluster methods developed to study transition-metal impurities in crystals.<sup>3</sup> Our calculations characterize the biomimetic materials, but more importantly, they are designed to assist in developing semiempirical models that will allow us to predict important parameters such as type of metal ion, redox properties, ligand composition, and geometry. These parameters are needed to describe the catalytic reaction for methane conversion. Based on these parameters, new catalyst materials can be experimentally prepared and tested.

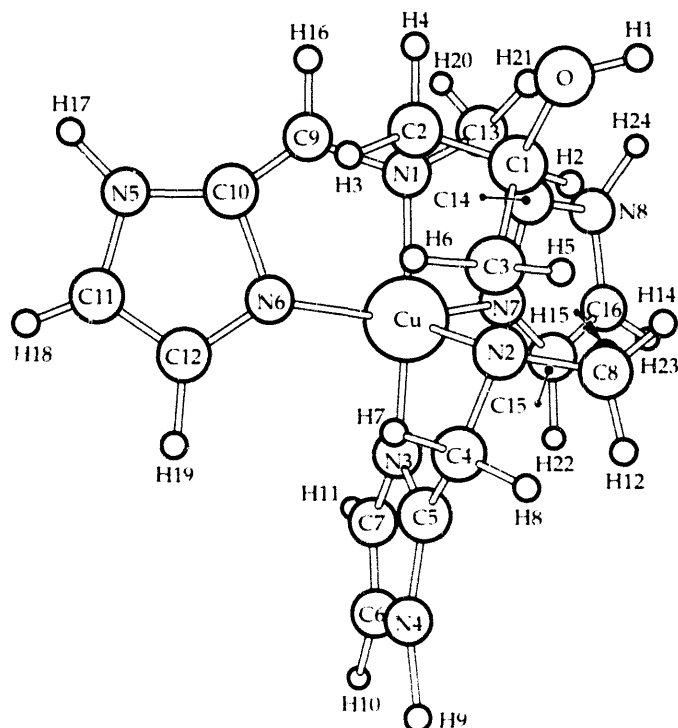
## Theory

The biomimetic transition metal complexes include mono- and binuclear copper and tetranuclear iron sites that promote the catalytic reaction. The metals are coordinated by benzimidazole ligands and are linked by aceto- and hydroxo-bridges. We have carried out first-principles Hartree-Fock calculations of the electronic structure for both the mono- and binuclear copper and the iron sites. To reduce the computational effort, we replaced the benzimidazole ligands of the mononuclear copper complex,

$\text{Cu}(\text{N}_8\text{C}_{31}\text{H}_{36}\text{O})$ , with simpler imidazole ligands. The resulting 50-atom model complex,  $\text{Cu}(\text{N}_8\text{C}_{16}\text{H}_{24}\text{O})$ , is shown in Fig. 1. We replaced the  $1s^22s^22p^63s^23p^6$  core electrons on the copper ion and the  $1s^2$  inner-shell electrons on carbon, nitrogen, and oxygen atoms with relativistic effective core potentials<sup>4</sup> to further reduce the number of electrons explicitly considered in the calculations. We used a Gaussian atomic orbital basis set<sup>5,6</sup> on each atom to describe the valence electrons and fixed the atomic positions at the experimental x-ray structure values.

The calculated atomic charges characterize the Hartree-Fock charge distribution and provide an important comparison between first-principles and semiempirical molecular

**Figure 1.** The structure of the  $\text{Cu}(\text{N}_8\text{C}_{16}\text{H}_{24}\text{O})$  model complex.



orbital methods. Table 1 summarizes the atomic orbital populations and total atomic charges as determined from the molecular orbital wavefunction for the mononuclear complex. The labeling of the atomic sites is keyed to Fig. 1. Formally, copper is  $3d^9$  with a charge of +2. The calculations indicate a valence electron configuration of  $3d^{9.02}4s^{0.34}4p^{0.16}$

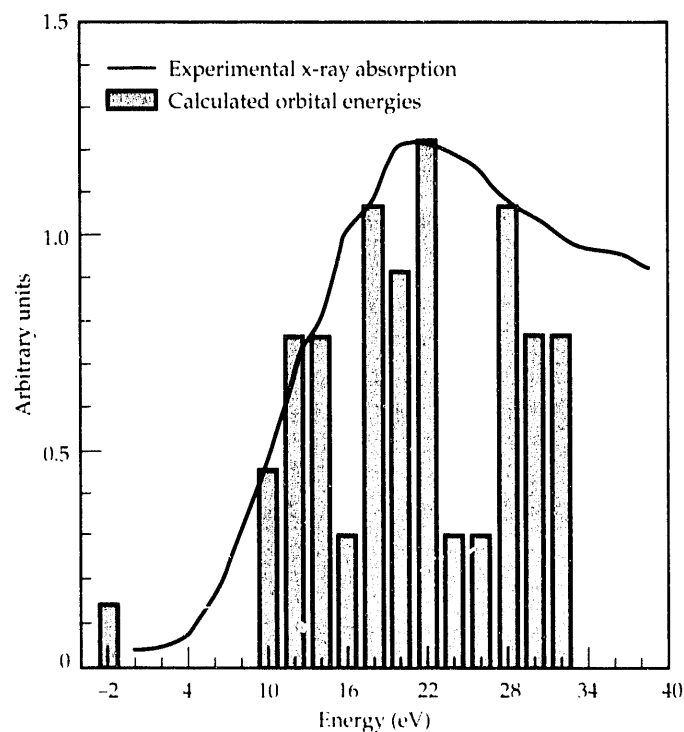
**Table 1.** Calculated charges from the Hartree-Fock wavefunctions for the  $\text{Cu}(\text{N}_8\text{C}_{16}\text{H}_{24}\text{O})$  model complex.

Atom	s	p	d	Total	Charge
Cu	0.34	0.16	9.02	9.52	1.48
O	1.82	4.73		6.55	-0.55
N <sub>1</sub>	1.59	3.86		5.45	-0.45
N <sub>2</sub>	1.57	3.87		5.45	-0.45
N <sub>3</sub>	1.67	3.85		5.52	-0.52
N <sub>4</sub>	1.58	3.90		5.48	-0.48
N <sub>5</sub>	1.58	3.89		5.47	-0.47
N <sub>6</sub>	1.67	3.84		5.51	-0.51
N <sub>7</sub>	1.67	3.86		5.53	-0.53
N <sub>8</sub>	1.58	3.89		5.48	-0.48
C <sub>1</sub>	1.22	2.88		4.11	-0.11
C <sub>2</sub>	1.28	3.07		4.36	-0.36
C <sub>3</sub>	1.28	3.08		4.36	-0.36
C <sub>4</sub>	1.28	3.12		4.40	-0.40
C <sub>5</sub>	1.19	2.62		3.82	0.18
C <sub>6</sub>	1.26	2.96		4.22	-0.22
C <sub>7</sub>	1.27	2.96		4.22	-0.22
C <sub>8</sub>	1.35	3.27		4.62	-0.62
C <sub>9</sub>	1.28	3.11		4.39	-0.39
C <sub>10</sub>	1.18	2.66		3.84	0.16
C <sub>11</sub>	1.26	2.96		4.22	-0.22
C <sub>12</sub>	1.26	2.94		4.20	-0.20
C <sub>13</sub>	1.27	3.13		4.40	-0.40
C <sub>14</sub>	1.19	2.64		3.83	0.17
C <sub>15</sub>	1.26	2.95		4.21	-0.21
C <sub>16</sub>	1.26	2.95		4.22	-0.22
H <sub>1</sub>	0.63		0.63	0.63	0.37
H <sub>2</sub>	0.73		0.73	0.73	0.27
H <sub>3</sub>	0.70		0.70	0.70	0.30
H <sub>4</sub>	0.71		0.71	0.71	0.29
H <sub>5</sub>	0.71		0.71	0.71	0.29
H <sub>6</sub>	0.72		0.72	0.72	0.28
H <sub>7</sub>	0.68		0.68	0.68	0.32
H <sub>8</sub>	0.69		0.69	0.69	0.31
H <sub>9</sub>	0.47		0.47	0.47	0.53
H <sub>10</sub>	0.63		0.63	0.63	0.37
H <sub>11</sub>	0.62		0.62	0.62	0.38
H <sub>12</sub>	0.72		0.72	0.72	0.28
H <sub>13</sub>	0.71		0.71	0.71	0.29
H <sub>14</sub>	0.73		0.73	0.73	0.27
H <sub>15</sub>	0.68		0.68	0.68	0.32
H <sub>16</sub>	0.69		0.69	0.69	0.31
H <sub>17</sub>	0.47		0.47	0.47	0.53
H <sub>18</sub>	0.63		0.63	0.63	0.37
H <sub>19</sub>	0.62		0.62	0.62	0.38
H <sub>20</sub>	0.68		0.68	0.68	0.32
H <sub>21</sub>	0.68		0.68	0.68	0.32
H <sub>22</sub>	0.61		0.61	0.61	0.39
H <sub>23</sub>	0.62		0.62	0.62	0.38
H <sub>24</sub>	0.47		0.47	0.47	0.53

and a charge of +1.5. The open-shell 3d orbital is atomic-like, with essentially no admixture of ligand orbitals. The significant participation of the empty 4s and 4p orbitals in the metal-ligand interaction demonstrates the importance of these orbitals in describing reaction intermediates that involve the transition-metal site and indicates that semiempirical models cannot be parameterized solely on the basis of the 3d orbitals. Similar results were obtained for the binuclear copper complex.

The one-electron energy levels for the mononuclear copper complex have been charted in a histogram with 2 eV bins to give an approximate density of states. The results are compared to the experimental  $\text{Cu}(\text{N}_8\text{C}_{31}\text{H}_{36}\text{O})$  x-ray absorption spectra for the  $1s \rightarrow 4l$  transitions in Fig. 2. The theoretical energy scale has been adjusted to match the observed  $1s \rightarrow 3d$  pre-edge feature. No absorption was calculated in the near-edge region, but the calculated  $\text{Cu}(4s, 4p)$  and ligand energy levels qualitatively reproduce the shape of the main absorption peak. The binuclear copper complex showed similar agreement. This comparison verifies that the model calculations accurately reproduce the copper environment and should be adequate for further study of reaction intermediates at the metal site.

**Figure 2.** Comparison of the calculated Hartree-Fock one-electron density of states for  $\text{Cu}(\text{N}_8\text{C}_{16}\text{H}_{24}\text{O})$  to the experimental x-ray absorption of the  $\text{Cu}(\text{N}_8\text{C}_{31}\text{H}_{36}\text{O})$  complex.



## Summary

Our first-principles calculation of the electronic structure of the copper complexes has demonstrated our ability to characterize the transition-metal sites in candidate catalyst materials. The analysis indicates that the imidazole groups show considerable similarity in their charge distributions, even though no symmetry was enforced in the calculations. This result suggests that it may be possible to further simplify the description of the ligands without significant loss of accuracy, making possible the calculation of the potential-energy surfaces for the interaction with O<sub>2</sub> and CH<sub>4</sub>.

*This work was funded by Laboratory Directed Research and Development.*

\*Physics Department, LLNL

## References

1. D. M. Kurtz, "Oxo- and Hydroxo-Bridged Diiron Complexes: A Chemical Perspective on a Biological Unit," *Chem. Rev.* **90**, 585 (1990).
2. P. A. Frey, "Importance of Organic Radicals in Enzymatic Cleavage of Unactivated C-H Bonds," *Chem. Rev.* **90**, 1343 (1990).
3. N. W. Winter, D. K. Temple, V. Luana, and R. M. Pitzer, "Calculation of the Electronic Structure of Transition Metal Impurities in Ionic Crystals," *Advances in Molecular Electronic Structure Theory*, Vol 2, T. H. Dunning, Ed. (JAI Press Inc., 1991).
4. W. C. Ermler, R. B. Ross, and P. A. Christiansen, "Ab Initio Relativistic Effective Potentials with Spin-Orbit Operators," *Adv. Quantum Chem.* **19**, 139 (1988).
5. M. M. Hurley, L. Fernandez Pacios, P. A. Christiansen, R. B. Ross, and W. C. Ermler, "Ab Initio Relativistic Effective Potentials with Spin-Orbit Operators. II—K through Kr," *J. Chem. Phys.* **84**, 6840 (1986).
6. L. Fernandez Pacios and P. A. Christiansen, "Ab Initio Relativistic Effective Potentials with Spin-Orbit Operators. I—Li through Ar," *J. Chem. Phys.* **82**, 2664 (1985).

# Subunit Resolution for Active Site Identification of *Methylosinus trichosporium* OB3b Soluble Methane Monooxygenase

M. M. Himmelsbach,  
R. T. Taylor, and  
M. W. Droege

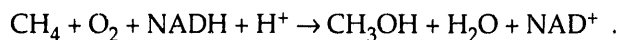
*We have developed a procedure for the dissociation and resolution of the three distinct subunits of the soluble methane monooxygenase protein A. Using the net charge differences between the subunits to effect a separation by ion exchange chromatography, the individual subunits are isolated under denaturing conditions.*

## Introduction

Information concerning the selective transformation of methane to methanol, which occurs in a special group of microorganisms, would be of great value for several reasons. First, economic factors motivate the production of methanol from methane. Second, the ability to produce methanol selectively from methane is unique from a chemical perspective, as little selectivity for the alcohol is observed in the known oxidation reactions of methane. One way to design and synthesize catalysts that produce methanol on an industrial scale is to carefully study enzyme systems that can convert methane to methanol. Identification of unique chemical features in these systems should facilitate a more rational approach to the synthesis of biomimetic industrial catalysts. We have therefore chosen to examine the active site structure of the cytoplasmic methane-oxidizing enzyme produced by the bacterium *Methylosinus trichosporium* OB3b.

Within this bacterium, methane monooxygenase (MMO) is the specific enzyme complex that converts methane to methanol. Under ambient conditions, the soluble form of

MMO (sMMO) produces methanol at the rate of approximately four molecules per molecule of enzyme per second<sup>1</sup>; the cell then uses methanol as a source of carbon for biomass generation and for energy storage.<sup>1</sup> The production of methanol (CH<sub>3</sub>OH) by sMMO requires stoichiometric amounts of methane (CH<sub>4</sub>), molecular oxygen (O<sub>2</sub>), and a source of intracellular electrons that are supplied by reduced nicotinamide adenine dinucleotide (NADH):

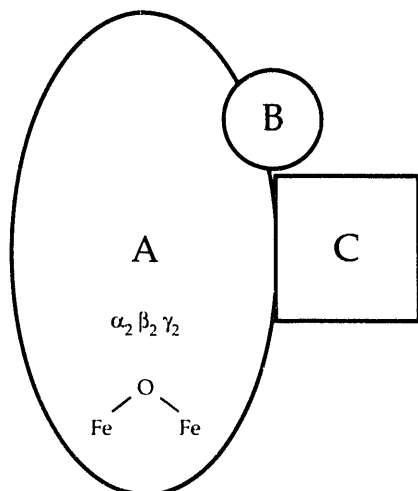


Three proteins (A, B, and C) facilitate this complex interaction, which results in a controlled partial oxidation of methane. Figure 1 shows these three proteins that comprise the soluble enzyme system. According to current understanding, methane oxidation occurs at a hydroxo-bridged dinuclear iron center in protein A, while proteins B and C participate in the transfer of electrons from NADH to the iron center in protein A.

Our investigation focuses on protein A because it appears to have the key features necessary for CH<sub>4</sub> activation. It is an oligomeric protein, composed of three distinct subunits in an  $\alpha_2 \beta_2 \gamma_2$  configuration, with a molecular weight of 245,000 daltons. Currently, the location of the iron center in protein A is not known. It is also not known whether this cofactor links with the amino-acid side chains of only one type of subunit, or whether it bridges an interface between two unlike polypeptide subunits. Our project aims to identify portions of the amino-acid sequence within protein A that surround the iron center. To do this, it was necessary to first determine conditions for separating and resolving the  $\alpha$ ,  $\beta$ , and  $\gamma$  subunits of protein A. This will allow us to define more accurately the location of the enzyme's active site, to understand the subunit interactions and their impact on CH<sub>4</sub> activation, and to simplify the purification of polypeptide fragments derived from the active site.

**Figure 1.**

Protein components of the soluble methane monooxygenase system.



## Experimental Methods

We obtained purified protein A by modifying published procedures.<sup>2,3</sup> Initially, we guided enzyme purification at each step by correlating the enzymatic activity with the ultraviolet (UV) absorption profile (280 nm) and determined purity by sodium dodecyl sulfate polyacrylamide gel electrophoresis (SDS-PAGE). Later purifications relied solely on the UV profile and the protein subunit composition indicated by gel electrophoresis.

We grew *M. trichosporium* OB3b according to the method of Park et al.<sup>4</sup> A typical purification used 12 to 16 g of dry cell weight equivalent, which was suspended in 25 mM 3-(N-morpholino)propanesulfonic acid (MOPS), 5 mM MgCl<sub>2</sub>, and 5 mM dithiothreitol (DTT). Two passages through a Manton-Gaulin homogenizer ruptured the cells, which we then stirred at 4°C with DNase. Centrifuging at 40,000 × gravity for 1 h produced the cell-breakage supernatant fluid. We then transferred this cytoplasmic material into an Amicon ultrafiltration cell under nitrogen (this and all subsequent steps were carried out at 4°C). Passage across an XM 300 membrane concentrated the supernatant fluid and provided a bulk discrimination between the high- and low-molecular-weight protein components. Next, we loaded the high-molecular-weight XM 300 retentate onto a diethylaminoethyl (DEAE) Sepharose Fast Flow anion-exchange column, equilibrated with 25 mM MOPS and 5 mM DTT, and eluted with a linear salt gradient from 0 to 0.25 M NaCl. We pooled and concentrated the peak that eluted at approximately 0.14 M NaCl and took it onto a second anion-exchange column. Gel filtration chromatography in the same buffer completed the final purification of protein A. We obtained approximately 240 to 480 mg of protein, which we judged to be ~95% pure using SDS-PAGE.

To generate subunits, we denatured protein A by incubating the protein in buffered urea solutions for 1 h at 21°C. Gel filtration chromatography was carried out at room temperature in an attempt to improve the flow rate and resolution by this technique. Later, we obtained subunit separations more successfully by denaturing anion-exchange chromatography at pH 8 in tris(hydroxymethyl)aminomethane buffer (Tris), which was performed at 4°C.

## Results and Discussion

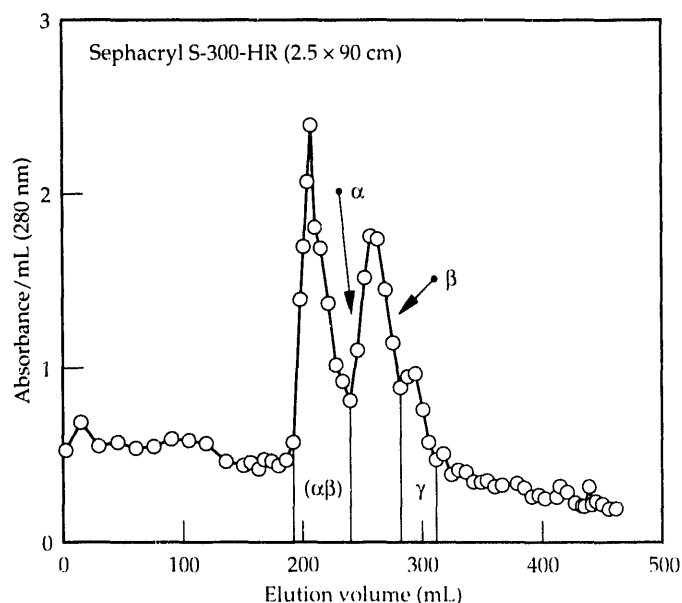
SDS-PAGE of purified protein A showed three distinct bands, indicating the expected subunit composition and molecular weights:  $\alpha$  (54,000),  $\beta$  (43,000),  $\gamma$  (23,000). Other than the electrophoretic separation of microgram quantities of the subunits achieved in the polyacrylamide gel matrix, the individual properties of the subunits have not been reported or explored. To carry out studies such as these, milligram quantities of each subunit are required.

To dissociate protein A in an aqueous solution, we attempted a number of denaturing conditions. The chemical denaturants included sodium dodecyl sulfate, guanidine

hydrochloride, and urea, coupled with variations in the salt concentration, temperature, and pH. For an oligomeric protein in a denaturing medium, dissociation followed by subunit unfolding is thought to occur in a stepwise manner. One of the most difficult problems was to define conditions that maintained the solubility of the dissociated subunits. This problem is common in protein unfolding because the hydrophobic interactions that stabilized the globular protein now drive the interchain association of the unfolded strands and result in aggregation and precipitation.<sup>5</sup> Using a combination of the factors listed above, we obtained the only satisfactory results with the reversible denaturant urea. Treating the protein with urea in the presence of DTT prevented disulfide formation. Initially, we tried gel filtration chromatography to resolve the individual subunits and to provide information regarding the extent of dissociation.

A precipitate formed on our first effort to dissociate protein A in urea (pH 7). Analysis of the supernatant indicated that most of the  $\gamma$  subunit remained in solution. We dissolved the precipitated protein under alkaline conditions and then subjected the solution to gel filtration chromatography. The elution profile (see Fig. 2) showed three major peaks, which we analyzed using SDS-PAGE. The earliest eluting peak, corresponding to material with the highest molecular weight, was identified as a complex containing both  $\alpha$  and  $\beta$ . This indicated that the subunits of protein A had not been completely dissociated. The second peak corresponded to the sequential elution of  $\alpha$  and  $\beta$ — $\alpha$  eluting on the front half and  $\beta$  eluting on the back half—and the last peak contained only the  $\gamma$  fraction. Observation of the  $\gamma$  subunit in solution following precipitation of the  $\alpha$  and  $\beta$  subunits, coupled with the

**Figure 2.** Gel filtration profile in 50 mM MOPS (pH 7), 6 M urea, and 5 mM DTT, following a 1-h incubation at 21°C in the same buffer.



partial retention of an ( $\alpha\beta$ ) complex under alkaline conditions, indicates that the  $\alpha$  and  $\beta$  subunits have higher affinities for each other than for  $\gamma$ .

To determine the effect on dissociation of the subunits and their chromatographic separation, we then probed other factors. We examined the salt concentration by adding 0.3 M sodium chloride to a 6 M urea solution at pH 7. Analysis of the solution by gel filtration chromatography, followed by electrophoresis, again indicated that incomplete dissociation had occurred, as the ( $\alpha\beta$ ) complex remained the major component in solution. Protein unfolding and denaturation is known to be a very sensitive function of temperature,<sup>6</sup> and

**Figure 3.** Gel filtration profile in 50 mM glycine (pH 9.3), 7 M urea, 5 mM DTT, following a 1-h incubation at 21°C in the same buffer.

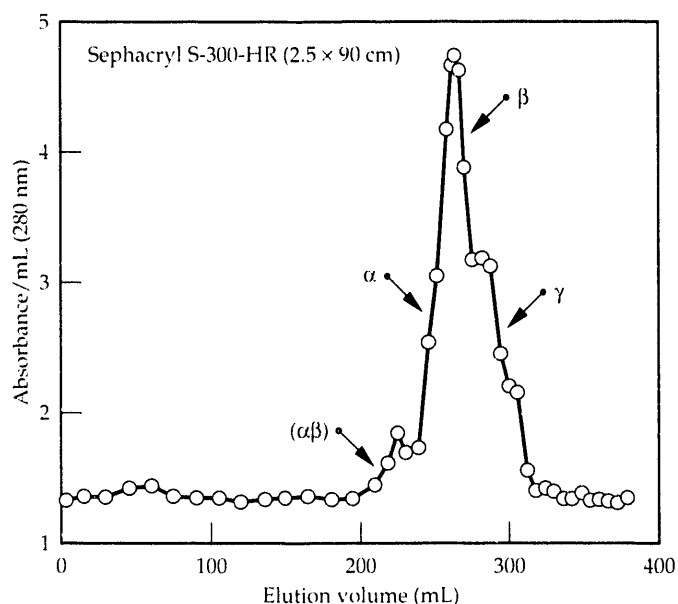
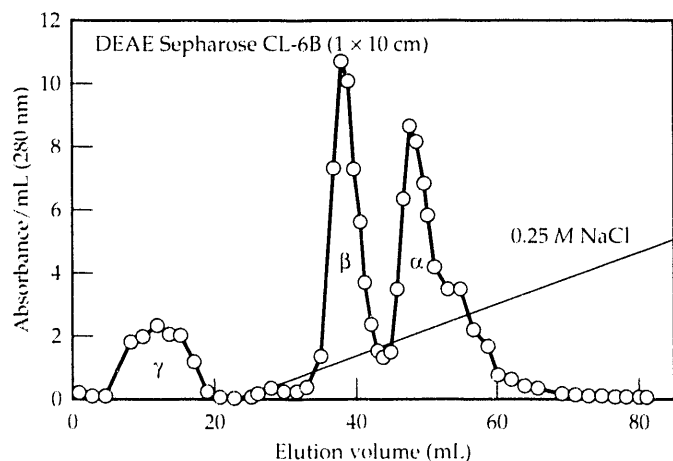


**Figure 4.** Anion exchange profile in 25 mM Tris (pH 8), 7 M urea, 5 mM DTT, following a 1-h incubation at 21°C in the same buffer.

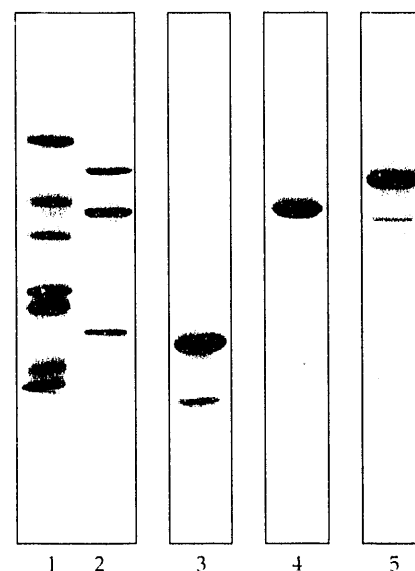


we determined that protein A was very easily heat-denatured with precipitation, even at 40°C. Consequently, temperatures above 21°C cannot be used to enhance subunit dissociation. Finally, we found that adjusting the pH to 8 or higher would optimize the dissociation of the subunits, presumably because of electrostatic repulsion between the negatively charged side chains. In addition, we raised the urea concentration to 7 M to maintain the solubility of the polypeptides. Gel-filtration chromatography of protein A in glycine buffer at pH 9.3 (see Fig. 3) showed that very little of the ( $\alpha\beta$ ) complex was present. However, as the profile indicates, very little resolution of the dissociated subunits was achieved with this chromatographic technique.

Anion-exchange chromatography provided much higher resolution of the dissociated subunits under the window of conditions discussed here. Chromatography of denatured protein A on DEAE Sepharose CL-6B resulted in three distinct peaks, corresponding to each of the subunits (see Fig. 4). Because ion-exchange chromatography does not discriminate on the basis of size, but rather on charge, the elution profile provides some measure of the subunit net-charge properties. The  $\gamma$  subunit is not bound by the anion-exchange resin under these conditions, which suggests that it is positively charged at pH 8. The  $\alpha$  and  $\beta$  subunits bind to the column, indicating that they both possess a negative charge at this pH. We again detected a small amount of the ( $\alpha\beta$ ) complex in this mixture and found it to elute as a shoulder on the trailing edge of the  $\alpha$  subunit. SDS-PAGE of the peak fractions (see Fig. 5) clearly indicates a high degree of subunit resolution.

**Figure 5.**

SDS-PAGE of the individual subunits obtained by denaturing anion-exchange chromatography (fraction number corresponds to elution volume in Fig. 4).



**Lanes:**

1. Molecular-weight standards
2. Column load
3. Fraction 12
4. Fraction 38
5. Fraction 48



## Conclusions

We have defined conditions that allow us to dissociate the sMMO protein A into its constituent subunits. Given the high mutual affinity of the  $\alpha$  and  $\beta$  subunits, these subunits could be dissociated only under slightly alkaline conditions in 7 M urea. We achieved the resolution of these three subunits—for the first time on a preparative (milligram) scale—by anion-exchange chromatography.

*This work was funded by Laboratory Directed Research and Development.*

\* Both a soluble form and a particulate form of this enzyme are known for *Methylosinus trichosporium* OB3b. We discuss only the soluble form (sMMO) here.

## References

1. C. Anthony, "Bacterial Oxidation of Methane and Methanol," *Adv. Microbial Physiol.* **27**, 113 (1986).
2. H. Dalton and S. J. Pilkington, "Soluble Methane Monooxygenase from *Methylococcus capsulatus* Bath," in *Methods in Enzymology* **188**, M. E. Lidstrom, Ed. (Academic Press, San Diego, CA, 1990), p. 181.
3. B. G. Fox, W. A. Froland, D. R. Jollie, and J. D. Lipscomb, "Methane Monooxygenase from *Methylosinus trichosporium* OB3b," in *Methods in Enzymology* **188**, M. E. Lidstrom, Ed. (Academic Press, San Diego, CA, 1990), p. 191.
4. S. Park, M. L. Hanna, R. T. Taylor, and M. W. Droegge, "Batch Cultivation of *Methylosinus trichosporium* OB3b. I: Production of Soluble Methane Monooxygenase," *Biotechnol. Bioeng.* **38**, 423 (1991).
5. R. Jaenicke and R. Rudolph, "Refolding and Association of Oligomeric Proteins," in *Methods in Enzymology* **131**, C. H. W. Hirs and S. N. Timasheff, Eds. (Academic Press, Orlando, FL, 1986), p. 228.
6. K. A. Dill, "Dominant Forces in Protein Folding," *Biochem.* **29**, 7133 (1990).

# Bioreactor Cultivation of *Methylophilus* *trichosporium* OB3b for the Production of Particulate Methane Monooxygenase

N. N. Shah, R. T. Taylor,  
and M. W. Droegge

***Methane monooxygenases (MMOs) are enzymes that oxidize a wide variety of saturated hydrocarbons to alcohols and alkenes to epoxides. We studied the effects of two important medium components, copper and nitrate, on the production of a membrane-bound, particulate form of the enzyme (pMMO) in Methylophilus trichosporium OB3b for batch and continuous bioreactor culturing of this bacterium. Studies of pMMO-vs-soluble MMO structure-function relationships will provide useful information for the synthesis of catalytic materials needed to convert methane to liquid fuels.***

## Introduction

We are developing new materials that can catalyze the partial oxidation of methane to a liquid fuel such as methanol. Current oxidative processes that transform methane to a mixture of methanol plus some higher hydrocarbons require high operating temperatures (700 to 800°C) and have unacceptably low product yields because of overoxidation of the gas to CO and CO<sub>2</sub>. An ideal catalyst should control the activation of the oxygen and methane C-H bond and yield a specific desired product. Efforts to synthesize such catalysts chemically can benefit from a structure-function study of biological catalysts that can partially and very efficiently oxidize methane to methanol under ambient conditions.

The only known biological catalysts that can selectively convert methane to methanol are methane monooxygenases (MMOs). In nature, they exist exclusively in a group of bacteria called methanotrophs.<sup>1</sup> In some methanotrophs, such as *Methylophilus trichosporium* OB3b and *Methylococcus capsulatus* (bath), two distinct forms of MMO—one soluble (sMMO) and the other particulate (pMMO)—occur, depending on the availability of copper in the culture medium.<sup>2,3</sup> A membrane-bound pMMO forms when copper is sufficient, while an sMMO forms when copper availability is very low.

These two intracellular forms of MMO exhibit some remarkable differences in their catalytic activities for various substrates (e.g., *n*-alkanes, *n*-alkenes, aromatic and alicyclic compounds). The sMMO displays a much broader substrate specificity, but the pMMO is more active with methane and propene. Isolation of MMOs for structure-function studies requires a bulk production of the bacterial

biomass. Previously, we optimized the growth conditions for sMMO biosynthesis by *M. trichosporium* OB3b.<sup>2</sup> As a result, the purification and further characterization of this enzyme system is in progress.<sup>4</sup>

More recently, we have focused our attention on the bioreactor cultivation of *M. trichosporium* OB3b containing exclusively pMMO. Our objective was to obtain a reproducible growth of cells containing a maximal level of expressed pMMO activity for comparative structure-function studies of the pMMO (copper-dependent enzyme) vs the sMMO (copper-independent enzyme) system within a single strain of methanotroph. We first examined the effects of two important medium components, copper and nitrate, on cell growth and whole-cell specific pMMO under fixed-batch culturing conditions. Subsequently, we established the conditions for maximally expressing whole-cell pMMO activity under continuous culturing conditions.

## Experimental Methods

We grew *M. trichosporium* OB3b in a modified Higgin's nitrate minimal salts medium<sup>2,3</sup> and performed fermentor-scale experiments in a 5-L bioreactor (Bioflo II, New Brunswick) at pH 6.8 to 7.2 and a 30°C incubation temperature. Gaseous substrates, 10% CO<sub>2</sub>-containing air and methane (3:1 v/v), were sparged continuously. Bioreactor inocula were cultured under an air/methane gas mixture (1:1 v/v) in 2-L shake-flasks with 200 mL of Higgin's medium containing 10 μM CuSO<sub>4</sub>.<sup>3</sup> We operated the bioreactor either in a batch mode or switched it to a continuous feed mode after about 50 h of batch growth. Occasionally, we adjusted the impeller speeds and gas-flow rates to maintain dissolved oxygen levels above 5% during the

batch operations. However, we maintained the impeller speed and dilution rate at 500 rpm and  $0.06 \text{ h}^{-1}$ , respectively, during the continuous cultivations. To maintain a constant volume of bioreactor liquid, we used a peristaltic pump to continuously feed filter-sterilized medium to the bioreactor. We observed a steady state after maintaining the bioreactor under a desired set of culture conditions for more than three times the inverse of the dilution rate. (We assumed a steady state when two consecutive measurements of cell density and pMMO activity yielded approximately the same values.)

We determined cell densities from spectrophotometric measurements of the absorbance at 660 nm and determined nitrate concentrations with an ion-specific nitrate electrode and a double-junction reference electrode connected to a pH/ion meter. Using inductively coupled plasma-atomic emission spectroscopy (ICP-AES),\* we determined the copper content of the washed and freeze-dried cell samples. We measured the epoxidation rate of propene to determine the total MMO activity (sMMO plus pMMO) of the intact cells. Propene is a convenient surrogate substitute for methane because the whole-cell MMO-catalyzed product, propene oxide, cannot be further metabolized. In contrast, the natural initial intracellular product of methane conversion, methanol, can be oxidized to formaldehyde, formate, and carbon dioxide. To determine sMMO activity alone, we assayed the disappearance rate of chloroform because the pMMO of *M. trichosporium* OB3b cannot degrade chloroform.<sup>2,5</sup> We used a gas chromatograph equipped with a flame ionization detector to analyze propene oxide formation and chloroform disappearance.

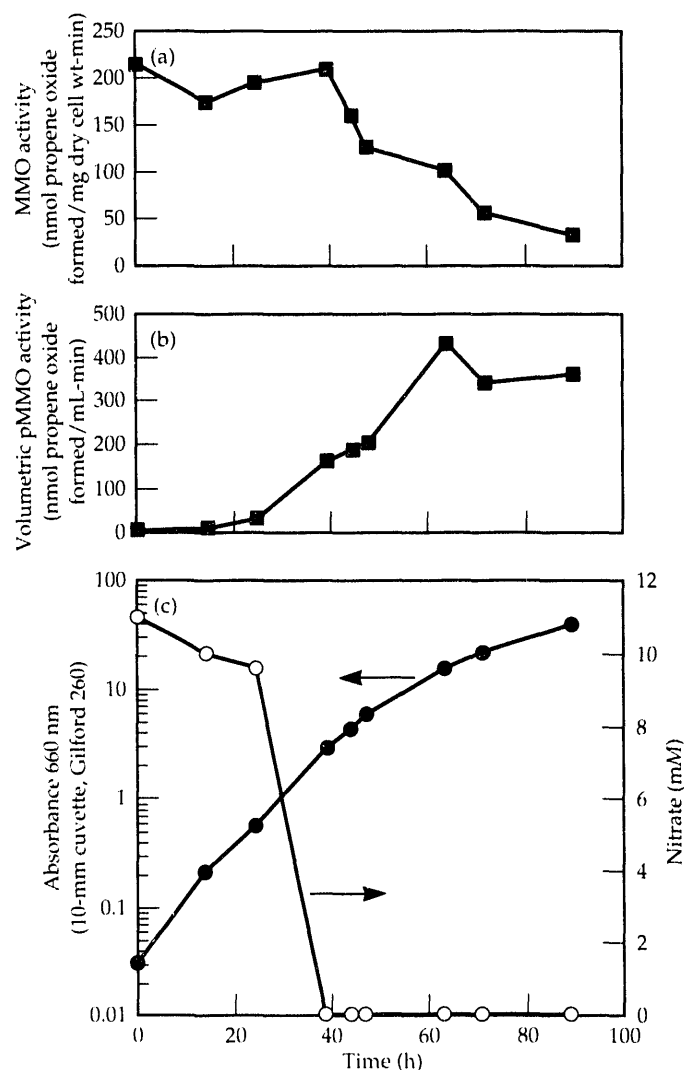
## Results and Discussion

Figure 1 shows profiles of cell growth and whole-cell specific MMO activity (exclusively resulting from the particulate form of the enzyme), as well as the variations in nitrate concentration and volumetric MMO activity for a batch culture experiment. We observed rapid exponential growth ( $\mu = 0.12 \text{ h}^{-1}$ ) and high whole-cell pMMO activity during the first 40 h after inoculation, after which time the pMMO activity began to decrease as nitrate depleted, yet well before the cell growth slowed. In a second experiment, addition of supplemental nitrate (30 mM) at 40 h (i.e., after depletion of the initial feed nitrate) restored the deteriorating whole-cell specific activity up to an absorbance (660 nm) of 11 (3 g dry cell wt/L) at about 54 h. This corresponded to a cell density 3.5 times higher than that in Fig. 1 at 40 h. To our surprise, simply raising the standard initial nitrate concentration of Higgin's medium (10 mM to 40 mM) failed to prevent the decline of pMMO activity and also resulted in a lower growth rate.

We next studied bacterial growth under continuous culturing conditions for the effects of copper and nitrate. The advantage of continuous culturing is that much larger amounts of biomass can be generated in a given time with a small 5-L bioreactor. Figure 2 shows the effects of copper concentration on the steady-state cell density, whole-cell sMMO, total MMO activity, and percentage of pMMO.

We raised the feed medium nitrate concentration in standard Higgin's medium to 20 mM to avoid nitrate limitation, which we had observed during batch cultivation with the standard 10 mM level. The cell density increased sharply when we added  $1 \mu\text{M}$  copper to a medium containing no copper and then increased gradually up to 10

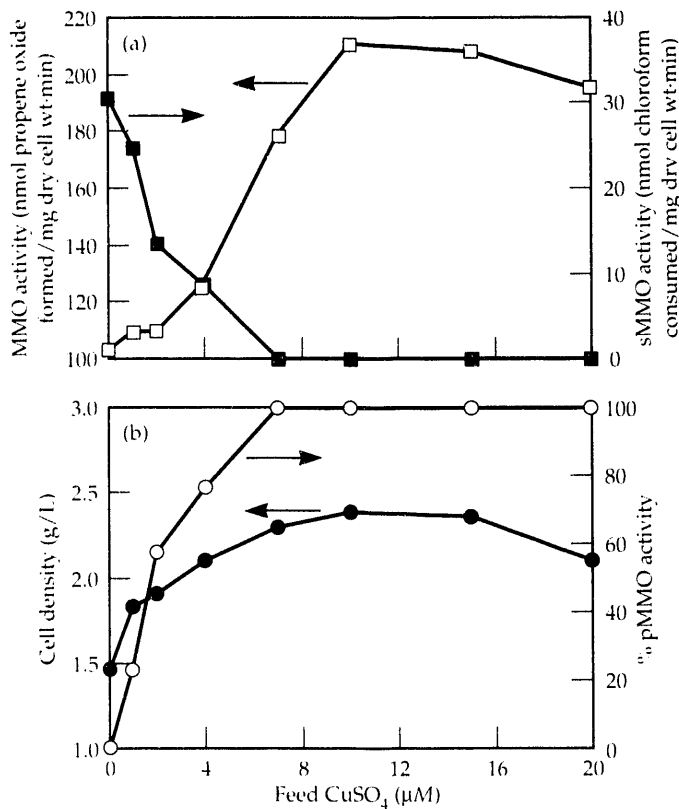
**Figure 1.** Bioreactor batch-culture profiles of whole-cell specific pMMO activity (a), volumetric pMMO activity (b), and cell growth and nitrate concentration (c). The cells were grown in Higgin's medium containing  $10 \mu\text{M}$   $\text{CuSO}_4$  and  $80 \mu\text{M}$  Fe under otherwise standard conditions.



before decreasing somewhat between 10 and 20  $\mu\text{M}$ . Because we did not change the bioreactor operating conditions that affect the oxygen transfer rate (e.g., agitation speed, air flow rate, and dissolved oxygen level), this trend suggests a correlation between the cell yield on oxygen ( $Y_{X/O}$ ) or oxygen-utilization efficiency and copper availability at lower  $\text{CuSO}_4$  concentrations (i.e.,  $<10 \mu\text{M}$ ). However, at  $\text{CuSO}_4$  concentrations well above 10  $\mu\text{M}$ , we observed that copper slightly inhibited both biomass production and total MMO activity.

Figure 2(a) depicts the whole-cell MMO activities measured with two separate substrates, propene and chloroform. The MMO activities with these two substrates show opposite trends: epoxidation increases and chloroform degradation decreases with increasing copper concentrations up to 7  $\mu\text{M}$ . Because chloroform is an sMMO-specific substrate, these catalysis profiles indicate that, over the  $\text{CuSO}_4$  range of 0 to 7  $\mu\text{M}$ , the intracellular form of MMO switches from 100% soluble to 100% particulate. Figure 2(b) demonstrates this switch more clearly [percentage of pMMO activity relative to total whole-cell propene epoxidation activity (pMMO plus sMMO)].

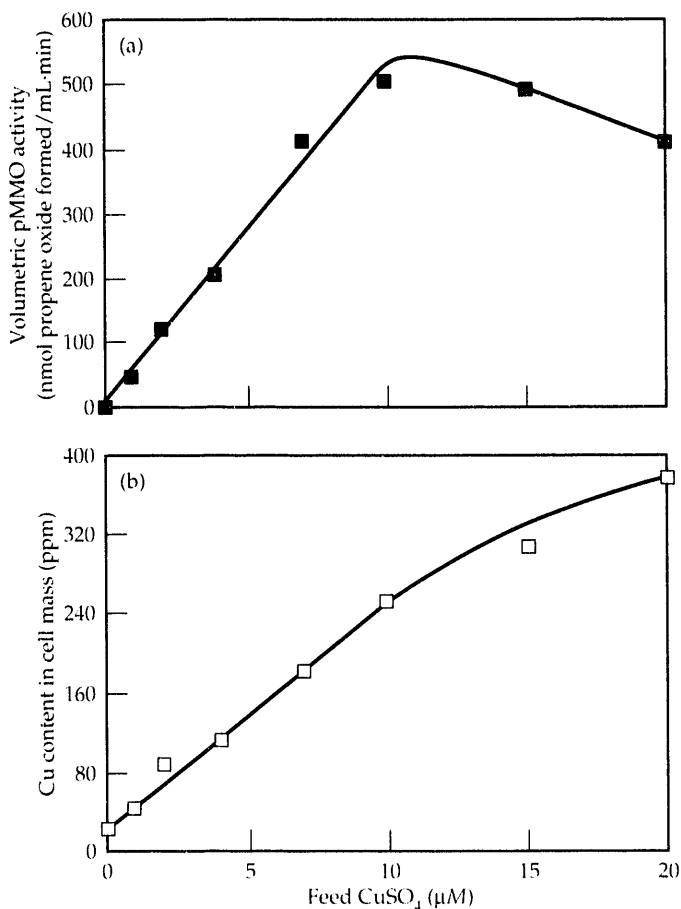
**Figure 2.** Effect of copper concentration on whole-cell sMMO activity and total MMO activity (a), and cell density and percentage of pMMO activity (b) in a 5-L bioreactor during oxygen-limited, continuous culturing conditions. Cells were grown in Higgin's medium containing 80  $\mu\text{M}$  Fe and 20 mM nitrate under standard conditions.



From the same continuous culture experiment depicted in Fig. 2, we used ICP-AES to determine the corresponding copper contents in freeze-dried cell masses. Figure 3 shows these results and the volumetric whole-cell pMMO activity as functions of the feed copper concentration. Both the volumetric pMMO activity and the copper content of the cell mass increased linearly as the culture medium copper concentration was elevated to 10  $\mu\text{M}$ . At higher copper concentrations, the former gradually declined, while the latter became nonlinear. Based on the volumetric pMMO data (0 to 10  $\mu\text{M}$   $\text{CuSO}_4$  range), we calculated  $Y_{X/\text{Cu}}$  (the quantitative amount of copper required to produce a certain cell mass containing 100% pMMO) to be  $3.9 \times 10^3$  g dry cell wt/g Cu, which is equivalent to  $4.0 \times 10^{-6}$  mol Cu/g dry cell wt (copper requirement or copper content). The latter value agrees very well with the ICP-AES copper analyses of the freeze-dried cells.

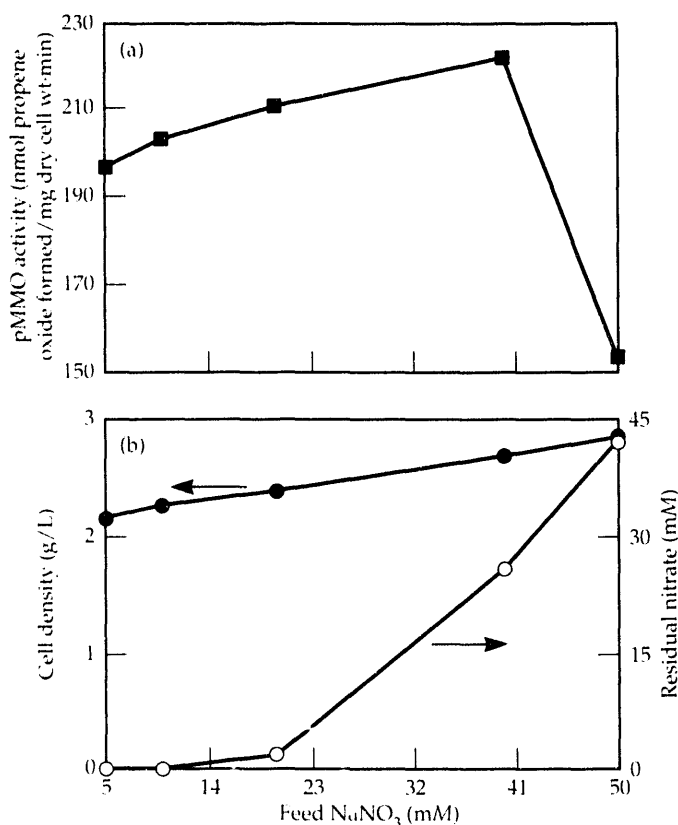
The second medium component studied in continuous culture was nitrate. Figure 4 shows the effects of the feed nitrate concentration on steady-state cell density and activity of the pMMO enzyme. We maintained the feed

**Figure 3.** Effect of feed medium copper concentration on volumetric pMMO activity (a) and copper content of the biomass (b) during the continuous culturing experiment shown in Fig. 2.



medium copper concentration at 10  $\mu\text{M}$  to exclusively produce pMMO. When we raised the feed nitrate level from 5 to 40 mM, both the steady-state cell density and pMMO activity increased. Moreover, at feed concentrations from 5 to 20 mM, most of the available medium nitrate was consumed (90 to 100%). However, when we raised the incoming nitrate concentration to 40 mM, only 30 to 35% of it was used, and the cells derived their remaining nitrogen by fixing gaseous  $\text{N}_2$ . When we further increased the feed nitrate concentration to 50 mM, steady-state cell density increased slightly, but pMMO activity declined sharply. These changes were accompanied by a much-reduced nitrate utilization to about 15%, suggesting an inhibitory effect of nitrate at this concentration. These data established that feed nitrate concentrations of 30 to 40 mM

**Figure 4.** Effect of feed medium nitrate concentration on whole-cell specific pMMO (a) and cell density and residual steady-state nitrate concentration (b). The cells were grown in Higgin's medium containing 80  $\mu\text{M}$  Fe and 10  $\mu\text{M}$  Cu under standard continuous culture conditions.



provide a maximal whole-cell pMMO activity and optimal biomass generation under continuous culture conditions.

## Conclusions

We studied the effects of the medium copper and nitrate concentrations on the cell growth and whole-cell pMMO activity of an obligatory methanotroph, *M. trichosporium* OB3b, during bioreactor cultivation. Supplemental addition of nitrate during batch cultivation allowed a cell density of 3 g dry cell wt/L to be reached, and it elicited a high pMMO activity in Higgin's medium containing 10  $\mu\text{M}$  Cu and 80  $\mu\text{M}$  Fe. During continuous culturing, we detected both soluble and particulate forms of the MMO at copper concentrations up to 7  $\mu\text{M}$ . Maximal cell density and whole-cell specific pMMO activity was elicited with 10  $\mu\text{M}$  copper in the feed medium. *M. trichosporium* OB3b requires  $2.6 \times 10^{-4}$  g Cu/g dry cell wt for the exclusive production of pMMO. The optimal feed nitrate concentration for pMMO production is 30 to 40 mM under continuous cultivation conditions.

*This work was funded by Laboratory Directed Research and Development.*

\* ICP-AES analyses for the cellular copper contents were performed by Theresa I. Duewer in the LLNL Chemistry and Materials Science Department.

## References

1. C. Anthony, *The Biochemistry of Methyloprotophys* (Academic Press, New York, 1982).
2. S. Park, M. L. Hanna, R. T. Taylor, and M. W. Droege, "Batch Cultivation of *Methylosinus trichosporium* OB3b. I: Production of Soluble Methane Monooxygenase," *Biotechnol. Bioeng.* **38**, 423 (1991).
3. S. Park, N. N. Shah, R. T. Taylor, and M. W. Droege, "Batch Cultivation of *Methylosinus trichosporium* OB3b. II: Production of Particulate Methane Monooxygenase," *Biotechnol. Bioeng.* **40**, 151 (1992).
4. M. M. Himmelsbach, R. T. Taylor, and M. W. Droege, "Subunit Resolution for Active Site Identification of *Methylosinus trichosporium* OB3b Soluble Methane Monooxygenase," elsewhere in this Report.
5. R. T. Taylor, M. L. Hanna, S. Park, and M. W. Droege, "Chloroform Oxidation by *Methylosinus trichosporium* OB3b—A Specific Catalytic Activity of the Soluble Form of Methane Monooxygenase," *Abstracts of the 90th Annual Meeting of the American Society for Microbiology*, 221 (1990).

# Coking and Cracking Reactions of Oil Vapor Over Oxidized Shale

P. H. Wallman,  
M. F. Singleton, and  
C. B. Thorsness

*We investigated cracking and coking reactions of oil-shale vapor in the presence of hot oxidized oil shale, both for its intrinsic importance and in support of the modeling effort on the oil-shale process. Our model includes mass transfer of vapor through the gas film surrounding the shale particles with countercurrent flow of cracked low-molecular-weight products, diffusion through the pore system, adsorption onto the internal surfaces, chemical reaction of the adsorbate, and desorption of oil and light gas.*

## Introduction

Hot-recycle-solids (HRS) oil-shale processes<sup>1</sup> provide the heat for reaching pyrolysis temperatures by recycling a burned shale stream. The contact between primary oil vapors and recycled burned solids results in changes in oil properties that are mostly favorable but can also result in loss of oil yield to coke and noncondensable gases. Previous work at LLNL<sup>2,3</sup> and at the Commonwealth Scientific and Industrial Research Organization (CSIRO) in Australia<sup>4</sup> has shown that partial coking of shale-oil vapors over oxidized shale minerals can favorably affect oil upgrading because of the cracking of heavy oil to lighter components. Hence, the degree of coking in HRS oil-shale processes may provide an opportunity to simultaneously improve oil quality and control the undesirable loss of product to excess coking and cracking. As a guide to this optimization, we have developed a coking model based on the HRS pilot-plant process developed at LLNL.

## Experimental Approach

The coking process is quite complex.<sup>2</sup> It resembles catalytic petroleum cracking in that both processes involve oil vapors in contact with a hot porous solid. The surface reactions on oxidized shale change with coke buildup,<sup>3</sup> leading to a slowdown of the overall coking rate.

We assume that the oil is a mixture of three pseudocomponents, each with a different boiling point, diffusion rate, and adsorption equilibrium. However, in the absence of experimental data, we assume the intrinsic coking kinetics to be alike. We also assume that the three oil components undergo the same coking reaction on the surface to produce coke and light gas with the same stoichiometry (2/3 coke and 1/3 gas). Because basic kinetic data do not exist, we did not include production of lighter oil components

from adsorbed heavy oil. The current model has several adjustable parameters that are determined by matching the model to experimental results.

Previously,<sup>3</sup> we used a simple packed-bed reactor with a constant oil feed. With that apparatus, we established the "oil-upgrading effect." That is, the partially coked oil is considerably lighter and more valuable than the starting oil. In modeling this effect, we postulate that coke originates from the heavy end of the boiling-point distribution without producing any light oil components. Such an explanation is a simplification of the real coking/cracking reactions that probably both produce and remove light oil. Still, this result provides a basis for the simple reaction stoichiometry adopted for the model. We also determined the intrinsic coking rate of shale oil adsorbed on a nonporous, well-coked quartz surface because the fresh surface is covered with coke in a fraction of the total elapsed time of each experiment. In previous experiments, we did not determine coking kinetics over freshly oxidized porous shale surfaces.

Our current apparatus consists of a fluidized bed for pyrolyzing a small shale sample and a packed bed of oxidized shale for coking reactions. An oil-vapor pulse from the fluidized bed enters the packed bed and emerges as an altered oil pulse. We determine the hydrocarbon concentrations of both of these pulses in separate experiments by oxidizing the oil pulse to  $\text{CO}_2 + \text{H}_2\text{O}$  in a combustion tube and monitoring the combustion products with a mass spectrometer. We determine the amount of coke deposited in the packed bed by adding more oxygen, burning it off, and measuring the combustion products.

In each experiment, we drop a series of shale samples into the fluidized bed. The resulting oil pulses pass through the packed bed, and the bed burns off at the end of the series. Consequently, the first oil pulse in each series encounters a freshly oxidized shale surface, whereas subsequent oil pulses encounter an increasingly coked surface. We adjust

the size of the packed bed to make the coke yield differential proportional to the oil pulse. That is, we use shorter beds for small particles because small particles show a greater overall coking tendency than do large particles.

### Coking Model

The basis for the current coking model is a computer code for heterogeneous reactions in a porous sphere. This code is quite rigorous; it incorporates the Stefan-Maxwell relationships for describing diffusion of gas species in the multicomponent system. In this article, we relate the experimental data to the results obtained from the code.

Table 1 specifies the properties of the three oil pseudo-components. This selection of components implies a three-point discretization of the continuous boiling-point curve of the shale oil. More components could easily be added. A typical porosity ( $\epsilon$ ) and total surface area of oxidized Green River formation oil shale are 0.3 and 5 m<sup>2</sup>/g, respectively.

The adsorption equilibrium relationships are based on the Langmuir isotherm: The equilibrium vapor pressure of component  $i$  is a function of the equilibrium constant of component  $i$  (related to the heat of adsorption according to the van't Hoff relationship and using Trouton's rule for heat of condensation) and the surface coverage factor for component  $i$  ( $[Oil_{i,ads}]/[Oil_{max,ads}]$ ). These equilibrium relationships contain two adjustable parameters: a pre-exponential factor in the van't Hoff relationship,  $k_o$ , and the total number of sites for adsorption,  $[Oil_{max,ads}]$ .

**Table 1.** Oil component properties used in the model.

Component	Boiling point (°C)	Molecular weight	Fraction (wt %)	Diffusivity @500°C cm <sup>2</sup> /s
1	200	155	50	0.27
2	400	338	25	0.17
3	500	451	25	0.15

A third adjustable parameter is the pre-exponential factor  $A$ , which appears in the first-order coking rate for the intrinsic coking rate on a freshly oxidized surface:

$$\frac{d[Oil_{i,ads}]}{dt} = -A \exp\left(\frac{-19270}{T}\right) [Oil_{i,ads}] \text{ (mineral surface) } \quad (1)$$

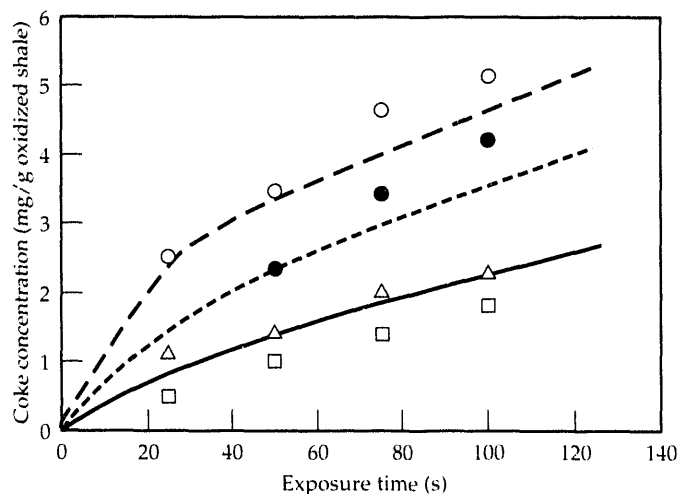
in which the activation energy is assumed to be the same as for the coking rate on a coked surface:

$$\frac{d[Oil_{i,ads}]}{dt} = -10^9 \exp\left(\frac{-19270}{T}\right) [Oil_{i,ads}] \text{ (coked surface) } \quad (2)$$

The model uses a weighted average of Eqs. (1) and (2) for the case of a partially coked surface.

### Results

The fitted parameters are:  $k_o = 3 \times 10^{-7}$  kPa<sup>-1</sup>,  $[Oil_{max,ads}] = 0.6$  mg/m<sup>2</sup>, and  $A = 10^{10}$  s<sup>-1</sup>. This set of parameters produces the best match of model and experimental results. Figure 1, an example of the match between model and experiment, shows that the particle size of oxidized shale has a strong effect on overall coking rate, which declines significantly at a coke coverage of approximately 3 mg/g. The slowdown is particularly strong for 1-mm particles because pore diffusion does not dominate the initial overall coking rate at this small particle size. The model matches the slowdown by switching from a combination of Eqs. (1) and (2) to Eq. (2) kinetics only at a coke coverage of 3 mg/g, which is equivalent to 0.6 mg/m<sup>2</sup> (approximately a monolayer). Significantly, the matching of the model produced the same monolayer limit for the maximum adsorbed oil concentration on the surface. The two sets of 5-mm differential particle data in Fig. 1 show the importance of reactor bed size (10-g bed vs 17-g bed).



Data	Model	Particle size (m)	Avg. oil conc. (mg/L)
○	---	1	15
●	-.-.-	2.5	17
△	—	5	18 (10-g bed)
□	—	5	18 (17-g bed)

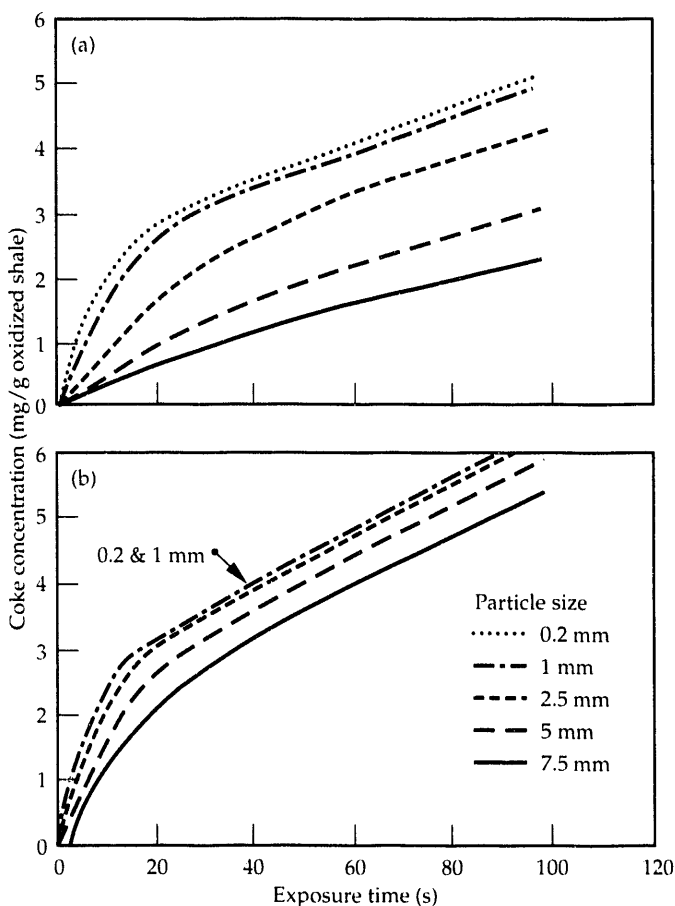
**Figure 1.**

Effect of particle size on coke buildup at a temperature of 530°C.

The consequence of a larger bed is a significant depletion of cokable reactants across the bed.

The maximum oil concentration expected in HRS oil-shale processes is a few hundred mg oil/L. Figure 2 shows that increasing oil concentration increases the coke yield, but with a proportionality much less than first order. Comparison of Fig. 2(a) and Fig. 2(b) reveals that the increased coke yield with higher oil concentration is mostly due to increased coking in the large particles. This factor is explained by pore diffusion responding to a higher driving

**Figure 2.** Model-predicted coke buildup at 500°C with constant oil-vapor concentrations of (a) 40 mg oil/L, and (b) 400 mg oil/L.



force. The pore-diffusion effect is evident in the coke profiles of the larger particle sizes: a coke wave penetrates gradually into the 5- and 7.5-mm particles.

## Conclusions and Future Plans

We compared experimental data with a model based on physical and chemical phenomena that govern coking of oil vapors over a porous medium. We conclude that mass transfer, phase equilibria, and intrinsic chemical kinetics are all important in determining the overall coking rates for oil-shale processes in which the product oil vapor contacts an oxidized recycle solid stream. We have used our model to extrapolate the experimental data to higher oil concentrations typical of the HRS processes and to larger particle sizes; oil losses to coke in the HRS process can be kept to a level of 10 to 15% of primary oil produced. We have also concluded that the physical adsorption step is at least partially responsible for the observed selectivity toward high-boiling components in the heterogeneous coking process. The high-boiling components also are likely to have higher reactivities than the low-boiling components, and we intend to study possible differences in reactivity as a function of molecular structure. Finally, cracking reactions for oil adsorbed on the surface should be added to the two competing processes (coking and desorption) included in this study.

*This work was funded by the DOE Energy Technology Center by direction of the DOE Assistant Secretary for Fossil Fuels.*

## References

1. P. W. Tamm, C. A. Bertelsen, G. M. Handel, B. G. Spars, and P. H. Wallman, "The Chevron STB Oil Shale Report," *Energy Progress* **2**, 37 (1982).
2. M. F. Singleton, P. H. Wallman, and R. Mallon, "Oil Cracking and Coking Experiments," in *Proc. Sixth Briefing on Oil Shale Research*, Lawrence Livermore National Laboratory, Livermore, CA, MISC-4892 (1989), pp. 103-140.
3. P. H. Wallman, M. F. Singleton, and R. W. Taylor, "Cracking and Coking of Shale Oil Vapors," in *23rd Oil Shale Symposium Proc.*, Colorado School of Mines, Golden, CO, RSBN-0-91-8062-84-5 (1990), pp. 125-132.
4. P. Udaja, G. J. Duffy, and M. D. Chensee, "Coking Reactivities of Australian Shale Oils," *Fuel* **69**, 1150 (1990).



---

## Overview

For several years, the Department has been involved in research and development regarding the processing and management of radioactive waste. Recent activities are reported here.

One of the major technical problems to be solved is the safe disposal of high-level wastes. The currently favored procedure calls for disposal in metal canisters that are then placed in a geologic repository. Because containment times in the canisters (1000 years) are well beyond any existing experimental data, the pitting corrosion rate of potential waste containers has been modeled.

Mixed waste—a mixture of hazardous waste such as toxic organic compounds with low-level radioactive

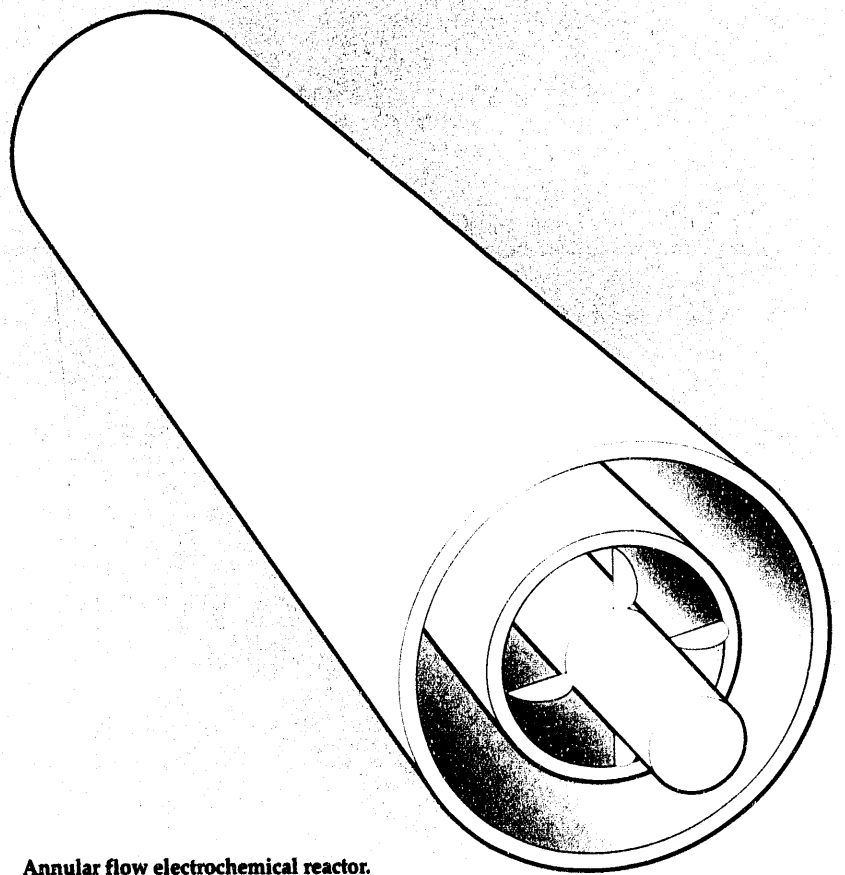
waste—presents a different kind of problem. No accepted procedure exists to treat such waste; it can only be stored, and repository space is rapidly filling up.

Two possible chemical treatment schemes are being developed. In one, a powerful inorganic oxidant is generated electrochemically on a continuous basis to oxidize the hazardous organic compounds into harmless products. In the other, a molten salt of mixed carbonates is used with an oxidant gas to pyrolyze and oxidize organic materials. Chlorine-containing compounds are converted to stable salts such as sodium chloride. With either method, the low-level radioactive waste is left as a small-volume residue that is relatively easy to dispose of.

---

Section 8

**Waste  
Processing and  
Management**



**Annular flow electrochemical reactor.**

# Stochastic Models for Predicting Pitting Corrosion Damage of Radioactive-Waste Containers

G. A. Henshall

*We explored stochastic models of pitting corrosion and found them to be potentially useful in predicting damage of radioactive-waste containers. These models can simulate pit initiation and growth under various environments, including those that change during exposure. Equally important is that they provide quantitative information useful to performance assessment models of the entire waste repository system. Valuable insights into the mechanisms of pit initiation and growth have resulted from this research.*

## Introduction

The Yucca Mountain site in Nevada currently is being evaluated as a potential geological repository for storing high-level radioactive waste (HLRW) by the U.S. Department of Energy. Prior to emplacement in the repository, the waste will be sealed in HLRW containers, which must be capable of containing radionuclides for at least 1000 years. Because the containment times are well beyond those for which experimental data can be collected, the design and analysis of the containers will depend extensively on model calculations. One area in which modeling will be crucial is in predicting degradation of the containers by pitting corrosion.<sup>1</sup> The objective of this study was to develop Monte Carlo computer codes based on stochastic pitting models and to evaluate their utility in predicting the performance of HLRW containers.

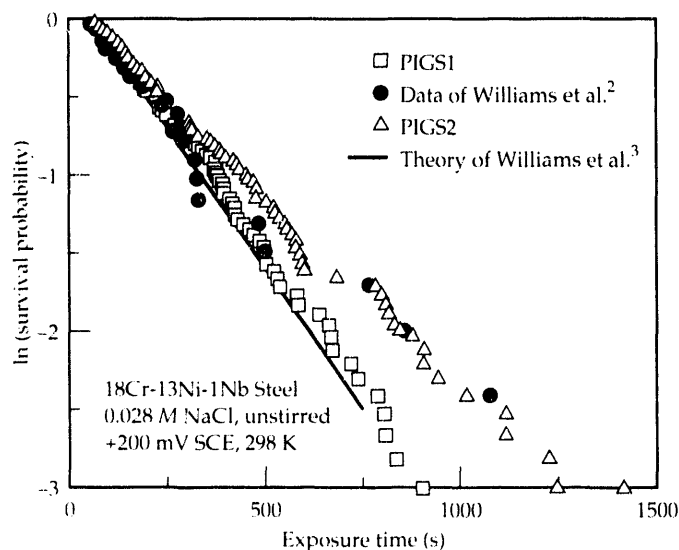
## Stochastic Pit Initiation and Growth Model

During the past decade, experimental evidence has accumulated that the initiation of corrosion pits is a stochastic process. For example, Fig. 1 presents the results of experiments by Williams et al.<sup>2</sup> in which the time required to initiate a pit was measured for many identical steel specimens in identical NaCl solutions. The data are given as the logarithm of the survival probability (i.e., the probability that a stable pit will *not* appear) as a function of exposure time. The wide distribution in failure times suggests that pit initiation is a stochastic process.

Experimental observations like these have led to the development of several stochastic pit initiation models,<sup>3-5</sup> with pit growth also being treated stochastically in one case.<sup>4</sup> In these models, small fluctuations in the local environment (e.g., solution chemistry, surface topography, surface metallurgy) cause local breakdown of the protective passive film on the metal surface, resulting in the "birth" of metastable pits or "embryos." Many of these embryos become unstable when local conditions change, and repassivation (i.e., "death") results. Once an embryo reaches a critical size or age, however, it becomes a "stable" (permanent) pit and cannot die. Stable pits then grow at a rate that can be computed by means of deterministic laws or a stochastic model.

In this study, we have written Monte Carlo computer codes based on the stochastic approach just described. These codes establish a unit area that is divided into individual cells to represent a metal surface in contact with an aggressive environment. Random numbers are generated, and their values are compared with the prescribed birth probability,  $\lambda$ , and death probability,  $\mu$ , to control the initiation, growth, and death of metastable pit embryos. This Monte Carlo process is repeated during each time step for each cell, with a cell capable of containing at most one pit. If a given embryo survives for a number of time steps equal to the critical age,  $\tau_c$ , then a stable pit is established in that cell. Stable pit growth also is treated stochastically

**Figure 1.** Effect of exposure time on survival probability. The data and simulation of Williams et al.<sup>2</sup> are compared with results of the Monte Carlo models PIGS1 and PIGS2.



because this approach was found to produce results superior to those of deterministic models.<sup>6</sup> Growth of a stable pit during a particular time step occurs only if a randomly generated number is less than the growth probability,  $\gamma$ .

### Simulations with the Model

**Pit Initiation.** Figure 1 shows quantitative simulations of pit initiation using this Monte Carlo model, PIGS1 (Pit Initiation and Growth Stochastic model No. 1). Although there is variability in the PIGS1 results, the model is consistent with the algebraic theory upon which it was based,<sup>3</sup> which is shown as the solid line in Fig. 1. Both models, however, accurately simulate the data only for short times and underpredict the survival probability for long times. Following the work of Shibata,<sup>5</sup> we obtained improved predictions by including an exponential decay in  $\lambda$  with exposure time<sup>6</sup> and incorporated these results into a second model, PIGS2 (see Fig. 1).

**Pit Growth.** The initiation of pits is of no consequence unless they grow to a depth that may degrade the capability of the HLRW container to prevent the release of

radionuclides. Thus, simulation of pit growth is of great importance. Of particular interest is simulating the distribution in pit depths for various exposure times because this can provide valuable information to the repository system performance assessment (PA) models.<sup>6</sup>

By using the stochastic pit growth model described previously and by employing the exponential decay in  $\lambda$ , we obtained qualitative agreement with available experimental data. Figure 2 shows the evolution of the simulated pit-depth distribution as a series of histograms. Note that the total number of pits initially increases with exposure time and then saturates as the distribution broadens and moves toward deeper pits. The experimental distributions show similar trends,<sup>6</sup> suggesting that the assumptions of decaying birth probability and stochastic stable growth may be appropriate. Equally important, predictions like those in Fig. 2 could provide useful information to the system PA models. For example, if the HLRW container wall thickness is 32 (arbitrary units), the time required for first penetration of the container is about 100 time steps [Fig. 2(c)]. After further exposure to 125 time steps, approximately 25 pits will have penetrated a unit area of the container [Fig. 2(d)].

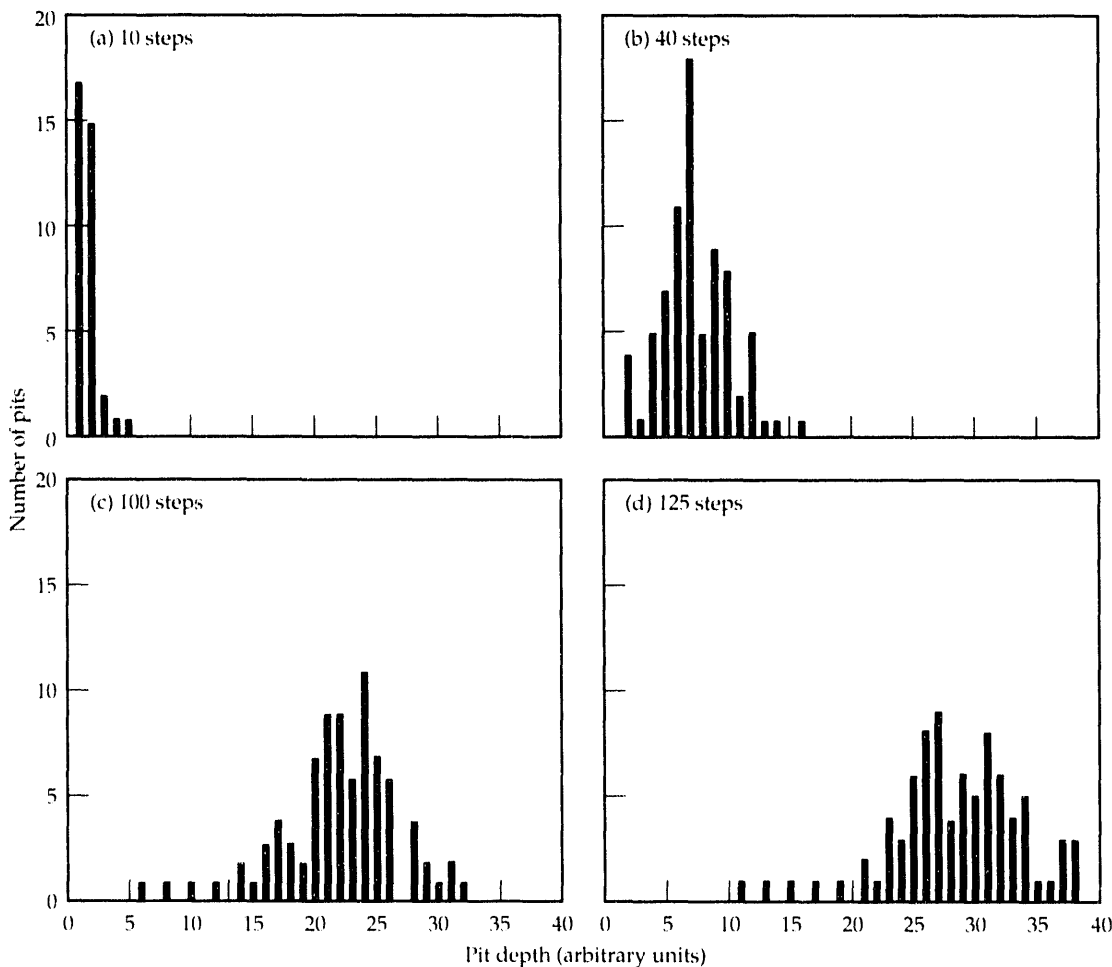


**Figure 2.**

Evolution of the pit-depth distribution computed by the Monte Carlo model.

**Environmental Effects.** One major purpose of modeling the localized corrosion of HLRW containers is to extrapolate short-time, or “accelerated,” test data to extremely long service times. Since accelerated testing will require environmental conditions more aggressive than those expected in the repository, these extrapolations will require quantitative predictions of the effects of environment on pit initiation and growth rates. Predicting the effects of environment on pitting will also be required to explore the performance of the containers under various environmental scenarios, including the expected case in which the environment changes with time.

In the context of stochastic pitting models, the goal is to model the environmental sensitivity of the stochastic parameters:  $\lambda$ ,  $\mu$ ,  $\tau_c$ , and  $\gamma$ . There is not yet enough experimental data with which to rigorously quantify these complex dependencies. Based on a variety of available data, however, we developed a simple phenomenological model and included it in the Monte Carlo code<sup>7</sup> to illustrate the potential power of the stochastic approach. We included three important environmental parameters in this simple model: applied electrical potential,  $E_{app}$ , chloride ion concentration,  $[Cl^-]$ , and absolute temperature,  $T$ .

Calculations with this model have demonstrated its ability to qualitatively simulate several important phenomena,<sup>7</sup> including (1) the complex dependence of pit initiation rate on  $T$ , (2) the effect of  $E_{app}$  on the distribution of pit depths, and (3) the effect of a changing environment on the evolution of the pit-depth distribution. One particular simulation that brought valuable insights into modeling the pitting of HLRW containers concerned the effect of  $[Cl^-]$  on pit growth. Figure 3 shows the results of a Monte Carlo simulation in which both the median pit depth,  $\langle d \rangle$ , and the maximum pit depth,  $d_{max}$ , are plotted as a function of  $[Cl^-]$ . The logarithmic dependence of  $\langle d \rangle$  on  $[Cl^-]$  follows directly from the equation describing the dependence of  $\gamma$  on  $[Cl^-]$  and is consistent with the data of Herbsleb and Engell.<sup>8</sup> However,  $d_{max}$  is larger at low  $[Cl^-]$  than would be expected from a simple extrapolation of the

behavior at high  $[Cl^-]$ . Although no data are available to confirm this prediction, it may have important implications for modeling the performance of HLRW containers because the deepest pits are of chief concern. If true, this prediction means that extrapolation of “accelerated” test data in concentrated environments to the more benign conditions expected in the repository may require stochastic models such as those explored in this study.

## Summary and Conclusions

We have demonstrated the potential usefulness of stochastic models for predicting the degradation of HLRW containers by aqueous pitting corrosion through simulations of a variety of experimental data. The calculations also have provided valuable insights into the modeling of pitting corrosion. Monte Carlo computer implementation of these stochastic pitting models represents a way in which detailed mechanistic knowledge can be “distilled” into a more concise and general model that may provide useful quantitative information to the system PA models. The stochastic models also may be useful for other applications in which pitting corrosion limits component lifetimes.

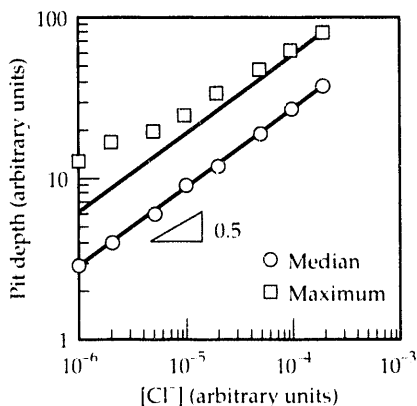
*This work was funded by the Yucca Mountain Project.*

## References

1. J. C. Farmer, G. E. Gdowski, R. D. McCright, and H. S. Ahluwalia, “Corrosion Models for Performance Assessment of High-Level Radioactive-Waste Containers,” *Nucl. Eng. Design* **129**, 57 (1991).
2. D. E. Williams, C. Westcott, and M. Fleischmann, “Stochastic Models of Pitting Corrosion of Stainless Steels—II. Measurement and Interpretation of Data at Constant Potential,” *J. Electrochem. Soc.* **132**, 1804 (1985).
3. D. E. Williams, C. Westcott, and M. Fleischmann, “Stochastic Models of Pitting Corrosion of Stainless Steels—I. Modeling of the Initiation and Growth of Pits at Constant Potential,” *J. Electrochem. Soc.* **132**, 1796 (1985).
4. E. E. Mola, B. Mellein, E. M. Rodriguez de Schiapparelli, J. L. Vicente, R.C. Salvarezza, and A. J. Ariva, “Stochastic Approach for Pitting Corrosion Modeling—I. The Case of Quasi-Hemispherical Pits,” *J. Electrochem. Soc.* **137**, 1384 (1990).
5. T. Shibata, “Stochastic Studies of Passivity Breakdown,” *Corr. Sci.* **31**, 413 (1990).
6. G. A. Henshall, “Stochastic Models for Predicting Pitting Corrosion Damage of HLRW Containers,” in *Proc. FOCUS '91: Nuclear Waste Packaging* (American Nuclear Society, La Grange Park, IL, 1992), p. 225–232.
7. G. A. Henshall, “Modeling Pitting Corrosion Damage of High-Level Radioactive-Waste Containers Using a Stochastic Approach,” *J. Nucl. Mater.*, in press [see LLNL Preprint UCRL-JC-109020 (1991)].
8. G. Herbsleb and H.-J. Engell, “Untersuchungen über die Lochfrasskorrosion des Passiven Eisens in Chlorionenhaltiger Schwefelsäure,” *Werkst. Korros.* **17**, 365 (1966).

**Figure 3.**

The median and maximum pit depth predicted by the Monte Carlo model as a function of  $[Cl^-]$ .



# Mediated Electrochemical Oxidation of Hazardous and Mixed Wastes

J. C. Farmer, F. T. Wang,  
R. G. Hickman,  
R. A. Hawley-Fedder,  
P. R. Lewis, L. J. Summers,  
and L. Foiles

*In the future, mediated electrochemical oxidation (MEO) may be used to destroy hazardous waste at ambient temperature and to convert mixed waste to low-level radioactive waste. We have studied the MEO of ethylene glycol and benzene, determining destruction and current efficiencies. We used gas chromatography with mass spectrometry (GC/MS) to identify reaction intermediates and developed a model that accounts for sequential formation of intermediates to predict the time dependence of CO<sub>2</sub> evolution.*

## Introduction

We are developing an electrochemical process for destroying hazardous waste at ambient temperature and converting mixed waste to low-level radioactive waste. This process depends on mediated electrochemical oxidation (MEO). Anodic oxidation generates mediators such as silver(II), cobalt(III), and iron(III) [Ag(II), Co(III), and Fe(III)] and uses them to oxidize organics dissolved in an aqueous phase.<sup>1</sup> Dissolved organics convert to CO<sub>2</sub> and H<sub>2</sub>O. When organic components of mixed wastes in a condensed phase oxidize at ambient temperature, the possibility of high-temperature volatilization of radionuclides during incineration is avoided.

Our work aims to demonstrate the complete conversion of real and surrogate organic wastes to CO<sub>2</sub>, determine the current efficiency of the process, and develop an understanding of reaction intermediates and mechanisms. Such data are unavailable in the published literature. The electrochemical reactor used to accomplish these objectives had a rotating cylinder anode (RCA) that we operated well below the limiting current for Ag(II) generation,  $i_L$ . The RCA enabled us to use a small apparatus to mimic mass-transport conditions in a pilot plant without using massive flow-through electrochemical cells and pumps. We measured rates of CO<sub>2</sub> generation and used gas chromatography with mass spectrometry (GC/MS) to identify reaction intermediates. We also developed a simple kinetic model to explain observed nonlinearity in conversion-time curves.

In this work, we focused on the destruction of ethylene glycol and benzene by Ag(II). We selected ethylene glycol as a surrogate waste because detailed investigations of its partial oxidation have been published previously.<sup>2</sup> We selected benzene because it will be a primary constituent of mixed waste generated by the Defense Waste Processing Facility

(DWPF) at the DOE's Savannah River Plant.<sup>3</sup> More specifically, benzene contaminated with <sup>137</sup>Cs will be produced by the formic acid hydrolysis of tetraphenyl borate precipitates.

## Process Chemistry

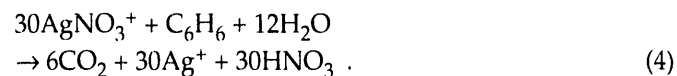
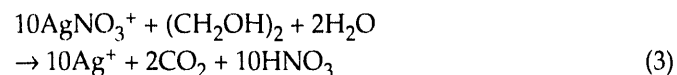
Ag(II) is generated by the anodic oxidation of Ag(I), as follows:



Most of the Ag(II) is present as a dark brown nitrate complex, AgNO<sub>3</sub><sup>+</sup>:



This complex completely oxidizes dissolved organics such as ethylene glycol and benzene:



## Experimental Procedures and Details

During the MEO of ethylene glycol and benzene, we measured rates of CO<sub>2</sub> evolution. We usually charged the electrochemical cell with 40 mL of anolyte, which consisted of 0.5 M AgNO<sub>3</sub> and 3.25 M HNO<sub>3</sub>, followed by either 8.8 × 10<sup>-3</sup> moles of ethylene glycol (0.22 mole/L of anolyte) or 3.0 × 10<sup>-3</sup> moles of benzene (0.075 mole/L of anolyte). The RCA was 1.2 cm in diameter, 1.78 cm long, and made of gold or platinum. We maintained the rotation speed of the

anode at 1500 rpm and performed experiments at three different combinations of cell current and steady-state temperature: 336 mA and 27°C (24%  $i_L$ ); 673 mA and 33°C (40%  $i_L$ ); and 1346 mA and 41 to 52°C (58%  $i_L$ ). Ohmic heating in the cell elevated the anolyte steady-state temperature above ambient. Because porous ceramic separators used in early experiments could not prevent the migration of nitrous acid from the anolyte to the catholyte, we used either a flat piece of Vycor microporous glass or a Nafion cation-exchange membrane to separate a stationary platinum cathode from the anode. So that all CO<sub>2</sub> could be captured, we conducted reactions in a closed vessel. The volume of this vessel was 38.2 L, which corresponds to approximately 1.5 moles of gas at ambient temperature and pressure. Using mass spectrometry, we periodically determined concentrations of CO<sub>2</sub> in the gas phase and used them to calculate percentage conversions of the organic substrate. To obtain reaction intermediates for identification by GC/MS, we partially oxidized ethylene glycol and benzene with the RCA at 673 mA and 33°C (40%  $i_L$ ).

## Results

**Complete oxidation of ethylene glycol.** Complete conversion of ethylene glycol to CO<sub>2</sub> required 8.4, 4.3, and 4.5 h, respectively. Current efficiency was 83 to 84% at 336 to 673 mA but decreased to 39% at 1346 mA. In similar experiments with a Vycor microporous glass separator, complete conversion actually required 8.3, 4.0, and 3.3 h, respectively. Current efficiency was 84 to 88% at 336 to 673 mA but decreased to 44% at 1346 mA.

**Complete oxidation of benzene.** At 336 mA, only 60% was converted after 5 h of electrolysis. Failure to achieve 100% conversion is attributed to the volatilization of benzene, or an intermediate such as acetone, from the anolyte. At 673 mA, 88% was converted after 3.8 h of electrolysis. The increase from 60 to 88% is attributed to a corresponding decrease in benzene volatilization from the anolyte (there was less time for volatilization at 673 mA than at 336 mA). At 1346 mA, 86% was converted in 3 h, an increase of only 33% over the rate at 673 mA. Because the theoretical rate of benzene oxidation is proportional to current, we expected the measured rate to double. Apparently, the Ag(II)-generation efficiency decreased as cell current increased above 673 mA.

**General observation.** The anolyte remained clear during oxidation of ethylene glycol and benzene, indicating that the bulk AgNO<sub>3</sub><sup>+</sup> concentration was essentially zero and that the organics were oxidized near the surface of the RCA. After ethylene glycol and its intermediates were completely

converted to CO<sub>2</sub>, the anolyte turned dark brown, indicative of AgNO<sub>3</sub><sup>+</sup> in the bulk anolyte. Note that AgNO<sub>3</sub><sup>+</sup> is strongly absorbent at approximately 390 nm.

**Intermediates formed during ethylene glycol oxidation.** CO<sub>2</sub>, N<sub>2</sub>O, and formaldehyde eluted from the GC/MS column simultaneously. The mass spectrum coincident with this elution was characterized by a peak at 29 daltons, which is attributed to a CHO fragment formed from formaldehyde, CH<sub>2</sub>O. We also detected a large amount of formic acid. We have found that formaldehyde and formic acid are primary intermediates formed during the MEO of ethylene glycol.

**Intermediates formed during benzene oxidation.**

Compounds found in the anolyte during the initial stage of benzene oxidation include phenol, hydroquinone, benzoquinone, benzaldehyde, benzoic acid, methyl benzoate, benzonitrile, benzonitrile aldehyde, and 4-nitro butylnitrile. A compound that has been tentatively identified as benzoquinone epoxide (C<sub>6</sub>H<sub>4</sub>O<sub>3</sub>) was present at the highest concentration and is believed to be a product of the oxidation of benzoquinone. Numerous nitrated aromatics detected include nitrobenzene, dinitrobenzene, nitrophenol, and nitrobenzonitrile. Compounds found in the anolyte as the oxidation approached completion include acetic acid, acetone, and methanol.

## Discussion

**Plausible mechanism for ethylene glycol oxidation.**

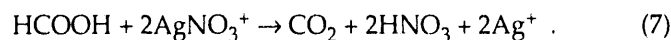
Based on published literature<sup>2,4,5</sup> and GC/MS analyses reported here, we have postulated a reaction mechanism for the complete MEO of ethylene glycol. The oxidation of ethylene glycol probably generates two molecules of formaldehyde or an aldehyde-like intermediate<sup>2</sup>:



This intermediate would then be oxidized by Ag(II) to produce formic acid<sup>4</sup>:



The last step toward the complete conversion of ethylene glycol to CO<sub>2</sub> probably involves the oxidation of formic acid<sup>5</sup>:



Because 10 AgNO<sub>3</sub><sup>+</sup> ions are reduced during the oxidation of a single ethylene glycol molecule, 10 electrons are required for regeneration.

**Plausible mechanism for benzene oxidation.** The MEO of benzene is much more complicated than that of ethylene glycol. We believe that the initial steps in the reaction sequence leading from benzene to  $\text{CO}_2$  are (1) benzene to phenol, (2) to hydroquinone, (3) to benzoquinone, and (4) to benzoquinone epoxide. Subsequent oxidation and fragmentation are not yet understood. We believe that acetone, acetic acid, and methanol formed as the oxidation of benzene approached completion.

**Observed nonlinearity in conversion-time curves.** The instantaneous conversion of ethylene glycol or benzene to  $\text{CO}_2$  would be characterized by (1) the absence of chemical intermediates in the anolyte and (2) a linear conversion-time ( $\text{CO}_2$ -evolution) curve. In such a case, conversion would increase linearly with time to 100%. To our surprise, we found nonlinearity (curvature) to be one of the most obvious features of actual conversion-time data. To explain this nonlinear behavior, we have formulated a simple model that takes into account the sequential oxidation of known and suspected chemical intermediates. The model assumes that all reactions occur in a thin reaction layer of anolyte at the anode surface.

The rate of accumulation of the  $i$ th intermediate in the anolyte,  $dC_i/dt$ , is equivalent to the difference between generation and loss terms:

$$dC_i/dt = \langle r_{i-1} \rangle - \langle r_i \rangle \quad (8)$$

The loss term for the  $i$ th intermediate,  $\langle r_i \rangle$ , is the volume-average rate of oxidation and is defined as follows:

$$\langle r_i \rangle = (1/V) (\Theta_i/m_i) (\pi d_R L) (i/F) \quad (9)$$

where  $V$  is the total volume of anolyte,  $\Theta_i$  is the fractional consumption of Ag(II) by reaction with the  $i$ th intermediate,  $m_i$  is the corresponding stoichiometric coefficient of Ag(II),  $d_R$  and  $L$  are the diameter and length of the anode,  $i$  is the current density of the anode, and  $F$  is Faraday's constant. The generation term,  $\langle r_{i-1} \rangle$ , is simply the loss term for the previous intermediate in the reaction sequence. The fractional consumption of Ag(II) by the  $i$ th reaction is

$$\Theta_i = \frac{m_i r_{i,\text{avg}}}{\sum_{j=1}^n m_j r_{j,\text{avg}}} \quad (10)$$

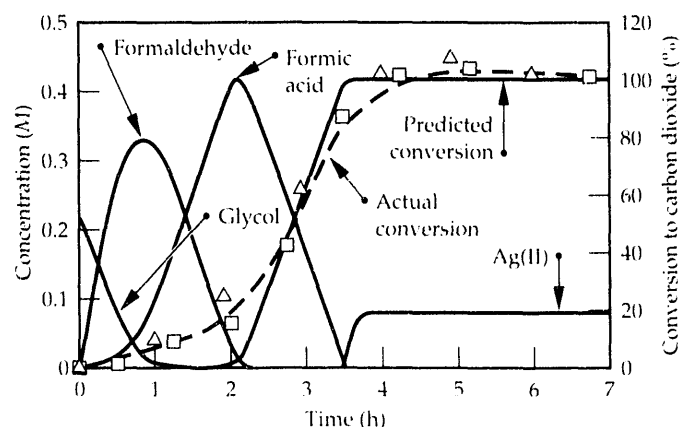
where  $r_{i,\text{avg}}$  is the average rate of reaction in the anolyte film, based on an average reactant concentration. Because all  $r_{i,\text{avg}}$  values are first order in Ag(II) concentration,  $[\text{Ag(II)}]$  appears in both the numerator and denominator of Eq. (10) and can be eliminated. Therefore,  $\Theta_i$  is independent of Ag(II) concentration. The average concentration of a reactant in the reaction layer is assumed to be approximately

$(1/2)C_i$ . The factor  $(1/2)$  also appears in both the numerator and denominator of Eq. (10) and can be eliminated. Therefore, the approximate value of  $\Theta_i$  can be calculated from the concentrations of organics in the bulk anolyte,  $C_i$ , and the corresponding rate constants. The system of ordinary differential equations represented by Eq. (8) can be integrated numerically with a fourth-order Runge-Kutta algorithm.

**Applying the model to MEO of ethylene glycol.** Now consider applying the model represented by Eq. (10) to the conversion of ethylene glycol to  $\text{CO}_2$ . Based on our GC/MS data, we believe that this process involves two primary intermediates, formaldehyde and formic acid. The partial oxidation of ethylene glycol to formaldehyde by Ag(II) in acidic perchlorate solutions has been investigated by Mentasti and Kirschenbaum.<sup>2</sup> Mentasti and Baiocchi<sup>4</sup> give an empirical rate equation for the oxidation of formaldehyde. The oxidation of formic acid by Ag(II) has been investigated by Miller and Morrow.<sup>5</sup> Values of equilibrium and rate constants for the oxidation of ethylene glycol, formaldehyde, and formic acid are available in these references.

**Predictions for ethylene glycol.** Figure 1 compares predictions and all experimental measurements of ethylene glycol conversion to  $\text{CO}_2$  at 673 mA and 33°C (40%  $i_L$ ). Calculated concentrations of ethylene glycol, formaldehyde, and formic acid are also shown. According to the model, ethylene glycol is consumed by its conversion to formaldehyde. Formaldehyde reaches a maximum level when its rate of generation, due to the oxidation of ethylene glycol, is equivalent to its rate of conversion to formic acid. Similarly, formic acid reaches a maximum level when its rate of generation, due to the oxidation of formaldehyde, is equivalent to its rate of conversion to  $\text{CO}_2$ . We successfully

**Figure 1.** Comparison of model predictions and experimental data for MEO of ethylene glycol at 336 mA and 27°C (24%  $i_L$ ). Square and triangular symbols represent data obtained during experiments with Nafion 117 cation-exchange membrane and Vycor microporous glass, respectively.





predicted the observed nonlinearity in the conversion-time curve by accounting for the sequential formation of reaction intermediates. Conversion-time curves for the oxidation of formic acid, a reaction with no accumulation of intermediates, exhibited no such nonlinearity.

**Steady-state Ag(II) concentration.** After all organics completely oxidize, Ag(II) begins to accumulate in the bulk anolyte and reaches a steady-state concentration when the rates of Ag(II) generation and loss are equivalent. This is possible after the dissolved organics completely oxidize. At this point, the only loss of Ag(II) is due to the reduction by H<sub>2</sub>O. Steady-state concentrations of Ag(II) in the bulk anolyte can be calculated by setting the accumulation term in the differential mass balance for Ag(II) to zero.

## Summary and Conclusions

We have studied the complete MEO of ethylene glycol and benzene by Ag(II) in a closed reactor equipped with an RCA. We operated the reactor as a closed system so that all of the product gas (CO<sub>2</sub>) could be captured, and we used the data obtained from this experiment to calculate destruction efficiencies and current efficiencies, resulting in significant insight into the mechanisms involved in this novel process.

**Ethylene glycol.** Ethylene glycol and its intermediates were completely converted to CO<sub>2</sub>. Current efficiencies of 83 to 88% were achieved at 336 to 673 mA (24 to 40%  $i_L$ ).

**Benzene.** Except for organics volatilized from the anolyte, benzene was also completely converted to CO<sub>2</sub>. Numerous reaction intermediates were identified by GC/MS: nitrated benzenes, phenol, nitrated phenols, hydroquinone, benzoquinone, benzoquinone epoxide, benzaldehyde, benzoic acid, methyl benzoate, benzonitrile, nitro benzonitrile, nitro butylnitrile, acetone, and acetic acid.

*This work was funded by the Advanced Process Technology Program, part of the Laser Program.*

## References

1. D. F. Steele, "Electrochemical Destruction of Toxic Organic Industrial Waste," *Platinum Met. Rev.* **34**, 10 (1990).
2. *Defense Waste Processing Facility (DWPF) Process Description: Overview of DWPF Process*, Savannah River Plant, Aiken, SC, DPSOP 257-8, Part 2, Item 100, Rev. 5, pp. 1-6 (1989).
3. E. Mentasti and L. J. Kirschenbaum, "Oxidation of Organic Compounds by Silver(II). Reactions of Aliphatic Diols and  $\alpha$ -Hydroxy Acids," *Inorg. Chim. Acta* **134**, 283 (1987).
4. E. Mentasti and C. Baiocchi, "Mechanistic Aspects of Reactions Involving Ag(II) as an Oxidant," *Coord. Chem. Rev.* **54**, 131 (1984).
5. L. Miller and J. I. Morrow, "Kinetics of the Oxidation of Formic Acid by Silver(II) in Nitric Acid Media," *Inorg. Chem.* **15**, 1797 (1976).

# Molten-Salt Destruction Process for Mixed Wastes

R. S. Upadhye and  
J. F. Cooper

*We are developing an advanced, two-stage process for treating mixed wastes that contain both hazardous and radioactive components. Pyrolysis and oxidation destroy the organic constituents of the mixed waste. The melt retains heteroatoms, such as chlorine, in the mixed waste and metathesizes them into stable salts, such as NaCl. The melt also retains radioactive actinides.*

## Introduction

Acceptable methods for treating mixed wastes (hazardous wastes that are also radioactive<sup>1</sup>) are not currently available. The molten-salt destruction process (MSD)<sup>2</sup> possibly answers this dilemma. Originally developed by Rockwell International as a single-stage process for coal gasification, MSD was later used as an alternative to incineration for treating hazardous wastes such as polychlorinated biphenyls (PCBs).<sup>3</sup> MSD differs from (and is superior to) incineration for treating mixed wastes in several ways: it uses no open flame; it contains actinides by chemical means (wetting and dissolution); its operating temperature is much lower, thus lowering the volatility of radioactive actinides; and it generates no acid gases.

As Fig. 1 shows, mixed wastes are injected with air or oxygen into a bed of molten salt (typically alkali-metal carbonates). The organic components of the mixed waste convert to CO<sub>2</sub> and water vapor, heteroatoms such as chlorine are metathesized into stable salts such as NaCl, and the melt retains the actinides by dissolution and wetting. The lower operating temperature of the process

(700 to 900°C, compared to 1000 to 1200°C for incineration) keeps the actinide volatilities lower than expected at higher temperatures. After a run, the salt can be removed and dissolved in water. The actinide oxides and salts—being insoluble in the alkaline solution of sodium, potassium, or lithium—precipitate and are filtered out, and the dissolved salts separate through crystallization. We recycle the carbonates back to the processor and discard the stable salts as low-level waste (LLW). The MSD process produces benign gases (CO<sub>2</sub>, H<sub>2</sub>O) and a much lower volume of LLW (concentrated actinide oxides/salts) than the original volume of mixed waste. Treatable waste streams include organic liquids (including the ones containing chlorinated solvents and PCBs), greases, and combustible solids (such as cellulosic matter, rubber, and plastics).

## Technical Basis

Molten salts, typically mixtures of alkali or alkaline-earth carbonates and halides, provide excellent heat-transfer and reaction media, catalyze oxidation of organics, and prevent formation of acidic gases (e.g., HCl, SO<sub>2</sub>, and P<sub>2</sub>O<sub>5</sub>)

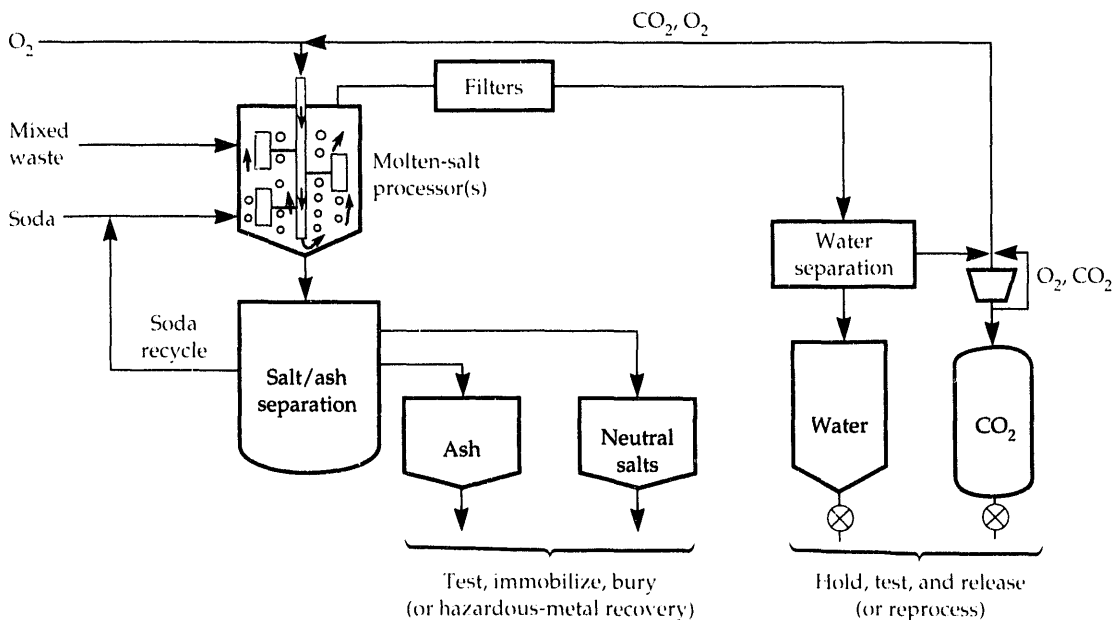


**Figure 1.**

The MSD process oxidizes mixed and radioactively contaminated wastes and retains the product gases as liquids pending assay and certified discharge.

by forming solutions of their neutral (and stable) salts (e.g., NaCl, Na<sub>2</sub>SO<sub>4</sub>, and Na<sub>3</sub>PO<sub>4</sub>).<sup>3,4</sup> The relatively high thermal inertia of the melt tends to resist changes in temperature resulting from sudden changes in the feed or heat transfer. The melt avoids forming potentially fugitive radioactive particulates and molecular species by a combination of particle wetting, encapsulation, and dissolution with complex formation. Therefore, containment of the radioactive material is based on a physicochemical process rather than on mechanical means alone, as is the case with incineration.

The melt must remain fluid to facilitate introducing oxygen, wetting the particulates, and transferring the melt. For wastes containing substantial quantities of inorganic oxides, (e.g., paper products containing kaolin), ash builds up as dissolved substances or as a two-phase slurry, resulting in increased viscosity. In this case, a fraction of the melt must be removed and replaced by fresh salt. Figure 1 illustrates the processing of the withdrawn melt.

Under oxidation alone, salt accumulates high concentrations (20 to 30%) of alumina and silica, which combine to form solid deposits on the vessel walls.<sup>2</sup> Because these deposits do not occur during oxygen-deficient conditions (i.e., during pyrolysis) or in the presence of silica or alumina alone, we developed the two-stage process. In the first stage, the organic portion of the waste is pyrolyzed

and then partially oxidized. Acid gases do not form because the salts are metathesized, and the melt retains both the actinides and the ash. The ash may now build up to higher levels than those that would inhibit operation under oxidation alone. The pyrolysis products from the first stage completely oxidize in the second stage, which operates with excess oxygen. The second stage also cleans up residual amounts of acid gases and retains any entrained actinide particles. The entire process operates without ash buildup under nearly optimal conditions.

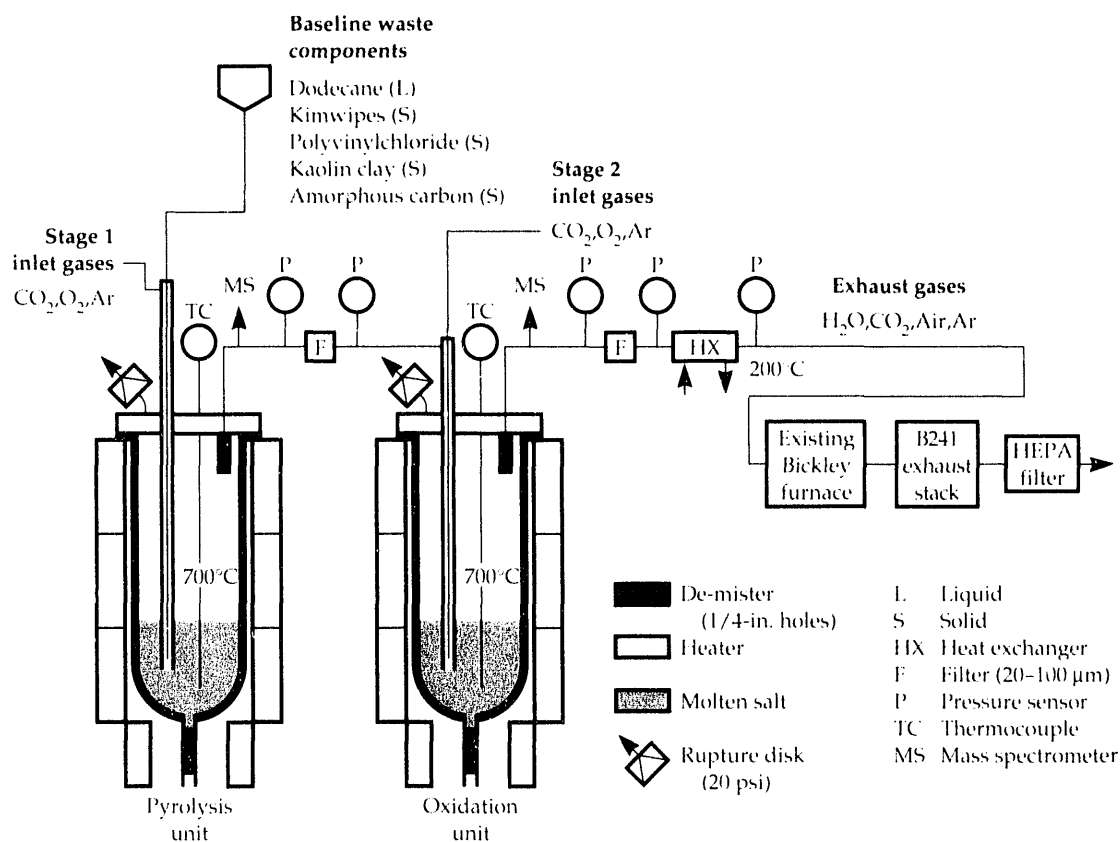
### Experimental Program

We have built a two-stage experimental unit to investigate the applicability of the MSD process for treating mixed wastes. Figure 2 shows a schematic of the current configuration, and Fig. 3 shows the unit in perspective.

The unit centers primarily around two identical stainless-steel crucibles. (Stainless steel is stable in the presence of alkali carbonates but is susceptible to stress corrosion in the presence of chlorides. However, these crucibles can withstand up to 47 thermal cycles, based on a safety analysis of the welds, considerably fewer than the limit imposed by chloride corrosion.) Each has a drain pipe, which leads to a bucket large enough to contain the molten-salt inventory.

**Figure 2.**

Separating MSD into two sequential stages of oxygen-deficient pyrolysis and oxygen-rich oxidation in tandem vessels is being studied as a means of reducing system operating temperature and overcoming limitations posed by construction materials.



We inject the untreated waste and the oxidant gases through two concentric tubes near the centers of the crucibles, which are in series. The gaseous product of the first crucible passes to the second crucible for complete oxidation. The second crucible receives its oxidant separately through its outer inlet tube. The product of each crucible first passes through a de-mister (which is packed with steel wool to capture entrained particles) and then through a 20- $\mu\text{m}$  filter to remove small particles.

Three cylindrical electrical heaters, each rated at 3 kW, are located outside each crucible, and a smaller, fourth heater is under each crucible, concentric with the drain pipe. A blower beneath the crucibles circulates air through the annular space between the crucibles and the heaters. The heaters initiate the process, and the blower removes heat generated by waste oxidation. The product from the second crucible passes through a water-cooled heat exchanger and then through a Bickley furnace to ensure complete oxidation of any trace contaminants. The product gas from the Bickley furnace passes through high-efficiency particulate air (HEPA) filters before being vented.

Thermocouples placed at various locations, both inside and outside the crucibles, monitor temperatures. We continuously monitor pressures within the crucibles, differential pressures around the filters, and the waste and oxidant-gas feed rates. A residual gas analyzer monitors gas composition. Gas samples can be taken through sampling ports for a

more accurate off-line analysis. We use a data logger/controller program for continuous data gathering and to control the operation of the unit.

We have completed the experimental unit, and shake-down runs are in progress.

## Results and Discussion

We have developed a spreadsheet heat-transfer model of the molten-salt system and use it to analyze the temperature profiles in the feed and oxidant tubes.<sup>5</sup> As a result of this analysis, we have improved the design of the feed nozzle system. It now cools externally to lower the temperature of the waste in the inner feed tube to the point where little, if any, pyrolysis will occur prior to its reaching the crucible. Our model is now being used to establish limits on the cooling capacity of the blower, which will place an upper bound on the rate at which any given waste stream can be processed. The model will be validated against experimental data.

We have correlated gas hold-up as a function of gas velocity, liquid height, and nozzle height, based on our experiments on an air-water system in a plexiglass model. We are now extending these correlations to liquids with surface tensions significantly different from that of water. After we complete these correlations, we can predict the froth height in the actual system for any configuration. In

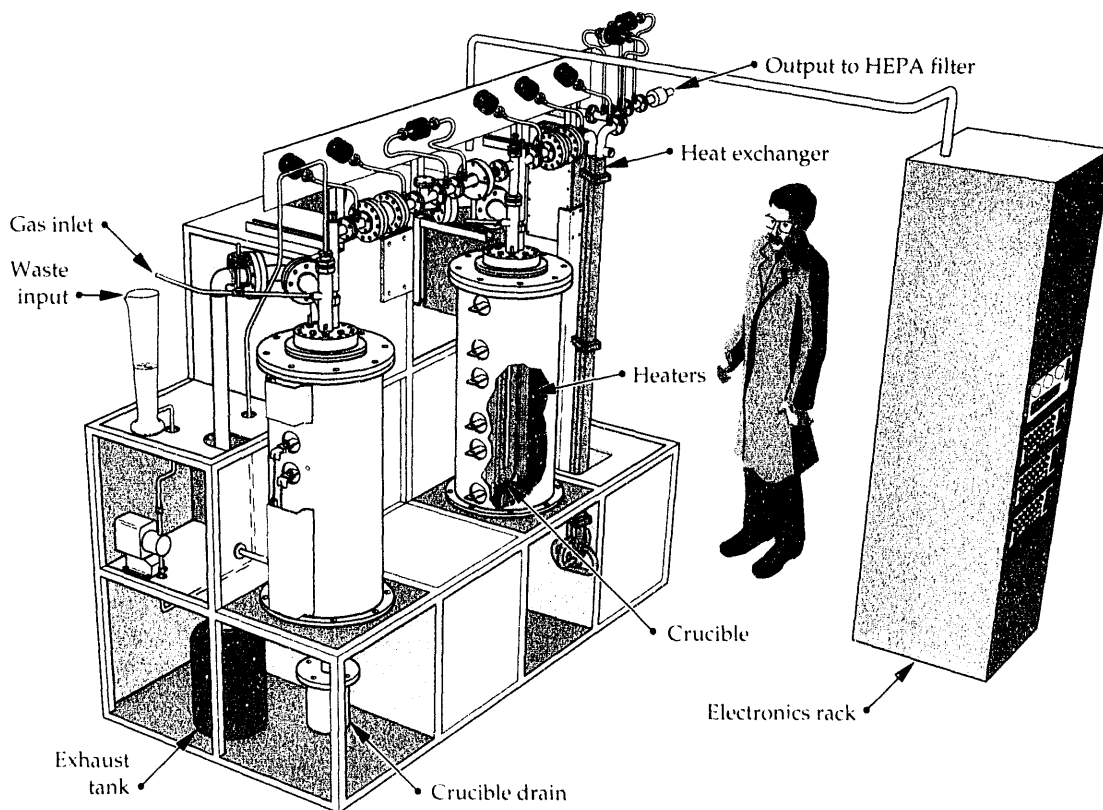


**Figure 3.**

LLNL's experimental two-stage unit for investigating the applicability of MSD to the treatment of mixed wastes.

addition, studies using color tracers have demonstrated that the contents of the liquid phase thoroughly mix at gas-flow rates significantly less than those anticipated in real operation.

Thermodynamic studies on the volatilities of radionuclides and toxic elements in the MSD process<sup>6</sup> and on the selection of salt mixtures<sup>7</sup> show that volatilities for actinides are orders of magnitude lower at molten-salt temperatures than at temperatures typical of incinerators.

## Conclusions

Process analyses<sup>8</sup> demonstrate that the MSD process is viable for treating mixed wastes. Several uncertainties, however, must be resolved:

- The effect of ash on melt stability under a variety of operating conditions.
- Processing of the spent salt under the limiting conditions of the buildup of ash and stable salts (such as NaCl).
- Retention of particulates in the molten-salt bed.
- Tolerance to upsets under a variety of operating conditions.

The experimental program currently under way addresses these issues and will obtain sufficient process-engineering data to design a pilot-scale unit.

## Acknowledgments

We gratefully acknowledge contributions from the following: Martyn Adamson, Gary Bradley, William Brummond, John Celeste, Edward Domning, Dawn Fairley, Joseph Farmer, Alfred Fontes, Joseph Glaser, Robert Hickman,

Beverly Hobson, Clarence Hoenig, Leroy Holmes, Russell Jones, Cory Karlsen, Oscar Krikorian, and Szu Wang.

*This project was jointly funded by LLNL's Laser and Environmental Technology Programs under the auspices of the DOE Office of Technology Development (EM).*

## References

1. J. F. Cooper et al., *Molten Salt Processing of Mixed Wastes with Offgas Condensation*, presented at the 1991 Incineration Conf., Knoxville, TN, March 13, 1991 (see LLNL Preprint UCRL-JC-107288, 1991).
2. M. L. Mendelsohn et al., "Final Report of the Director's Internal Panel on the Decontamination and Waste Treatment Facility (DWTF)," press release, Lawrence Livermore National Laboratory, Livermore, CA, February 21, 1990.
3. R. L. Gay et al., "Destruction of Toxic Wastes Using Molten Salts," *Proc. Nat. Meeting Am. Inst. Chem. Eng.*, Anaheim, CA, April 21, 1981 (AIChE, 1981).
4. D. E. McKenzie et al., "Volume Reduction of Radioactive Beta-Gamma and TRU Waste by Molten Salt Combustion," *Proc. ERDA/Georgia Tech Radwaste Management Symp.*, Atlanta, Georgia, May 1977 (Georgia Institute of Technology, Atlanta, GA, 1977).
5. R. S. Upadhye, D. Fairley, and L. Holmes, *A Spreadsheet Model for Analyzing Heat Transfer in the Molten-Salt Destruction Process*, Lawrence Livermore National Laboratory, Livermore, CA, in preparation (1992).
6. O. H. Krikorian, *Analysis of Plutonium and Uranium Volatilities from Mixed Wastes in the Molten Salt Processor*, presented at the 1991 Incineration Conference, Knoxville, TN, 13 May 1991 (see LLNL Preprint UCRL-JC-106163, 1991).
7. O. H. Krikorian, *Selection of Molten Salt Composition for Bench Scale Molten Salt Processor Tests*, Lawrence Livermore National Laboratory, Livermore, CA, UCRL-ID-107091 (1991).
8. A. E. Stewart et al., *Preconceptual Design of a Closed Molten Salt Destruction System for Mixed Waste*, Rockwell International, Energy Technology Engineering Center, Canoga Park, CA (March 20, 1991).

---

## Overview

One of the responsibilities of the Department is to analyze or characterize virtually any substance presented to its staff. A broad spectrum of conventional instrumentation and techniques for this purpose has been established over the years. New instruments and new ways to use existing instrumentation are constantly being discovered. From time to time, unusual programmatic responsibilities require us to develop entirely new devices or methods.

Among the newest technologies, synchrotron radiation has been developed to the next level of sophistication. Previously, the high intensity, high resolution, and tunability of a synchrotron light source made it possible to acquire detailed spectroscopic information such as extended x-ray absorption fine structure and near-edge structure. The more recent use of synchrotron radiation has taken advantage of the time structure of a synchrotron beam to acquire diffraction data in a few milliseconds, making it possible to study solid-state reactions with time constants in that range. In another advance, the focusing, intensity, and energy resolution inherent in a synchrotron beam have been combined to produce a three-dimensional image with elemental specificity of failure in a continuous-fiber metal-matrix composite. Spatial resolution of a few micrometers was necessary for this purpose.

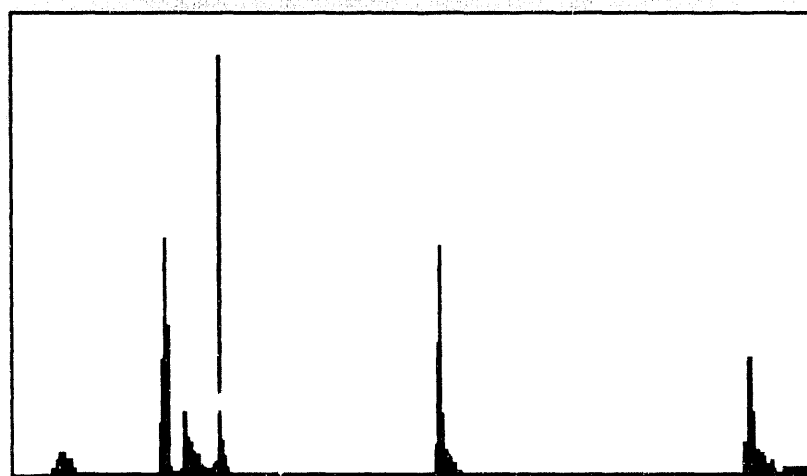
Scanning tunneling microscopy (STM) is almost a decade old, and its development has expanded in many directions. A related method of atomic force microscopy (AFM) has greatly extended the range of substances that could be investigated. STM has been used to determine the atomic structure of bio-organic molecules such as the DNA bases on surfaces, and AFM images were taken of mouse and bull sperm to follow their behavior on hydration.

In spite of the long usage of high-resolution optical spectroscopy, many elements have not yet been studied in detail. Reported here is the emission spectrum of cerium, for which the transition probabilities were deduced from transition intensities and upper-level lifetimes

Analysts constantly need new approaches to solve analytical problems. The ability to screen for and identify trace levels of nitrogen-containing compounds (potential explosives) and illicit drugs was presented as a challenge. The solution has been to combine capillary gas chromatography with a thermal energy analyzer and an ion-trap mass spectrometer.

Remote sensing by ion-selective sensors is a developing field with many applications. The use of ion implantation produces sensors with a wide concentration range and rapid response time. The particular application described here is to implant chloride ions in a silver substrate.

# Characterization and Analysis



**GC-TEA/TMS analysis  
of a standard organic mix-  
ture: (a) the GC-TEA  
chromatogram; (b) the  
GC-ITMS TIC.**

# A Time-Resolved Diffraction Study of the Ta-C Solid Combustion System

J. Wong, E. M. Larson,  
J. B. Holt, P. A. Waide,  
B. Rupp, and L. J. Terminello

**The adiabatic temperatures,  $T_{ad}$ , for the combustion synthesis of TaC and Ta<sub>2</sub>C are calculated from known thermodynamic data to be 2452 and 2376°C, respectively. These maximum reaction temperatures are well below the melting points of tantalum, carbon, and the corresponding products and eutectic temperatures known in the binary Ta-C phase diagram. Hence, a liquid phase does not form, and the syntheses are truly solid combustions. In the formation of TaC, a concurrent subcarbide Ta<sub>2</sub>C phase forms, persists for a couple of seconds, and decreases in intensity as the final TaC phase attains its maximum concentration. The formation of Ta<sub>2</sub>C proceeds directly with no discernible intermediate Ta-C phase within 50 ms. Our experimental approach can be used to study the chemical dynamics of high-temperature, solid-state phenomena and to provide the data base needed to test various models for the solid-combustion process.**

## Introduction

The combustion of gaseous reactants has been actively studied for many years.<sup>1</sup> However, a class of combustion exists in which at least one of the reactants is a solid, but it has received little attention from materials scientists thus far. The products of these "solid flames" are technologically important materials such as ceramics, intermetallics, and composites.<sup>2</sup> This class of solid-combustion reactions is universally accompanied by the release of a large amount of heat. Once initiated with an external source such as an electrically heated tungsten coil or a laser, these reactions become self-sustaining and propagate to completion within seconds. These self-propagating high-temperature synthesis (SHS) reactions are characterized by a fast-moving combustion front (1 to 100 mm/s) and a high self-generated reaction temperature (1000 to 4000 K).

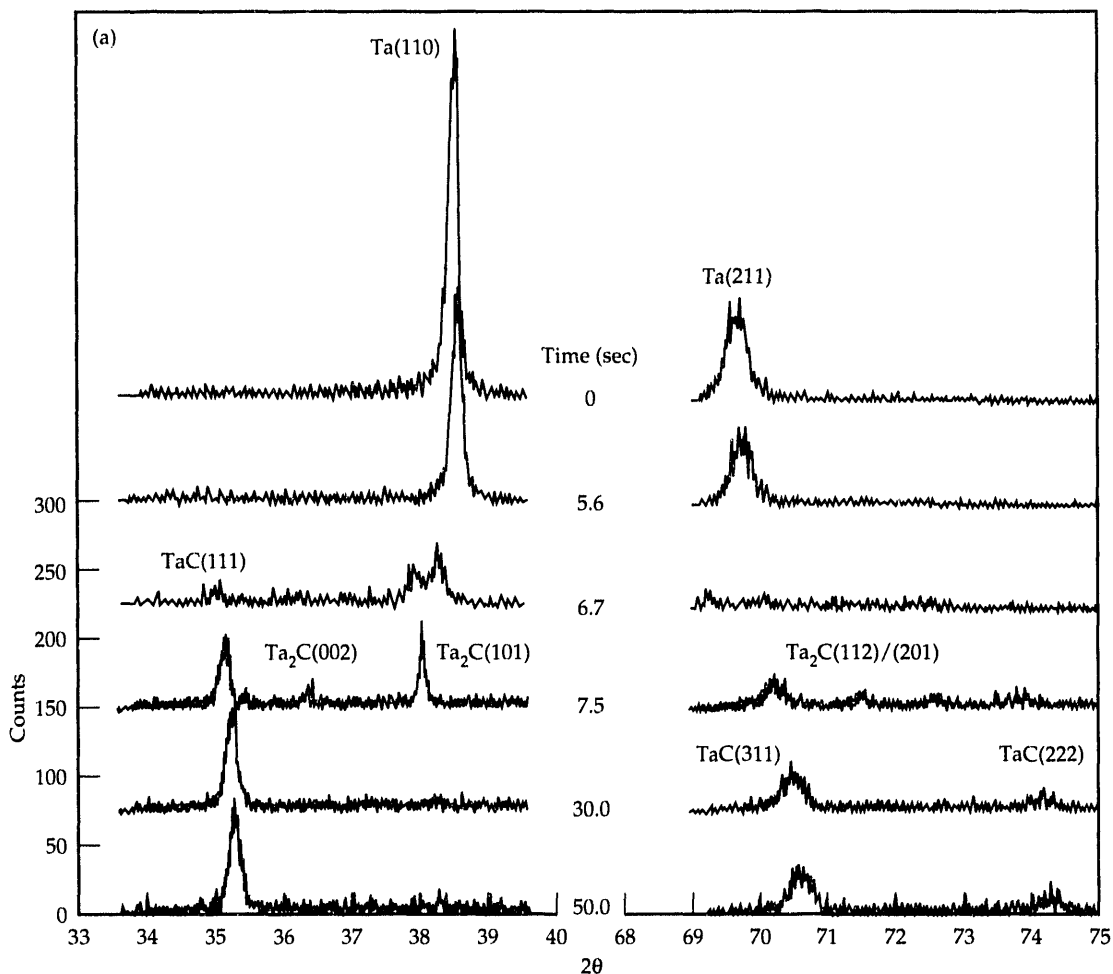
Although, in principle, the basic concepts of this method of material synthesis are relatively easy to apply, the chemical reactions and dynamics of phase transformations at the combustion front are not well understood.<sup>3</sup> This is true even of the simplest  $A + B \rightarrow AB$  class of combustion reactions. Until recently,<sup>4</sup> these reactions were difficult to investigate because of their high rates of combustion and extreme thermal conditions. Burn-front velocities and temperature profiles could be measured as functions of time and sample position, and the product

phase(s) and microstructure could be examined at the conclusion of the reaction. However, no conventional technique allowed *in situ* examination of phase transformations and chemical dynamics at the combustion front.

## Experiment

We used silicon photodiode array detectors manufactured by Princeton Instruments as position-sensitive detectors to record the time-resolved x-ray diffraction (TR-XRD) patterns from the specimen. The specimen was ignited in a specially designed reaction chamber-diffractometer with a vertical  $\theta$ -2 $\theta$  geometry. The detector is capable of recording a full scan of 1024 pixels in 4 ms. The reaction was ignited by the passage of a current through a tungsten coil adjacent to the pressed sample block. Concurrently, we recorded the temperature profile of the burn front with an imaging infrared camera (Inframetrics, Inc. Model 600). We then measured the sample temperature at a position  $\sim$ 1 cm upstream from the position of the x-ray beam and compared it to a preset triggering temperature. As soon as the measured value reached or exceeded this temperature, a pulse was sent to the array detector controller, and the diffraction data collection was activated, thus establishing a zero time for the scans. An IBM AT computer recorded the diffraction peaks at a fixed scan rate (e.g., 100 ms per scan) for a given number of scans (typically 500). Another method used was to trigger the TR-XRD recording with a thermocouple.<sup>4</sup> Details of the design and construction of



**Figure 1.**

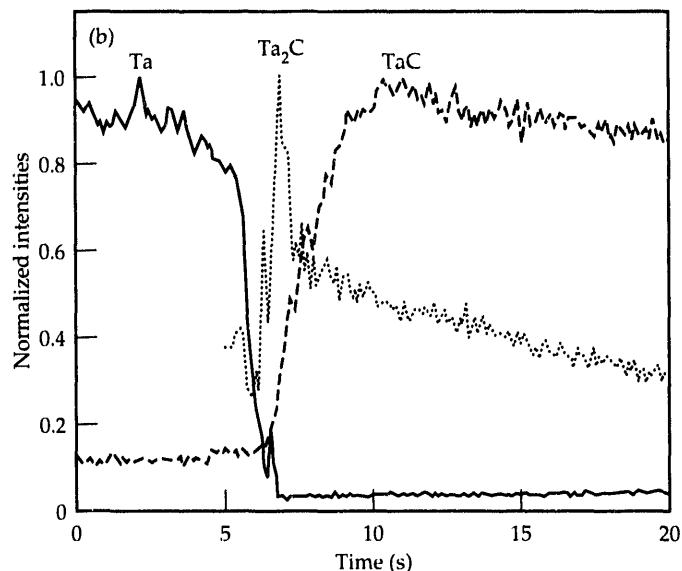
(a) Selected TR diffraction scans of the Ta + C → TaC reaction.  
 (b) Normalized integrated intensity plots from the TR scans shown in (a) vs time.

this high-speed, time-resolved, reaction chamber-diffractometer are described elsewhere.<sup>5,6</sup>

We performed time-resolved diffraction measurements on beam line X-11A at the Brookhaven National Synchrotron Light Source (NSLS), with the x-ray storage ring operating at an electron energy of 2.528 GeV and an injection current of ~200 mA. The synchrotron beam, 1 mrad (unfocused) or 2 mrad (focused), passed through a 1-mm vertical entrance slit and was monochromatized with a double Si(111) crystal at 8 keV. The estimated photon flux for the unfocused beam was  $\sim 10^{10}$  photons/s at the sample. Diffraction specimens in the form of 19-mm cubes or cylinders 19 mm in diameter and 19 mm long were pressed from dry-mixed weighed-out atomic mixtures of elemental powders. The average particle size was 2  $\mu\text{m}$ . We used submicrometer amorphous carbon from the Cabot Corporation as a Monarch 900 carbon black. The density of the pressed pellets was ~55 to 60% of the theoretical density.

## Results and Discussion

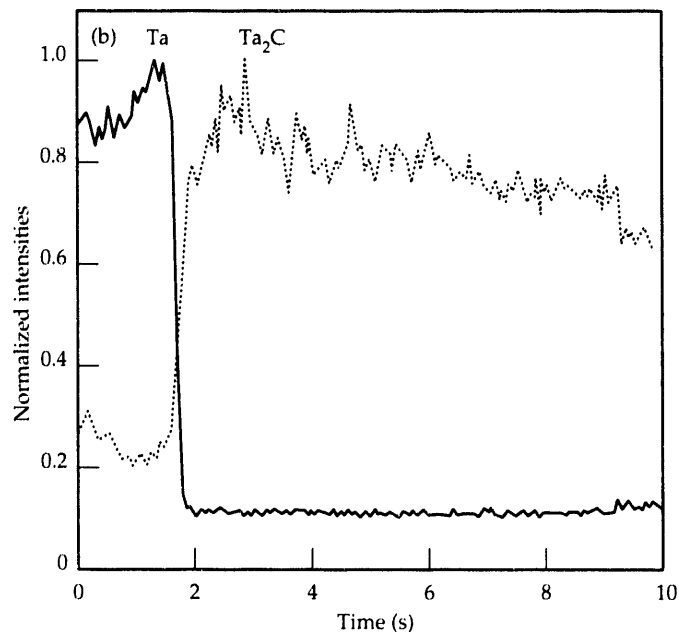
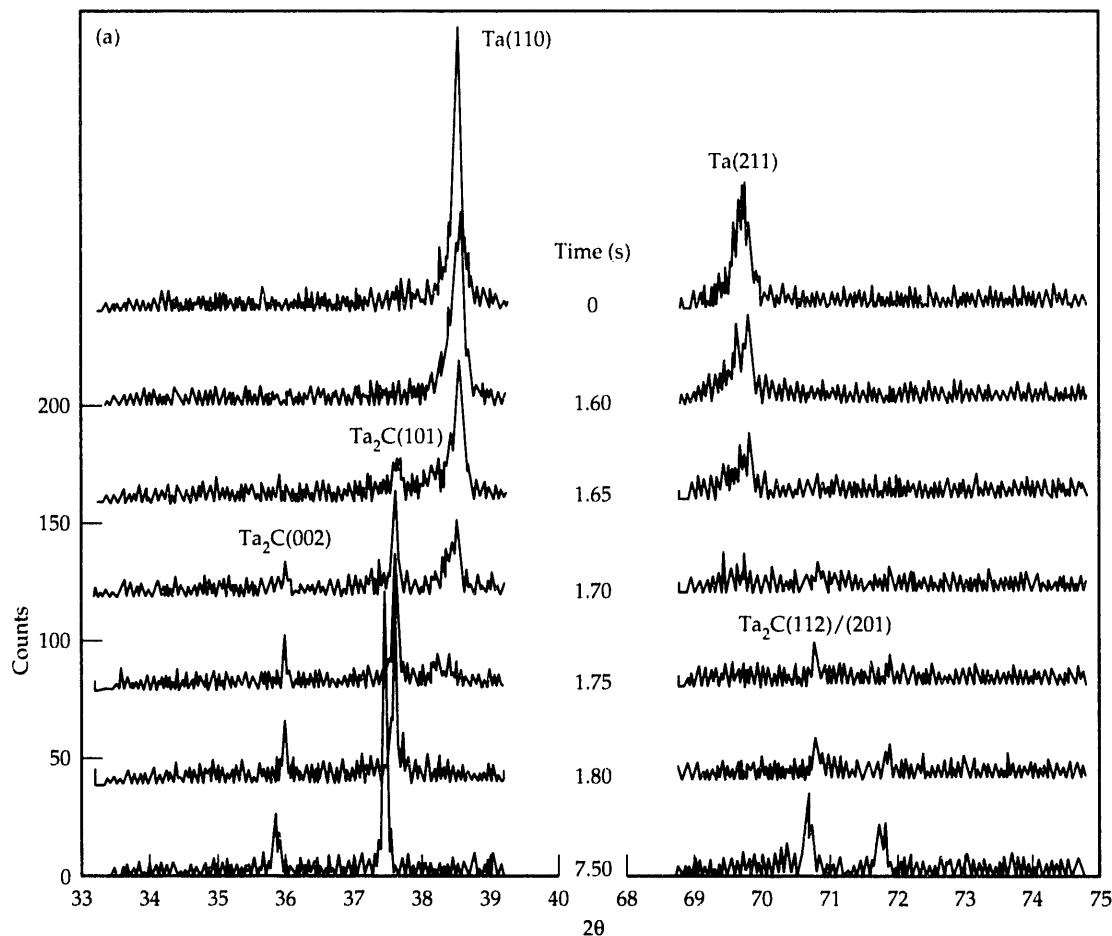
**Formation of TaC.** Figure 1(a) shows the TR-XRD results for the Ta + C → TaC reaction. Two detectors, one centered at 36.5° and a second one at 72°, simultaneously collected the



Bragg scattering of the Ta(110) and (211) peaks at the start of the reaction. Fortunately, the major peaks of both TaC and Ta<sub>2</sub>C are in these windows. Each TR-XRD scan was recorded in 100 ms. The two tantalum metal peaks are prominent until 5.6 s, at which time thermal effects broaden and diminish their intensities. The Ta(110) peak splits at

**Figure 2.**

(a) Selected TR diffraction scan of the  $2\text{Ta} + \text{C} \rightarrow \text{Ta}_2\text{C}$  reaction.  
 (b) Normalized integrated intensity plots from the TR scans shown in (a) vs time.



6.7 s, and another peak is observed at  $\sim 35^\circ$ . At this time, the Ta(211) has almost disappeared, and only a hint of scattering is observed in the center of the higher-angle detector. Both TaC and Ta<sub>2</sub>C are clearly evident at 7.5 s in both detectors. The burn-front velocity for this reaction is  $\sim 2.0$  mm/s, and with a beam size of 1.2 mm, the burn front would pass through the x-ray spot in 0.5 s. After 30 s, most of the scattering from Ta<sub>2</sub>C has disappeared, leaving only TaC as the final product of the reaction.

Figure 1(b) shows the integrated peak intensities of the reactants and products in the Ta + C combustion. The reduction in intensity of the tantalum peak as a result of thermal broadening from sample heating is largely responsible for the slope of the metal peak between 3 and 6 s. An intersection of the tantalum and TaC lines shows that TaC forms immediately upon passage of the burn front. However, the TaC intensity does not reach its maximum until the Ta<sub>2</sub>C peak has grown and then diminished. The appearance and disappearance of the Ta<sub>2</sub>C phase clearly indicates that it is an intermediate phase of the Ta + C reaction.

**Formation of Ta<sub>2</sub>C.** The burn-front velocity for the 2Ta + C → Ta<sub>2</sub>C reaction is about a factor of 3 faster than that for the formation of TaC discussed in the previous section. We monitored the subcarbide reaction on a 50-ms time scale. Figure 2(a) shows the TR-XRD data for this reaction. Within 50 ms, the tantalum peaks begin to decrease at 1.6 s, and the major Ta<sub>2</sub>C(101) peak appears at 1.65 s. In the next frame, at 1.7 s, all the subcarbide peaks are evident in both detectors, with no indication of any other species all the way to the end of reaction. The apparent shift to low angle in the last scan at 7.5 s is the result of a decrease in the height of the sample surface with respect to the beam as the whole sample contracts upon cooling. In Fig. 2(b), the integrated intensities of the tantalum reactant and the Ta<sub>2</sub>C product are plotted as a function of time. As can be seen, the slope of the curve showing the formation of the product is much steeper than that of the TaC reaction. Almost as soon as the tantalum disappears, the Ta<sub>2</sub>C product reaches its maximum intensity.

The adiabatic temperatures of this reaction and the TaC formation described in the previous section are calculated to be 2376 and 2452°C, respectively. These maximum reaction temperatures are below the melting points of tantalum (3020°C), carbon (~3800°C), and the corresponding products Ta<sub>2</sub>C (3300°C) and TaC (~3825°C) and the eutectic temperatures (2825 and 3375°C) known in the binary Ta-C phase diagram. Hence, no liquid phase forms, and the syntheses of these two carbides are truly solid-state combustion reactions.

## Conclusion

These experiments demonstrate that TR-XRD using synchrotron radiation is a very powerful and perhaps unique method of following the phase transformations and chemical dynamics of solid-combustion reactions *in*

*situ* at high temperature. When combustion-front velocity and temperature profile are measured synchronously and correlated with the TR-XRD scans, all participating phases can be identified as functions of time and temperature. Intrinsic, real-time kinetic data of this sort are much needed to permit testing of existing theoretical models of solid combustion and to provide the basis for developing new theories. Furthermore, using higher flux synchrotron sources currently available at wiggler beamlines (10<sup>12</sup> photons/s) or still brighter third-generation sources, we can achieve higher spatial resolution for a closer look at the combustion front in this interesting class of high-temperature solid-combustion reactions.

*This work was funded by Weapons-Supporting Research.*

\*Mechanical Engineering Department, LLNL

## References

1. See, for example, the volume of articles published in *Combustion and Flame* since 1957.
2. Z. A. Munir, "Synthesis of High-Temperature Materials by Self-Propagating Combustion Methods," *Ceram. Bull.* **27**, 342 (1988).
3. Z. A. Munir and U. Anselmi-Tamburini, "Self-Propagating Exothermic Reactions; the Synthesis of High-Temperature Materials by Combustions," *Mater. Sci. Rept.* **3**, 277 (1989).
4. J. Wong, E. M. Larson, J. B. Holt, P. A. Waide, B. Rupp, and R. Frahm, "Time-Resolved X-Ray Diffraction Study of Combustion Reactions," *Science* **249**, 406 (1990).
5. E. M. Larson, P. A. Waide, and J. Wong, "High-Speed Diffractometer Reaction Study Using Synchrotron Radiation," *Rev. Sci. Instrum.* **62**, 53, (1991).
6. E. M. Larson, J. B. Holt, J. Wong, P. A. Waide, B. Rupp, and L. Terminello, "A Time-Resolved Diffraction Study of the Ta-C Combustion System," submitted to *J. Mater. Res.* [see LLNL Preprint UCRL-JC-108303 (1991)].

# Preparation of Solid-Membrane Ion-Selective Electrodes by Ion Implantation

R. S. Glass, R. G. Musket,  
and K. C. Hong

*Ion implantation has been used to prepare solid-membrane ion-selective sensors. For example, a thin AgCl membrane (typically about 100 nm thick) is created by bombarding a silver substrate with 33- to 200-keV  $^{35}\text{Cl}^+$ . These surface-modified substrates act as sensors for chloride ion in solution over a concentration range of several decades and have rapid response times. We believe that ion implantation will prove to be a general method for fabricating a variety of ion-selective sensors that will have well-controlled properties.*

## Introduction

Ion-selective electrodes (ISEs) have had a major impact in analytical measurement science, and they will continue to have widespread application as sensors. They are commercially available in many shapes and sizes and in various chemical and material designs. Several completely solid-state ISEs are available. In recent years, a significant effort has been devoted to developing ion-sensitive field-effect transistors (ISFETs), which, like ISEs, are potentiometric sensors. (A membrane potential, which develops in the presence of selected ions in solution, is the measured response.) Several excellent recent monographs discuss the current state of ion-selective devices and the theory behind their operation.<sup>1-5</sup>

As an ISE for chloride ion, the solid-state membrane electrode has been available for some time. Common membrane materials include single crystals, disks cast from melts, sintered materials, and pressed polycrystalline pellets. These membranes consist of AgCl, or AgCl dispersed in a matrix of Ag<sub>2</sub>S. Membranes of this type display a Nernstian response to chloride ion in solution (i.e., for a constant activity coefficient, a linear membrane potential vs log [Cl<sup>-</sup>] curves with a slope of approximately 59 mV/decade). In general, many problems have been encountered when using conventional methods for ISE fabrication, including difficulty in pressing pellets, making contacts, and adhesion.

We found that if chloride ions are implanted into a silver substrate, a solid-state membrane ISE can be produced that shows (approximately) the expected Nernstian response in solutions containing chloride ion over a concentration range of several decades.<sup>6</sup> In addition, we found the potential-vs-concentration response between different implanted specimens to be very reproducible.

Our ultimate motivation in undertaking this work was to develop a convenient and reproducible method for fabricating arrays of ISEs and "micro-ISEs," with individual elements selective to different chemical species. Our work is a first step in that direction. Using ion implantation as a fabrication method allows precise control over the structure and composition of the ion-sensing membrane layer. Therefore, special properties can be realized (e.g., rapid response). In addition, the mass-production and low-cost features of this method of fabrication imply that it may be economical to discard ISEs after use.

## Experimental Methods

Specimens for implantation consisted of highly polished silver cylinders (0.64 cm in diameter by 1.27 cm high) and microdisks (10 μm in diameter). We mounted these specimens in a fixture, which we placed in a 200-kV ion implanter with the sample surfaces perpendicular to the ion beam. For our implantations, HCl gas was fed into the hot cathode ion source. The  $^{35}\text{Cl}^+$  ions were selected mass spectrometrically for implantation. We used three sequential ion beams with energies of 200, 70, and 33 keV, for which the fluences were 15, 5.9, and  $4.4 \times 10^{16}$  Cl/cm<sup>2</sup>, respectively. We used the Monte Carlo code TRIM89 (see Ref. 7) to calculate the low-fluence profiles for these energies and relative fluences. The half-maximum chloride concentration of the highest-energy implant indicated that the nominal depth of the implants was about 160 nm.

We used electron spectroscopy for chemical analysis (ESCA) to determine the composition of the surface layers and the chemical states of the silver and chlorine. A magnesium Kα x-ray source provided the primary x rays. For sputter profiling, a beam of 3-keV argon ions was used.

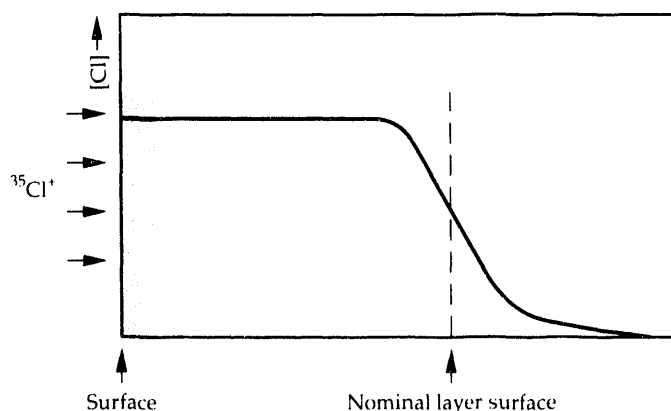
Reagent-grade AgCl in pelletized form and a non-implanted silver specimen were the standards. For evaluating the response of the implanted ISEs, we used a saturated calomel electrode (SCE) as a reference electrode. The remaining details of this experiment are reported elsewhere.<sup>6</sup>

## Results and Discussion

Figure 1 shows conceptually the structure of an ion-implanted ISE. For the experimental conditions we used, ESCA depth profiling revealed that impurities dominated the near-surface region (i.e., within about 3 nm) of the as-implanted specimen, which was subsequently exposed to the general atmosphere. However, the concentration of chlorine was still several atomic percent. After a short sputtering period of about 15 s, impurities were removed, leaving only silver and chlorine. The concentration of implanted chlorine after this treatment was about 14 at.%. Considering the relative sputtering rates for silver and a Ta<sub>2</sub>O<sub>5</sub> standard, we estimated the thickness of the implanted layer to be about 70 nm, suggesting that sputtering during the implantation had removed considerable amounts of chlorine. Consideration of the binding energies of the Ag 3d and Cl 2p electrons led us to the preliminary conclusion that the chlorine in the as-implanted silver was present mainly as Ag<sub>2</sub>Cl, with some evidence for AgCl. More detailed studies are needed to evaluate this conclusion.

To investigate reproducibility, we compared the potential response of three separate ion-implanted ISEs to chloride ion concentration in the range of 0.028 to 28 mM (1 to 1000 ppm). From the data shown in Fig. 2, we see that the reproducibility is quite good. Only the least-squares line for the total data set from all three ion-implanted ISEs is indicated (slope of -54 mV). When data for only the range of 0.28 to 28 mM are considered, the slopes for the individual electrodes increase, ranging from -55 to -58 mV for the three ISEs shown in Fig. 2, with correlation coefficients of 0.997 or better.

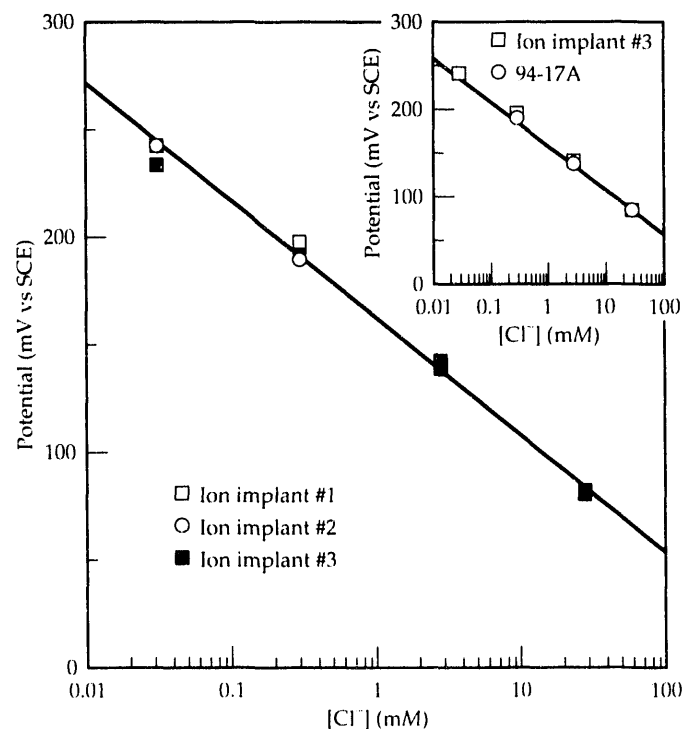
**Figure 1.** Conceptual drawing of the structure of an ion-implanted ISE.



The inset to Fig. 2 compares the response of a commercial Cl<sup>-</sup> ISE with that of one of the ion-implanted ISEs (#3 in the main figure). It is apparent that the response of the ion-implanted ISE is quite similar to that of the commercial electrode. This indicates that the interfacial processes are similar, as one might expect. However, concentrations of defects are no doubt different in the two cases. The defect structure of solid membranes is known to affect equilibrium potential values.<sup>5</sup>

Other criteria used to evaluate ISEs are the response time, the reproducibility of the final potential reached, and the rate at which equilibrium is attained. To evaluate these parameters for the ion-implanted ISEs, we alternately exposed them to chloride-ion solutions of 0.28 and 2.8 mM concentration and recorded the potential transients. Figure 3 shows the result of this study for one ion-implanted ISE. The response time,  $\tau_{90}$ , is defined as the time required for the potential to change by 90% of the difference between the initial and final potentials. For transitions in either direction,  $\tau_{90}$  is usually a little less than 1.5 s, and the results are reproducible. Because the membrane layer thickness affects response time and because ion implantation can generate solid-state membrane ISEs with well-defined thicknesses,

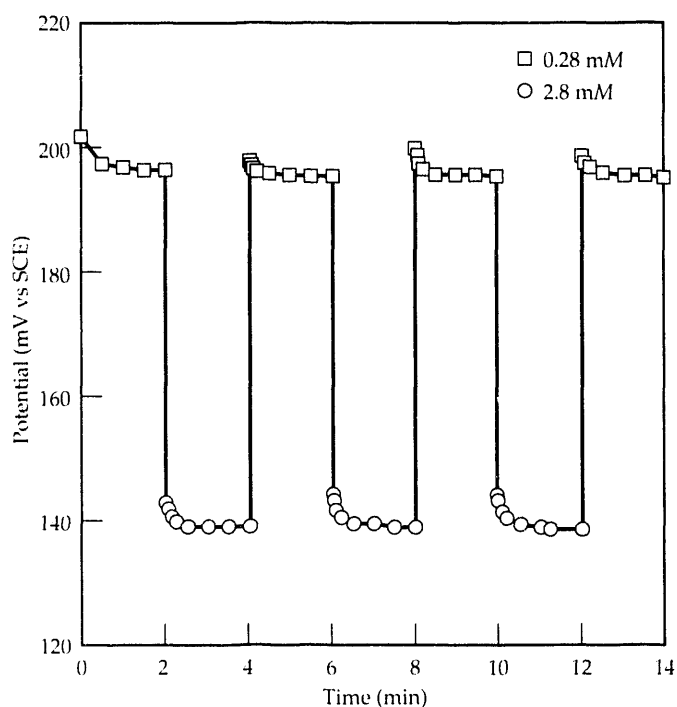
**Figure 2.** Electrode potentials as functions of chloride-ion concentration for three individual ion-implanted ISEs. The least-squares line is for the total data set from all three ISEs. The inset compares the responses of a commercial chloride ISE and an ion-implanted ISE. The least-squares line in the inset is only for the commercial electrode.



implantation should prove to be a useful method for accurately adjusting the response time.

In other experiments, we demonstrated that ion-implanted ISEs showed small hysteresis and conditioning (aging) effects. We are currently assessing several other criteria to evaluate ISEs, such as selectivity of response, detection limits, and long-term drift. We are also currently evaluating optimum beam parameters, such as fluence and energy, for implanting  $^{35}\text{Cl}^+$ . We may be able to use a much smaller dose than previously believed necessary and thereby diminish the implantation time required.

**Figure 3.** Demonstrated reproducibility of response times and equilibrium potentials for alternate immersion in 0.28- and 2.8-mM  $\text{Cl}^-$  solution for an ion-implanted ISE. The electrode was rinsed with deionized water between immersions.



## Summary

In summary, ion implantation appears to be a useful method for creating solid-state membrane ISEs. Because it is "line of sight" and because the fluence and energy of the ion beam are easily controlled, one can create modified layers of precise thickness and stoichiometry. While we have demonstrated the feasibility of creating chloride ISEs by using different ion beams for implantation, we should be able to produce novel materials that can function as ISEs and that show selective responses to a variety of other anions and cations. In particular, we are presently using ion implantation to develop solid-state pH sensors and sensors for heavy-metal ions. Because ion implantation readily lends itself to micropatterning, arrays of ISEs can be conveniently fabricated. The areas of most immediate application for these sensors are in environmental monitoring, process control, disposable bedside monitors of body fluids, or use *in vivo*.

This work was funded by the LLNL Special Projects Program and the LLNL Environmental Protection Department.

## References

1. J. Janata, *Principles of Chemical Sensors* (Plenum, New York, 1989).
2. M. J. Madou, S. R. Morrison, *Chemical Sensing with Solid State Devices* (Academic Press, Boston, 1989).
3. J. Koryta and K. Stulik, *Ion-Selective Electrodes*, 2nd ed. (Cambridge Univ. Press, New York, 1983).
4. W. E. Morf, *Studies in Analytical Chemistry 2, The Principles of Ion-Selective Electrodes and of Membrane Transport* (Elsevier, New York, 1981).
5. R. P. Buck, "Theory and Principles of Membrane Electrodes," *Ion-Selective Electrodes in Analytical Chemistry*; Vol. 1, H. Freiser, Ed. (Plenum, New York, 1978), pp. 1-137.
6. R. S. Glass, R. G. Musket, and K. C. Hong, "Preparation of Solid-Membrane Chloride Ion Selective Electrodes by Ion Implantation," *Anal. Chem.* **63**, 2203 (1991).
7. J. F. Ziegler, J. P. Biersack, and V. Littmark, *The Stopping and Range of Ions in Solids* (Pergamon, New York, 1985).

# Tensile Failure in Metal-Matrix Composites

J. H. Kinney, M. L. Sattler,  
E. Zywicki\*, R. A. Saroyan†,  
and M. C. Nichols‡

*We have shown that, because of the heterogeneous, two-phase microstructure of composites, failure may have a dual origin: properties of the fiber–matrix interface and defects that originate in the interior of the fiber. Although core and interior failure have been observed in single-fiber tensile tests, these are the first observations that indicate the possibility of significant failure near the fiber interior in a fabricated composite.*

## Introduction

Continuous fiber–metal-matrix composites (MMCs) have been extensively studied over the past several years with the hope that they might find use in advanced aerospace applications. Nevertheless, many fundamental questions remain regarding the mechanical response of these materials to applied loads. Especially difficult are fatigue and creep, in which the complex interplay between matrix and fibers in these heterogeneous structures greatly complicates the interpretation of test results and analytical modeling.

Mechanical-property measurements performed on MMCs rely on 1- and 2-D analytical techniques to explain what are, in reality, 3-D responses. A load–displacement curve is an example of a 1-D measurement that is often used to measure global deformation in a sample and to infer micromechanical mechanisms that might be operating during deformation. Scanning electron microscopy (SEM) and transmission electron microscopy (TEM) are essentially 2-D techniques that can be used to locate the origin of failure and determine if any dissipating forces, such as crack bridging or deflection, were operative during crack advance. However, few good ways exist for 3-D analysis of a material's microstructure, short of time-consuming serial sectioning—a technique that destroys the sample and is artifact prone.

The linear x-ray attenuation coefficient ( $\mu$ ) is a sensitive measure of atomic composition and density. If  $\mu$  could be measured nondestructively as a function of position in a sample, then a 3-D image of a sample's microstructure could be obtained without time-consuming and difficult sectioning. Subtle compositional changes from one position to the next would appear as differences in the attenuation coefficient. As long as the spatial resolution could be made small with respect to the microstructural features of interest, the 3-D x-ray images obtained from these measurements would provide valuable structural and compositional information.

Computed tomography (CT), a technique for measuring  $\mu$  in 3-D, is frequently used in medical diagnostic radiology and is slowly being developed for industrial

applications. Whereas the spatial resolution in medical CT is about 500  $\mu\text{m}$ , industrial CT systems designed to examine small samples typically have spatial resolutions between 50 and 100  $\mu\text{m}$ —high enough to detect many critically sized flaws but too low to image microstructural features such as second-phase precipitates, reinforcing particulates, or fibers in composite structures.

We have developed the technology to precisely measure x-ray attenuation on exceedingly small samples.<sup>1,2</sup> This technology, known as x-ray tomographic microscopy (XTM), is a form of x-ray microscopy that uses tomographic reconstruction techniques to build 3-D images of microstructures. In essence, XTM carries the industrial CT techniques to their extreme limit in spatial resolution and contrast sensitivity. The highest spatial resolution (2–3  $\mu\text{m}$ ) is obtained with monochromatic (single-energy) synchrotron radiation, and its use is limited to inspecting small (usually less than 1-cm-diam) specimens.

Because XTM is 3-D and noninvasive, it can enhance our understanding of failure in advanced composite materials. Although its spatial resolution is lower than that of electron microscopy, XTM can image the microstructures before, during, and after mechanical loading or fracture. Because of this capability, XTM can image the initial microstructure of a test sample, sequence and locate the origin of induced damage, and follow the evolution of damage to catastrophic failure. Then, higher resolution analytical techniques used in post-mortem examination of samples can more efficiently interpret the causes of failure in the sample.

## Experiment

In recent experiments, we used XTM to examine an aluminum-matrix/SiC SCS-8 fiber composite during a monotonic load sequence.<sup>3,4</sup> With these experiments, we aimed to determine if XTM had sufficient spatial resolution and contrast sensitivity to detect the microstructural damage that develops under loading at stress levels exceeding the yield strength of the aluminum matrix. Figure 1 shows the types of damage that might occur during loading. The

important microstructural features include interfacial disbonding, fiber breaking, and matrix and fiber microcracking. Because these features might not occur in any single plane, a 3-D image is advantageous to assess the nature of the damage expected in these materials.

Figure 2 is the XTM image of the as-received microstructure in the composite. Clearly visible are the carbon cores of the SCS-8 fibers (approximately 30  $\mu\text{m}$  in diameter). Sufficient contrast exists to distinguish between the SiC layer and the 6061 aluminum matrix, although the calculated contrast difference at the x-ray energy used to obtain this image is less than 10%. Furthermore, when 10 or more pixels in any region are averaged to reduce statistical noise, the measured and calculated  $\mu$  values agree within a few percent, even over a factor-of-100 spread in  $\mu$  value (see Table 1). The excellent agreement between the values measured using XTM and those calculated from the tabulated attenuation coefficients is a good indication that XTM is an imaging tool and, to a limited extent, an analytical tool as well.

As a further indication of XTM's analytical value, it can be used to map very accurately the variations of the carbon concentration in the SiC sheath. In Fig. 2, small halos surround the carbon cores and extend outward several micrometers. These halos, representing changes in the x-ray attenuation coefficient, are caused by a carbon gradient radiating outward from the core. From high-resolution TEM images, we believe that the microstructure near the carbon core consists of a two-phase mixture of small SiC crystallites in a matrix of amorphous (or turbostratic) carbon. The presence of a second-phase, low-modulus carbon greatly impacts the local stress fields near the core and can therefore influence the fiber's overall fracture behavior.

Therefore, obtaining accurate volume-fraction distributions of the carbon and the SiC is important in order to understand failures in composites fabricated with these fibers.

It is possible to use the electron energy loss spectrum (EELS) from a TEM to quantify the ratio of silicon atoms to carbon atoms with a spatial resolution of 1  $\mu\text{m}$  or better. Measuring the EELS spectrum, however, requires very thin sections (a few hundred angstroms thick) to be made from the fiber—a time-consuming and difficult task. Nevertheless, we prepared a thin section of SCS-8 fiber and used EELS spectroscopy to determine the C/Si ratio. In stoichiometric SiC, this ratio should be exactly 1:1. What we found, however, was a ratio varying from 2:1 near the carbon core to 1:1 midway through the fiber. If we assume that the  $\mu$  values measured from XTM arise from a mixture of SiC and amorphous carbon, then the C/Si ratio calculated from the XTM data is in excellent agreement with that obtained from the more time-consuming EELS spectroscopy (see Fig. 3). This agreement is important because it indicates that XTM can be used to obtain accurate compositional variations throughout the composite.

We fabricated tensile samples from the composite shown in Fig. 2 and stressed them in a monotonic load series extending up to the ultimate tensile strength of the composite. At applied tensile stress levels greater than the yield strength of the matrix, the fibers appeared to rearrange themselves into a configuration more closely packed

**Figure 1.** The important microstructural features in an aligned fiber-MMC that can be imaged using XTM. The microstructural features include fiber-matrix disbonding, broken and cracked fibers, and matrix microcracking. XTM can image fiber architecture and variations in fiber orientation as well.

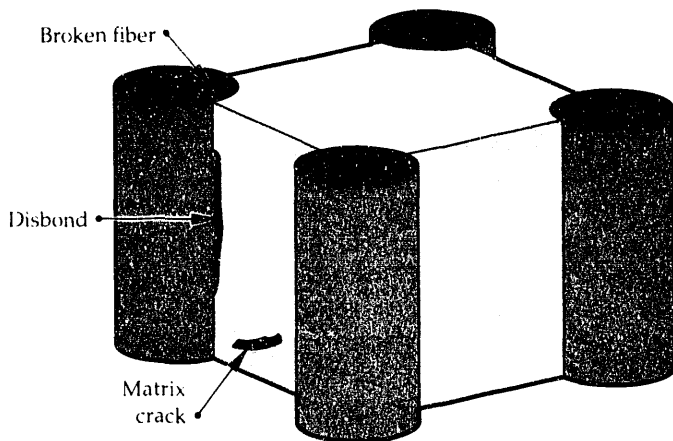


**Figure 2.**

XTM image of the as-received microstructure in an aluminum matrix/SCS-8 SiC fiber composite. The pre-existing matrix microcracking in the outer plies is probably due to incomplete matrix consolidation during fabrication.

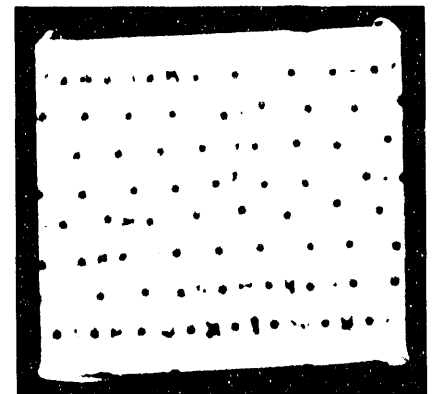


**Table 1.** Calculated x-ray attenuation coefficients<sup>a</sup> compared to XTM measurements in an MMC.<sup>3</sup>

Material	$\mu_{\text{obs}}$ ( $\text{cm}^{-1}$ )	$\mu_{\text{calc}}$ ( $\text{cm}^{-1}$ )	$\mu_{\text{calc}}/\mu_{\text{obs}}$
Crack	$0.07 \pm 0.04$	0	—
Graphite	$0.88 \pm 0.44$	0.84	0.95
Aluminum (pure)	$8.09 \pm 0.21$	7.93	0.98
Aluminum (6061)	$8.15 \pm 0.18$	8.26	1.01
Silicon carbide	$8.70 \pm 0.73$	8.89	1.02

<sup>a</sup> Coefficients were calculated using x-ray energy of 21 keV and densities of 3.22 and 2.2  $\text{g}/\text{cm}^3$  for SiC and graphite, respectively.



than their as-received distribution. Also, at applied stress levels near 50% of the ultimate tensile strength of the composite, the carbon cores began to break and continued to do so with ever-increasing frequency up to composite failure. Because no catastrophic fiber failures occurred after core breaking, it appears that core failure does not immediately affect fiber integrity. However, this lack of effect on the fiber might be explained by the low modulus of the carbon monofilament core; that is, the carbon core does not carry much of the fiber load. Nevertheless, the separation of the core alters the stress state along the interior wall of the SiC fiber and may eventually lead to failure from inside the fiber.

Figure 4 shows an XTM cross section taken vertically through the fracture surface of a composite tensile specimen that was loaded to failure. The fracture surface is very irregular and rough, and the visible subsurface damage (multiple fiber fractures located beneath the fracture surface) is consistent with numerous observations of failed aligned-fiber tensile samples.

**Figure 3.** Comparison of EELS and XTM data, showing the carbon-to-SiC ratio outward from the carbon core. The XTM data is consistent with the presence of a two-phase mixture of SiC and amorphous carbon.

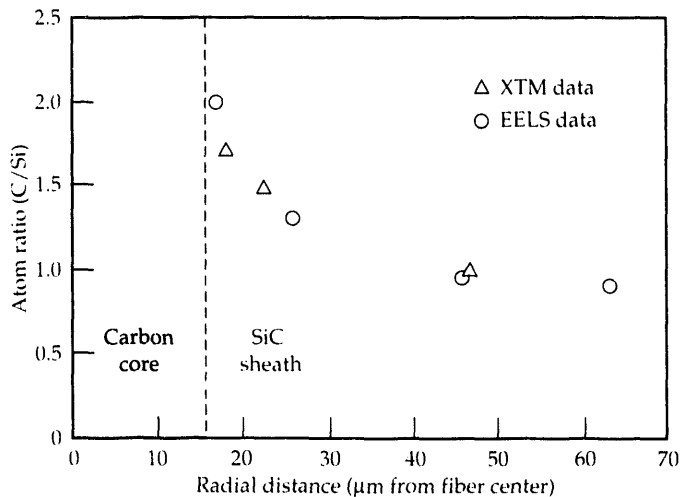


**Figure 4.**

XTM cross section taken through the fracture surface of the composite tensile specimen loaded to failure. The cross section is perpendicular to the load axis. The fiber fractures are not perpendicular to the applied tensile load. The fracture surface is rough, and much subsurface damage is visible.

Figure 5 is a 3-D rendering of the multiple fiber fractures lying beneath a single pulled-out fiber. We inverted the XTM data to show space and very low-density regions as being opaque, and matrix and fiber material as being transparent. Figure 5, therefore, is an image of the pulled-out region, the carbon core, and the fracture surfaces in the fiber. What is interesting here is that the fracture surface is approximately 45° rather than 90° to the load axis. This difference indicates that internally initiated failure, at least in these fibers, may be of great importance. Three-dimensional mechanical models do predict such a shear-like mode of failure when the fiber is subjected to a large state of residual compressive stress and then loaded axially. From what we have observed of the microstructure and fiber processing to date, however, this is probably unlikely.<sup>5,6</sup>

## Discussion

Detailed examination of the XTM data provides evidence for two modes of failure in the composite. First, XTM images provide evidence for planar fracture in the fibers (i.e., the fracture surface is normal to the tensile axis). Second, the XTM images also show a curved or shear-like fracture trajectory, frequently lying at 45° in the near-core region and often deflecting to a planar fracture around the mid-radius of the fiber, where the microstructure becomes single phase. The planar fracture is easy to interpret in terms of a fracture originating near the matrix-fiber interface. In this case, fracture-mechanics theory indicates that planar crack propagation is the minimal-energy mode for failure. Curved or shear-like

**Figure 5.**



A 3-D rendering of a broken fiber still imbedded in the aluminum matrix. The XTM data are inverted to show space as opaque and the matrix and fiber material as transparent. The image shows the carbon core and the fractures in the fiber. For the first time, fractures can be observed *in situ*, and the shapes, positions, and separations can be recorded and compared to models.

fracture originating from the matrix–fiber interface cannot be explained from what is known about the fiber microstructure. Some strong evidence exists that this type of failure might originate in the fiber interior.

Reporting results from failure studies of single SiC fibers similar to those used in this study, Bhatt and Hull<sup>7</sup> found it difficult to identify the primary fracture surface or the critical flaw responsible for fiber failure because the fibers tended to shatter. Nevertheless, SEM fractographic analysis revealed that the as-received fibers failed from an unidentified flaw near the fiber core. Because XTM allows us to image the fibers while they are still in the matrix, the fiber remains contained, and we can analyze the fracture at the point of failure. The evidence in Ref. 7 of failure near the core in single fibers is consistent with XTM observations of core failure prior to total fiber failure in the fabricated composite. Hence, without interfacial reactions or flaws at the fiber–matrix interface, one might argue that ultimate fiber failure in the SCS fibers initiates near the fiber core.

We have developed a scenario for fracture originating near the fiber core. First, a first-order stress analysis indicates that the nominal critical flaw size near the core is larger than that near the fiber surface. However, the small SiC grains near the fiber core may act as local stress concentrators and fracture-initiation sites, thereby greatly increasing the stress and reducing the critical flaw size. Second, because the modulus increases with distance from the fiber core (due to the decreasing volume fraction of amorphous carbon), an advancing inclined crack would want to minimize its mode II component by deflecting away from planar growth. Finally, when the crack reaches the mid-radial region of constant modulus, the behavior reverses, and propagation proceeds along a planar path toward the lower-modulus aluminum matrix. Thus, it is possible that planar fractures originate at the fiber surface and propagate inward, while nonplanar fractures originate near the fiber core and propagate outward.

## Summary

Our study illustrates how the noninvasive nature of XTM can be used to study dynamic response in materials—the time sequence of fiber failure during tensile loading and the 3-D distribution of the damage created in the composite before and after fracture. The XTM images have features that cannot easily be explained by existing models of tensile failure in these composites. Existing models hold that failure is

dominated by the fiber–matrix interface. Our results show that, because of the heterogeneous, two-phase microstructure of composites, failure may have a dual origin: properties of the fiber–matrix interface and defects that originate in the interior of the fiber. Although core and interior failure have been observed in single-fiber tensile tests, these are the first observations that indicate the possibility of significant failure near the fiber interior in a fabricated composite.

## Acknowledgments

The authors acknowledge the support of the staff of the Cornell High Energy Synchrotron Source (CHESS), funded by grants to B. W. Batterman from NSF, and to the staff of the Stanford Synchrotron Radiation Laboratory (SSRL).

*This work was funded by the DOE Advanced Industrial Concepts Materials Program.*

\* Nuclear Explosives Engineering Division, LLNL

† Computations Directorate, LLNL

‡ Materials Department, Sandia National Laboratories, Livermore, CA

## References

1. J. H. Kinney and M. C. Nichols, "X-Ray Tomographic Microscopy Using Synchrotron Radiation," *Ann. Rev. Mater. Sci.* **22**, 121 (1992).
2. J. H. Kinney, M. C. Nichols, U. Bonse, S. R. Stock, T. M. Breunig, A. Guvenilir, and R. A. Saroyan, "Nondestructive Imaging of Materials Microstructures Using X-Ray Tomographic Microscopy," in *Advanced Tomographic Imaging Methods for the Analysis of Materials*, Vol. 217 (Materials Research Society, Pittsburgh, PA, 1991), p. 81.
3. J. H. Kinney, S. R. Stock, M. C. Nichols, U. Bonse, T. M. Breunig, R. A. Saroyan, R. Nusshardt, Q. C. Johnson, F. Busch, and S. D. Antolovich, "Nondestructive Investigation of Damage in Composites Using X-Ray Tomographic Microscopy," *J. Mater. Res.* **5**, 1123 (1990).
4. T. M. Breunig, S. R. Stock, J. H. Kinney, A. Guvenilir, and M. C. Nichols, "Impact of X-Ray Tomographic Microscopy on Deformation Studies of SiC/Al MMC," in *Advanced Tomographic Imaging Methods for the Analysis of Materials*, Vol. 217 (Materials Research Society, Pittsburgh, PA, 1991), p. 135.
5. M. L. Sattler, J. H. Kinney, M. C. Nichols, and R. Alani, *The Microstructures of SCS-6 and SCS-8 SiC Reinforcing Fibers*, presented at the 16th Ann. Conf. Composites and Advanced Ceramics, The American Ceramic Society, Cocoa Beach, FL, January 7–10, 1992 [see LLNL Preprint UCRL-JC-107929 (1991)].
6. X. J. Ning and P. Pirouz, "The Microstructure of SCS-6 SiC Fiber," *J. Mater. Res.* **6**, 2234 (1991).
7. R. T. Bhatt and D. R. Hull, "Microstructural and Strength Stability of CVD SiC Fibers in Argon Environment," *Ceramic Eng. Sci. Proc.* **12**, 1832 (1991).

# Determination of Absolute Transition Probabilities in Neutral Cerium

S. E. Bisson,<sup>\*</sup> F. F. Worden,  
J. G. Conway,<sup>†</sup> and  
B. Comaskev<sup>‡</sup>

*We used a 1-m Fourier transform spectrometer to obtain the cerium emission spectrum from an electrodeless discharge lamp. Branching ratios from the intensity data, combined with upper-level lifetimes measured by laser techniques, yielded weighted Einstein A values (gA values) for 30 transitions. A plot of the natural logarithm of intensity divided by gA as a function of upper-level energy gives the source excitation temperature and gA values for all lines of neutral cerium with known upper level.*

## Introduction

No transition probabilities of neutral cerium, Ce I, were reported until our recent investigation.<sup>1</sup> Of the many methods for determining transition probabilities, or Einstein *A* values, the method of Corliss and Bozman<sup>2</sup> is the most powerful for rapidly determining large numbers of *A* values from emission intensities and upper-level energies through the relation

$$I = C g A \exp(-E/k_B T) . \quad (1)$$

In this expression, *I* is transition intensity, *C* is a known proportionality constant, *g* is the statistical weight ( $2J + 1$ ) of the upper level, *E* is the upper-level energy,  $k_B$  is Boltzmann's constant, and *T* is the excitation temperature of the source. If *gA* values are known for a sufficient number of transitions over a large energy range ( $\sim 10,000 \text{ cm}^{-1}$ ), then *T* can be determined. Absolute *gA* values for other transitions can then be derived from the observed emission intensities and known upper-level energies. This method has been used by numerous investigators to obtain absolute *gA* values for the spectra of many elements.<sup>2-5</sup>

We have applied this method to determine absolute transition probabilities in Ce I. Our recently published work<sup>1</sup> appears to be the first report of Ce I transition probabilities. In this work, we also tested the use of an electrodeless discharge lamp (EDL) as the excitation source. We believe this to be the first use of this source for determining branching ratios.

The branching ratio,  $\beta_{ki}$ , is the fraction of the total intensity from an upper level *k* that goes to a specific lower level *i* and is given by

$$\beta_{ki} = \frac{I_{ki}}{\sum_n I_{kn}} . \quad (2)$$

Here,  $I_{ki}$  is the line intensity for the transition from level *k* to level *i*, and the denominator is the intensity sum of all transitions from the upper level. The branching ratio divided by the upper-level lifetime,  $\tau_k$ , yields the  $A_{ki}$  value for the transition.

## Spectra

We used the 1-m Fourier transform spectrometer (FTS) at the National Solar Observatory, Kitt Peak, AZ, to observe the cerium emission spectrum from 4000 to 27,600  $\text{cm}^{-1}$ . The FTS is well known for its excellent frequency and intensity capabilities,<sup>3-5</sup> and it observes all spectral elements simultaneously, thereby avoiding the problem of source-intensity fluctuations. We obtained the spectral response function by using a source traceable to the National Institute of Standards and Technology (calibrated tungsten-filament lamp) to obtain accurate relative intensities for calculating branching ratios. We used an EDL with 99.7%  $^{140}\text{Ce}$  because this single, even-even isotope source avoided complications caused by isotope shift and hyperfine structure.

We assigned the observed lines as Ce I transitions by comparing their frequencies (using windows of 0.01 to 0.05  $\text{cm}^{-1}$ ) with predicted frequencies generated from the known 287 odd and 686 even energy levels.<sup>6</sup> Finally, we formed branching-ratio tables from these assigned lines.

## Lifetimes

We measured lifetimes of selected upper levels by using the delayed photoionization technique,<sup>7</sup> in which a level of an atomic beam is populated by one or two pulsed lasers, and the photoionization signal is measured as a function of delay time for one or more additional photoionization lasers. A plot of the natural log of photoion signal vs delay time yields the lifetime (see Fig. 1). Reference 1 gives details of the technique, which was automated in this work.

## Results and Discussion

We measured the lifetimes of 32 levels, ranging in energy from 12,114 to 30,542  $\text{cm}^{-1}$ . Thirty of these levels yielded satisfactory branching ratios, from which we calculated  $gA$  values and plotted  $\ln(I_{ki}/1.499gA_{ki})$  vs upper-level energy  $E_k$  (see Fig. 2). We found that self-absorption influenced (i.e., decreased) many of the  $I_{ki}$  values for transitions to the ground and low-lying metastable levels. Therefore, we developed methods to detect and correct for this influence in lines emitted by the EDL.<sup>1</sup> A least-squares fit to the data plotted in Fig. 1 yields the linear relation

$$\ln(I_{ki}/1.499gA_{ki}) = 13.433 - (2.870 \times 10^{-4})E_k \quad (3)$$

**Figure 1.** Lifetime-decay data for the 18,313- $\text{cm}^{-1}$  level of cerium, obtained by delayed photoionization.

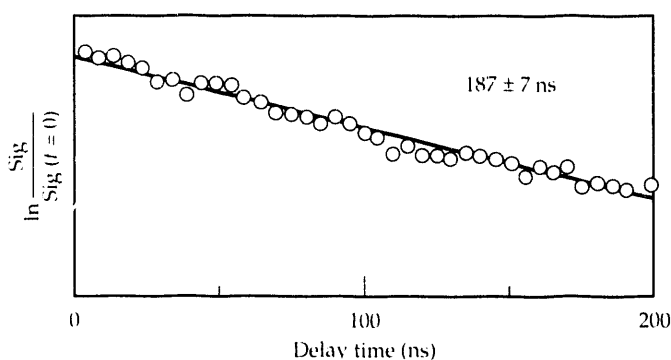
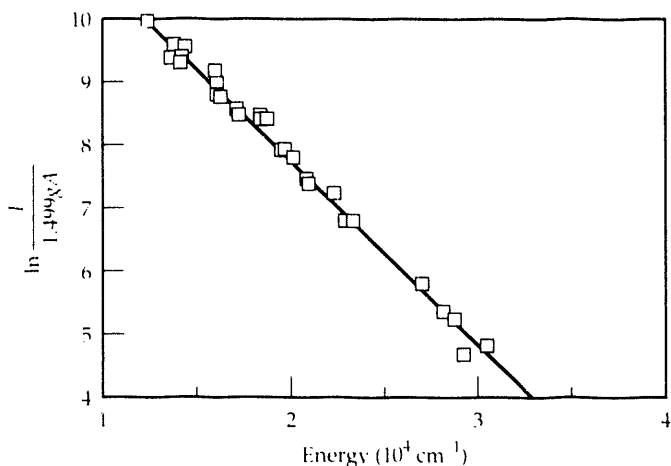


**Figure 2.** A least-squares fit to  $\ln(I/1.499gA)$  vs upper-level energy for neutral cerium yields a straight line, from which we find that the excitation temperature for the EDL is 5014  $\pm$  111 K.



The slope of this straight line is equal to  $-1/k_B T$ , where  $k_B$  is Boltzmann's constant ( $0.695 \text{ cm}^{-1}/\text{K}$ ) and  $T$  is the excitation temperature for the EDL. From this slope we get  $T = 5014 \pm 111 \text{ K}$ . The intensity  $I_{ki}$  of any transition with known upper-level energy  $E_k$  can be used in Eq. (3) to solve for  $gA_{ki}$ , the transition probability. We have observed over 5900 lines assigned to transitions in Ce I. After validity checks, we found that the intensities of all these lines could be converted to  $gA$  values by using Eq. (3).

## Conclusion

In Ref. 1, we reported 228  $gA$  values for the strongest Ce I lines emitted by an EDL in the range of 4000 to 27,600  $\text{cm}^{-1}$  (all of which were corrected for self-absorption effects). The number of lines reported was limited by the editorial policy of the journal. We have shown that an EDL may be used to obtain intensities for branching-ratio determination and for deriving transition probabilities when the source excitation temperature has been determined. Self-absorption must be recognized and corrected to obtain accurate transition probabilities.

*This work was funded by the AVLIS Program of Y Division.*

\* Current address: Sandia National Laboratories, Livermore, CA

† Lawrence Berkeley Laboratory, Berkeley, CA

‡ Laser Program, LLNL

## References

1. S. E. Bisson, E. F. Worden, J. G. Conway, B. Comaskey, J. A. D. Stockdale, and F. Nehring, "Determination of Absolute Transition Probabilities in Neutral Cerium Ions from Branching Ratios and Lifetime Measurements," *J. Opt. Soc. Am.* **B6**, 1545 (1991).
2. C. H. Corliss and W. R. Bozman, *Experimental Transition Probabilities for Spectral Lines of Seventy Elements*, U.S. National Bureau of Standards monograph 53 (U.S. GPO, Washington, DC, 1962).
3. W. Whaling and J. W. Brault, "Comprehensive Transition Probabilities in Mo I," *Phys. Scr.* **38**, 707 (1988).
4. T. R. O'Brian, M. E. Wickliffe, J. E. Lawler, W. Whaling, and J. W. Brault, "Lifetimes, Transition Probabilities, and Level Energies in Fe I," *J. Opt. Soc. Am.* **B8**, 1185 (1991).
5. J. E. Lawler and J. T. Dakin, "Absolute Transition Probabilities in Sc I and Sc II," *J. Opt. Soc. Am.* **B6**, 1457 (1989).
6. W. C. Martin, R. Zalubas, and L. Hagan, *Atomic Energy Levels—The Rare Earth Elements*, NSRDS-NBS 60 (U.S. GPO, Washington, DC, 1978).
7. L. R. Carlson, J. A. Paisner, E. F. Worden, S. A. Johnson, C. A. May, and R. W. Solarz, "Radiative Lifetimes, Absorption Cross Sections and the Observation of New High Lying Levels of  $^{238}\text{U}$  Using Multistep Laser Photoionization," *J. Opt. Soc. Am.* **66**, 846 (1976).

# New Analytical Approach for Screening and Identifying Trace Levels of Nitrogen-Containing Compounds

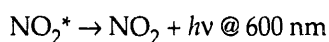
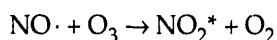
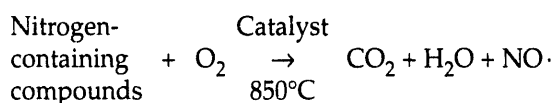
A. Alcaraz, W. H. Martin,  
and B. D. Andresen†

*We have developed a new approach for screening and identifying nitrogen-containing explosives and illicit drugs. This trace-component analysis simultaneously links capillary gas chromatography (GC) to both a thermal energy analyzer (TEA) and an ion trap mass spectrometer (ITMS). The new GC-TEA/ITMS system can screen for and identify trace levels of nitrogen-containing compounds. The TEA is a highly specific nitrogen detector that is used to locate the nitrogen-containing compounds in a total ion chromatogram (TIC). The ITMS can confirm known components and identify unknown chemicals. Both instrumental methods, when linked, have ultra-trace detection levels in the picogram range ( $10^{-12}$  g).*

## Introduction

The use of a thermal energy analyzer (TEA) as an ultrasensitive gas chromatography (GC) and liquid chromatography detector for nitrogen compounds has been demonstrated.<sup>1,2</sup> In the TEA nitrogen mode of operation, compounds are pyrolyzed with oxygen at 850°C under catalytic conditions. Pyrolysis by-products (water and carbon dioxide) are removed with a cold trap, and any nitrogen-containing compounds will remain in a transfer gas in the form of nitrosyl radicals ( $\text{NO}\cdot$ ).

The nitrosyl radical is then allowed to react with ozone under a reduced pressure, producing electronically excited  $\text{NO}_2^*$ . The  $\text{NO}_2^*$  then decays, generating a photon (chemiluminescence), which is detectable at 600 nm. The overall sequence of events in the operation of the TEA nitrogen detector is as follows:



Part of the new detection system is an ion storage device, the ion trap mass spectrometer (ITMS), that has gained wide acceptance in mass analysis of ions.<sup>3-5</sup> The capability of the ITMS to detect and identify organics at

picogram levels makes it a powerful analytical tool to link with a TEA.

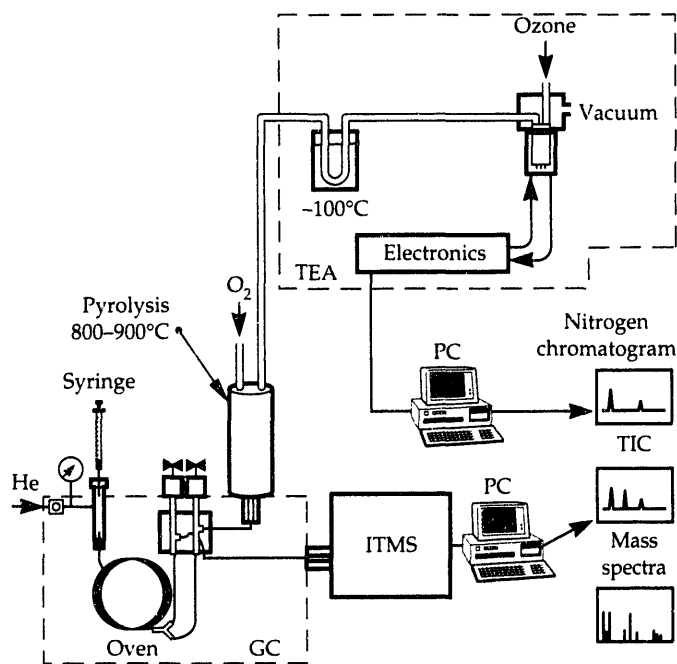
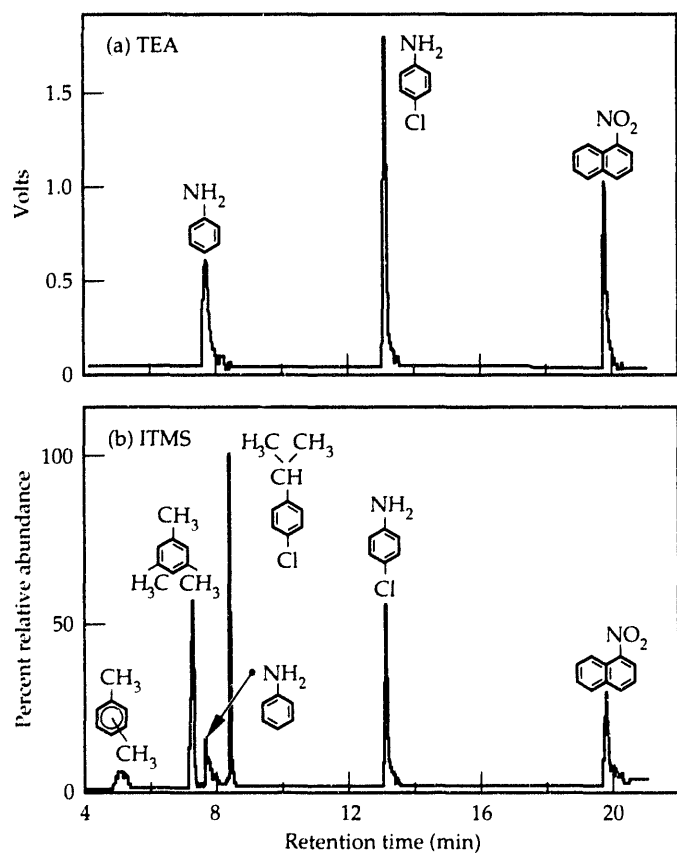
The ability to distinguish trace levels of nitrogen-containing compounds from other non-nitrogen components is a difficult task by GC/MS. Nitrogen compounds generate few diagnostic ions and often form unstable molecular ions, and their fragment ions are often misinterpreted as background.

A linked GC-TEA analysis is very useful for detecting nitrogen-containing compounds. However, because retention times are used to identify compounds by GC-TEA and several compounds may have similar retention times, the GC-TEA system cannot easily provide unambiguous identifications.

The capability of comparing a nitrogen chromatogram generated from the TEA with a total ion chromatogram (TIC) from the ITMS provides a means of screening for and identifying trace levels of nitrogen-containing compounds. In addition, mass spectral data from ITMS can be used to identify unknown species. Prior to the work described here, it was not possible to simultaneously acquire TEA and MS data. What was needed was a viable GC-TEA/ITMS interface to combine the capabilities of both instruments. We have now accomplished this goal.

## Experiment

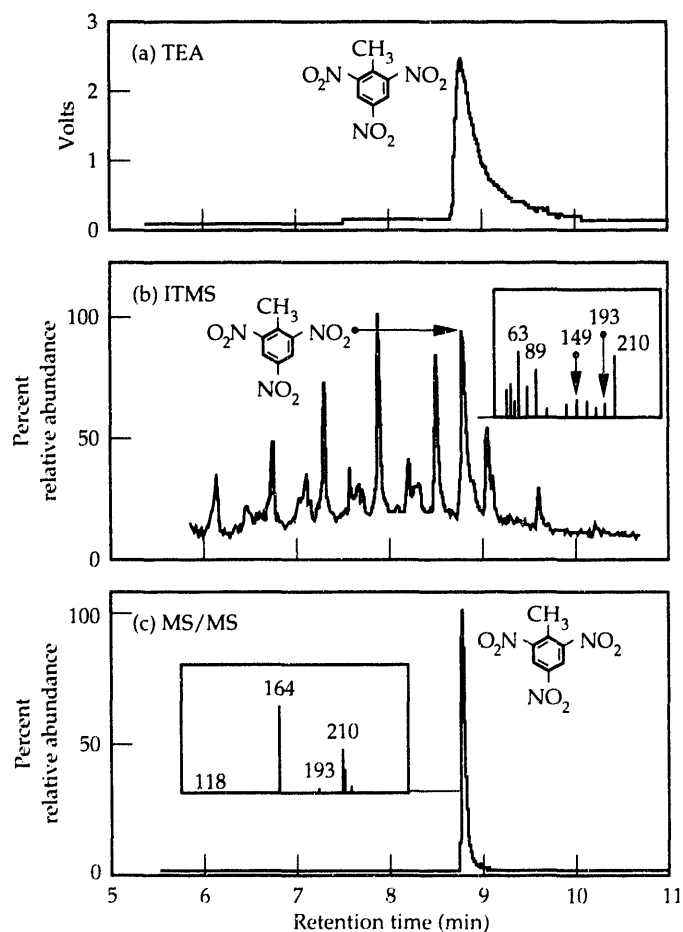
We installed the TEA pyrolyzer vertically on the GC oven box and drilled a hole through an existing GC oven to insert the pyrolyzer transfer line. At the exit of the GC

**Figure 1.** Schematic of the GC-TEA/ITMS system.**Figure 2.** GC-TEA/ITMS analysis of a standard organic mixture: (a) the GC-TEA chromatogram and (b) the GC-ITMS TIC.

capillary, we attached a glass "Y" connector with a split ratio of 1:1. We then connected the ends to two separate, low-dead-volume valves, which we placed in a specially machined heating block. A heating cartridge in the center of the heating block provided stable heating (using the alternate heater controller from the GC) during the variable temperature ranges of the GC oven. We connected the outlet of one valve to the ITMS interface (via a capillary guard column), and the other to the TEA interface. Figure 1 shows a complete schematic of the linked GC-TEA/ITMS system. The linear velocity of the GC carrier gas did not change with respect to the ITMS when the system was operating in the GC-TEA/ITMS mode. To acquire data for the TEA, we used a stand-alone personal computer. Various unique data-manipulation software programs were designed to offer the user a full range of processing options when using the new GC-TEA/ITMS system.

## Results

Figure 2 illustrates the capability of the GC-TEA/ITMS to screen for and identify nitrogen-containing compounds. Only the peak retention times of the nitrogen-containing

**Figure 3.** GC-TEA/ITMS analysis of TNT in diesel fuel and SRM of TNT: (a) GC-TEA chromatogram, (b) the GC-ITMS TIC, (c) TIC of TNT using selective reaction monitoring ( $m/z$  210 precursor ion to  $m/z$  164 product ion).

compounds from the TEA chromatogram [Fig. 2(a)] have a corresponding peak in the TICs [Fig. 2(b)]. Explosives in a complex matrix can be seen easily with GC-TEA/ITMS (see Fig. 3). Figure 3(a) demonstrates how a sample of diesel fuel was screened for explosives by use of the TEA chromatogram. The TEA response for TNT can be confirmed by locating the corresponding peak in the TIC [by retention time, Fig. 3(b)] and by extracting the mass spectrum of TNT [Fig. 3(b) inset]. Once the nitrogen compounds are identified, and if there are several samples of this type, an MS/MS scan function can be generated for exclusive identification of the target compounds.

For example, single reaction monitoring (SRM) of TNT [fragmentation of  $m/z$  210 (precursor ion) to  $m/z$  164 (product ion), see Fig. 3(c) inset] removes all superfluous peaks contributed by diesel fuel from the TIC [Fig. 3(c)]. This clearly shows the analytical power of ITMS for linked GC-TEA/MS/MS.

Another application of this new system is drug detection. Figure 4 illustrates how phencyclidine (PCP) can be detected [Fig. 4(a)] and identified [Fig. 4(b) inset] in marijuana extract. In addition to PCP, we also identified 1,3-benzothiazole, a rubber product residue. A strong 1,3-benzothiazole-TEA response [Fig. 4(a)] facilitated the location of 1,3-benzothiazole in the TIC for mass spectral identification. The use of the new GC-TEA/ITMS for drug screening shows that many other diluents and contaminants are in illicit street drugs.

We have not attempted to perform quantitative studies or optimize detection limits for specific compounds. We are now addressing these issues. Our results so far indicate that linking TEA with mass spectrometry will provide a new analytical tool for screening and identifying trace levels of nitrogen compounds.

*This work was funded by Laboratory Directed Research and Development.*

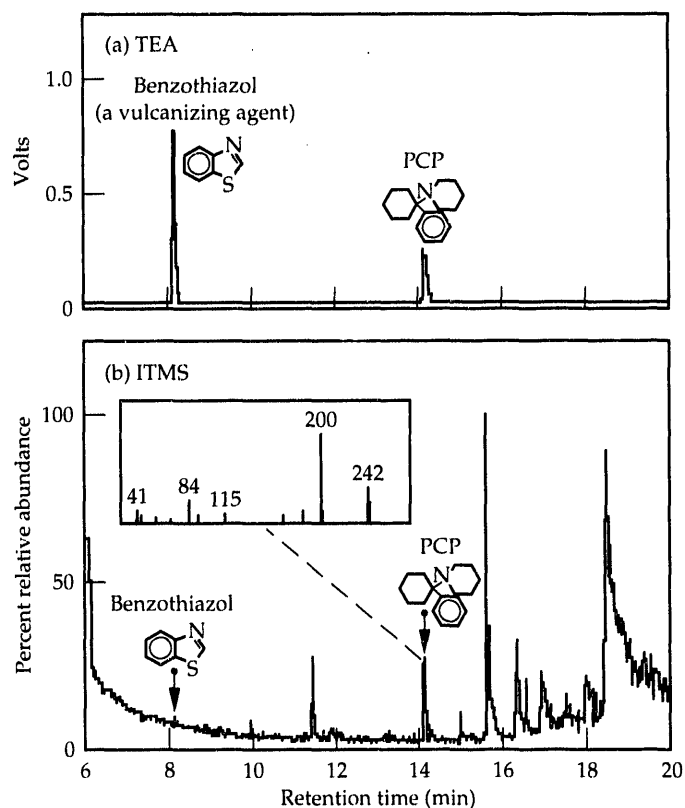
\* D-Division, LLNL

† Special Projects Division, LLNL

## References

1. A. L. Lafleur and K. M. Mills, "Trace-Level Determination of Selected Nitroaromatic Compounds by Gas Chromatography with Pyrolysis/Chemiluminescent Detection," *Anal. Chem.* **53**, 1202 (1981).
2. A. L. Lafleur and B. D. Morriseau, "Identification of Explosives at Trace Levels by High-Performance Liquid Chromatography with a Nitrosyl-Specific Detector," *Anal. Chem.* **52**, 1313 (1980).
3. J. N. Louris, R. G. Cooks, J. E. P. Syka, P. E. Kelly, and G. C. Stafford, "Instrumentation, Applications, and Energy Deposition in Quadrupole Ion-Trap Tandem Mass Spectrometry," *Anal. Chem.* **59**, 1677 (1987).
4. P. H. Dawson, Ed., *Quadrupole Mass Spectrometry And Its Applications* (Elsevier, New York, 1976).
5. R. E. March, R. J. Hughes, and J. F. J. Todd, *Quadrupole Storage Mass Spectrometry* (Wiley, New York, 1989).

**Figure 4.** GC-TEA/ITMS analysis of marijuana laced with PCP and rubber residue: (a) the GC-TEA chromatogram and (b) the GC-ITMS TIC.



# Bio-organic Molecules on Surfaces: Atomic Structure of Ordered Monolayers of Adenine on Graphite by Scanning Tunneling Microscopy and Analysis of Sperm Nuclear Volumes by Atomic Force Microscopy

W. J. Siekhaus, M. Balooch,  
R. J. Tench, R. Balhorn,  
M. J. Allen, N. V. Hud,  
C. Lee, G. Pogany,<sup>1</sup>  
and S. Subbiah<sup>1</sup>

*We have applied scanning probe microscopy to biomolecules of widely different size. On the angstrom scale, we have examined the molecular arrangements of adenine and thymine (two of the four DNA bases that comprise the genetic code) attached to the basal plane of highly oriented pyrolytic graphite. Both molecules form highly organized lattices. Images of these molecules at atomic resolution reveal that the aromatic regions are strongly detected in both molecules, whereas the various side-groups are not well resolved. These studies provide the first evidence that tunneling microscopy can be used to discriminate between purines and pyrimidines. On the micrometer scale, we have determined the volumes of individual mouse and bull sperm nuclei both dried in air and fully hydrated in a fluid cell. Sperm nuclei are shown to expand significantly upon hydration, contradicting previous serial section results by electron microscopy.*

## Introduction

Analysis of organic biomolecules at high resolution has been hampered because these molecules are stable only in their natural environment and denature in the vacuum environment required for structural analysis by electron microscopy (EM). Optical microscopy is limited in resolution. In both microscopies, three-dimensional analysis is difficult, and as a consequence, neither the *in vivo* volume nor the packing density of DNA in a sperm-head are known.

Scanning tunneling microscopy (STM) and atomic force microscopy (AFM) are particularly well suited to analyze biomolecules because they can operate in all fluids of low electrical conductivity. They provide three-dimensional information between the angstrom and the 100- $\mu\text{m}$  scales and therefore can resolve the structure of surfaces with atomic resolution and can determine the morphology of micrometer-size objects adsorbed on surfaces with high precision.

STM requires that the object under analysis conduct electrons well enough that the resistance across the object to the substrate is smaller than the resistance of the tunneling gap. Because most biological entities are bad electrical

conductors, STM analysis is restricted to biological objects of nanometer size. Here we used STM to image the bases of DNA.

On the other hand, AFM is ideally suited for analyzing larger biological molecules because it does not require the object or the substrate to be electrically conducting. It performs best when the objects are immersed in liquids. Tip-induced artifacts reduce AFM's usefulness for analyzing nanometer-size objects. Here we used AFM to determine the packing density of DNA in sperm-heads.

## Experimental Method and Results

To prepare and image adenine and thymine lattices,<sup>1</sup> we applied a 10- $\mu\text{L}$  droplet of distilled water containing 1 mg/mL of adenine or thymine to a freshly cleaved, highly oriented, pyrolytic graphite surface held at 80°C. After the droplet vaporized, we imaged the adsorbed layers in air at room temperature. To determine the adsorbate's epitaxy, we "brushed off" the adsorbate layer with the STM's tip by operating with a very low tunneling gap resistance, thus forcing the tip through the overlying adenine lattice onto the graphite surface.



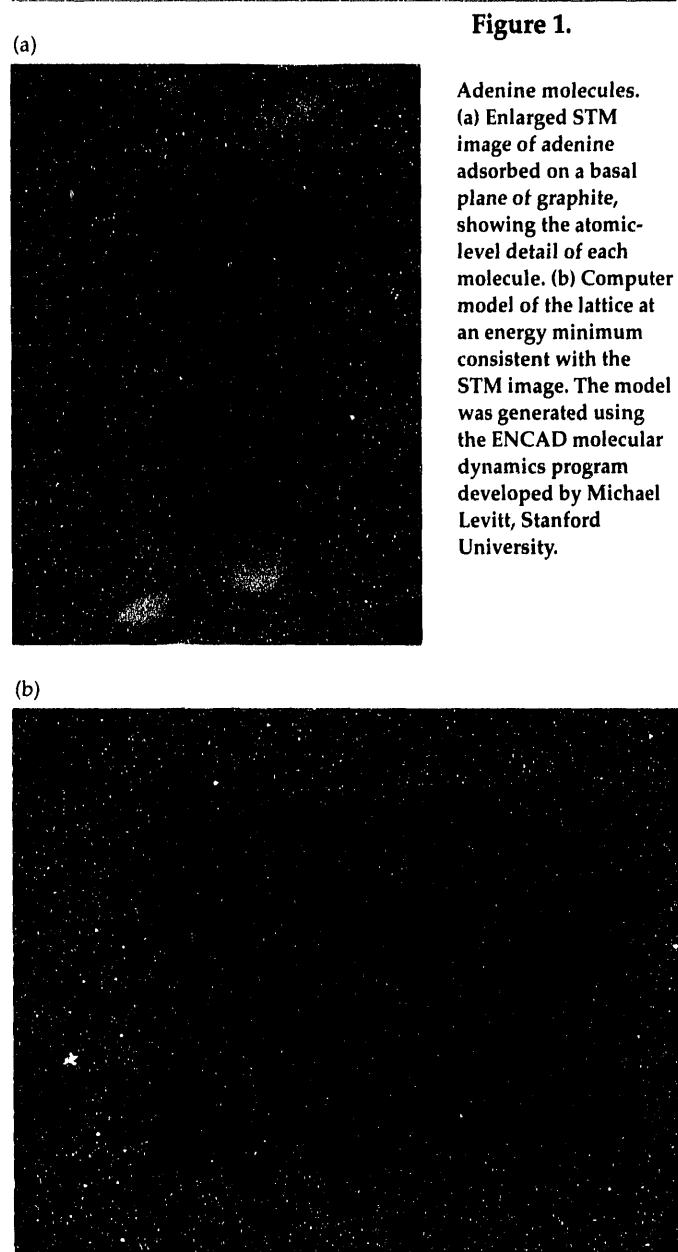
Using the program ENCAD (courtesy of Michael Levitt, Stanford University), we modeled the formation of an adenine lattice on a graphite substrate. Prior to minimization, we placed the adenine and water molecules on the graphite surface separated by distances suggested by STM measurements, and gave the water molecules random rotational orientations. The modeling program rotated and shifted the adenine molecules on the graphite lattice until the aromatic rings of adenine stacked onto the graphite in an A-B-A-B configuration. Subsequent layers of hexagonally coordinated carbon atoms stack in an A-B-A-B configuration; since the six- and five-membered rings of adenine are approximately similar in shape and size to the graphite hexagons, adenines may be expected to stack above the graphite substrate in an A-B-A-B manner. The molecules then assumed their most stable positions after several iterations of energy minimization. Both STM and modeling show that adenine lattices on graphite consist of bimolecular rows running head to tail and roughly parallel (see Fig. 1).

We measure the peak-to-peak length of each adenine molecule to be 5.4 Å [standard deviation (s.d.) = 0.9 Å] with a peak-to-peak separation of 3.2 Å (s.d. = 0.7 Å) between molecules along one monomolecular row. The average center-to-center distances between adenines in the same row (positioned head to tail) and between molecules in adjacent rows of a single bimolecular row are 8.75 Å (s.d. = 1.4 Å) and 5.8 Å (s.d. = 0.7 Å), respectively. These distances allow no room for water molecules between the purines within the row and correspond to tight van der Waals packing. Regularly spaced channels on either side of each bimolecular row appear to be imposed by water molecules bound within the lattice. The N-6 atom is the most charged atomic species of adenine and has the greatest affinity for water. Therefore, we suggest that the amino groups remain hydrated in these lattices and project out into the channels that are seen to either side of the bimolecular rows. The center-to-center distance between bimolecular rows is 22 Å (s.d. = 1.9 Å), with the proposed water channel measuring 11.3 Å (s.d. = 1.0 Å) wide. The individual aromatic rings within a single adenine molecule appear to be resolved. The peak-to-peak diameter of the larger ring is 3.1 Å (s.d. = 0.7 Å), and the smaller ring measures 2.2 Å (s.d. = 0.3 Å). These measurements agree with x-ray crystallography data on adenine hydrochloride. The amino group is not detected other than for a smear, which appears near the N-6 position in all but a few images. As with the alkylcyanobiphenyls, the hydrogen atoms are not clearly resolved.

For the structural analysis of sperm nuclei,<sup>2</sup> we briefly sonicated mouse or bull sperm to eliminate the acrosome and tails. We then prepared air-dried samples by adding a drop of diluted sperm nuclei in saline to an ethanol-cleaned coverslip and allowed the nuclei to settle and attach to the

glass for 30 min. After drying overnight, we imaged a 10,000- × 10,000-nm area containing the nuclei by AFM at minimum force (see Fig. 2). To image fully hydrated nuclei of mouse or bull sperm, we used the AFM's fluid cell. Immediately after the nuclei settled onto the glass, we injected saline solution into the cell to rinse the nuclei and began imaging.

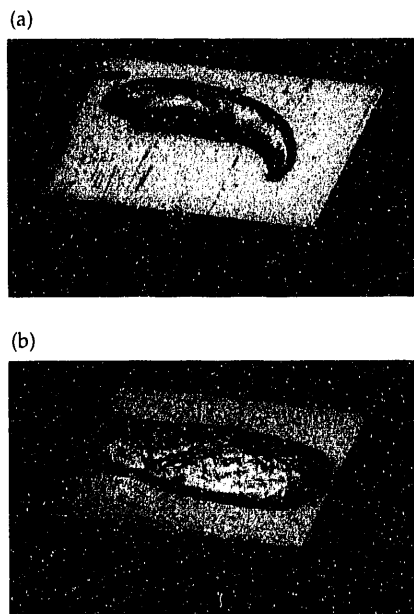
We obtained sperm chromatin particles by treating the sperm with mixed alkyltrimethylammonium bromide and dithiothreitol. The volumes of the mouse and bull sperm nuclei and chromatin particles imaged in the fluid cell



proved to be several times larger than those imaged in air. Repeated analyses performed on the same nucleus as it dehydrated in air showed that the volume of the sperm nucleus decreased dramatically as water was lost from the chromatin. Sperm nuclei also rapidly expanded when rehydrated. The results in Table 1 reveal that both mouse and bull sperm chromatin are extensively hydrated *in vivo* and provide evidence that the individual sperm chromatin fibers are not as tightly packed inside the nucleus as we previously thought.

**Figure 2.**

AFM scans of air-dried mouse (a) and bull (b) amembraneous sperm nuclei on glass, contrasting the three-dimensional morphologies of the species. The nuclei are shadowed by an artificial light source from above. The images are about  $10 \times 10\text{-}\mu\text{m}$  and are scaled proportionally in height.



## Summary

By using scanning probe microscopy to determine the epitaxy of DNA bases on graphite and the packing density of DNA in sperm nuclei, we demonstrated that STM in air clarifies how organic biomolecules bond to surfaces and that AFM may revitalize research in structural biology.

*This work was funded by Laboratory Directed Research and Development and by the DOE Biological and Environmental Research Program.*

## References

1. M. J. Allen, M. Balooch, S. Subbiah, R. J. Tench, W. Siekhaus, and R. Balhorn, "Scanning Tunneling Microscope Images of Adenine and Thymine at Atomic Resolution," *Scanning Microsc.* (1992), in press.
2. M. J. Allen, N. V. Hud, C. Lee, G. Pogany, W. J. Siekhaus, and R. Balhorn, "Analysis of Sperm Nuclear Volumes and Extent of Chromatin Compaction by Atomic Force Microscopy," *J. Cell Biol.* 50a, 115 (1991).

**Table 1.** Comparison of sperm volumes measured in dry and hydrated states by AFM and in dry state by serial section electron microscopy.

State	Volume ( $\mu\text{m}^3$ )	
	Mouse	Bull
Serial section EM	$4.01 \pm 0.03$	—
Sonicated (dry)	$5.88 \pm 0.28$	$7.67 \pm 0.30$
Dry	$6.26 \pm 0.23$	$7.65 \pm 0.32$
Sonicated (hydrated)	—	$18.03 \pm 2.54$

\*LLNL Biomedical Sciences Division

†Department of Biological Sciences, Northern Arizona University, Flagstaff

‡Department of Cell Biology, Stanford University, Stanford, CA

---

## Overview

In this section, we describe two major new facilities and some changes in the Department's institutional structure.

As laser technology has advanced to systems of shorter and shorter pulse width (into the femtosecond regime), time-resolved studies of condensed-phase energy transfer, chemical-reaction dynamics, and structural phase transitions have become possible. The new femtosecond system now undergoing initial trials will be used first to study shock sensitivity in energetic materials.

Modern materials science uses ion beams for a variety of synthesis and processing purposes: to implant ions, modify surfaces and internal layers, amorphize crystalline structures, and otherwise cause or produce nonequilibrium systems. Ion beams are also used to analyze and characterize materials by such standard methods as Rutherford backscattering and particle-induced x-ray emission. The advent of a versatile new accelerator capable of maintaining 4 MV on the terminal makes possible a variety of beams with energies up to 4 MeV times the charge on the accelerated ion.

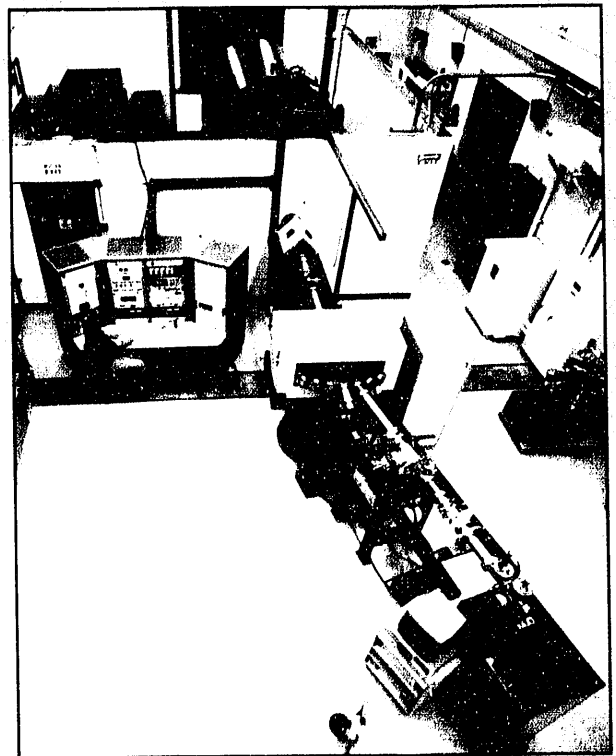
When the Department decided in 1987 to begin a major new program in high-transition-temperature superconductivity, it was immediately clear that the Laboratory would have neither the experienced staff nor suitable major equipment at adequate levels to mount a serious effort for several years. Fortunately, the Physics Department at the University of California at Davis had recently hired a new chairman, Robert N. Shelton, a solid-state physicist with interests and experience in superconductivity. A collaboration between LLNL and UCD was immediately seen to be advantageous to both parties. The current status of the collaboration is reported here.

As the original workers from the Manhattan Project era retire, one of the areas in which scientific personnel are disappearing is heavy-element science—the science and technology of the elements beyond actinium. LLNL has taken the lead to reverse this trend by providing opportunities for education and training of the next generation of heavy-element scientists. The vehicle selected to achieve these goals is an institute based in Livermore and cosponsored by Lawrence Berkeley Laboratory and the University of California at Berkeley.

---

Section 10

**Facilities and  
Instrumentation**



Overview of the 4-MV  
accelerator system.

# Applications of Ultrashort-Pulse Laser Technology to Materials Characterization and Investigations of Condensed-Phase Energy-Transfer Dynamics

A. J. Ruggiero

*New high-repetition-rate, high-power, femtosecond-pulse laser technology is being implemented in the study of condensed-phase energy-transfer dynamics. Uses of the new system include (1) precise determination of vibrational lifetimes and dephasing rates in energetic materials and (2) studies of phonon-mediated energy-transfer dynamics in aerogels.*

## Introduction

Our understanding of physical and chemical phenomena is advancing with the development of new optical sources and spectroscopic techniques. Several recent developments in ultrashort-pulse laser technology have removed the technical limitations to the routine generation of amplified optical pulses with durations under 100 fs. Consequently, a wide variety of experimental investigations have become feasible for the first time. The emphasis in experimental, time-resolved spectroscopy has shifted from issues regarding time resolution to the search for appropriate light-matter interactions to initiate and observe dynamical phenomena of interest. The use of optical pulses that have times shorter than those required for most nuclear motions—including collective vibrational modes, molecular orientational motion, intermolecular collisions, and intramolecular vibrations—has made possible the “impulsive” generation and direct observation of individual cycles of vibrational motion and associated relaxational phenomena.<sup>1</sup> Time-domain analogs of conventional frequency-domain spectroscopic techniques have emerged.<sup>2</sup> In addition, the prospect exists for direct time-resolved observation of events of chemical and physical interest (e.g., condensed-phase energy transfer, chemical-reaction dynamics, and structural phase transitions) with unprecedented detail.

## Shock Sensitivity of Energetic Materials

Minimizing the shock sensitivity of homogeneous energetic materials while maximizing their performance is a major goal of the energetic-materials community. Although the general performance of explosives and propellants can be satisfactorily understood by means of a macroscopic hydrodynamic picture, the difficult problem of shock sensitivity

and molecular reactivity must be interpreted microscopically. This solution includes a comprehensive microscopic theory of sensitivity that can accurately predict materials properties and lead to a molecular-engineering approach to the synthesis of energetic materials.

To understand the molecular basis of condensed-phase shock sensitivity and shock-induced chemical reaction, we first must identify intrinsic material properties that can be precisely determined and correlated with molecular structure and reactivity. A reasonable approach is to focus attention on the fundamental material excitations that are directly involved in the inter-to-intramolecular energy transfer that precedes shock-induced reaction (i.e., the dynamics and interactions of the phonons and vibrons in the system). Phonon and vibron dynamics can be quantified by their experimentally determined energy and phase-relaxation times. These system-specific dynamic quantities are governed by the anharmonic phonon-phonon and phonon-vibron coupling terms.<sup>3,4</sup> These terms describe the material's intermolecular potential energy surface and consequently provide a direct link to molecular structure.

Intra- and intermolecular vibrational energy redistribution and relaxation in condensed phases occur on picosecond and subpicosecond time scales. The material excitations relevant to the problem of shock sensitivity involve energies in the 10- to 400-cm<sup>-1</sup> (THz) range. Characterization of these relatively low-frequency vibrational modes in the time domain by using recently developed femtosecond spectroscopic techniques provides a convenient means of obtaining information on both energy and phase relaxation, as well as the specific details regarding the coupling of different material modes. Time-resolved coherent Raman or infrared spectroscopy provides experimental information on the lifetimes of optically active phonons and vibrons in the time domain. The experimental results are then interpreted in terms of many-body perturbation techniques<sup>5</sup> or

molecular dynamics (MD) simulation.<sup>6–8</sup> The latter is particularly useful for the types of large organic molecules that constitute most energetic materials of interest. Because the technique does not use any perturbative expansion, it incorporates the full anharmonicity of the potential used and does not truncate higher-order terms. The method directly furnishes space- and time-correlation functions of the dynamical variables that are the spectroscopic quantities of interest. Analysis of the appropriate correlation functions permits a direct comparison with experimental time-domain data.

The coupling of diamond anvil cell (DAC) technology with femtosecond time-resolved spectroscopy is a logical and powerful tool for studying condensed-phase dynamics in energetic materials. It enables material-specific dynamic parameters to be probed at temperatures and pressures approaching those found in a shock wave. Pressure-induced changes in the experimentally measured femtosecond coherent Raman decays can be correlated with pressure-induced anharmonicities in the intermolecular potential energy function. This correlation will allow us to determine the accuracy of the phenomenological atom–atom potential functions used in the MD simulations and to assess the necessity of including higher order electrostatic interactions. Exploring the temperature dependence of the experimentally determined quantities at a given pressure will permit us to evaluate the contributions of different relaxation mechanisms such as stimulated phonon emission and absorption.

### Thermal Conduction in Aerogels

The characterization of the fundamental mechanisms and structural parameters responsible for the thermal and acoustic properties of aerogels relates to this area of interest. With time-domain impulsive stimulated light scattering and femtosecond pump/probe spectroscopy, we can examine coherent optical and acoustic phonon dynamics in pure aerogels and relaxational phenomena involving non-equilibrium incoherent phonon populations in doped aerogels. Optical generation and detection of acoustic phonons by means of time-domain impulsive stimulated Brillouin scattering (ISBS) permit direct determination of acoustic velocities, acoustic attenuations, temperature coefficients of the acoustic velocity, and photoelastic constants.<sup>2</sup> In general, any acoustic mode that the material can support—pure shear, quasi-shear, quasi-longitudinal, and pure longitudinal—can be selectively generated and detected. Acoustic frequencies can be tuned continuously from 3 MHz to 1 THz by using this technique. Traditional ultrasonic methods permit efficient study of acoustic vibrations in solids only up to about 10 GHz. The ISBS technique allows access to

the higher frequencies up to the zone boundary frequencies of the acoustic branches in the THz range.

Acoustic phonons at these frequencies play an important role in the thermal properties of materials. The main source of information on the kinetics of phonons outside the conventional ultrasonic region is thermal conduction data, which yield only averages related to all phonons excited at a given temperature. Both spectral and temporal information about the phonon distribution can be obtained by using ISBS.

Higher-frequency–optic phonon dynamics in aerogels can be characterized through femtosecond time-resolved measurements of energy and phase relaxation by using impulsive stimulated Raman scattering (ISRS).<sup>1,2</sup> The relaxation of incoherent phonons detected by transient Raman spectroscopy after optical excitation of impurity centers (dopants) provides another microscopic probe of aerogel structure and properties. Local heat dissipation over molecular-length scales can be investigated in this manner. The correlation of synthetically modified aerogel structures with time-domain spectroscopic studies of phonon properties should provide a powerful approach to the detailed understanding of these materials.

The key to successfully implementing the previously outlined experimental approaches is the amplified femtosecond laser system currently under development. This system uses an ultrafast optical technology that is custom designed and optimized for use in condensed-phase spectroscopic investigations. The amplified femtosecond-pulse source for this work is based on a recently developed and demonstrated high-repetition-rate (100-kHz) solid-state regenerative amplifier and pulse-compression technology.<sup>9,10</sup> The unique high pulse-repetition rate of this system allows operation in a regime where an ideal compromise can be achieved between the peak powers necessary to enhance desired nonlinear optical processes and the ability to exploit high-repetition-rate signal averaging and multiple modulation techniques. This compromise is particularly important for the nondestructive spectral characterization of energetic materials in the DAC, where small sample volumes require focused laser beams and a delicate balance exists between optical damage and an acceptable experimental signal-to-noise ratio. Tunability in terms of wavelength, pulsewidth, and pulse repetition rate are intrinsic aspects of the type of broadband, high-repetition-rate, high-energy system design being implemented. Spectral tunability from the ultraviolet to the infrared will be possible via a combination of femtosecond continuum generation, harmonic generation, and optical mixing. Amplified pulse-sequence generation (via spectral windowing and/or interferometric addition) will also be feasible.

## Summary

We are in the process of developing a unique spectroscopic resource at LLNL based on recently developed and demonstrated short-pulse technologies. The system is ideally suited for time-resolved studies of condensed phases. Combined theory and experiment are expected to increase our understanding of energy transfer in energetic materials and aerogels and impact other fundamental areas of research involving phonon-mediated processes.

*This work was funded by Weapons-Supporting Research.*

## References

1. K. A. Nelson and E. P. Ippen, "Femtosecond Coherent Spectroscopy," *Adv. Chem. Phys.* **75**, 1 (1989) and references therein.
2. Y. X. Yan, L. T. Cheng, and K. A. Nelson, "Impulsive Stimulated Light Scattering," Ch. 7, *Advances in Nonlinear Spectroscopy*, R. J. H. Clark and R. E. Hester, Eds. (Wiley, New York, 1987), p. 299.
3. J. R. Hill, E. L. Chronister, T. C. Chang, H. Kim, J. C. Postlewaite, and D. D. Dlott, "Vibrational Relaxation and Vibrational Cooling in Low Temperature Molecular Crystals," *J. Chem. Phys.* **88**, 949 (1988).
4. S. Velsko and R. M. Hochstrasser, "Studies of Vibrational Relaxation in Low Temperature Molecular Crystals," *J. Phys. Chem.* **89**, 2240 (1985).
5. S. Califano, V. Schettino, and N. Neto, "Lattice dynamics of Molecular Crystals," *Lecture Notes in Chemistry*, Vol 16 (Springer, Berlin, 1981).
6. G. Cardini, R. Righini, and S. Califano, "Computer Simulation of the Dynamics of the Plastic Phase of Succinonitrile," *J. Chem. Phys.* **95**, 679 (1991).
7. J. M. Dickey and A. Paskin, "Computer Simulation of the Lattice Dynamics of Solids," *Phys. Rev.* **188**, 1407 (1969).
8. P. Procacci, G. Cardini, R. Righini, and S. Califano, "Anharmonic Lattice Dynamics and Computer Simulation for Simple Model Systems," *Phys. Rev. B* **45**, 2113 (1992).
9. A. J. Ruggiero, N. F. Scherer, G. M. Mitchell, and G. R. Fleming, "Regenerative Amplification of Picosecond Pulses in Nd:YAG at Repetition Rates in the 100 kHz Range," *J. Opt. Soc. Am. B* **8**, 2061 (1991).
10. A. J. Ruggiero, N. F. Scherer, and G. R. Fleming, "100-kHz Synchronous Amplification of 50-Femtosecond Optical Pulses and White Light Continuum Generation," *Opt. Lett.*, submitted.

# 4-MV Ion-Accelerator System for Materials Studies

R. G. Musket

*With the addition of a 4-MV ion-accelerator system, we have enhanced the Laboratory's capabilities for characterizing and modifying materials. This system generates MeV ions that can be used to perform quantitative, nondestructive analysis of materials by four ion-beam techniques: ion backscattering, particle-induced x-ray emission, ion-induced nuclear-reaction analysis, and forward-recoil spectroscopy. In addition, we can modify materials by using high-energy ion implantation and irradiation.*

## Introduction

We recently purchased and installed a 4-MV ion-accelerator system that is dedicated to the characterization and modification of materials. With this system, we can meet increasingly stringent materials requirements for weapons research and other Laboratory programs. In this article, we describe the system, present some basic concepts of ion-material interactions, summarize the four major techniques used in the ion-beam analysis of materials, discuss an example of ion-beam characterization of a material, and outline ion-beam modification procedures.<sup>1</sup>

## Description of 4-MV Ion-Accelerator System

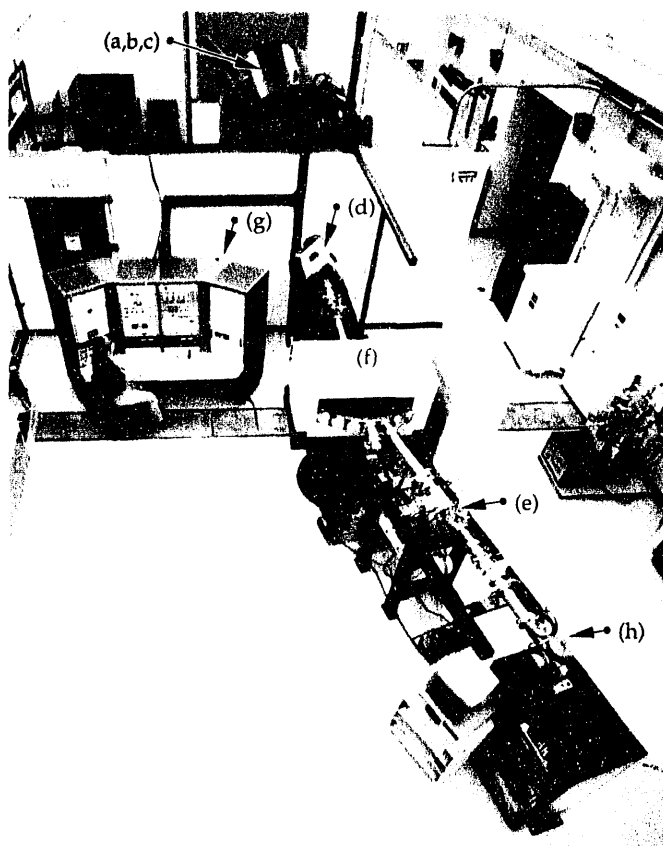
The present system with the main analytical beam line (see Fig. 1) consists of (a) the 4-MV, single-ended ion accelerator that relies on a pelletron chain for charging, (b) the tank containing the SF<sub>6</sub> insulating gas, (c) a cold-cathode ion source located at the high-voltage terminal potential, (d) a magnetic quadrupole focusing unit, (e) various beam diagnostic and feedback units, (f) an analyzing magnet with a chamber to permit selection of the ion to be sent to the specified end station, (g) a control console, and (h) the present, small analytical end station.

The cold-cathode source can produce ions from any gas. For example, the accelerator can deliver more than 10  $\mu$ A of analyzed hydrogen, helium, or argon ions and more than 1  $\mu$ A of doubly charged nitrogen ions to the analytical end station. The existing analytical end station will soon be replaced with a larger, more versatile, automated end station. The analyzing magnet has a mass-energy product of at least 500 MeV amu, which means that 3.8-MeV xenon ions can be deflected into the  $\pm 15^\circ$  beamlines. The chamber in the analyzing magnet can accommodate as many as six analyzed beamlines at  $\pm 15$ , 30, and 45°. The other five beamlines will be installed in the future as programmatic and research needs dictate. A beamline for ion-beam modification of materials, including a rastering capability, will be installed on the other 15° direction to permit implantations and irradiations.

## Ion-Material Interactions

After monoenergetic ions with energies between 0.4 and 8 MeV enter a material, they begin to slow down as a result of scattering with electrons and with the atomic nuclei. The number of ions is preserved at any depth associated with the straight-line part of the trajectory, which is related to the region where interactions with electrons dominate. However, ion energies decrease slowly and

**Figure 1.** Overview of the 4-MV accelerator system. See text for explanation of the callouts. In this photo, Steve Holmes monitors the 4-MV accelerator during an experiment.





spread increasingly about the average as a result of interactions with the electrons. Because the directed ion flux (ions/cm<sup>2</sup>/s) can be specified throughout the straight-line path, meaningful material characterizations over this depth can be obtained directly from the known cross sections of rare ion-atom interactions and the well-documented values of  $dE/dx$ , the energy loss per unit depth. These values provide a “window” into the material by virtue of the nearly linear relationship between ion energy loss and the amount of material traversed. This relationship forms the basis for using MeV ions to analyze a material as a function of depth.

### Ion-Beam Analysis

Ions with energies between 0.4 and 8 MeV are well suited to probing materials using four major quantitative, nondestructive techniques: ion backscattering (BS), particle-induced x-ray emission (PIXE), ion-induced nuclear reaction analysis (NRA), and forward-recoil spectroscopy (FRS). Ion-beam analyses are quantitative because the cross sections for the interactions of the ions with the atoms in the materials are either well known or can be determined by using known standards. By judiciously selecting the ion species, its incident energy, and the specific ion-beam technique, we can tailor the analysis for each element in the periodic table. One or more of these techniques can provide detection sensitivities for various elements of about 10<sup>-3</sup> monolayer (about 10<sup>12</sup> atoms/cm<sup>2</sup>) for surface layers, or less than one atomic part per million (appm) for bulk levels.

All four techniques rely on interactions between the ion and the target atom that occur only when the two particles come within about 0.01 nm—a very small distance compared with the typical interatomic spacing in solids (0.3 nm). A combination of one of these close-encounter analysis techniques together with channeling of ions through the open directions (axial or planar channels) of monocrystalline materials can be used to determine the location of impurity atoms in either interstitial or substitutional sites or to assess the extent of lattice imperfections in the near-surface region.<sup>2</sup>

In ion BS spectrometry,<sup>3</sup> the energies of ions elastically scattered back from nuclei in the sample are measured. Simple Coulombic or **Rutherford backscattering (RBS)** using helium ions and protons has proven to be most generally useful. Interpretation of the BS spectra yields information about both the mass and the depth distribution of the elemental constituents of the specimen with a depth resolution of about 30 nm for energy-dispersive detectors.

**PIXE**, which is characteristic of the atomic species in the bombarded target, results from inner-shell ionizations. PIXE and RBS are well matched as complementary techniques

because, for a given ion energy, the x-ray production cross section decreases dramatically with the atomic number ( $Z$ ) of the target atoms (e.g.,  $\sim 1/Z^8$  for K-shell x-ray production), whereas the Rutherford cross section increases as the square of the atomic number ( $Z^2$ ). In addition, PIXE provides a clear distinction between atoms with similar atomic numbers, but RBS does not always yield an unambiguous identification for high- $Z$  atoms.<sup>4</sup>

Ion-induced nuclear reactions can emit prompt products (such as ions and/or gamma rays) that are uniquely related to the nuclei of the reacting particles (the incident ions and the target atoms). Thus, **NRA** consists of energy spectrometry of the reaction products and yields an unambiguous identification of the reacting nuclei. The reaction cross sections of many ion-induced nuclear reactions have sharp resonances as a function of ion energy. If these resonances have a narrow energy width and are well separated in energy, then depth profiling can be performed by starting with the ion energy that places the resonance reaction at the surface. Then, as the energy of the ion is increased, the resonance occurs at increasingly greater depths in the sample. Because the reaction yield at each depth is proportional to the concentration of the isotope of interest, the isotopic depth distribution can be determined from the known energy loss of the ion in the material.

When the mass of the incident particle is equal to or greater than the mass of the target atom, elastic BS cannot occur. However, a large part of the incident ion energy can be transferred to the lighter target atom, which then recoils into a forward angle. In **FRS**, energy spectrometry of these elastically recoiled atoms yields the initial depth distributions of the recoiled atoms. Generally, the incident ion and the detected recoiled atom have paths at small angles (<30°) with the surface of thick specimens. Thin, freestanding foils are an exception because the recoiled atoms can escape through the foil to a detector.

### Ion-Beam Materials Characterization

During the 1980s, we used MeV ions from a 3-MV accelerator, which no longer exists, to characterize materials for a variety of LLNL projects. The applications included analysis of thin foils<sup>5,6</sup>; coatings; interfaces related to bonding and adhesion failures; polishing damage on the surface of crystals; ion-, electron-, and laser-modified materials; and materials after they had reacted with gases.<sup>7,8</sup>

A representative example of these analyses is shown in Fig. 2. We determined the composition and thickness of a free-standing, deposited carbon foil by simultaneous RBS and PIXE using 2-MeV helium ions.<sup>6</sup> Although most of the ions passed through the thin foil, a very small fraction of them were backscattered through an angle of 168° to the energy-dispersive detector. In the backscattering spectrum

shown in Fig. 2, the subscripts "T" and "B" refer to the energy position for helium scattered from the indicated element at the top or base of the foil, as originally deposited on a substrate. The corresponding PIXE spectrum revealed peaks for C(K), O(K), Si(K), Ar(K), Fe(L), and Cu(L) x rays. Knowing which elements were present removed uncertainties related to the interpretation of the RBS results, which showed that contamination by oxygen (1.6 at.%), argon (0.2 at.%), iron (0.5 at.%) and copper (0.6 at.%) existed uniformly throughout the entire foil thickness. In contrast, silicon inside the foil near the center caused a very small BS peak. We made a quantitative evaluation of the carbon-atom areal density ( $4.62 \times 10^{18}$  carbon atoms/cm<sup>2</sup> or 92.0  $\mu\text{g}$  carbon/cm<sup>2</sup>) and of the amounts of the impurities, assuming that the stopping matrix was pure carbon. Taking 2.0 g/cm<sup>3</sup> as the density of the deposited carbon converts the areal density obtained by RBS to a thickness of 460 nm.

### Ion-Beam Modification

High-energy ion-beam modification of materials can be divided into two distinctive classes: implantation and irradiation. Although essentially all of the ions become implanted in both classes, implantation includes procedures for which the implanted layer is the desired end effect. Examples of implantation applications are calibration standards for analysis techniques and other experiments, low-concentration doping, synthesis of compounds or alloys, and formation of subsurface elemental layers.

Irradiation includes processes in which the important features are the interactions of the ions with the material before they come to rest. Two examples are "mixing" and

"stitching" at interfaces. Passage of ions through interfaces between dissimilar materials can lead to the formation of interfacial alloys or compounds. This results from atomic intermixing caused by collision cascades and radiation-enhanced diffusion. In addition, mixing and stitching can be used to enhance the adherence of a coating to a substrate as ions are passed through the interface. The term "mixing" generally describes this enhancement phenomenon when the dominant energy deposition process at the interface leads to atomic displacements, because significant atomic exchange across the interface is expected. When electronic excitation dominates, very little atomic exchange occurs between the coating and the substrate; however, the electronic bonding configurations across the interface are modified, and "stitching" may occur.

### Summary

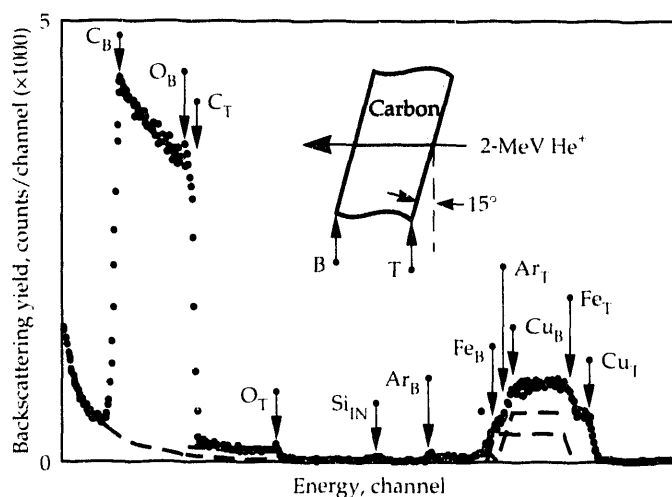
The quantitative, nondestructive nature of the major ion-beam analysis techniques accessible with our new 4-MV accelerator system should continue to prove invaluable for resolving a variety of materials questions. In addition, MeV ion implantations and irradiations hold promise for developing new materials.

*This work was supported jointly by Defense Sciences and by Weapons-Supporting Research.*

### References

1. R. G. Musket, "Using MeV Ions to Characterize and Modify Materials," *Energy and Technology Review*, Lawrence Livermore National Laboratory, Livermore, CA, UCRL-52000-90-10 (1990), p. 26.
2. L. C. Feldman, J. W. Mayer, and S. T. Picraux, *Materials Analysis by Ion Channeling* (Academic Press, New York, 1982).
3. W.-K. Chu, J. W. Mayer, and M. A. Nicolet, *Backscattering Spectrometry* (Academic Press, New York, 1978).
4. R. G. Musket, "Applications of Simultaneous Ion Backscattering and Ion-Induced X-Ray Emission," *Nucl. Instrum. Meth.* **218**, 420 (1983).
5. R. G. Musket, "Analysis of Oxygen on and in Beryllium Using 2-MeV Helium Ions," *Nucl. Instrum. Meth.* **B24/25**, 698 (1987).
6. R. G. Musket, "Composition and Thickness of Multilayer Foils Using MeV Ion-Beam Techniques," *Proc. SPIE*, **911**, 177 (1988).
7. E. N. Kaufmann, R. G. Musket, C. A. Colmenares, and B. R. Appleton, "Enhancement of Uranium Oxidation Resistance by Molybdenum Implantation," in *Mater. Res. Soc. Symp. Proc.* **27** (1984), p. 747.
8. E. N. Kaufmann, R. G. Musket, J. J. Truhan, K. S. Grabowski, C. R. Gossett, and I. L. Singer, "High-Temperature Oxidation of Ion-Implanted Tantalum," *Nucl. Instrum. Meth.* **209/210**, 953 (1983).

**Figure 2.** Helium-ion backscattering spectrum for free-standing, 460-nm-thick carbon foil.



# LLNL/UC Davis High- $T_c$ Collaboration: Highlights of the University Program

R. N. Shelton\*

*LLNL and UC Davis have completed the third year of a collaborative research program that focuses on high-temperature, superconducting materials. Emphasizing experimental work, individual projects have covered the spectrum from investigations of the intrinsic origins of high- $T_c$  superconductivity to experiments with a strong orientation toward applications and device fabrication.*

## Introduction

For the past three years, LLNL and the University of California, Davis have collaborated on research on high-temperature, superconducting materials. Collaborators have included senior investigators and postdoctoral researchers from both institutions and UC Davis graduate students. Some collaborators have been experimentalists, others theorists. Experimental facilities were used at the two institutions in complementary ways because neither institution is fully equipped for a broadly based research program in high-temperature superconductivity.

## Doctoral Program

Through direct sponsorship provided by this program, two students have completed their doctorates. They are continuing their careers as a research physicist and as a postdoctoral researcher at major universities. Two other graduate students will finish their doctorates this academic year. This rapid graduation rate is made possible through the high-quality research program sponsored by LLNL. Through this support, we can attract top-quality students to work on important research projects that lead to publications and conference participation. The high visibility of these projects results in postdoctoral opportunities for these students.

## Productivity

In addition to student support and the accompanying benefits to this collaborative research program, the numerous publications sponsored by this program manifest its overall productivity. Since its inception, the program has produced 26 collaborative publications in refereed journals. Additional conference proceedings, invited and contributed talks, and institutional seminars based on this

program are too numerous to itemize. Eighteen publications appeared in FY90–91 alone.<sup>1–18</sup> The research leading to this exceptional productivity is described according to the materials under study.

## Single-Crystal Research

The exceptional ability of our research collaboration to produce the highest quality single crystals of multinary oxides gives us a competitive edge in experimental studies. This single-crystal capability has enabled us to perform unique, leading-edge experiments on  $\text{YBa}_2\text{Cu}_3\text{O}_{7-x}$  (YBCO) and on crystals derived from YBCO via substitutional methods. For YBCO, a recent article in *Physical Review Letters* presented our analysis of twin boundary effects on magnetic vortex motion. In the same prestigious journal, we reported the first direct experimental determination of the Fermi surface in YBCO. Overall, our program has contributed fundamentally to the understanding of the flux creep mechanism and the role of anisotropy in this material.

Using our crystal-growth capabilities, we completed the first series of experiments on two sets of doped YBCO crystals. The complex and controversial system of praseodymium-doped YBCO required single-crystal studies to complement earlier polycrystalline work. In a project related to the effect of twin boundaries on the superconducting properties, we successfully doped iron into YBCO and determined the interactive effects of the magnetic iron ions and the changing twin boundary spacing.

Our collaborative program extends beyond YBCO and derivative systems. Recent published work includes single-crystal studies on systems as diverse as  $\text{Tl-Ba-Ca-Cu-O}$  (which includes the current world record  $T_c = 125$  K material),  $\text{Bi-Sr-Ca-Cu-O}$ , and the electron-based superconductors  $\text{Nd}_{2-x}\text{Ce}_x\text{CuO}_{4-y}$ . In the bismuth system, we extended the most recent theoretical model to obtain a complete picture of the phenomenon of magnetic relaxation. Previous work had treated only selected regions of the field–temperature–time parameter space. Our new method of crystal growth

for the electron-based materials led to collaborative research on the electronic structure. The role of electron doping by cerium (and thorium) into the neodymium site was determined through x-ray absorption studies.

## Summary

The LLNL/UC Davis collaborative research program in high- $T_c$  superconductivity has shown exceptional productivity. The rate of publication in the highest quality journals attests to the importance of the topics selected for study. Strong student participation has developed young scientists who are now contributing independently to the interdisciplinary field of materials physics. Through this interactive, multidisciplinary approach to research, we have created a team of scientists with expertise across the broad range of experimental physics, chemistry, and materials science. The effect of this team approach to research extends beyond the specific program focus of high-temperature superconductivity. Details of some of these projects are given elsewhere in this *Report*.

*This work was funded by Weapons-Supporting Research.*

\* University of California, Davis

## References

1. K. F. McCarty, J. Z. Liu, R. N. Shelton, and H. B. Radousky, "Electronic Raman Scattering of  $\text{YBa}_2\text{Cu}_3\text{O}_7$  Using C-Axis Polarization—Evidence for Two Characteristic Superconducting Energies," *Phys. Rev. B* **42**, 9973 (1990).
2. Z. Tan, J. I. Budnick, J. L. Peng, L. Zhang, and R. N. Shelton, "X-Ray Absorption Studies of Atomic and Electronic Structures of  $\text{Nd}_{2-x}\text{M}_x\text{CuO}_4$  ( $M=\text{Ce}$  and  $\text{Th}$ )," *Physica* **B163**, 13 (1990).
3. J. Z. Liu, Y. X. Jia, P. Klavins, R. N. Shelton, J. Downey, and D. J. Lam, "Preparation and Magnetic Measurements of Single Crystal  $\text{Tl}_2\text{BaCaCu}_2\text{O}_8$ ," *J. Cryst. Growth* **109**, 436 (1990).
4. N. E. Phillips, R. A. Fisher, R. Caspary, A. Amato, H. B. Radousky, J. L. Peng, L. Zhang, and R. N. Shelton, "Magnetic Ordering, Hyperfine, and 'Linear' Contributions to the Low-Temperature Specific Heat of  $(\text{Y}_{1-x}\text{Pr}_x)\text{Ba}_2\text{Cu}_3\text{O}_{7-\delta}$ ," *Phys. Rev. B* **43**, 11488 (1991).
5. L. Zhang, J. Z. Liu, M. D. Lan, P. Klavins, and R. N. Shelton, "Single Crystal Growth of  $\text{Nd}_{2-x}\text{Ce}_x\text{CuO}_{4-y}$ ," *Physica* **C174**, 431 (1991).
6. S. T. Weir, W. J. Nellis, Y. Dalichaouch, B. W. Lee, M. J. Maple, J. Z. Liu, and R. N. Shelton, "Evidence for a Time-Dependent Crossover from Surfacerlike to Bulklike Flux Relaxation in  $\text{YBa}_2\text{Cu}_3\text{O}_{7-\delta}$ ," *Phys. Rev. B* **43**, 3034 (1991).
7. J. Z. Liu, Y. X. Jia, R. N. Shelton, and M. J. Fluss, "In-Plane Anisotropy of the Interaction Between Vortex and Twin Boundary in  $\text{YBa}_2\text{Cu}_3\text{O}_7$  Single Crystals," *Phys. Rev. Lett.* **66**, 1354 (1991).
8. K. F. McCarty, H. B. Radousky, J. Z. Liu, and R. N. Shelton, "Temperature Dependence of the Linewidths of the Raman-Active Phonons of  $\text{YBa}_2\text{Cu}_3\text{O}_7$ : Evidence for a Superconducting Gap Between 440 and 500  $\text{cm}^{-1}$ ," *Phys. Rev. B* **43**, 13751 (1991).
9. H. Haghighi, J. H. Kaiser, S. Rayner, R. N. West, J. Z. Liu, R. Shelton, R. H. Howell, F. Solal, and M. J. Fluss, "Direct Observation of Fermi Surface in  $\text{YBa}_2\text{Cu}_3\text{O}_{7-\delta}$ ," *Phys. Rev. Lett.* **67**, 382 (1991).
10. M. D. Lan, J. Z. Liu, and R. N. Shelton, "Effects of Cu Substitution by Fe on the Magnetic Properties of  $\text{YBa}_2\text{Cu}_3\text{O}_{7-y}$  Single Crystals," *Phys. Rev. B* **43**, 12989 (1991).
11. M. D. Lan, J. Z. Liu, and R. N. Shelton, "Critical Current Density in Iron-Doped Y-Ba-Cu-O Single Crystals," *Phys. Rev. B* **44**, 233 (1991).
12. M. D. Lan, J. Z. Liu, and R. N. Shelton, "Flux Creep in Iron-Doped Y-Ba-Cu-O Single Crystals," *Phys. Rev. B* **44**, 2751 (1991).
13. K. F. McCarty, J. Z. Liu, Y. X. Jia, R. N. Shelton, and H. B. Radousky, "Effect of Gold-Doping on the Energy Gap of  $\text{YBa}_2\text{Cu}_3\text{O}_7$  as Determined by Raman Scattering," *Solid State Commun.* **79**, 359 (1991).
14. H. A. Blackstead, D. B. Pulling, P. J. McGinn, and J. Z. Liu, "Flux-Flow and Phase-Slip Dissipation in Crystalline  $\text{Bi}_2\text{Sr}_2\text{CaCu}_2\text{O}_{8+x}$  and  $\text{YBa}_2\text{Cu}_3\text{O}_{7-x}$ ," *Physica* **C174**, 394 (1991).
15. J. Chen, L. Chow, and J. Z. Liu, "Response of the High Temperature Superconductors to Weak AC Magnetic Field," *Physica* **C175**, 634 (1991).
16. E. K. Moser, W. J. Tomasch, P. J. McGinn, and J. Z. Liu, "Microwave Magneto-Dissipation in Crystalline  $\text{YBa}_2\text{Cu}_3\text{O}_{6+x}$  and  $\text{Bi}_2\text{Sr}_2\text{CaCu}_2\text{O}_8$ ," *Physica* **C176**, 235 (1991).
17. A. Amato, R. Caspary, R. A. Fisher, N. E. Phillips, H. B. Radousky, J. L. Peng, R. Zhang, and R. N. Shelton, "Specific Heat of  $(\text{Y}_{1-x}\text{Pr}_x)\text{Ba}_2\text{Cu}_3\text{O}_7$ : Magnetic Ordering, Magnetic Hyperfine Fields," *Physica* **B165**, 1347 (1990).
18. H. B. Radousky, R. S. Glass, D. Back, A. H. Chin, M. J. Fluss, J. Z. Liu, W. D. Mosley, P. Klavins, and R. N. Shelton, "Processing Parameters and Kinetics of Bromination and Chlorination in the  $\text{YBa}_2\text{Cu}_3\text{O}_{6+x}$  System," *IEEE Trans. Magn.* **27**, 2512 (1991).

# Glenn T. Seaborg Institute for Transactinium Science

T. T. Sugihara

*We have organized a new institute that will focus its activities on the science and technology of the transactinium elements. One of its major purposes is to educate and train new scientists in this field.*

## Background

The science and technology of the heaviest elements has long been a specialty at the Lawrence Livermore National Laboratory and its sister institutions: the Lawrence Berkeley Laboratory (LBL) and the University of California at Berkeley (UCB). This area of research is of great technical interest, not only because of the unusual chemical, physical, and nuclear properties of these elements, but also because of their importance in national security, environmental studies, waste minimization and processing, and national energy policy.

In 1989, the Chemistry and Materials Science Department at LLNL surveyed the field and concluded that the supply of trained professionals was diminishing to the detriment of national goals. We needed a mechanism that would provide new personnel who could promote, expand, and strengthen basic and applied understanding of the elements from thorium ( $Z = 90$ ) up to the heaviest known ( $Z = 109$ ). In addition, we needed a way to focus the nation's activities in this field.

To achieve these goals, we explored, with LLNL management and colleagues, the concept of forming an institute and subsequently consulted our counterparts at LBL and UCB. One of the main purposes of the institute would be education and training based on research and development in transactinium science. The concept was endorsed unanimously and enthusiastically. We chose LLNL as the site of the institute because it can satisfy the unusual needs of a research institute for heavy element work: physical security for safety reasons, specialized equipment and facilities, and proximity to major academic institutions.

## Early Activities—Starting the Institute

Having arrived at a concept, we next had to define an agenda, at least for the early years of the proposed institute, and present a focused plan to various managers who ultimately would be asked to endorse the institute. We also needed the support of the heavy-element community of the

United States and, to the extent possible, of other countries as well. To this end, an international workshop, organized by E. K. Hulet, was held in June 1990 at the Claremont Hotel in Oakland, California. This well-attended meeting assessed the state of the art in a variety of areas that constituted the field of heavy-element science and technology. The proceedings of the workshop<sup>1</sup> are intended to be a guide for the institute in the near term.

By the winter of 1990–91, the creation of an institute had been approved by the chief executives of elements of the University of California system who would be associated with the new institute: David P. Gardner, President, University of California; John H. Nuckolls, Director, LLNL; Charles V. Shank, Director, LBL; and Chang-Lin Tien, Chancellor, UCB. In addition, President Gardner approved the addition of "Glenn T. Seaborg" to the name of the new "Institute for Transactinium Science" in recognition of Seaborg's historic contributions to the field in his many years of affiliation with UCB, LBL, and the Department of Energy (and its predecessor agencies as far back as the Manhattan Project).

The formal announcement of the formation of the Glenn T. Seaborg Institute for Transactinium Science came in February 1991 at a celebration of the 50th anniversary of the discovery of plutonium. Darleane C. Hoffman, professor of chemistry at UCB and a strong contributor to the literature in the chemistry and physics of the heavy elements, was named the first director of the Institute. Subsequently, Patricia A. Baisden and Lawrence R. Newkirk, both of LLNL, were named deputy directors to assist Director Hoffman. Administratively, the Institute is part of the Chemistry and Materials Science Department, and the Institute director reports to the Associate Director for Chemistry and Materials Science.

The first funding for the Institute came in April 1991 through Weapons-Supporting Research at LLNL. The Institute's charter called for the formation of an Advisory Council whose principal function was to advise the Associate Director for Chemistry and Materials Science on policy matters related to the management and operation of the Institute. The Advisory Council was appointed in April 1991 and met for the first time in July 1991.

Members of the Advisory Council were chosen because of their extensive management, policy, or technical expertise across a broad spectrum of transactinium science, technology, and educational topics. Current members include the following:

- Glenn T. Seaborg, LBL, chair
- Roger E. Batzel, LLNL
- Gregory R. Choppin, Florida State University
- Floyd L. Culler, Electric Power Research Institute
- Jean Fuger, Commission of European Communities
- Gerhart Friedlander, Brookhaven National Laboratory
- Dieter M. Gruen, Argonne National Laboratory
- Guenter Herrmann, University of Mainz
- John R. Huizenga, University of Rochester
- M. Brian Maple, University of California at San Diego
- Don R. Olander, UCB
- Hirokazu Umezawa, Japan Atomic Energy Research Institute
- Eugene M. Wewerka, Los Alamos National Laboratory
- Ray E. Wildung, Battelle Pacific Northwest Laboratories
- Ray G. Wymer, Oak Ridge National Laboratory

### Current Activities

It was essential that the Institute get off to a flying start. From the point of view of existing experimental programs at LBL and LLNL and the availability of facilities, the best choice in the fall of 1991 for immediate involvement of graduate students was in the environmental chemistry of plutonium and other actinide elements. Subsequently, a postdoctoral associate was named in solid-state chemistry, and most recently, a postdoctoral theorist was appointed who will interpret electronic structures of transactinium species.

In parallel with the startup of scientific activities, substantial effort has been devoted to a search for additional funding, principally within offices of the Department of Energy. A broad-gauged field work proposal (FWP) has been prepared to secure funding for scientific staff and student fellowships and for safe and environmentally

responsible operation of the complex facilities needed for transactinium research. In the near term, the FWP also requests funds to refurbish and upgrade existing facilities. In the longer term, a new facility specifically designed for education and training as well as research and development is proposed.

Activities proposed in the FWP include education and training in areas relevant to the mission of Defense Programs, such as modernization and design of weapons facilities, nuclear materials processing, stockpile reduction, nuclear test diagnostics, and surveillance and detection of proliferation activities. Another DOE office that would benefit from the education and training activities of the Institute is Environmental Restoration and Waste Management, particularly in addressing environmental contamination by transactinium elements and in developing, testing, and improving methods and technologies for environmental restoration.

The Institute's activities also overlap strongly with the mission of the DOE's Office of Energy Research in the chemical sciences, materials science, and nuclear physics. In the Bay Area, ER already strongly supports research programs in heavy element nuclear chemistry, physical chemistry, metallurgy, solid-state chemistry, and synchrotron-related science as well as major research facilities such as the LBL cyclotron and the soon-to-operate Advanced Light Source.

The Glenn T. Seaborg Institute for Transactinium Science is off to an impressive start. In future issues of this *Report*, we will relate its scientific accomplishments in a section on transactinium science.

*This work was funded by Weapons-Supporting Research in FY91 and Laboratory Directed Research and Development in FY92.*

### References

1. E. K. Hulet, Ed., *Report of a Workshop on Transactinium Science*, Lawrence Livermore National Laboratory, Livermore, CA, UCRL-LR-104538 (1990).

---

## Overview

L. M. Brown

These last pages of this *Report* for 1990–91 are intended to supplement the preceding articles in order to present a more complete picture of the C&MS organization, staff, activities, and (in the final section) budget.

In strict terms, C&MS is a directorate, headed by an associate director. The Personnel section of this *Report* lists C&MS employees in four groups: those working directly on the staff of the associate director and those assigned to one of the three divisions (Chemical Sciences, Condensed Matter and Analytical Sciences, and Materials). Like most LLNL organizations, C&MS is dynamic, with terminations and retirements, a limited number of hires from the outside, and transfers to and from other LLNL organizations occurring throughout the year. The personnel listed here were those present toward the end of calendar year 1991.

An area of special emphasis in recent years has been the expansion of the C&MS postdoctoral research program. The number of postdoctoral research staff members has increased from 1 to 2 in 1985 to a steady state of about 20 in 1991; postdoctoral research terms are generally 2 to 3 years and, as seen in the listing, a number of postdoctoral research associates have subsequently joined the Laboratory as career staff. Postdoctoral research staff members play an important role in C&MS, as evidenced by their contributions to the research presented in this *Report*. C&MS also supports the work of graduate students, primarily from the University of California at Davis.

Interactions with a broad spectrum of the national and international scientific and technical communities are vital to the success of C&MS programs, and we list here the

consultants, advisory committees, and collaborations of the directorate. In particular, the Chemistry Review Committee and the Materials Review Committee play key roles in evaluating the respective research programs and advising the associate director and senior staff on both quality and direction. The collaborations listed are primarily with educational institutions. In future editions of this *Report*, many more collaborations with industry will be presented, in response to DOE's increasing emphasis on technology transfer.

The section on Research Communications emphasizes the breadth of research and programmatic activities in C&MS. Input for this section was solicited from all directorate personnel, and the response was impressive: for calendar years 1990 and 1991, C&MS personnel were responsible for over 230 journal articles, 140 conference proceedings, 75 Laboratory-issued reports, 20 articles in books, and 4 edited books. In addition, they gave over 80 lectures and more than 360 presentations at technical meetings and conferences. (The latter number does not include the numerous briefings C&MS staff present to government, educational, and industrial visitors to the Laboratory, nor does it list programmatic briefings delivered to sponsoring agencies.) C&MS personnel who work primarily on classified projects frequently cannot publish in the open literature; some of their efforts, however, are listed in the "Presentations" category. Finally, we list 26 patents issued to C&MS staff members during this two-year period.

---

Section 11

**Department  
Personnel and  
Professional  
Contributions**



# Personnel

## Chemistry & Materials Science Directorate

C. Gatrousis  
Associate Director for Chemistry & Materials Science

T. Sugihara  
Deputy Associate Director for Research

L. Schwartz  
Deputy Associate Director for Administration

R. Beach  
Deputy Associate Director for Assurances

### Critical Facilities

A. Garcia  
Plutonium Facility Manager

A. Toy  
Tritium Facility Manager

### Directorate Staff

J. Campbell, P. Crawford, E. Ernst, R. Failor, L. Frahm,  
J. Johnson, A. Mode, V. Oversby, D. Seaton, P. Shell, M. Taie

## Chemical Sciences Division

J. Richardson, Division Leader  
J. H. de Pruneda, Deputy Division Leader

### Division Staff

R. Hopper, J. Oldani, M. Schwab

## Chemical Engineering Section

C. Thorsness,  
Section Leader

D. Aldis  
J. Britten  
D. Camp  
R. Cena

J. Creighton  
J. Diaz  
D. Fields  
K. Foster  
D. Gregg  
R. Hickman  
R. Homsy

J. Kolb  
Assistant Associate Director for Weapons Program  
Support

D. La Curtis  
Assistant Associate Director for Resources

## Division Leaders

M. Fluss, Condensed Matter and Analytical Sciences  
Division

J. Kass, Materials Division

J. Richardson, Chemical Sciences Division

### Administrative Staff

L. Brown, L. Ellis, M. Governor, J. Jensen, B. Parashis,  
K. Spurlin, E. Waller, A. Altenbach, K. Common, G. Glasscox,  
J. Jackson, L. Jones, V. Maness, C. Spolerich, S. Woodard

### Administrative Staff

Y. Villa, M. Lewis, D. Coronado, S. Crowder,  
B. McCollough, B. Royval, C. Ynzunza

W. Hui  
R. Kanna  
M. Kozlowski  
S. Mayer  
S. Mayhugh  
M. McClelland  
L. Murguia

B. Musgrave  
R. Quong  
R. Taylor  
R. Upadhye  
H. Wallman  
B. Watkins  
Y. Zundeleovich

**Energetic Materials Section**

R. Simpson,  
Section Leader

W. Black  
D. Calef  
T. Cook  
C. Coon  
L. Daniels  
M. Foltz  
F. Garcia

R. Garza  
H. Golopol  
L. Green  
F. Helm  
M. Hoffman  
E. Jessop  
J. Kury  
C. Lee  
J. Maienschein

A. Mitchell  
G. Moody  
M. Murphy  
A. Nichols  
D. Ornellas  
P. Pagoria  
K. Pederson  
C. Pruneda  
A. Ruggiero

K. Scribner  
L. Simpson  
C. Souers  
W. Tao  
C. Tarver  
P. Urtiew  
E. von Holtz  
C. Walkup  
J. Walton

**Physical Chemistry Section**

L. Hair,  
Section Leader

W. Burks-Houck  
G. Collins  
W. Conaway

P. Coronado  
A. Droege  
M. Droege  
E. Fearon  
M. Himmelsbach  
H. Leider

L. Logoteta  
F. McMurphy  
D. Miller  
F. Miller  
J. Nielsen  
D. Olness

R. Sanner  
N. Shah  
C. Stevens  
S. Steward  
R. Tsugawa

**Polymers Section**

R. Pekala,  
Section Leader

R. Alexander  
C. Alviso  
S. Buckley  
I. Chiu

R. Cook  
M. Gebert  
K. Hong  
L. Hrubesh  
B. Haendler  
S. Hulsey

F. Kong  
J. LeMay  
S. Letts  
B. Mendoza  
E. Mones  
R. Morrison

G. Overturf  
J. Poco  
J. Satcher  
L. Spellman  
W. Sunderland  
T. Tillotson

**Condensed Matter and Analytical Sciences Division**

M. Fluss, Division Leader  
R. Rozsa, Deputy Division Leader  
M. Weber, Associate Division Leader, Special Programs

**Division Staff**

J. Fischer, M. Guinan, G. Roberts

**Administrative Staff**

K. Jautaikis, R. Quigley, D. Baker, B. Briggs, K. Clark,  
R. Coleman, N. Poggio

## Analytical Chemistry Section

P. Baisden,  
Deputy Division Leader

### Plutonium

J. Magana, Group Leader  
D. Del Giudice  
W. Morris  
M. Sharp  
E. Worden

### Solutions

R. Torres, Group Leader  
B. Armstrong  
N. Butler  
J. Happe  
J. Harrar  
P. Perry  
R. Ward

### Organic

R. Hawley-Fedder,  
Group Leader  
A. Alcaraz  
D. Chambers  
J. Clarkson  
J. Cupps  
L. Foiles  
J. Haas  
R. Whipple

### Environmental

P. Russ, Group Leader  
A. Conover  
J. Deering  
P. Epperson  
S. Gagner  
J. Hirschfeld  
R. Lim  
S. Lombard

### Inorganic

P. Miller, Group Leader  
C. Bartholdi  
T. Duewer  
C. Otto Jr.  
D. Pugh

### Energy

H. Gregg, Group Leader  
R. Bedford  
T. Coburn  
K. King  
J. Lindsey  
C. Morris  
J. Reynolds  
M. Singleton  
R. Swansiger

## Condensed Matter and Materials Characterization Section

L. Chase,  
Deputy Division Leader

### Surface Science

M. Balooch  
C. Colmenares  
A. Connor  
C. Evans  
T. Gouder  
A. Hamza  
W. Siekhaus  
L. Terminello

### Theory And Modeling

T. Diaz de la Rubia  
A. Gonis  
G. Nutt  
L. Reinhard  
P. Singh  
E. Sowa  
P. Sterne  
P. Turchi

### Particle Laboratory

K. Gels  
R. Meisenheimer  
H. Newkirk

### Electron Microscopy

G. Campbell  
V. Chen  
W. King  
D. McCoy  
M. Sattler  
W. Wien  
J. Yoshiyama

### Experimental Solid State

J. De Yoreo  
C. Ebbers  
V. Kresin  
E. Larson  
K. Ralls  
B. Rupp  
J. Tobin  
D. Waddill  
J. Wong

### X-Ray Characterization

W. Bell  
J. Kinney  
G. Smith

### Program Assignment

J. Atherton  
J. Cooper  
L. DeLoach  
M. Elder  
R. Reibold  
L. Summers  
F. Wang

## Materials Division

J. Kass, Division Leader  
 A. Lingenfelter, Deputy Division Leader  
 L. Newkirk, Deputy Division Leader

### Division Staff

T. Barbee, R. Christensen, M. Kassner

### Administrative Staff

J. Strickland, A. Moser, S. Cowan, J. Gomez, M. Manipis,  
 H. Meredith, J. Prince

## Physical Metallurgy, Joining, and Coating Section

W. Gourdin, Section Leader

### Physical Metallurgy

R. Daley  
 G. Henshall  
 P. Johnson  
 R. Musket

N. Nguyen  
 C. Price  
 R. Rosen  
 A. Schwartz  
 M. Sluiter  
 L. Tanner  
 N. Thomas  
 M. Wall

### Joining

J. Elmer, Group Leader  
 M. Gauthier  
 D. Hoffman  
 D. Kautz  
 B. Olsen  
 T. Ramos  
 M. Strum  
 L. Wagner  
 B. Westfall

### Coatings

D. Makowiecki, Group  
 Leader  
 C. Alford  
 C. Chen  
 R. Foreman  
 R. Juntz

## Metals Processing Section

G. Gallegos,  
 Section Leader

J. Hanafee  
 R. Wallace

### Forming and Processing

L. Summers, Group Leader  
 R. Burns  
 M. Coops  
 F. Dishong  
 L. Keene  
 P. Landon  
 T. Quick  
 E. Sedillo  
 M. Stratman  
 C. Tallman  
 S. Torres  
 D. Wood

### Metallography

R. Kershaw  
 J. Canfield  
 K. Miller  
 H. Olson

### Deposition

A. Jankowski, Group  
 Leader  
 F. Genin  
 J. Huang  
 E. Randich  
 H. Rizzo  
 E. Stiles  
 T. Summers

## Plutonium Technology Section

A. Lingenfelter,  
 Section Leader

C. Cate  
 R. Condit  
 T. Crawford  
 J. Furr  
 R. Gomez

D. Hagerty  
 R. Krueger  
 V. Mason-Reed  
 D. McAvoy  
 B. Vallier

### **Ceramics and Composites Section**

R. Landingham,  
Section Leader

#### **Ceramics**

K. Wilfinger, Group Leader  
M. Costantino  
P. Curtis  
B. Ebbinghaus

C. Hoenig  
B. Holt  
O. Krikorian  
J. Lakner  
J. Marion  
R. Otto  
T. Shell  
A. Tesar  
S. Weinland

#### **Polymer Based Fiber Composites**

S. DeTeresa, Group Leader  
L. Chiao  
R. Lyon  
J. Matthews  
W. Steele

### **Corrosion and Electrochemical Processes Section**

W. Clarke,  
Section Leader

J. Estill  
J. Farmer  
M. Farris

D. Fleming  
R. Glass  
P. Lewis  
B. Lum  
D. McCright  
J. Mitchell

#### **Radiation Effects**

W. Halsey  
R. VanKonynenburg

## Postdoctoral Research Staff Members

Ph.D. Institution and Fiscal Year of Appointment			
J. D. Bauer	Columbia University (1989–1991)	E. Larson	Arizona State University (1988–1991)
G. H. Campbell	University of California, Santa Barbara (1990–1992)	L. T. Reinhard	University of Zurich (1991–1992)
R. Daley	University of California, Los Angeles (1992)	A. J. Ruggiero	University of Oregon (1990–1991; to career employee in 1992)
T. Diaz de la Rubia	State University of New York (1989–1991; to career employee in 1992)	B. Rupp	Technical University of Vienna (1989–1992)
C. A. Ebbers	University of California, Davis (1992)	A. J. Schwartz	University of Pittsburgh (1991–1992)
B. B. Ebbinghaus	University of California, Berkeley (1991–1992)	N. N. Shah	Cornell University (1991–1992)
M. F. Foltz	University of California, Berkeley (1989–1992)	P. Singh	University of North Carolina, Chapel Hill (1991–1992)
M. Gebert	Northwestern University of Illinois (1992)	M. H. Sluiter	University of California, Berkeley (1990–1992)
F. Genin	Carnegie Mellon University (1991–1992)	F. R. Solal	University of Paris (1990–1991)
T. H. Gouder	University of Namur (1990–1992)	E. C. Sowa	University of California, Berkeley (1988–1990; to career employee in 1991)
H. Hall	University of California, Berkeley (1991)	J. W. Stephens	Rice University (1989–1991)
M. M. Himmelsbach	University of Colorado (1990–1992)	P. A. Sterne	Cambridge University (1989–1991)
P. E. Johnson	University of California, Berkeley (1992)	T. S. Summers	University of California, Berkeley (1991–1992)
V. V. Kresin	University of California, Berkeley (1991–1992)	J. Systma	University of Utrecht (1991–1992)
		G. D. Waddill	Indiana University (1991–1992)
		H. Wallman	University of California, Berkeley (1990; to career employee in 1991)

## Graduate Students

S. Bosson	University of California, Davis	J. Satcher	University of California, Davis
D. Bradley	Stanford University	M. Schildbach	University of California, Davis
M. Connor	University of California, Davis	D. Storms	University of California, Davis
D. Halverson	University of California, Davis	A. Sunwoo	University of California, Berkeley
K. Harding	Saint Olaf College	E. Suranyi	University of California, Davis
J. Mikalopas	University of California, Davis	R. Tench	University of California, Davis
M. Prieto	University of California, Davis	L. Wang	University of California, Davis

## Consultants

John G. Albright	Texas Christian University	Digby D. McDonald	SRI International
Amos Alexander	Custom Analytical Engineering Systems, Inc.	Hugh J. McQueen	Concordia University
Michael J. Aziz	Harvard University	Marc H. Mehlman	University of California, Riverside
Carl F. Beckner	Finnigan	Dale J. Meier	Michigan Molecular Institute
Thomas B. Brill	University of Delaware	Alan K. Miller	Stanford University
Daniel Bullen	DG Engineering, Inc.	Roger J. Morgan	Michigan Molecular Institute
Kenneth D. Challenger	University of Cincinnati	John W. Morris, Jr.	University of California, Berkeley
Leroy Chauffe	California State University, Hayward	Amiya K. Mukherjee	University of California, Davis
Peter H. Dederichs	Institut für Fostkörperforschung, Germany	Zuhair A. Munir	University of California, Davis
Morton Denn	University of California, Berkeley	Paul M. Naghdi	University of California, Berkeley
Mildred S. Dresselhaus	Massachusetts Institute of Technology	Robert J. Naylor	Maryville College
Geoffrey Egan	Aptech Engineering Services, Inc.	Richard E. Norberg	Washington University
Peter A. Fedders	Washington University	Steven R. Nutt	Brown University
Leonard C. Feldman	AT&T Bell Laboratories	Donald R. Olander	University of California, Berkeley
James R. Gaines	University of Hawaii	Martin Prager	Materials Property Council
Richard P. Gangloff	University of Virginia	William E. Preeg	Schlumberger-Doll Research
Richard W. Gaver	San Jose State University	George W. Reed, Jr.	Argonne National Laboratory (Ret.)
Warren H. Giedt	University of California, Davis	Edgar A. Rinehart	University of Wyoming
Randy Golding	Tracer Research Corporation	Robert O. Ritchie	University of California, Berkeley
Hong T. Hahn	Pennsylvania State University	Alan E. Schoen	Finnigan
John R. Hardy	University of Nebraska	Dominique Schryvers	University of Antwerp
Robert J. Hardy	University of Nebraska	Andre W. Sleeswyk	University of Groningen
Gary M. Hieftje	Indiana University	Deane K. Smith	Pennsylvania State University
John Huizenga	University of Rochester	George Springer	Stanford University
Robin Jones	Electric Power Research Institute	Urs Steiner	Finnigan
Robert Long	G. P. U. Nuclear	Albert J. Stonehouse	Iowa State University
Robert K. MacCrone	Rensselaer Polytechnic Institute	Richard M. Teeter	Chevron (Ret.)
James M. MacLaren	Tulane University	T. Darrah Thomas	Oregon State University
Thaddeus B. Massalski	Carnegie-Mellon University	Thomas A. Tombrello	California Institute of Technology
Bernard J. Matkowsky	Northwestern University	Thomas Tsakalakos	Rutgers University
Edwin D. McClanahan, Jr.	Rice University	Gustaf Van Tendeloo	University of Antwerp
		Frank R. Villalovoz	San Joaquin Delta College
		Manfred Wuttig	University of Maryland
		Richard N. Zare	Stanford University

## Scientific Advisory Committees

### Chemistry Review Committee

Thomas A. Tombrello,  
California Institute of Technology, Chair  
Thomas B. Brill, University of Delaware  
John G. Curro, Sandia National Laboratories  
Morton Denn, University of California, Berkeley  
John R. Huizenga, University of Rochester  
Richard E. Norberg, Washington University  
William E. Preeg, Schlumberger-Doll Research  
T. Darrah Thomas, Oregon State University

### Materials Review Committee

Thomas A. Tombrello,  
California Institute of Technology, Chair  
Martin Blume, Brookhaven National Laboratory  
Robert Eagan, Sandia National Laboratories  
Dieter M. Gruen, Argonne National Laboratory  
M. Brian Maple, University of California, San Diego  
John W. Morris, University of California, Berkeley

## Collaborations

Research and development programs in C&MS frequently involve collaborations with researchers at universities and other research institutions. The following is a partial list of collaborating organizations.

### U.S. Universities

Brown University	University of Illinois
University of California	University of Maryland
Berkeley	University of Massachusetts
Davis	Massachusetts Institute of Technology
Irvine	Miami University (Ohio)
Los Angeles	University of Minnesota
San Diego	University of Missouri—Kansas City
San Francisco	University of Nebraska
Santa Barbara	North Carolina Agricultural and Technical State University
California Institute of Technology	Northwestern University
California State University	Ohio State University
Northridge	Oregon State University
San Jose	Princeton University
Hayward	Rutgers University
Carnegie-Mellon University	University of South Carolina
Case Western Reserve University	Stanford University
University of Cincinnati	Syracuse University
University of Connecticut	University of Texas—Arlington
Cornell University	Texas Christian University
Florida Atlantic University	University of Virginia
Georgia Institute of Technology	Washington University (St. Louis)
Harvard University	University of Wisconsin
University of Hawaii	Madison
University of Houston	Milwaukee

### Foreign Universities

University of Antwerp (Belgium)	University of Guelph (Ontario)
University of Bristol (United Kingdom)	Queen's University (Ontario)
Concordia University (Montreal)	University of Tokyo (Japan)
Dortmund University (Germany)	Technical University of Vienna (Austria)
University of Groningen (Netherlands)	University of Würzburg (Germany)



## U.S. Laboratories

Ames Laboratory  
Argonne National Laboratory  
Brookhaven National Laboratory  
National Synchrotron Light Source  
Department of Defense  
Army Research and Development Center  
(Picatinny Arsenal)  
Naval Ordnance Station (Indian Head, MD)  
Naval Surface Weapons Center (White Oak, MD)  
Naval Research Laboratory  
Naval Warfare Station (Yorktown, VA)

Naval Weapons Center (China Lake, CA)  
Rocket Propulsion Laboratory (Edwards AFB, CA)  
Lawrence Berkeley Laboratory  
Los Alamos National Laboratory  
National Aeronautics and Space Administration  
Oak Ridge National Laboratory  
Sandia National Laboratories  
Albuquerque  
Livermore  
Stanford Synchrotron Radiation Laboratory

## Foreign Laboratories

Centre National Recherche Scientifique, Laboratory of  
Electronic Properties of Solids (Grenoble, France)  
European Institute for Transuranium Elements  
(Karlsruhe, Germany)  
HASYLAB, Deutsches Elektronen Synchrotron  
(Hamburg, Germany)  
Kernforschungsanlage Jülich, Institut für  
Festkörperforschung (Jülich, Germany)

Max Planck Institut für Metallforschung  
(Stuttgart, Germany)  
National Institute for Research in Inorganic Materials  
(Tsukuba, Japan)  
Office National d'Etudes et de Recherches Aérospatiale  
(Chatillon, France)  
Solid State Physics Institute, Academy of Science (Moscow)  
S. I. Vavilov State Optical Institute (St. Petersburg)

# Research Communications

## Articles in Journals

D. F. Aldis and D. Gidaspow, "A Two-Dimensional Analysis of a Dust Explosion," *AIChE J.* **36**(7), 1087 (1990).

C. Alford, F. Serduke, D. Makowiecki, A. Jankowski, and M. Wall, "X-Ray Fiducial Foils," *Thin Solid Films* **206**, 306 (1991).

M. J. Allen, R. J. Tench, J. A. Mazimas, M. Balooch, W. J. Siekhaus, and R. Balhorn, "A Pulse Deposition Method for Scanning Tunneling Microscopy of Deoxyribonucleic Acid on Graphite," *J. Vac. Sci. Technol.* **9**, 1272 (1991).

C. T. Alviso and R. W. Pekala, "Melamine-Formaldehyde Aerogels," *Polym. Preprints* **32**(3), 242 (1991).

A. Amato, R. Caspary, R. A. Fisher, N. E. Phillips, H. B. Radousky, J. L. Peng, R. Zhang, and R. N. Shelton, "Specific Heat of  $(Y_{1-x}Pr_x)Ba_2Cu_3O_7$ : Magnetic Ordering, Magnetic Hyperfine Fields," *Phys. B* **165**, 1347 (1990).

L. J. Atherton, J. J. DeYoreo, S. A. Payne, D. H. Roberts, J. F. Cooper, and R. W. Martin, "Growth of  $Cr:LiCaAlF_6$ ," *AACG Newsletter* **21**, 10 (1991).

R. Balhorn, M. Corzett, J. Mazrimas, and B. Watkins, "Identification of Bull Protamine Disulfides," *Biochem.* **30**, 175 (1991).

M. Balooch, D. R. Olander, W. J. Siekhaus, and D. E. Miller, "Reaction of Chlorine and Molybdenum by Modulated Molecular Beam Mass Spectrometry," *Surf. Sci.* **248**, 322 (1991).

M. Balooch, M. A. Schildbach, R. J. Tench, M. Allen, and W. J. Siekhaus, "Surface Site Specificity on the Basal Plane of Graphite: 1.06 Micron Laser Damage Threshold and Reactivity with Oxygen Between 350 and 2300 K," *J. Vac. Sci. Technol.* **9**, 1088 (1991).

M. Balooch, R. J. Tench, W. J. Siekhaus, M. J. Allen, A. L. Connor, and D. R. Olander, "Deposition of SiC Films by Pulsed Excimer Laser Ablation," *Appl. Phys. Lett.* **57**, 1540 (1990).

T. W. Barbee, Jr., "Advances in Multilayer X-Ray/EUV Optics: Synthesis, Performance, and Instrumentation," *Opt. Eng.* **29**, 711 (1990).

T. W. Barbee, Jr., "Multilayer Optics for the Soft X-Ray and Extreme Ultraviolet," *Phys. Scripta* **T31**, 147 (1990).

T. W. Barbee, Jr., "Multilayer Optics for the Soft X-Ray and Extreme Ultraviolet," *MRS Bull.* **XV**(2), 37 (1990).

T. W. Barbee, Jr., J. V. Bixler, and D. D. Dietrich, "Performance of Multilayer Coated Gratings at Near Normal Incidence in the Extreme Ultraviolet," *Phys. Scripta* **41**, 740 (1990).

T. W. Barbee, Jr., J. C. Rife, W. R. Hunter, R. G. Cruddace, and P. Pianetta, "Multilayer Diffraction Gratings: Application to Synchrotron Radiation Instrumentation," *Opt. Eng.* **29**, 738 (1990).

T. W. Barbee, Jr., J. W. Weed, R. B. Hoover, M. J. Allen, J. F. Lindblom, R. H. O'Neal, C. C. Kankelborg, C. E. DeForest, E. S. Paris, A. B. C. Walker, Jr., T. D. Willis, E. Gluskin, P. Pianetta, and P. C. Baker, "Multi-Spectral Solar Telescope Array II: Soft X-Ray/EUV Reflectivity of the Multilayer Mirrors," *Opt. Eng.* **30**, 1067 (1990).

J. D. Bauer and D. F. Calef, "Harmonic Analysis of Phonon Echoes in Liquids," *Chem. Phys. Lett.* **187**(4), 391 (1991).

J. V. Bixler, T. W. Barbee, Jr., and D. D. Dietrich, "Multilayer Coated Concave Diffraction Grating Resolution and Efficiency in the Extreme Ultraviolet," *Opt. Eng.* **29**, 733 (1990).

H. A. Blackstead, D. B. Pulling, P. J. McGinn, and J. Z. Liu, "Flux-Flow and Phase-Slip Dissipation in Crystalline  $Bi_2Sr_2CaCu_2O_{8+x}$  and  $YBa_2Cu_3O_{7-x}$ ," *Phys. C* **174**, 394 (1991).

D. W. Brown, Z. A. Munir, and R. G. Musket, "A Precipitate Coarsening Mechanism for Buried Layer Formation by Ion Implantation," *Nucl. Instrum. Methods B* **59**(60), 627 (1991).

D. W. Brown, R. G. Musket, and Z. A. Munir, "Buried Monocrystalline Aluminum Layers in Beryllium using Ion Implantation," *Appl. Phys. Lett.* **57**, 2651 (1990).

D. W. Camp, R. L. Braun, and J. C. Diaz, "Results of Mathematical Modeling of an Oil Shale Retort Having a Fluidized-Bed Pyrolyzer and a Lift-Pipe Combustor," *Fuel Processing Technol.* **21**, 135 (1989).

D. W. Camp, S. B. Tantekin, and W. B. Krantz, "Darcy Flow to a Vertical Fracture Intersecting a Cylindrical Cavity—Application to Water Permeation in UCG," *In Situ* **12**(1&2), 15 (1988).

N. M. Ceglio, A. M. Hawryluk, D. G. Stearns, D. P. Gaines, R. S. Rosen, and S. P. Vernon, "Soft X-Ray Projection Lithography," *J. Vac. Sci. Technol. B* **8**(6), 1325 (1990).

- T.-M. Chang, J. D. Bauer, and J. L. Skinner, "Critical Exponents for Anderson Localization," *J. Chem. Phys.* **93**(12), 8973 (1990).
- L. L. Chase, "Laser-Induced Surface Ablation as a Probe of Optical Surface Damage Mechanisms," *Nucl. Instrum. Methods B* **46**, 252 (1990).
- L. L. Chase, H. W. H. Lee, and R. S. Hughes, "Investigation of Laser-surface Interactions and Optical Damage Mechanisms Using Excitation by Pairs of Picosecond Laser Pulses," *Appl. Phys. Lett.* **57**, 443 (1990).
- L. L. Chase and S. A. Payne, "New Tunable Solid State Lasers,  $\text{Cr}^{3+}:\text{LiCaAlF}_6$  and  $\text{Cr}^{3+}:\text{LiSrAlF}_6$ ," *Opt. Photonics News*, August 1990, 16 (1990).
- J. Chen, L. Chow, and J. Z. Liu, "Response of the High Temperature Superconductors to Weak AC Magnetic Field," *Phys. C* **175**, 634 (1991).
- L. Chiao, "Application of Mechanistic Chemical Kinetics to Thermoset Composites Processing," *High Perform. Polym.* **1**(2), 109 (1990).
- L. Chiao, "Mechanistic Modeling of Epoxy Resins," *SAMPE J.* **26**(1), 27 (1990).
- L. Chiao, "Mechanistic Reaction Kinetics of 4,4'-Diaminodiphenyl/Sulfone Cured Tetraglycidyl-4,4'-diaminodiphenylmethane Epoxy Resins," *Macromol.* **23**, 1286 (1990).
- L. Chiao and R. E. Lyon, "A Fundamental Approach to Resin Cure Kinetics," *J. Composite Mater.* **24**(7), 739 (1990).
- M. Choi, J. I. Budnick, D. M. Pease, G. H. Hayes, and J. Wong, "A Method of Obtaining the Empirical Scattering Parameters for the Fe-B Pair from the EXAFS Data for  $\text{Fe}_2\text{B}$ : Possible Limitations," *Phys. Rev. B* **41**, 9654 (1990).
- D. C. Chrzan, L. M. Falicov, J. M. MacLaren, X.-G. Zhang, and A. Gonis, "Magnetism of {111} Stacking Faults in Ni," *Phys. Rev. B* **43**, 9442 (1991).
- T. T. Coburn and C. J. Morris, "Bench Scale Studies of Oil Shale Flash Pyrolysis Under Hot-Recycled-Solid Conditions," *Fuel* **70**, 1362 (1991).
- G. W. Collins, E. M. Fearon, J. L. Maienschein, E. R. Mapoles, R. T. Tsugawa, and P. C. Souers, "Triggered Energy Releases in Solid Hydrogen Hosts Containing Unpaired Atoms," *Phys. Rev. Lett.* **65**, 444 (1990).
- G. W. Collins, E. M. Fearon, E. R. Mapoles, P. C. Souers, and P. A. Fedders, "J=1-to-0 Conversion In Solid  $\text{D}_2$ ," *Phys. Rev. B* **44**, 6598 (1991).
- G. W. Collins, P. C. Souers, E. M. Fearon, E. R. Mapoles, R. T. Tsugawa, and J. R. Gaines, "Thermal Conductivity of Condensed D-T and  $\text{T}_2$ ," *Phys. Rev. B* **41**, 1816 (1990).
- C. Colmenares, M. Connor, and C. Evans, "Photoactivated Heterogeneous Catalysis on Aerogels," *Eur. J. Solid State Inorg. Chem.* **28**, 429 (1991).
- V. L. Colvin, A. P. Alivisatos, and J. G. Tobin, "Valence Band Photoemission from a Quantum Dot System," *Phys. Rev. Lett.* **66**, 2786 (1991).
- R. C. Cook, "Iron-Doped Polymers for Capsule Impulsion Diagnostics," *ICF Quarterly Report* **1**, 47 (1991).
- R. C. Cook, R. D. Johnson, C. G. Wade, D. J. O'Leary, B. Munoz, and M. M. Green, "Solvent Dependence of the Chain Dimensions of Poly(n-hexyl-isocyanate)," *Macromol.* **23**, 3454 (1990).
- M. S. Costantino, "A High Pressure-High Temperature Valve Packing," *Rev. Sci. Instrum.* **62**(6), 2 (1991).
- M. S. Costantino and C. S. Firpo, "High Pressure Combustion Synthesis of Aluminum Nitride," *J. Mater. Res.* **6**(11), 6 (1991).
- M. S. Costantino, J. F. Lakner, and R. Bastasz, "Synthesis of Monolithic Uranium Hydride and Uranium Deuteride," *J. Less-Common Metals* **159**, 97 (1990).
- M. S. Costantino, J. F. Lakner, and R. Bastasz, "Supercritical Phase Separation in  $\text{H}_2\text{O}-\text{N}_2$  Mixtures," *J. Phys. Chem.* **95**, 3 (1991).
- P. M. Cotts and R. W. Pekala, "Dynamic Light Scattering Studies of Resorcinol-Formaldehyde Gels as Precursors of Organic Aerogels," *Polym. Preprints* **32**(3), 451 (1991).
- R. G. Cruddace, T. W. Barbee, Jr., J. C. Rife, and W. R. Hunter, "Measurements of the Normal-Incidence X-Ray Reflectance of a Molybdenum-Silicon Multilayer Deposited on a 2000 1/mm Grating," *Phys. Scripta* **41**, 396 (1990).
- C. E. DeForest, C. C. Kankelborg, M. J. Allen, E. S. Paris, T. D. Willis, J. F. Lindblom, R. H. O'Neal, A. B. C. Walker, Jr., T. W. Barbee, Jr., R. B. Hoover, and T. W. Barbee, III, "Multi-Spectral Solar Telescope Array V: Temperature Diagnostic Response to the Optically Thin Solar Plasma," *Opt. Eng.* **30**, 1125 (1991).
- S. J. DeTeresa, "Piezoresistivity and Failure of Carbon Filaments in Axial Compression," *Carbon* **29**(3), 397 (1991).
- J. J. DeYoreo, L. J. Atherton, and D. H. Roberts, "Elimination of Scattering Centers from  $\text{Cr}:\text{LiCaAlF}_6$ ," *J. Cryst. Growth* **113**, 691 (1991).

- J. J. DeYoreo, D. R. Lux, and C. V. Guidotti, "Thermal Modelling in Low-pressure Metamorphic Belts," *Tectonophys.* **188**, 209 (1991).
- J. J. DeYoreo, A. Navrotsky, and D. B. Dingwell, "Energetics of the Charge-Coupled Substitution  $\text{Si}^{4+} \rightleftharpoons \text{Na}^{1+} + \text{T}^{3+}$  in the Glasses  $\text{NaTO}_2\text{-SiO}_2$  (T = Al, Fe, Ga, B)," *J. Am. Ceram. Soc.* **73**, 2068 (1990).
- H. Dindi, J. A. Britten, and W. B. Krantz, "Combustion and Dielectric Breakdown Instabilities in Porous Media," *Earth-Sci. Rev.* **29**, 401 (1990).
- M. W. Droege and R. G. Finke, "A Novel Triperoxy niobium Containing Heteropolyanion,  $\text{SiW}_9(\text{NbO}_2)_3\text{O}_{40}^{7-}$ : Catalytic Allylic Epoxidations with  $\text{H}_2\text{O}_2$  and Preliminary Kinetic Studies," *J. Mol. Cat.* **69**, 323 (1991).
- C. A. Ebberts and D. Eimerl, "New Materials For High Average Power Electro-Optic Switches," *Ceramic Trans.* **14**, 67 (1990).
- J. W. Elmer, S. M. Allen, and T. W. Eagar, "Microstructural Development During Solidification of Stainless Steel Alloys," *Metall. Trans. A* **20A**(10), 2117 (1989).
- J. W. Elmer and T. W. Eagar, "Measuring the Residual Ferrite Content of Rapidly Solidified Stainless Steel Alloys," *Weld. J.* **69**(4), 141 (1990).
- J. W. Elmer, W. H. Giedt, and T. W. Eagar, "The Transition from Shallow to Deep Penetration During Electron-Beam Welding," *Weld. J.* **69**(5), 167 (1990).
- J. C. Farmer, G. E. Gdowski, R. D. McCright, and H. S. Ahluwalia, "Corrosion Models for Performance Assessment of High-Level Radioactive Waste Containers," *Nucl. Eng. Des.* **129**, 57 (1991).
- J. C. Farmer, F. T. Wang, R. A. Hawley-Fedder, P. R. Lewis, L. J. Summers, and L. Foiles, "Electrochemical Treatment of Mixed and Hazardous Wastes: Oxidation of Ethylene Glycol and Benzene by Ag(II)," *J. Electrochem. Soc.* **138**(3), 654 (1992).
- R. Frahm, T. W. Barbee, Jr., and W. Warburton, "In Situ Structural Study of Thin-Film Growth by Quick-Scanning X-Ray-Absorption Spectroscopy," *Phys. Rev. B* **44**, 2822 (1991).
- R. S. Glass, "Electrochemical Microsensors," *Verif. Tech. Rev.* **2**(3), 18 (1990).
- R. S. Glass, R. G. Musket, and K. C. Hong, "Preparation of Solid Membrane Chloride Ion-Selective Electrodes by Ion Implantation," *Anal. Chem.* **63**(19), 2203 (1991).
- R. S. Glass, S. P. Perone, and D. R. Ciarlo, "Application of Information Theory to Electroanalytical Measurements Using a Disposable Multielement Microelectrode Array Sensor," *Anal. Chem.* **62**(18), 1914 (1990).
- A. Gonis, M. Sluiter, P. E. A. Turchi, G. M. Stocks, and D. M. Nicholson, "Electronic Structure, Alloy Phase Stability, and Phase Diagrams," *J. Less-Common Metals* **168**, 127 (1990).
- A. Gonis, E. C. Sowa, and P. A. Sterne, "Exact Treatment of Poisson's Equation in Solids with Space-Filling Cells," *Phys. Rev. Lett.* **66**, 2207 (1991).
- A. Gonis, R. Zeller, P. H. Dederichs, J. S. Faulkner, B. L. Györffy, D. M. Nicholson, G. M. Stocks, L. T. Wille, and X.-G. Zhang, "Comment on Exact Eigenvalue Equation for Finite and Infinite Collections of Muffin-Tin Potentials," *Phys. Rev. B* **41**, 10224 (1990).
- A. Gonis, X.-G. Zhang, J. M. MacLaren, and S. Crampin, "Green Function Method for Electronic Structure Calculations of Surfaces and Coherent Interfaces," *Phys. Rev. B* **42**, 3798 (1990).
- W. H. Gourdin and J. W. Dini, "Evaluation of Electroformed Copper for Shaped Charge Applications," *Plating Surf. Finishing* **77**, 54 (1990).
- W. H. Gourdin and D. Lassila, "Flow Stress of OFE Copper at Strain Rates from  $10^{-3}$  to  $10^4 \text{ s}^{-1}$ : Grain-Size Effects and Comparison to the Mechanical Threshold Stress Model," *Acta Metall. Mater.* **39**(10), 2337 (1991).
- E. Gregory, L. R. Motowidlo, G. M. Ozeryansky, and L. T. Summers, "High Strength  $\text{Nb}_3\text{Sn}$  Conductors for High Magnetic Field Applications," *IEEE Trans. Magn.* **27**, 2033 (1991).
- H. Haghighi, J. H. Kaiser, S. Rayner, R. N. West, M. J. Fluss, R. H. Howell, P. E. A. Turchi, A. L. Wachs, Y. C. Jean, and Z. Z. Wang, "A Positron Study of the Electronic Structure of  $\text{YBa}_2\text{Cu}_3\text{O}_{7-\delta}$ ," *J. Phys. Condens. Matt.* **2**, 1911 (1990).
- H. Haghighi, J. H. Kaiser, S. Rayner, R. N. West, J. Z. Liu, R. Shelton, R. H. Howell, F. Solal, and M. J. Fluss, "Direct Observation of Fermi Surface in  $\text{YBa}_2\text{Cu}_3\text{O}_{7-\delta}$ ," *Phys. Rev. Lett.* **67**, 382 (1991).
- P. A. Hahn, M. W. Guinan, L. T. Summers, T. Okada, and D. B. Smathers, "Fusion Neutron Irradiation Effects in Commercial  $\text{Nb}_3\text{Sn}$  Superconductors," *J. Nucl. Mater.* **179**, 1127 (1991).
- L. M. Hair, W. J. Pitz, M. W. Droege, and C. K. Westbrook, "Modeling of Catalytic Coupling of Methane," *Preprints Div. Fuel Chem.* **36**, 370 (1991).

- H. L. Hall, K. E. Gregorich, R. A. Henderson, C. M. Gannett, R. B. Chadwick, J. D. Leyba, K. R. Czerwinski, B. Kadkhodayan, S. A. Kreek, N. J. Hannink, D. M. Lee, M. J. Nurmia, D. C. Hoffman, C. E. A. Palmer, and P. A. Baisden, "Electron-Capture-Delayed Fission Properties of  $^{232}\text{Am}$ ," *Phys. Rev. C* **42**, 1480 (1990).
- H. L. Hall, K. E. Gregorich, R. A. Henderson, C. M. Gannett, R. B. Chadwick, J. D. Leyba, K. R. Kadkhodayan, S. A. Kreek, D. M. Lee, M. J. Nurmia, D. C. Hoffman, C. E. A. Palmer, and P. A. Baisden, "EC-Delayed Fission Properties of  $^{234}\text{Am}$ ," *Phys. Rev. C* **41**, 618 (1990).
- D. D. Heinrich, K. Folting, J. C. Huffman, J. G. Reynolds, and G. Christou, "Preparation and Properties of Mononuclear Vanadium Thiolates: Structural Characterization of the  $[\text{V}(\text{SBU}^t)_4]^{0,1}$  Pair, and C-S Bond Cleavage in  $\text{V}(\text{SBU}^t)_4$  in the Gas Phase," *Inorg. Chem.* **30**, 300 (1991).
- G. A. Henshall and A. K. Miller, "Simplifications and Improvements in Unified Constitutive Equations for Creep and Plasticity with Solute Effects: Part I—Equations Development," *Acta Metall. Mater.* **38**, 2101 (1990).
- G. A. Henshall and A. K. Miller, "Simplifications and Improvements in Unified Constitutive Equations for Creep and Plasticity with Solute Effects: Part II—Behavior and Capabilities of the Model," *Acta Metall. Mater.* **38**, 2117 (1990).
- G. A. Henshall, R. S. Rosen, M. E. Kassner, and R. G. Whirley, "Finite-Element Analysis of Interlayer Welds Loaded in Tension," *Weld. J.* **69**(9), 337 (1990).
- K. Hong, R. B. Rosner, and M. F. Rubner, "Langmuir-Blodgett Manipulation of Electrically Conductive Polypyrroles," *Chem. Mater.* **2**, 82 (1990).
- K. C. Hong and R. S. Glass, "Chemically Modified Electrode Sensors," *Environtech* **2**(9), 2 (1991).
- R. B. Hoover, D. L. Shealy, B. R. Brinkley, P. C. Baker, T. W. Barbee, Jr., and A. B. C. Walker, Jr., "Development of the Water Window Imaging X-Ray Microscope Utilizing Normal-Incidence Multilayer Optics," *Opt. Eng.* **30**, 1086 (1990).
- R. W. Hopper, "Plane Stokes Flow Driven by Capillarity on a Free Surface," *J. Fluid Mech.* **213**, 349 (1990).
- R. W. Hopper, "Plane Stokes Flow Driven by Capillarity on a Free Surface, 2: Further Developments," *J. Fluid Mech.* **230**, 355 (1991).
- L. W. Hrubesh, "Aerogels: The World's Lightest Solids," *Chem. & Industry* **24**, 824 (1990).
- H. G. Hsieh, C. W. Price, E. L. Pierce, and R. G. Wirtenson, "Effects of Nitrogen Pulsing on Sputter-Deposited Beryllium Films," *J. Vac. Sci. Technol. A* **8**, 2165 (1990).
- J. S. Huang, "Carbide Formation in Nb and Ta Implanted by Carbon Ions at Room Temperature," *Nucl. Instrum. Methods B* **59**(60), 652 (1991).
- J. S. Huang and G. F. Gallegos, "Embrittlement by Liquid U in some Group VB and VIB Metals and Alloys during Tensile Loading at 1473 K," *Metall. Trans.* **21A**, 1959 (1990).
- J. S. Huang and Y. W. Kim, "Creep Deformation and Fracture of a Two-Phase TiAl alloy," *Scripta Metall.* **25**(8), 1901 (1991).
- K. Y. Jang, K. Kim, and R. S. Upadhye, "Study of Sol-Gel Processing for Fabrication of Hollow Silica Aerogel Spheres," *J. Vac. Sci. Technol. A* **8**(3), 1732 (1990).
- A. Jankowski and T. Tsakalakos, "Interface Phenomena in Multilayers," *Mater. Sci. Eng. B* **6**, 87 (1990).
- A. F. Jankowski, "On the Deposition Optimization of W/C Multilayer Mirrors," *Opt. Eng.* **29**, 968 (1990).
- A. F. Jankowski, "Short Period Multilayers: Interface Dominated Structures," *Mater. Sci. Eng. B* **6**, 191 (1990).
- A. F. Jankowski and D. M. Makowiecki, "W/B<sub>4</sub>C Multilayer X-Ray Mirrors," *Opt. Eng.* **30**, 2003 (1991).
- A. F. Jankowski and P. L. Perry, "Microstructure of Au/Nb Multilayers," *Thin Solid Films* **194**, 799 (1990).
- A. F. Jankowski and P. L. Perry, "Characterization of Mo/B<sub>4</sub>C Multilayers," *Thin Solid Films* **206**, 365 (1991).
- A. F. Jankowski and L. R. Schrawyer, "Reactive Sputtering of Molybdenum," *Thin Solid Films* **193**, 61 (1990).
- A. F. Jankowski, L. R. Schrawyer, and P. L. Perry, "Reactive Sputtering of Molybdenum-Oxide Gradient-Index Filters," *J. Vac. Sci. Technol. A* **9**, 1184 (1991).
- A. F. Jankowski, L. R. Schrawyer, and M. A. Wall, "Structural Stability of Heat Treated W/C and W/B<sub>4</sub>C Multilayers," *J. Appl. Phys.* **68**, 5162 (1990).
- A. F. Jankowski, M. A. Wall, and P. E. A. Turchi, "Crystallization of Amorphous Ti-Pd," *J. Less-Common Metals* **161**, 115 (1990).

- Y. C. Jean, C. S. Sundar, A. Bharathi, J. Kyle, H. Nakanishi, P. K. Tseng, P. H. Hor, R. L. Meng, Z. J. Huang, C. W. Chu, Z. Z. Wang, P. E. A. Turchi, R. H. Howell, A. L. Wachs, and M. J. Fluss, "Local Charge Density and Superconductivity: a Positron Study," *Phys. Rev. Lett.* **64**, 1593 (1990).
- M. E. Kassner, N. Q. Nguyen, G. A. Henshall, and H. J. McQueen, "The Effects of Temperature and Strain Rate on the Extended Ductility of Aluminum," *J. Mater. Sci. Eng. A* **132**, 97 (1991).
- M. E. Kassner, R. S. Rosen, and G. A. Henshall, "Delayed Mechanical Failure of Silver Interlayer Bonds," *Metall. Trans.* **21A**, 3085 (1990).
- M. E. Kassner, R. S. Rosen, G. A. Henshall, and K. D. Challenger, "Time-Dependent Failure of Silver-Interlayer Diffusion Welds Between Elastically Deforming Base Metals," *Scripta Metall. Mater.* **24**(3), 587 (1990).
- D. D. Kautz, D. L. Olson, P. Burgardt, and G. R. Edwards, "A Characterization of Pulsed Electron Beam Welding Parameters," *Weld. J.* **70**(4), 100 (1991).
- W. E. King and J. H. Park, "Effect of Y on Cation and Anion Diffusion in Chromia," *Colloq. Phys.* **C1 51**, 551 (1990).
- T. Krekels, G. VanTendeloo, D. Broddin, S. Amelinckx, L. E. Tanner, M. Mehbod, E. VanLathen, and R. Detour, "Tweed Structure of Fe-Doped  $\text{YBa}_2\text{Cu}_3\text{O}_{7-\delta}$ ," *Phys. C* **173**, 361 (1991).
- O. H. Krikorian and D. C. Hagerty, "Exchange Reactions of Plutonium with Silicides and Estimation of the Enthalpy of Formation of  $\text{Pu}_5\text{Si}_3$ ," *J. Nucl. Mater.* **171**, 237 (1990).
- W. F. Krupke and L. L. Chase, "Ground State Depleted Solid State Lasers: Principles, Characteristics, and Scaling," *Opt. Quant. Electron.* **22**, 51 (1990).
- M. D. Lan, J. Z. Liu, and R. N. Shelton, "Critical Current Density in Iron-Doped Y-Ba-Cu-O Single Crystals," *Phys. Rev. B* **44**, 233 (1991).
- M. D. Lan, J. Z. Liu, and R. N. Shelton, "Effects of Cu Substitution by Fe on the Magnetic Properties of  $\text{YBa}_2\text{Cu}_3\text{O}_{7-y}$  Single Crystals," *Phys. Rev. B* **43**, 12989 (1991).
- M. D. Lan, J. Z. Liu, and R. N. Shelton, "Flux Creep in Iron-Doped Y-Ba-Cu-O Single Crystals," *Phys. Rev. B* **44**, 2751 (1991).
- R. A. Lange, J. J. DeYoreo, and A. Navrotsky, "Scanning Calorimetric Measurement of the Heat Capacity During Incongruent Melting of Diopside," *Am. Min.* **76**, 904 (1990).
- D. A. Lapiano-Smith, E. A. Eklund, F. J. Himpsel, and L. J. Terminello, "Epitaxy of LiF on Ge(001)," *Appl. Phys. Lett.* **59**, 2174 (1991).
- E. M. Larson, A. J. G. Ellison, F. W. Lytle, A. Navrotsky, R. B. Gregor, and J. Wong, "XAS Study of La Ion Speciation in High Silica Glasses of the System  $\text{K}_2\text{O-SiO}_2\text{-La}_2\text{O}_3$ ," *J. Non-Cryst. Solids* **130**, 260 (1991).
- E. M. Larson, P. A. Waide, and J. Wong, "High Speed Diffractometer Reaction Chamber Using Synchrotron Radiation," *Rev. Sci. Instrum.* **62**, 53 (1991).
- J. D. LeMay, R. W. Hopper, L. W. Hrubesh, and R. W. Pekala, "Low-Density Microcellular Materials," *MRS Bull.* **XV**(12), 19 (1990).
- J. F. Lindblom, R. H. O'Neal, A. B. C. Walker, Jr., F. R. Powell, T. W. Barbee, Jr., R. B. Hoover, and S. F. Powell, "Multi-Spectral Solar Telescope Array IV: the Soft X-Ray and Extreme Ultraviolet Filters," *Opt. Eng.* **30**, 1134 (1991).
- J. Z. Liu, Y. X. Jia, P. Klavins, R. N. Shelton, J. Downey, and D. J. Lam, "Preparation and Magnetic Measurements of Single Crystal  $\text{Tl}_2\text{BaCaCu}_2\text{O}_8$ ," *J. Cryst. Growth* **109**, 436 (1990).
- J. Z. Liu, Y. X. Jia, R. N. Shelton, and M. J. Fluss, "In-Plane Anisotropy of the Interaction Between Vortex and Twin Boundary in  $\text{YBa}_2\text{Cu}_3\text{O}_7$  Single Crystals," *Phys. Rev. Lett.* **66**, 1354 (1991).
- R. E. Lyon, "Shear Strength of Ductile Material from Solid Cylinder Torsion," *J. Test. Eval.* **19**(3), 240 (1991).
- R. E. Lyon and R. J. Farris, "Analysis of Heat-Flux Calorimeter Signals," *Thermochim. Acta* **161**, 287 (1990).
- F. W. Lytle, G. Van der Laan, R. B. Gregor, E. M. Larson, and J. Wong, "Determination of the Valence of Pr, Gd, and Ho in  $\text{YBa}_2\text{Cu}_3\text{O}_7$  by X-Ray Absorption Spectroscopy," *Phys. Rev. B* **41**, 8955 (1990).
- J. L. Maienschein, P. E. Barry, F. E. McMurphy, and J. S. Bowers, "Synthesis and Properties of a Low Density, High Porosity Lithium Hydride-Beryllium Hydride Foam," *Mater. Sci. Eng. A* **132**, 143 (1991).
- D. M. Makowiecki, A. F. Jankowski, M. A. McKernan, and R. J. Foreman, "Magnetron Sputtered Boron Films and Ti/B Multilayer Structures," *J. Vac. Sci. Technol. A* **8**, 3910 (1990).
- E. R. Mapoles, F. Magnotta, G. W. Collins, and P. C. Souers, "Optical Pulses in Tritiated Solid Hydrogen," *Phys. Rev. B* **41**, 11653 (1990).

- J. E. Marion and M. J. Weber, "Phosphate Laser Glass," *Eur. J. Solid State Inorg. Chem.* **28**, 271 (1991).
- M. G. Mason, J. G. Tobin, D. A. Shirley, Z. Hussain, and R. F. Davis, "Energy Bandmapping of Silver(110) by Angle-Resolved Photoemission," *Arab. J. Sci. Eng.* **15**, 309 (1990).
- R. Mathew, J. G. Albright, D. G. Miller, and J. A. Rard, "Isothermal Diffusion Coefficients for NaCl-MgCl<sub>2</sub>-H<sub>2</sub>O at 25°C. 4. Solute Concentration Ratio of 1:3," *J. Phys. Chem.* **94**, 6875 (1990).
- K. F. McCarty, J. Z. Liu, Y. X. Jia, R. N. Shelton, and H. B. Radousky, "Effect of Gold-Doping on the Energy Gap of YBa<sub>2</sub>Cu<sub>3</sub>O<sub>7</sub> as Determined by Raman Scattering," *Solid State Commun.* **79**, 359 (1991).
- K. F. McCarty, J. Z. Liu, R. N. Shelton, and H. B. Radousky, "Electronic Raman Scattering of YBa<sub>2</sub>Cu<sub>3</sub>O<sub>7</sub> Using C-Axis Polarization: Evidence for Two Characteristic Superconducting Energies," *Phys. Rev. B* **42**, 9973 (1990).
- K. F. McCarty, H. B. Radousky, J. Z. Liu, and R. N. Shelton, "Temperature Dependence of the Linewidths of the Raman-Active Phonons of YBa<sub>2</sub>Cu<sub>3</sub>O<sub>7</sub>: Evidence for a Superconducting Gap Between 440 and 500 cm<sup>-1</sup>," *Phys. Rev. B* **43**, 13751 (1991).
- M. McKernan, D. Makowiecki, P. Ramsey, and A. Jankowski, "Magnetron Sputter Deposition of Boron and Boron Carbide," *Surf. Coatings Technol.* **49**, 411 (1991).
- N. Merk and L. E. Tanner, "Solid-State Amorphization and Contamination of Ni-Ta Powders During Ball Milling," *Scripta Metall.* **26**, 381 (1991).
- E. K. Moser, W. J. Tomasch, P. J. McGinn, and J. Z. Liu, "Microwave Magneto-Dissipation in Crystalline YBa<sub>2</sub>Cu<sub>3</sub>O<sub>6+x</sub> and Bi<sub>2</sub>Sr<sub>2</sub>CaCu<sub>2</sub>O<sub>8</sub>," *Phys. C* **176**, 235 (1991).
- R. W. Murray, M. B. Buchholz ten Brink, D. L. Jones, D. C. Gerlach, and G. P. Russ III, "Rare-Earth Elements as Indicators of Different Marine Depositional Environments in Chert and Shale," *Geology* **18**, 268 (1990).
- R. G. Musket, "X-Ray Fluorescence Analysis for Oxygen on and in Materials," *X-Ray Spectrom.* **19**, 185 (1990).
- R. G. Musket, "Extracting the Net 0(K) X-Ray Peak from Si(Li)-Detector Spectra," *Nucl. Instrum. Methods B* **61**, 322 (1991).
- R. G. Musket, R. A. Hawley-Fedder, and W. L. Bell, "Proton Irradiation of Thin Films of C<sub>60</sub> Molecules," *Rad. Effects Defects Solids* **118**, 225 (1990).
- R. G. Musket and S. J. Holmes, "Apparatus for Low-Energy X-Ray Fluorescence Using an Al(K) X-Ray Source and a Si(Li) Detector," *X-Ray Spectrom.* **19**, 177 (1990).
- A. L. Nichols III and D. F. Calef, "Structure and Thermodynamics of Asymmetric Molecules: Application to Linear Triatomic Dipolar Molecules," *Mol. Phys.* **71**, 269 (1990).
- Y. Noda, S. M. Shapiro, G. Shirane, Y. Yamada, and L. E. Tanner, "Martensite Transformation of a Ni-Al Alloy. I. Experimental Results and Approximate Structure of the 7-Layered Phase," *Phys. Rev. B* **42**, 10397 (1990).
- C. G. Olson, J. G. Tobin, F. R. Solal, C. Guo, J. Z. Liu, M. J. Fluss, R. H. Howell, J. C. O'Brien, H. B. Radousky, and P. A. Sterne, "High Resolution Photoemission Studies of Untwinned YBa<sub>2</sub>Cu<sub>3</sub>O<sub>6.9</sub>," *J. Phys. Chem. Solids* **52**, 1419 (1991).
- D. L. Ornellas, J. S. Thrasher, M. E. Sitzman, and W. H. G. Nigan, "Polynitroaliphatic Explosives Containing the Pentafluorosulfanyl (SF<sub>5</sub>) Group: The Selection and Study of a Model Compound," *J. Energetic Mater.* **8**(4), 352 (1990).
- L. Paduano, R. Sartorio, V. Vitagliano, J. G. Albright, D. G. Miller, and J. Mitchell, "Diffusion Coefficients in Systems with Inclusion Compounds. 1.  $\alpha$ -Cyclodextrin-L-Phenylalanine-Water at 25°C," *J. Phys. Chem.* **94**, 6885 (1990).
- R. Pahl, U. Bonse, R. W. Pekala, and J. H. Kinney, "SAXS Investigations on Organic Aerogels," *J. Appl. Cryst.* **24**, 771 (1991).
- S. Park, M. L. Hanna, R. T. Taylor, and M. W. Droege, "Cultivation of Methylosinus Trichosporium 0B3b: I. Production of Soluble Methane Monooxygenase," *Biotechnol. Bioeng.* **38**, 423 (1991).
- S. A. Payne, J. A. Caird, L. L. Chase, L. K. Smith, N. D. Nielson, and W. F. Krupke, "Spectroscopy and Gain Measurements of Nd<sup>3+</sup> in SrF<sub>2</sub> and Other Fluorite-Structure Hosts," *J. Opt. Soc. Am. B* **8**, 726 (1991).
- S. A. Payne, L. L. Chase, L. K. Smith, and B. H. T. Chai, "Flashlamp-Pumped Laser Performance of LiCaAlF<sub>6</sub>:Cr<sup>3+</sup>," *Opt. Quant. Electron.* **22**, 5259 (1990).
- R. W. Pekala, C. T. Alviso, and J. D. LeMay, "Organic Aerogels: Microstructural Dependence of Mechanical Properties in Compression," *J. Non-Cryst. Solids* **125**, 67 (1990).
- R. W. Pekala and R. L. Ward, "<sup>13</sup>C NMR Investigation of Crosslinking in Organic Aerogels," *Polym. Preprints* **31**(1), 167 (1990).

- N. E. Phillips, R. A. Fisher, R. Caspary, A. Amato, H. B. Radousky, J. L. Peng, L. Zhang, and R. N. Shelton, "Magnetic Ordering, Hyperfine and 'Linear' Contributions to the Low-Temperature Specific Heat of  $(Y_{1-x}Pr_x)Ba_2Cu_3O_{7-\delta}$ ," *Phys. Rev. B* **43**, 11488 (1991).
- R. C. Powell, S. A. Payne, L. L. Chase, and G. D. Wilke, "Four-wave Mixing of  $Nd^{3+}$ -Doped Crystals and Glasses," *Phys. Rev. B* **13**, 8593 (1990).
- C. W. Price, "Use of Johnson-Mehl-Avrami Kinetics in Recrystallization of Metals and Crystallization of Metallic Glasses," *Acta Metall. Mater.* **38**, 727 (1990).
- C. W. Price, "Analysis of Models for Grain-Impingement Compensation and Their Effect on Recrystallization Kinetics," *Acta Metall. Mater.* **39**, 1807 (1991).
- H. B. Radousky, R. S. Glass, D. Back, A. H. Chi, M. J. Fluss, J. Z. Liu, W. D. Mosly, P. Klavins, and R. N. Shelton, "Processing Parameters and Kinetics of Bromination and Chlorination in the  $YBa_2Cu_3O_{6+x}$  System," *IEEE Trans. Magn.* **27**(2), 2512 (1991).
- H. B. Radousky, R. S. Glass, P. A. Hahn, M. J. Fluss, R. G. Meisenheimer, B. P. Bonner, C. I. Merzbacher, E. M. Larson, K. McKeegan, J. C. O'Brien, J. L. Peng, R. N. Shelton, and K. F. McCarty, "Metallization and Superconducting Properties of  $YBa_2Cu_3O_{6.2}Br_y$ ," *Phys. Rev. B* **41**(16), 11140 (1990).
- K. S. Ralls and R. A. Buhrman, "A Microscopic Study of 1/f Noise in Metal Nanobridges," *Phys. Rev. B* **44**, 5800 (1991).
- J. A. Rard and D. G. Miller, "Ternary Mutual Diffusion Coefficients of  $ZnCl_2$ -KCl- $H_2O$  at 25°C by Rayleigh Interferometry," *J. Solution Chem.* **19**, 129 (1990).
- J. A. Rard and D. G. Miller, "Corrected Values of Osmotic and Activity Coefficients of Aqueous  $NaTcO_4$  and  $HTcO_4$  at 25°C," *J. Solution Chem.* **20**, 1139 (1991).
- S. P. Regan, A. P. Zwicker, M. Finkenthal, H. W. Moos, and T. W. Barbee, Jr., "Evaluation of a Multilayer Mirror Spectrometer in the 230–304 Å Wavelength Range," *Rev. Sci. Instrum.* **61**, 2789 (1990).
- B. A. Remington, S. W. Haan, S. G. Glendinning, J. D. Kilkenny, D. H. Munro, and R. J. Wallace, "Indirect-Drive Rayleigh-Taylor Experiments Using Shaped Laser Pulses," *ICF Quarterly Report* **1**(1), 7 (1990).
- B. A. Remington, S. W. Haan, S. G. Glendinning, J. D. Kilkenny, D. H. Munro, and R. J. Wallace, "Large Growth Rayleigh-Taylor Experiments Using Shaped Laser Pulses," *Phys. Rev. Lett.* **67**, 3259 (1991).
- J. G. Reynolds, "Can Size Exclusion Chromatography with Element Specific Detection, the D 2007-80 with Asphaltene Precipitation (SARA) Separation, and Hydrogen Distribution by NMR Help at All in Predicting Residuum Processability?" *Fuel Sci. Technol. Int.* **9**(5), 613 (1991).
- J. G. Reynolds, R. W. Crawford, and A. K. Burnham, "Analysis of Oil Shale and Petroleum Source Rock Pyrolysis by Triple Quadrupole Mass Spectrometry: Comparisons of Gas Evolution at the Heating Rate of 10°C/Min," *Energy & Fuels* **5**, 507 (1991).
- S. F. Rice and M. F. Foltz, "Very High Pressure Combustion: Reaction Propagation Rates of Nitromethane within a Diamond Anvil Cell," *Comb. Flame* **87**, 109 (1991).
- J. C. Rife, T. W. Barbee, Jr., W. R. Hunter, and R. G. Cruddace, "Performance of a Tungsten/Carbon Multilayer-Coated Blazed Grating from 80 to 1700 eV," *Phys. Scripta* **41**, 406 (1990).
- R. S. Rosen and M. E. Kassner, "Diffusion Welding of Silver Interlayers Coated onto Base Metals by Planar-Magnetron Sputtering," *J. Vac. Sci. Technol. A* **8**(1), 19 (1990).
- P. J. Rous, X.-G. Zhang, J. M. MacLaren, A. Gonis, M. A. V. Hove, and G. A. Samorjai, "A Real Space Multiple Scattering Theory of LEED: A New Approach for the Determination of Stepped Surfaces," *Surf. Sci.* **239**, 103 (1990).
- B. Rupp, B. Smith, and J. Wong, "SEXIE: a Microcomputer Program for the Calculation of Coordination Shells and Geometries," *J. Appl. Crystallogr.* **24**, 263 (1991).
- J. J. Sanchez and R. S. Upadhye, "A Non-Destructive Method for Measuring  $D_2/DT$  Fill Pressure and Permeability for Direct Drive Plastic Shells," *J. Nucl. Fusion* **31**(3), 459 (1991).
- A. Santoni, L. J. Terminello, and F. J. Himpsel, "Mapping of Fermi Surfaces with a Display-Type Photoelectron Spectrometer," *Appl. Phys. A* **52**, 299 (1991).
- J. H. Schloss, L. L. Chase, and L. K. Smith, "Dynamics of Laser-pumped  $Nd^{3+}$  Laser Media at High Excitation Density," *J. Lumin.* **49**, 857 (1991).
- D. Schryvers and L. E. Tanner, "On the Interpretation of High-Resolution Electron Microscopy Images of Premartensitic Microstructures in Ni-Al Beta Phase," *Ultramicroscopy* **32**, 241 (1990).
- S. Shapiro, L. E. Tanner, Y. Noda, and D. Schryvers, "Neutron Scattering and Electron-Microscopy Studies of the Premartensitic Phenomena in  $Ni_xAl_{(100-x)}$ ," *Phys. Rev. B* **44**, 9301 (1991).



- D. L. Shealy, R. B. Hoover, T. W. Barbee, Jr., and A. B. C. Walker, Jr., "Design and Analysis of a Schwarzschild Imaging Multilayer X-Ray Microscope," *Opt. Eng.* **29**, 721 (1990).
- P. P. Singh, "An Efficient Formulation of the Korringa-Kohn-Rostoker Method in the Coherent Potential Approximation for Substitutionally Disordered Alloys," *Solid State Commun.* **76**, 1223 (1990).
- P. P. Singh, "Evolution of Bulk-Like Properties in Mercury Microclusters," *J. Phys. D* **17**, 309 (1990).
- P. P. Singh, "First-Principles Calculations of the Electronic Properties of 3d-Transition-Metal Impurities in Al," *J. Phys. C* **3**, 3285 (1991).
- P. P. Singh, "Self-Consistent Electronic Structure of 3d-Transition-Metal Impurities in Aluminum Using the Recursion Method," *Phys. Rev. B* **43**, 3975 (1991).
- P. P. Singh, D. de Fontaine, and A. Gonis, "Self-Consistent-Field Korringa-Kohn-Rostoker Coherent-Potential-Approximation Calculations in the Atomic-Sphere Approximation," *Phys. Rev. B* **44**, 8578 (1991).
- M. Sluiter, D. de Fontaine, X. Guo, R. Podloucky, and A. J. Freeman, "First-Principles Calculation of Aluminum-Lithium Phase Diagram," *Phys. Rev. B* **42**, 10460 (1990).
- M. Sluiter and P. Turchi, "Theoretical Investigation of Phase Stability in Ti-V and Ti-Cr," *Phys. Rev. B* **43**, 12251 (1991).
- J. P. Sokoloff, L. L. Chase, and L. A. Boatner, "Low Frequency Relaxation Modes and Structural Disorder in  $\text{KTa}_{1-x}\text{Nb}_x\text{O}_3$ ," *Phys. Rev.* **41**, 2398 (1990).
- D. G. Stearns, R. S. Rosen, and S. P. Vernon, "Fabrication of High-Reflectance Mo-Si Multilayer Mirrors by Planar-Magnetron Sputtering," *J. Vac. Sci. Technol. A* **9**(5), 2662 (1991).
- D. G. Stearns, R. S. Rosen, and S. P. Vernon, "A Normal Incidence X-Ray Mirror for 70 Å," *Optics Lett.* **16**(16), 1283 (1991).
- L. T. Summers, A. R. Duenas, C. E. Karlsen, G. M. Ozeryansky, and E. Gregory, "A Characterization of Internal-Sn Superconductors for Use in the Proof of Principles (POP) Coil," *IEEE Trans. Magn.* **27**, 1763 (1991).
- L. T. Summers, M. W. Guinan, J. R. Miller, and P. A. Hahn, "A Model for the Prediction of  $\text{Nb}_3\text{Sn}$  Critical Current as a Function of Field, Temperature, Strain, and Radiation Damage," *IEEE Trans. Magn.* **27**, 2041 (1991).
- L. T. Summers and J. R. Miller, "Further Studies of Transverse Stress Effects in Cable-in-Conduit Conductors," *Adv. Cryo. Eng.* **36A**, 101 (1990).
- L. T. Summers, J. R. Miller, and J. R. Heim, "The International Thermonuclear Experimental Reactor (ITER); Design and Materials Selection," *Adv. Cryo. Eng.* **36A**, 769 (1990).
- L. T. Summers, M. J. Strum, and J. R. Miller, "The Characterization of  $\text{Nb}_3\text{Sn}$  Superconductors for Use in Magnets of 19 T and Greater," *Adv. Cryo. Eng.* **36A**, 77 (1990).
- Z. Tan, J. I. Budnic, J. L. Peng, L. Zhang, and R. N. Shelton, "X-Ray Absorption Studies of Atomic and Electronic Structures of  $\text{Nd}_{2-x}\text{M}_x\text{CuO}_4$  (M=Ce and Th)," *Phys. B* **163**, 13 (1990).
- L. E. Tanner, A. R. Pelton, G. VanTendeloo, D. Schryvers, and M. E. Wall, "Premartensitic Microstructures in Ni-Al Ordered Beta Phase: I. Effects Induced by Cooling," *Scripta Metall.* **24**, 1731 (1990).
- W. C. Tao and C. W. Frank, "Energy Migration in the Aromatic Vinyl Polymers. 7. Application of a One-Dimensional Electronic Excitation Transport Model for Transient Fluorescence of Poly(2-vinylnaphthalene) in Alkylbenzene Solution and Polystyrene Blends," *J. Phys. Chem.* **93**(2), 776 (1989).
- W. C. Tao, J. W. Thomas, and C. W. Frank, "Excimer Fluorescence as a Molecular Probe of Polymer Blend Miscibility. 8. Polymeric and Glassy Solvent Host Matrices," *Polymer* **29**(9), 1625 (1988).
- C. M. Tarver, "Modeling Shock Initiation and Detonation Divergence Tests on TATB-Based Explosives," *Propellants, Explosives and Pyrotechnics* **15**, 132 (1990).
- R. J. Tench, M. Balooch, L. Bernardez, M. J. Allen, W. J. Siekhaus, D. R. Olander, and W. Wang, "Clusters Formed in Laser-Induced Ablation of Si, SiC, Pt,  $\text{UO}_2$  and Evaporation of  $\text{UO}_2$  Observed by Laser Ionization Time-of-Flight Mass Spectrometry and Scanning Tunneling Microscopy," *J. Vac. Sci. Technol.* **9**, 820 (1991).
- L. J. Terminello and J. J. Barton, "Auger Electron Angular Distributions from Surfaces: A Comparison of Isoenergetic Photoelectrons and Auger Electrons," *Science* **251**, 1219 (1991).
- L. J. Terminello, D. K. Shuh, F. J. Himpsel, D. A. Lapiano-Smith, J. Stöhr, D. S. Bethune, and G. Meijer, "Unfilled Orbitals of  $\text{C}_{60}$  and  $\text{C}_{70}$  from Carbon K-Shell X-Ray Absorption Fine Structure," *Chem. Phys. Lett.* **182**, 491 (1991).

- A. A. Tesar, "Nonradiative Properties of Nd Doped Fluoride Glasses," *J. Quant. Spec. Rad. Trans.* **46**, 425 (1991).
- C. B. Thorsness and J. A. Britten, "Influence of Finite Jets on Mass Transfer in Radial-Flow, Multijet CVD Reactors," *AIChE J.* **36**, 801 (1990).
- J. G. Tobin, V. L. Colvin, and A. P. Alivisatos, "Photoemission Investigation of Compound Semiconductor Monodisperse Clusters," *J. Vac. Sci. Technol. A* **9**, 852 (1991).
- J. G. Tobin, J. C. Hansen, and M. K. Wagner, "Probing Bimetallic Surfaces with Photoelectron Diffraction: Au/Cu(001) and Fe/Cu(001)," *J. Vac. Sci. Technol. A* **8**, 2494 (1990).
- R. A. Torres, C. E. A. Palmer, P. A. Baisden, R. E. Russo, and R. J. Silva, "A Comparison of Photoacoustic Spectroscopy, Conventional Absorption Spectroscopy, and Potentiometry as Probes of Lanthanide Speciation," *Anal. Chem.* **62**, 298 (1990).
- R. T. Tsugawa, J. S. Bowers, J. A. Emig, R. S. Hafner, J. L. Maienschein, and A. S. Nicolosi, "Determination of Tritium in Mercury from Sprengel Pumps," *J. Nucl. Mater.* **172**, 239 (1991).
- P. E. A. Turchi, "Electronic Structure and Phase Stability: Effect of a Bain Transformation on the Thermodynamic Properties of Substitutional Alloys," *Mater. Sci. Eng. A* **127**, 145 (1990).
- P. E. A. Turchi and A. Finel, "New Possible Ordered States Based on the A15 Crystalline Structure," *J. Phys. Soc. Jpn.* **60**, 942 (1991).
- P. E. A. Turchi and A. Finel, "Phase Stability Properties in Complex Substitutional Alloys," *J. Less-Common Metals* **168**, 103 (1991).
- P. E. A. Turchi, M. Sluiter, F. J. Pinski, D. D. Johnson, D. M. Nicholson, G. M. Stocks, and J. B. Staunton, "A First-Principles Description of Phase Stability in Cu-Zn Substitutional Alloys," *Phys. Rev. Lett.* **67**, 1779 (1991).
- P. E. A. Turchi, A. L. Wachs, K. H. Wetzler, J. H. Kaiser, R. N. West, Y. C. Jean, R. H. Howell, and M. J. Fluss, "Electron Momentum Density Studies in High  $T_c$  Materials by Positron Annihilation Spectroscopy: Theory and Experiment," *J. Phys. Condens. Matt.* **2**, 1635 (1990).
- K. W. Turteltaub, B. E. Watkins, M. Vanderlaan, and J. S. Felton, "Role of Metabolism of the DNA-Binding of MeIQx in Mice and Bacteria," *Carcinogenesis* **11**, 43 (1990).
- R. S. Upadhye and E. J. Hsieh, "A Unified Integrated Model for Sputter Coating Uniformity," *J. Vac. Sci. Technol. A* **8**(3), 1348 (1990).
- P. A. Urtiew and B. Hayes, "Empirical Estimates of Detonation Parameters in Condensed Explosives," *J. Energetic Mater.* **9**(4), 297 (1991).
- M. Vanderlaan, J. Alexander, C. Thomas, T. Djanegara, M. Hwang, B. E. Watkins, and H. E. Walling, "Immunochemical Detection of Rodent Hepatic and Urinary Metabolites of Cooking-Induced Food Mutagens," *Carcinogenesis* **12**, 349 (1991).
- G. VanTendeloo, D. Broddin, C. Leroux, D. Schryvers, L. E. Tanner, and S. Amelinckx, "Electron Microscopy Observations of Pretransition Effects in Alloys," *Phase Transitions* **27**, 61 (1990).
- E. M. Vogel, M. J. Weber, and D. Krol, "Nonlinear Optical Phenomena in Glass," *Phys. Chem. Glass* **32**, 231 (1991).
- M. K. Wagner, J. C. Hansen, R. de Souza-Machado, S. Liang, J. G. Tobin, M. G. Mason, S. Brandt, Y. T. Tan, A.-B. Yang, and F. C. Brown, "Surface Morphology and Growth of AgBr on Ag(111)," *Phys. Rev. B* **43**, 6405 (1991).
- A. B. C. Walker, Jr., J. F. Lindblom, R. H. O'Neal, M. J. Allen, T. W. Barbee, Jr., and R. B. Hoover, "Multi Spectral Solar Telescope Array," *Opt. Eng.* **29**, 581 (1990).
- A. B. C. Walker, Jr., J. F. Lindblom, J. G. Timothy, T. W. Barbee, Jr., R. B. Hoover, and E. Tandberg-Hanssen, "The Ultra High Resolution XUV Spectroheliograph," *Opt. Eng.* **29**, 698 (1990).
- P. H. Wallman and W. J. Fisk, "Exhaust-Air Heat Pump Performance with Unsteady State Operation," *Heat Recovery Systems & CHP* **10**, 234 (1990).
- W. K. Warburton, T. W. Barbee, Jr., and Z. U. Rek, "Characterization Tests on Layered Synthetic Microstructures as X-Ray Optical Elements," *Nucl. Instrum. Methods A* **291**, 165 (1990).
- I. Watanabe, K. Hong, and M. F. Rubner, "Langmuir-Blodgett Manipulation of Poly(3-alkylthiophenes)," *Langmuir* **6**, 1164 (1990).
- B. E. Watkins, H. Esumi, K. Wakabayashi, M. Nagao, and T. Sugimura, "Fate and Distribution of 2-amino-1-methyl-6-phenylimidazo [4,5-*b*]pyridine (PhIP) in Rats," *Carcinogenesis* **12**, 1073 (1991).

B. E. Watkins, M. Suzuki, H. Wallin, K. Wakabayashi, J. Alexander, M. Vanderlaan, T. Sugimura, and H. H. Esumi, "The Effect of Dose and Enzyme Inducers on the Metabolism of 2-amino-1-methyl-6-phenylimidazo[4,5-b]pyridine (PhIP) in Rats," *Carcinogenesis* **12**, 2291 (1991).

M. J. Weber, "Science and Technology of Laser Glass," *J. Non-Cryst. Solids* **123**, 208 (1990).

S. T. Weir, W. J. Nellis, Y. Dalichaouch, B. W. Lee, M. B. Maple, J. Z. Liu, and R. N. Shelton, "Evidence for a Time-Dependent Crossover from Surfacerlike to Bulklike Flux Relaxation in  $\text{YBa}_2\text{Cu}_3\text{O}_{7-\delta}$ ," *Phys. Rev. B* **43**, 3034 (1991).

D. Wild, B. E. Watkins, and M. Vanderlaan, "Azido-PhIP and Nitro-PhIP, Relatives of the Heterocyclic Arylamine and Food Mutagen PhIP—Mechanism of their Mutagenicity in Salmonella," *Carcinogenesis* **12**, 1091 (1991).

K. R. Wilfinger, W. R. Cannon, and T. Tsakalakos, "RMS Matrix Strains in Transformation Toughened Alumina," *J. Mater. Sci.* **25**(10), 4402 (1990).

## Papers in Proceedings

J. G. Albright and D. G. Miller, "Calculation of the  $L_{ij}$  Transport Coefficients for  $\text{NaCl-MgCl}_2\text{-H}_2\text{O}$  at  $25^\circ\text{C}$ ," in *Proc. Fundamentals and Applications of Ternary Diffusion*, 29th Ann. Conf. Metallurgists CIM, G. R. Purdy, Ed. (Pergamon Press, New York, 1990), p. 101.

A. Alcaraz, R. W. Crawford, and J. G. Reynolds, "Analysis of Oil Shale by On-line TQMS," in *Proc. 38th ASMS Conf. Mass Spectrometry Applied Topics* (American Society for Mass Spectrometry, Tucson, AZ, 1990), p. 597.

M. Asta, M. Sluiter, P. Singh, D. de Fontaine, T. Hong, and A. J. Freeman, "First Principles Study of Phase Stability in the AL-Ti System," in *Mater. Res. Soc. Symp. Proc.* **186**, G. M. Stocks, D. P. Pope and A. F. Giamei, Eds. (Materials Research Society, Pittsburgh, PA, 1991), p. 33.

S. P. Baker, A. F. Jankowski, S. Hong, and W. D. Nix, "Mechanical Properties of Compositional Modulated Au/Ni Films Using Indentation and Microbeam Deflection Techniques," in *Thin Films: Stresses and Mechanical Properties II*, *Mater. Res. Soc. Symp. Proc.* **188**, W. Oliver, M. Doerner, G. Pharr and F. R. Brotzen, Eds. (Materials Research Society, Pittsburgh, PA, 1990), p. 289.

M. Balooch, D. R. Olander, R. E. Russo, and W. J. Siekhaus, "Long Laser-pulse Method of Producing Y-Ba-Cu-O Superconducting Films," in *Mater. Res. Society Symp. Proc.* **169** (Materials Research Society, Pittsburgh, PA, 1990), p. 447.

J. Wong, E. Larson, J. Holt, P. Waide, B. Rupp, and R. Frahm, "Time-Resolved Diffraction Study of Solid Combustion Reactions," *Science* **249**, 1906 (1990).

J. Wong, G. Shimkaveg, and W. Goldstein, "Synchrotron Radiation," *Nucl. Instrum. Methods A* **291**, 243 (1990).

L. Zhang, J. Z. Liu, M. D. Lan, P. Klavins, and R. N. Shelton, "Single Crystal Growth of  $\text{Nd}_{2-x}\text{Ce}_x\text{CuO}_{4-y}$ ," *Phys. C* **174**, 431 (1991).

X.-G. Zhang, M. A. VanHove, G. A. Samorjai, P. J. Rous, D. Tobin, A. Gonis, J. M. MacLaren, K. Heinz, M. Michl, H. Linden, K. Müller, E. Ehsasi, and J. H. Block, "Efficient Determination of Multilayer Relaxation in the Pt (210) Stepped and Densely Kinked Surface," *Phys. Rev. Lett.* **67**, 1298 (1991).

Y. Zundelevich and R. Glaser, "Activity of Growth Centers During Spiral Growth of KDP in Aqueous Solution: a Statistical Approach," *J. Cryst. Growth* **102**, 69 (1990).

T. W. Barbee, Jr., J. W. Weed, R. B. Hoover, M. J. Allen, J. F. Lindblom, R. H. O'Neal, C. C. Kankelborg, C. E. DeForest, E. S. Paris, A. B. C. Walker, Jr., T. D. Willis, E. S. Gluskin, P. Pianetta, and P. C. Baker, "Multispectral Solar Telescope Array II: Soft X-ray/EUV Reflectivity of the Multilayer Mirrors," in *Multilayer and Grazing Incidence X-Ray/EUV Optics*, *SPIE Symp. Proc.* **1546**, R. Hoover, Ed. (International Society for Optical Engineering, Bellingham, WA, 1991), p. 432.

A. Baron, T. W. Barbee, Jr., and G. Brown, "Multilayer Monochromator for Synchrotron Radiation Angiography," in *X-Ray/EUV Optics for Astronomy, Polarimetry and Projection Lithograph*, *SPIE Symp. Proc.* **1343**, R. Hoover and A. Walker, Eds. (International Society for Optical Engineering, Bellingham, WA, 1990), p. 84.

J. A. Britten, J. Tong, and C. K. Westbrook, "A Numerical Study of Silane Combustion," in *Proc. 23rd Symp. (Int.) on Combustion* (The Combustion Institute, Pittsburgh, PA, 1991), p. 195.

D. W. Camp, "Mild Coal Gasification—Screw Pyrolyzer Development and Design," in *Proc. 10th Ann. Gasification and Gas-Stream Cleanup Systems Contractors Rev.*, V. P. Kothari and J. L. Beeson, Eds. (DOE, Morgantown Energy Technol. Center, Morgantown, WV, 1990), p. 528.

- D. W. Camp, T. T. Coburn, and P. H. Wallman, "Mild Coal Gasification—Product Separation, Pilot-Unit Support, Twin Screw Heat Transfer, and H<sub>2</sub>S Evolution," in *Proc. 11th Ann. Gasification and Gas-Stream Cleanup Systems Contractors Rev.* **1** (DOE, Morgantown Energy Technol. Center, Morgantown, WV, 1991), p. 133.
- G. H. Campbell, S. M. Foiles, W. E. King, M. Rühle, and W. Wien, "HREM Investigation of the Structure of S5(210)/[001] Symmetric Tilt Grain Boundaries in Nb," in *Structure/Property Relationships for Metal/Metal Interfaces, Mater. Res. Soc. Symp. Proc.* **229**, J. Alton, D. Romig, D. E. Fowler and P. D. Bristowe, Eds. (Materials Research Society, Pittsburgh, PA, 1991), p. 191.
- R. J. Cena, "Hot-Recycled-Solid Pilot Plant 1991 Status Report," in *Proc. 24th Oil Shale Symp.* **83(4)** (Colorado School of Mines, Golden, CO, 1991), p. 60.
- L. L. Chase, "Solar Pumping of Solid State Lasers: Rapporteur's Report," in *Proc. National Academy of Sciences Workshop, Potential Applications of Solar Photons* (National Academy Press, Washington, DC, 1991), p. 93.
- L. L. Chase, A. V. Hamza, and H. W. H. Lee, "Laser Ablation and Optical Surface Damage," in *Proc. Workshop on Laser Ablation Mechanisms and Applications* **389**, J. C. Miller and R. F. Haglund, Eds. (Springer-Verlag, Berlin, 1991), p. 193.
- L. L. Chase, S. A. Payne, L. K. Smith, W. L. Kway, and W. F. Krupke, "Emission Cross Sections and Energy Extraction for the Mid-Infrared Transitions of Er, Tm, and Ho in Oxide and Fluoride Crystals," in *Proc. Advanced Solid State Lasers* **10**, G. Dube and L. Chase, Eds. (Optical Society of America, Washington, DC, 1991), p. 14.
- J. Chaudhuri, V. Gondhalekar, and A. F. Jankowski, "Analysis of the Strain Profile in Thin Au/Ni Multilayers by X-Ray Diffraction," in *Advances in Surface and Thin Film Diffraction, Mater. Res. Soc. Symp. Proc.* **208**, P. I. Cohen, D. J. Eaglesham and T. C. Huang, Eds. (Materials Research Society, Pittsburgh, PA, 1991), p. 211.
- J. Chaudhuri, S. Shah, V. Gondhalekar, and A. F. Jankowski, "Analysis of Au/Ni Multilayers by X-Ray Diffraction," in *Layered Structures—Heteroepitaxy, Superlattices, Strain and Metastability, Mater. Res. Soc. Symp. Proc.* **160**, L. J. Schowalter, F. H. Pollak, B. W. Dodson and J. E. Cunningham, Eds. (Materials Research Society, Pittsburgh, PA, 1990), p. 195.
- W. L. Clarke, J. C. Farmer, W. G. Halsey, and R. D. McCright, "Container Material Selection, Modeling and Testing," in *Proc. Int. Topical Meeting, High-Level Radiation Waste Management* **1** (American Nuclear Society and American Society of Civil Engineers, 1990), p. 437.
- T. T. Coburn, K. G. Foster, H. R. Gregg, and J. A. Lindsey, "Tests of a Mechanism for H<sub>2</sub>S Release during Coal Pyrolysis," in *Proc. 1991 Int. Conf. Coal Science* (1991), p. 616.
- T. T. Coburn and C. J. Morris, "New Albany Shale Flash Pyrolysis Under Hot-Recycled-Solid Conditions, Chemistry and Kinetics II," in *Proc. 1990 Eastern Oil Shale Symposium*, J. Stivers, Ed. (1990), p. 289.
- T. T. Coburn, R. W. Taylor, C. J. Morris, and R. W. Crawford, "Oil Shale Sulfur Chemistry," in *Proc. Oil Shale and Tar Sand Contractors Revi. Meeting* **90/6111**, T. C. Barke, Ed. (DOE, Morgantown Energy Technol. Center, Morgantown, WV, 1990), p. 103.
- G. W. Collins, J. R. Gaines, E. M. Fearon, J. L. Maienschein, E. R. Mapoles, R. T. Tsugawa, and P. C. Souers, "Triggered Energy Releases in Solid Hydrogen Hosts Containing Unpaired Atoms," in *Proc. High Energy Density Mater. Contractors Conf.*, L. P. Davis and F. J. Wodarczyk, Eds. (Air Force Office of Scientific Research, Long Beach, CA, 1990), p. 47.
- G. W. Collins, P. C. Souers, E. R. Mapoles, P. A. Fedders, F. Magnotta, and J. R. Gaines, "Extremely Large Atom Densities in Tritiated Solid Hydrogen," in *Proc. High Energy Density Mater. Contractors Conf.*, L. P. Davis and F. J. Wodarczyk, Eds. (Air Force Office of Scientific Research, Long Beach, CA, 1990), p. 235.
- G. W. Collins, P. C. Souers, E. R. Mapoles, and F. Magnotta, "Enhancing Atom Densities in Solid Hydrogen by Isotopic Substitution," in *Proc. High Energy Density Mater. Contractors Conf.*, M. E. Cordonnier, Ed. (Air Force Office of Scientific Research, Albuquerque, NM, 1991), p. 43.
- J. F. Cooper, W. Brummond, J. Celeste, J. Farmer, C. Hoenig, O. H. Krikorian, R. Upadhye, R. L. Gay, A. Stewart, and S. Yosim, "Molten Salt Processing of Mixed Wastes with Offgas Condensation," in *Proc. 1991 Incineration Conf.* (Univ. of California, Irvine, 1991), p. 31.
- J. J. DeYoreo and B. W. Woods, "Investigation of Strain Birefringence and Wavefront Distortion in 001 Plates of KD<sub>2</sub>PO<sub>4</sub>," in *Inorganic Crystals for Optics, Electro-Optics and Frequency Conversion, SPIE Conf. Proc.* **1561**, P. F. Bordui, Ed. (International Society for Optical Engineering, Bellingham, WA, 1991), p. 50.
- J. W. Elmer, "Non-Equilibrium Microstructures Produced During Electron-Beam and Laser-Beam Surface Modification of Metallic Alloys," in *Proc. TMS Metal Science of Joining Symposium* (The Metallurgical Society, Warrendale, PA, 1991), p. 123.

- J. W. Elmer and T. W. Eagar, "The Influence Of Cooling Rate On The Ferrite Content Of Stainless Steel Alloys," in *Proc. Recent Trends In Welding Sci. and Technol.*, S. A. David and J. M. Vitek, Eds. (American Society for Metals, Metals Park, OH, 1990), p. 165.
- J. W. Elmer, T. W. Eagar, and S. M. Allen, "Modeling Second-Phase Formation During Rapid Resolidification of Stainless Steel Alloys," in *Proc. ISIJ Stainless Steels 1991 Conf.* (The Iron and Steel Institute of Japan, 1991), p. 669.
- J. W. Elmer, T. W. Eagar, and S. M. Allen, "Single-Phase Solidification During Rapid Resolidification Of Stainless Steel Alloys," in *Proc. ASM Mater. Weldability of Mater. Symposium*, R. A. Patterson and K. W. Martins, Eds. (American Society for Metals, Metals Park, OH, 1990), p. 143.
- J. S. Felton, M. G. Knize, M. Roper, K. W. Turteltaub, K. Carroll, C. B. Thomas, B. E. Watkins, and M. Vanderlaan, "Isolation, Identification and Low Level Detection of Heterocyclic Amines in Cooked Foods," in *Proc. 15th Int. Cancer Cong., J. Cancer Res. and Clinical Oncology* **116**, 927 (1990).
- A. M. Frank and W. C. Tao, "Photography of Shock Waves in Explosive Crystals," in *Proc. SPIE Annual Meeting on Ultra High Speed Photography* (International Society for Optical Engineering, Bellingham, WA, 1991), in press [see LLNL Preprint JC-107195 (1991)].
- R. S. Glass, "Electrochemical Microsensors," in *Proc. DOE Conf. Technol. Res. and Development for Arms Control Verification* (Los Alamos National Laboratory, Los Alamos, NM, LA-11818-C, 1990), p. 115.
- R. S. Glass, K. C. Hong, K. Ashley, and R. L. Jones, "Electrochemical Array Sensors for Environmental Monitoring," in *Proc. 179th Meeting of The Electrochemical Soc.* **91-1** (The Electrochemical Society, Inc., Pennington, NJ, 1991), p. 1152.
- A. Gonis, P. E. A. Turchi, M. Sluiter, F. J. Pinski, and D. D. Johnson, "Phase Stability and Phase Diagrams of Al-Li Alloys," in *Mater. Res. Soc. Symp. Proc.* **186**, G. M. Stocks, D. P. Pope and A. F. Giamei, Eds. (Materials Research Society, Pittsburgh, PA, 1991), p. 89.
- L. W. Gray, R. G. Hickman, and J. C. Farmer, "Mediated Electrochemical Oxidation of Organics," in *Proc. First Int. Conf. Solvent Substitution*, E. Helminski, Ed. (Weapons Complex Monitor Forums, Washington, DC, 1990), p. 281.
- G. A. Henshall, M. E. Kassner, and R. S. Rosen, "Ambient-Temperature Creep Failure of Silver-Aided Diffusion Bonds Between Steel," in *Proc. 2nd Int. Conf. Diffusion Bonding*, D. J. Stephenson, Ed. (Elsevier, London, 1990), p. 13.
- R. G. Hickman, L. W. Gray, and Z. Chiba, "Mixed Waste Treatment with a Mediated Electrochemical Process," in *Proc. National Meeting of Am. Nucl. Soc.* **63**, I. O. Macke, Ed. (American Nuclear Society, LaGrange Park, IL, 1991), p. 69.
- R. B. Hoover, D. L. Shealy, P. C. Baker, T. W. Barbee, Jr., and A. B. C. Walker, Jr., "Development of the Water-window Imaging X-ray Microscope," in *Multilayer and Grazing Incidence X-Ray/EUV Optics, SPIE Symp. Proc.* **1546**, R. Hoover, Ed. (International Society for Optical Engineering, Bellingham, WA, 1991), p. 125.
- R. B. Hoover, D. L. Shealy, B. R. Brinkley, P. C. Baker, T. W. Barbee, Jr., and A. B. C. Walker, Jr., "X-Ray Imaging Microscope for Cancer Research," in *Proc. Technology 2000* (NASA, Washington, DC, NASA Con. Pub. 3109, Vol. 1, 1991), p. 73.
- R. B. Hoover, A. B. C. Walker, Jr., J. F. Lindblom, M. J. Allen, R. H. O'Neal, C. E. DeForest, and T. W. Barbee, Jr., "Solar Observations with the Multispectral Solar Telescope Array," in *Multilayer and Grazing Incidence X-Ray/EUV Optics, SPIE Symp. Proc.* **1546**, R. Hoover, Ed. (International Society for Optical Engineering, Bellingham, WA, 1991), p. 175.
- L. W. Hrubesh, T. M. Tillotson, and J. F. Poco, "Characterization of Ultralow-Density Silica Aerogel made from a Condensed Silica Precursor," in *Better Ceramics Through Chemistry IV, Mater. Res. Soc. Symp. Proc.* **180**, C. J. Brinker, D. E. Clark, D. R. Ulrich and B. J. Zelinski, Eds. (Materials Research Society, Pittsburgh, PA, 1990), p. 315.
- J. S. Huang, "Formation of Niobium Carbides in High-Dose Carbon-Ion-Implanted and Annealed Niobium," in *Mater. Res. Soc. Symp. Proc.* **157** (Materials Research Society, Pittsburgh, PA, 1990), p. 137.
- J. S. Huang and G. F. Gallegos, "The Behavior of Single Crystal Ta and W and Polycrystalline Nb-xTa Alloys in Liquid U during Tensile Testing at 1473K," in *Proc. 6th Int. Conf. Mechanical Behavior of Mater.* (Pergamon Press, New York, 1991), p. 657.
- A. F. Jankowski, "Implications of Interface Structure on the Elastic Properties of Metallic Multilayers—The Case of the Supermodulus Effect," in *Structure/Property Relationships For Metal/Metal Interfaces, Mater. Res. Soc. Symp. Proc.* **229**, A. D. Romig, Jr., D. E. Fowler and P. D. Bristowe, Eds. (Materials Research Society, Pittsburgh, PA, 1991), p. 53.
- A. F. Jankowski, "Structural Stability of Heat Treated W/B<sub>4</sub>C Multilayers," in *Layered Structures - Heteroepitaxy, Superlattices, Strain and Metastability, Mater. Res. Soc. Symp. Proc.* **160**, L. J. Schowalter, F. H. Pollak, B. W. Dodson and J. E. Cunningham, Eds. (Materials Research Society, Pittsburgh, PA, 1990), p. 611.

- A. F. Jankowski, R. J. Foreman, and D. M. Makowiecki, "Fabrication of Advanced X-Ray Optics with Magnetron Mini-Source Arrays," in *Multilayer Optics for Advanced X-Ray Applications*, SPIE Conf. Proc. **1547**, N. Ceglio, Ed. (International Society for Optical Engineering, Bellingham, WA, 1991), p. 14.
- A. F. Jankowski, D. M. Makowiecki, R. J. Foreman, M. A. McKernan, and R. G. Patterson, "Deposition Controlled Uniformity of Multilayer Mirrors," in *X-Ray/EUV Optics for Astronomy, Microscopy, Polarimetry, and Projection Lithography*, SPIE Conf. Proc. **1343**, R. B. Hoover and A.B.C. Walker, Jr., Eds. (International Society for Optical Engineering, Bellingham, WA, 1990), p. 32.
- A. F. Jankowski and D. G. Stearns, "Layer Formation in CuNi/C X-Ray Optics," in *Evolution of Thin Film and Surface Microstructure*, Mater. Res. Soc. Symp. Proc. **202**, C. V. Thompson, J. Y. Tsao and D. J. Srolovitz, Eds. (Materials Research Society, Pittsburgh, PA, 1991), p. 695.
- A. F. Jankowski, M. A. Wall, and D. M. Makowiecki, "Solid-State Amorphization in a Ti/B Multilayer," in *Proc. Annual Electron Microscopy Society of America Meeting* **49**, G. W. Bailey and E. L. Hall, Eds. (San Francisco Press, San Francisco, CA, 1991), p. 904.
- D. D. Johnson, P. E. A. Turchi, M. Sluiter, F. Pinski, G. M. Stocks, and D. M. Nicholson, "First-Principles Study of Phase Stability in Pd-Rh Substitutional Alloys," in *Mater. Res. Soc. Symp. Proc.* **186**, G. M. Stocks, D. P. Pope and A. F. Giamei, Eds. (Materials Research Society, Pittsburgh, PA, 1991), p. 21.
- M. E. Kassner, G. A. Henshall, and H. J. McQueen, "The Ductility and Microstructure of Aluminum and Aluminum-Magnesium Alloys Deformed to Large Strains at Elevated Temperatures," in *Proc. Hot Deformation of Aluminum Alloys*, TMS Conference, T. G. Langdon, H. D. Merchant, J. G. Morris and M. A. Zaidi, Eds. (The Metallurgical Society, Warrendale, PA, 1991), p. 261.
- M. E. Kassner, N. Q. Nguyen, G. A. Henshall, and H. J. McQueen, "The Effects of Temperature and Strain-Rate on the Extended Ductility of Aluminum," in *Proc. Advanced Aluminum and Magnesium Alloys*, ASM, T. Kahn and G. Effenberg, Eds. (American Society for Metals, Metals Park, OH, 1990), p. 591.
- M. E. Kassner, R. S. Rosen, G. A. Henshall, and K. D. Challenger, "Time-Dependent Failure of Silver-Interlayer Diffusion Bonds Between Non-Deforming Base-Metals," in *Proc. Inter. Conf. on Creep and Fracture of Eng. Mater. and Structures*, B. Wilshire and R. W. Evans, Eds. (Institute of Metals, London, 1990), p. 179.
- M. E. Kassner, M. C. Tolle, R. S. Rosen, G. A. Henshall, and J. W. Elmer, "Recent Advances in Understanding the Mechanical Behavior of Constrained Thin Metals in Brazes and Solid-State Bonds," in *Proc. TMS Metal Science of Joining Symp.* (The Metallurgical Society, Warrendale, PA, 1991), p. 223.
- D. D. Kautz, C. D. Anglin, and T. J. Ramos, "Precision Laser Cutting," in *Proc. The Laser Vs. Electron Beam in Welding, Cutting, and Surface Treatment, State of the Art 1989* **2**, R. Bakish, Ed. (Bakish Materials Corp., Englewood, NJ, 1990), p. 107.
- D. D. Kautz and J. J. Oldani, "The Use of 308L for Laser Welding," in *Proc. 46th Meeting of Interagency Manufacturing Operations Group—Subgroup on Joining*, H. A. Hancock, Jr., Ed. (Westinghouse Savannah River Co., Aiken, SC, 1991), p. 119.
- W. E. King, G. H. Campbell, A. Coombs, M. J. Mills, and M. Rühle, "HREM Investigation of the Structure of the S5(310)/[001] Symmetric Tilt Grain Boundary in Nb," in *Defects in Mater., Mater. Res. Soc. Symp. Proc.* **209**, P. D. Bristowe, J. E. Epperson, J. E. Griffith and Z. Liliental-Weber, Eds. (Materials Research Society, Pittsburgh, PA, 1991), p. 39.
- O. H. Krikorian, "Analysis of Plutonium and Uranium Volatilities from Mixed Wastes in the Molten Salt Processor," in *Proc. 1991 Incineration Conf* (Univ. of California, Irvine, 1991), p. 311.
- J. D. LeMay, T. M. Tillotson, L. W. Hrubesh, and R. W. Pekala, "Microstructural Dependence of Aerogel Mechanical Properties," in *Better Ceramics Through Chemistry IV*, Mater. Res. Soc. Symp. Proc. **180**, C. J. Brinker, D. E. Clar, D. R. Ulrich and B. J. Zelinski, Eds. (Materials Research Society, Pittsburgh, PA, 1990), p. 321.
- S. A. Letts, S. R. Buckley, F. M. Kong, E. F. Lindsay, and M. L. Sattler, "Structure and Properties of Resorcinol-Formaldehyde Gels," in *Macromolecular Liquids*, Mater. Res. Soc. Symp. Proc. **177**, C. R. Safinya, S. A. Safran and P. A. Pincus, Eds. (Materials Research Society, Pittsburgh, PA, 1990), p. 275.
- J. L. Maienschein, P. E. Barry, F. E. McMurphy, and J. S. Bowers, "A New Low Density, High Porosity Lithium Hydride-Beryllium Hydride Foam," in *X-ray/EUV Optics for Astronomy, Microscopy, Polarimetry, and Projection Lithography*, SPIE Conf. Proc. **1343** (International Society for Optical Engineering, Bellingham, WA, 1990), p. 477.

- E. R. Mapoles, F. Magnotta, G. W. Collins, and P. C. Souers, "Optical and Thermal Energy Discharge from Tritiated Solid Hydrogen," in *Proc. High Energy Density Mater. Contractors Conf.*, M. E. Cordonnier, Ed. (Air Force Office of Scientific Research, Albuquerque, NM, 1991), p. 209.
- R. D. McCright, J. C. Farmer, and D. L. Fleming, "An Electrochemical Approach to Predicting Corrosion Performance of Container Materials," in *Proc. 2nd Ann. Int. High-Level Radiation Waste Management Conf. 2* (American Nuclear Society and American Society of Civil Engineers, LaGrange Park, IL, 1991), p. 940.
- J. Mikalopas, M. Sluiter, P. E. A. Turchi, and P. A. Sterne, "A First-Principles Examination of Phase Stability in Ni-V Alloys," in *Mater. Res. Soc. Symp. Proc. 186*, G. M. Stocks, D. P. Pope and A. F. Giamei, Eds. (Materials Research Society, Pittsburgh, PA, 1991), p. 83.
- J. Mikalopas, P. A. Sterne, M. Sluiter, and P. E. A. Turchi, "First Principles Calculation of Phase Stability of High Temperature Intermetallic Alloys," in *Mater. Res. Soc. Symp. Proc. 213*, L. A. Johnson, D. P. Pope and J. O. Stiegler, Eds. (Materials Research Society, Pittsburgh, PA, 1991), p. 119.
- D. G. Miller, "Equal Eigenvalues in Multicomponent Diffusion: the Extraction of Diffusion Coefficients from Experimental Data in Ternary Systems," in *Proc. Fundamentals and Applications of Ternary Diffusion, 29th Ann. Conf. of Metallurgists of CIM*, G. R. Purdy, Ed. (Pergamon Press, New York, 1990), p. 29.
- Y. Noda, S. M. Shapiro, G. Shirane, Y. Yamada, K. Fuchizaki, and L. E. Tanner, "Structure Analysis of Ni-Al Martensite," in *Proc. International Conference on Martensite Transformations, ICOMAT '89, Mater. Sci. Forum 56-8*, B. C. Muddle, Ed. (Materials Research Society, Pittsburgh, PA, 1990), p. 299.
- M. A. Norton, D. Eimerl, C. A. Ebberts, S. P. Velsko, and C. S. Petty, "KD\*P Frequency Doubler for High Average Power Applications," in *Solid State Lasers, SPIE Conf. Proc. 1223*, (International Society for Optical Engineering, Bellingham, WA, 1990), p. 75.
- M. S. Oh and V. M. Oversby, "The Effect of Sample Preparation Methods on Glass Performance," in *XIV Symp. Scientific Basis for Nucl. Waste Management, Mater. Res. Soc. Symp. Proc. 212* (Materials Research Society, Pittsburgh, PA, 1990), p. 123.
- S. A. Payne, L. L. Chase, L. J. Atherton, J. A. Caird, W. L. Kway, M. D. Shinn, R. S. Hughes, and L. K. Smith, "Properties and Performance of the  $\text{LiCaAlF}_6:\text{Cr}^{3+}$  Laser Material," in *SPIE Proc. 1223* (International Society for Optical Engineering, Bellingham, WA, 1990), p. 84.
- R. W. Pekala, "Synthetic Control of Molecular Structure in Organic Aerogels," in *Polymer-Based Molecular Composites, Mater. Res. Soc. Symp. Proc. 171*, D. W. Schaefer and J. E. Marks, Eds. (Materials Research Society, Pittsburgh, PA, 1990), p. 285.
- R. W. Pekala and C. T. Alviso, "A New Synthetic Route to Organic Aerogels," in *Better Ceramics Through Chemistry IV, Mater. Res. Soc. Symp. Proc. 180*, C. J. Brinker, D. E. Clark, D. R. Ulrich and B. J. Zelinski, Eds. (Materials Research Society, Pittsburgh, PA, 1990), p. 791.
- R. W. Pekala, L. W. Hrubesh, T. M. Tillotson, C. T. Alviso, J. F. Poco, and J. D. LeMay, "A Comparison of Mechanical Properties and Scaling Law Relationships for Silica Aerogels and Their Organic Counterparts," in *Mechanical Properties of Porous and Cellular Mater., Mater. Res. Soc. Symp. Proc. 207*, L. Gibson, D. Green and K. Sieradski, Eds. (Materials Research Society, Pittsburgh, PA, 1991), p. 197.
- R. S. Porter, S. J. DeTeresa, J. A. Donovan, and R. L. Brady, "On the Compression of Organic Fibers and their Transverse Properties in Composites," in *Proc. 2nd Jpn. Int. SAMPE Symp.* (SAMPE, Covina, CA, 1991), p. 24.
- C. W. Price, "Analysis of Electroless Nickel Thin Films," in *Proc. 49th Annual Meeting of the Electron Microscopy Society of America*, G. W. Bailey, Ed. (San Francisco Press, Inc., San Francisco, CA, 1991), p. 510.
- C. W. Price, "Comparison of Low- and High-Voltage SEM Images of Beryllium," in *Proc. XII International Congress for Electron Microscopy*, G. W. Bailey, Ed. (San Francisco Press, Inc., San Francisco, CA, 1990), p. 400.
- C. W. Price, "The Concept of 'Axial-Symmetry Constraint' and Its Significance in Recrystallization," in *Proc. Recrystallization '90*, T. Chandra, Ed. (The Metallurgical Society, Warrendale, PA, 1990), p. 199.
- C. W. Price, "Use of Computer Simulations to Analyze Limitations of Kinetic Models for Recrystallization," in *Proc. Recrystallization '90*, T. Chandra, Ed. (The Metallurgical Society, Warrendale, PA, 1990), p. 789.
- C. W. Price and E. F. Lindsey, "Ground Surface Finishes in Carbonized Resorcinol/Formaldehyde Foam," in *Proc. XII International Congress for Electron Microscopy*, G. W. Bailey, Ed. (San Francisco Press, Inc., San Francisco, CA, 1990), p. 864.
- C. W. Price, E. F. Lindsey, and S. A. Letts, "EDS Analysis of Bromine in Polymers," in *Proc. 49th Annual Meeting of the Electron Microscopy Society of America*, G. W. Bailey, Ed. (San Francisco Press, Inc., San Francisco, CA, 1991), p. 1046.

- C. W. Price and J. C. Norberg, "Analyses of Particles in Beryllium by Ion Imaging," in *Proc. Secondary Ion Mass Spectroscopy (SIMS VII)*, A. Benninghoven, C. A. Evans, K. D. McKeegan, H. A. Storms and H. W. Werner, Eds. (Wiley and Sons, Chichester, England, 1990), p. 935.
- C. W. Price and J. C. Norberg, "Analysis of Nitrogen-Pulsed Sputtered Beryllium," in *Proc. Secondary Ion Mass Spectroscopy (SIMS VII)*, A. Benninghoven, C. A. Evans, K. D. McKeegan, H. A. Storms and H. W. Werner, Eds. (Wiley and Sons, Chichester, England, 1990), p. 727.
- C. O. Pruneda, E. S. Jessop, and R. R. McGuire, "Low-Vulnerability Explosives (LOVEX) for Mass-Use Warheads," in *Proc. Technol. of Polymer Compounds and Energetic Mater., 21st Int. Ann. Conf. of the ICT*, K. Menke, Ed. (Fraunhofer-Institut für Chemische Technologie, Karlsruhe, FRG, 1990), p. 96.
- C. O. Pruneda, R. R. McGuire, and R. Clements, "Development of a High Tensile Strain Plastic-Bonded Explosive," in *Proc. Technol. of Polymer Compounds and Energetic Mater., 21st Int. Ann. Conf. of the ICT*, K. Menke, Ed. (Fraunhofer-Institut für Chemische Technologie, Karlsruhe, FRG, 1990), p. 99.
- D. T. Reed, V. Swayambunathan, B. S. Tani, and R. A. Van Konynenburg, "Corrosion Product Identification and Relative Rates of Corrosion of Candidate Metals in an Irradiated Air-Steam Environment," in *Scientific Basis for Nucl. Waste Management XIII*, *Mater. Res. Soc. Symp. Proc.* **176**, V. M. Oversby and P. W. Brown, Eds. (Materials Research Society, Pittsburgh, PA, 1990), p. 517.
- D. T. Reed and R. A. Van Konynenburg, "Corrosion of Copper-based Materials in Irradiated Moist Air Systems," in *Scientific Basis for Nucl. Waste Management XIV*, *Mater. Res. Soc. Symp. Proc.* **212**, T. Abrajano, Jr. and L. H. Johnson, Eds. (Materials Research Society, Pittsburgh, PA, 1991), p. 317.
- D. T. Reed and R. A. Van Konynenburg, "Effect of Ionizing Radiation on the Waste Package Environment," in *Proc. High Level Radioactive Waste Management, Second Annual International Conference 2*, L. McClure, Ed. (American Nuclear Society, LaGrange Park, IL, 1991), p. 1396.
- S. P. Regan, L. K. Huang, M. Finkenthal, H. W. Moos, and T. W. Barbee, Jr., "Plasma Imaging in the XUV Wavelength Range (175 Å) Using Curved Layered-Synthetic-Microstructure Coated Surfaces," in *Multilayer and Grazing Incidence X-Ray/EUV Optics, SPIE Symp. Proc.* **1546**, R. Hoover, Ed. (International Society for Optical Engineering, Bellingham, WA, 1991), p. 322.
- R. S. Rosen, M. A. Viliardos, M. E. Kassner, D. G. Stearns, and S. P. Vernon, "Thermal Stability of Mo/Si Multilayers," in *Multilayer Optics for Advanced X-Ray Applications, SPIE Conf. Proc.* **1547** (International Society for Optical Engineering, Bellingham, WA, 1991), p. 212.
- G. C. Ruben and R. W. Pekala, "High Resolution TEM of Organic and Inorganic Aerogels," in *Better Ceramics Through Chemistry IV, Mater. Res. Soc. Symp. Proc.* **180**, C. J. Brinker, D. E. Clark, D. R. Ulrich and B. J. Zelinski, Eds. (Materials Research Society, Pittsburgh, PA, 1990), p. 785.
- M. Schilbach, L. L. Chase, and A. V. Hamza, "Investigation of Neutral and Ion Emission During Laser Conditioning of Multilayer HfO<sub>2</sub> - SiO<sub>2</sub> Coatings," in *Proc. 22nd Ann. Boulder Damage Symp., Laser-Induced Damage in Opt. Mater.: 1990* **1441**, H. E. Bennett, L. L. Chase, A. H. Guenther, B. E. Newnam and M. J. Soileau, Eds. (International Society for Optical Engineering, Bellingham, WA, 1990), p. 287.
- M. Schilbach, R. Tench, W. Siekhaus, M. Balooch, and L. L. Chase, "Nanometer Scale Pulsed Laser Modification of the Basal Plane of Graphite Observed With Scanning Tunneling Microscopy," in *Laser Ablation for Mater. Synthesis, Mater. Res. Soc. Symp. Proc.* **191** (Materials Research Society, Pittsburgh, PA, 1991), p. 79.
- M. A. Schilbach and A. V. Hamza, "Interaction of 1064 nm Photons With the Al<sub>2</sub>O<sub>3</sub> (11 $\bar{2}$ 0) Surface," in *Proc. 22nd Ann. Boulder Damage Symp., Laser-Induced Damage in Opt. Mater.: 1990* **1441**, H. E. Bennett, L. L. Chase, A. H. Guenther, B. E. Newnam and M. J. Soileau, Eds. (International Society for Optical Engineering, Bellingham, WA, 1990), p. 139.
- D. Schryvers and L. E. Tanner, "HREM Observations of the Omega Phase in Ti-Mo Alloys," in *Proc. Int. Conf. on Martensite Transformations, ICOMAT '89, Mater. Sci. Forum* **56-8**, B. C. Muddle, Ed. (1990), p. 329.
- M. D. Shinn, L. L. Chase, J. A. Caird, S. A. Payne, L. J. Atherton, and W. L. Kway, "Progress in the Development of LiCaF:Cr Laser Crystals," in *Proc. Advanced Solid State Lasers*, H. P. Jepsen and G. Dube, Eds. (Optical Society of America, Washington, DC, 1991), p. 48.
- M. Sluiter and P. E. A. Turchi, "The Role of Off-Diagonal Disorder on Alloy Phase Stability: An Application to the Ni-Pt System," in *Mater. Res. Soc. Symp. Proc.* **213**, L. A. Johnson, D. P. Pope and J. O. Stiegler, Eds. (Materials Research Society, Pittsburgh, PA, 1991), p. 101.



- M. Sluiter and P. E. A. Turchi, "Theoretical Investigation of Phase Stability in Non-Magnetic Fe-V Substitutional Alloys," in *Mater. Res. Soc. Symp. Proc.* **213**, L. A. Johnson, D. P. Pope and J. O. Stiegler, Eds. (Materials Research Society, Pittsburgh, PA, 1991), p. 37.
- M. Sluiter and P. E. A. Turchi, "Theoretical Investigation of Phase Stability in Paramagnetic Cu-Ni Alloys," in *Mater. Res. Soc. Symp. Proc.* **186**, G. M. Stocks, D. P. Pope and A. F. Giamei, Eds. (Materials Research Society, Pittsburgh, PA, 1991), p. 77.
- M. Sluiter and P. E. A. Turchi, "Theoretical Investigation of Phase Stability in Ti-V and Ti-Cr Substitutional Alloys," in *Mater. Res. Soc. Symp. Proc.* **186**, G. M. Stocks, D. P. Pope and A. F. Giamei, Eds. (Materials Research Society, Pittsburgh, PA, 1991), p. 95.
- M. Sluiter, P. E. A. Turchi, D. D. Johnson, F. J. Pinski, D. M. Nicholson, and G. M. Stocks, "A First Principles Study of Short Range Order in Cu-Zn," in *Mater. Res. Soc. Symp. Proc.* **166**, S. M. Shapiro, S. C. Moss and J. D. Jorgensen, Eds. (Materials Research Society, Pittsburgh, PA, 1990), p. 225.
- E. C. Sowa, A. Gonis, and X.-G. Zhang, "Electronic Structure of Grain Boundaries in Nb," in *Defects in Mater., Mater. Res. Soc. Symp. Proc.* **209**, P. D. Bristowe, J. E. Epperson, J. E. Griffith and Z. Liliental-Weber, Eds. (Materials Research Society, Pittsburgh, PA, 1991), p. 131.
- E. C. Sowa, A. Gonis, and X.-G. Zhang, "The Electronic Structure of S5 Grain Boundaries in Cu," in *Mater. Res. Soc. Symp. Proc.* **159** (Materials Research Society, Pittsburgh, PA, 1990), p. 395.
- E. C. Sowa, A. Gonis, and X.-G. Zhang, "First-Principles Calculations of the Electronic Structure of Grain Boundaries," in *Proc. Int. Cong. on Intergranular and Interphase Boundaries in Mater.: II* **B89** (Les Editions de Physique, Paris, France, 1990), p. 335.
- E. C. Sowa, A. Gonis, and X.-G. Zhang, "The Real-Space Multiple-Scattering Theory and The Electronic Structure of Grain Boundaries," in *Mater. Res. Soc. Symp. Proc.* **229** (Materials Research Society, Pittsburgh, PA, 1991), p. 129.
- D. G. Stearns, N. M. Ceglio, A. M. Hawryluk, R. S. Rosen, and S. P. Vernon, "Multilayer Optics for Soft X-Ray Projection Lithography: Problems and Prospects," in *Proc. Electron-Beam, X-Ray, and Ion-Beam Submicrometer Lithographies for Manufacturing* **1465** (International Society for Optical Engineering, Bellingham, WA, 1991), p. 80.
- D. G. Stearns, R. S. Rosen, and S. P. Vernon, "High Performance Multilayer Mirrors for Soft X-ray Projection Lithography," in *Multilayer Optics for Advanced X-Ray Applications, SPIE Conf. Proc.* **1547** (International Society for Optical Engineering, Bellingham, WA, 1991), p. 2.
- D. G. Stearns, R. S. Rosen, and S. P. Vernon, "High Performance Multilayer X-ray Optics," in *Proc. Short Wavelength Coherent Radiation: Generation and Applications* **11** (Optical Society of America, Washington, DC, 1991), p. 152.
- D. G. Stearns, R. S. Rosen, and S. P. Vernon, "Structural Characterization of Ru-B<sub>4</sub>C Multilayers Fabricated by Magnetron Sputtering," in *Advances in Surface and Thin Film Diffraction, Mater. Res. Soc. Symp. Proc.* **208** (Materials Research Society, Pittsburgh, PA, 1990), p. 143.
- L. E. Tanner, D. Schryvers, and S. M. Shapiro, "High-Resolution Electron Microscopy and Neutron Scattering Studies of a Martensitic Ni-Al Beta-phase Alloy," in *Proc. Workshop on First-Order Displacive Phase Transformations, Mater. Sci. Eng. A* **127**, L. E. Tanner and M. Wuttig, Eds. (1990), p. 205.
- L. E. Tanner and M. Wuttig, "Review of the Workshop on First-Order Displacive Phase Transformations," in *Proc. Workshop on First-Order Displacive Phase Transformations, Mater. Sci. Eng. A* **127-2**, L. E. Tanner and M. Wuttig, Eds. (1990), p. 137.
- R. J. Tench, M. Balooch, M. J. Allen, W. J. Siekhaus, D. R. Olander, and W. Wang, "SiC Films Deposition by Pulsed Laser Ablation," in *Mater. Res. Soc. Symp. Proc.* **191** (Materials Research Society, Pittsburgh, PA, 1990), p. 61.
- R. J. Tench, M. Balooch, L. Bernardez, B. L. Olson, W. J. Siekhaus, and D. R. Olander, "Observation of Cluster Formation in the Laser Ablation of Metals, Carbides and Oxides by Scanning Tunneling Microscopy and Laser Ionization Time-of-Flight Mass Spectrometry," in *Mater. Res. Soc. Symp. Proc.* **191** (Materials Research Society, Pittsburgh, PA, 1990), p. 85.
- A. A. Tesar, M. Balooch, K. W. Shotts, and W. J. Siekhaus, "Morphology and Laser Damage Studies by Atomic Force Microscopy of E-Beam Deposited AR and HR Coatings," in *Optical Mater. for High Power Lasers, SPIE Conf. Proc.* **1441** (International Society for Optical Engineering, Bellingham, WA, 1990), p. 228.
- A. A. Tesar, M. Balooch, B. Tench, C. Stolz, T. Sarginson, and W. Siekhaus, "Examination of Laser Conditioning Using Atomic Force Microscopy," in *Optical Mater. for High Power Lasers, SPIE Conf. Proc.* **1624** (International Society for Optical Engineering, Bellingham, WA, 1991), p. 12.

- A. A. Tesar, N. J. Brown, J. R. Taylor, and C. Stolz, "Subsurface Polishing Damage of Fused Silica: Nature and Effect on Laser Damage of Coated Surfaces," in *Optical Mater. for High Power Lasers, SPIE Conf. Proc.* **1441** (International Society for Optical Engineering, Bellingham, WA, 1990), p. 154.
- A. A. Tesar and B. Fuchs, "Removal Rates of Fused Silica with Cerium Oxide/Pitch Polishing," in *Advanced Manufacturing and Testing, SPIE Conf. Proc.* **1531** (International Society for Optical Engineering, Bellingham, WA, 1991), p. 80.
- T. M. Tillotson and L. W. Hrubesh, "Characterization of Partially Condensed Silica Formed from the Partial Hydrolysis of TMOS," in *Better Ceramics Through Chemistry IV, Mater. Res. Soc. Symp. Proc.* **180**, D. E. Clark, D. R. Ulrich and B. J. Zelinski, Eds. (Materials Research Society, Pittsburgh, PA, 1990), p. 309.
- J. G. Tobin, M. K. Wagner, X. Q. Guo, and S. Y. Tong, "Photoelectron Diffraction of Magnetic Ultrathin Films: Fe/Cu(001)," in *Mater. Res. Soc. Symp. Proc.* **208** (Materials Research Society, Pittsburgh, PA, 1991), p. 283.
- P. E. A. Turchi, "Interplay between Local Environment Effect and Electronic Structure Properties in Close Packed Structures," in *Mater. Res. Soc. Symp. Proc.* **206**, R. S. Averback, D. L. Nelson and J. Bernholc, Eds. (Materials Research Society, Pittsburgh, PA, 1991), p. 265.
- P. E. A. Turchi, R. H. Howell, A. L. Wachs, M. J. Fluss, F. J. Pinski, D. D. Johnson, G. M. Stocks, D. M. Nicholson, and W. Schweika, "Ordering Mechanism in Ni-Cr Alloys: Theory and Experiments," in *Mater. Res. Soc. Symp. Proc.* **166**, S. M. Shapiro, S. C. Moss and J. D. Jorgensen, Eds. (Materials Research Society, Pittsburgh, PA, 1990), p. 231.
- P. E. A. Turchi, M. Sluiter, F. J. Pinski, and D. D. Johnson, "A Comparative First Principles Study of Phase Stability in Ni-Al and Ni-Ti Alloys at Near-Equiatomic Composition," in *Mater. Res. Soc. Symp. Proc.* **186**, G. M. Stocks, D. P. Pope and A. F. Giamei, Eds. (Materials Research Society, Pittsburgh, PA, 1991), p. 59.
- P. E. A. Turchi, M. Sluiter, F. J. Pinski, D. D. Johnson, and G. M. Stocks, "From Electronic Structure to Alloy Phase Stability," in *Proc. Int. Symp. on Intermetallic Compounds: Structure and Mechanical Properties JIMIS-6*, O. Izumi, Ed. (Japan Institute for Metals, Sendai, Jpn, 1991), p. 215.
- P. E. A. Turchi, M. Sluiter, and G. M. Stocks, "A Comparative Study of Short Range Order in Fe-Cr and Fe-V Alloys around Equiatomic Composition," in *Mater. Res. Soc. Symp. Proc.* **213**, L. A. Johnson, D. P. Pope and J. O. Stiegler, Eds. (Materials Research Society, Pittsburgh, PA, 1991), p. 75.
- P. A. Urtiew and L. M. Erickson, "Multiple Gauges for *In Situ* Measurements of Pressure and Particle Velocity in Condensed Materials," in *Proc. 12th Int. Colloq. on Dynamics of Explosions and Reactive Systems, Dynamics of Detonations and Explosions: Detonations* **133**, *Progress in Astronautics and Aeronautics*, A. L. Kuhl, J. C. Leyer, A. A. Borisov and W. A. Sirignano, Eds. (American Institute of Aeronautics and Astronautics, Washington, DC, 1991), p. 371.
- R. A. Van Konynenburg, "Gaseous Release of Carbon-14: Why the High Level Waste Regulations Should Be Changed," in *Proc. High Level Radioactive Waste Management, 2nd Ann. Int. Conf.* **1**, L. McClure, Ed. (American Nuclear Society, LaGrange Park, IL, 1991), p. 313.
- M. Vanderlaan, B. E. Watkins, T. Djanegara, and J. S. Felton, "Immunochemical Detection of Cooked Meat Mutagens and Metabolites in Human Urine," in *Proc. 15th Int. Cancer Cong., J. Cancer Res. and Clinical Oncology* **116**, 106 (1990).
- S. P. Vernon, D. G. Stearns, R. S. Rosen, N. M. Ceglie, D. P. Gaines, M. Krumrey, and J. P. Muller, "Multilayer coatings on figured optics," in *Multilayer Optics for Advanced X-Ray Applications, SPIE Conf. Proc.* **1547** (International Society for Optical Engineering, Bellingham, WA, 1991), p. 39.
- E. von Holtz, K. Scribner, G. Moody, and R. McGuire, "The Search for High Energy Low Vulnerability Explosives," in *Proc. Technol. of Polymer Compounds and Energetic Mater., 21st Int. Ann. Conf. of ICT* (Fraunhofer-Institut für Chemische Technologie, Karlsruhe, FRG, 1990), p. 12.
- E. von Holtz, K. Scribner, R. Whipple, and J. Carley, "Paste Extrudable Explosives: Their History and Their Current Status," in *Proc. Technol. of Polymer Compounds and Energetic Mater., 21st Int. Ann. Conf. of ICT* (Fraunhofer-Institut für Chemische Technologie, Karlsruhe, FRG, 1990), p. 16.
- A. B. C. Walker Jr, J. F. Lindblom, J. G. Timothy, T. W. Barbee, Jr., R. B. Hoover, E. Tandberg-Hanssen, S. T. Wu, and J. Sahada, "Solar/stellar Coronal Explorer and the Solar/stellar Coronal Observatory," in *Multilayer and Grazing Incidence X-Ray/EUV Optics, SPIE Symp. Proc.* **1546**, R. Hoover, Ed. (International Society for Optical Engineering, Bellingham, WA, 1991), p. 281.
- A. B. C. Walker, Jr., C. C. Kankelborg, R. B. Hoover, T. W. Barbee, Jr., and P. C. Baker, "Narrow-band Solar Images in the Soft X-ray Regime with Multilayer Optics," in *Multilayer and Grazing Incidence X-Ray/EUV Optics, SPIE Symp. Proc.* **1546**, R. Hoover, Ed. (International Society for Optical Engineering, Bellingham, WA, 1991), p. 345.

A. B. C. Walker, Jr., J. F. Lindblom, J. G. Timothy, R. B. Hoover, E. Tandberg-Hanssen, and T. W. Barbee, Jr., "Ultrahigh-resolution XUV Spectroheliograph III: a Modified Configuration for a Free-flying Platform," in *Multilayer and Grazing Incidence X-Ray/EUV Optics*, SPIE Symp. Proc. **1546**, R. Hoover, Ed. (International Society for Optical Engineering, Bellingham, WA, 1991), p. 265.

M. A. Wall and A. F. Jankowski, "In Situ Observation of Solid-State Amorphization in a Ni/Ti Multilayer," in *Proc. 12th Int. Cong. for Electron Microscopy* **4**, L. D. Peachey and D. B. Williams, Eds. (San Francisco Press, Inc., San Francisco, CA, 1990), p. 128.

P. H. Wallman and R. C. J. Carlsson, "Fluidized Bed Combustion Kinetics at Elevated Pressures," in *Proc. 11th Int. Conf. on Fluidized-Bed Combustion* (American Society for Mechanical Engineers, New York, 1991), p. 1517.

P. H. Wallman, R. C. J. Carlsson, and E. L. Ivasson, "NO<sub>x</sub> and N<sub>2</sub>O Formation in Pressurized Fluidized-Bed Combustion Tests," in *Proc. 11th Int. Conf. on Fluidized-Bed Combustion* (American Society for Mechanical Engineers, New York, 1991), p. 1021.

P. H. Wallman, D. B. Fields, C. J. Morris, M. F. Singleton, C. B. Thorsness, and B. E. Watkins, "Oil Vapor Coking Kinetics over Oxidized Colorado Oil Shale," in *Proc. 6th Australian Workshop on Oil Shale* (Univ. of Queensland, St. Lucia, Brisbane, 1991), p. 47.

## Articles in Books

W. Brostow, R. C. Cook, and J. Kubat, "Molecular Dynamics and Monte Carlo Simulation of Polymeric Materials: Chain Relaxation Dynamics," in *Integral Methods in Science and Engineering—90*, A. Haji-Sheikh, Ed. (Hemisphere Publishing Corp., Washington, DC, 1991), p. 24.

L. Chiao, "Process Modeling, Cure," in *International Encyclopedia of Composites*, S. M. Lee, Ed. (VCH Publishers, New York, 1991), p. 483.

M. S. Costantino and J. B. Holt, "High Pressure Burning Rate of Silicon in Nitrogen," in *Combustion and Plasma Synthesis of High Temperature Materials*, Z. A. Munir and J. B. Holt, Eds. (VCH Publishers, New York, 1990), p. 315.

C. E. Walter, J. H. VanSant, J. E. Kammeraad, and R. A. Van Konynenburg, "Thulium Heat Source for High-Endurance and High-Energy-Density Power Systems," in *Proc. 26th Intersociety Energy Conversion Eng. Conf.* **2**, T. J. Bland, Ed. (American Nuclear Society, LaGrange Park, IL (1991), p. 234.

D. L. Windt, W. K. Waskiewicz, G. D. Kubiak, T. W. Barbee, Jr., and R. N. Watts, "XUV Characterization Comparison of Mo/Si Multilayer Coatings," in *X-Ray/EUV Optics for Astronomy, Microscopy, Polarimetry, and Projection Lithography*, SPIE Symp. Proc. **1343**, R. Hoover and A. Walker, Eds. (International Society for Optical Engineering, Bellingham, WA, 1990), p. 274.

X.-G. Zhang, P. J. Rous, J. M. MacLaren, A. Gonis, M. A. V. Hove, and G. A. Samorjai, "Real-Space Multiple Scattering Theory Calculations of LEED Intensities for Stepped Surfaces," in *Proc. ICSOS-3* (Springer-Verlag, New York, 1990).

J. L. Zhao, R. J. Willey, and R. W. Pekala, "Carbon Aerogels as Catalyst Supports," in *Synthesis and Properties of New Catalysts: Utilization of Novel Mater. Components and Synthetic Techniques*, Mater. Res. Soc. Symp. Proc. **24**, E. W. Corcoran, Jr., M. J. Ledoux and J. R. Knox, Eds. (Materials Research Society, Pittsburgh, PA, 1990), p. 145.

S. J. Zinkle and J. S. Huang, "Mechanical Properties of Carbon-Implanted Niobium," in *Mater. Res. Soc. Symp. Proc.* **188**, W. Oliver, M. Doerner, G. Pharr and F. R. Brotzen, Eds. (Materials Research Society, Pittsburgh, PA, 1990), p. 121.

L. M. Hair and S. A. Letts, "Gels and Foams from Ultra-High Molecular Weight Polyethylene," in *Advances in Chemistry*, C. D. Craver and T. Provder, Eds. Series No. 227, Polymer Characterization (American Chemical Society, Washington, D.C., 1990), Ch. 8.

D. W. Hall and M. J. Weber, "Glass Lasers," in *Handbook of Laser Science and Technology, Suppl. 1: Lasers*, (CRC Press, Boca Raton, FL, 1991), p. 137.

D. D. Kautz, "Laser Cutting Safety," in *Welding Handbook*, R. L. O'Brien, Ed. (American Welding Society, Miami, FL, 1991), p. 522.

D. D. Kautz and A. C. Lingenfelter, "Thin Section Welding," in *Welding Handbook*, R. L. O'Brien, Ed. (American Welding Society, Miami, FL, 1991), p. 728.

- W. E. King and B. S. Lawver, "Refinement of Interface Atomic Structure from HREM Images," in *Microbeam Analysis*, D. G. Howitt, Ed. (San Francisco Press, San Francisco, CA, 1991), p. 217.
- D. G. Miller and J. G. Albright, "Measurement of the Transport Properties of Fluids: Experimental Thermodynamics," in *Optical Methods*, W. A. Wakeham, A. Nagashima, and J. V. Sengers, Eds. (Blackwell Scientific Publications, Oxford, England, 1991), p. 272.
- A. R. Mitchell, A. Rahman, and R. B. Merrifield, "Preparation and Use of 2-*t*-Butoxyphenol for the Synthesis of Monoaminoacyl Catechol Derivatives," in *Peptides 1990*, E. Giralt and D. Andreu, Eds. (Escom Science Publishers, Leiden, The Netherlands, 1990), p. 39.
- J. G. Reynolds, "Effect of Asphaltene Precipitation on the Size of Vanadium-, Nickel- and Sulfur-Containing Compounds in Heavy Crude Oils and Residua," in *Asphaltene and Asphalt* (Elsevier, Amsterdam, 1991), Ch. 5.
- L. Stanker, M. Vanderlaan, B. E. Watkins, R. Ellis and J. Rajan, "An Immunoassay for Heptachlor in Animal Fats," in *Immunoassays for Trace Chemical Analysis*, M. Vanderlaan, L. Stanker, and B. E. Watkins, Eds. (American Chemical Society, Washington, DC, 1991), p. 2.
- L. H. Stanker, B. E. Watkins, and M. Vanderlaan, "Environmental Monitoring by Immunoassay," in *Pesticide Chemistry*, H. Frehse, Ed. (VCH Publishers, New York, 1991), p. 398.
- W. C. Tao and C. W. Frank, "Energy Migration in Polymeric Blends and Solutions," in *Lasers in Polymer Science and Technology: Applications*, J. P. Fouassier and J. F. Rabek, Eds. (CRC Press, Boca Raton, FL, 1989).
- A. A. Tesar, W. K. Eickelberg, and J. R. Taylor, "Interferometric Measurements of Refractive Index Inhomogeneity in Fused Silica Windows," in *Solid State Optical Materials*, A. Bruce and B. Hiremath, Eds. (American Ceramic Soc., Columbus, OH, 1991), p. 62.
- M. Vanderlaan, M. Hwang, M. G. Knize, B. E. Watkins, and J. S. Felton, "Monoclonal Antibody Based Immunoassays for Cooking-Induced Meat Mutagens," in *Mutation and the Environment. Part E: Environmental Genotoxicity, Risk, and Modulation*, M. Mendelsohn and R. J. Albertini, Eds. (Wiley-Liss, Inc., New York, 1990), p. 189.
- M. Vanderlaan, L. Stanker, and B. E. Watkins, "Immunochemical Techniques in Trace Residue Analysis," in *Immunoassays for Trace Chemical Analysis*, M. Vanderlaan, L. Stanker, B. E. Watkins, and D. Roberts, Eds. (American Chemical Society, Washington, DC, 1991), p. 108.
- M. J. Weber, "Optical Properties," in *Glasses and Amorphous Materials, Materials Science and Technology*, J. Zarzycki, Ed. (VCH Publishers, New York, 1991), p. 619.
- M. J. Weber, "Solid State Dye Lasers," in *Handbook of Laser Science and Technology, Supplement 1: Lasers* (CRC Press, Boca Raton, FL, 1991), p. 159.
- J. D. Young and A. R. Mitchell, "Use of *N*-Benzylglycine as a Replacement for Aromatic Amino Acid Residues. Synthesis of [*N*-Benzylglycine<sup>7</sup>]-Bradykinin," in *Peptides: Structure and Function*, J. E. Rivier and G. R. Marshall, Eds. (Escom Science Publishers, Leiden, The Netherlands, 1989), p. 155.
- X.-G. Zhang, E. C. Sowa, and A. Gonis, "A First-Principles Method for the Determination of the Electronic Structure of Grain Boundaries," in *Metal-Ceramic Interfaces*, M. Rühle, A. G. Evans, M. F. Ashby, and J. P. Hirth, Eds. (Pergamon Press, New York, 1990), p. 25.

## Edited Books, Journals, and Proceedings

- Multilayer Materials*, T. W. Barbee, Jr., Guest Ed., *MRS Bull.* **XV**(2) (1990).
- Proc. Fourth Int. Otto Schott Colloquium*, W. Höland and M. J. Weber, Eds., *J. Non-Cryst. Solids* **129** (1991).
- Scientific Basis for Nucl. Waste Management XIII, Mater. Res. Soc. Symp. Proc.* **176**, V. M. Oversby and P. W. Brown, Eds. (Materials Research Society, Pittsburgh, PA, 1990).
- Handbook of Laser Science and Technology, Suppl. 1: Lasers*, M. J. Weber, Ed. (CRC Press, Boca Raton, FL, 1991).

## Reports

A. Alcaraz, B. D. Andresen, R. J. Eagle, J. S. Haas, W. H. Martin, R. R. McGuire, and R. D. Sanner, *Results of Analysis International Round Robin Three in Support of the CWC*, Lawrence Livermore National Laboratory, Livermore, CA, UCRL-ID-109085 (1991).

A. Alcaraz, B. D. Andresen, and W. H. Martin, *Finnigan Ion Trap Mass Spectrometer Detection Limits and Thermal Energy Analyzer Interface Status Report and Present Capabilities*, Lawrence Livermore National Laboratory, Livermore, CA, UCRL-ID-105197 (1990).

D. F. Aldis, W. Quirk, and R. D. Breithaupt, *The Effect of Detonation Curvature on Cylindrical Wall Motion*, Lawrence Livermore National Laboratory, Livermore, CA, UCRL-ID-107480 (1991).

C. Alford, F. Serduke, D. Makowiecki, A. Jankowski, and M. Wall, *X-Ray Fiducial Foils*, Lawrence Livermore National Laboratory, Livermore, CA, UCRL-JC-105704 (1991).

B. D. Andresen, R. J. Eagle, J. S. Haas, A. Alcaraz, and W. H. Martin, *Characterization of Round-Robin II Samples*, Lawrence Livermore National Laboratory, Livermore, CA, UCRL-ID-195955 (1990).

W. L. Clarke, J. C. Farmer, W. G. Halsey, and R. D. McCright, *Container Material Selection, Modeling, and Testing*, Lawrence Livermore National Laboratory, Livermore, CA, UCRL-101877 (1991).

R. C. Cook, G. E. Overturf III, B. L. Haendler, F.-M. Kong, and S. A. Letts, *Low-Density Foam Materials from Styrene-Ethylbenzene Inverse Emulsions*, Lawrence Livermore National Laboratory, Livermore, CA, UCRL-LR-109207 (1991).

J. C. Farmer, Z. Chiba, and R. G. Hickman, *Annular-Flow Electrochemical Cell for Silver(II) Generation: Steady-State Performance Calculations*, Lawrence Livermore National Laboratory, Livermore, CA, UCRL-LR-106858 (1991).

J. C. Farmer, R. G. Hickman, F. T. Wang, P. R. Lewis, and L. J. Summers, *Electrochemical Treatment of Mixed and Hazardous Wastes: Oxidation of Ethylene Glycol by Ag(II)*, Lawrence Livermore National Laboratory, Livermore, CA, UCRL-JC-106947, Rev. 2 (1991).

J. C. Farmer, R. G. Hickman, F. T. Wang, P. R. Lewis, and L. J. Summers, *Initial Study of the Complete Mediated Electrochemical Oxidation of Ethylene Glycol*, Lawrence Livermore National Laboratory, Livermore, CA, UCRL-LR-106479 (1991).

J. C. Farmer, F. T. Wang, R. A. Hawley-Fedder, P. R. Lewis, L. J. Summers, and L. Foiles, *Electrochemical Treatment of Mixed and Hazardous Wastes: Oxidation of Benzene by Ag(II)*, Lawrence Livermore National Laboratory, Livermore, CA, UCRL-JC-107043, Rev. 2 (1991).

J. C. Farmer, F. T. Wang, R. A. Hawley-Fedder, P. R. Lewis, L. J. Summers, and L. Foiles, *Initial Study of Halide-Tolerant Mediators for the Electrochemical Treatment of Mixed and Hazardous Wastes*, Lawrence Livermore National Laboratory, Livermore, CA, UCRL-LR-107781 (1991).

J. C. Farmer, F. T. Wang, P. R. Lewis, and L. J. Summers, *Electrochemical Treatment of Mixed and Hazardous Wastes: Oxidation of Ethylene Glycol by Cobalt(III) and Iron(III)*, Lawrence Livermore National Laboratory, Livermore, CA, UCRL-JC-109134 (1991).

A. L. Frahm, K. J. Scribner, and E. von Holtz, *Extrusion Cast Explosives (ECX) in the TOW-2 Warhead*, Lawrence Livermore National Laboratory, Livermore, CA, UCRL-ID-106755 (1991).

R. S. Glass, K. C. Hong, K. Ashley, and V. E. Granstaff, *Versatile Electrochemical Microsensors for Environmental Monitoring*, Lawrence Livermore National Laboratory, Livermore, CA, UCRL-JC-108143 (1991).

W. G. Halsey, *Selection Criteria for Container Materials at the Proposed Yucca Mountain High Level Nuclear Waste Repository*, Lawrence Livermore National Laboratory, Livermore, CA, UCRL-102285 (1989).

W. G. Halsey, *Preliminary Selection Criteria for the Yucca Mountain Project Waste Package Container Material*, Lawrence Livermore National Laboratory, Livermore, CA, UCRL-ID-104552 (1991).

R. A. Hawley-Fedder and B. Andresen, *Sampling and Extraction Techniques for Organic Analysis of Soil Samples*, Lawrence Livermore National Laboratory, Livermore, CA, UCRL-ID-106599 (1991).

G. A. Henshall and N. Q. Nguyen, *Ambient Temperature Fracture Strength of Pure Alumina*, Lawrence Livermore National Laboratory, Livermore, CA, UCRL-ID-105842 (1990).

R. W. Hopper, *Plane Stokes Flow Driven by Capillarity on the Free Surfaces of a Doubly Connected Region*, Lawrence Livermore National Laboratory, Livermore, CA, UCRL-ID-105872 (1991).

- L. W. Hrubesh and J. Poco, *Development of Low-Density Silica Aerogels as a Capture Medium for Hypervelocity Particles—Summary Report FY91*, Lawrence Livermore National Laboratory, Livermore, CA, UCRL-CR-105858-91 (1991).
- L. W. Hrubesh and J. F. Poco, *Development of Low-Density Silica Aerogel as a Capture Medium for Hypervelocity Particles: Summary Report FY90*, Lawrence Livermore National Laboratory, Livermore, CA, UCRL-CR-105466 (1990).
- L. W. Hrubesh and T. M. Tillotson, *Development of Optically Active Aerogels*, Lawrence Livermore National Laboratory, Livermore, CA, UCRL-CR-105363 (1990).
- D. D. Kautz and R. P. Decofano, *Enable Kit (MC-4246) for the DOT Charged Line System*, Lawrence Livermore National Laboratory, Livermore, CA, UCRL-ID-104523 (1991).
- D. D. Kautz, D. E. Hoffman, and C. N. Westrich, *Weldability of AerMet 100*, Lawrence Livermore National Laboratory, Livermore, CA, UCRL-ID-106142 (1991).
- F.-M. Kong, S. R. Buckley, C. L. Giles, Jr., B. L. Haendler, L. M. Hair, S. A. Letts, G. E. Overturf III, C. W. Price, and R. C. Cook, *Low-Density Carbonized Resorcinol-Formaldehyde Foams*, Lawrence Livermore National Laboratory, Livermore, CA, UCRL-LR-106946 (1991).
- O. H. Krikorian, *A Preliminary Assessment of Salt and Radionuclide Volatilities in the Molten Salt Processor*, Lawrence Livermore National Laboratory, Livermore, CA, UCRL-ID-105173 (1990).
- O. H. Krikorian, *Estimation of Uranyl Acetate Volatilities in the Molten Salt Processor Under Pyrolytic Operating Conditions*, Lawrence Livermore National Laboratory, Livermore, CA, UCRL-ID-107877 (1991).
- O. H. Krikorian, *Selection of Molten Salt Compositions for Bench-Scale Molten Salt Processor Tests*, Lawrence Livermore National Laboratory, Livermore, CA, UCRL-ID-107091 (1991).
- E. M. Larson, A. F. Jankowski, W. A. Hamilton, and G. S. Smith, *Reflectivity Studies of Ni/Ti Neutron Mirrors*, Los Alamos National Laboratory, Los Alamos, NM, LANL-LA-11933-PR (1990).
- E. M. Larson, A. F. Jankowski, W. A. Hamilton, and G. S. Smith, *Reflectivity Studies of Nickel Titanium Neutron Mirrors*, Los Alamos National Laboratory, Los Alamos, NM, LANL-LA-12194-PR (1990).
- H. R. Leider, S. N. Nguyen, R. B. Stout, and H. C. Weed, *Estimating the Time for Dissolution of Spent Fuel Exposed to Unlimited Water*, Lawrence Livermore National Laboratory, Livermore, CA, UCRL-ID-107289 (1991).
- J. L. Maienschein and F. E. McMurphy, *Infrared Spectra of Crystalline and Amorphous Beryllium Hydride*, Lawrence Livermore National Laboratory, Livermore, CA, UCRL-JC-108814 (1991).
- D. Munro, G. Glendinning, R. Wallace, and J. Kilkenny, *Nova Rayleigh-Taylor Experiment*, Lawrence Livermore National Laboratory, Livermore, CA, UCRL-ID-106304 (1991).
- A. L. Nichols III and F. H. Ree, *CHEQ 2.0 User's Manual*, Lawrence Livermore National Laboratory, Livermore, CA, UCRL-MA-106754 (1990).
- D. U. Olness and A. S. Warshawsky, *Technique for Evaluating Combat Potential Subsequent to a Deep Attack*, Lawrence Livermore National Laboratory, Livermore, CA, UCRL-ID-105975 (1991).
- D. U. Olness, A. S. Warshawsky, and M. J. Uzelac, *Modeling the MLRS/TGW Weapon System in Janus*, Lawrence Livermore National Laboratory, Livermore, CA, UCRL-ID-104129 (1990).
- V. M. Oversby, *The Need for a Full-System Analysis when Evaluating Energy Options*, Lawrence Livermore National Laboratory, Livermore, CA, UCRL-JC-103606 (1990).
- V. M. Oversby, *Low-Cost Energy Production: The Responsibility of the Developed Countries toward the Less-Developed*, Lawrence Livermore National Laboratory, Livermore, CA, UCRL-JC-109004 (1991).
- V. M. Oversby and D. L. Phinney, *The Structure of Alteration Layers on Case Glass Surfaces*, Lawrence Livermore National Laboratory, Livermore, CA, UCRL-JC-107901 (1991).
- P. F. Pagoria, C. L. Coon, A. R. Mitchell, D. R. Breithaupt, and R. L. Simpson, *Synthesis of a New, Insensitive Explosive*, UCRL-LR-105446-91-1 (1991).
- P. F. Pagoria and A. R. Mitchell, *The Synthesis, Scale-Up and Characterization of a New Explosive*, Sandia National Laboratories, Livermore, CA, SAND-90-1104 (1990).
- P. F. Pagoria, A. R. Mitchell, C. L. Coon, and D. R. Breithaupt, *Synthesis, Scale-Up and Characterization of 2-Oxo-1,3,5-triaza-1,3,5-trinitrocyclohexane (K-6)*, Joint DOD/DOE Munitions Technology Development Program-FY89, Lawrence Livermore National Laboratory, UCRL-ID-103486-89 (1990).

P. F. Pagoria, A. R. Mitchell, C. L. Coon, and R. L. Simpson, *Synthesis, Scale-Up, and Characterization of a New Insensitive Explosive*, Joint DOE/DOE Munitions Technology Development Program-FY90, UCRL-ID-103486-90 (1991).

C. O. Pruneda, E. S. Jessop, and R. R. McGuire, *Low-Vulnerability Explosives for Mass-Use Warheads*, Lawrence Livermore National Laboratory, Livermore, CA, UCRL-102391 (1990).

C. O. Pruneda, E. S. Jessop, R. R. McGuire, C. M. Walkup, W. R. Black, and F. H. Helm, *Low-Vulnerability Explosives (LOVEX) for Mass-Use Warheads Part I: The Processing and Vulnerability Testing of LOVEX Formulations RX-35-AQ, RX-35-AS, and RX-35-AT*, Lawrence Livermore National Laboratory, Livermore CA, UCRL-ID-106441 (1991).

C. O. Pruneda, R. R. McGuire, and R. Clements, *Development of a High Tensile Strain Plastic-Bonded Explosive*, Lawrence Livermore National Laboratory, Livermore, CA, UCRL-102395 (1990).

D. Ress, L. J. Suter, S. G. Glendinning, D. W. Phillion, G. Stone, and R. J. Wallace, *Low-Z/High-Z-Interface Motion in Radiatively Driven Composite Targets*, Lawrence Livermore National Laboratory, Livermore, CA, UCRL-JC-105522 (1991).

R. S. Rosen, *Time-Dependent Failure of Silver Interlayer Welds*, Lawrence Livermore National Laboratory, Livermore, CA, UCRL-53945 (1990).

G. P. Russ III, M. W. Caffee, G. B. Hudson, and N. A. Storch, *Reduction of Multi-element Mass Spectra*, Lawrence Livermore National Laboratory, Livermore, CA, UCRL-CR-104525 (1990).

G. P. Russ III and G. F. Hunt, *Operation of Inductively Coupled Plasma Source Mass Spectrometers in the Peak-Jumping Mode*, Lawrence Livermore National Laboratory, Livermore, CA, UCRL-CR-104524 (1990).

J. J. Sanchez and R. S. Upadhye, *A Non-Destructive Method for Measuring the Fill Pressure and Permeability of Fuel-filled Plastic Shells*, Lawrence Livermore National Laboratory, UCRL-LR-105821-91-1 (1991).

R. D. Sanner, *Chemistry of GB and GD Precursors and Decontamination Products on Environmental Surfaces*, Lawrence Livermore National Laboratory, Livermore, CA, UCRL-ID-109418 (1991).

M. Sluiter and P. E. A. Turchi, *Phase Stability of Artificial Metallic Superlattices: Chemical Order Effect*, Lawrence Livermore National Laboratory, Livermore, CA, UCRL-JC-108156 (1991).

M. Sluiter and P. E. A. Turchi, *The Role of Chemical Interactions in the Stability of Artificial Metallic Superlattices*, Lawrence Livermore National Laboratory, Livermore, CA, UCRL-JC-107696 (1991).

M. Sluiter, P. E. A. Turchi, F. J. Pinski, and G. M. Stocks, *A First-Principles Study of Phase Stability in Ni-Al and Ni-Ti Alloys*, Lawrence Livermore National Laboratory, Livermore, CA, UCRL-JC-108606 (1991).

M. Sluiter, P. E. A. Turchi, F. J. Pinski, and G. M. Stocks, *Theoretical Study of Phase Stability in Ni-Al and Ni-Ti Alloys*, Lawrence Livermore National Laboratory, Livermore, CA, UCRL-JC-108775 (1991).

M. P. Stratman, *Tensile Testing at High Temperatures in a Glovebox*, Lawrence Livermore National Laboratory, Livermore, CA, UCRL-ID-104929 (1990).

M. J. Strum, T. J. Ramos, and J. R. Murchie, *ALT 328 Laser Weld Characterization*, Lawrence Livermore National Laboratory, Livermore, CA, UCRL-ID-107017 (1991).

P. E. A. Turchi and M. Sluiter, *Stability of Metallic Superlattices*, Lawrence Livermore National Laboratory, Livermore, CA, UCRL-JC-108838 (1991).

P. E. A. Turchi, M. Sluiter, and G. M. Stocks, *First-Principles Prediction of Alloy Phase Stability*, Lawrence Livermore National Laboratory, Livermore, CA, UCRL-JC-109140 (1991).

R. S. Upadhye and J. G. Wilder, *An Improved Method for Making Polystyrene Microspheres*, Lawrence Livermore National Laboratory, UCRL-LR-105821-91-1 (1991).

P. A. Urtiew and B. Hayes, *Parametric Study of the Dynamic JWL-EOS for Detonation Products*, Lawrence Livermore National Laboratory, Livermore, CA, UCRL-JC-103219 (1990).

P. A. Urtiew and T. M. Cook, *Pressure Measurements During the W79 ALT SOC Explosive Propagation (1804 M) Test*, Lawrence Livermore National Laboratory Livermore, CA, UCRL-ID-104167 (1990).

S. P. Velsko and L. M. Hair, *Harmonic Generation in Ferroelectric Liquid Crystals and Chiral Polymers*, Lawrence Livermore National Laboratory, Livermore, CA, UCRL-53689-90 (1990).

E. von Holtz, J. D. LeMay, J. F. Carley, and G. L. Flowers, *Dependence of the Specific Volume of RX-08-FK High-Energy Paste on Temperature and Pressure*, Lawrence Livermore National Laboratory, Livermore, CA, UCRL-JC-107078 (1991).

P. H. Wallman, *Separation of Products from Mild Coal Gasification Processes*, Lawrence Livermore National Laboratory, Livermore, CA, UCRL-ID-108327 (1991).

A. S. Warshawsky and D. U. Olness, *Quantifying the Effectiveness of TNF and ACM*, Lawrence Livermore National Laboratory, Livermore, CA, UCRL-JC-107814 (1991).

A. S. Warshawsky, D. U. Olness, J. E. Pimper, M. J. Uzelac, and J. Wilson, *Effectiveness of Tiltrotor Aircraft Support to Ground Combat*, Lawrence Livermore National Laboratory, Livermore, CA, UCRL-ID-106416 (1991).

C. E. Witherell, *Wastage-Resistant FBC Evaporator Tubing Through Microalloying*, Lawrence Livermore National Laboratory, Livermore, CA, UCRL-CR-109002 (1991).

F. Ze, R. L. Kaufmann, R. K. Turner, L. J. Suter, N. Landen, H. N. Kornblum, S. M. Pollaine, and R. J. Wallace, *Results of Laser Transport and Energy Deposition in Hohlraums Driven by Shaped Laser Pulses*, Lawrence Livermore National Laboratory, Livermore, CA, UCRL-MI-105503 (1991).

Y. Zundelevich, *The Mediated Electrochemical Dissolution of Plutonium Oxide: Kinetics and Mechanism*, Lawrence Livermore National Laboratory, Livermore, CA, UCRL-JC-106889 (1991).

## Lectures

T. W. Barbee, Jr., "Multilayer Materials: X-Ray Optics and Atomically Engineered Materials," at IBM, Almaden Research Laboratory, San Jose, CA, December 13, 1990.

T. W. Barbee, Jr., "Multilayer Structures: X-Ray Optics and Atomically Engineered Materials," at Advanced Photon Source, Argonne National Laboratory, Argonne, IL, June 19, 1990.

T. W. Barbee, Jr., "Multilayer Structures: Atomic Engineering in Its Infancy," at Stanford Univ., Stanford, CA, October 11, 1991.

L. Chiao, "Using Indigenous Materials for Future Lunar and Mars Missions," at Lawrence Livermore National Laboratory, Livermore, CA, June 13, 1991.

G. W. Collins, "The Quest for a Nuclear Spin Temperature Near 0 K in a Hot Quantum Solid," at Univ. of California at Davis, Department of Applied Science, Livermore, CA, May 29, 1990.

R. C. Cook, "Solution Properties of Rigid Rod Polymers," at Univ. of Alabama, Birmingham, AL, October 1990.

R. C. Cook, "Solvent Dependence at the Chain Dimensions of Poly (n-hexylisoryante)," at Colorado State Univ., Fort Collins, CO, October 1990.

R. C. Cook, "Doped Polymer Needs at LLNL," at DuPont, Wilmington, DE, April 1991.

R. C. Cook, "Doped Polymer Needs at LLNL—An Update," at DuPont, Wilmington, DE, December 1991.

R. C. Cook, "Polymeric Materials and Coatings for Direct Drive ICF Experiments," at California Polytechnic Univ., San Luis Obispo, CA, November 1991.

M. S. Costantino, "High-Pressure, High-Temperature Mechanical Equation-of-State Research," at Case-Western Reserve Univ., Cleveland, OH, September 1990, and at Aluminum Company of America, Alcoa Center, PA, September 1990.

J. J. DeYoreo, "The Role of Magmatism in the Formation of Low-Pressure Metamorphic Belts," at IV Summer School on the Petrological and Structural Analysis of Plutonic Complexes, Sienna, Italy, September 23–October 6, 1990.

J. J. DeYoreo, "Characterization, Identification and Elimination of Defects in  $\text{LiCaAlF}_6:\text{Cr}^{3+}$ ," at Oklahoma State Univ., Stillwater, OK, January 1991.

J. J. DeYoreo, "Design and Materials Issues for the Beamlet Pockels Cell," at Commission Energie Atomique Laboratory, Limeill, France, June 1991.

J. J. DeYoreo, "The Formation, Growth, and Elimination of Defects in  $\text{Cr}:\text{LiCaAlF}_6$ ," at Cornell Univ., Ithaca, NY, November 1991.

R. S. Glass, "Versatile Electrochemical Microsensors for Environmental, Corrosion, and Process Monitoring," at General Electric Company Vallecitos Nuclear Center, Pleasanton, CA, October 30, 1991, and at Northrop Corporation, Los Angeles, CA, November 6, 1991.

A. Gonis, "Multiple Scattering Theory for Space-Filling Potential Cells," at Univ. of Kentucky Supercomputer Center, Lexington, KY, June 4, 1991.

A. V. Hamza, "Photon Absorption by Sapphire Surfaces," at Fakultät für Physik der Technischen Universität München, München, FRG, September 18, 1991.



- R. G. Hickman, "Aqueous Process Development at LLNL," at Los Alamos National Laboratory, Los Alamos, NM, March 1991.
- L. W. Hrubesh, "Silica Aerogel: A High-Tech Material with Fascinating Properties," at California Institute of Technology, Pasadena, CA, May 1990, at Wisconsin State Univ., Eau Claire, WI, September 1990, and at Univ. of California at Davis, Department of Applied Science, Livermore, CA, January 1991.
- L. W. Hrubesh, "Aerogel Materials for He Superfluid Studies," at Pennsylvania State Univ., State College, PA, September 1991.
- L. W. Hrubesh, "Development of Silica Aerogel for Cerenkov Detectors," at California Institute of Technology, Pasadena, CA, April 5, 1991.
- A. F. Jankowski, "Synthesis and Structure of Sputtered Materials," at Department of Materials Science and Engineering, Univ. of California at Los Angeles, Los Angeles, CA, January 18, 1991.
- W. E. King, "The Important Role of Bicrystals in Interface Science," at Max Planck Institut, Stuttgart, FRG, July 9, 1991.
- W. E. King, "Use of Shock Waves to Measure the Bond Strength at Metal/Ceramic Interfaces," at AT&T Bell Labs, Murray Hill, NJ, September 10, 1991.
- R. L. Landingham, "Molten Metal Infiltration for Economical Processing Ceramic Metal Hybrids," at American Society for Metals International, San Diego Chapter, San Diego, CA, May 16, 1991.
- R. W. Pekala, "Organic Aerogels: Synthesis and Structural Characterization," at Shell Development Company, Houston, TX, June 1990.
- R. W. Pekala, "Aerogels: Controlling Structure at the Nanometer Scale," at Univ. of California at Los Angeles, Los Angeles, CA, May 1991.
- R. W. Pekala, "Aerogels: Structure and Property Control at the Nanometer Scale," at Rockwell Science Center, Thousand Oaks, CA, January 1991.
- R. W. Pekala, "Inorganic and Organic Aerogels," at Ames Laboratory, Iowa State Univ., Ames, IA, March 1991.
- R. W. Pekala, "Low Density Microcellular Materials," at Univ. of Massachusetts, Amherst, MA, April 1991.
- C. O. Pruneda, "Energetic Materials Development at the Lawrence Livermore National Laboratory," at The Fraunhofer-Institut für Chemische Technologie (ICT), Pfinztal, FRG, July 1990.
- C. O. Pruneda, "The Development of Insensitive Energetic Materials at the Lawrence Livermore National Laboratory," at Defence Research Agency, Fort Halstead, England, November 1991.
- K. S. Ralls, "Noise in Nanobridges: A Window on Microscopic Processes in Metals," at AT&T Bell Laboratories, Murray Hill, NJ, September 1991.
- M. Sluiter, "The Role of Off-Diagonal Disorder on Alloy Phase Stability," at Center for Computational Sciences, Univ. of Kentucky, Lexington, KY, June 1991.
- E. C. Sowa, "Basic Research in Interface Science at LLNL," at Univ. of Southern Indiana, Evansville, IN, March 22, 1991.
- L. E. Tanner, "TEM Observations of the Pretransformation Behavior in Metallic Alloys," at Department of Materials, Univ. of California at Los Angeles, Los Angeles, CA, December 1990.
- L. E. Tanner, "Premartensitic Behavior and Martensite Nucleation in Ni-Al Alloys," at Argonne National Laboratory, Argonne, IL, January 1991.
- L. E. Tanner, "The Systematics of Phase Transformations," at Oak Ridge National Laboratory, Oak Ridge, TN, January 1991, and at Los Alamos National Laboratory, Los Alamos, NM, February 1991.
- T. M. Tillotson, "An Overview of Aerogels—Synthesis, Characterization, and Use," at Hewlett Packard, Palo Alto, CA, May 1990.
- J. G. Tobin, "Reversible Formation of a Surface Alloy: Au/Cu(001)," at Sandia National Laboratories, Livermore, CA, June 1990.
- J. G. Tobin, "Synchrotron Radiation Photoemission Studies of Nanoscale Structures: Magnetic Ultrathin Films, Monodisperse Semiconductor Clusters, and High-Temperature Superconductors," at Physics Department, Montana State Univ., Bozeman, MT, February 1991.

- J. G. Tobin, "The Unexpected Photoemission Spectral Structure of Untwinned, Single-Crystal  $\text{YBa}_2\text{Cu}_3\text{O}_{6.9}$ ," at Naval Research Laboratory, Washington, DC, March 1991.
- P. E. A. Turchi, "First Principles Studies of Alloy Phase Stability," at Hokkaido Univ., Hokkaido, Jpn., June 24, 1991, at Osaka Univ., Osaka, Jpn., June 26, 1991, and at Institute for Solid State Physics, the Univ. of Tokyo, Tokyo, Jpn., July 2, 1991.
- P. E. A. Turchi, "From Electronic Structure to Alloy Phase Stability," at Materials Research Center, Los Alamos National Laboratory, Los Alamos, NM, January 1991.
- R. S. Upadhye, "Dealing with Mixed Wastes," at Contra Costa College, San Pablo, CA, April 13, 1991.
- R. S. Upadhye, "Mixed Waste Treatment Technologies," at NORCAL AIChE Annual Symposium, Berkeley, CA, March 19, 1991.
- R. S. Upadhye, "Process Modeling using ASPEN," at NORCAL AIChE South Bay Section, San Jose, CA, October 24, 1991.
- P. A. Urtiew, "Experimental Techniques for Measuring Pressure and Particle Velocity in Condensed Materials under Dynamic Loading," at Ioffe Physico-Technical Institute, Leningrad, USSR, September 25, 1990.
- P. A. Urtiew, "Experimental Diagnostic Techniques in High Explosive Research," at Lavrentiev's Institute of Hydrodynamics, Akademgorodok—Novosibirsk, USSR, August 14, 1991.
- R. A. Van Konynenburg, "Cold Fusion," at California State Univ., Sacramento, CA, April 1990, and at Santa Clara Valley Branch of the American Electroplating and Surface Finishing Society, San Jose, CA, October 1990.
- R. A. VanKonynenburg, "Theory and Applications of Solid State Physics," at Univ. of California at Davis, Department of Applied Science, Livermore, CA, September 1990–June 1991.
- B. E. Watkins and R. T. Taylor, "Biomimetic Methane Oxidation," at Gas Research Institute, Los Angeles, CA, November 1991.
- M. J. Weber, "Local Structure at Rare Earth Sites in Laser Glass," at Rutgers Univ., Piscataway, NJ, October 17, 1990.
- M. J. Weber, "Recent Advances in Glasses for Fiber and Fusion Lasers," at Bell Communications Research, Red Bank, NJ, October 18, 1990.
- J. Wong, "Real-Time Studies of High-Temperature Ceramic Processing," at General Electric R&D Center, Schenectady, NY, April 3, 1990.
- J. Wong, "Time-Resolved Synchrotron Studies of Combustion Synthesis," at Rensselaer Polytechnic Institute, Troy, NY, April 4, 1990.
- J. Wong, "Time-Resolved Diffraction and Spectroscopic Studies of SHS Reactions," at Univ. of California at Berkeley, Materials Science Department, Berkeley, CA, September 23, 1990.
- J. Wong, "Applications of  $\text{YB}_{66}$  as a New Soft X-Ray Monochromator," at National Institute for Research in Inorganic Materials (NIRIM), Tsukuba City, Jpn., February 21, 1991.
- J. Wong, "Time-Resolved Capabilities in Materials Science," at Institute of Molecular Science, Okazaki, Jpn., March 1, 1991.
- J. Wong, "Real-Time Probes of SHS Reactions Using Synchrotron Radiation," at Ryukoku Univ., Seta, Jpn., March 2, 1991.
- J. Wong, "TR Diffraction and XAS studies in Materials Science," at Electrotechnical Laboratory, Tsukuba City, Jpn., March 4, 1991.
- J. Wong, " $\text{YB}_{66}$  as a Soft X-Ray Monochromator for Synchrotron Radiation," at Electrotechnical Laboratory, Tsukuba City, Jpn., March 4, 1991.
- J. Wong, " $\text{YB}_{66}$  as a Monochromator in the 1–2 keV Region," at Photon Factory, Tsukuba City, Jpn., March 5, 1991.
- J. Wong, "Applications of  $\text{YB}_{66}$  in SR Instrumentation," at Chemistry Department, Univ. of Tokyo, Tokyo, Jpn., March 11, 1991.
- J. Wong, "Time-Resolved Synchrotron Study of Solid Combustions," at National Institute for Research in Inorganic Materials (NIRIM), Tsukuba City, Jpn., March 12, 1991.
- J. Wong, "Chemical Dynamics of High-Temperature, Solid-State Reactions Using SR," at Bochum Univ., Bochum, FRG, July 5, 1991.
- J. Wong, " $\text{YB}_{66}$  as a New Soft X-Ray Monochromator for SR," at European Synchrotron Radiation Facility (ESRF), Grenoble, France, September 13, 1991.
- J. Wong, "Time-Resolved Synchrotron Studies of Solid Combustions," at LURE Synchrotron Radiation Facility, Orsay, France, October 7, 1991.

J. Wong, "Chemical Dynamics of Solid Combustions by Time-Resolved Diffraction and XAS," at Mineralogisches Institut, Bonn Univ., Bonn, Germany, October 31, 1991.

J. Wong, "Synchrotron Studies of Solid Combustions in the Sub-Second Time Scale," at Frascati Synchrotron Radiation Laboratory, Frascati, Italy, November 4, 1991.

## Technical Presentations

### Gordon Conference on Solid Hydrogen, Oxnard, CA, January 1990

G. W. Collins, "Atomic Hydrogen is Solid Tritiated Hydrogen."

### First U.S.-Japanese Workshop on Combustion Synthesis, Ibaraki, Jpn., January 3-7, 1990

J. B. Holt and J. Wong, "A New Experimental Approach to Solid Combustion Reactions Using Synchrotron Radiation."

### American Society for Metals Conference on Thermodynamics and Phase Relations of Exotic Materials, 119th Annual Meeting of The Metallurgical Society, Anaheim CA, February 18-22, 1990

A. Gonis, M. Sluiter, P. E. A. Turchi, G. M. Stocks, and D. M. Nicholson, "Electronic Structure, Alloy Stability, and Phase Diagrams."

P. E. A. Turchi, "Electronic Structure and Phase Stability of A15-Based Substitutional Alloys."

### DOE Containment Workshop, Golden, CO, February 23, 1990

D. D. Kautz, "Tubulation Designs."

### Topical Conference on Advanced Solid State Lasers, Salt Lake City, UT, March 5-7, 1990

L. L. Chase, S. A. Payne, R. S. Hughes, B. W. Woods, and L. E. DeLoach, "Measurement of Thermal Lensing for the LiCaAlF<sub>6</sub>:Cr<sup>3+</sup> Laser Material."

S. A. Payne, J. A. Caird, L. L. Chase, L. K. Smith, N. D. Nielsen, and W. F. Krupke, "Spectroscopy and Laser Properties of Nd<sup>3+</sup>-Doped CaF<sub>2</sub>, SrF<sub>2</sub>, and BaF<sub>2</sub>."

J. Wong, "Time-Resolved Diffraction and QEXAFS Studies of Solid Combustions," at HASYLAB, Hamburg, Germany, November 5, 1991.

J. Wong, "Study of Fast Chemical Reactions Using Synchrotron Radiation," at Hamburg Univ., Hamburg, Germany, November 12, 1991.

M. D. Shinn, L. L. Chase, J. A. Caird, S. A. Payne, L. J. Atherton, and W. L. Kway, "Progress in Material Development of LiCaAlF<sub>6</sub>:Cr<sup>3+</sup> Lasers."

### Pittsburgh Conference on Analytical Chemistry, New York, NY, March 5-9, 1990

J. W. Pyper, A. Alcaraz, B. H. Armstrong, N. L. Butler, J. F. Carley, T. T. Coburn, R. W. Crawford, J. E. Harrar, W. F. Morris, and J. C. Newton, "Quality Control Standards for Various Analytical Techniques When Analyzing Non-routine Samples."

### American Physical Society, Anaheim, CA, March 12-16, 1990

M. Asta, M. Sluiter, D. de Fontaine, T. Hong, P. P. Singh, and A. J. Freeman, "Ab Initio Study of Phase Stability in the Al-Ti System," *Bull. Am. Phys. Soc.* **35**, 576 (1990).

D. C. Chrzan, L. M. Falicov, J. M. MacLaren, X.-G. Zhang, and A. Gonis, "Magnetic Structure of {111} Stacking Faults in Ni," *Bull. Am. Phys. Soc.* **35**, 374 (1990).

R. C. Cook, "Solvent Dependence of the Chain Dimensions of Poly(*n*-hexylisocyanate)," *Bull. Am. Phys. Soc.* **35**, 508 (1990).

A. Gonis, P. E. A. Turchi, M. Sluiter, F. J. Pinski, and D. D. Johnson, "First-Principles Electronic Structure Calculations of Phase Stability and Phase Diagrams of Al-Li Alloys," *Bull. Am. Phys. Soc.* **35**, 251 (1990).

R. H. Howell, J. C. O'Brien, P. Sterne, H. B. Radousky, P. E. A. Turchi, M. J. Fluss, J. L. Peng, T. J. Folkerts, and R. N. Shelton, "Positron Annihilation Lifetime Analysis of Superconducting Oxides," *Bull. Am. Phys. Soc.* **35**, 482 (1990).

N. Kioussis, J. Berkowitz, E. C. Sowa, A. Gonis, and X.-G. Zhang, "The Electronic Structure of Unrelaxed and Relaxed Dislocations in Cu," *Bull. Am. Phys. Soc.* **35**, 334 (1990).

A. L. Nichols III, "The Effect of Molecular Solvation on Bond Stretching."

H. B. Radousky, R. S. Glass, M. J. Fluss, J. C. O'Brien, B. P. Bonner, C. I. Merzbacher, E. M. Larson, R. G. Meisenheimer, J. L. Peng, R. N. Shelton, and K. F. McCarty, "Superconductivity in Bromine Doped  $\text{YBa}_2\text{Cu}_3\text{O}_{6.2}$ ," *Bull. Amer. Phys. Soc.* **36**, 831 (1991).

P. P. Singh and D. de Fontaine, "Linear Muffin-tin Orbital Method in the Coherent Potential Approximation for Substitutionally Disordered Alloys," *Bull. Am. Phys. Soc.* **35**, 468 (1990).

M. Sluiter, P. E. A. Turchi, F. J. Pinski, and D. D. Johnson, "Electronic Structure and Ordering Phenomena in Ni-Ti and Ni-Al near Equiatomic Composition," *Bull. Am. Phys. Soc.* **35**, 602 (1990).

E. C. Sowa, A. Gonis, and X.-G. Zhang, "Electronic Structure Calculations of Grain Boundaries in Cu," *Bull. Am. Phys. Soc.* **35**, 624 (1990).

J. G. Tobin, "Photoemission Studies of Fe/Cu(001)."

X.-G. Zhang, P. J. Rous, J. M. MacLaren, A. Gonis, M. A. VanHove, and G. A. Samorjai, "LEED from Stepped Surfaces: A New Method Based on Removal Invariance in Angular Momentum Space," *Bull. Am. Phys. Soc.* **35**, 251 (1990).

**Gordon Conference on Crystal Growth, Oxnard, CA, March 12-16, 1990**

J. J. DeYoreo, L. J. Atherton, D. H. Roberts, and R. W. Martin, "Solid State Chemistry and Large Crystal Growth of  $\text{LiCaAlF}_6\cdot\text{Cr}^{3+}$ ."

**Beryllium Coordinating Committee, Oak Ridge, TN, March 13-14, 1990**

J. E. Hanafee, M. L. Sattler, and C. L. Hoenig, "Beryllium Technology at LLNL."

**Recent Advances in Research on Heterocyclic Amines, Kauai, HI, March 17-24, 1990**

J. F. Felton, M. G. Knize, M. Vanderlaan, B. E. Watkins, J. D. Tucker, and K. W. Turteltaub, "Predictive Steady State Model of Annular-Flow Electrochemical Reactor."

**Combat Vehicle Survivability Symposium, Gaithersburg, MD, March 26-29, 1990**

R. L. Landingham and T. Shell, "Processing and Performance of Advanced Ceramic Composite Armor."

**Solid State NMR Meeting, Pleasanton, CA, March 30, 1990**

R. L. Ward, "NMR Studies of Resorcinol-Formaldehyde Aerogels."

**American Crystallographic Association Meeting, New Orleans, LA, April 1990**

A. G. Clare, A. C. Wright, M. J. Weber, and R. N. Sinclair, "An Investigation of the Structural Role of  $\text{Dy}^{3+}$  in a Sodium Fluoroberyllate Glass Using Neutron Scattering."

**31st Experimental NMR Conference, Pacific Grove, CA, April 1-5, 1990**

R. L. Ward and R. Balhorn, " $^{13}\text{C}$ -CPMAS Studies of Bull Sperm DNA-Protamine-1 Complex."

**17th International Conference on Metallurgical Coatings, San Diego, CA, April 2-6, 1990**

A. F. Jankowski and P. L. Perry, "Microstructure of Au/Nb Multilayers."

A. F. Jankowski and L. R. Schrawyer, "Reactive Sputtering of Molybdenum."

**JANNAF Propulsion Systems Hazard Meeting, April 3-6, 1990**

W. C. Tao, M. Costantino, and D. Ornellas, "Burning Mechanism and Regression Rate of RX-40-AP as a Function of HMX Particle Size and Moduli."

**Spring Meeting of The Materials Research Society, San Francisco, CA, April 16-20, 1990**

R. S. Glass, D. R. Ciarlo, F. U. Dowla, J. S. Haas, G. T. Jameson, J. F. Kimmons, and S. P. Perone, "Disposable Electrochemical Array Sensors."

A. Gonis, P. E. A. Turchi, M. Sluiter, F. J. Pinski, and D. D. Johnson, "Electronic Structure and Phase Stability Properties of Al-Li Alloys."

D. D. Johnson, P. E. A. Turchi, M. Sluiter, F. J. Pinski, G. M. Stocks, and D. M. Nicholson, "First-Principles Study of Phase Stability in Pd-Rh Alloys."

J. Mikalopas, P. E. A. Turchi, M. Sluiter, and P. A. Sterne, "A First-Principles Examination of Phase Stability in fcc-Based Ni-V Substitutional Alloys."

M. Sluiter, P. E. A. Turchi, F. J. Pinski, and D. D. Johnson, "A Comparative First-Principles Study of Phase Stability in Ni-Al and Ni-Ti Alloys at Near Equiatomic Composition."

M. Sluiter and P. E. A. Turchi, "Theoretical Investigation of Phase Stability in Nonmagnetic Copper-Nickel Alloys."

P. E. A. Turchi and A. Finel, "Order-Disorder Phenomena in Complex Alloys: the Case of Al<sub>15</sub>-Based Substitutional Alloys."

P. E. A. Turchi, A. Gonis, M. Sluiter, F. J. Pinski, D. D. Johnson, and G. M. Stocks, "First-Principles Study of Phase Stability in Pd-Rh Substitutional Alloys."

**4th Annual Oil Shale Contractors' Meeting, Morgantown, WV, April 18–19, 1990**

R. J. Cena, "LLNL Oil Shale Project Review."

P. H. Wallman, R. W. Taylor, and M. F. Singleton, "Shale Oil Cracking and Coking Kinetics."

**American Ceramic Society Meeting, Dallas, TX, April 22–26, 1990**

R. W. Hopper, "Crack Blunting by Viscous Flow."

M. J. Weber, M. D. Shinn, I. M. Thomas, E. J. A. Pope, and J. D. Mackenzie, "Optical and EXAFS Studies of the Local Environment of Nd<sup>3+</sup> in Fused Silica."

**American Chemical Society, Boston, MA, April 22–27, 1990**

R. B. Rosner, K. Hong, and M. F. Rubner, "Electrical Properties of Langmuir-Blodgett Films of Polypyrrole."

**National Association of Corrosion Engineers, Corrosion-90, Las Vegas, NV, April 23–27, 1990**

W. G. Halsey, "Preliminary Selection Criteria for Container Materials at the Proposed Yucca Mountain High Level Nuclear Waste Repository."

**71st Annual Meeting of the American Welding Society, Anaheim, CA, April 24, 1990**

J. W. Elmer, T. W. Eagar, and S. M. Allen, "Solute Redistribution and Second-Phase Formation During Rapid Solidification of Stainless Steel Alloys."

D. D. Kautz, "Comparison of Laser Welding to Other Processes for Dissimilar Metal Joining."

**16th DOE Compatibility Meeting, Livermore, CA, April 24–26, 1990**

C. Colmenares and H. R. Leider, "Alpha Radiolysis of the Fluorinert FC-43."

**23rd Annual Oil Shale Symposium, Golden, CO, May 1–2, 1990**

T. T. Coburn, R. W. Taylor, R. W. Crawford, and C. J. Morris, "Sulfur Release from a Hot-Recycled-Solids Retort."

P. H. Wallman, M. F. Singleton, and R. W. Taylor, "Cracking and Coking of Shale Oil Vapors."

**SUBWOG 12A, Livermore, CA, May 8–9, 1990**

D. M. Makowiecki, A. F. Jankowski, M. A. McKernan, and R. J. Foreman, "Magnetron Sputtered Boron Films and Ti/B Multilayer Structures."

R. A. VanKonynenburg, "Cold Fusion."

**American Society of Microbiology, Anaheim, CA, May 13–17, 1990**

R. T. Taylor, M. L. Hanna, S. Park, and M. W. Droege, "Chloroform Oxidation by *Methylosinus trichosporium* 0B3b—A Specific Catalytic Activity of the Soluble Form of Methane Monooxygenase."

**14th Annual Actinide Separation Conference, Gatlinburg, TN, May 14–17, 1990**

Y. Zundelevich, "Suspension of Solids by Turbulent Jets."

**International Quantum Electronics Conference, Anaheim, CA, May 21–25, 1990**

S. A. Payne, L. L. Chase, and R. C. Powell, "Four-Wave Mixing of Nd<sup>3+</sup> Impurities in Glasses and Crystals."

J. H. Schloss, L. L. Chase, and S. A. Payne, "Sequential Two-Photon Excitation of Nd<sup>3+</sup>:SrF<sub>2</sub>."

**Subwog 12-D, Tritium Technology Meeting, Aiken, SC, May 21–25, 1990**

J. L. Maienschein, F. R. Holdener, J. T. Merrill, Y. Chang, S. W. Wilson, and D. I. Chambers, "Review of the LLNL Tritium Facility Upgrade as It Nears Completion."

R. T. Tsugawa, J. S. Bowers, J. A. Emig, R. S. Hafner, J. L. Maienschein, and A. S. Nicolosi, "Determination of Tritium in Mercury from Sprengel Pumps."

**Plutonium Containment Conference, Los Alamos, NM, May 29–30, 1990**

J. E. Hanafee, "Tube Containment Model."

J. E. Hanafee and R. L. Krueger, "Containment by High-Strain-Rate Formed Metals."

**Gordon Conference on Energetic Materials, New Hampton, NH, June 1990**

S. F. Rice and M. F. Foltz, "High-Pressure Reaction Measurements."

**The 64th Colloidal and Surface Science Symposium, Bethlehem, PA, June 1990**

G. W. Wilemski and R. C. Cook, "Simulations of Colloidal Suspensions."

**Workshop on Computational Methods for the Electronic Structure and Related Properties of Metallic Alloys, Lexington, KY, June 4–5, 1990**

M. Sluiter, "Electronic Structure Calculations and Alloy Phase Stability."

E. C. Sowa, A. Gonis, and X.-G. Zhang, "Real-Space Multiple-Scattering Theory (RSMST): The Electronic Structure of Interfaces."

P. E. A. Turchi, "From Quantum Mechanics to Statistical Thermodynamics."

**Ninth Annual Working Group Institute on Synthesis of High Energy Density Materials, Monticello, NY, June 4–7, 1990**

A. R. Mitchell, P. F. Pagoria, and C. L. Coon, "New Nitrourea Compounds."

**16th DOE Surface Studies Conference, Golden, CO, June 5–7, 1990**

R. G. Musket, "X-Ray Fluorescence Analysis of Oxygen on and in Materials."

**International Colloquium on Free Boundary Problems: Theory and Applications, Montreal, Canada, June 13–22, 1990**

R. W. Hopper, "Plane Stokes Flow Driven by Capillarity on a Free Surface: Overview and Status."

**13th Surface/Interface Research Meeting of the Northern California Chapter of the American Vacuum Society, Menlo Park, CA, June 19, 1990**

A. V. Hamza and M. A. Schildbach, "Low-Energy Electron Diffraction Investigation of the  $\text{Al}_2\text{O}_3(11\bar{2}0)$  Surface Structure."

J. G. Tobin, "Photoelectron Diffraction of Magnetic Ultrathin Films."

**JOWOG 28B Meeting, Livermore, CA, June 19–21, 1990**

R. C. Cook, B. L. Haendler, and G. E. Overturf, "Completion of Development of Low-Density Polystyrene Foams for Laser Inertial Confinement Fusion."

M. S. Costantino and C. S. Firpo, "High-Pressure Combustion Synthesis of Aluminum Nitride."

F. M. Kong, S. R. Buckley, R. C. Cook, B. L. Haendler, S. A. Letts, and G. E. Overturf, "Pyrolysis of Low-Density Polymer Foams."

**NWD DEA 5660 Meeting on New Energetic Ingredients, China Lake, CA, June 20–21, 1990**

A. R. Mitchell, P. F. Pagoria, and C. L. Coon, "New Nitrourea Compounds."

**45th Annual Calorimetry Conference, Ann Arbor, MI, July 1990**

P. A. Baisden, "The Development of a Variable-Temperature/Pressure Titration Calorimeter for Aqueous Solution Studies."

**International Conference on Electron Microscopy, Seattle, WA, July 1990**

D. Schryvers and L. E. Tanner, "HREM Studies of Ni-Al Beta-Phase Alloy Transformations."

**The Fellowship Forum, Stanford Univ., Stanford, CA, July 1990**

T. M. Tillotson, "Silica Aerogels: Scientific Curiosity or Technological Breakthrough?"

**Annual Meeting of the Japanese National Cancer Society, Hokkaido, Jpn., July 1990**

B. E. Watkins, "Fate, and Distribution of 2-amino-1-methyl-6-phenylimidazo [4,5-*b*] pyridine (PhIP) in Rats."

**International Society for Optical Engineering Conference, San Diego, CA, July 9–13, 1990**

D. Breithaupt and C. Tarver, "Uses of Fabry Perot Velocimeter in Studies of High-Explosive Detonation."

**20th Intersociety Conference on Environmental Systems, Williamsburg, VA, July 10, 1990**

E. Cantwell, T. Shenk, P. Robinson, and R. S. Upadhye, "Automated Simulation as Part of a Design Workstation."

**Eighth American Conference on Crystal Growth, Vail, CO, July 15–20, 1990**

J. J. DeYoreo, L. J. Atherton, D. H. Roberts, and R. W. Martin, "Characterization, Identification, and Elimination of Microscopic Defects in  $\text{LiCaAlF}_6:\text{Cr}^{3+}$ ."

**International Luminescence Conference, Lisbon, Portugal, July 16–20, 1990**

J. H. Schlarb, L. L. Chase, and L. K. Smith, "Dynamics of Laser-Tuned  $\text{Nd}^{3+}$  Laser at High Excitation Density."

**Third International Workshop on Positron and Positronium Chemistry, Milwaukee, WI, July 16–18, 1990**

P. E. A. Turchi, "Positron Behavior in some High- $T_c$  Materials and Related Oxides."

**Gordon Conference on High Temperature Chemistry, New Hampton, NH, July 21–25, 1990**

J. Wong, "Time-Resolved Synchrotron Studies of Solid Combustion Reactions."

**23rd Combustion Symposium, New Orleans, LA, July 22–27, 1990**

W. C. Tao, A. Frank, J. Shepherd, and R. Clements, "The Combustion Kinetics of Aluminum Metal in Composite Explosives Revealed by Ultrahigh-Speed Microphotography."

W. C. Tao, R. Hampton, and D. Ornellas, "Burning Rates of Cast Nitramine Explosives Using a Hybrid Closed Bomb-Strand Burner."

**Fourth International Otto Schott Colloquium, Jena, FRG, July 23–27, 1990**

M. J. Weber, "Local Structure and Properties of Rare Earth Ions in Laser Glasses."

**Fifth Semiannual Review, Technology Coordination Group for Energetic Materials, Los Alamos, NM, July 25–26, 1990**

P. F. Pagoria, C. L. Coon, and A. R. Mitchell, "Synthesis Efforts."

**11th Biennial Conference on Chemical Education, Atlanta, GA, August 1990**

P. A. Baisden, "Options for Nuclear Waste Disposal."

**Topical Meeting on Optical Amplifiers, Optical Society of America, Monterey, CA, August 6–8, 1990**

M. J. Weber, "Materials Considerations for Rare Earth Doped Glasses."

**EXPLOMET '90—International Conference on Shock-Wave and High-Strain-Rate Phenomena in Materials, San Diego, CA, August 12–17, 1990**

W. H. Gourdin, "Characterization of Copper Shaped-Charge Liner Materials at Tensile Strain Rates of  $10^4 \text{ s}^{-1}$ ."

W. H. Gourdin, "Correlation Between the Ultimate Elongations of Rapidly Expanding Rings and Stretching Metal Jets."

**200th National American Chemical Society Meeting, Washington, D.C., August 26–31, 1990**

P. A. Baisden, "Summer School in Nuclear Chemistry—Can Summer Programs Really Work?"

P. F. Pagoria, A. R. Mitchell, and E. S. Jessop, "Synthesis of Mono- and Dinitroureas."

**VI Interdisciplinary Laser Science Conference, Minneapolis, MN, September 1990**

C. G. Stevens, and W. E. Conaway, "Bond Selective Dissociation of HOD by 2-Step Laser Excitation."

**Finnish-Swedish Flame Days, Åbo, Finland, September 1990**

R. C. J. Carlsson, E. L. Ivarsson, and P. H. Wallman, " $\text{NO}_x$  and  $\text{N}_2\text{O}$  Formation in Bench-Scale Fluidized-Bed Combustion of Coal."

**Association of Analytical Chemists, New Orleans, LA, September 9–13, 1990**

L. H. Stanker, B. E. Watkins, and M. Vanderlaan, "Immunoassay for Pyrethroid Insecticides."

L. H. Stanker, B. E. Watkins, and M. Vanderlaan, "Immunoassay for Cyclodiene Insecticides."

**Ion Beam Modification of Materials 1990, Knoxville, TN, September 9–14, 1990**

D. W. Brown, Z. A. Munir, and R. G. Musket, "A Precipitate Coarsening Mechanism for Buried Layer Formation."

**World Congress on Superconductivity, Houston, TX, September 10–13, 1990**

H. B. Radousky, R. S. Glass, M. J. Fluss, J. L. Peng, R. N. Shelton, and J. Z. Liu, "Chemical Evidence for Charge Transfer Doping on YBCO: The Case for Halogenation."

**26th Meeting of JOWOG-12 and 11th Meeting of SUB-WOG-12B, Aldermaston, England, September 10–14, 1990**

C. A. Colmenares and H. R. Leider, "Compatibility of Pu and Other Metals with Fluorinert."

H. R. Leider and C. A. Colmenares, "Alpha Radiolysis of Fluorinert."

**The Third International Conference "Lavrentiev's Readings," Novosibirsk, USSR, September 10–14, 1990**

P. A. Urtiew and B. Hayes, "Parametric Study of The Dynamic JWL-EOS for Detonation Products."

**TTCP Composite Explosives Workshop, White Oak, MD, September 18–20, 1990**

W. C. Tao, "The Future of Composite Explosives."

**Yucca Mountain Integrated Performance Model Workshop, Redmond, WA, September 19–21, 1990**

W. G. Halsey, "Container Material Performance Models."

**International Conference Dedicated to V.A. Michelson, USSR Academy of Science, Institute of Chemical Physics, Moscow, USSR, September 19–21, 1990**

P. A. Urtiew and B. Hayes, "Empirical Estimates of Detonation Parameters in Condensed Explosives."

**1990 Applied Superconductivity Conference, Snowmass, CO, September 24–28, 1990**

H. B. Radousky, R. S. Glass, D. Back, A. H. Chin, M. J. Fluss, J. Z. Liu, W. D. Mosly, P. Klavins, and R. N. Shelton, "Processing Parameters and Kinetics of Bromination and Chlorination in the  $\text{YBa}_2\text{Cu}_3\text{O}_{6+x}$  System."

**Stanford Synchrotron Radiation Laboratory Users Group Meeting, Stanford, CA, October 1990**

J. G. Tobin, "A Photoemission Investigation of Compound Semiconductor Quantum Dots."

J. G. Tobin, "Photoelectron Diffraction of Magnetic Ultrathin Films: Fe/Cu(001)."

**DARPA High Temperature Superconductor Workshop, Danvers, MA, October 3–5, 1990**

H. B. Radousky, R. S. Glass, M. J. Fluss, J. L. Peng, R. N. Shelton, and J. Z. Liu, "Chemical Evidence for Charge Transfer Doping on YBCO: The Case for Halogenation."

**The Metallurgical Society Fall Meeting, Detroit, MI, October 7–11, 1990**

M. Sluiter and P. E. A. Turchi, "Phase Stability of Ni-Al Intermetallics from First-Principles Electronic Structure Calculations."

M. Sluiter, P. E. A. Turchi, and G. M. Stocks, "Phase Stability of Ni-Al Intermetallics from First-Principles Electronic Structure Calculations."

P. E. A. Turchi, M. Sluiter, F. J. Pinski, D. D. Johnson, and G. M. Stocks, "A First-Principles Electronic Structure Description of the Thermodynamic Stability of Intermetallics in the Ni-Ti System."

**37th Annual Symposium of the American Vacuum Society, Toronto, Canada, October 8–12, 1990**

E. J. Hsieh, R. S. Upadhye, E. L. Pierce, and L. A. Witt, "Application of a Sputter Coating Uniformity Model to Bouncing Pan Coating of Microspheres."

A. F. Jankowski, L. R. Schrawyer, and P. L. Perry, "Reactive Sputtering of Molybdenum-Oxide Gradient-Index Filters."

J. G. Tobin, "A Photoemission Investigation of Quantum Confinement in Compound Semiconductor Monodisperse Clusters."

J. G. Tobin, "Photoemission Investigation of the Fermi Surface of Untwinned Single Crystal  $\text{YBa}_2\text{Cu}_3\text{O}_{6.9}$ ."

J. G. Tobin, "Photoelectron Diffraction of Magnetic Ultrathin Films: Fe/Cu(001)."



**JOWOG 22B, Aldermaston, England, October 9–12, 1990**

J. E. Hanafee, "Overview of Beryllium Science and Technology in the United States."

J. E. Hanafee, "Characterization of Atomized Beryllium Powder."

**178th Electrochemical Society Meeting, Seattle, WA, October 14–19, 1990**

J. Farmer, P. Grant, P. Robouch, F. Wang, Z. Chiba, and P. Lewis, "Design of Electrochemical Reactor for Enhanced Dissolution of Plutonium Oxide."

**JOWOG 22A, Livermore, CA, October 16–17, 1990**

J. E. Hanafee, "Tube Containment Model."

J. E. Hanafee and R. L. Krueger, "Containment Performance of High-Strain-Rate Formed Metals."

**U.S. Nuclear Regulatory Commission Advisory Committee on Nuclear Waste, Bethesda, MD, October 26, 1990**

R. A. VanKonynenburg, "Review of Carbon-14 Release from a High-Level Nuclear Waste Repository."

**University of Wisconsin Synchrotron Radiation Center Users Meeting, Stoughton, WI, November 1990**

J. G. Tobin, "Photoemission Investigation of the Fermi Surface of Untwinned, Single-Crystal  $\text{YBa}_2\text{Cu}_3\text{O}_{6.9}$ ."

**Natural Gas R&D Contractors Review Meeting, Morgantown, WV, November 1990**

L. M. Hair and M. W. Droege, "The Synthesis, Characterization, and Catalytic Reactions of Metal Silicate Catalysts for the Partial Oxidation of Methane."

**1990 Pacific Conference on Chemistry and Spectroscopy, San Francisco, CA, November 1, 1990**

P. Robinson and R. S. Upadhye, "Learning to Resolve Competing Influences in a Qualitative Simulator."

**11th International Conference on the Application of Accelerators in Research and Industry, Denton, TX, November 5–8, 1990**

R. G. Musket, "Spectroscopy of Sub-keV, Ion-Induced X Rays using Si(Li) Detectors," *Bull. Am. Phys. Soc.* **35**, 1760 (1990).

**JANNAF Combustion Subcommittee, Cheyenne, WY, November 5–9, 1990**

M. S. Costantino, W. C. Tao, C. M. Tarver, D. R. Breithaupt, and D. L. Ornellas, "Understanding Composite Explosive Energetics: II. The Combustion Kinetics of Metallic Additives in Different Oxidizing Environments."

W. C. Tao, M. S. Costantino, D. L. Ornellas, L. G. Green, and E. S. Jessop, "The Effects of HMX Particle Size and Binder Stiffness on the Burning Mechanism and Regression Rate of a Series of Fast-Burning Propellants."

W. C. Tao, C. M. Tarver, D. R. Breithaupt, and D. L. Ornellas, "Understanding Composite Explosives Energetics: II. The Combustion Kinetics of Metallic Additives in Different Oxidizing Environments."

**1990 Eastern Oil Shale Symposium, Lexington, KY, November 6–8, 1990**

R. J. Cena and C. B. Thorsness, "LLNL Oil Shale Pilot Plant Status Report."

**International Symposium on New Directions and Future Aspects of HVEM, Osaka, Jpn., November 8–10, 1990**

W. E. King, "Novel *In Situ* Experiments in the HVEM and Potential Future Applications."

**Materials Research Society Fall Meeting, Boston, MA, November 26–30, 1990**

P. A. Baisden, "Development of High-Temperature UV-VIS-NIR Spectroscopy for the Measurement of Free Energies of Complexation at Elevated Temperatures."

J. Chaudhuri, V. Gondhalekar, and A. F. Jankowski, "Analysis of the Strain Profile in Thin Au/Ni Multilayers by X-Ray Diffraction."

A. V. Hamza and M. A. Schilbach, "Laser- $\text{Al}_2\text{O}_3(11\bar{2}0)$  Surface Interactions."

A. F. Jankowski and D. G. Stearns, "Layer Formation in CuNi/C X-Ray Optics."

H. B. Radousky, R. S. Glass, M. J. Fluss, J. Z. Liu, and R. N. Shelton, "Superconducting Properties and Processing Parameters of  $\text{YBa}_2\text{Cu}_3\text{O}_{6+x}\text{Br}_y$ ."

J. G. Tobin, "A Photoemission Investigation of Compound Semiconductor Quantum Dots."

J. G. Tobin, "Photoelectron Diffraction of Magnetic Ultrathin Films: Fe/Cu(001)."

J. G. Tobin, "Photoemission Investigation of the Fermi Surface of Untwinned, Single-Crystal  $\text{YBa}_2\text{Cu}_3\text{O}_{6.9}$ ."

**Ninth Biennial CUBE Symposium, Santa Fe, NM, November 27–30, 1990**

A. L. Nichols III, "Chemical Reaction Modeling in TOPAZ."

**University of Miami Workshop on Electronic Structure and Mechanisms for High Temperature Superconductivity, Miami, FL, January 1991**

J. G. Tobin, "The Unexpected Photoemission Spectral Structure of Untwinned, Single-Crystal  $\text{YBa}_2\text{Cu}_3\text{O}_{6.9}$ ."

**Arizona State Univ. Winter Workshop on the Structure and Properties on Interfaces, Wickenburg, AZ, January 3–6, 1991**

W. E. King, G. Campbell, A. Coombs, S. M. Foiles, M. J. Mills, and M. Rühle, "HREM Investigation of the Structure of the S5(310)/[001] Symmetric Tilt Grain Boundary in Nb."

**American Mathematical Society, San Francisco, CA, January 16–19, 1991**

R. W. Hopper, "Plane Stokes Flow Driven by Capillarity on a Moving Free Boundary."

**NMR Meeting of DOE Contractors, Albuquerque, NM, January 17, 1991**

R. L. Ward, " $^{13}\text{C}$ -CPMAS Studies of Organic Aerogels."

**10th Annual Pyrochemical Workshop, Charleston, SC, January 30, 1991**

C. Cate, "Equipment Development for Salt Preparation."

**Gordon Conference on Superconductivity, Ventura, CA, February 1991**

J. G. Tobin, "The Unexpected Photoemission Spectral Structure of Untwinned, Single-Crystal  $\text{YBa}_2\text{Cu}_3\text{O}_{6.9}$ ."

**U.S. Workshop on Superconductors for High Magnetic Fields, Tiburon, CA, February 4, 1991**

L. T. Summers, "Superconductors for ITER Magnet Systems."

**Golden Gate Materials Technology Conference, San Mateo, CA, February 5–7, 1991**

W. G. Halsey, "Container Materials for High-Level Nuclear Waste."

A. F. Jankowski, "Mechanical Properties of Multilayers."

**4th Topical Meeting on Microphysics of Surfaces: Beam-Induced Processes, Santa Fe, NM, February 11–13, 1991**

A. V. Hamza, M. A. Schildbach, J. R. S. Hughes, and H. W. H. Lee, "The Absorption of 1.17 eV Photons by  $\text{Al}_2\text{O}_3(11\bar{2}0)$ ."

**Sixth Semi-annual Review, Technology Coordination Group for Energetic Materials, Livermore, CA, February 12–13, 1991**

C. L. Coon, P. F. Pagoria, and A. R. Mitchell, "Synthesis Efforts."

**LLNL-LANL High Explosives Information Exchange, Livermore, CA, February 14, 1991**

A. R. Mitchell, "Synthesis, Scale-Up, and Characterization of K-6."

P. F. Pagoria, "Synthesis and Characterization of a New Insensitive Explosive."

E. von Holtz and K. J. Scribner, "Higher Energy, Nonfreezing PEX."

**Fifth International Conference on Ultrastructure Processing of D.C., Glasses, Composites, Ordered Polymers, and Advanced Optical Materials, Orlando, FL, February 18–21, 1991**

L. W. Hrubesh, T. M. Tillotson, and J. F. Poco, "A Sol-Gel Route to Very High-Porosity Silica Aerogels."

R. W. Pekala, "Organic Aerogels: A New Type of Ultrastructured Polymer."

**Annual Meeting of The Metallurgical Society, New Orleans, LA, February 17–21, 1991**

M. E. Kassner and G. A. Henshall, "A New Dislocation-Hardening Equation that Describes Elevated Temperature."

**Workshop on Fermiology of High- $T_c$  Superconductors, Argonne, IL, March 1991**

J. G. Tobin, "The Unexpected Photoemission Spectral Structure of Untwinned, Single-Crystal  $\text{YBa}_2\text{Cu}_3\text{O}_{6.9}$ ."

**Spring Meeting of the Combustion Institute, Boulder, CO, March 1991**

P. H. Wallman, "Kinetic Combustion Experiments in a Pressurized Fluidized Bed."

**JOWOG-9 Mechanical Properties of Explosives,  
Livermore, CA, March 12–13, 1991**

C. O. Pruneda, "High-Tensile-Strength HE."

E. von Holtz, K. Scribner, R. Whipple, and G. Flowers, "Paste Extrudable Explosive Rheology."

**KKR-CPA Workshop, Cincinnati, OH, March 16, 1991**

E. C. Sowa, A. Gonis, and P. A. Sterne, "Exact Treatment of Poisson's Equation in Solids with Space-Filling Cells."

**Topical Meeting on Advanced Solid State Lasers, Hilton Head, SC, March 18–20, 1991**

L. L. Chase, S. A. Payne, L. K. Smith, W. L. Kway, and W. F. Krupke, "Emission Cross Sections and Energy Extraction for the Mid-Infrared Laser Transitions of  $\text{Er}^{3+}$ ,  $\text{Tm}^{3+}$ , and  $\text{Ho}^{3+}$ ."

**American Physical Society, Cincinnati, OH,  
March 18–22, 1991**

M. Asta, P. P. Singh, and D. de Fontaine, "Study of Stable Ground States in the Cu-Au-Pd System," *Bull. Am. Phys. Soc.* **36**, 522 (1991).

W. H. Butler, A. Gonis, and R. Brown, "Basis Functions for Non-Muffin Tin Multiple Scattering Theory," *Bull. Am. Phys. Soc.* **36**, 570 (1991).

G. W. Collins, E. M. Fearon, E. R. Mapoles, P. C. Souers, and P. A. Fedders, " $J=1$ -to- $0$   $D_2$  Conversion in Solid D-T."

G. W. Collins, R. T. Tsugawa, E. R. Mapoles, P. C. Souers, and J. R. Gaines, "Quantum Tunneling of Unpaired Hydrogen Atoms in Isotopic Mixtures of Solid Hydrogen Containing Tritium."

J. W. Elmer, L. E. Tanner, and M. J. Aziz, "Model for the Formation of Bands of Ultrafine Particles During Rapid Solidification."

A. Gonis, P. E. A. Turchi, M. Sluiter, F. J. Pinski, and D. D. Johnson, "Phase Stability and Phase Diagrams of Al-Li Alloys," *Bull. Am. Phys. Soc.* **36**, 620 (1991).

A. Gonis and W. H. Butler, "Variational derivation of Multiple Scattering Theory for Space-Filling Potentials," *Bull. Am. Phys. Soc.* **36**, 569 (1991).

R. H. Howell, C. Berger, F. Solal, Y. Calvayrac, and P. E. A. Turchi, "Structural Features in Icosahedral  $\text{Al}_{63}\text{Cu}_{25}\text{Fe}_{12}$ ," *Bull. Am. Phys. Soc.* **36**, 988 (1991).

N. Kioussis, R. G. Hemker, E. C. Sowa, A. Gonis, and X.-G. Zhang, "Electronic Structure and Energetics of Edge Dislocations in Copper," *Bull. Am. Phys. Soc.* **36**, 731 (1991).

J. M. MacLaren, S. Crampin, A. Gonis, and G. Schadler, "Electronic Structure of Disordered Interfaces," *Bull. Am. Phys. Soc.* **36**, 731 (1991).

J. Mikalopas, M. Sluiter, P. A. Sterne, and P. E. A. Turchi, "First-Principles Calculation of Phase Stability of Intermetallic Alloys," *Bull. Am. Phys. Soc.* **36**, 619 (1991).

K. S. Ralls and R. A. Buhrman, "Defect Interactions and the Ubiquity of  $1/f$  Noise," *Bull. Am. Phys. Soc.* **36**, 354 (1991).

S. P. Regan, A. P. Zwicker, L. K. Huang, M. Finkenthal, H. W. Moos, and T. W. Barbee, Jr., "An Evaluation of a Multilayer Mirror Spectrometer for Plasma Imaging in the 10-25 Å Wavelength Range."

M. A. Schilbach and A. V. Hamza, "Absorption of 1064- and 355-nm Laser Light by  $\text{Al}_2\text{O}_3$  Surfaces."

P. P. Singh, D. de Fontaine, and A. Gonis, "Charge Self-Consistent KKR-ASA-CPA Calculations of Cu-Pd Alloys," *Bull. Am. Phys. Soc.* **36**, 619 (1991).

M. Sluiter and P. E. A. Turchi, "The Role of Off-Diagonal Order in the Phase Stability of Some Transition Metal Alloys," *Bull. Am. Phys. Soc.* **36**, 619 (1991).

E. C. Sowa, A. Gonis, and X.-G. Zhang, "Electronic Structure Calculations for Extended Defects: Grain Boundaries in Nb," *Bull. Am. Phys. Soc.* **36**, 730 (1991).

P. A. Sterne, E. C. Sowa, and A. Gonis, "Exact Treatment of Poisson's Equation in Solids with Space-filling cells," *Bull. Am. Phys. Soc.* **36**, 570 (1991).

E. Suranyi and A. Gonis, "Analytic Properties of the Korringa-Kohn-Rostoker Coherent Potential Approximation," *Bull. Am. Phys. Soc.* **36**, 619 (1991).

R. J. Tench, M. A. Schilbach, L. L. Chase, and W. J. Siekhaus, "8-ns Nd:YAG Laser-Induced Surface Damage on  $\text{Al}_2\text{O}_3$ : Damage Morphology and Correlation Between Surface Structure and Damage Threshold Studied by Atomic Force Microscopy."

L. J. Terminello, "Photoelectron Holography and Auger Electron Angular Distributions Measured Using Synchrotron Radiation."

L. J. Terminello, D. K. Shuh, D. A. Lapiano-Smith, F. J. Himpsel, J. Stöhr, D. S. Bethune, and G. Meijer, "Unfilled Orbitals of  $\text{C}_{60}$  and  $\text{C}_{70}$  from C 1s Near Edge X-Ray Absorption Fine Structure."

P. E. A. Turchi, M. Sluiter, and G. M. Stocks, "Ni-Al: A First-Principles Study of the Interplay between Chemical Order and Structural Effects," *Bull. Am. Phys. Soc.* **36**, 619 (1991).

X.-G. Zhang, A. Gonis, D. Jentz, M. A. VanHove, G. A. Samorjai, P. J. Rous, K. Heinz, H. Lindner, K. Müller, M. Ehsasi, and J. H. Block, "Studies of Clean Stepped Surfaces Using LEED," *Bull. Am. Phys. Soc.* **36**, 811 (1991).

**22nd Lunar and Planetary Science Conference, Houston, TX, March 18–22, 1991**

L. W. Hrubesh and J. F. Poco, "Development of Silica Aerogel as a Capture Medium—Status Report."

**Workshop on Fermiology of High  $T_c$  Superconductors, Argonne, IL, March 25–27, 1991**

P. E. A. Turchi, "A Molecular Orbital Approach to Electron-Positron Annihilation in High- $T_c$  Materials."

**2nd European Conference on Industrial Furnaces and Boilers, Algarve, Portugal, April 1991**

R. C. J. Carlsson, R. Hernberg, J. Stenberg, and P. H. Wallman, "Pyrometric and Combustion Kinetic Measurements in a Pressurized Fluidized Bed."

**72nd Annual American Welding Society Conference, Detroit, MI, April 1991**

J. W. Elmer, A. T. Teruya, and D. W. O'Brien, "Tomographic Determination of the Power Distribution in Electron Beams."

D. W. O'Brien and J. W. Elmer, "Measurement and Study of Keyhole Dynamics in Electron Beam Welding."

**DOE Containment Workshop, Livermore, CA, April 3–4, 1991**

J. E. Hanafee, "Reuse Systems."

J. E. Hanafee, "Containment by Vanadium."

J. E. Hanafee, R. L. Krueger, E. M. Sedillo, and B. F. Vallier, "Pu-Be Studies."

J. E. Hanafee, "Tube Containment—Baseline Review."

G. A. Henshall, "Microstructure and Mechanical Properties of Commercially Pure Vanadium."

D. D. Kautz, "Joining Issues—Liquid Metal Containment."

**32nd Experimental NMR Conference, St. Louis, MO, April 7–11, 1991**

R. L. Ward and R. W. Pekala, "NMR Investigations of Crosslinking in Melamine-Formaldehyde Aerogels."

**American Chemical Society, Atlanta, GA, April 10–14, 1991**

L. M. Hair, W. J. Pitz, M. W. Droegge, and C. K. Westbrook, "Modeling of Catalytic Coupling of Methane."

J. Stephens and C. G. Stevens, "Shock-Wave Desorption for Trace Analysis."

**International Conference on Metallurgical Coatings and Thin Films, San Diego, CA, April 22–26, 1991**

C. Alford, F. Serduke, D. Makowiecki, A. Jankowski, and M. Wall, "X-Ray Fiducial Foils."

A. F. Jankowski and P. L. Perry, "Characterization of Mo/ $B_4C$  Multilayers."

M. McKernan, D. Makowiecki, P. Ramsey, and A. Jankowski, "Magnetron Sputter Deposition of Boron and Boron Carbide."

**24th Oil Shale Symposium, Golden, Colorado, April 23, 1991**

D. F. Aldis and C. B. Thorsness, "Analysis of Particle Slip and Drag in a Lift-Pipe Used in the Hot Recycle-Solid Oil Shale Retort."

**International Group on Radiation Damage Mechanisms—Workshop on Damage Exposure Units for Ferritic Steel Embrittlement Correlations, Raleigh, NC, April 26, 1991**

R. A. VanKonynenburg, "Recent Results of Molecular Dynamics Modelling of Radiation Damage Cascades."

**American Ceramic Society, Cincinnati, OH, April 29–May 2, 1991**

M. L. Elder, S. A. Payne, M. J. Weber, G. D. Wilke, and J. A. Caird, "Concentration Dependent Quantum Efficiency and Relaxation in Nd-Doped Laser Glasses."

S. A. Payne, M. L. Elder, J. H. Campbell, and M. J. Weber, "Optimization of Laser Glass for Fusion Systems."

A. A. Tesar, W. K. Eickelberg, and J. F. Taylor, "Interferometric Measurements of Refractive Index Inhomogeneity in Fused Silica Windows."

M. J. Weber, "Recent Developments in Glasses for Fiber and Fusion Lasers."

**The Materials Research Society, Anaheim, CA, April 29–May 3, 1991**

K. C. Hong and R. S. Glass, "Chemically Modified Microelectrode Arrays for Environmental Monitoring."

E. C. Sowa, A. Gonis, and X.-G. Zhang, "The Real-Space Multiple-Scattering Theory and the Electronic Structure of Grain Boundaries."

J. G. Tobin, "Spin-Integrated and Spin-Dependent Photoelectron Diffraction of Fe/Cu(001)."

J. G. Tobin, "Concentration-Dependent Binding Energy Shifts in a Surface Alloy State."

J. G. Tobin, "The Unexpected Photoemission Spectral Structure of Untwinned, Single-Crystal  $\text{YBa}_2\text{Cu}_3\text{O}_{6.9}$ ."

**JANNAF Meeting, CL-20 Symposium, China Lake, CA, April 29–May 3, 1991**

M. F. Foltz, "High-Pressure Combustion of CL-20 Polymorphs in a Diamond Anvil Cell."

D. L. Ornellas, "Calorimetric Determination of the Heat and Products of Detonation of Hexanitrahexazaisowurtzitane (E-CL-20)."

**Interagency Manufacturing Operations Group–Subgroup on Joining, Largo, FL, April 30–May 2, 1991**

D. D. Kautz, "Preliminary Results of Cutting Studies with High-Brightness Lasers."

D. D. Kautz, "Weldability of AerMet 100."

M. J. Strum, "Atmospheric Effects on Vanadium Laser Weld Properties."

**Northern California Crystal Growth Society, Sunol, CA, May 1991**

W. E. King, "The Important Role of Bicrystals in Interface Science."

**39th ASMS Conference on Mass Spectrometry and Applied Topics, Nashville, TN, May 1991**

A. Alcaraz, B. D. Andresen, and W. H. Martin, "Linked Gas Chromatograph-Thermal Energy Analyzer/Ion Trap Mass Spectrometer."

**Workshop on Nitrous Oxide Emissions from Fluidized Bed Combustion, Morgantown, WV, May 1991**

P. H. Wallman, "Chemistry of  $\text{N}_2\text{O}$  Formation and Destruction."

**ESF Workshop on Holography and Diffraction, Coventry, England, May 3, 1991**

L. J. Terminello, "Auger Electron Angular Distributions and Photoelectron Holograms."

**179th Meeting of the Electrochemical Society, Washington, D.C., May 5–10, 1991**

J. C. Farmer, R. G. Hickman, F. T. Wang, and P. R. Lewis, "Mediated Electrochemical Oxidation of Ethylene Glycol."

R. M. Yamamoto et al., "The Design of an Electrochemical Waste Treatment System."

**Conference on Laser Ablation: Mechanisms and Applications, Oak Ridge TN, May 8–10, 1991**

L. L. Chase, "Role of Laser Ablation in Causing and Investigating Optical Surface Damage."

**1991 Incineration Conference, Knoxville, TN, May 13–17, 1991**

O. H. Krikorian, "Analysis of Plutonium and Uranium Volatilities from Mixed Wastes in the Molten Salt Processor."

**Conference on Lasers and Electro-optics (CLEO), Baltimore, MD, May 13–17, 1991**

S. A. Payne, L. L. Chase, L. K. Smith, W. L. Kway, and W. F. Krupke, "Emission Cross Sections of the Mid-Infrared Laser Transitions of  $\text{Er}^{3+}$ ,  $\text{Tm}^{3+}$ , and  $\text{Ho}^{3+}$  in Fluoride and Oxide Crystals."

**Strategic Defense Initiative Technical Achievements Symposium, Cleveland, OH, May 14–15, 1991**

S. K. Ault, N. J. Colella, R. L. Landingham, and J. Rego Jr., "Low-Areal Density Micropellet/Space Debris Shield for LEO Satellites."

**National Light Source Annual Users Meeting, Upton, NY, May 22, 1991**

L. J. Terminello, "Photoelectron Holography Using Synchrotron Radiation."

**Twelfth Conference on Crystal Growth, Fallen Leaf Lake, CA, May 28–31, 1991**

M. J. Weber, "Glass is Characterized by an Infinitely Large Unit Cell; Glass vs Crystals from One Spectroscopist's Viewpoint."

**U.S. Cryogenic Structural Materials Workshop, Boulder, CO, May 29, 1991**

L. T. Summers, "NDE Requirements for ITER Superconducting Magnets."

**Physical Electronics Conference, Rutgers, NJ, June 1991**

J. G. Tobin, "A Photoemission Investigation of Compound Semiconductor Quantum Dots."

**Northern California Chapter of the American Vacuum Society, Stanford, CA, June 1991**

J. G. Tobin, "A Photoemission Investigation of Compound Semiconductor Quantum Dots."

**Tenth Annual Working Group Institute on Synthesis of High Energy Density Materials, Monticello, NY, June 3–6, 1991**

A. R. Mitchell, "Use of *N*-tert-Butoxycarbonyl (BOC) Derivatives for the Synthesis of Nitramines."

**JOWOG 9, Los Alamos, NM, June 10–14, 1991**

C. O. Pruneda, E. H. von Holtz, K. J. Scribner, and R. E. Whipple, "Higher-Energy, Reduced-Sensitivity Explosives."

W. C. Tao, "Energetic Materials Research and Development at LLNL."

**21st Annual DOE Adhesives Symposium, Livermore, CA, June 11–12, 1991**

L. Chiao, "Mechanistic Modeling of Cure."

S. J. DeTeresa and R. E. Lyon, "Matrix Property Translation into Advanced Fiber Composites."

J. D. LeMay, R. E. Lyon, and I. Chiu, "Fracture Toughness of Candidate Adhesives for BeO-BeO Bond."

R. E. Lyon, "Surface Tension Measurements of Liquid Epoxies."

R. E. Lyon, "High-Modulus/Low-Viscosity Epoxy Resin for Wet-Filament Winding and Resin Transfer Molding."

M. L. Myrick, S. M. Angel, and R. E. Lyon, "Raman Fiber Optic Sensors for Epoxy Cure Monitoring."

**12th American Peptide Symposium, Cambridge, MA, June 16–21, 1991**

A. R. Mitchell, F. Ghofrani, and J. D. Young, "Improved Methodologies for Solid Phase Peptide Synthesis. Use of a Fmoc Strategy with Benzhydryl Resins."

**1991 Topical Conference on Shock Compression of Condensed Matter, American Physical Society, Williamsburg, VA, June 17–20, 1991**

W. H. Gourdin, "Deformation Behavior of Pre-shocked Copper as a Function of Strain Rate and Temperature."

W. C. Tao, C. M. Tarver, and D. R. Breithaupt, "Fundamental Chemical Interactions in Metal-Filled Composite Explosives."

**15th Annual Actinide Separation Conference, Charleston, SC, June 17–21, 1991**

Y. Zundelevich, "The Mediated Electrochemical Dissolution of Plutonium Oxide: Kinetics and Mechanism."

**JOWOG-22C, Aldermaston, England, June 18–20, 1991**

M. J. Strum, "Fatigue Behavior of U-6Nb."

**JOWOG Meeting—Organic Materials Section, Livermore, CA, June 19–21, 1991**

R. W. Pekala, "A New Synthetic Route to Organic Aerogels."

R. W. Pekala, "Low-Density Carbon Foams."

**Actinide Separation Conference, Charleston, SC, June 20, 1991**

J. C. Farmer and Z. Chiba, "Predictive Steady-State Model of Annular-Flow Electrochemical Reactor."

**Gordon Research Conference, Plymouth, NH, July 1991**

J. W. Elmer, L. E. Tanner, and M. J. Aziz, "Model for the Formation of Bands of Ultrafine Particles During Rapid Solidification."

**Scanned Probe Microscopies Conference, Santa Barbara, CA, July 1991**

R. J. Tench, M. A. Schildbach, M. Balooch, W. J. Siekhaus, and A. A. Tesar, "In Situ Scanned Probe Studies on Site Specificity of Laser Surface Damage."

**International Symposium on Metal/Ceramic Interfaces, Irsee, Germany, July 1-4, 1991**

W. E. King, "Shock-Wave Exfoliation."

**Gordon Research Conference, New London, NH, July 1-5, 1991**

S. J. DeTeresa, "Compressive Behavior of High-Performance Fibers and Their Composites."

**Second International Conference on Lasers in Materials Engineering, Medicine, and Biology, Physics, and Chemistry, Grenoble, France, July 9-11, 1991**

L. L. Chase, "Laser Media for Diode Laser-Pumped Solid-State Lasers."

**Gordon Research Conference on Crystal Growth, Plymouth, NH, July 15-19, 1991**

J. J. DeYoreo, L. J. Atherton, D. H. Roberts, and R. W. Martin, "The Formation, Growth, and Elimination of Defects in Cr:LiCaAlF<sub>6</sub>."

**Gordon Research Conference on High Temperature Corrosion, New London, NH, July 15-19, 1991**

W. E. King, "Measurement of Metal/Scale Interface Bond Strength."

**International Society for Optical Engineering Symposium on Optical Applied Science and Engineering, San Diego, CA, July 21-26, 1991**

J. J. DeYoreo, B. W. Woods, and L. J. Atherton, "The Effect of Strain on the Performance of Large-Aperture KD\*P Pockels Cells."

N. Thomas and C. G. Stevens, "Echelle-Prism Spectrograph for Remote Sensing of Chemical Efficients at 2-5  $\mu\text{m}$ ."

**International Conference on Materials and Mechanisms of Superconductivity—High Temperature Superconductors, Kanazawa, Jpn., July 22-26, 1991**

M. J. Fluss, H. B. Radousky, and R. S. Glass, "On the Chemical Origin of the Hole Carriers in YBCO."

**Society of Photo-Optical Instrumentation Engineers, San Diego, CA, July 22-24, 1991**

T. W. Barbee, Jr., "Multilayer Structures: Historical Perspective and Future Potential."

**International Conference of Point Defects in Glass, Riga, Latvia, July 29-31, 1991**

M. J. Weber, "Local Structure of Rare Earth Ions in Glass."

**Workshop on Spectroscopic Imaging, Diffraction and Holography with X-Ray Photoemission, Berkeley, CA, August 1991**

J. G. Tobin, "Photoelectron Diffraction of Magnetic Ultrathin Films."

**Seventh Semiannual Review, Technology Coordination Group for Energetic Materials, White Oak, MD, August 1991**

P. F. Pagoria, C. L. Coon, A. R. Mitchell, and R. L. Simpson, "Synthesis and Scale-Up."

**CONFAB 91, Silver Creek, CO, August 1991**

B. E. Watkins, D. F. Aldis, C. J. Morris, T. T. Coburn, and C. B. Thorsness, "Retorting of 7-mm-Diameter Particles of Oil Shale."

**VII International Conference on the Physics of Non-Crystalline Solids, Cambridge, England, August 4-9, 1991**

M. J. Weber, "Physics of Laser Glass."

**The 5th All Union Meeting on Detonation—International Symposium on Chemistry of Shock Waves, Krasnoyarsk, USSR, August 4-11, 1991**

P. A. Urtiew, C. M. Tarver, and L. G. Green, "Response of LX-10 Explosive to Low-Pressure Dynamic Loading."

**Electron Microscopy Society of America, San Jose, CA, August 5-8, 1991**

M. Wall and T. W. Barbee, Jr., "Structural Characterization of Macroscopic Copper-304/Stainless-Steel Multilayer Materials."

**Pacific International Congress on X-ray Analytical Methods, Honolulu, HI, August 12-16, 1991**

T. W. Barbee Jr., "Spatially and Spectrally Imaging Multilayer X-Ray Optics and Instrumentation."

**NATO Advanced Study Institute, Equilibrium Structure and Properties of Surfaces and Interfaces, Porto Carras, Greece, August 18–30, 1991**

E. C. Sowa and A. Gonis, "The Real-Space Multiple-Scattering Theory: A First-Principles Method for the Computation of the Electronic Structure of Defects."

**American Institute of Chemical Engineers, Pittsburgh, PA, August 19, 1991**

R. G. Hickman, L. W. Gray, and J. C. Farmer, "Mediated Electrochemical Process for Mixed Waste Treatment."

**American Chemical Society, New York, NY, August 26–30, 1991**

A. C. Jones, C. Stevens, W. Conaway, and A. Droege, "Laser Generated Hydrocarbon Plasmas: Determination of Temperature by C<sub>2</sub> Emission Spectroscopy."

**9th International Conference on Positron Annihilation, Szombathely, Hungary, August 26–31, 1991**

R. H. Howell, C. Berger, F. Solal, Y. Calvayrac, and P. E. A. Turchi, "Structural Features in Icosahedral Al<sub>63</sub>Cu<sub>25</sub>Fe<sub>12</sub>."

**DOE Workshop on Scientific Issues Related to Intermetallic Compounds, La Jolla, CA, September 1991**

L. E. Tanner, "Phonon Behavior and Microstructural Development Leading to Martensitic Transformations."

**American Society of Metals, International Conference on High Temperature Aluminides and Intermetallics, San Diego, CA, September 16–19, 1991**

H. Li, F. C. Chen, A. J. Ardell, A. F. Jankowski, and D. F. Pedraza, "Mechanical Behavior of 1-MeV Proton-Irradiated Ni<sub>3</sub>Al."

M. Sluiter, P. E. A. Turchi, F. J. Pinski, D. D. Johnson, and G. M. Stocks, "A First-Principles Study of Phase Stability in Ni-Al and Ni-Ti Alloys."

**JOWOG 28B, Aldermaston, England, September 17, 1991**

J. LeMay, K. Wilfinger, C. Hoenig, and G. Thomas, "HIP Bonding of Ag-Be Laminated Test Components."

T. M. Tillotson, L. W. Hrubesh, and W. E. Sunderland, "Silica Aerogels with Improved Optical Properties."

**Interdisciplinary Laser Science Conference, ILS-VI, Monterey, CA, September 22–26, 1991**

A. V. Hamza, "Photon Absorption by Sapphire Surfaces."

L. L. Chase, A. V. Hamza, and H. W. H. Lee, "Mechanisms of Laser-Induced Damage in SiO<sub>2</sub> and HfO<sub>2</sub> Coatings."

**Eighth Target Fabrication Specialists Meeting, Albuquerque, NM, September 23–25, 1991**

S. R. Buckley, G. E. Overturf, and R. C. Cook, "Brominated Polystyrene at Preselected Atom %."

R. C. Cook, G. E. Overturf, and S. R. Buckley, "Diagnostic Dopants in Direct-Drive Laser ICF Target Mandrels."

S. A. Letts, M. D. Saculla, F.-M. Kong, E. F. Lindsey, C. W. Price, and S. R. Buckley, "Bromine-Containing Plasma Polymer Coatings."

C. E. Moore and R. J. Wallace, "Target Metrology Upgrade."

G. E. Overturf, S. R. Buckley, and R. C. Cook, "Synthesis and Characterization of Iodinated Polystyrene."

C. W. Price, E. F. Lindsey, and S. A. Letts, "Bromine Analysis in Hydrocarbon Films by Energy-Dispersive Spectroscopy."

C. W. Price, E. F. Lindsey, and S. A. Letts, "Bromine-Rich Precipitates on Brominated Hydrocarbon Films."

C. W. Price, G. J. Greiner, and C. E. Moore, "X-Ray Microfluorescence Capabilities at LLNL."

C. W. Price, E. F. Lindsey, T. P. Bernat, R. E. Turner, W. J. Siekhaus, M. Balooch, and R. J. Tench, "Use of Atomic Force Microscopy for Surface-Finish Measurements."

C. W. Price and E. F. Lindsey, "Thickness Measurements of Thin Films."

M. D. Saculla and S. A. Letts, "Quantitative Radiography of Bromine-Containing Plasma Polymer Coatings."

J. Sanchez, G. W. Collins, and E. M. Fearon, "Burst-Pressure Measurements of PVA-Coated Polystyrene Capsules for Direct-Drive Experiments."

R. J. Wallace, G. J. Mauger, G. J. Greiner, M. Spragge, and R. Levesque, "Improved Target Assembly Workstation."



L. Witt, S. A. Letts, and E. F. Lindsey, "Atomic Force Microscopy of Plasma Polymer Coatings."

**6th Symposium on the Containment of Underground Nuclear Explosions, Reno, NV, September 23–27, 1991**

H. L. McKague, J. R. Hearst, and R. L. Ward, "Nuclear Magnetic Resonance Determination of the Non-Pore Water Content of Zeolitic Tuffs and Its Application to Correction of Epithermal-Neutron-Derived Water Content."

**Focus 91—Nuclear Waste Packaging, Las Vegas, NV, September 29–October 2, 1991**

W. L. Clarke, G. E. Gdowski, W. G. Halsey, and R. D. McCright, "Candidate Container Materials for Yucca Mountain."

G. A. Henshall, "Stochastic Models for Predicting Pitting Corrosion Damage of HLRW Containers."

**Fourth Topical Meeting on Tritium Technology, Albuquerque, NM, September 29–October 4, 1991**

J. L. Maienschein, S. W. Wilson, and F. Garcia, "Design and Operational Experience with a Portable Tritium Cleanup System."

J. L. Maienschein, R. S. Hudson, R. T. Tsugawa, E. M. Fearon, P. C. Souers, and G. W. Collins, "Production of Ultrapure D-T Gas by Removal of Molecular Tritium by Selective Adsorption."

J. L. Maienschein, F. Garcia, R. G. Garza, R. L. Kanna, S. R. Mayhugh, and D. T. Taylor, "Experiences with Decontaminating Tritium-Handling Apparatus."

**Third International Symposium on Aerogels, Wurzburg, Germany, September 30–October 2, 1991**

R. W. Pekala, "Aerogels Derived from Multifunctional Organic Monomers."

T. M. Tillotson and L. W. Hrubesh, "Transparent Ultralow-Density Silica Aerogels by a Two-Step Sol-Gel Process."

**University of Wisconsin Synchrotron Radiation Center Users Meeting, Madison, WI, October 1991**

J. G. Tobin, "Utilization of an SGM Beamline for Studies with High Resolution and Helically Polarized X Rays at SSRL."

**DOE Workshop on Synchrotron Radiation Beamlines, Gatlinburg, TN, October 1991**

J. G. Tobin, "Spectromicroscopy IDT."

**Emerging Technologies for Hazardous Waste Management, Atlanta, GA, October 1–3, 1991**

R. G. Hickman, J. C. Farmer, and F. Wang, "Mediated Electrochemical Hazardous Waste Destruction."

**Institute of Electrical and Electronics Engineers 14th Symposium on Fusion Engineering, San Diego, CA, October 3, 1991**

L. T. Summers, "The Impact of Fatigue and Structural Design on the Operation and Reliability of ITER Magnet Systems."

**International Symposium on the Physics and Chemistry of Finite Systems, Richmond, VA, October 8–12, 1991**

V. Kresin, "Inelastic Electron Scattering and Response Properties of Alkali Clusters."

**DOE 17th Surface Studies Conference, Pleasanton, CA, October 15–18, 1991**

L. L. Chase, A. V. Hamza, and H. W. H. Lee, "Investigation of Optical Damage in SiO<sub>2</sub> and HfO<sub>2</sub> Coatings Using Pairs of Picosecond Laser Pulses."

C. A. Colmenares, J. Z. Liu, and C. Evans, "UPS and XPS Studies of *In Situ* Cleaved Single Crystals of YBa<sub>2</sub>Cu<sub>3</sub>O<sub>7</sub>."

T. H. Gouder and C. A. Colmenares, "Formation and Interconversion of Uranium Surface Oxides and Oxycarbides Studied by UPS/XPS/HREELS."

T. H. Gouder and C. A. Colmenares, "Electronic Structure and Surface Reactivity of Sputtered Thin Films of Uranium on Silicon."

M. A. Schildbach and A. V. Hamza, "Interaction of Pulsed Laser Light with Sapphire Surfaces."

L. J. Terminello and J. J. Barton, "Surface Structure Determination Using Photoelectron Holography."

J. G. Tobin, "Spin-Integrated and Spin-Dependent Photoelectron Diffraction of Fe/Cu(001)."

**Electronics, Glass, and Optical Materials Meeting,  
American Ceramic Society, Arlington, VA,  
October 20–23, 1991**

L. L. Chase, R. W. Adair, and S. A. Payne, "Characterization of the Nonlinear Refractive Properties of Optical Materials and Laser Media."

**The Metallurgical Society Fall Meeting, American  
Society of Metals Conference on Phase Diagram  
Computation, Cincinnati OH, October 21–24, 1991**

J. E. Hanafee, "Characterization and Consolidation of Gas Atomized Beryllium Powder."

J. Mikalopas, M. Sluiter, P. A. Sterne, and P. E. A. Turchi, "First-Principles Calculation of Phase Stability of Ni-V and Pd-V Alloys."

M. Sluiter, P. E. A. Turchi, F. J. Pinski, and G. M. Stocks, "Theoretical Study of Phase Stability in Ni-Al and Ni-Ti Alloys."

G. M. Stocks, D. M. Nicholson, W. A. Shelton, F. J. Pinski, D. D. Johnson, J. B. Staunton, A. Barbieri, B. L. Gyorffy, B. Ginatempo, P. E. A. Turchi, and M. Sluiter, "Ordering Mechanisms in Metallic Alloys."

L. E. Tanner, "Premartensitic Behavior and Martensite Nucleation in Ni-Al Alloys."

P. E. A. Turchi, M. Sluiter, and G. M. Stocks, "First-Principles Prediction of Alloy Phase Stability."

**23rd Annual Boulder Damage Symposium on Optical  
Materials for High-Power Lasers, Boulder, CO,  
October 23–24, 1991**

L. L. Chase, A. V. Hamza, and H. W. H. Lee, "Investigation of Optical Damage in SiO<sub>2</sub> and HfO<sub>2</sub> Coatings Using Pairs of Picosecond Laser Pulses."

A. V. Hamza, R. S. Hughes, L. L. Chase, and H. W. H. Lee, "Investigation of the Laser-Al<sub>2</sub>O<sub>3</sub>(11 $\bar{2}$ 0) Surface Interactions Using Pairs of Picosecond Pulses."

**4th European Symposium on Space Environmental  
Control Systems, Florence, Italy, October 23, 1991**

A. Waleh, V. Kanevsky, R. S. Upadhye, and T. Wydeven, "Impact of Diet on the Design of Waste Processors in CELSS."

**2nd Peoples Republic of China Detonation Symposium,  
Beijing, China, October 28–November 1, 1991**

W. C. Tao, C. M. Tarver, and D. L. Ornellas, "Understanding Composite Explosives Energetics: III. Reactive Flow Modelling of Aluminum Reaction Kinetics in PETN and TNT."

**7th National Conference on Synchrotron Radiation  
Instrumentation 91, Baton Rouge, LA, October 29, 1991**

L. J. Terminello, G. D. Waddill, and J. G. Tobin, "High-Resolution Photoabsorption and Magnetic Circular Dichroism Measurements on the Univ. of California/National Laboratory Spherical Grating Monochromator Beamline."

**Interagency Manufacturing Operations Group—Subgroup  
on Joining, Livermore, CA, October 31, 1991**

D. D. Kautz, "Laser Materials Processing Update."

**Stanford Synchrotron Radiation Laboratory Users  
Meeting, Stanford, CA, November 1991**

J. G. Tobin, "Synchrotron Radiation-Based Investigation of Magnetic Ultrathin Films: Fe/Cu(001)."

**Optical Society of America Symposium—Optical  
Fabrication, San Jose, CA, November 1991**

A. A. Tesar, B. A. Fuchs, and P. P. Hed, "Polishing Compounds: An In-Depth Study of Polishing Behaviors and Surface Characteristics."

**The Laser and Electron Beam in Welding, Cutting, and  
Surface Treatment State of the Art 1991 Conference,  
Reno, NV, November 1991**

A. T. Teruya, J. W. Elmer, and D. W. O'Brien, "A Method for Imaging the Power Distribution in Electron Beams."

**Royal Society Meeting, London, England,  
November 5–6, 1991**

C. O. Pruneda, E. S. Jessop, C. M. Walkup, and D. M. Hoffman, "LOVEX-BX, A High-Performance, Low-Vulnerability, and Low-Cost Composite Explosive."

**Stanford Synchrotron Radiation Laboratory User's  
Meeting, Stanford, CA, November 8, 1991**

L. J. Terminello, "High-Resolution Photoabsorption of O<sub>2</sub>, N<sub>2</sub>, and CO K-Shells on the Univ. of California/National Laboratory Spherical Grating Monochromator Beamline."

**38th National Symposium of the American Vacuum Society, Seattle, WA, November 11–15, 1991**

R. C. Cook, G. E. Overturf, and S. R. Buckley, "Covalent Inclusion of Diagnostic Dopant Atoms in Polymeric Materials for ICF Experiments."

A. F. Jankowski, "Synthesis and Structure of a Superconducting Au-Nb Superlattice."

S. A. Letts, M. D. Saculla, F.-M. Kong, E. F. Lindsey, C. W. Price, and S. R. Buckley, "Bromine-Containing Plasma Polymer Coatings."

S. A. Letts, E. F. Lindsey, and L. Witt, "Atomic Force Microscopy of Plasma Polymer Coatings."

J. Sanchez, G. W. Collins, and E. M. Fearon, "D-T and D<sub>2</sub> Retention in Plastic Shells."

L. J. Terminello and J. J. Barton, "Photoelectron Holography of Cu(001) and Cl/CU(001) Measured Using Synchrotron Radiation."

J. G. Tobin, "The Valence Bands and Fermiology of Untwinned Single-Crystal YBa<sub>2</sub>Cu<sub>3</sub>O<sub>6.9</sub>."

**Mechanics of Composites Review, Dayton, OH, November 12–13, 1991**

S. J. DeTeresa, "Maximizing the Axial Compressive Strength of Filament-Wound Composite Cylinders."

**High-Resolution Conflict Simulation Conference, Livermore, CA, November 13–15, 1991**

D. U. Olness, "Comparing the Relative Effectiveness of Tactical Yield Nuclear Weapons and Developmental Advanced Conventional Munitions."

**1991 Eastern Oil Shale Symposium, Lexington, KY, November 13–15, 1991**

T. I. Duewer, K. G. Foster, and T. T. Coburn, "Raw Shale Dissolution as an Aid in Determining Mineralogy."

D. F. Aldis, "Attrition and Abrasion Models for Oil Shale Process Modeling."

**11th Annual Pyrochemical Workshop, Oakbrook, IL, November 13, 1991**

C. Cate, "Plutonium Chloride Preparation by Hydride Chlorination."

R. S. Upadhye, "Molten Salt Destruction Process for the Treatment of Pu-Containing Wastes."

**1991 Annual Meeting of The American Institute of Chemical Engineers, Symposium on Electrochemical Sensors, Los Angeles, CA, November 17–22, 1991**

R. S. Glass, K. C. Hong, K. Ashley, and V. E. Granstaff, "Versatile Electrochemical Microsensors for Environmental Monitoring."

**Performance Assessment Total System Analysis Workshop, Las Vegas, NV, November 19–20, 1991**

W. G. Halsey and A. D. Lamont, "Yucca Mountain Integrating Model."

**Seminar on Nuclear Physics Concepts in Atomic Cluster Physics, Nad Honnef, Germany, November 26–29, 1991**

V. Kresin, "Inelastic Electron-Cluster Collisions and Response Properties of Metal Clusters."

**Materials Research Society, Boston, MA, December 2–6, 1991**

A. V. Hamza and M. A. Schildbach, "The Effect of an H<sub>2</sub>O Adlayer on the Laser-A1203(1102) Surface Interaction."

A. F. Jankowski and M. A. Wall, "The Stabilization of Face-Centered-Cubic Titanium."

J. Ma, A. P. Y. Wong, S. B. Kim, M. H. W. Chan, W. I. Goldberg, and L. W. Hrubesh, "Superfluid and Liquid-Vapor Critical Phase Transition of N<sub>2</sub> Confined in Aerogel."

R. G. Musket, R. H. Hawley-Fedder, and W. L. Bell, "Interactions of Protons with Thin Films of C<sub>60</sub> Molecules."

D. Schryvers and L. E. Tanner, "Electron Microscopy of Stress-Induced Martensite and Pretransition Microstructures in Ni<sub>62.5</sub>Al<sub>37.5</sub>."

P. P. Singh, A. Gonis, and D. de Fontaine, "Self-Consistent-Field KKR-CPA Calculations in the Atomic-Sphere Approximation."

M. Sluiter and P. E. A. Turchi, "The Role of Chemical Interactions in the Stability of Artificial Metallic Superlattices."

L. E. Tanner, "Phonon Behavior and Microstructural Development Leading to Martensitic Transformations in Ni<sub>x</sub>Al<sub>(100-x)</sub> Alloys."

J. G. Tobin, "The Valence Bands and Fermiology of Untwinned Single-Crystal  $\text{YBa}_2\text{Cu}_3\text{O}_{6.9}$ ."

P. E. A. Turchi and M. Sluiter, "Real-Space Multiple-Scattering Theory of Phase Stability in Alloys."

P. E. A. Turchi and M. Sluiter, "Statics of Phase Transformation in Ni-Al, Ni-Ti, and Cu-Zn: A First-Principles Study."

**Yucca Mountain Project Geochemistry Integration Meeting: Role of Geochemistry in Performance Assessment, Henderson, NV, December 4-5, 1991**

W. G. Halsey, "Waste Package Performance Assessment Needs for Geochemical Data."

**Sixth Australian Workshop on Oil Shale, Brisbane, Queensland, Australia, December 5-6, 1991**

R. J. Cena and P. H. Wallman, "The LLNL HRS Retorting Process Pilot Plant and Conceptual Design Studies."

**International Conference on Lasers '91, San Diego, CA, December 9-13, 1991**

D. D. Kautz, "Preliminary Cutting and Drilling Studies with High-Power, High-Radiance Lasers."

M. J. Strum, "Interstitial Embrittlement of Vanadium Laser Welds."

## Patents

L. J. Atherton, J. J. DeYoreo, and D. H. Roberts, *Method for Reducing Passive Scattering Losses in LiCAF*, U.S. Patent No. 5,099,490 (1991).

T. W. Barbee, Jr., *Multilayer Diffraction Grating*, U.S. Patent No. 4,915,463 (1990).

J. A. Britten, C. B. Thorsness, R. M. Brusasco, J. H. Campbell, W. Johnson, and M. W. Scrivener, *Flat High-Temperature Plasma CVD Coater*, DOE Patent Application No. IL-8274 (1990).

C. A. Colmenares, *Catalysts for Synthesizing Various Short Chain Hydrocarbons*, U.S. Patent No. 5,030,607 (1991).

S. J. DeTeresa, *Conducting-Fiber Compression Tester*, U.S. Patent No. 4,974,451 (1990).

C. A. Ebbers, L. DeLoach, and M. Webb, *Frequency-Conversion Material*, DOE Patent Application No. IL-8491 (1991).

J. C. Farmer and R. G. Hickman, *Potential-Controlled Electrochemical Reactor for Mediated Electrochemical Oxidation*, DOE Patent Application No. IL-8627 (1990).

J. C. Farmer, R. G. Hickman, F. T. Wang, P. R. Lewis, and L. J. Summers, *Rotating-Anode Electrochemical Reactor for Mediated Electrochemical Oxidation*, DOE Patent Application No. IL-8626 (1990).

J. C. Farmer, F. T. Wang, R. G. Hickman, P. R. Lewis, and L. J. Summers, *Mediated Electrochemical Oxidation of Hazardous Organic Wastes without Electrode Separators*, DOE Patent Application No. IL-8851 (1991).

K. G. Foster, E. J. Frohwein, and R. W. Taylor, *Tube Furnace*, U.S. Patent No. 5,072,094 (1991).

R. S. Glass, S. P. Perone, D. R. Ciarlo, and J. F. Kimmons, *Electrochemical Sensor/Detector System and Method*, DOE Patent Application No. IL-8043 (1991).

B. L. Haendler, *Stable Emulsified Bleaching Composition*, U.S. Patent No. 4,929,383 (1990).

B. L. Haendler and R. J. Cramer, *Bleaching and Bluing Composition and Method*, U.S. Patent No. 5,075,029 (1991).

F.-M. Kong, *Carbonization of HIPE Polystyrene Foam*, U.S. Patent No. 4,992,254 (1991).

F.-M. Kong, *Low-Density Carbonized Composite Foams*, U.S. Patent No. 5,047,225 (1991).

J. D. LeMay, *Low-Density Microcellular Foams*, U.S. Patent No. 5,066,684 (1991).

J. L. Maienschein and P. E. Barry, *Low-Density Metal Hydride Foams*, U.S. Patent No. 5,026,670 (1991).

D. M. Makowiecki and A. F. Jankowski, *Fabrication of Multilayered Optical Coatings with Arrays of Small Magnetron Sputtering Sources*, DOE Patent Application No. S-72,127 (1990).

D. M. Makowiecki and A. F. Jankowski, *Magnetron Sputtered Boron Films and Ti/B Multilayer Structures*, DOE Patent Application No. S-71,298 (1991).

R. G. Musket, D. W. Brown, and Z. A. Munir, *Process for Forming One or More Substantially Pure Layers in Substrate Materials using Ion Implantation*, U.S. Patent No. 4,976,987 (1991).

G. L. Nutt, *Method for Enhancing Stability of High Explosives for Purposes of Transport or Storage, and the Stabilized High Explosives*, U.S. Patent No. 5,067,995 (1991).

D. U. Olness and T. B. Hirschfeld, *Elastomer Degradation Sensor Using a Piezoelectric Material*, U.S. Patent No. 4,906,917 (1990).

R. W. Pekala, *Low-Density Resorcinol-Formaldehyde Aerogels*, U.S. Patent No. 4,997,804 (1991).

C. G. Stevens and N. Thomas, *Echelle-Prism Spectrograph for Remote Sensing*, DOE Patent Application No. IL-8795 (1991).

M. Vanderlaan, B. E. Watkins, and L. H. Stanker, *Monoclonal Antibodies for the Separate Detection of Halodexyuridines and Method for their Use*, U.S. Patent No. 5,053,336 (1991).

F. T. Wang, J. C. Farmer, R. G. Hickman, and L. W. Gray, *Anodic Oxidation of Oxalic Acid and Oxalate Ion in Aqueous Solutions*, DOE Patent Application No. IL-8840 (1991).



---

Section 12

**Budget  
Information**

**Table 1.** Distribution of effort and funds for the C&MS Department in FY91.

C&MS Cost Center	Number of FTE		Cost (\$K)
	C&MS	Other	
<b>Direct Programs</b>			
Weapons Supporting Research	14.7	6.9	6722
Departmental LDRD/exploratory research	3.3	5.2	2074
Departmental LDRD/supporting research	1.0	0.7	312
Labwide LDRD	0.7	0.0	96
DOE/Basic Energy Sciences	4.4	3.8	1886
DoD/Reimbursables	1.1	0.3	415
Miscellaneous WFO	1.0	0.5	302
DOE Direct	0.8	1.1	356
	<b>27.0</b>	<b>18.5</b>	<b>12163</b>
<b>Distributed Services</b>			
Plutonium Facility	6.6	22.8	6371
Tritium Facility	2.6	8.2	1759
	<b>9.2</b>	<b>31.0</b>	<b>8130</b>
<b>Indirect Activities</b>			
Support Burden	47.3	4.8	5147
Maintenance/Noncapital	10.3	22.5	5448
Capital Equipment/Fabrication	0.1	0.4	1216
	<b>57.7</b>	<b>27.7</b>	<b>11811</b>
<b>Subtotal, C&amp;MS Cost Centers</b>	<b>93.9</b>	<b>77.2</b>	<b>32104</b>
<b>Support to Other Programs</b>			
Defense Systems	75.7		
Special Projects	7.5		
Laser Programs	41.7		
Energy Program	27.3		
Miscellaneous DOE	22.9		
Reimbursables/WFO	38.2		
LDRD	20.0		
	<b>233.3</b>		
<b>Total C&amp;MS Department</b>	<b>327.2</b>		

**Figure 1.** FTE distribution in FY 91. (a) Direct programs, 27.0 FTE. (b) Distributed services and indirect activities, 66.9 FTE. (c) Support to other programs, 233.3 FTE.

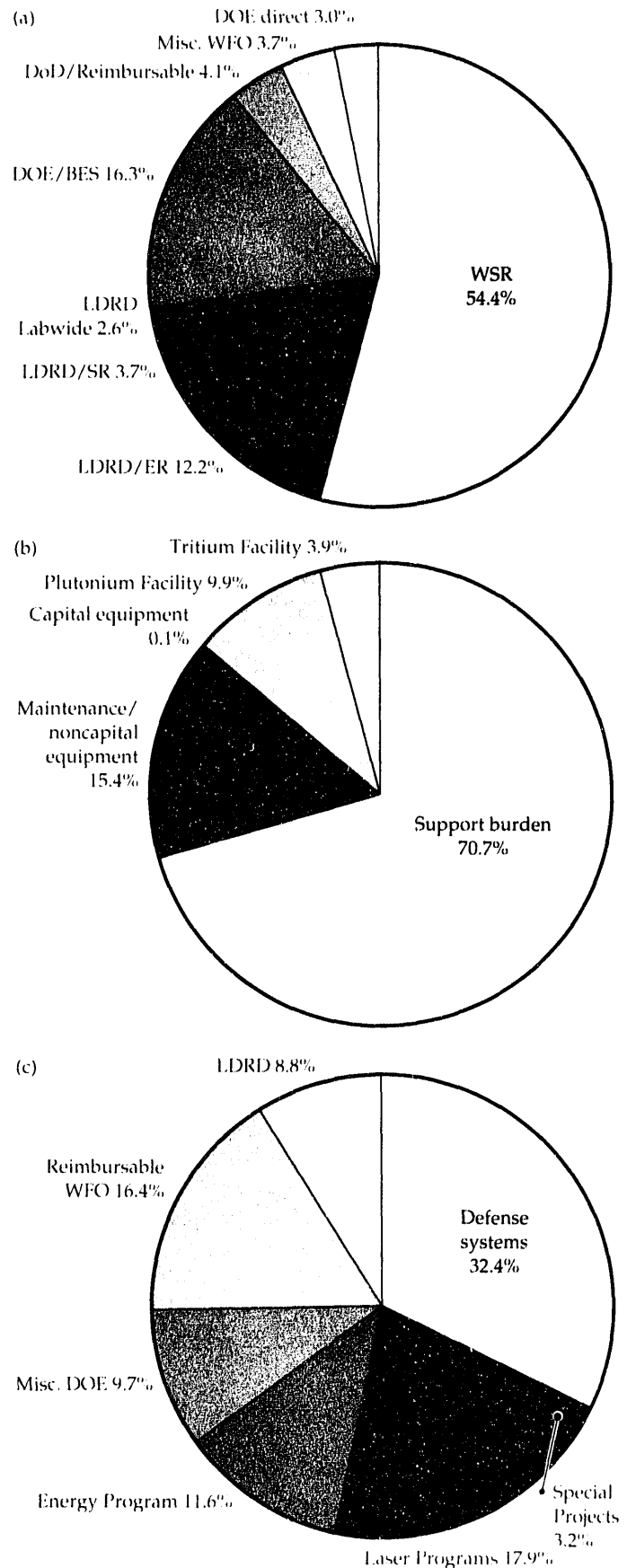




**Table 2.** C&MS Weapons-Supporting Research program and budgets for FY90 and FY91 (\$K).

Thrust Area	Leader	FY90	FY91
Energetic Materials	R. Simpson	685	705
Fundamentals of the Physics & Processing of Metals	M. Kassner/ W. Gourdin	850	850
High-Transition-Temperature Superconductivity	M. Fluss	600	600
Interfaces, Adhesion & Bonding	W. King	500	500
Plutonium Research	L. Newkirk	750	800
Synchrotron Radiation-Based Materials Science	J. Wong	750	750
Tritium Research	C. Souers	300	472
<b>Total</b>		<b>4935</b>	<b>4677</b>
Group	Leader	FY90	FY91
Interactions of Surfaces with the Environment	C. Colmenares		400
Molecular Approach to Aerogels	L. Hrubesh		200
<b>Total</b>			<b>600</b>
Individual project	Principal investigator	FY90	FY91
Ultratrace Analysis	B. Andresen	120	
Photocatalysis on Doped Aerogels	C. Colmenares	200	
Bond-Selective Chemistry	W. Conaway	150	
Chemistry of Defects	J. De Yoreo	70	
DTA Equipment Development	J. De Yoreo	50	
Laser-Produced Molecular Plasmas	A. Droege	170	
Structural Transformation & Precursor Phenomena in Advanced Materials	P. Turchi	150	
<sup>15</sup> N NMR Investigation of Crosslinking	R. Ward	40	
Surface Magnetism in Ultrathin Films	J. Tobin	60	
Damage Initiation and Accumulation	J. Kinney	35	
Actinide Physics	P. Baisden		60
Properties of Graphite Fibers	R. Christensen		100
Diffusion of Point Defects in Fluorides	J. De Yoreo		40
Synthesis of Buried Layers	R. Musket		150
<b>Total</b>		<b>1045</b>	<b>350</b>
<b>Total Weapons-Supporting Research</b>		<b>5980</b>	<b>5627</b>

**Table 3.** C&MS Laboratory Directed Research & Development projects and budgets for FY90 and FY91 (\$K).

Department project	Principal investigator	FY90	FY91
Chemistry & Physics of High-Transition-Temperature Superconductivity	M. Fluss	1208	1125
Thermodynamics & Mechanical Properties of Al-Li Alloys	A. Gonis	172	
Structure-Property Link in Sub-nanometer Materials	A. Jankowski	220	238
Nuclear Spin Polarization	C. Souers	645	323
Structure & Properties of Ultrathin Magnetic Films	J. Tobin		195
Structural Transformation & Precursor Phenomena in Advanced Materials	P. Turchi		194
<b>Total</b>		<b>2245</b>	<b>2075</b>
Laboratory-wide project	Principal investigator	FY90	FY91
Application of <sup>67</sup> Zn Mossbauer Spectroscopy to Hole- and Electron-Doped Copper Oxide	C. Violet	124	
Changes in Material Structure over Extremely Short Periods	Q. Johnson	88	
Synthesis & Characterization of Melamine-Formaldehyde Aerogels	R. Pekala		97
<b>Total</b>		<b>212</b>	<b>97</b>
<b>Total Laboratory Directed Research &amp; Development</b>		<b>2457</b>	<b>2172</b>

# Acronyms and Abbreviations

<b>ACAR</b>	Angular correlation of annihilation radiation	<b>FWHM</b>	Full width at half maximum
<b>ADNT</b>	3,5-dinitro-1,2,4-triazolate	<b>FWP</b>	Field work proposal
<b>AES</b>	Auger electron spectroscopy	<b>GC</b>	Gas chromatography
<b>AFM</b>	Atomic force microscopy	<b>GC/MS</b>	Gas chromatography/mass spectrometry
<b>ANTA</b>	3-amino-5-nitro-1,2,4-triazole	<b>GPM</b>	Generalized perturbation method
<b>APB</b>	Antiphase boundary	<b>hcp</b>	Hexagonally close-packed
<b>ASTM</b>	American Society for Testing Materials	<b>HF</b>	Hartree-Fock
<b>bcc</b>	Body-centered cubic	<b>HLRW</b>	High-level radioactive waste
<b>bct</b>	Body-centered tetragonal	<b>HMX</b>	1,3,5,7-tetranitro-1,3,5,7-tetraazacyclooctane
<b>BET</b>	Nitrogen adsorption porosimetry	<b>HOPG</b>	Highly ordered pyrolytic graphite
<b>BF</b>	Bright field	<b>HREM</b>	High-resolution electron microscopy
<b>BS</b>	Backscattering	<b>HRS</b>	Hot-recycle solids (oil shale process)
<b>BSCCO</b>	$\text{Bi}_2\text{Sr}_2\text{CaCu}_2\text{O}_8$	<b>HRTEM</b>	High-resolution transmission electron microscopy
<b>CBM</b>	Conduction band minimum	<b>ICF</b>	Inertial confinement fusion
<b>CFC</b>	Chlorofluorocarbon	<b>ICP-AES</b>	Inductively coupled plasma-atomic emission spectroscopy
<b>CFT</b>	Concentration functional theory	<b>IM</b>	Insensitive munition
<b>CI</b>	Configuration interaction	<b>IR</b>	Infrared
<b>CMA</b>	Cylindrical mirror analyzer	<b>ISBS</b>	Impulsive stimulated Brillouin scattering
<b>CPA</b>	Coherent potential approximation	<b>ISE</b>	Ion-selective electrodes
<b>CSL</b>	Coincident site lattice	<b>ISFET</b>	Ion-sensitive field-effect transistor
<b>CT</b>	Computed tomography	<b>ISRS</b>	Impulsive stimulated Raman scattering
<b>CTBN</b>	Carboxy-terminated butadiene-acrylonitrile	<b>ITMS</b>	Ion trap mass spectrometer
<b>CTEM</b>	Contrast transmission electron microscopy	<b>KKR</b>	Korringa, Kohn, and Rostoker
<b>CVM</b>	Cluster variation method	<b>LA</b>	Longitudinal acoustic
<b>CZ</b>	Czochralski	<b>LAXS</b>	Large-angle x-ray spectroscopy
<b>DABCO</b>	Brand name of Air Products, Inc.	<b>LBL</b>	Lawrence Berkeley Laboratory
<b>DAT</b>	3,5-diamino-1,2,4-triazole	<b>LCW</b>	Lock-Crisp-West (theorem)
<b>DCHA</b>	dicyclohexyammonium	<b>LEED</b>	Low-energy electron diffraction
<b>DCPD</b>	Direct-current potential-drop	<b>LiCAF</b>	$\text{Cr}^{3+}:\text{LiCaAlF}_6$
<b>DEAE</b>	Diethylaminoethyl	<b>LiGaF</b>	$\text{Cr}^{3+}:\text{LiSrGaF}_6$
<b>DMF</b>	Dimethylformamide	<b>LiSAF</b>	$\text{Cr}^{3+}:\text{LiSrAlF}_6$
<b>DNT</b>	3,5-dinitro-1,2,4-triazole	<b>LKKR</b>	Layer Korringa, Kohn, and Rostoker (computer code)
<b>DOE</b>	(U.S.) Department of Energy	<b>LMTO</b>	Linear muffin tin orbital (method)
<b>DOS</b>	Density of states	<b>LOVEX</b>	Low-vulnerability explosives
<b>DSC</b>	Differential scanning calorimetry	<b>LPN</b>	Liquid-phase nucleation
<b>DTT</b>	Dithiothreitol	<b>LPS</b>	Long-period superstructure
<b>DWPF</b>	Defense Waste Processing Facility	<b>L/S</b>	Liquid/solid
<b>EAM</b>	Embedded-atom method	<b>LSCO</b>	$\text{La}_{2-x}\text{Sr}_x\text{CuO}_4$
<b>ED</b>	Electron diffraction	<b>MEO</b>	Mediated electrochemical oxidation
<b>EDL</b>	Electrodeless discharge lamp	<b>MF</b>	Melamine-formaldehyde
<b>EDS</b>	Energy-dispersive spectrometer	<b>MGPT</b>	Model-generalized pseudopotential theory
<b>EELS</b>	Electron-energy-loss spectrum	<b>MMC</b>	Metal-matrix composite
<b>ELS</b>	Electron-energy-loss spectroscopy	<b>MMO</b>	Methane monooxygenase
<b>EM</b>	Electron microscopy	<b>MOPS</b>	Morpholino propanesulfonic acid
<b>EPI</b>	Electronic pair interaction	<b>MS</b>	Mass spectrometry
<b>ER</b>	(DOE Office of) Energy Research	<b>MST</b>	Multiple-scattering theory
<b>ESCA</b>	Electron spectroscopy for chemical analysis	<b>MTS</b>	Mechanical threshold stress
<b>ESR</b>	Electron spin resonance	<b>NADH</b>	Nicotinamide adenine dinucleotide
<b>EXAFS</b>	Extended x-ray absorption fine structure	<b>NIR</b>	Normal-incidence reflectivity
<b>fcc</b>	Face-centered cubic	<b>NMR</b>	Nuclear magnetic resonance
<b>FCGR</b>	Fatigue crack growth rate		
<b>FTS</b>	Fourier transform spectrometer		
<b>FRS</b>	Forward-recoil spectroscopy		

<b>NQ</b>	Nitroguanidine	<b>STEM</b>	Scanning transmission electron microscopy
<b>NRA</b>	Nuclear reaction analysis	<b>STM</b>	Scanning tunneling microscope (microscopy)
<b>NLSL</b>	National Synchrotron Light Source	<b>STS</b>	Stockpile-to-target sequence
<b>OFE</b>	Oxygen-free electronic	<b>SXPL</b>	Soft x-ray projection lithography
<b>O-T</b>	Orthorhombic-tetragonal (phase transition)	<b>TA</b>	Transverse acoustic
<b>PA</b>	Performance assessment	<b>TATB</b>	1,3,5-triamino-2,4,6-trinitrobenzene
<b>PBX</b>	Plastic bonded explosive	<b>TEA</b>	Thermal energy analyzer
<b>PCP</b>	Phencyclidine	<b>TEGDN</b>	Trimethyleneglycol dinitrate
<b>PES</b>	Photo-electron spectroscopy	<b>TEM</b>	Transmission electron microscope (microscopy)
<b>PETN</b>	Pentaerythritol tetranitrate (an explosive)	<b>TEOS</b>	Tetraethoxysilane
<b>PIXE</b>	Particle-induced x-ray emission	<b>TIC</b>	Total ion chromatogram
<b>pMMO</b>	Particulate form of methane monooxygenase	<b>TMD</b>	Theoretical maximum density
<b>PVD</b>	Physical vapor deposition	<b>TMETN</b>	Trimethylol ethane trinitrate
<b>RBS</b>	Rutherford backscattering	<b>TMOS</b>	Tetramethoxysilane
<b>RCA</b>	Rotating cylinder anode	<b>TNT</b>	Trinitrotoluene
<b>RDX</b>	Hexahydro-1,3,5-trinitro-1,3,5-triazine	<b>TOF</b>	Time of flight
<b>REELS</b>	Reflection electron energy loss spectroscopy	<b>TONE</b>	Brand name of Union Carbide Corporation
<b>RPR</b>	Reaction propagation rate	<b>Tris</b>	Tris(hydroxymethyl)aminomethane
<b>RSMST</b>	Real scattering multiple scattering theory	<b>TR-XRD</b>	Time-resolved x-ray diffraction
<b>SAD</b>	Selected area diffraction	<b>UCB</b>	The University of California at Berkeley
<b>SAED</b>	Selected-area electron diffraction	<b>UCD</b>	The University of California at Davis
<b>SAXS</b>	Small-angle x-ray spectroscopy	<b>UHV</b>	Ultrahigh vacuum
<b>SCC</b>	Stress corrosion cracking	<b>UPS</b>	Ultraviolet photoelectron spectroscopy
<b>SCE</b>	Saturated calomel electrode	<b>UV</b>	Ultraviolet
<b>SDS-PAGE</b>	Sodium dodecyl sulfate polyacrylamide gel electrophoresis	<b>UV/VIS</b>	Ultraviolet/visible spectrum
<b>SEM</b>	Scanning electron microscopy	<b>VBM</b>	Valence band maximum
<b>SIP</b>	Semi-infinite periodicity	<b>XPS</b>	X-ray photoelectron spectroscopy
<b>sMMO</b>	Soluble form of methane monooxygenase	<b>XRCA</b>	X-ray crystallographic analysis
<b>SHPB</b>	Split Hopkinson pressure bar	<b>XRMF</b>	X-ray microfluorescence
<b>SPM</b>	Scanning probe microscopy	<b>XTM</b>	X-ray tomographic microscopy
<b>SRO</b>	Short-range order	<b>YBCO</b>	YBa <sub>2</sub> Cu <sub>3</sub> O <sub>7-x</sub> (sometimes subscript <i>x</i> is a <i>y</i> or <i>δ</i> )

**END**

**DATE  
FILMED**

**11 / 20 / 92**

